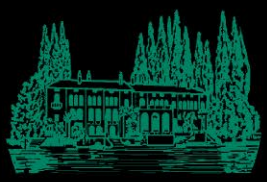

PROCEEDINGS
INTERNATIONAL SCHOOL OF PHYSICS «ENRICO FERMI»

COURSE 201

Nuclear Physics with Stable and Radioactive Ion Beams

edited by F. Gramegna, P. Van Duppen, A. Vitturi and S. Pirrone

14 - 19 July 2017

Villa Monastero
Varenna, Lake Como

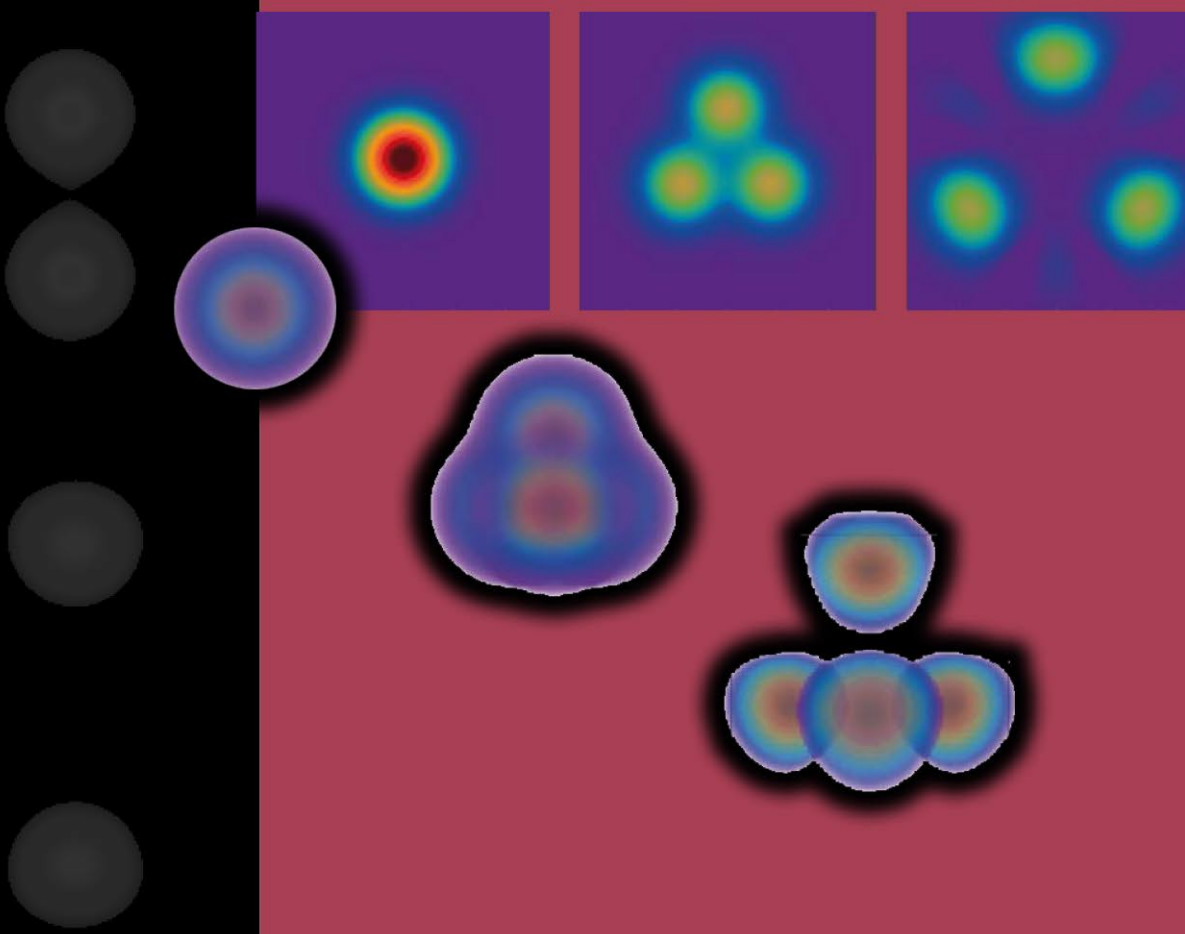

SOCIETÀ ITALIANA DI FISICA

SOCIETÀ ITALIANA DI FISICA

RENDICONTI

DELLA

SCUOLA INTERNAZIONALE DI FISICA

"ENRICO FERMI"

CCI Corso

a cura di F. Gramegna, P. Van Duppen e A. Vitturi

Direttori del Corso

e di

S. Pirrone

VARENNA SUL LAGO DI COMO

VILLA MONASTERO

14 – 19 Luglio 2017

Fisica nucleare con fasci di ioni stabili e radioattivi

2019

SOCIETÀ ITALIANA DI FISICA
BOLOGNA-ITALY

ITALIAN PHYSICAL SOCIETY

PROCEEDINGS

OF THE

INTERNATIONAL SCHOOL OF PHYSICS

"ENRICO FERMI"

Course 201

edited by F. Gramegna, P. Van Duppen and A. Vitturi

Directors of the Course

and

S. Pirrone

VARENNA ON LAKE COMO

VILLA MONASTERO

14 – 19 July 2017

Nuclear Physics with Stable and Radioactive Ion Beams

2019

IOS Press

AMSTERDAM, OXFORD, TOKIO, WASHINGTON DC

ISSN 0074-784X (print)
ISSN 1879-8195 (online)

ISBN 978-1-61499-956-0 (print) (IOS Press)
ISBN 978-1-61499-957-7 (online) (IOS Press)
ISBN 978-88-7438-117-3 (SIF)

LCCN 2019934680

jointly published and distributed by:

IOS PRESS
Nieuwe Hemweg 6B
1013 BG Amsterdam
The Netherlands
fax: +31 20 687 0019
info@iospress.nl

SOCIETÀ ITALIANA DI FISICA
Via Saragozza 12
40123 Bologna
Italy
fax: +39 051 581340
order@sif.it

Distributor in the USA and Canada
IOS Press, Inc.
4502 Rachael Manor Drive
Fairfax, VA 22032
USA
fax: +1 703 323 3668
sales@iospress.com

Supported by

Camera di Commercio di Lecco

Istituto Nazionale di Fisica Nucleare (INFN)

Istituto Nazionale di Geofisica e Vulcanologia (INGV)

Univerlecco

Museo Storico della Fisica e Centro Studi e Ricerche “Enrico Fermi”

Istituto Nazionale di Ricerca Metrologica (INRiM)

Università di Roma Tor Vergata

Gran Sasso Science Institute (GSSI)

Produced by the SIF Editorial Staff

Production Editor: Marcella Missiroli

Cover: see F. Iachello, *Algebraic models of quantum many-body systems: The algebraic cluster model*, p. 31.

Cover figure reproduced with permission from V. Della Rocca, R. Bijker and F. Iachello, "Single-particle levels in cluster potentials", *Nucl. Phys. A*, **966** (2017) 158, © Elsevier (2017).

Graphic elaboration by Simona Oleandri

Printed in Italy by nuova MONOGRAF snc - Bologna

CONTENTS

The electronic version of volumes from 124 to 198 is available online at the IOS Press web site

http://ebooks.iospress.nl/bookseries/proceedings-of-the-international-school-of-physics-enrico-fermi

Figures with colour source files will appear in colour in the online version.

SIF Members are granted free access to these volumes at
https://members.sif.it

For a complete list of published courses see
https://en.sif.it/books/series/proceedings_fermi

Preface

The 201st International School of Physics "Enrico Fermi" addressed the fundamental features associated with the study of nuclear systems far from the valley of stability. Studies performed with stable beams and with radioactive ion beams produced at first generation facilities hint to a number of new insight in the way nuclei are built from their constituents. By studying the properties of the so-called exotic nuclei that possess an unbalanced number of protons to number of neutrons ratio, hidden aspects of the strong and weak force acting in the nuclear medium can be uncovered.

The field of radioactive ion beam research has evolved over the last three decades and several medium and large size facilities are currently undergoing a major upgrade or are under construction. In Europe, these include ISOLDE - CERN (Switzerland), SPIRAL2 - GANIL (France), FAIR - GSI (Germany) and SPES (Italy) while RIBF - RIKEN (Japan), TRIUMF (Canada) and FRIB - MSU (USA) are the major undertakings elsewhere. These facilities will create unprecedented opportunities to extend our knowledge in so far unexplored regions of the nuclear chart and to address key questions in nuclear physics, fundamental interactions and astrophysics, but also link to other fields of science including life science.

The lectures and seminars of the school focused on the structural and dynamical aspects from both a theoretical and experimental point of view. Recent advances in theoretical and experimental approaches were discussed. The former included advanced shell-model, density functional applications, and symmetry-based methods as well as cluster and reaction models. The latter dealt with state-of-the-art experimental themes covering reaction, decay and laser spectroscopy studies and Coulomb excitation experiments. On the occasion of the 90th birthday of Professor R.A. Ricci, a dedicated session was organized including a number of topical seminars. During this session, the pioneer work of Prof. Ricci in nuclear structure was recalled, together with his important contribution in the evolution of nuclear physics in Italy. He was especially one of the founders of heavy-ion-induced reaction studies in Italy devoted to deepen the knowledge on nuclear structure and dynamics coordinating the efforts at the Legnaro National Laboratory for the advent of the Tandem XTU in the 80's and suggesting the development and installation of the LINAC ALPI in the 90's.

The organization of the school with participants from ten different countries was a success thanks to the excellent lecturers and seminar speakers and to the highly appreciated work of the school's administrative staff. The directors would like to express on behalf of all participants their sincere gratitude.

F. Gramegna, P. Van Duppen, A. Vitturi and S. Pirrone

Italian Physical Society
INTERNATIONAL SCHOOL OF PHYSICS «E. FERMI»
COURSE 201
14 - 19 July 2017
VILLA MONASTERO − VARENNA, LAKE COMO

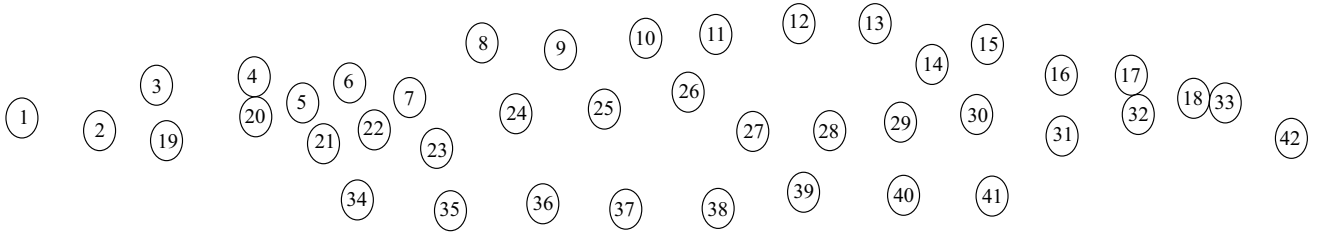

1) Ramona Brigatti
2) Barbara Alzani
3) Brunilde Gnoffo
4) Denise Piatti
5) Diego Gruyer
6) Magda Cicerchia
7) Riccardo Raabe
8) Silvia Vignals i Onses
9) Elena Santopinto
10) Asli Kusoglu
11) Pietro Ottanelli
12) Federico Pinna
13) Salvatore Calabrese
14) Nunzia Martorana
15) Giuseppe Pastore
16) Alberto Camaiani
17) Oleskii Poleshchuk
18) Marek Stryjczyk
19) Fabiana Gramegna
20) Gianluca Colò
21) Yoshiko Kanada-En'yo
22) Giorgia Mantovani
23) Elena Fumagalli
24) Vira Bondar
25) Petra Colovic
26) Simone Perrotta
27) Giovanna Benzoni
28) Silvia Lenzi
29) Jiecheng Yang
30) Andrea Vitturi
31) Korneliya Spasova Yordanova
32) Sara Pirrone
33) Kushal Kapoor
34) Piet Van Duppen
35) Wilfried Nörtershäuser
36) Takaharu Otsuka
37) Francesco Iachello
38) Renato Angelo Ricci
39) Luciano Moretto
40) Antonio Moro
41) Wolfram Korten
42) Angelo Pagano

This page intentionally left blank

Proceedings of the International School of Physics "Enrico Fermi"
Course 201 "Nuclear Physics with Stable and Radioactive Ion Beams", edited by F. Gramegna,
P. Van Duppen, A. Vitturi and S. Pirrone
(IOS, Amsterdam; SIF, Bologna) 2019
DOI 10.3254/978-1-61499-957-7-1

Recent developments in shell model studies of atomic nuclei

T. Otsuka

Department of Physics and Center for Nuclear Study, University of Tokyo
Hongo, Bunkyo-ku, Tokyo 113-0033, Japan

RIKEN Nishina Center - 2-1 Hirosawa, Wako, Saitama 351-0198, Japan

Instituut voor Kern- en Stralingsfysica, Katholieke Universiteit Leuven
B-3001 Leuven, Belgium

National Superconducting Cyclotron Laboratory and Department of Physics and Astronomy
Michigan State University - East Lansing, Michigan 48824, USA

Summary. — An introduction and recent developments in the nuclear shell model are presented. The basic concepts are explained starting from the work of Mayer and Jensen. The conventional and Monte Carlo Shell Model are illustrated in a pedagogical way. Some important points of the Monte Carlo Shell Model are explained to some details. The monopole interaction and the shell evolution are discussed. The shape evolutions are also discussed with Type-II shell evolution. Finally the quantum self-organization is presented.

1. – Introduction

The atomic nucleus is composed of Z protons and N neutrons in a compact volume isolated in the vacuum. It determines its own quantum many-body structure by itself. In this sense, the atomic nucleus is a rather unique quantal object. I present, in this lecture,

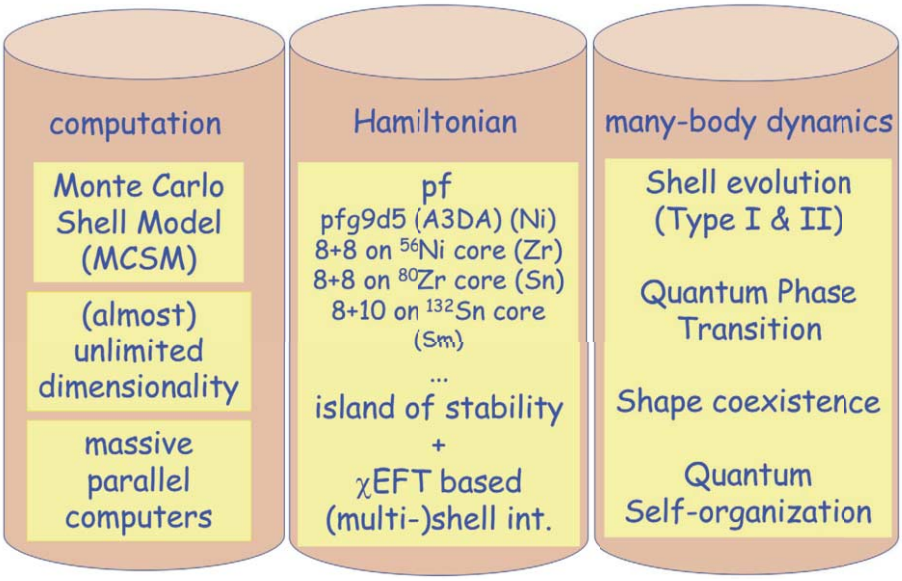

Fig. 1. – Three pillars for nuclear structure studies.

recent developments and expected further developments of the nuclear shell model, which is one of the general frameworks to describe such quantal structure.

2. – Basic points of the shell model

The lecture is formed by three pillars as shown in fig. 1. Let me start with a brief introduction of these pillars. The first pillar is computational. For the current shell model achievement, this primarily means the Monte Carlo Shell Model (MCSM). The MCSM can be characterized by almost unlimited dimensionality, and its applicability is enhanced enormously by the advances in massive parallel computers. Thus, we are in the right moment for a rapid growth of the shell model calculations. I shall explain these points.

The second pillar is the Hamiltonian. The shell model Hamiltonian has been set up for challenging regions on the nuclear chart: the A3DA (or A3DA-m) interaction has been successfully applied to the model space comprised of the full pf shell + the $g9/2$ orbit + the $d5/2$ orbit. This model space is too big for the conventional shell model calculation. I shall touch on some properties of Ni isotopes. The MCSM has been advanced to heavier nuclei. The second example is the MCSM calculations on Zr isotopes, and the third one is on Sm isotopes. In parallel to such developments, the nuclear forces have been treated in recent years in a more *ab initio* way. I discussed, in my lecture, some topics on the island of inversion, based on the EKK method for deriving the effective nucleon-nucleon (NN) interaction on nuclei but will skip this discussion in this lecture note.

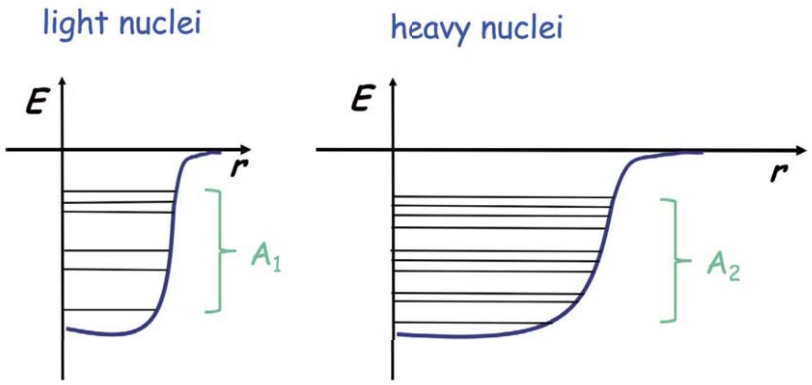

Fig. 2. – Schematic illustration of the mean potential for (left) light, A_1 small, and (right) heavy, A_2 large, nuclei.

The third pillar refers to recent conceptual advances such as Type-I and -II shell evolutions, quantum phase transition, some new aspects in shape coexistence and quantum self-organization. We shall see how these concepts and aspects appear in the shell model, and how they are related to various nuclear properties. We thus try to include most recent developments from the shell model viewpoint, highlighting some intriguing points.

We start with the picture that nucleons forming the atomic nucleus are moving in a mean potential, which is generated by those nucleons themselves. This picture has to be reasonable, because the nucleus exists as an isolated quantum many-body system, and the combination of the density saturation and the short-range strong attraction leads us to a potential like those shown in fig. 2. In other words, the depth of the potential should be almost constant in the inner part of the nucleus, because the density is nearly constant there and hence the number of nucleons within the range of the nuclear forces is also almost constant. This constancy does not hold near the surface as the density becomes lower. The potential becomes shallower around the nuclear surface, and vanishes quickly outside the nucleus due to the short-range character of the nuclear forces.

Because the nucleon density inside the nucleus is constant (as is referred to as the density saturation), the potential depth inside the nucleus is basically independent of the nucleus. On the other hand, as a function of the mass number, A $(= Z + N)$, the nuclear radius increases in proportion to $A^{-1/3}$ consistent with the density saturation. This increase of the radius results in another increase of the radius of the potential as shown in fig. 2, and the potential with a larger radius can hold more nucleons within the same energy range, as shown in fig. 2. In fact, the mean potentials with the same depth can hold A nucleons because of the varying potential radius.

The mean potential depends on the radius, r, from the center of the nucleus (see fig. 2). This r dependence is similar to that of the Harmonic Oscillator potential, inside

the nuclear surface. It is then expected that various properties, including single-particle wave functions, in fig. 2 can be replaced, in a rather good approximation, by those of the Harmonic Oscillator potential. The 3-dimensional Harmonic Oscillator potential gives the well-known pattern of its energy eigenvalues characterized by $(N+3/2)\hbar\omega$, where N denotes the Harmonic Oscillator quanta. This N has the same character as the one for the neutron number, but it is usually assumed that no confusion occurs because of completely different meanings. Such properties of single-particle states can be represented as "shell structure", where shell structure means the grouping of the eigenenergies of the single-particle states. The 3-dimensional Harmonic Oscillator potential produces degenerate single-particle states and the constant gap of $\hbar\omega$ between neighboring groups. This explains the shell structure of some light nuclei, but there are other properties which cannot be accounted for.

Mayer [1] and Jensen [2] introduced the spin-orbit splitting in addition to the Harmonic Oscillator potential, and have succeeded in describing the observed shell structure, leading to the *shell model (SM)* as an *independent-particle model (IPM)* [3]. Due to the spin-orbit splitting and another minor correction, the final shell structure is modified from that of the Harmonic Oscillator potential. The single-particle orbits are grouped into *shells*. The standard shell structure has thus been established in 1949, as described also in many textbooks, for instance, [4-6].

Although the Mayer-Jensen's independent-particle model explains many properties including magic numbers, the nuclear structure cannot be described, in general, only by the single-particle motion in the mean potential. We shall consider cases with Z and N differing from their magic numbers. Figure 3 represents such cases. In fig. 3, single-particle orbits in proton and neutron mean potentials are shown by horizontal bars, and protons and neutrons shown by circles can occupy those orbits. Each single-particle orbit has total angular momentum $\vec{j}$ with magnitude j, where $\vec{j}=\vec{\ell}+\vec{s}$, with $\vec{\ell}$ ($\vec{s}$) being the orbital (spin) angular momentum. Each j orbit has magnetic substates depicted by the z-component of $\vec{j}$, denoted by $j_z=-j,-j+1,\ldots,j-1,j$. Such (magnetic sub-) states are referred to as *single-particle states* hereafter. Because of the rotational invariance of the Hamiltonian, the single-particle states belonging to the orbit j have the same *single-particle energy (SPE)*, ϵ_j, and the j orbit has the degeneracy of $(2j+1)$. In fig. 3, some circles are on the same bar, reflecting this property. Single-particle orbits are grouped, forming shells. The energy gap between neighboring shells is called *shell gap* or *magic gap*.

In fig. 3, several lowest single-particle orbits are shaded. These single-particle orbits are completely occupied. Lowest shells which are completely occupied are called collectively *closed shells* (or sometimes *inert core*). The shaded parts in fig. 3 are indeed closed shells for protons and neutrons. The total number of protons (neutrons) in a closed shell is called *magic number*. The scheme introduced by Mayer and Jensen thus provides the shell structure and resulting magic numbers. The actual values of such magic numbers are $2,8,20,28,50,82,126,\ldots$, the first three of which are the same as the magic numbers given by the pure Harmonic Oscillator potential. The nucleus with Z or N equal to one of the magic numbers is called a *(single-)closed* or *(semi-)magic* nucleus. If both Z and

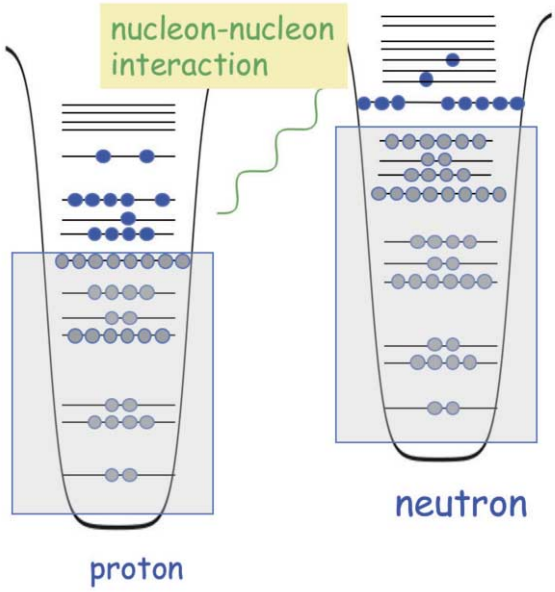

Fig. 3. – Schematic illustration of the shell structure of proton-neutron open shell nucleus.

N are magic numbers, the nucleus is called *doubly magic*. The spin/parity of the closed shell is $J^P = 0^+$. This is because no nucleon can change its magnetic substate, meaning that the z-component of its angular momentum cannot be raised or lowered, *i.e.*, being zero. The completely occupied orbit should have an even number of nucleons, making its parity even. Thus, any closed shell has $J^P = 0^+$, which is the same as a vacuum, and the degrees of freedom of the closed shell are completely frozen in the shell model calculation unless otherwise stated.

The nucleus shown in fig. 3 is not a magic nucleus. In fact, neither Z nor N is equal to one of the magic numbers. Such nuclei are called *open-shell nuclei* in contrast to *closed-shell nuclei* mentioned just above. Single-particle orbits on top of the shaded part, which is a closed shell, are only partly occupied. Such single-particle orbits are called *valence orbits*, and the shell containing a valence orbit is referred to as *valence shell*. Nucleons in the valence shell are called *valence protons* or *valence neutrons*.

There is a distinct difference between the nucleon in the closed shell and the nucleon in the valence shell. The former cannot move within the closed shell because the shell is fully packed, whereas the latter can move from a state (one of the magnetic substates of an orbit) to another because there are vacancies. At present, we do not consider the cases where nucleons in the closed shell are excited to valence shells.

Suppose that two valence nucleons are in the states m_1 and m_2, which belong to the orbits j_1 and j_2, respectively. The valence nucleons can move to other states, if they are vacant. This occurs by the nuclear forces acting on these nucleons. In other words, these

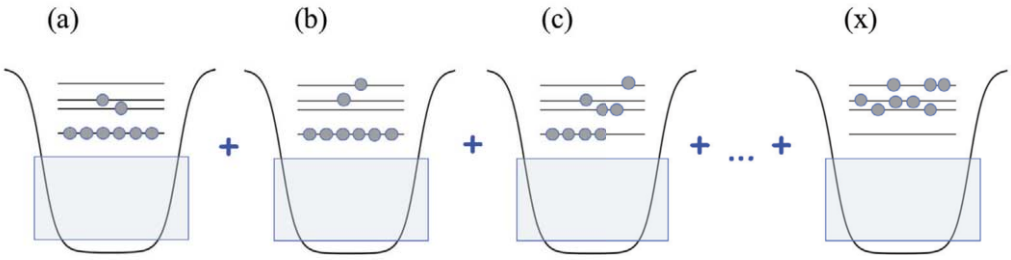

Fig. 4. – Schematic illustration of occupancies of valence protons (or neutrons).

two nucleons interact with each other through the nuclear forces in general. This process can be viewed as a collision of these two nucleons. After this interaction (or collision), the two nucleons can be in some states different from those before the collision. Figure 4 shows that valence nucleons can change their states, for instance, the top two nucleons in panel (a) can be moved to other states shown in panel (b). The panel (x) displays an occupation pattern which completes all the possibilities. The wave function of the nucleus is expressed by a superposition of such states. The pattern of the occupation is called *configuration*. Various configurations can be mixed in an eigenstate producing additional binding energy. This is very important as we shall see. Such additional energy is often called *correlation energy*. The word *correlation* is often used in the SM discussions, meaning some effects or phenomena beyond simple independent-particle picture.

The nuclear forces causing this superposition are called *(effective) nucleon-nucleon interactions* as seen in fig. 3. The word "effective" is placed occasionally in front of "nucleon-nucleon interaction", so as to emphasize that this interaction not only contains effects of nuclear forces for the scattering of free nucleons, but also includes various modifications for the description of the motion of nucleons in a nucleus, for instance, some medium corrections. Sometimes, these forces or interactions are called *"residual" interaction* or *force*, in the sense that they are residual in comparison to the mean potential; the mean potential implies the major thing and the residual force serves as a kind of minor additional factor. However, this does not represent the full physics contents, and this nomenclature may cause an inadequate impression. It will not be used in this lecture, whereas one may encounter it in the literatures or talks. Anyway, it may be stated that *"the residual interaction, though may not be minor at all, causes various correlations beyond simple structures, and the shell model treats it as it is."*

We now come to concrete processes of the shell model. As mentioned above, we concentrate on the valence shells and handle only valence nucleons. Their Hamiltonian is written in general as

$$H = \sum_i \epsilon_i \, n_i + \frac{1}{4} \sum_{i,j,k,l} v_{i,j,k,l} a_i^\dagger \, a_j^\dagger \, a_l \, a_k, \tag{1}$$

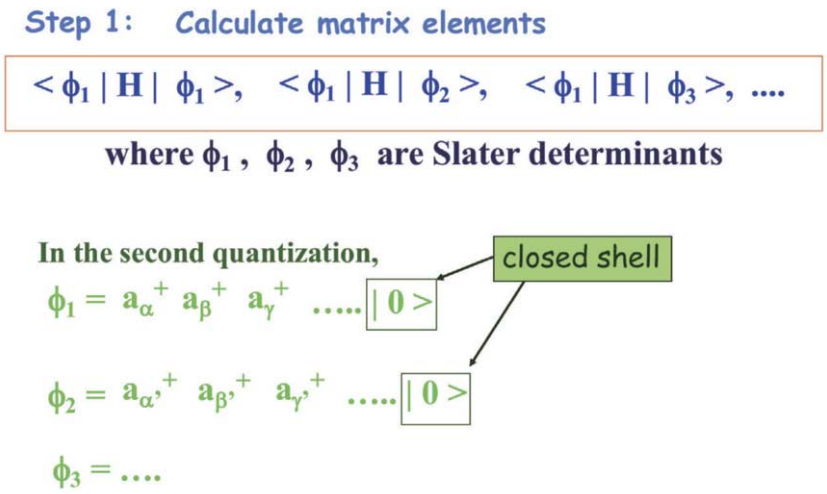

Fig. 5. – Step 1 of the shell model calculation. Slater determinants $\phi_1, \phi_2, \phi_3, \ldots$ are constructed from single-particle states $\alpha, \beta, \gamma, \ldots$, $\alpha', \beta', \gamma', \ldots$, which are magnetic substates of valence orbits. Matrix elements of the Hamiltonian, H, are calculated with respect to those Slater determinants.

where the subscripts i, j, k, l denote magnetic substates of single-particle valence orbits, the summation runs over all possible states, n_i is the number operator of the state i, $v_{i,j,k,l}$ means antisymmetrized two-body matrix element of the nuclear forces being considered, and $a^\dagger$ and a are nucleon creation and annihilation operators, respectively.

The valence nucleons occupy some single-particle states in the valence shells. Their number is fixed. In step 1 of the shell model calculation, we prepare all Slater determinants of the valence nucleons. One can do this for protons and neutrons separately, and take all their possible direct products. This process is displayed in fig. 5, where $\phi_1, \phi_2, \phi_3, \ldots$ stand for such Slater determinants. There, the subscript $\alpha, \beta, \gamma, \ldots$, $\alpha', \beta', \gamma', \ldots$, denote single-particle states (*i.e.*, magnetic substates of valence orbits). As shown in the figure, $|0\rangle$ means the relevant closed shell. Once Slater determinants are prepared, as shown in fig. 5, we calculate matrix elements of the Hamiltonian H in eq. (1) with respect to these Slater determinants: $\langle\phi_1|H|\phi_1\rangle, \langle\phi_1|H|\phi_2\rangle, \ldots$, $\langle\phi_2|H|\phi_2\rangle, \langle\phi_2|H|\phi_3\rangle, \ldots$. Note that, because of the hermiticity of the Hamiltonian, we can utilize the relation $\langle\phi_i|H|\phi_j\rangle = \langle\phi_j|H|\phi_i\rangle^*$, where the symbol * refers to the complex conjugate. Once all calculations of this step 1 are carried out, the matrix of the Hamiltonian, H, is completed, as illustrated as step 2 in fig. 6.

The Schrödinger equation of the many-body system is

$$H\Psi = E\Psi, \tag{2}$$

where Ψ is the eigenstate and E stands for the energy eigenvalue. In the SM, the wave

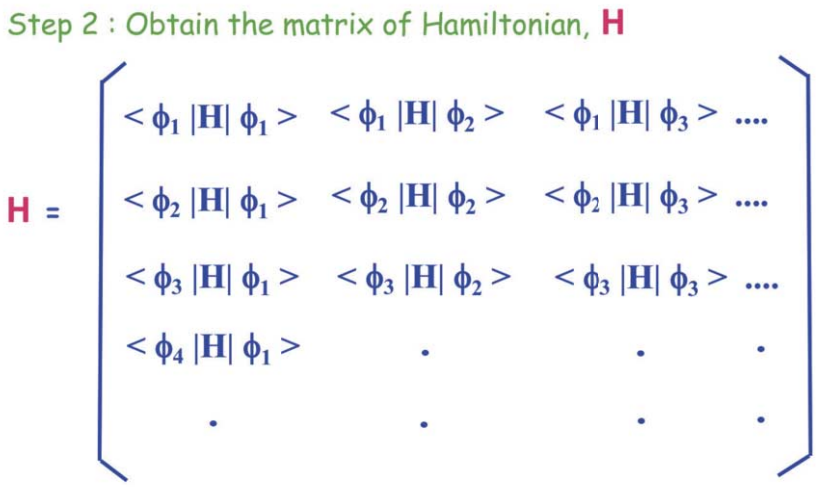

Fig. 6. – Step 2 of the shell model calculation. The Hamiltonian matrix is completed.

function of the eigenstate Ψ is represented in the form of a superposition of the Slater determinants, $\phi_1, \phi_2, \phi_3, \ldots$,

$$\Psi = c_1\,\phi_1 + c_2\,\phi_2 + c_3\,\phi_3 + \ldots, \tag{3}$$

with $c_1, c_2, c_3, \ldots$ being probability amplitudes. The eigenvalue and the eigenvector are determined by the diagonalization of the Hamiltonian matrix as shown in fig. 7. The complete set of the many-body basis vectors must be taken, and this can be achieved by taking all possible Slater determinants for the given valence shell and valence nucleons.

After the Hamiltonian matrix in eq. (6) is diagonalized as step 3, we have the energy eigenvalue, E, and its eigenvectors $(c_1, c_2, c_3, \ldots)$, with c_i being nothing but the probability amplitude of the i-th Slater determinant. For the diagonalization, the Lanczos method is used in most cases, as it is suitable for large matrices [7]. By using this representation of the eigenstate Ψ, one can calculate many physical observables and analyze various properties of the eigenstate Ψ, for instance the occupation numbers of the individual orbit j. As an example, see the review article [7]. We note that the SM calculation is quite similar to the configuration interaction (CI) calculation in other fields of science.

The processes presented so far are indeed carried out in conventional shell model calculations. Its summary is shown in fig. 8. The dimension of the eigenvector, *i.e.*, that of the Hilbert space, is called the *SM dimension*. The valence shell taken for such SM calculation is often called *model space*. The SM dimension is nothing but the dimension of the model space. This model space dimension is the major factor to determine the difficulty of the SM calculation from the computational point of view. By combining the progress in the algorithm and coding of the SM calculation with the development

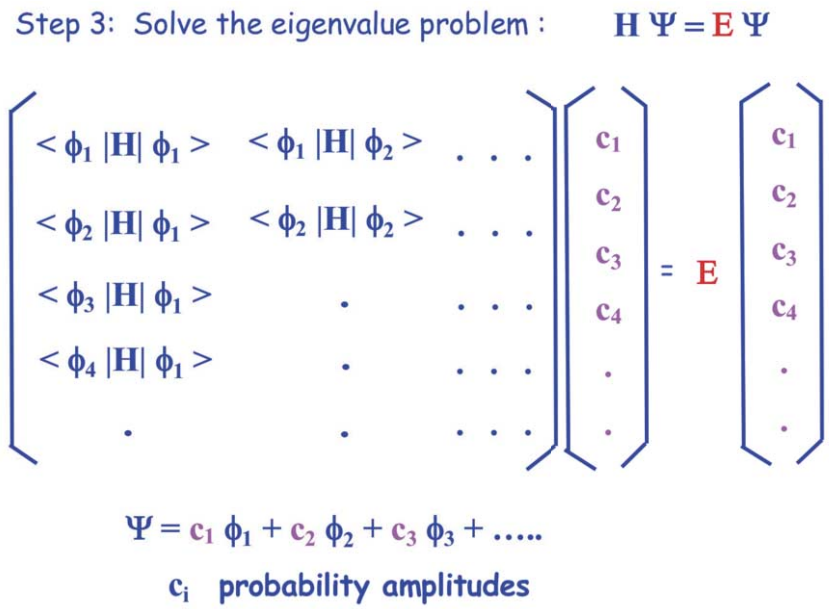

Fig. 7. – Step 3 of the shell model calculation. The Hamiltonian matrix is diagonalized with its eigenvalue E and eigenvector Ψ.

of the computers, the maximum tractable dimension has been enormously enlarged. As of today, this is a few times 10^{10}, *i.e.*, a few tens of billions. By utilizing the most advanced computer codes such as NuShell (OXBASH) [8], ANTOINE/NATHAN [9], KSHELL/MSHELL64 [10], MFDn [11], BIGSTICK [12], etc., SM calculations with huge SM dimensions are being carried out for a variety of subjects of nuclear physics.

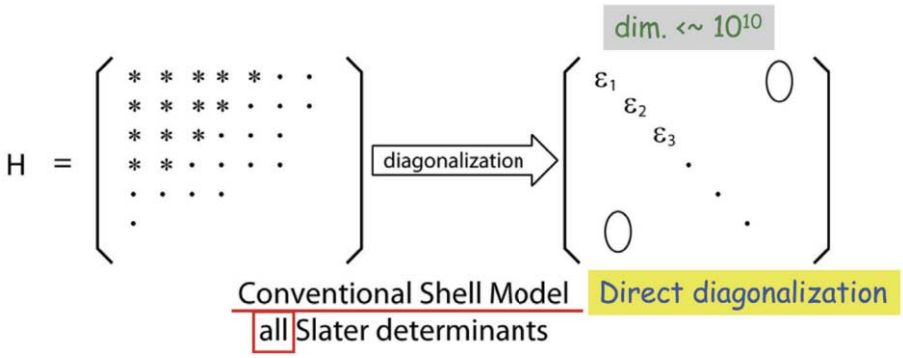

Fig. 8. – Conventional shell model calculation. The eigenvalues are obtained form the Hamiltonian matrix.

There is a number of interesting and/or important physics problems beyond the upper limit of the SM dimension, however. This is particularly crucial for heavy nuclei with many valence orbits and valence nucleons. The SM dimension becomes larger also if one studies exotic nuclei, because the conventional shell structure discussed so far is broken and some orbits in the conventional closed shell become valence orbits, as we shall see later. Thus, another methodology of the SM calculation is needed. The Monte Carlo shell model calculation has been introduced as a key method in this direction, and we shall move on to it now.

3. – Computational aspect—Monte Carlo Shell Model

After having a quick overview of the basic features of the SM studies, I would like to come to one of the three pillars in fig. 1, a computational frontline by the Monte Carlo Shell Model (MCSM) [13, 14]. The MCSM is a recent method to obtain eigensolutions of the SM calculation. In conventional shell model calculations, the matrix of the Hamiltonian with respect to many Slater determinants is diagonalized. As stated in the previous section, the SM dimension, *i.e.*, the number of the Slater determinants, can be enormous, making the calculation unfeasible. On the other hand, many interesting and important problems lie beyond this limit. The MCSM provides a breakthrough in this regard. The MCSM is very different from the conventional shell model calculation. A set of Slater determinants, called MCSM basis vectors, is introduced, and the diagonalization is performed in the Hilbert subspace spanned by the MCSM basis vectors. Practically speaking, the number of the MCSM basis vectors is a few hundreds at most.

I shall describe the MCSM procedure in some detail now. By the SM calculation, as stated above, we obtain the eigensolution of the many-body Schrödinger equation. In the MCSM, its solution, which is supposed to be a good approximation to the exact eigenstate, is expressed as

$$|\Psi(\mathbf{D})\rangle = \sum_{n=1}^{N_B} c_n \, P^{J^\pi} |\phi^{(n)}\rangle, \tag{4}$$

where P^{J^π} is the projection operator onto the spin-parity J^π of the eigenstate being considered, $|\phi^{(n)}\rangle$ denotes the n-th MCSM basis vector (a deformed Slater determinant as described below) with N_B and c_n implying, respectively, the number of such basis vectors and the probability amplitude. The state in eq. (4) will be referred to as MCSM eigenstate hereafter. Here, $\mathbf{D}$ stands for a set of matrices $D^{(n)}$ $(n = 1, 2, \ldots)$, the matrix elements of which appear in the Slater determinant expressed as the direct product,

$$|\phi^{(n)}\rangle = \prod_{\alpha=1}^{N_p} \left(\sum_{i=1}^{N_s} a_i^\dagger \, D_{i\alpha}^{(n)} \right) |0\rangle, \tag{5}$$

where N_p (N_s) is the number of valence particles (the number of single-particle states), $a_i^\dagger$ means the creation operator of the i-th original valence single-particle state, and $|0\rangle$

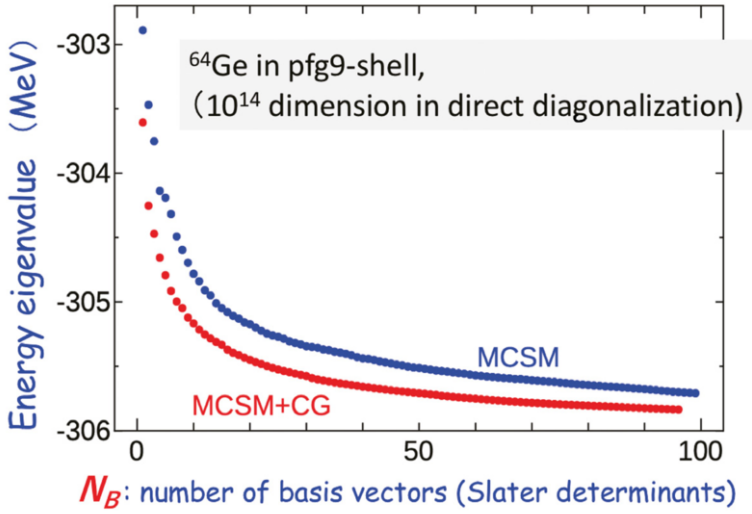

Fig. 9. – Energy eigenvalue as a function of the number of MCSM basis vectors. Two calculations are carried out: one with stochastic process only and the other stochastic + variational processes.

denotes the closed shell. In other words, $D^{(n)}_{i\alpha}$ are the amplitudes to expand the α-th deformed single-particle state (forming the Slater determinant) by the original single-particle states with index i, with respect to the n-th MCSM basis vector. The set of the matrices $\mathbf{D}$ are determined by combining stochastic, variational and diagonalization procedures [13, 14]. To be more precise, suppose that we have obtained already the first $(n-1)$ MCSM basis vectors, and that we are looking for the n-th MCSM basis vector, $|\phi^{(n)}\rangle$. We can generate many candidates by trying various $D^{(n)}$ by stochastic (or quantum Monte Carlo) ways. Once a good candidate is chosen from them, we can polish it by a variational way. In these processes, we always monitor the energy eigenvalue of the requested J^π obtained by the basis vectors $|\phi^{(1)}\rangle, |\phi^{(2)}\rangle, \ldots |\phi^{(n-1)}\rangle$ and the working candidate $|\phi^{(n)}\rangle$. Once we find the solution for the n-th candidate, we can move onto the $(n+1)$-th basis vector. As more basis vectors are determined, the energy eigenvalue goes down. Figure 9 depicts how this occurs with two types of MCSM calculations: one with the stochastic sampling and optimization only, and the other including the additional variational improvements. We see that the energy eigenvalue is lowered as more MCSM basis vectors are included. The MCSM concept is summarized in fig. 10. Even when the dimensions are in the order of 10^{23} [15] or more for the conventional shell model, the problem can be solved, to a good approximation, with up to approximately 100 MCSM basis vectors. I would like to point out that the procedures presented so far can be applied not only to the ground state but also to excited states in the same way.

On top of the procedure shown so far, we further perform the extrapolation of the energy eigenvalue by means of the energy variance [16], but we do not discuss it here as it is beyond the current scope.

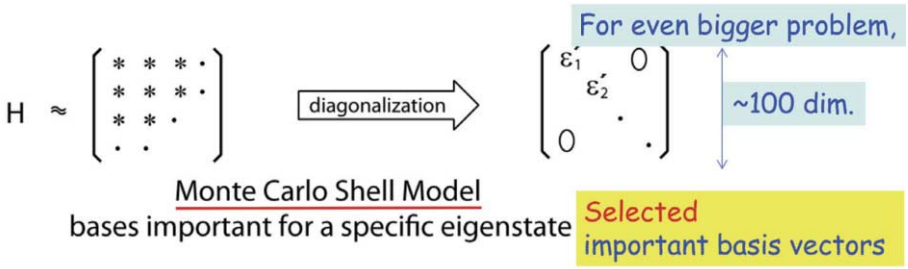

Fig. 10. – Monte Carlo shell model calculation. The eigenvalues are obtained from a much smaller Hamiltonian matrix than the one shown in fig. 8.

It may be useful to compare the conventional SM calculation and the MCSM calculation in their computational methods. The eigenstate is expanded in terms of the naive Slater determinants, composed from single-particle states given by the single-particle potential (for instance the Harmonic Oscillator), as shown in fig. 5. The diagonalization procedure gives us eigenstates with good J^P values by means of proper superposition of those Slater determinants. The number of these Slater determinants can become prohibitively large. The Slater determinant of the MCSM is very different. Each single-particle state is a superposition over all original single-particle states as shown in eq. (5). The amplitudes of this superposition are expressed by $D^{(n)}_{i\alpha}$ (see eq. (5)), and their values are

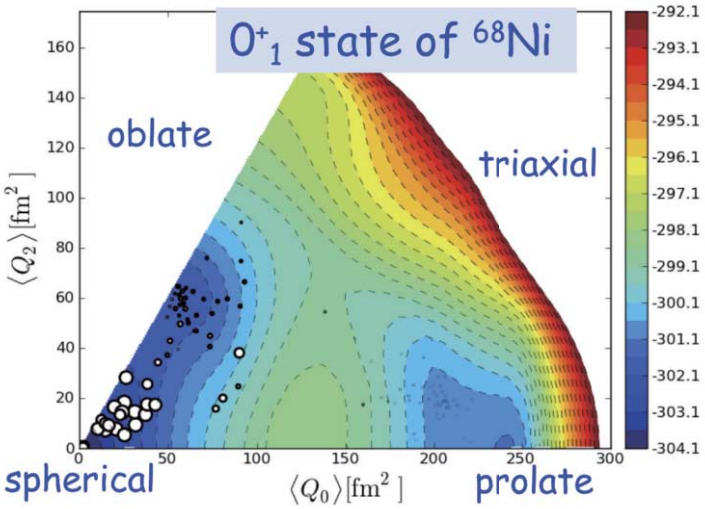

Fig. 11. – T-plot on the potential energy surface obtained from the same shell model Hamiltonian. The ground state of ^{68}Ni is taken.

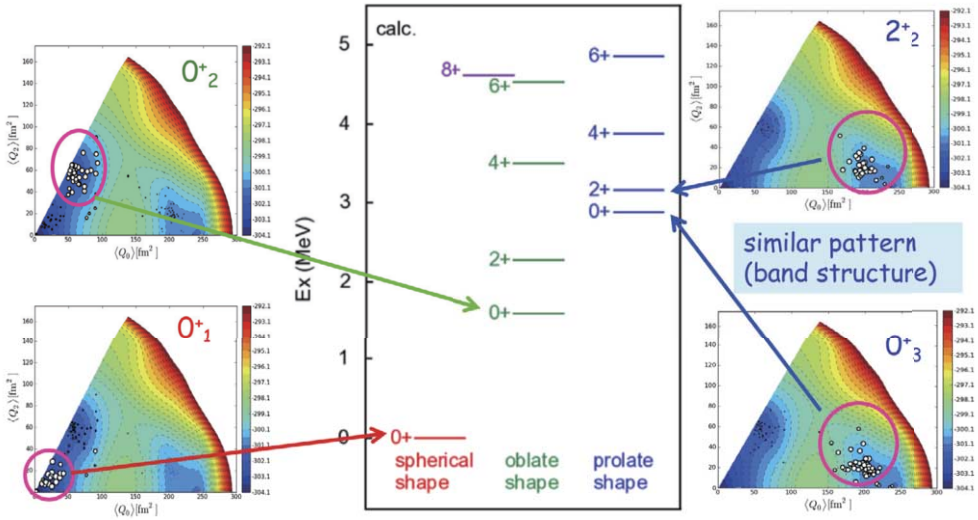

Fig. 12. – T-plot on the potential energy surface obtained from the same shell model Hamiltonian. Four low-lying states of ^{68}Ni are taken.

optimized so that we can describe the eigenstate with much smaller number of Slater determinants.

I introduce one of the useful outcomes of the MCSM calculations, the *T-plot* [17,18]. The MCSM eigenstate is expressed by the MCSM basis vectors as shown in eq. (4). As each MCSM basis vector is a deformed Slater determinant, one can calculate its intrinsic quadrupole moments by diagonalizing its quadrupole matrix. Such quadrupole property is expressed in terms of Q_0 and Q_2. In parallel, we can calculate the potential energy surface (PES) from the SM Hamiltonian used for the SM calculation. Figure 11 displays an example of T-plot for the ground state of ^{68}Ni, where the circles indicate pairs of Q_0 and Q_2 for individual MCSM basis vector, and the size (or area) presents their overlap probabilities with the eigenstate as an indicator of their importance. In this particular example, big circles are concentrated near the spherical limit, suggesting the spherical shape of the ground state of ^{68}Ni.

Figure 12 depicts the T-plot for the three lowest 0^+ states and the second 2^+ state. One can see very clearly that the $0^+_{1,2,3}$ states show spherical, oblate and prolate shapes, respectively. The 0^+_3 state and the 2^+_2 state are obtained independently, but exhibit a very similar T-plot. This suggests that these two states are in the same band. The T-plot produces many circles around the same shape. This is because the T-plot shows the shape of the MCSM basis vector, which is nothing but a Slater determinant. The pairing interaction mixes different Slater determinants, while it cannot change the shape too much. Thus, the concentration of the T-plot circles is quite natural. We are utilizing the T-plot to a great extent in the MCSM calculations.

4. – Hamiltonians

The second pillar in fig. 1 is Hamiltonians. The shell model Hamiltonian has been set up for challenging regions on the nuclear chart: the A3DA (or A3DA-m) interaction has been successfully applied to the model space comprised of the full pf shell + the $g9/2$ orbit + the $d5/2$ orbit [17]. This model space is too big for the conventional shell model calculation. Many MCSM calculations have been performed for Ni, Cu and other neighboring isotopes [19-25].

The MCSM has been advanced to heavier nuclei. The second example is the MCSM calculations on Zr and Sr isotopes [15, 26-28], and the third one is on Sm isotopes.

In parallel to such developments, the nuclear forces have been treated in recent years in a more *ab initio* way. I discussed, in my lecture, some topics on the island of inversion, based on the EKK method for deriving the effective nucleon-nucleon (NN) interaction on nuclei [29, 30].

I shall present some discussions on this subject in the next sections in relation to the emerging concept.

5. – Emerging concepts on many-body dynamics

The third pillar in fig. 1 is about many-body dynamics, including some new concepts and ideas. Obviously, the underlying mechanisms of the many-body structure of atomic nuclei have been studied over decades as one of the major objectives of nuclear physics. It has then been understood that there are two basic types of the motion of nucleons in the atomic nucleus: one is the single-particle motion and the other is collective motion. Regarding the single-particle states representing the single-particle motion, we have discussed them in sect. **2**, starting from Mayer and Jensen [1-3], with a general description of the shell structure and associated magic numbers. The nuclear shell model has been developed starting from the independent particle model (IPM) and has become a framework of solving the many-body problem of atomic nuclei (see sect. **2**). It has been shown to be extremely successful in the description of the structure of many nuclei. The interested reader can refer to textbooks, for example, [5] and/or [6], and review articles [7, 31]. Thus, the shell model presently stands for an approach to various correlations among valence nucleons rather than the single-particle motion. On the other hand, the single-particle states are the building blocks of shell model states as well as the effective NN interaction. There has been a significant progress in the properties of the single-particle states in exotic nuclei, particularly as a function of the neutron number (N) within the same isotopic chain. We shall discuss this point first.

6. – Shell evolution and monopole interaction

The magic numbers (corresponding to major closed shells) proposed with the independent particle model by Mayer and Jensen [1, 2] have been considered to be constants for all nuclei, taking the values $2, 8, 20, 28, 50, 82, 126, \ldots$. This paradigm of the magic-number constancy has been working very well for stable nuclei and their neighborhood,

but is being challenged for exotic nuclei. Here, exotic nuclei mean atomic nuclei with an unbalanced ratio N/Z with N (Z) being the neutron (proton) number, and have short half-lives due to this feature. In contrast, stable nuclei have a well-balanced ratio N/Z (from 1 for ^{4}He up to 1.5 for ^{208}Pb) and have infinite (or almost infinite) life times.

Although this shell structure is certainly a valid starting point in stable nuclei, as more neutrons are added within a given isotope chain, nuclei move to the right on the Segrè chart and enter the region of exotic nuclei. The shell structure may change, or *evolve*, as we shall show. This change is called *shell evolution* [32]. I shall start discussing the mechanism of this shell evolution.

The canonical (or standard) shell structure/magic numbers can be obtained basically using a harmonic oscillator potential and the spin-orbit splitting. This model already includes a good fraction of the nuclear forces, but may not incorporate other sizable effects.

6˙1. *Monopole interaction.* – We start with a single-particle valence orbit j with its single-particle energy, ϵ_j. In the case of one nucleon + core system, if this nucleon is on the orbit j, ϵ_j consists of the kinetic energy and the effects of nuclear forces from all nucleons in the core. In the case of a one nucleon outside a stable closed-shell nucleus, the ϵ_j are well described by the standard independent-particle picture. As the nucleus moves away from such a case with more neutrons (*i.e.*, neutron-rich exotic nuclei), ϵ_j will change in general. A smooth A ($= Z + N$) dependence arises, but the change is gradual and minor. The kinetic-energy part changes very gradually as a function of A, and is assumed, in this article, to remain unchanged within the region of interest on the Segrè chart [4]. The ϵ_j can change, however, due to nuclear forces, as N (or Z) changes.

We show how to evaluate or understand this change. To this purpose, we first introduce the monopole component of a general two-body interaction $\hat{v}$ [7, 31, 18, 33-35]. The monopole matrix element is defined as [31]

$$v_m(j,j') = \frac{\sum_{\mu,\mu'} \langle j,\mu,j',\mu'|\hat{v}|j,\mu,j',\mu'\rangle}{\sum_{\mu,\mu'} 1}\,, \tag{6}$$

with j and j' shorthand notation for (n,l,j) of the orbit, μ and μ' being their magnetic substates, respectively, and $\langle \ldots|\hat{v}|\ldots\rangle$ standing for the two-body matrix element. This expression is a general one, and $\hat{v}$ implies a general two-body interaction. The monopole matrix element is obtained, for a given pair of orbits j and j', as the average over all possible orientations of the two-particle states, $\mu \otimes \mu'$. The denominator in eq. (6) is the number of such two-particle states. This average property then becomes

$$v_m(j,j') = \frac{\sum_J (2J+1)\langle j,j';J|\hat{v}|j,j';J\rangle}{\sum_J (2J+1)}\,, \tag{7}$$

where J denotes the angular momentum resulting from the angular momenta of the two orbits, as $\vec{J} = \vec{j} + \vec{j'}$. The factor $(2J+1)$ is the degeneracy of the two-particle states having the same value of J. In the latter equation, some J values can be forbidden by

the antisymmetrization, but this is not the case if only the proton-neutron monopole interaction is considered. From the monopole matrix element, one can derive the monopole component, $\hat{v}_m$, of the interaction $\hat{v}$, which can be called the *monopole interaction*.

The monopole interaction we discuss in the present contribution is limited, almost exclusively, to the one between a proton and a neutron, for the sake of clarity. We then obtain

$$\hat{v}_m = \sum_{j,j'} v_m(j,j')\,\hat{n}_j\,\hat{n}_{j'}, \tag{8}$$

where the orbit j refers to a proton and j' to a neutron, or vice versa. The (total) monopole interaction, consisting of not only this proton-neutron interaction but also the proton-proton and the neutron-neutron interactions, is an important part of the original interaction $\hat{v}$. The remaining part is called the *multipole interaction*, in order to distinguish it from the monopole interaction. The multipole interaction is often expressed as $\hat{v}_M$, and it includes in particular the quadrupole interaction.

6˙2. *Effect of monopole interaction.* – The most important effect of the monopole interaction is the change of the single-particle energy of the orbit j due to the occupancy of the orbit j'. Such a shifted SPE is called, in general, effective SPE (*ESPE*). By calculating the expectation value of the operator $\hat{n}_{j'}$ with respect to a many-body reference state, the induced change of ESPE is given by

$$\Delta\epsilon_j = v_m(j,j')n_{j'}, \tag{9}$$

where $n_{j'}$ stands for the expectation value $n_{j'} = \langle\hat{n}_{j'}\rangle$. This equation means that the single-particle energy of the orbit j is changed effectively in proportion to $n_{j'}$. This relation leads to a very amusing feature: the effects of the multipole interaction vanish if the shell (or orbit) j' is completely filled, whereas the effect of the monopole interaction not only remains finite but also maximal.

An interesting issue is related to the appearance pattern of major effects of the monopole interaction, with changing the nuclear forces. As an extreme case, if $\hat{v}$ is isotropic with infinite range, $v_m(j,j')$ does not depends on j or j', being a constant. If $\hat{v}$ is an attractive force, $v_m(j,j')$ takes a constant negative value. This implies that if more neutrons occupy the orbit j', all proton orbits j become more bound to the same extent. In other words, the proton shell is conserved but becomes more deeply bound.

On the other hand, if $\hat{v}$ is given by a δ-function with a strength parameter, $v_m(j,j')$ becomes sensitive to the overlap between the wave functions of the orbit j and that of the orbit j'. This implies that if more neutrons occupy the orbit j', proton orbits, j's, become more bound to different extents. In other words, the ordering of the proton single-particle states may change to a certain extent but become more deeply bound as a whole.

These are properties that one can expect from different central forces, while the actual situation should be somewhere in between. We point out a common feature that if the

nuclear force, $\hat{v}$, is an attractive central force, the monopole effect depicted in eq. (9) is always attractive for all orbits j.

7. – Shell evolution due to nuclear forces

As shown in the previous section, the monopole interaction varies in general the shell structure through the mechanism shown in eq. (9). This variation is represented quantitatively in terms of the *ESPEs* discussed above, which are configuration-dependent in principle, and the multipole interaction, such as the quadrupole interaction, will act on top of them. Even for the same multipole interaction, its effects can be different for different ESPEs. For instance, for the same quadrupole interaction, the quadrupole deformation will change due to the shell evolution resulting in different ESPEs. Thus, the shell evolution can affect not only single-particle-type but also various other nuclear properties. We note that ESPEs here mean the so-called spherical ones, as the mechanism in eq. (9) is scalar. On the other hand, such spherical ESPEs (obtained from appropriate reference states which can be the eigenstate being calculated, implying *self-consistency*) are relevant not only to spherical states but also to all kinds of deformed states. We note also that the monopole and multipole interactions are parts of the Hamiltonian, and their effects are automatically included if the Hamiltonian is diagonalized in the shell model calculation.

7˙1. *Type-I shell evolution.* – We start considering a chain of isotopes. If more neutrons are added beyond a closed shell, the nucleus moves to the right on the Segrè chart. We now take, for the sake of simplicity, a filling scheme where neutrons occupy the lowest possible single-particle orbits. We emphasize that the filling scheme is just a simplest and easiest treatment to see the ESPEs. As more neutrons (or protons) occupy the orbit j' at the Fermi level, its occupation number $n_{j'}$ increases (see eq. (9)). Thus, type-I shell evolution occurs. In subsect. **6**˙2, this case was discussed with an extremely simple force, infinite-range central force. We then found that the shell structure does not change, but the whole shell becomes more bound. We now study the shell evolution due to more realistic nuclear forces.

7˙2. *Shell evolution due to tensor force.* – The tensor force has been known for a long time, and its effects have been studied from many angles. Those studies include an extraction of the tensor-force component in the empirical nucleon-nucleon interaction by Schiffer and True [36], a derivation of microscopic effective NN interaction (*i.e.*, so-called "G-matrix interaction") including second-order effects of the tensor force by Kuo and Brown [37], a calculation of magnetic moments also including second-order tensor-force contributions by Arima and his collaborators [38] and by Towner [39], etc.

The robust, systematic and first-order effects of the tensor force on the shell structure have, however, been discussed since 2005 [32]. We present the basic properties of the monopole interaction of the tensor force, by using an illustrative example. Figure 13(a)

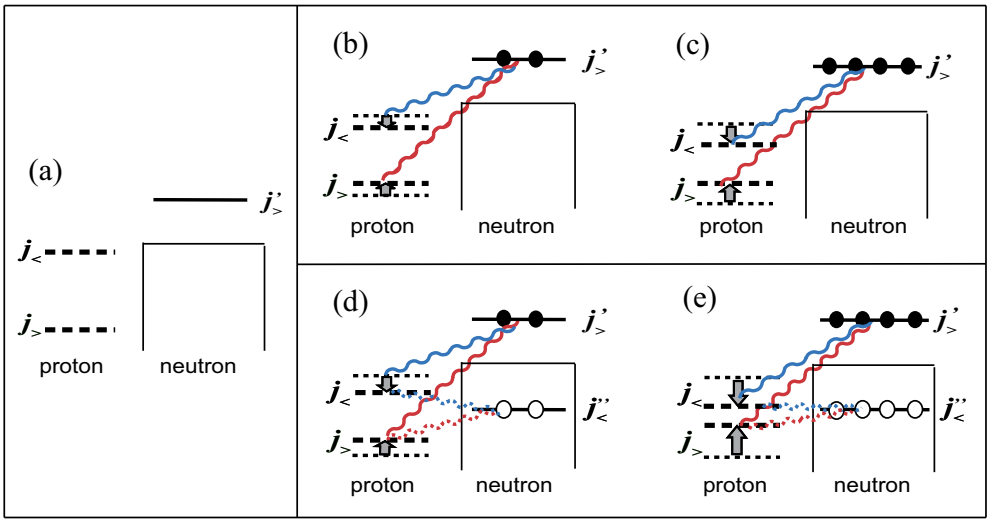

Fig. 13. – Illustration of the type-I and -II shell evolutions.

shows proton orbits and a neutron orbit. The proton orbits are spin-orbit partners

$$j_> = l + 1/2, \qquad j_< = l - 1/2, \tag{10}$$

where l denotes the orbital angular momentum, and $1/2$ represents the spin. As shown in ref. [32] with an intuitive picture, the coupling between $j_>$ and $j'_<$ orbits is attractive for the tensor force. On the other hand, the coupling between $j_>$ and $j'_>$ is repulsive as well as the coupling between $j_<$ and $j'_<$. (For more elaborate intuitive explanation, see [40].) In fig. 13(a), a neutron $j'_>$ orbit is shown on top of the core. Figure 13(b) illustrates how the tensor force works, if two neutrons occupy this $j'_>$ orbit. Due to the repulsive monopole interaction (red wavy line), the ESPE of the proton $j_>$ orbit is raised. On the other hand, owing to the attractive monopole interaction (blue wavy line), the ESPE of the proton $j_<$ orbit is lowered. These combined changes produce the reduction of spin-orbit splitting.

Since the monopole effect is linear, four neutrons in the $j'_>$ orbit as shown in fig. 13(c) double the effect exhibited in fig. 13(b). Thus, the proton spin-orbit splitting becomes smaller and smaller, as more neutrons occupy the $j'_>$ orbit.

This change of the shell structure is very different from the changes discussed in subsect. **6**˙2 with central forces. In the present case, the sign of the effect changes for different combinations of the orbits, whereas the sign is the same in the discussions on the central forces made in subsect. **6**˙2. Thus, the tensor force produces very unique monopole interaction, which may show various shell evolutions with significant changes such as the disappearance of traditional magic numbers, the appearance of new magic numbers, the crossing of two orbits, etc., which provide intriguing research programs [41, 42].

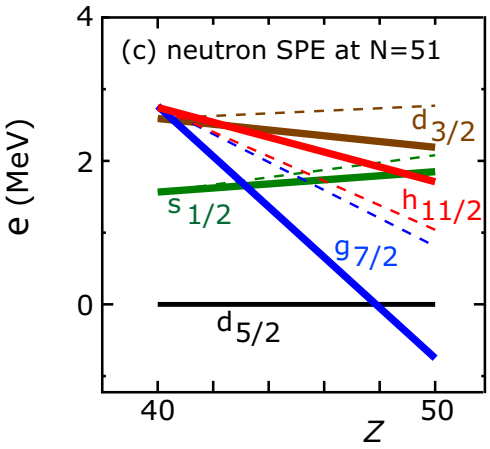

Fig. 14. – Shell evolution of neutrons from $Z = 40$ to 50. Taken from fig. 3 of ref. [55].

We note that the actual values of the monopole matrix element depend on the radial wave functions of the orbits j and j' in eq. (8) also in the case of the tensor force. Large magnitudes are expected between the same orbits ($j = j'$) or between spin-orbit partners, as well as for a pair of orbits both having no radial node and high orbital angular momenta close to each other [32].

The tensor-force component has been included by now in various types of nuclear models. They include the shell model analysis based on the spin-tensor decomposition [43, 44], showing contributions from various channels. Regarding the mean-field models, the extention of the Gogny model was made in 2006 [45]. For the Skyrme model, while an early concrete attempt was carried out in 1977 [46], the tensor force has not in general been activated until recently [47]. The research activity is, however, quite high with many publications after 2006 [48-52]. Relativistic approach is also of interest [53,54], with more expectations towards future developments because of closer relations to meson exchange processes.

One typical case of the application of the tensor-force-driven shell evolution is shown in fig. 14 taken from [55]. Here, from ^{90}Zr to ^{100}Sn, the number of protons in the $1g_{9/2}$ orbit increases from 0 to 10, because of the simple filling approximation assumed. The neutron orbits on top of the $N = 50$ core change their single-particle energies, as shown in fig. 14. There are two sets of calculated results: one (solid lines) is obtained with the central and tensor forces, while the other (dashed lines) is only with the central force. Note that the tensor force used in fig. 14 was obtained from the π-meson + ρ-meson exchange potential [56, 55], and that the central force here is of a Gaussian type, which can reproduce basic properties of the central part of microscopic effective NN interactions based on G-matrix calculation [57] (see ref. [55] for details). We mention some important features: i) the $1g_{7/2}$ and $1h_{11/2}$ orbits come down together if the central force only is taken. In contrast, these two orbits exhibit an increasing energy splitting

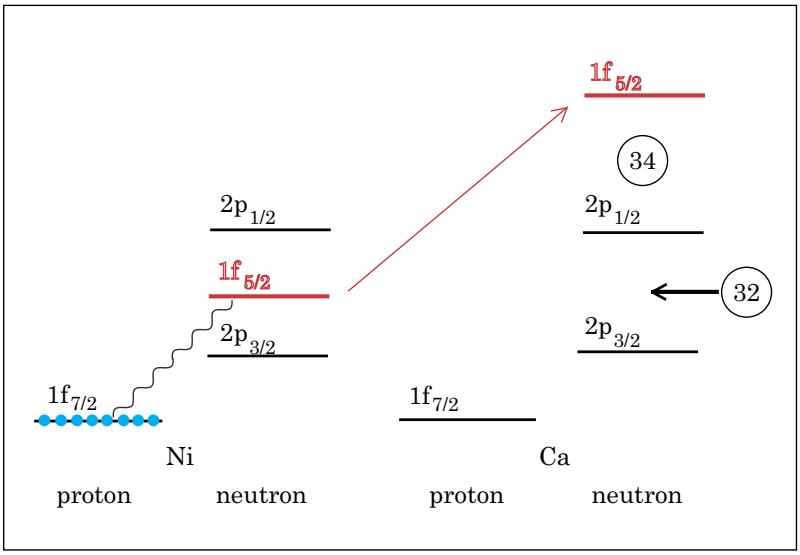

Fig. 15. – Schematic illustration of shell evolution from Ni back to Ca for neutron orbits. Light blue circles are protons. The wavy line is the interaction between the proton $1f_{7/2}$ orbit and the neutron $1f_{5/2}$ orbit. The numbers in circles indicate (semi-) magic numbers. Taken from [18].

approaching $Z = 50$ if the tensor force is included. The lowering of the $1g_{7/2}$ orbit has been known experimentally [58,59], consistently with a significant monopole effect of the tensor force. The stronger coupling between the proton $1g_{9/2}$ orbit and the neutron $1g_{7/2}$ orbit was discussed as an effect of the central force in the $^3S_1$ channel by Federman and Pittel [60], consistently with the central-force contribution in fig. 14.

We mention, from a more general viewpoint, that the strong attraction between proton-neutron spin-orbit partners was noticed in relation to the onset of deformation in Zr isotopes [61]. The monopole interaction between proton $2p_{3/2,1/2}$ orbit and neutron $2d_{5/2}$ orbit was discussed for the description of Zr-Sr isotopes in [62] by using the empirical interaction introduced in [36]. Such monopole effects presented in earlier works without mentioning the tensor force, *e.g.*, [60-64], can be understood now quite consistently as appearances of the shell evolution involving the tensor-force monopole effect. There were earlier shell model calculations with realistic effective NN interactions which somehow contain tensor-force component and consequently show certain monopole contributions, for instance [65,66].

A recent typical example of the shell evolution is the appearance of a new magic number $N = 34$. Figure 15 shows the shell evolution for the neutron orbits in the pf shell from Ni to Ca. In Ni, there are eight protons on top of the $Z = 20$ core, and they are assumed to be in the $1f_{7/2}$ orbit. Due to the strong attractive interaction between the $1f_{7/2}$ proton and $1f_{5/2}$ neutron orbits where the tensor and central forces contribute additively, the addition of protons lowers the ESPE of the neutron $1f_{5/2}$ orbit. This is

the case for Ni isotopes, where the $1f_{5/2}$ orbit is located between the $2p_{3/2}$ and $2p_{1/2}$ orbits. In the Ca isotopes, the proton $1f_{7/2}$ orbit is unoccupied in the picture of the ^{40}Ca magic core, so the above-mentioned monopole shift for the $1f_{5/2}$ orbit is vanished. This moves the neutron $1f_{5/2}$ orbit upwards even above the $2p_{1/2}$ orbit, leaving a gap at $N = 32$ and creating another gap at $N = 34$. Thus, $N = 34$ becomes a magic number for the Ca isotopes. In this argument, the $j_>$-$j_<$ proton-neutron coupling within a major shell is important, and is the mechanism for the shell evolution between Ca and Ni. This was basically the prediction in ref. [34] in 2001, and the corresponding text is quoted as "*we can predict other magic numbers, for instance,* $N = 34$ *associated with the* $0f_{7/2}$-$0f_{5/2}$ *interaction*". The experimental investigation of the $N = 34$ magic number in the Ca isotopes, however, had been unfeasible for a long time, casting doubt over this magic number [67, 68]. In 2013, finally, the 2^+ excitation energy was measured in RIBF [69] consistently with a $N = 34$ gap. The $N = 32$ gap in the Ca isotopes was investigated experimentally in ISOLDE in 1985 in terms of the 2^+ excitation energy [70]. The magic structures of Ca isotopes attracted much attention in recent years [71-87].

We here comment that the tensor force in the free space like the one obtained from one-π-meson + one-ρ-meson exchange potential does not change much after the renormalization procedures for the short-range repulsion and the in-medium corrections, as referred to as *renormalization persistency* [55, 88]. The tensor-force component of the effective NN interaction can be obtained by its spin-tensor decomposition [89-94]. The tensor forces obtained by different approaches are known to be rather similar at least at the level of the monopole interaction for the valence shell because of the renormalization persistency. Thus, we can discuss rather well general features of the monopole effects of the tensor force.

8. – Nuclear shape

The shell evolution is one of the correlation effects, reflecting the monopole interaction. There are other components in the NN interaction, which produce other correlations. As consequences of such correlations, one can find certain modes with strong coherence among many participating nucleons, referred to as collective modes usually. Among such collective modes, the one causing the deformation of the nuclear shape is particularly important, as pointed out by Rainwater [95], and Bohr and Mottelson [96, 97]. With this collective mode, the shape of the nucleus is changed from a sphere to an ellipsoid, and this mode is called quadrupole deformation. Besides the quadrupole deformation of the shape, there are various collective modes such as octupole deformation, or other correlations with weaker coherence.

8˙1. *Nuclear shapes and quantum phase transition.* – We shall first focus on the quadrupole deformation of the nuclear shape as a function of the neutron number N. Figure 16 exhibits the excitation energy of the 2_1^+ state, or the 2_1^+ level, for Sm and Zr isotopes as a function of N. In the Sm chain, the 2^+ level comes down rather gradually, similarly to many other isotopic chains. As shown in fig. 16, a higher 2^+ level corre-

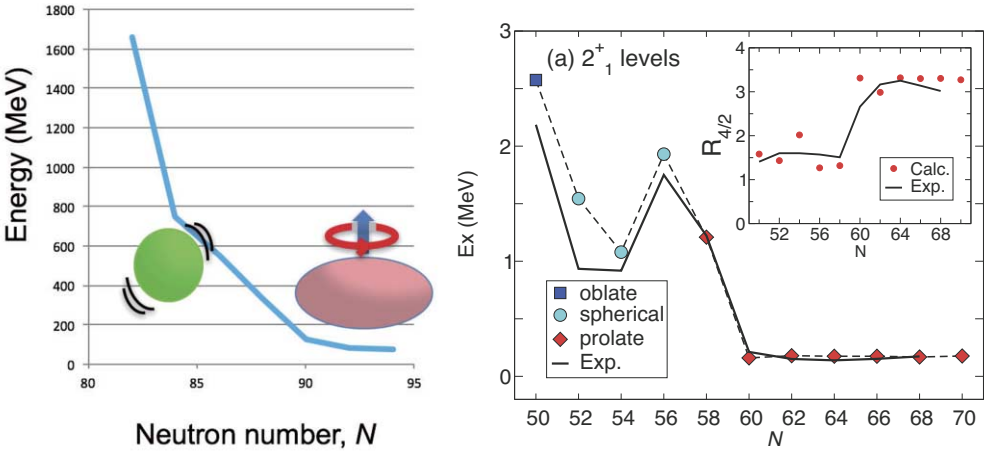

Fig. 16. – Systematic changes of the 2_1^+ level in (left) Sm and (right) Zr isotopes, as functions of N. Data taken from [98] for Sm. The right panel is based on [15].

sponds to a spherical shape and its surface oscillation, while a lower 2^+ level implies an ellipsoidal deformed shape and the rotation of the ellipsoid. On the other hand, in the Zr chain, the 2^+ level drops down abruptly in moving from $N = 58$ to 60. Due to this abrupt change, this phenomenon can be referred to as a quantum phase transition [15]. Likewise, the ground-state structure of the Zr isotopes is changed drastically between $N = 58$ and 60, also from the sphere to the strongly deformed ellipsoid. The Monte Carlo Shell Model (MCSM) describes both situations including the abrupt change with the same Hamiltonian [15, 26].

8˙2. *Quantum phase transition in Zr isotopes.* – We shall now look into the structure changes in Zr isotopes based on the MCSM calculation. The upper panel of fig. 17 shows the occupation numbers of proton orbits for some states. The $g_{9/2}$ orbit is almost empty in the 0_1^+ state of ^{98}Zr, whereas it is occupied by about 3.5 protons in its 0_2^+ state. Note that this 0_1^+ (0_2^+) state is spherical (deformed). Such changes, including the numbers of proton holes in the pf orbits, result in substantial shifts of the neutron ESPEs as shown schematically in the upper right panel of fig. 17. The proton-neutron monopole interaction (wavy line in the figure) generates those shifts. The lower panel depicts the actual neutron ESPEs. One notices substantial changes in the ESPEs for different states. One sees that the spacing between the $d_{5/2}$ and $g_{7/2}$ orbits is nearly 5 MeV for the 0_1^+ state of ^{98}Zr, but it is reduced to about 2 MeV in 0_2^+ state. Such a reduced splitting is found also in the 0_1^+ state of ^{100}Zr which is also strongly deformed.

We now discuss why the ESPEs are so different between spherical and deformed states. We first point out that the nuclear deformation at low excitation energy is a Jahn-Teller effect [99], meaning that the collective motion causing the deformation occurs as a consequence of coherent contributions from some relevant orbits near the Fermi energy. For

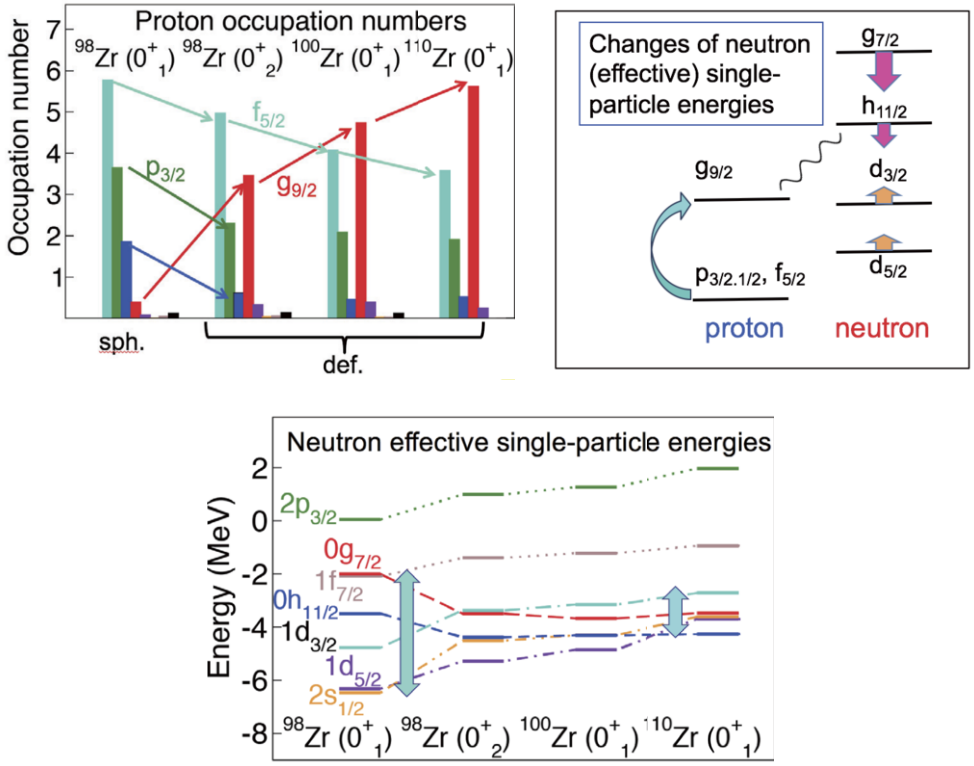

Fig. 17. – Top left: occupation numbers of proton orbits of Zr isotopes. Top right: schematic illustration of the changes of neutron (effective) single-particle energies in Zr isotopes. Bottom: Actual values of neutron (effective) single-particle energies obtained in the calculation of [15]. The top left panel and the bottom one are based on [15].

such coherent effects, larger splittings of ESPEs weaken the coherence, leading to a lower collectivity. On the other hand, the monopole interaction with other valence nucleons can change the ESPEs depending on the occupancy of the other nucleons. If the monopole interaction were uniform, no configuration dependence would appear, and this change should be absent. The tensor-force component of the nuclear force makes the monopole interaction attractive or repulsive, depending on the combination of the orbits [32, 55]. This is certainly against the uniformity, and its effect can be crucial. The central-force component changes its magnitude also depending on the combination of the orbits mainly due to varying overlaps of radial wave functions of single-particle states [55]. Thus, the monopole interaction is indeed far from being uniform, and the selection of favored configurations can move the ESPEs of relevant orbits substantially. If relevant ESPEs can be made closer to being degenerate, it helps the deformation. We shall formulate this novel mechanism in the next section.

8˙3. *Quantum self-organization.* – The nuclear shapes have been one of the major focuses of the nuclear structure physics, including spherical, vibrational and rotational ones [100]. The relation between the single-particle states and the collective modes has naturally become of much interest, as described by Bohr and Mottelson in [100] as "the problem of reconciling the simultaneous occurrence of single-particle and collective degrees of freedom and exploring the variety of phenomena that arise from their interplay".

The atomic nucleus is a many-body quantum system made of protons and neutrons, which is often considered to be described in terms of Landau's Fermi Liquid picture. In a somewhat simplified expression of this picture, protons and neutrons of a nucleus are in a mean potential which is like a rigid "vase", and nucleons are like free particles moving in this vase, interacting weakly among themselves through a "residual interaction". The ESPEs of such a system exhibit some shell structure, and are split in general. If the splitting is large enough, the many-body structure is dominated by the ESPEs: nucleons occupy the lowest single-particle states in the ground state, the next lowest configuration gives us the first excited state, and so forth. In such cases, the correlations due to the interaction between nucleons may contribute, but their effects are minor, more or less, compared to the effects of ESPE splittings. However, if the energy gain from such correlations overcomes the relevant ESPE splittings, a collective mode dominates the structure of the ground and low-lying states. Although the understanding of the relation between the single-particle states and the collective modes has been pursued in many ways, it seems to remain an open problem. For instance, G.E. Brown had kept, throughout his life, the question, "how can single-particle states coexist with collective modes?" as quoted from "*Fermi liquid theory: A brief survey in memory of Gerald E. Brown*" in [101]. We shall present a novel mechanism which is closely related to this problem.

The nuclear deformation is determined by the balance between the effect of the collective-mode driving force and the resistance power against this collective mode. A schematic expression of this property is

$$\text{deformation} = \frac{\text{quadrupole force}}{\text{resistance power}}\,. \tag{11}$$

The collective-mode driving force is the quadrupole (or quadrupole-quadrupole) interaction in the case of the ellipsoidal shape. This interaction is one of the major components of the proton-neutron realistic force. A typical example of the resistance power is the pairing interaction, which tends to make the shape more spherical because all time-reversal pairs are equally favored. Keeping the pairing interaction aside, we shall consider another source of the resistance power. That is, the effects of the monopole interaction on the ESPEs.

We here propose a novel mechanism called, *Quantum Self-Organization*. This mechanism implies the following property: Atomic nuclei can "organize" their single-particle energies by taking particular configurations of protons and neutrons, optimized for each eigenstate, thanks to orbit dependences of monopole components of nuclear forces (*e.g.*,

tensor and central forces). This results in an enhancement of the Jahn-Teller effect, *i.e.*, an enhancement of the collective mode. The deformation and quantum self-organization can be linked in a non-linear way with a positive feedback: once some nucleons are excited to particular favorable orbits, the ESPEs can be shifted in favor of a larger deformation. A larger deformation can promote such excitations with more nucleons. This cycle continues until self-consistency is achieved, whereas intermediate situations are skipped. In many cases, massive excitations are involved, and the particle-hole hierarchy is broken, for instance, a $6p$-$6h$ deformed state comes right after a $2p$-$2h$ near-spherical state, skipping the $4p$-$4h$ state [18].

The property shown in eq. (11) is somewhat analogous to the relation

$$\text{electric current} = \frac{\text{voltage}}{\text{resistance}}\,, \tag{12}$$

where the electric current, voltage and resistance mean the usual quantities regarding the electricity. The higher voltage produces a higher current, but the current can be increased also by decreasing the resistance. The quantum self-organization implies that the atomic nucleus finds particular configurations which decrease the resistance power.

The most favorable configurations and associated ESPEs vary for individual eigenstate even within the same type of the collective mode. For instance, prolate, oblate or triaxial shapes belong to the quadrupole deformation, but can appear with different patterns of the ESPEs within the same nucleus. The oblate shape is less affected by the quantum self-organization, because smaller numbers of nucleons on unique-parity orbits are the key element of the oblate shape in most cases. In those cases, the organizations of many orbits are rather irrelevant, and the quantum self-organization may not occur to a sizable extent. This feature has been verified with concrete cases. On the other hand, many orbits contribute coherently to the prolate deformation, and the quantum self-organization can produce crucial effects. This has been confirmed by changing the monopole interactions, for instance, closer to the uniform one.

We present a concrete example by taking the case of the prolate band in ^{68}Ni [18]. The monopole interaction between the neutron $1g_{9/2}$ orbit and the proton $1f_{5/2}$ orbit is more attractive than that between the neutron $1g_{9/2}$ orbit and the proton $1f_{7/2}$ orbit mainly due to the robust property of the monopole interaction of the tensor force, and this difference serves as the major origin of the quantum self-organization in this particular case: more neutrons in the $1g_{9/2}$ orbit reduces the $1f_{7/2}$-$1f_{5/2}$ spin-orbit splitting for protons [17,32,55]. The effect of this difference on the deformation can be seen quantitatively by replacing the strengths of these monopole interactions with the average of their original values, *i.e.*, the same value. Likewise, we reset the monopole interaction between the neutron $1f_{5/2}$ and the proton $1f_{7/2}$ orbits and that between the neutron $1f_{5/2}$ and the proton $1f_{5/2}$ orbits. These modifications correspond basically to the removal of the tensor-force monopole contributions, and are nothing but the suppression of the present effects of the quantum self-organization. The resulting Potential Energy Surface is shown in fig. 18 for the axially symmetric deformation compared with that obtained

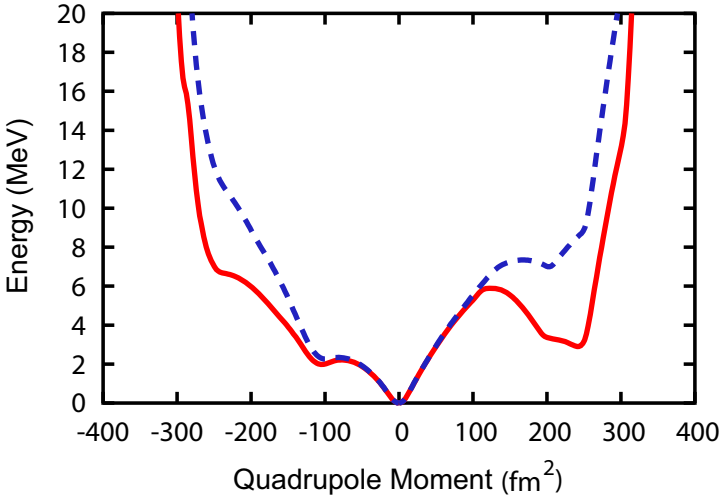

Fig. 18. – Potential Energy Surface with the axially symmetric deformation for ^{68}Ni. The red solid line denotes the energy of the constrained Hartree-Fock calculation with the original Hamiltonian. The blue dashed line implies the same calculation except that the quantum self-organization is suppressed (see text). Figure taken from [18].

from the original Hamiltonian. Around the spherical minimum the energy curves of the two calculations are similar, however, when going to stronger deformation values, the two approaches differ substantially. In particular, the prolate profound local minimum, seen in the original calculation (red solid line), is pushed up by about 4 MeV, if the quantum self-organization is suppressed as described above (blue dashed line). Thus, the quantum self-organization is a part of the crucial mechanisms producing the nuclear deformation.

At this point, we mention that the ESPE being discussed corresponds somehow to the spherical terms in the Nilsson model [100] which are comprised of the $\ell\ell$ and ℓs terms as well as the harmonic-oscillator-quanta term. As their strengths are independent of the deformation, the present effect is not included in the Nilsson model.

Type-II shell evolution [18] has been discussed, for instance, in the Co/Ni region [17, 22, 25], where neutrons are excited from the pf shell to $g_{9/2}$ across the $N = 40$ sub-magic gap. The neutrons in $g_{9/2}$ and neutron holes in $f_{5/2}$ provide sizable monopole effects similarly to the ^{68}Ni case discussed above. A smaller $1f_{7/2}$-$1f_{5/2}$ spin-orbit splitting for protons reduces the resistance power against deformation, pulling down the prolate band as seen in fig. 18. Type-II shell evolution was introduced as the particle-hole excitation over a magic or sub-magic gap. Clearly, this kind of mechanism is a very simple and visible case of the quantum self-organization. On the other hand, the quantum self-organization can occur certainly in more complex ways. Such a complex way may be found in the shape transition of Sm isotopes (see fig. 16), where no magic or sub-magic gap is involved. We can see the spherical-vibrational-rotational shape evolution in MCSM calculations, as will be reported in detail elsewhere.

The structure of Sm isotopes has been one of the focal points of the nuclear structure physics. This is largely because the whole picture of the gradual change form the spherical to strongly deformed shapes has been seen experimentally from an earlier time. We have succeeded in describing this shape evolution by the MCSM with a large model space. As the results are preliminary, they are not shown here, but will be presented somewhere in a near future.

Likewise, the shape coexistence in Hg/Pb isotopes has been studied. In those cases, the quantum self-organization gives intriguing contributions on the pattern of the shape coexistence, as reported also elsewhere.

9. – Summary and perspectives

We presented an overview on the shell model studies on atomic nuclei, covering from the beginning to very recent results.

The shell model calculation can include various effects of the nuclear forces. Although it faced the difficulty of the matrix dimension size, this difficulty has been removed by the MCSM. The T-plot was explained.

In parallel to this development, the effects of the monopole component, or interaction, have been discussed. The central and tensor monopole interactions produce crucial and characteristic contributions to the structure of exotic nuclei. Those contributions can be seen not only in single-particle properties but also in other properties due to strong multipole correlation effects. The mechanism of the monopole interaction has been referred to as the Type-I and -II Shell Evolutions [18].

Some examples are shown for Ni and Zr isotopes to some detail and some perspectives are given for Sm amd Hg/Pb nuclei. The Zr case involves the first-order quantum phase transition.

Finally, a comprehensive and basic mechanism on the relation between single-particle states and collective modes was presented. This is called the *quantum self-organization*, and a summary on this is given below.

- The atomic nuclei are not like simple rigid vases containing almost free nucleons interacting only weakly: the naive Fermi liquid picture.
- Nuclear forces are rich enough to change effective single-particle energies for each eigenstate, and can lead to the quantum self-organization.
- Single-particle energies can be self-organized, being enhanced by
  - i) two quantum liquids (*e.g.*, protons and neutrons)
  - ii) two major force components
    - *e.g.*, quadrupole interaction: to drive collective mode
      - monopole interaction: to control resistance power.
- Type-II shell evolution is a simple visible case involving excitations across (sub)magic gap.

– Actual cases such as shape coexistence, quantum phase transition, octupole vibration/deformation, super deformation, etc. can be studied with this scope.

– The quantum self-organization becomes more important in heavier nuclei where the number of active orbits and the number of active nucleons are larger. With larger numbers of them, the effects of the organization can be more significant. This feature may be linked to fission and superheavy elements. On the other hand, the quantum self-organization may not be so visible in light nuclei except for particular cases like intruder bands or cluster (or multiple particle-hole excited) states.

– Time-dependent version of quantum self-organization may be of another interest for reactions and fission.

The nuclear structure is becoming more and more interesting and exciting with many aspects and ideas.

* * *

The MCSM calculations were performed on the K computer at RIKEN AICS (hp140210, hp150224, hp160211, hp170230). This work was also supported in part by the HPCI Strategic Program (The origin of matter and the universe) and "Priority Issue on Post-K computer" (Elucidation of the Fundamental Laws and Evolution of the Universe) from MEXT and JICFuS.

REFERENCES

[1] Mayer M. G., *Phys. Rev.*, **75** (1949) 1969.
[2] Haxel O., Jensen J. H. D. and Suess H. E., *Phys. Rev.*, **75** (1949) 1766.
[3] Mayer M. G. and Jensen J. H. D., *Elementary Theory of Nuclear Shell Structure* (Wiley, New York) 1955.
[4] Bohr A. and Mottelson B. R., *Nuclear structure I* (Benjamin, New York) 1949.
[5] de-Shalit A. and Talmi I., *Nuclear Shell Theory* (Dover) 2004.
[6] Heyde K. L. G., *The Nuclear Shell Model* (Springer, Berlin) 1990.
[7] Caurier E., Martinez-Pinedo G., Nowacki F., Poves A. and Zuker A. P., *Rev. Mod. Phys.*, **77** (2005) 427.
[8] Brown B. A. and Rae W. D. M., *Nucl. Data Sheets*, **120** (2014) 115.
[9] Caurier E. and Nowacki F., *Acta Phys. Pol. B*, **30** (1999) 705.
[10] Shimizu N., arXiv:1310.5431 (2013).
[11] Aktulga H. M., Yang C., Ng E. G., Maris P. and Vary J. P., *Concurr. Comput.: Pract. Exper.*, **26** (2014) 2631.
[12] Johnson C. W., Ormand W. E., McElvain K. S. and Shan H., arXiv:1801.08432 (2018).
[13] Otsuka T. *et al.*, *Prog. Part. Nucl. Phys.*, **47** (2001) 319.
[14] Shimizu N. *et al.*, *Prog. Theor. Exp. Phys.*, **2012** (2012) 01A205.
[15] Togashi T., Tsunoda Y. Otsuka T. and Shimizu N., *Phys. Rev. Lett.*, **117** (2016) 172502.
[16] Shimizu N. *et al.*, *Phys. Rev. C*, **82** (2010) 061305.
[17] Tsunoda Y. *et al.*, *Phys. Rev. C*, **89** (2014) 031301.

[18] OTSUKA T. and TSUNODA Y., *J. Phys. G: Nucl. Part. Phys.*, **43** (2016) 024009.
[19] SUCHYTA S. *et al.*, *Phys. Rev. C*, **89** (2014) 021301.
[20] CHIARA C. J. *et al.*, *Phys. Rev. C*, **91** (2015) 044309.
[21] CRIDER B. P. *et al.*, *Phys. Lett. B*, **763** (2016) 108.
[22] LEONI S., FORNAL B. *et al.*, *Phys. Rev. Lett.*, **118** (2017) 162502.
[23] SAHIN E. *et al.*, *Phys. Rev. Lett.*, **118** (2017) 242502.
[24] OLIVIER L. *et al.*, *Phys. Rev. Lett.*, **119** (2017) 192501.
[25] MORALES A. I., BENZONI G. *et al.*, *Phys. Lett. B*, **765** (2017) 328.
[26] KREMER C. *et al.*, *Phys. Rev. Lett.*, **117** (2016) 172503.
[27] PAUL N. *et al.*, *Phys. Rev. Lett.*, **118** (2017) 032501.
[28] RÉGIS J. M. *et al.*, *Phys. Rev. C*, **95** (2017) 054319.
[29] TSUNODA N. *et al.*, *Phys. Rev. C*, **89** (2014) 024313.
[30] TSUNODA N. *et al.*, *Phys. Rev. C*, **95** (2017) 021304.
[31] OTSUKA T., GADE A., SORLIN O., SUZUKI T. and UTSUNO T., arXiv:1805.06501 [nucl-th].
[32] OTSUKA T. *et al.*, *Phys. Rev. Lett.*, **95** (2005) 232502.
[33] BANSAL R. K. and FRENCH J. B., *Phys. Lett.*, **11** (1964) 145.
[34] OTSUKA T. *et al.*, *Phys. Rev. Lett.*, **87** (2001) 082502.
[35] POVES A. and ZUKER A., *Phys. Rep.*, **70** (1981) 235.
[36] JOHN P. SCHIFFER and WILLIAM W. TRUE, *Rev. Mod. Phys.*, **48** (1976) 191.
[37] KUO T. T. S. and BROWN G. E., *Nucl. Phys.*, **85** (1966) 40.
[38] SHIMIZU K., ICHIMURA M. and ARIMA A., *Nucl. Phys. A*, **226** (1974) 282.
[39] TOWNER I. S., *Phys. Rep.*, **155** (1987) 263.
[40] TAKAHARU OTSUKA, *Phys. Scr.*, **T152** (2013) 014007.
[41] ALEXANDRA GADE and THOMAS GLASMACHER, *Prog. Part. Nucl. Phys.*, **60** (2008) 161.
[42] SORLIN O. and PORQUET M.-G., *Prog. Part. Nucl. Phys.*, **61** (2008) 602.
[43] SMIRNOVA N. A. *et al.*, *Phys. Lett. B*, **686** (2010) 109.
[44] SMIRNOVA N. A. *et al.*, *Phys. Rev. C*, **86** (2012) 034314.
[45] OTSUKA T. *et al.*, *Phys. Rev. Lett.*, **97** (2006) 162501.
[46] STANCU FI. *et al.*, *Phys. Lett. B*, **68** (1977) 108.
[47] BENDER M. *et al.*, *Rev. Mod. Phys.*, **75** (2003) 121.
[48] BROWN B. A. *et al.*, *Phys. Rev. C*, **74** (2006) 061303.
[49] BRINK D. M. and STANCU FL., *Phys. Rev. C*, **75** (2007) 064311.
[50] LESINSKI T. *et al.*, *Phys. Rev. C*, **76** (2007) 014312.
[51] COLO G. *et al.*, *Phys. Lett. B*, **646** (2007) 227.
[52] BENDER M. *et al.*, *Phys. Rev. C*, **80** (2009) 064302.
[53] LALAZISSIS G. A. *et al.*, *Phys. Rev. C*, **80** (2009) 041301.
[54] LONG W.-H. *et al.*, *Phys. Lett. B*, **640** (2006) 150.
[55] OTSUKA T. *et al.*, *Phys. Rev. Lett.*, **104** (2010) 012501.
[56] OSTERFELD F. *et al.*, *Rev. Mod. Phys.*, **64** (1992) 491.
[57] MORTEN HJORTH-JENSEN, THOMAS T. S. KUO and EIVIND OSNES, *Phys. Rep.*, **261** (1995) 125.
[58] SEWERYNIAK D. *et al.*, *Phys. Rev. Lett.*, **99** (2007) 022504.
[59] DARBY I. G. *et al.*, *Phys. Rev. Lett.*, **105** (2010) 162502.
[60] FEDERMAN P. and PITTEL S., *Phys. Lett. B*, **69** (1977) 385.
[61] FEDERMAN P. and PITTEL S., *Phys. Lett. B*, **82** (1979) 9.
[62] FEDERMAN P., PITTEL S. and ETCHEGOYE A., *Phys. Lett. B*, **140** (1984) 269.
[63] FEDERMAN P. and PITTEL S., *Phys. Rev. C*, **20** (1979) 820.
[64] PITTEL S. *et al.*, *Phys. Rev. C*, **48** (1993) 1050.
[65] ALAN L. GOODMAN, *Nucl. Phys. A*, **287** (1977) 1.

[66] Zeldes N., Dumitrescu T. S. and Kohler H. S., *Nucl. Phys. A*, **399** (1983) 11.
[67] Warner D., *Nature*, **430** (2004) 517.
[68] Janssens R. V. F. *et al.*, *Nature*, **459** (2009) 1069.
[69] Steppenbeck D. *et al.*, *Nature*, **502** (2013) 207.
[70] Huck A. *et al.*, *Phys. Rev. C*, **31** (1985) 2226.
[71] Prisciandaro J. I. *et al.*, *Phys. Lett. B*, **510** (2001) 17.
[72] Janssens R. V. F. *et al.*, *Phys. Lett. B*, **546** (2002) 55.
[73] Liddick S. N. *et al.*, *Phys. Rev. Lett.*, **92** (2004) 072502.
[74] Burger A. *et al.*, *Phys. Lett. B*, **622** (2005) 29.
[75] Dinca D.-C. *et al.*, *Phys. Rev. C*, **71** (2005) 041302.
[76] Gade A. *et al.*, *Phys. Rev. C*, **74** (2006) 021302.
[77] Rodriguez T. R. *et al.*, *Phys. Rev. Lett.*, **99** (2007) 062501.
[78] Rejmund M. *et al.*, *Phys. Rev. C*, **76** (2007) 021304.
[79] Honma M. *et al.*, *RIKEN Accel. Prog. Rep.*, **41** (2008) 32.
[80] Coraggio L. *et al.*, *Phys. Rev. C*, **80** (2009) 044311.
[81] Crawford H. L. *et al.*, *Phys. Rev. C*, **82** (2010) 014311.
[82] Kaneko K. *et al.*, *Phys. Rev. C*, **83** (2011) 014320.
[83] Holt J. *et al.*, *J. Phys. G: Nucl. Part. Phys.*, **39** (2012) 085111.
[84] Utsuno Y. *et al.*, *Prog. Theor. Phys. Suppl.*, **196** (2012) 304.
[85] Hagen G. *et al.*, *Phys. Rev. Lett.*, **109** (2012) 032502.
[86] Wienholtz F. *et al.*, *Nature*, **498** (2013) 346.
[87] Steppenbeck D. *et al.*, *Phys. Rev. Lett.*, **114** (2015) 252501.
[88] Tsunoda N. *et al.*, *Phys. Rev. C*, **84** (2011) 044302.
[89] Elliott J. P. *et al.*, *Nucl. Phys. A*, **121** (1968) 241.
[90] Kirson M. *et al.*, *Phys. Lett. B*, **47** (1973) 110.
[91] Klingenbeck K. *et al.*, *Phys. Rev. C*, **15** (1977) 1483.
[92] Yoro K. *et al.*, *Nucl. Phys. A*, **333** (1980) 67.
[93] Brown B. A. *et al.*, *Ann. Phys.*, **182** (1988) 191.
[94] Osnes E. *et al.*, *Phys. Rev. C*, **45** (1992) 662.
[95] Rainwater J., *Phys. Rev.*, **79** (1950) 432.
[96] Bohr A., *Mat. Fys. Medd. Dan. Vid. Selsk.*, **26** (1952) 14.
[97] Bohr A. and Mottelson B. R., *Mat. Fys. Medd. Dan. Vid. Selsk.*, **27** (1952) 16.
[98] NNDC, NuDat 2 `http://www.nndc.bnl.gov/nudat2/`.
[99] Jahn H. A. and Teller E., *Proc. R. Soc. A*, **161** (1937) 220.
[100] Bohr A. and Mottelson B. R., *Nuclear structure II* (Benjamin, New York) 1975.
[101] Schaefer T. *et al.*, *Nucl. Phys. A*, **928** (2014) 180.

Proceedings of the International School of Physics "Enrico Fermi"
Course 201 "Nuclear Physics with Stable and Radioactive Ion Beams", edited by F. Gramegna,
P. Van Duppen, A. Vitturi and S. Pirrone
(IOS, Amsterdam; SIF, Bologna) 2019
DOI 10.3254/978-1-61499-957-7-31

Algebraic models of quantum many-body systems: The algebraic cluster model

F. Iachello

Center for Theoretical Physics, Sloane Laboratory, Yale University
New Haven, CT 06520-8120, USA

Summary. — A brief account of the algebraic cluster model (ACM) is given. Applications to cluster structures composed of k α-particles with $k = 2$ (Z_2 symmetry), $k = 3$ (D_{3h} symmetry) and $k = 4$ (T_d symmetry) are presented. Experimental evidence for the occurrence of these symmetries in ^{8}Be (Z_2), ^{12}C (D_{3h}), and ^{16}O (T_d) is shown.

1. – Introduction

Algebraic methods and their associated group theoretical methods have been used extensively in physics since their introduction by Wigner [1] and Racah [2, 3]. Since 1974, a general formulation of algebraic methods has emerged [4]. In this formulation, a quantum-mechanical many-body system is mapped onto an algebraic structure. The logic of the method is

Many-body system
↓
Choice of relevant degrees of freedom
↓
Quantization in terms of boson and/or fermion operators
↓
Algebraic structure (Lie algebra, Graded Lie algebra, ...)
↓
Computation of observables
↓
Comparison with experiment

The main ingredient of the method is the algebraic structure. The large majority of the applications make use of Lie algebras [5], although in recent years also graded Lie algebra (super-algebras) have been used [6].

In the last 40 years many algebraic models of physical systems have been introduced and developed, encompassing all fields of physics. Some of these models are:

a) Nuclear physics [7, 8]

The Interacting Boson Model, IBM-1, the Proton-Neutron Interacting Boson Model, IBM-2, the Interacting Boson Fermion Model, IBFM-1, and the Proton-Neutron Interacting Boson-Fermion Model, IBFM-2, have provided since 1974 a detailed description of medium mass and heavy nuclei.

b) Molecular physics [9]

The Vibron Model (VM) and the Electron-Vibron Model, EVM, have provided since 1981 a detailed description of molecules.

c) Hadronic physics [10, 11]

An algebraic model of hadrons was introduced in 1994 and used to describe both mesons and baryons.

d) Polymer physics [12, 13]

An algebraic model of polymer chains was introduced in 1999 and used to describe finite polymer chains, in particular the paraffin and related structures.

e) Cluster physics [14, 15]

The algebraic cluster model (ACM) was introduced in 2002 and used to describe properties of light nuclei.

f) Crystal physics [16, 17]

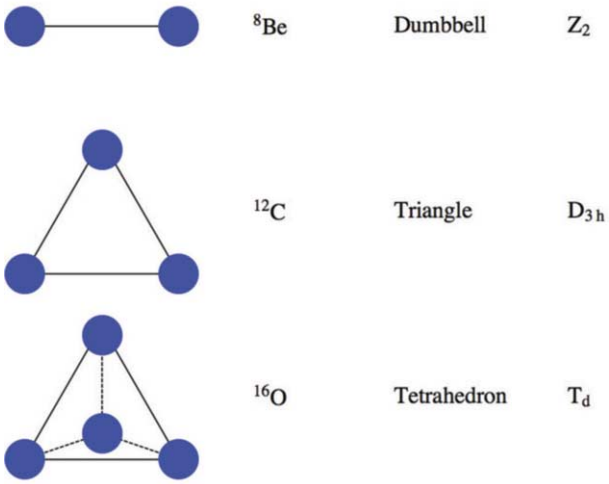

Fig. 1. – Cluster configurations for $k = 2, 3, 4$. Reproduced from [26] with permission.

The algebraic model of crystal vibrations (ACV) is the latest addition to the list as it was introduced in 2015 to describe properties of one- and two-dimensional crystals, in particular graphene sheets.

Reviews of the Interacting Boson Model and Interacting Boson Fermion Model have been given at previous "Enrico Fermi" schools [18, 19]. I will provide here a review of the Algebraic Cluster Model (ACM).

2. – Cluster structure of light nuclei

The cluster structure of light nuclei has a long history dating back to the 1930's with work of Wheeler [20] and Hafstad and Teller [21], followed by Dennison [22], and Kameny [23]. In 1965, Brink [24, 25] suggested specific geometric configurations for nuclei composed of k α-particles, here referred as $k\alpha$ nuclei. In particular, the suggested configurations of the ground state were, for $k = 2$ (^{8}Be) a dumbbell configuration with Z_2 symmetry, for $k = 3$ (^{12}C) an equilateral triangle with $D_{3\mathrm{h}}$ symmetry, and for $k = 4$ (^{16}O) a tetrahedron with T_d symmetry, as shown in fig. 1. In these lectures, an algebraic description of the geometric configurations of fig. 1 in terms of the algebraic cluster model (ACM) is given.

3. – The algebraic cluster model

The algebraic cluster model is based on the algebraic theory of molecules introduced in 1981 [27] and reviewed in [9]. It amounts to a bosonic quantization of the Jacobi variables according to the general quantization scheme [4] for problems with ν degrees of freedom in terms of the Lie algebra $U(\nu + 1)$. For $k\alpha$ structures, the number of degrees

TABLE I. – *Summary of ACM cases explicitly constructed.*

k	Nucleus	$U(3k-2)$	Discrete symmetry	Jacobi variables
2	^{8}Be	$U(4)$	Z_2	$\boldsymbol{\rho}$
3	^{12}C	$U(7)$	$D_{3\mathrm{h}}$	$\boldsymbol{\rho}, \boldsymbol{\lambda}$
4	^{16}O	$U(10)$	T_{d}	$\boldsymbol{\rho}$, $\boldsymbol{\lambda}$, $\boldsymbol{\eta}$

of freedom, removing the center-of-mass motion, is $\nu = 3k-3$, leading to the Lie algebra of $U(3k-2)$.

An explicit construction of the algebra and derivation of analytic formulas for energy levels, electromagnetic transition rates, matter and charge densities and associated form factors in electron scattering has been completed for cases $k = 2$ [27], $k = 3$ [14, 28] and $k = 4$ [15, 29-31]. It is summarized in table I and results will be given in the following subsections.

3˙1. *Classification of states*. – The discrete symmetry of clusters imposes conditions on the allowed quantum states. The mathematical method for determining the allowed states (*i.e.* constructing representations of the discrete group G) is the diagonalization of the so-called symmetry adapter operators. For cases $k = 2, 3, 4$ and identical constituents, one can exploit the isomorphism of the discrete point group with the permutation group S_{n}. The associated symmetry adapter operators are given in table II. For the ACM,

TABLE II. – *Symmetry adapter operators of* S_{n}.

Group G	Symmetry adapter
$Z_2 \sim S_2 \sim P$	Transposition (12)
$D_3 \sim S_3$	Transposition (12), Cyclic permutation (123)
$T_{\mathrm{d}} \sim S_4$	Transposition (12), Cyclic permutation (1234)

TABLE III. – *Labelling of representations.*

Group G	G label	S_{n} label	Degeneracy
$Z_2 \sim S_2 \sim P$	A	[2]	Singly
$D_3 \sim S_3$	A	[3]	Singly
	E	[21]	Doubly
$T_{\mathrm{d}} \sim S_4$	A	[4]	Singly
	F	[31]	Triply
	E	[22]	Doubly

formulated in terms of $U(3k-2)$ the construction is even simpler, since $U(3k-2)$ contains the harmonic oscillator group $U(3k-3)$ and the breaking of $U(3k-3)$ onto $S_{\rm n}$ was studied years ago by Kramers and Moshinsky [32]. One can therefore find the angular momentum and parity, L^P, content in a given representation of the discrete group, G. Representations can be labeled either by $S_{\rm n}$ or by the isomorphic discrete group G, as in table III. Here the representations of $S_{\rm n}$ are labelled by the Young tableau, while those of G are labelled by the standard notation used in molecular physics [33].

3˙1.1. Dumbbell configuration, $k=2$. Z_2 symmetry. An algebraic description of this configuration is given by the algebra of $U(4)$ [27], reviewed in [9]. This algebra is constructed with boson creation and annihilation operators, $b^\dagger_{\rho,m}, s^\dagger \equiv c_\alpha$ and $b_{\rho,m}, s \equiv c_\alpha$. Here $b^\dagger_{\rho,m}$, $b_{\rho,m}$ $(m=0,\pm1)$ are the quantization of the Jacobi variable $\boldsymbol{\rho}$, fig. 2 and its conjugate momentum, and $s^\dagger$, s is an auxiliary boson.

The bilinear products $G_{\alpha\beta} = c^\dagger_\alpha c_\beta$ $(\alpha,\beta = 1,\ldots,4)$ of creation and annihilation operators generate the Lie algebra of $U(4)$. Specifically these are

$$
\begin{aligned}
&(s^\dagger \times \tilde{s})^{(0)}, \\
&\left(b^\dagger_\rho \times \tilde{b}_\rho\right)^{(L)} \quad (L=0,1,2), \\
&\left(b^\dagger_\rho \times \tilde{s}\right)^{(1)}, \qquad \left(s^\dagger \times \tilde{b}_\rho\right)^{(1)},
\end{aligned}
\tag{3.1}
$$

where $\tilde{b}_{\rho,m} = (-)b_{\rho,-m}$, $\tilde{s} = s$. We consider here rotations and vibrations of the dumbbell configuration. States can be classified by a vibrational quantum number $v = 0,1,2,\ldots$ and a rotational quantum number L, $|v,L,M_L\rangle$. In the case in which the two constituents are identical (two α-particles) the dumbbell has $Z_2 \sim S_2 \sim P$ symmetry. All vibrational states v have symmetry A under Z_2 since the two particles are identical (fig. 2). The angular momentum content of each vibrational band is $A : L^P = 0^+, 2^+, 4^+, \ldots$, where the parity P has been added, although here is not an independent quantum number, $P = (-)^L$. The expected states $|v, L^P\rangle$ of a rotating and vibrating dumbbell are shown in fig. 3.

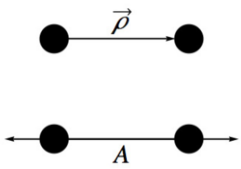

Fig. 2. – Jacobi vector $\boldsymbol{\rho}$ for a dumbbell configuration and its vibrations.

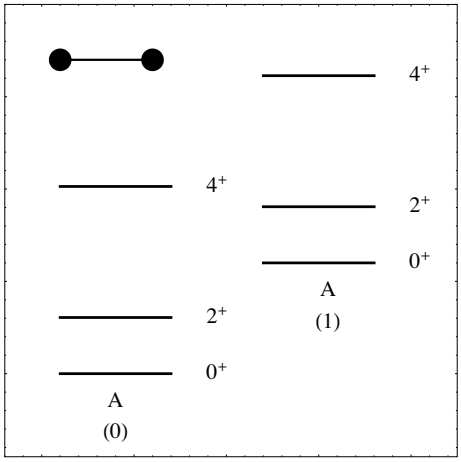

Fig. 3. – Expected states of a rotating and vibrating dumbbell configuration. Only states up to $v = 1$ are shown.

3˙1.2. Equilateral-triangle configuration, $k = 3$. D_{3h} symmetry. An algebraic description of this configuration is given by the algebra $U(7)$ [14, 28]. This algebra is constructed with boson creation operators $b^\dagger_{\rho,m}$, $b^\dagger_{\lambda,m}$, $s^\dagger \equiv c^\dagger_\alpha$, $(m = 0, \pm 1)$, $(\alpha = 1, \ldots, 7)$ and associated annihilation operators $b_{\rho,m}$, $b_{\lambda,m}$, s.

The two vector boson operators $b^\dagger_{\rho,m}$, $b^\dagger_{\lambda,m}$, $b_{\rho,m}$, $b_{\lambda,m}$ are the quantization of the two Jacobi variables

$$\vec{\rho} = (\vec{r}_1 - \vec{r}_2)/\sqrt{2}, \tag{3.2}$$

$$\vec{\lambda} = (\vec{r}_1 + \vec{r}_2 - 2\vec{r}_3)/\sqrt{6}.$$

The bilinear products $G_{\alpha\beta} = c^\dagger_\alpha c_\beta$ $(\alpha, \beta = 1, \ldots, 7)$ generate the Lie algebra of $U(7)$. A specific form is given in [14].

We consider here rotations and vibrations of an equilateral-triangle configuration. States can be classified as

$$\left| \left(v_1, v_2^{\ell_2} \right); t, K, L^P, M_L \right\rangle, \tag{3.3}$$

where t denotes the representations of D_{3h}, K the projection of the angular momentum on the intrinsic axis, L the angular momentum, and M_L its projection.

In the case in which the three constituents are identical (three α-particles), the triangular configuration of fig. 4 has D_{3h} symmetry. This imposes some conditions on the allowed values of K and L. In eq. (3.3), $(v_1, v_2^{\ell_2})$ label the vibrational states, with $v_1 = 0, 1, 2, \ldots$; $v_2 = 0, 1, 2 \ldots$; $\ell_2 = v, v-2, \ldots, 1$ or 0 (v_2 = odd or even). The fundamental vibrations of a triangular configuration are shown in fig. 5.

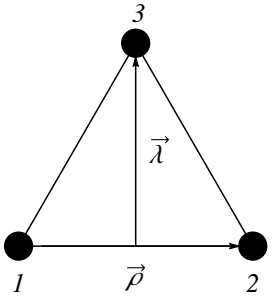

Fig. 4. – Jacobi variables $\boldsymbol{\rho}$, $\boldsymbol{\lambda}$ for an equilateral-triangle configuration.

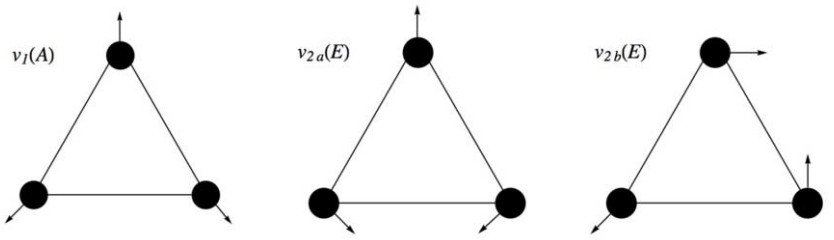

Fig. 5. – Fundamental vibrations of a triangular configuration (point group D_{3h}). The A vibration is singly degenerate, while E is doubly degenerate with components v_{2a}, v_{2b}.

For vibrational bands with $\ell_2 = 0, 1$, the allowed values of the angular momentum are for $(v_1, v_2^{\ell_2=0})$:

(3.4a)
$$\begin{aligned} &K = 3n, \quad n = 0, 1, 2, \ldots, \\ &L = 0, 2, 4, \ldots, \quad \text{for } K = 0, \\ &L = K, K+1, K+2, \ldots, \quad \text{for } K \neq 0, \end{aligned}$$

and for $(v_1, v_2^{\ell_2=1})$:

(3.4b)
$$\begin{aligned} &K = 3n+1, 3n+2, \quad n = 0, 1, 2 \ldots, \\ &L = K, K+1, K+2, \ldots. \end{aligned}$$

The parity is $P = (-)^K$. The vibrational band $(1,0^0)$ has the angular momenta $L^P = 0^+, 2^+, 3^-, 4^\pm, \ldots$, as the ground $(0,0^0)$, while the angular-momentum content of the doubly degenerate vibration $(0,1^1)$ is given by $L^P = 1^-, 2^\mp, 3^\mp, \ldots$. The expected states of a triangular configuration are shown in fig. 6.

3˙1.3. Tetrahedral configuration, $k = 4$. T_d symmetry. An algebraic description of this configuration is given by the algebra of $U(10)$ [15, 29-31]. This algebra is constructed with boson creation operators $b^\dagger_{\rho,m}$, $b^\dagger_{\lambda,m}$, $b^\dagger_{\eta,m}$, $s^\dagger \equiv c^\dagger_\alpha$ $(m = 0, \pm 1)$ $(\alpha = 1, \ldots, 10)$ and

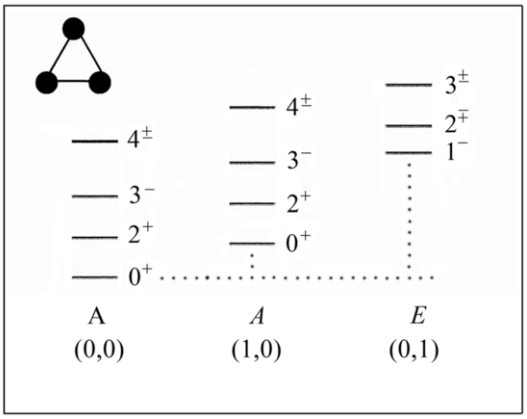

Fig. 6. – Expected states of a triangular configuration with D_{3h} symmetry.

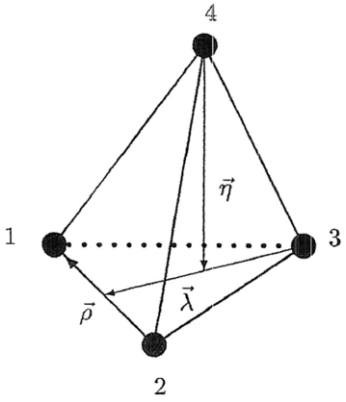

Fig. 7. – Jacobi coordinates in a tetrahedral configuration.

associated annihilation operators $b_{\rho,m}$, $b_{\lambda,m}$, $b_{\eta,m}$, s. The three vector boson operators $b^{\dagger}_{\rho,m}$, $b^{\dagger}_{\lambda,m}$, $b^{\dagger}_{\eta,m}$, $b_{\rho,m}$, $b_{\lambda,m}$, $b_{\eta,m}$ are the quantization of the three Jacobi variables

$$\vec{\rho} = (\vec{r}_1 - \vec{r}_2)/\sqrt{2}, \tag{3.5}$$

$$\vec{\lambda} = (\vec{r}_1 + \vec{r}_2 - 2\vec{r}_3)/\sqrt{6},$$

$$\vec{\eta} = (\vec{r}_1 + \vec{r}_2 + \vec{r}_3 - 3\vec{r}_4)/\sqrt{12},$$

shown in fig. 7. The bilinear products $G_{\alpha\beta} = c^{\dagger}_{\alpha} c_{\beta}$ $(\alpha, \beta = 1, \ldots, 10)$ generate the Lie algebra of $U(10)$. A specific form is given in [15].

We consider here rotations and vibrations of a tetrahedral configuration. States can

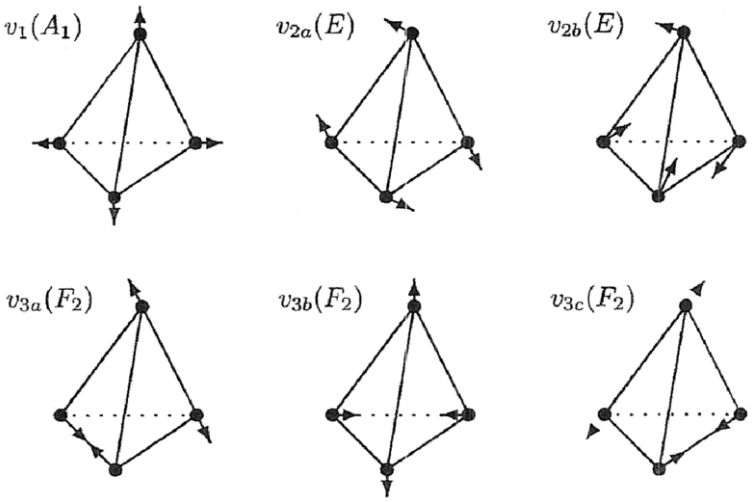

Fig. 8. – Fundamental vibrations of a tetrahedral configuration (point group T_d). The A_1 vibration is singly degenerate, E is doubly degenerate v_{2a}, v_{2b} and F_2 is triply degenerate, v_{3a}, v_{3b}, v_{3c}.

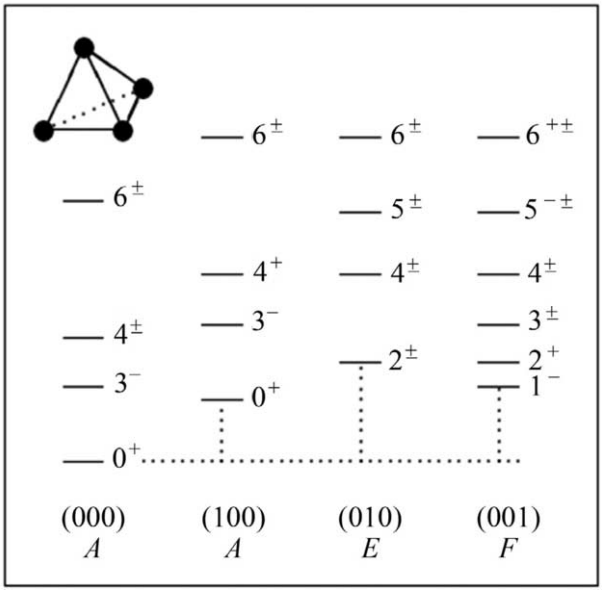

Fig. 9. – Expected states of a tetrahedral configuration. The rotational bands are labelled by (v_1, v_2, v_3); t. All states are symmetric under $S_4 \sim T_\mathrm{d}$. Note the unusual angular-momentum content of the rotational bands, with parity doubling.

be classified as

$$\left|\left(v_1, v_2^{\ell_2}, v_3^{\ell_3}\right); t, L^P, M_L\right\rangle, \tag{3.6}$$

where v_1, $v_2^{\ell_2}$, $v_3^{\ell_3}$ denote vibrational quantum numbers and t labels the representations of $T_{\rm d}$. In the case in which the constituents are identical (four α-particles), the tetrahedral configuration of fig. 7 has $T_{\rm d}$ symmetry. This imposes some conditions on the allowed values of L, which depend on t. A derivation of the allowed values is given in [15]. For the ground state, $t = A_1$, and for the fundamental vibrations, fig. 8, $t = A_1$, E, F_2, it can be summarized as follows:

$$
\begin{aligned}
&t = A_1, \quad L^P = 0^+, 3^-, 4^+, 6^\pm, \ldots, \text{ singly degenerate} \\
&t = E, \quad L^P = 2^\pm, 4^\pm, 5^\pm, 6^\pm, \ldots, \text{ doubly degenerate} \\
&t = F_2, \quad L^P = 1^-, 2^+, 3^\pm, 4^\pm, 5^{-,\pm}, 6^{+,\pm}, \ldots, \text{ triply degenerate.}
\end{aligned} \tag{3.7}
$$

The expected states of a tetrahedral configuration are shown in fig. 9.

3˙2. *Energy formulas.* – Energy levels in ACM can be obtained by diagonalizing the Hamiltonian, H. Computer programs have been written for all three cases, $U(4)$, $U(7)$, $U(10)$ [34]. These programs can deal with all situations encountered in 2-, 3- and 4-body problems, including both soft and rigid situations. For applications here, we consider only rigid situations and write down analytic formulas that can be used to analyze experimental data.

3˙2.1. Dumbbell configuration. Z_2 symmetry. The algebraic Hamiltonian describing roto-vibrations of a dumbbell configuration (diatomic molecule) is given in eqs. (2.108) and (2.112) of [9]. Written explicitly in terms of boson operators, it has the form

$$
\hat{H} = E_0' + A(\hat{D}^2 + \hat{L}^2) + B\hat{L}^2 \tag{3.8}
$$

with

$$
\begin{aligned}
\hat{D}_m &= \left(b_\rho^\dagger \tilde{s} + s^\dagger \tilde{b}_\rho\right)^{(1)}_m, \quad (m = 0, \pm 1), \\
\hat{L}_m &= \sqrt{2}\left(b_\rho^\dagger \times \tilde{b}_\rho\right)^{(1)}_m, \quad (m = 0, \pm 1).
\end{aligned} \tag{3.9}
$$

In this case, the Hamiltonian $\hat{H}$ has a dynamic symmetry $U(4) \supset SO(4) \supset SO(3) \supset SO(2)$.

The eigenvalues of H can be written in explicit analytic form as

$$
E(N, v, L, M_L) = E_0' - 4A(N+1)\left[v - \frac{v^2}{N+1}\right] + BL(L+1). \tag{3.10}
$$

Here N is the so-called vibron number, that is the boson number that characterizes the irreducible representations of $U(4)$. The vibrational quantum number v takes the values

$$
v = 0, 1, \ldots, \frac{N-1}{2} \quad \text{or} \quad \frac{N}{2}, \tag{3.11}
$$

for $N =$ odd or even, and the rotational quantum number L takes the integer values

$$L = 0, 1, 2, \ldots, (N - 2v). \tag{3.12}$$

For identical constituents, Z_2 symmetry, $L =$ even $= 0, 2, \ldots, (N-2v)$. In the limit $N \to \infty$, one obtains the semiclassical formula for the energy levels of a dumbbell configuration

$$E(v, L, M_L) = E_0 + \omega \left(v + \frac{1}{2} \right) + BL(L + 1), \tag{3.13}$$

where ω is the vibrational energy and B the inertial parameter $B = \frac{\hbar}{2I}$.

3˙2.2. Equilateral-triangle configuration. $D_{3\mathrm{h}}$ symmetry. The situation here is more complicated than in the previous subsection, since there is no dynamic symmetry corresponding to the rotation and vibration of a rigid symmetric top. The explicit form of the Hamiltonian is

$$\begin{aligned} H = {} & \xi_1 \left(s^\dagger s^\dagger - b^\dagger_\rho \cdot b^\dagger_\rho - b^\dagger_\lambda \cdot b^\dagger_\lambda \right) \left(\tilde{s}\tilde{s} - \tilde{b}_\rho \cdot \tilde{b}_\rho - \tilde{b}_\lambda \tilde{b}_\lambda \right) \\ & + \xi_2 \left[\left(b^\dagger_\rho \cdot b^\dagger_\rho - b^\dagger_\lambda \cdot b^\dagger_\lambda \right) \left(\tilde{b}_\rho \cdot \tilde{b}_\rho - \tilde{b}_\lambda \cdot \tilde{b}_\lambda \right) + 4 \left(b^\dagger_\rho \cdot b^\dagger_\lambda \right) \left(\tilde{b}_\lambda \cdot \tilde{b}_\rho \right) \right] \\ & + 2\kappa_1 \left(b^\dagger_\rho \times \tilde{b}_\rho + b^\dagger_\lambda \times \tilde{b}_\lambda \right)^{(1)} \cdot \left(b^\dagger_\rho \times \tilde{b}_\rho + b^\dagger_\lambda \times \tilde{b}_\lambda \right)^{(1)} \\ & + 3\kappa_2 \left(b^\dagger_\rho \times \tilde{b}_\lambda - b^\dagger_\lambda \times \tilde{b}_\rho \right)^{(0)} \cdot \left(b^\dagger_\lambda \times \tilde{b}_\rho - b^\dagger_\rho \times \tilde{b}_\lambda \right)^{(0)} . \end{aligned} \tag{3.14}$$

In a generic situation, this Hamiltonian needs to be diagonalized in the space of given vibron number N. However, in the limit $N \to \infty$, one can write down a semiclassical formula

$$\begin{aligned} E\left(v_1, v_2^{\ell_2}, K, L, M_L \right) = {} & E_0 + \omega_1 \left(v_1 + \frac{1}{2} \right) \\ & + \omega_2 (v_2 + 1) + BL(L + 1) + \kappa_2 \left(K \mp 2\ell_2 \right)^2 , \end{aligned} \tag{3.15}$$

which describes the energy levels of a symmetric top. States are classified as in eq. (3.3) and the values of K and L for given v_1 and v_2 are as in eq. (3.4).

3˙2.3. Tetrahedral configuration. T_{d} symmetry. Also here the situation is rather complicated since there is no dynamic symmetry corresponding to the rotation and vibration

of a spherical top. The explicit form of the Hamiltonian describing the vibrations is

$$
\begin{aligned}
H_{vib} = \xi_1 &\left(s^\dagger s^\dagger - b^\dagger_\rho \cdot b^\dagger_\rho - b^\dagger_\lambda \cdot b^\dagger_\lambda - b^\dagger_\eta \cdot b^\dagger_\eta\right) (\text{h.c.}) \\
&+\xi_2 \left[\left(-2\sqrt{2} b^\dagger_\rho \cdot b^\dagger_\eta + 2 b^\dagger_\rho \cdot b^\dagger_\lambda\right) (\text{h.c.})\right. \\
&\left. + \left(-2\sqrt{2} b^\dagger_\lambda \cdot b^\dagger_\eta + \left(b^\dagger_\rho \cdot b^\dagger_\rho - b^\dagger_\lambda \cdot b^\dagger_\lambda\right)\right) (\text{h.c.})\right] \\
&+\xi_3 \left[\left(2 b^\dagger_\rho \cdot b^\dagger_\eta + 2\sqrt{2} b^\dagger_\rho \cdot b^\dagger_\lambda\right) (\text{h.c.})\right. \\
&+ \left(2 b^\dagger_\lambda \cdot b^\dagger_\rho + \sqrt{2}\left(b^\dagger_\rho \cdot b^\dagger_\rho - b^\dagger_\lambda \cdot b^\dagger_\lambda\right)\right) (\text{h.c.}) \\
&\left. + \left(b^\dagger_\rho \cdot b^\dagger_\rho + b^\dagger_\lambda \cdot b^\dagger_\lambda - 2 b^\dagger_\eta \cdot b^\dagger_\eta\right) (\text{h.c.})\right] .
\end{aligned} \tag{3.16}
$$

The Hamiltonian describing rotations can be written as

$$
H_{rot} = \kappa_1 \vec{L} \cdot \vec{L} + \kappa_2 \left(\vec{L} \cdot \vec{L} + \vec{I}' \cdot \vec{I}'\right) , \tag{3.17}
$$

where $\vec{L}$ and $\vec{I}'$ denote the angular momentum in coordinate space and index space, respectively [15], the explicit form of which is

$$
\begin{aligned}
L_m &= \sqrt{2} \left[b^\dagger_\rho \times \tilde{b}_\rho + b^\dagger_\lambda \times b^\dagger_\lambda + b^\dagger_\eta \times b^\dagger_\eta\right]^{(1)}_m , \\
I'_\rho &= \sqrt{3}(-i) \left[b^\dagger_\lambda \times \tilde{b}_\eta - b^\dagger_\eta \times \tilde{b}_\lambda\right]^{(0)} , \\
I'_\lambda &= \sqrt{3}(-i) \left[b^\dagger_\eta \times \tilde{b}_\rho - b^\dagger_\rho \times \tilde{b}_\eta\right]^{(0)} , \\
I'_\eta &= \sqrt{3}(-i) \left[b^\dagger_\rho \times \tilde{b}_\lambda - b^\dagger_\lambda \times \tilde{b}_\rho\right]^{(0)} .
\end{aligned} \tag{3.18}
$$

Again, in a generic situation, this Hamiltonian needs to be diagonalized in the space of given vibron number N. For $N \to \infty$, one can write down a semiclassical formula

$$
\begin{aligned}
E(v_1, v_2, v_3; t, L^P, M_L) = E &+ \omega_1 \left(v_1 + \frac{1}{2}\right) \\
&+ \omega_2 (v_2 + 1) + \omega_3 \left(v_3 + \frac{3}{2}\right) + BL(L+1),
\end{aligned} \tag{3.19}
$$

which describes the energy levels of a spherical top. States are classified as in eq. (3.6) and the values of t and L^P for the ground state band and the fundamental vibrations are given in eq. (3.7).

3˙3. *Form factors and transition probabilities.* – The transition form factors are the matrix elements of $\sum_{i=1}^{k} \exp(i\vec{q} \cdot \vec{r}_i)$, where $\vec{q}$ is the momentum transfer and $\vec{r}_i$ is the

location of the α-particles. To do this calculation in ACM, one first converts the transition operator to algebraic form and then calculates the form factors

$$F_M(i \to f; q) = \left\langle \gamma_f, L_f, M | \hat{T}(q) | \gamma_i, L_i, M \right\rangle . \tag{3.20}$$

The transition probabilities $B(EL)$ can be extracted from the form factors in the long-wavelength limit

$$B(EL; i \to f) = (Ze)^2 \frac{[(2L+1)!!]^2}{4\pi(2L_i+1)} \lim_{q\to 0} \sum_M \frac{|F_M(i \to f; q)|^2}{q^{2L}} , \tag{3.21}$$

where Ze is the total electric charge of the cluster.

3˙3.1. Dumbbell configuration. Z_2 symmetry. Choosing the z-axis along the direction of the momentum transfer and using the fact that the two particles are identical, it is sufficient to consider the matrix elements of $e^{iqr_{2z}}$. After converting to Jacobi coordinates one has $e^{-iq\rho_z}$. The matrix elements of this operator can be obtained algebraically by the replacement

$$\rho_z \to \beta \hat{D}_z / X_D, \tag{3.22}$$

where β represents the scale of the coordinate and X_D is given by the reduced matrix elements of the dipole operator, eq. (3.9).

Explicit evaluation in the large-N limit gives

$$\begin{aligned} &F(0^+ \to L^P; q) = c_L j_L(q\beta), \\ &c_L^2 = \frac{2L+1}{4}[2 + 2P_L(-1)], \\ &c_0^2 = 1, \qquad c_2^2 = 5, \qquad c_4^2 = 9, \end{aligned} \tag{3.23}$$

where j_L is the spherical Bessel function, and P_L the Legendre polynomial. From these, one can obtain the $B(EL)$ values

$$B(EL; 0 \to L) = \left(\frac{Ze\beta^L}{2}\right)^2 \left(\frac{2L+1}{4\pi}\right) [2 + 2P_L(-1)]. \tag{3.24}$$

3˙3.2. Equilateral-triangle configuration. $D_{3\mathrm{h}}$ symmetry. Choosing again the z-axis along the direction of the momentum transfer and using the fact that the three particles are identical, it is sufficient here to consider the matrix elements of $\exp(-iq\sqrt{\frac{2}{3}}\lambda_z)$. By making the replacement

$$\sqrt{\frac{2}{3}}\lambda_z \to \beta \hat{D}_{\lambda,z} / X_D, \tag{3.25}$$

one can obtain the form factors, given explicitly, for $N \to \infty$, by

$$
\begin{aligned}
& F(0^+ \to L^P; q) = c_L j_L(q\beta), \\
& c_L^2 = \frac{2L+1}{9}\left[3 + 6P_L\left(-\frac{1}{2}\right)\right], \\
& c_0^2 = 1, \qquad c_2^2 = \frac{5}{4}, \qquad c_3^2 = \frac{35}{8}, \qquad c_4^2 = \frac{81}{64}.
\end{aligned} \tag{3.26}
$$

The corresponding $B(EL)$ values are

$$
B(EL; 0 \to L) = \left(\frac{Ze\beta^L}{3}\right)^2 \frac{2L+1}{4\pi}\left[3 + 6P_L\left(-\frac{1}{2}\right)\right]. \tag{3.27}
$$

3˙3.3. Tetrahedral configuration. $T_{\rm d}$ symmetry. The operator here is $\exp(-iq\sqrt{\frac{3}{4}}\eta_z)$ and the replacement is

$$
\sqrt{\frac{3}{4}}\eta_z \to \beta \hat{D}_{\eta,z}/X_D. \tag{3.28}
$$

One obtains

$$
\begin{aligned}
& F(0^+ \to L^P; q) = c_L j_L(q\beta), \\
& c_L^2 = \frac{2L+1}{16}\left[4 + 12P_L\left(-\frac{1}{3}\right)\right], \\
& c_0^2 = 1, \qquad c_3^2 = \frac{35}{9}, \qquad c_4^2 = \frac{7}{3}, \qquad c_6^2 = \frac{416}{8}
\end{aligned} \tag{3.29}
$$

and

$$
B(EL; 0 \to L) = \left(\frac{Ze\beta^L}{4}\right)^2 \frac{2L+1}{4\pi}\left[4 + 12P_L\left(-\frac{1}{3}\right)\right]. \tag{3.30}
$$

3˙4. *Cluster densities*. – All results in sect. **3**˙3 are for point-like constituents, with density

$$
\rho(\vec{r}) = \sum_{i=1}^{k} \delta(\vec{r} - \vec{r}_i). \tag{3.31}
$$

This situation is not realistic, since the constituent α-particles are not point-like. Assuming a Gaussian form of the density of the α-particle, one has the realistic cluster density

$$
\rho(\vec{r}) = \left(\frac{\alpha}{\pi}\right)^{3/2} \sum_{i=1}^{k} \exp\left[-\alpha(\vec{r} - \vec{r}_i)^2\right]. \tag{3.32}
$$

Here $\alpha = 0.56\,\mathrm{fm}^{-2}$ describes the form factor of the α-particle [35]. With the density eq. (3.32), the form factors become

$$F(0^+ \to L^P; q) = c_L j_L(q\beta) e^{-\frac{q^2}{4\alpha}}, \tag{3.33}$$

which represents the convolution of the form factor of the cluster with that of the α-particle. $B(EL)$ values, however, remain the same as in sect. **3**˙3 since in the limit $q \to 0$, $e^{-q^2/4\alpha} \to 1$.

The density of eq. (3.32) can be visualized by making an expansion into multipoles. By placing the particles at a distance β from the center of mass with spherical coordinates $(\beta, \theta_i, \phi_i)$ we then have [26]

$$\begin{aligned}\rho(\vec{r}) &= \left(\frac{\alpha}{\pi}\right)^{3/2} \sum_{i=1}^{k} \exp\left[-\alpha(\vec{r} - \vec{r}_i)^2\right] \\ &= \left(\frac{\alpha}{\pi}\right)^{3/2} e^{-\alpha(r^2+\beta^2)} 4\pi \sum_{\lambda\mu} i_\lambda(2\alpha\beta r) Y_{\lambda\mu}(\theta,\phi) \sum_{i=1}^{k} Y^*_{\lambda\mu}(\theta_i, \phi_i),\end{aligned} \tag{3.34}$$

where $i_\lambda(x) = j_\lambda(ix)/i^\lambda$ is the modified spherical Bessel function. The matter density and charge density for each configuration can be obtained from eq. (3.34) by multiplying it by A/k and Z/k, respectively. One should note that all results in sect. **3**˙3 can also be obtained from eq. (3.34) without making use of the algebraic approach, by taking the Fourier transform of the density.

3˙4.1. Dumbbell configuration. Z_2 symmetry. For Z_2 symmetry, the angles of the particles in eq. (3.34) are given by $(\theta_1, \phi_1) = (0, -)$ and $(\theta_2, \phi_2) = (\pi, -)$, and

$$\begin{aligned}\sum_{i=1}^{2} Y^*_{\lambda\mu}(\theta_i, \phi_i) &= \sqrt{\frac{2\lambda+1}{4\pi}} \left[\delta_{\mu,0} + \sqrt{\frac{(\lambda+\mu)!}{(\lambda-\mu)!}} P_\lambda^{-\mu}(-1)\right] \\ &= \delta_{\mu,0} \sqrt{\frac{2\lambda+1}{4\pi}} [1 + P_\lambda(-1)].\end{aligned} \tag{3.35}$$

This configuration has axial symmetry. In the multipole expansion, eq. (3.34), only $\mu = 0$ and $\lambda = \text{even} = 0, 2, 4, \ldots$ remain. The charge and matter densities of the dumbbell configuration are shown in fig. 10 as a function of β, in the range $\beta = 0$–$4\,\mathrm{fm}$. Figure 10 shows that the density, eq. (3.34) describes the entire range from united-constituent-particles ($\beta = 0$) to separated constituent particles ($\beta \to \infty$). Note that the density, eq. (3.34) describes also break-up into two fragments, as shown in the panel on the right-hand side of fig. 10.

3˙4.2. Equilateral-triangle configuration. $D_{3\mathrm{h}}$ symmetry. For the symmetry $D_{3\mathrm{h}}$ (equilateral triangle), the angles of the particles are given by $(\theta_1, \phi_1) = (0, -)$, $(\theta_2, \phi_2) = (2\pi/3, 0)$

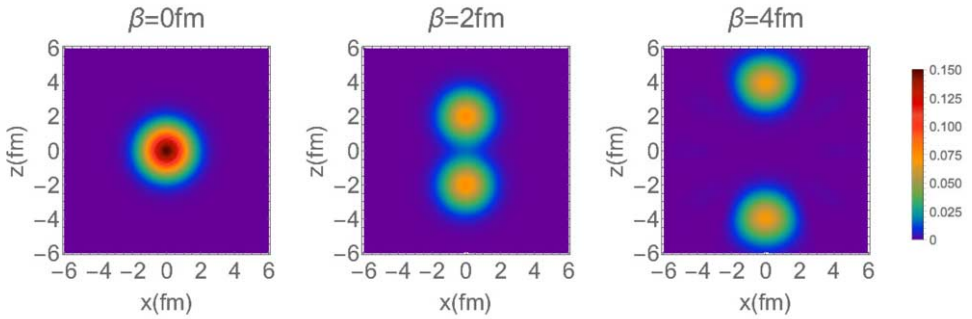

Fig. 10. – Densities of a $k = 2$ α-cluster as given in eq. (3.34). The value of $\alpha = 0.56\,\mathrm{fm}^{-2}$. The color scale is in fm^{-3}. Reproduced from [26] with permission.

and $(\theta_3, \phi_3) = (2\pi/3, \pi)$, and

$$\sum_{i=1}^{3} Y^*_{\lambda\mu}(\theta_i, \phi_i) = \sqrt{\frac{2\lambda+1}{4\pi}} \left[\delta_{\mu,0} + \sqrt{\frac{(\lambda+\mu)!}{(\lambda-\mu)!}} P_\lambda^{-\mu}\left(-\frac{1}{2}\right)\left(1+(-1)^\mu\right)\right] \tag{3.36}$$
$$= \left\{ \begin{array}{ll} \sqrt{\frac{2\lambda+1}{4\pi}}\left[1+2P_\lambda\left(-\frac{1}{2}\right)\right]; & \mu = 0 \\ \sqrt{\frac{2\lambda+1}{4\pi}}\sqrt{\frac{(\lambda+\mu)!}{(\lambda-\mu)!}}\,2P_\lambda^{-\mu}\left(-\frac{1}{2}\right); & \mu = 2\kappa \neq 0 \end{array} \right\},$$

where $\kappa = 1, 2, \ldots$, and $\mu \leq \lambda$.

For this configuration, the remaining multipoles are $\lambda = 0, 2, 3, 4, \ldots$, corresponding to the fact that the density is invariant under D_3 transformations and thus belongs to the A representation of D_3 [14]. The charge (and matter) densities of a triangular configuration are shown in fig. 11 as a function of β.

3˙4.3. Tetrahedral configuration. T_d symmetry. For the symmetry T_d (tetrahedron), the angles of the particles are given by $(\theta_1, \phi_1) = (0, -)$, $(\theta_2, \phi_2) = (\gamma, 0)$, $(\theta_3, \phi_3) = (\gamma, 2\pi/3)$ and $(\theta_4, \phi_4) = (\gamma, 4\pi/3)$ with $\cos\gamma = -1/3$, and

$$\sum_{i=1}^{4} Y^*_{\lambda\mu}(\theta_i, \phi_i) = \sqrt{\frac{2\lambda+1}{4\pi}} \left[\delta_{\mu,0} + \sqrt{\frac{(\lambda+\mu)!}{(\lambda-\mu)!}} P_\lambda^{-\mu}\left(-\frac{1}{3}\right)\left(1+2\cos\frac{2\mu\pi}{3}\right)\right] \tag{3.37}$$
$$= \left\{ \begin{array}{ll} \sqrt{\frac{2\lambda+1}{4\pi}}\left[1+3P_\lambda\left(-\frac{1}{3}\right)\right]; & \mu = 0 \\ \sqrt{\frac{2\lambda+1}{4\pi}}\sqrt{\frac{(\lambda+\mu)!}{(\lambda-\mu)!}}\,3P_\lambda^{-\mu}\left(-\frac{1}{3}\right); & \mu = 3\kappa \neq 0 \end{array} \right\},$$

where $\kappa = 1, 2, 3, \ldots$, and $\mu \leq \lambda$.

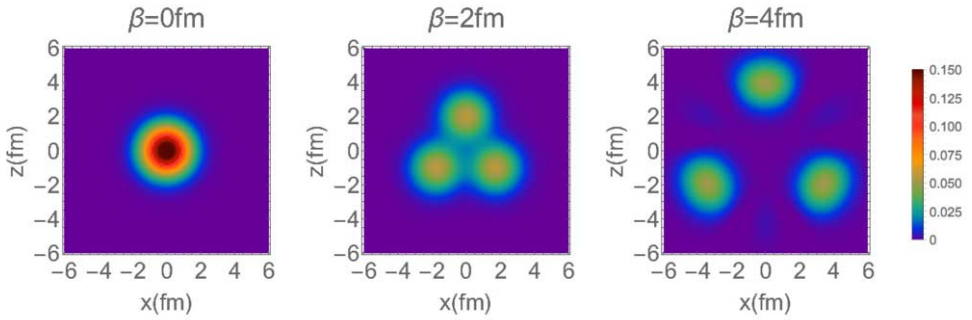

Fig. 11. – Densities of a $k = 3$ α-cluster as given in eq. (3.34). The value of $\alpha = 0.56\,\mathrm{fm}^{-2}$. The color scale is in fm^{-3}. Reproduced from [26] with permission.

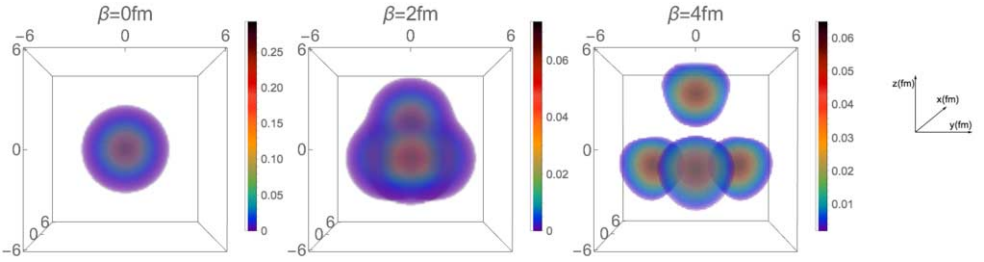

Fig. 12. – Densities of a $k = 4$ α-cluster as given in eq. (3.37). The value of $\alpha = 0.56\,\mathrm{fm}^{-2}$. The color scale is in fm^{-3}. Reproduced from [26] with permission.

For this configuration, the remaining multipoles are $\lambda = 0, 3, 4, 6, \ldots$, corresponding to the A representation of the tetrahedral group, T_d [15]. The charge and matter densities of a tetrahedral configuration are shown in fig. 12.

3˙5. *Moments of inertia and radii.* – From the density eq. (3.34) one can calculate the moments of inertia and radii. The three components of the moment of inertia are given by

$$I_x = \int (y^2 + z^2)\rho(\vec{r})\mathrm{d}^3\vec{r}, \tag{3.38}$$

$$I_y = \int (x^2 + z^2)\rho(\vec{r})\mathrm{d}^3\vec{r},$$

$$I_z = \int (x^2 + y^2)\rho(\vec{r})\mathrm{d}^3\vec{r},$$

and radii by

$$\langle r^2 \rangle = \int r^2 \rho(\vec{r})\mathrm{d}^3\vec{r}. \tag{3.39}$$

3˙5.1. Dumbbell configuration. Z_2 symmetry. Introducing the appropriate normalization, one has

$$I_x = I_y = Am\beta^2 + \frac{Am}{\alpha}\,, \qquad I_z = \frac{Am}{\alpha}\,, \tag{3.40}$$

where $A = 4k = 8$, corresponding to a prolate top, and

$$\langle r^2\rangle^{1/2} = \sqrt{\frac{3}{2\alpha} + \beta^2}. \tag{3.41}$$

3˙5.2. Equilateral-triangle configuration, $k = 3$. $D_{3\mathrm{h}}$ symmetry. In this case [14]

$$I_x = I_z = \frac{1}{2}Am\beta^2 + \frac{Am}{\alpha}\,, \qquad I_y = Am\beta^2 + \frac{Am}{\alpha}\,, \tag{3.42}$$

where $A = 4k = 12$, corresponding to an oblate top, and

$$\langle r^2\rangle^{1/2} = \sqrt{\frac{3}{2\alpha} + \beta^2}. \tag{3.43}$$

3˙5.3. Tetrahedral configuration, $k = 4$. T_{d} symmetry. Here

$$I_x = I_y = I_z = \frac{2}{3}Am\beta^2 + \frac{Am}{\alpha}\,, \tag{3.44}$$

where $A = 4k = 16$, corresponding to a spherical top, and

$$\langle r^2\rangle^{1/2} = \sqrt{\frac{3}{2\alpha} + \beta^2}. \tag{3.45}$$

4. – Evidence for cluster structures

The ACM provides a simple way to analyze experimental data, thus determining whether or not the symmetries Z_2, $D_{3\mathrm{h}}$, and T_{d} appear in the spectra of ^{8}Be, ^{12}C and ^{16}O.

4˙1. *Energies*.

4˙1.1. Dumbbell configuration. Z_2 symmetry. Energy levels for this configuration can be analyzed with eq. (3.13). A comparison with data in ^{8}Be [36] is shown in fig. 13. The occurrence of a rotational band in the experimental spectrum is clearly seen in fig. 14, where the energy of the states is shown as a function of $L(L+1)$. No evidence for the vibrational bands is reported in [36].

From the value of $B = \frac{\hbar}{2I}$ extracted from the experimental energy difference $E_{2_1^+} - E_{0_1^+}$, one can determine the moment of inertia $I \equiv I_x = I_y$ and from eq. (3.40) the value of $\beta = 1.82\,\mathrm{fm}$ [37].

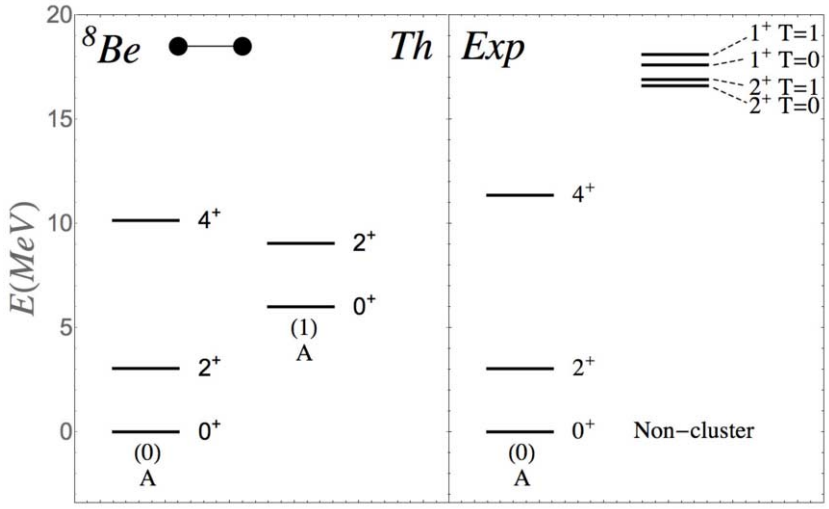

Fig. 13. – Comparison between the cluster spectrum and the experimental spectrum [36] of ^{8}Be. In panel (Th), $D = 6\,\text{MeV}$, $B = 0.507\,\text{MeV}$. Figure adapted from [37].

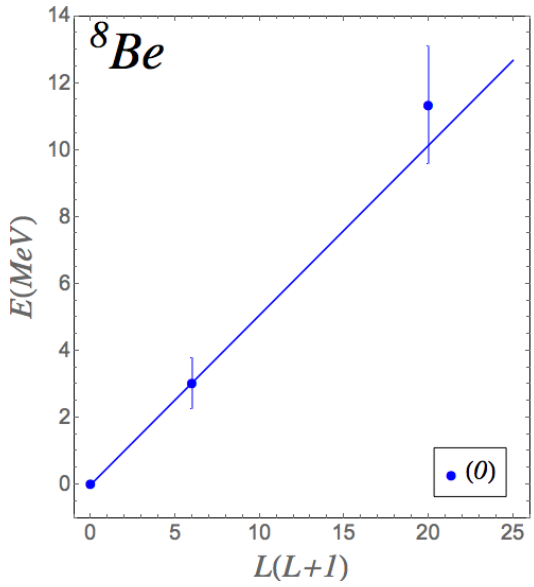

Fig. 14. – Observed cluster rotational band in ^{8}Be, $v = 0$. The theoretical line is given by eq. (3.13) with $B = 0.507\,\text{MeV}$. The experimental bar is the width Γ. Figure adapted from [37].

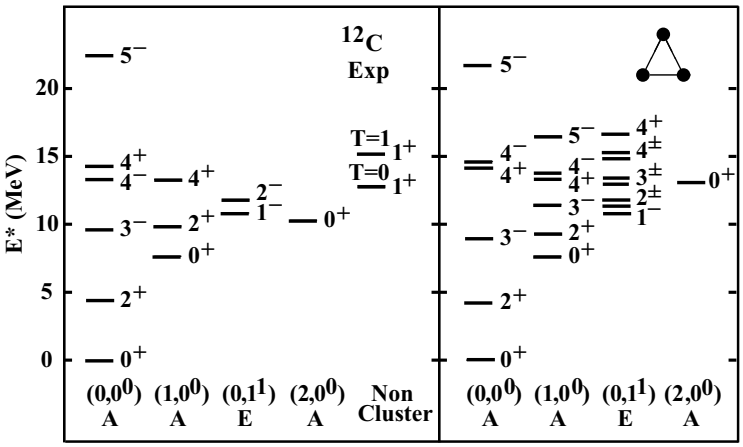

Fig. 15. – Comparison between the cluster spectrum and the experimental spectrum of ^{12}C [39-41]. Figure reproduced from [41] with permission.

4˙1.2. Equilateral-triangle configuration. D_{3h} symmetry. Recent experiments [38-41] have confirmed the occurrence of D_{3h} symmetry in ^{12}C. Energy levels have been analyzed with a variation of eq. (3.15) which includes anharmonic terms. The results are shown in figs. 15 and 16. One can see here the occurrence of not only rotational bands with angular-momentum content expected from D_{3h} symmetry, but also the occurrence of the fundamental vibrations of the triangle of fig. 5 $(1, 0^0)$ and $(0, 1^1)$ with symmetry A and E, respectively.

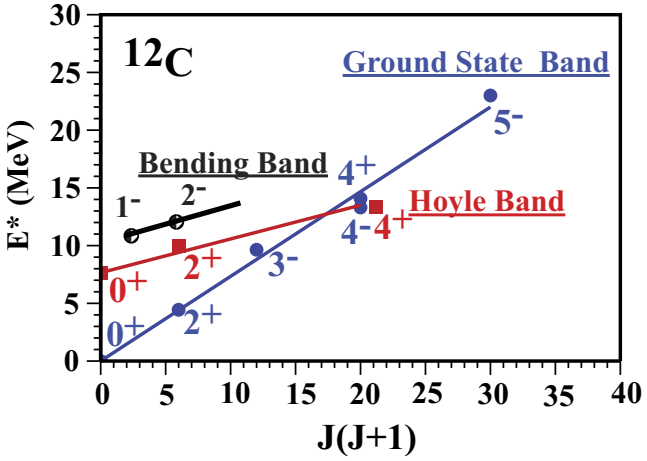

Fig. 16. – Rotational bands in ^{12}C. Figure reproduced from [41] with permission.

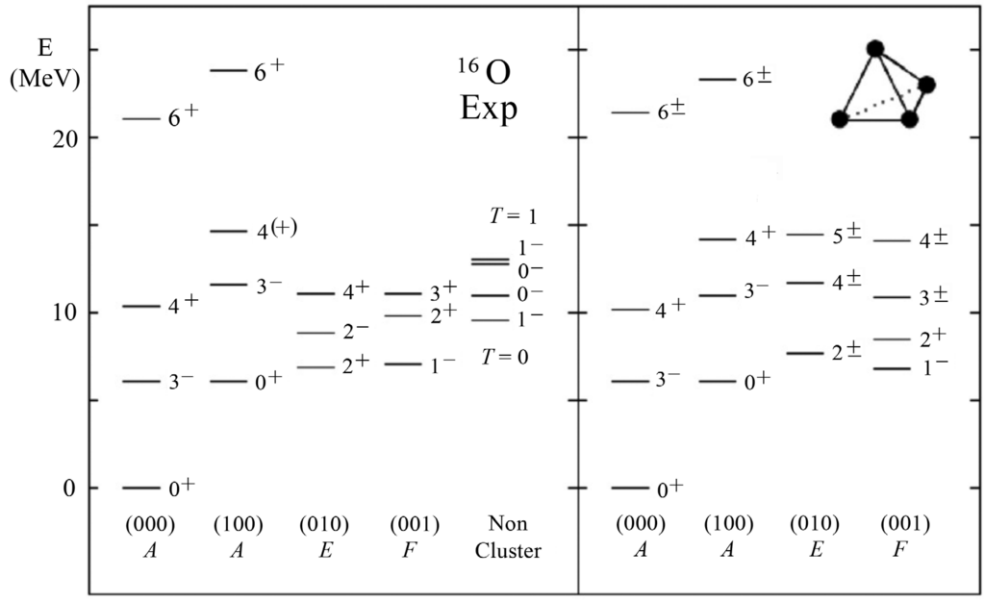

Fig. 17. – Comparison between the cluster spectrum and the experimental spectrum of ^{16}O. Figure reproduced from [15] with permission.

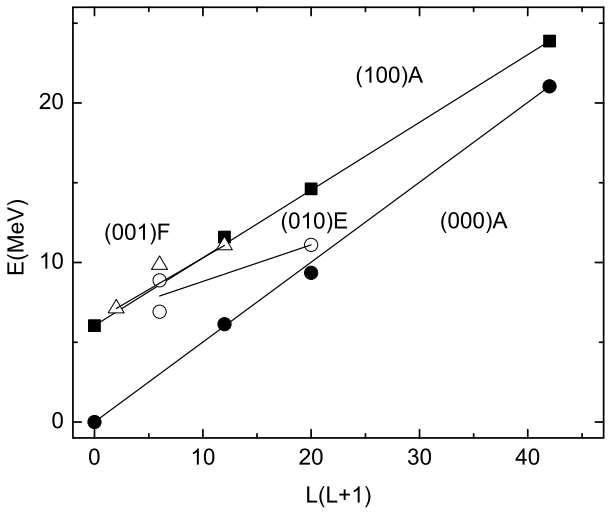

Fig. 18. – Rotational bands in ^{16}O. Figure reproduced from [15] with permission.

4˙1.3. Tetrahedral configuration. $T_{\rm d}$ symmetry. The occurrence of $T_{\rm d}$ symmetry in ^{16}O was emphasized by Robson [42, 43] in the 1970's and more recently revisited in [15]. Energy levels have been analyzed with eq. (3.19). A comparison with data is shown in figs. 17 and 18.

TABLE IV. – *Comparison between calculated and experimental $B(EL)$ values in* ^{8}Be. *Units* e^2fm^{2L}.

$B(EL; L^P \to 0^+)$	Th	Exp	$E(L^P)$	Th	Exp
$B(E2; 2^+ \to 0^+)$	14.0	21.0(23)	$E(2^+)$	3060	3030
$B(E4; 4^+ \to 0^+)$	153.3		$E(4^+)$	10200	11350

TABLE V. – *Comparison between calculated and experimental $B(EL)$ values in* ^{12}C. *Units* e^2fm^{2L}. *The value* $\beta = 1.9$ fm *is estimated from the elastic form factor measured in electron scattering.*

$B(EL; L^P \to 0^+)$	Th	Exp	$E(L^P)$	Th	Exp
$B(E2; 2^+ \to 0^+)$	9.3	7.6(4)	$E(2^+)$	4400	4439
$B(E3; 3^- \to 0^+)$	84	103(17)	$E(3^-)$	9640	9641
$B(E4; 4^+ \to 0^+)$			$E(4^+)$	14670	14080

4˙2. *Electromagnetic transition rates.*

4˙2.1. Dumbbell configuration. Z_2 symmetry. Electromagnetic transition rates and $B(EL)$ values can be analyzed by making use of eq. (3.24). A comparison with data is shown in table IV. In this table, the experimental value is estimated from ref. [44] using the Green's function Monte Carlo method (GFMC). The value of $\beta = 1.82$ fm is obtained from the moment of inertia.

4˙2.2. Equilateral-triangle configuration. D_{3h} symmetry. $B(EL)$ values along the ground state band can be analyzed using eq. (3.27). A comparison with data is shown in table V.

4˙2.3. Tetrahedral configuration. T_d symmetry. $B(EL)$ values for this configuration can be analyzed using eq. (3.29). A comparison with data is shown in table VI.

4˙3. *Form factors.* – Form factors in electron scattering can be simply derived by making use of the formulas given in sect. **3˙3** in the rigid case, or, in the more general

TABLE VI. – *Comparison between calculated and experimental $B(EL)$ values in* ^{16}O. *Units* e^2fm^{2L}. *The value* $\beta = 2.0$ fm *is estimated form the elastic form factor.*

$B(EL; L^P \to 0^+)$	Th	Exp	$E(L^P)$	Th	Exp
$B(E3; 3^- \to 0^+)$	181	205(10)	$E(3^-)$	6132	6130
$B(E4; 4^+ \to 0^+)$	338	378(133)	$E(4^+)$	10220	10356
$B(E6; 6^+ \to 0^+)$	8245		$E(6^+)$	21462	21052

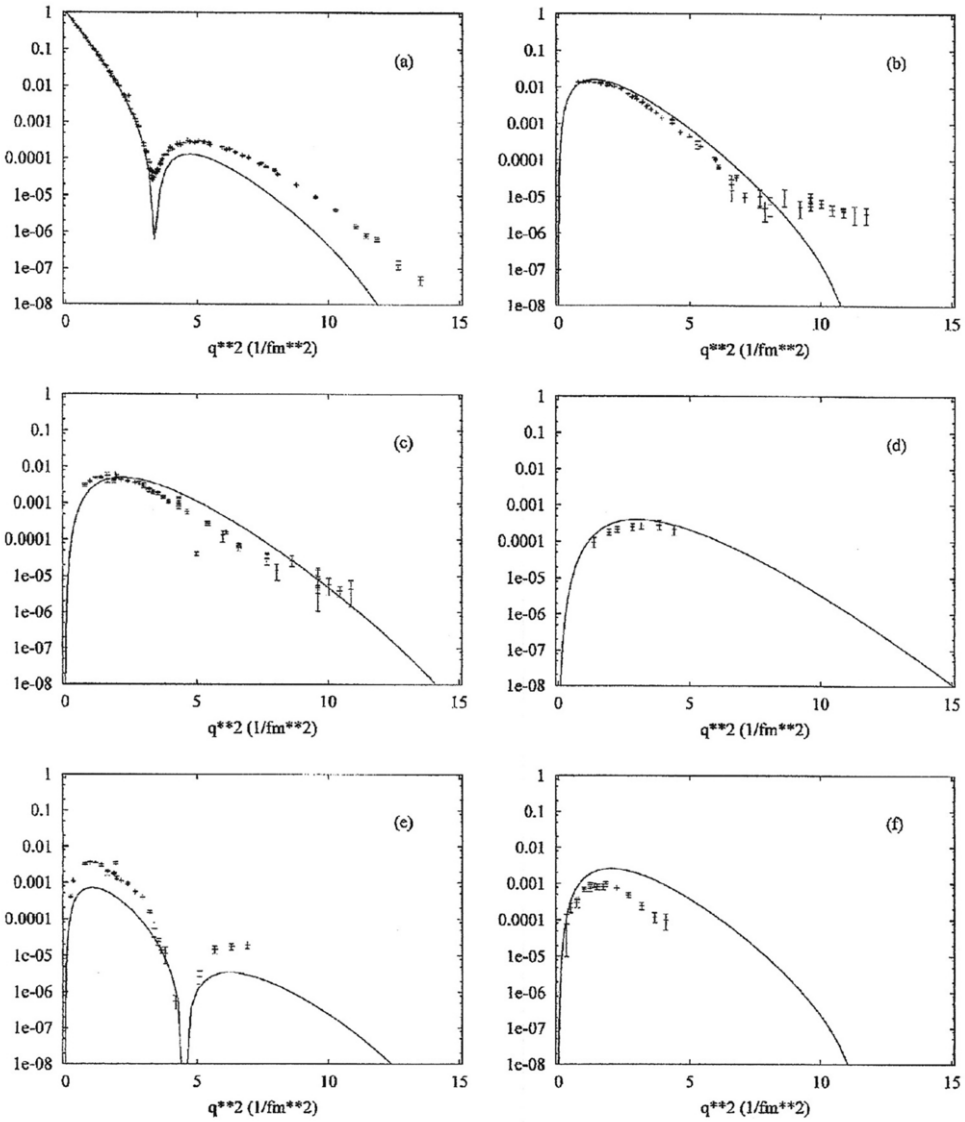

Fig. 19. – Comparison between the experimental form factors $|F(0_1^+ \to L_i^P; q)|^2$ of ^{12}C for the final states (a) $L_i^P = 0_1^+$ (elastic), (b) $L_i^P = 2_1^+$, (c) $L_i^P = 3_1^-$, (d) $L_i^P = 4_1^+$, (e) $L_i^P = 0_2^+$, and (f) $L_i^P = 1_1^-$ and those obtained for the oblate top. Reproduced from [14] with permission.

situation, by evaluating the matrix elements of the operator $\hat{T}(q)$ of eq. (3.20) in the wave functions obtained by diagonalizing the Hamiltonian of sect. **3**˙2.

4˙3.1. Dumbbell configuration. Z_2 symmetry. The nucleus ^{8}Be is unstable and therefore form factors in electron scattering cannot be measured.

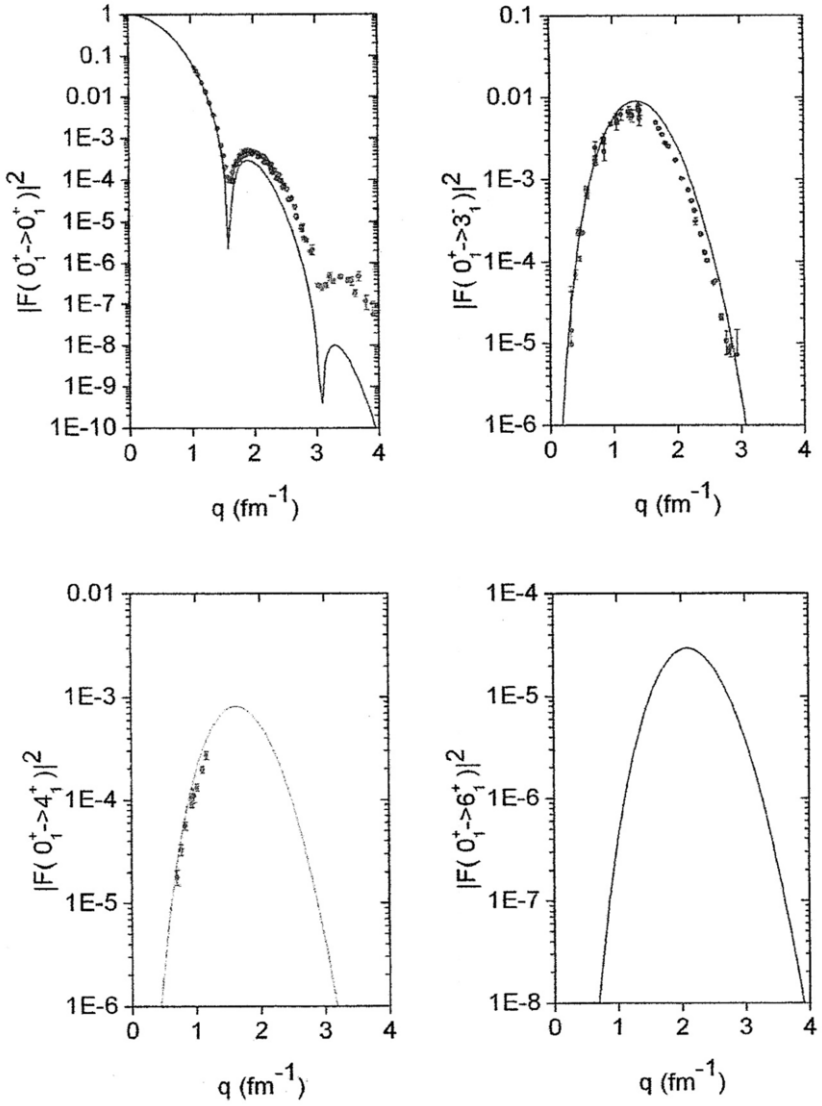

Fig. 20. – Comparison between the experimental form factors $|F(0_1^+ \rightarrow L_i^P)|^2$ of ^{16}O for the final states $L_i^P = 0_1^+, 3_1^-, 4_1^+, 6_1^+$ and those obtained for the spherical top. Reproduced from [15] with permission.

4˙3.2. Equilateral-triangle configuration. D_{3h} symmetry. Form factors in ^{12}C have been extensively investigated. In the rigid case, only states in the ground-state band are excited with form factors given by eq. (3.26) and no excitation of the vibrational bands occurs. Since experimentally excitation of these bands occurs, although with a small strength, one needs in this case to do a calculation with the general algebraic Hamiltonian, eq. (3.14) [14]. The resulting form factors are shown in fig. 19, where they are compared with experimental data.

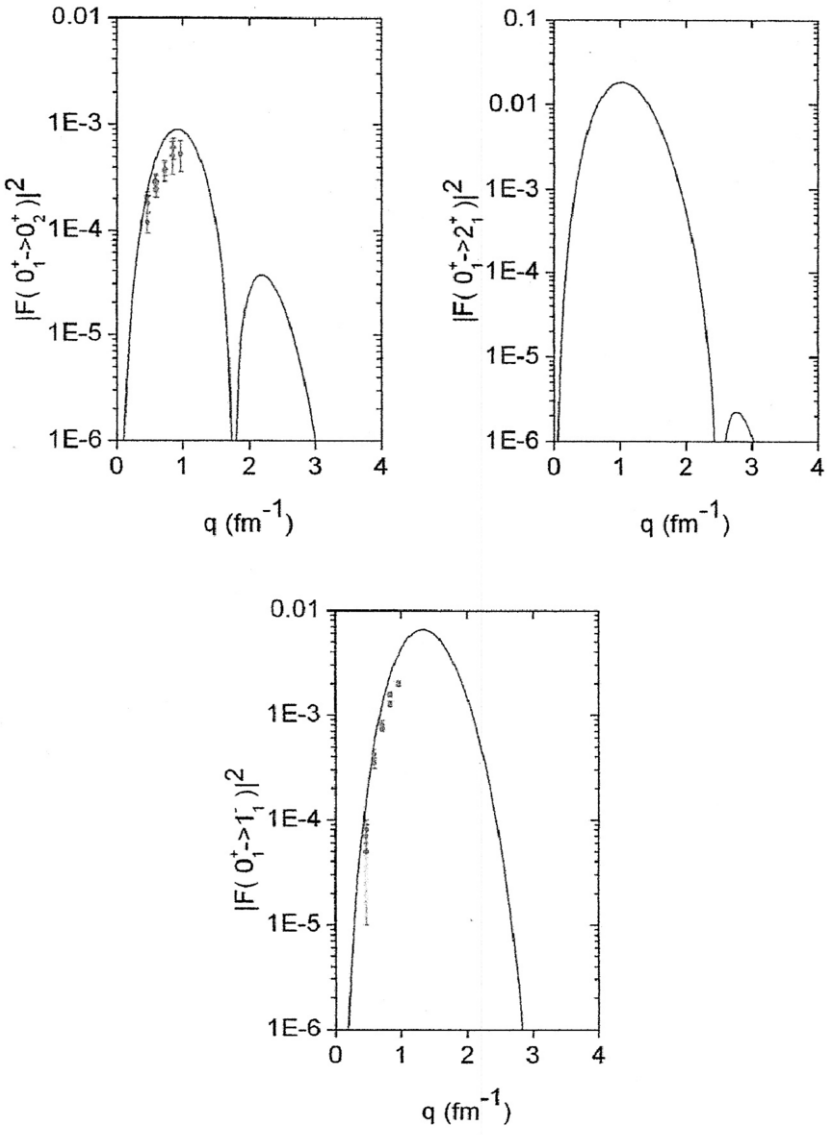

Fig. 21. – Comparison between the experimental form factors $|F(0_1^+ \to L_i^P)|^2$ of ^{16}O for the final states $L_i^P = 0_2^+, 2_1^+, 1_1^-$ and those obtained for the spherical top. Reproduced from [15] with permission.

4·3.3. Tetrahedral configuration. $T_{\rm d}$ symmetry. Form factors in ^{16}O have also been extensively investigated. In the rigid case, the form factors are given by eq. (3.29). Since also here excitation of the vibrational bands occurs, one needs to do a full calculation [15]. The resulting form factors are shown in figs. 20 and 21, where they are compared with experimental data.

5. – Breaking of the cluster structure. Non-cluster states

The cluster model assumes that $k\alpha$ nuclei are composed of α-particles. However, these in turn are composed of two protons and two neutrons. At some excitation energy in the nucleus, the α-particle structure may break. Non-cluster states can be in some cases clearly identified, since some states are forbidden by the discrete symmetry. Specifically, for Z_2 symmetry (^{8}Be), 1^+ states cannot be formed, for D_{3h} symmetry (^{12}C), 1^+ states cannot be formed, and for T_d symmetry (^{16}O), 0^- states cannot be formed. These are signatures of non-cluster states. In addition, since α-particles have isospin $T = 0$, states with $T = 1$ cannot be formed. This is another signature of non-cluster states. The energy at which non-cluster states occur is shown in figs. 13, 15 and 17. It is ~ 15 MeV in ^{8}Be, ~ 13 MeV in ^{12}C and ~ 10 MeV in ^{16}O. Above these energies, cluster states co-exist with non-cluster states.

6. – Softness and higher-order corrections

Equations (3.13), (3.15) and (3.19) describe rigid situations. As mentioned in previous sections, soft (non-rigid) situations can be described by diagonalizing the full algebraic Hamiltonian. However, one can also write, for comparison with experimental data, simpler analytic expressions for non-rigid situations.

6˙1. *Dumbbell configuration. Z symmetry.* – An analytic formula including anharmonic corrections and vibration-rotation interaction is

$$E = E_0 + \omega\left(v+\frac{1}{2}\right)\left(1-\frac{v+1/2}{N}\right) + BL(L+1) + B'[L(L+1)]^2 + \lambda\left(v+\frac{1}{2}\right)L(L+1), \tag{6.1}$$

where $1/N$ is called anharmonicity parameter.

6˙2. *Equilateral-triangle configuration. D_{3h} symmetry.* – In this case an analytic expression is

$$E = E_0 + \omega_1\left(v_1+\frac{1}{2}\right)\left(1-\frac{v_1+1/2}{N}\right) + \omega_2(v_2+1)\left(1-\frac{v_2+1}{N+1/2}\right) + BL(L+1) + (A-B)(K\mp 2\ell_2)^2 + B'[L(L+1)]^2 + \left[\lambda_1\left(v_1+\frac{1}{2}\right)+\lambda_2(v_2+1)\right]L(L+1). \tag{6.2}$$

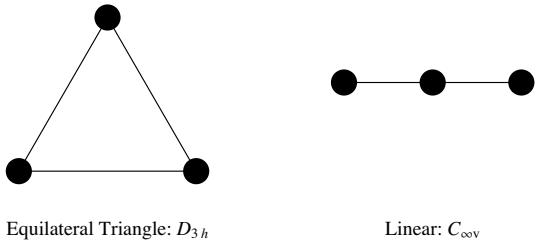

Fig. 22. – Possible cluster configurations of three particles.

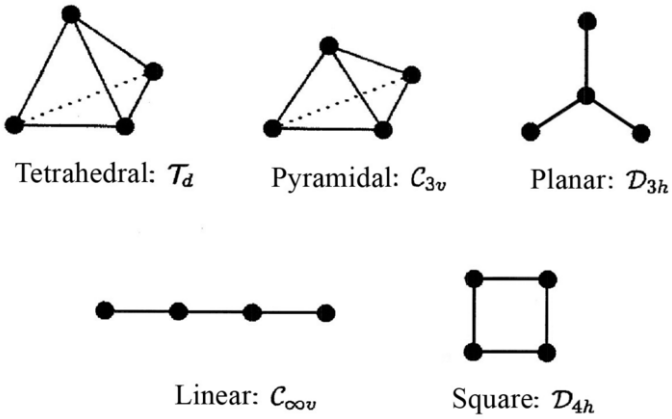

Fig. 23. – Possible cluster configurations of four particles.

6˙3. *Tetrahedral configuration. $T_{\rm d}$ symmetry.* – The effect of anharmonicities here can be written as

$$E = E_0 + \sum_{i=1}^{3} \omega_i v_i + \sum_{i,j=1}^{3} x_{ij} v_i v_j + BL(L+1) + \left(\sum_{i=1}^{3} \lambda_i v_i \right) L(L+1) + B'[L(L+1)]^2. \tag{6.3}$$

7. – Other geometric configurations

Within the ACM it is possible to provide analytic formulas for energies and electromagnetic transition rates for all possible geometric configurations and, most importantly, by diagonalizing the full algebraic Hamiltonian, it is possible to study non-rigid situation intermediate between two or more geometric situations and thus study the transitions between these, called ground-state phase transitions [45]. The possible geometric configurations for three and four α-particles are shown in figs. 22 and 23.

Another situation that can be studied with ACM is that in which the ground state has a different geometric configuration than the excited states. In the interpretation of the previous sect. **4**, the excited states are (large amplitude) vibrations of the ground state configuration. An alternative interpretation was given by Brink [24, 25], in which the excited states have a different geometric configuration of the ground state. Specifically, in ^{12}C, the ground state was suggested to be an equilateral triangle (D_{3h} symmetry) while the excited state was suggested to be linear ($C_{\infty v}$ symmetry). Similarly in ^{16}O, the ground state was suggested to be a tetrahedron (T_d symmetry) while the excited state was suggested to be a square (D_{4h} symmetry). This situation, in which the symmetry of the state changes as a function of excitation energy is called an excited state quantum phase transitions (ESQPT) [46].

8. – Conclusions

The algebraic cluster model (ACM) provides a framework in which experimental data in $k\alpha$ nuclei can be analyzed. The data show evidence of cluster structure in ^{8}Be, (Z_2 symmetry), in ^{12}C (D_{3h} symmetry) and ^{16}O (T_d symmetry). The evidence is clear for the ground-state rotational bands, but less so for the vibrational bands.

A remaining questions is the extent to which clustering appears in other $k\alpha$ nuclei, specifically, ^{20}Ne, ^{24}Mg and ^{28}Si which were assigned by Brink [24, 25] to D_{3h}, D_{2h} and D_{3v} symmetry, respectively.

* * *

This work was performed in part under DOE Grant DE-FG02-91ER40608. I wish to thank V. Della Rocca for preparing some of the figures (figs. 2–5, 13, 22) shown in these lecture notes and M. Gai for giving permission and providing files of figs. 15 and 16.

REFERENCES

[1] WIGNER E., *Phys. Rev.*, **51** (1937) 106.
[2] RACAH G., *Phys. Rev.*, **76** (1949) 1352.
[3] RACAH G., *Group Theory and Spectroscopy*, Mimeographed Lecture Notes, Princeton, New Jersey (1951). Reprinted in *Springer Tracts Mod. Phys.*, **37** (1965) 28.
[4] IACHELLO F., in *Lie Algebras, Cohomologies and Applications of Quantum Mechanics*, edited by KAMRAN N. and OLVER P., *Contemporary Mathematics*, **160** (American Mathematical Society, Providence, RI, USA) 1994, p. 151.
[5] IACHELLO F., *Lie Algebras and Applications*, 2nd edition, *Lect. Notes Phys.*, Vol. **891** (Springer, Berlin) 2015.
[6] IACHELLO F., in *Latin-American School of Physics XXXV ELAF*, *AIP Conf. Proc.*, **744** (2015) 85.
[7] IACHELLO F. and ARIMA A., *The Interacting Boson Model* (Cambridge University Press, Cambridge) 1987.
[8] IACHELLO F. and VAN ISACKER P., *The Interacting Boson-Fermion Model* (Cambridge University Press, Cambridge) 1991.

[9] IACHELLO F. and LEVINE R. D., *Algebraic Theory of Molecules* (Oxford University Press, Oxford) 1995.
[10] BIJKER R., IACHELLO F. and LEVIATAN A., *Ann. Phys. (N.Y.)*, **236** (1994) 69.
[11] BIJKER R., IACHELLO F. and LEVIATAN A., *Ann. Phys. (N.Y.)*, **284** (2000) 89.
[12] IACHELLO F. and TRUINI P., *Ann. Phys. (N.Y.)*, **276** (1999) 120.
[13] IACHELLO F. and OSS S., *Eur. Phys. J. D*, **19** (2002) 307.
[14] BIJKER R. and IACHELLO F., *Ann. Phys. (N.Y.)*, **298** (2002) 334.
[15] BIJKER R. and IACHELLO F., *Nucl. Phys. A*, **957** (2017) 154.
[16] IACHELLO F., DIETZ B., MISKI-OGLU M. and RICHTER A., *Phys. Rev. B*, **91** (2015) 214307.
[17] DIETZ B., IACHELLO F. and MACEK M., *Crystals*, **7** (2017) 246.
[18] IACHELLO F., *Proceedings of the International School "Enrico Fermi", Course CLIII*, edited by MOLINARI A., RICCATI L., ALBERICO W. M. and MORANDO M. (SIF, Bologna and IOS Press, Amsterdam) 2003, p. 1.
[19] VAN ISACKER P., *Proceedings of the International School "Enrico Fermi", Course CLXIX*, edited by COVELLO A., IACHELLO F., RICCI R. A. and MAINO G. (SIF, Bologna and IOS Press, Amsterdam) 2008, p. 347.
[20] WHEELER J. A., *Phys. Rev.*, **52** (1937) 1083.
[21] HAFSTAD L. R. and TELLER E., *Phys. Rev.*, **54** (1938) 681.
[22] DENNISON D. M., *Phys. Rev.*, **96** (1954) 378.
[23] KAMENY S. L., *Phys. Rev.*, **103** (1956) 358.
[24] BRINK D. M., in *Proceedings of the International School "Enrico Fermi", Course XXXVI*, (Academic Press, New York) 1966, pp. 247–277.
[25] BRINK D. M., FRIEDRICH H., WEIGUNY A. and WONG C. W., *Phys. Lett. B*, **33** (1970) 143.
[26] DELLA ROCCA V., BIJKER R. and IACHELLO F., *Nucl. Phys. A*, **966** (2017) 158.
[27] IACHELLO F., *Chem. Phys. Lett.*, **78** (1981) 581.
[28] BIJKER R. and IACHELLO F., *Phys. Rev. C*, **61** (2000) 067305.
[29] BIJKER R., *AIP Conf. Proc.*, **1323** (2010) 28.
[30] BIJKER R., *J. Phys. Conf. Ser.*, **380** (2012) 012003.
[31] BIJKER R. and IACHELLO F., *Phys. Rev. Lett.*, **112** (2014) 152501.
[32] KRAMER P. and MOSHINSKY M., *Nucl. Phys.*, **82** (1966) 241.
[33] BRIGHT WILSON JR E., DECIUS J. C. and CROSS P. C., *Molecular Vibrations* (McGraw-Hill, New York) 1955.
[34] BIJKER R., *Computer Program ACM*, unpublished.
[35] SICK I. and MCCARTHY J. S., *Nucl. Phys. A*, **150** (1970) 631.
[36] TILLEY D. R. *et al.*, *Nucl. Phys. A*, **745** (2004) 155.
[37] DELLA ROCCA V. and IACHELLO F., *Nucl. Phys. A*, **973** (2018) 1.
[38] FREER M. and FYNBO H. O. U., *Prog. Part. Nucl. Phys.*, **78** (2014) 1.
[39] FREER M. *et al.*, *Phys. Rev. C*, **76** (2007) 034320.
[40] KIRSEBOM O. S. *et al.*, *Phys. Rev. C*, **81** (2010) 064313.
[41] MARIN-LAMBARRI D. J., BIJKER R., FREER M., GAI M., KOKALOVA TZ., PARKER D. J. and WHELDON C., *Phys. Rev. Lett.*, **113** (2014) 012502.
[42] ROBSON D., *Nucl. Phys. A*, **308** (1978) 381.
[43] ROBSON D., *Prog. Part. Nucl. Phys.*, **8** (1982) 257.
[44] DAKER D. M. *et al.*, *Phys. Rev. Lett.*, **111** (2013) 062502.
[45] IACHELLO F., *Rivista del Nuovo Cimento*, **34** (2011) 617.
[46] CAPRIO M. A., CEJNAR P. and IACHELLO F., *Ann. Phys. (N.Y.)*, **323** (2008) 1106.

This page intentionally left blank

Proceedings of the International School of Physics "Enrico Fermi"
Course 201 "Nuclear Physics with Stable and Radioactive Ion Beams", edited by F. Gramegna,
P. Van Duppen, A. Vitturi and S. Pirrone
(IOS, Amsterdam; SIF, Bologna) 2019
DOI 10.3254/978-1-61499-957-7-61

Clustering in light neutron-rich nuclei

Y. Kanada-En'yo

Department of Physics, Kyoto University - Kyoto, Japan

Summary. — Nuclear clustering is one of the essential features of nuclear systems. Various rich cluster phenomena have been discovered in a wide region of nuclear chart as functions of proton and neutron numbers and excitation energy. Examples are cluster formation/breaking at nuclear surface in low-lying states, cluster excitation and resonances in highly excited states, molecular orbital structures in neutron-rich Be and Ne, cluster gas and linear chain structures in multi-cluster systems. To make systematic study of such cluster phenomena, we apply a method of antisymmetrized molecular dynamics (AMD) and its extended versions. The method is a useful approach applicable to the ground and excited states of general nuclei. One of the advantages of the method is that it is able to describe various cluster phenomena including cluster formation and breaking as well as shell-model like structures. In this paper, we discuss some topics of cluster phenomena in light nuclei based on AMD calculations.

1. – Introduction

A nucleus is a finite quantum many-body system consisting of protons and neutrons. It has analogies with and differences from an atomic system. An important difference is that a nucleus is a self-bound system, in which nucleons are attracted by the nuclear forces. It is a clear difference from an electron system, in which electrons are bound in an external Coulomb potential from a nucleus located at the center of the atom.

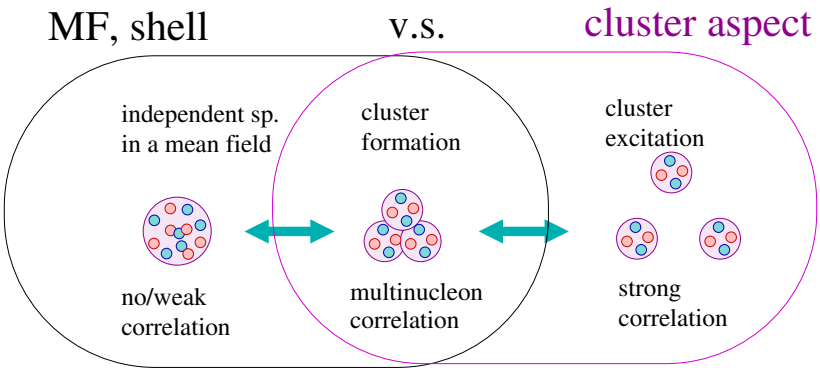

Fig. 1. – Schematic figures for cluster formation and development caused by many-body correlations.

Nevertheless, it is widely known that, at the leading order, nucleons in a nucleus behave as independent particles in a mean field resulting in shell structures. However, because of attractive nuclear forces, correlations between nucleons are not negligible but rather strong. A typical example of spatial correlations is "cluster", which is a subunit formed by spatially correlated nucleons. In other words, nuclear systems have two different natures, the independent-particle feature in a mean field and the cluster feature. Because of the coexistence of these two natures, rich phenomena appears in nuclear systems depending on proton and neutron numbers, energy, and density.

If there is no correlation between nucleons, all nucleons should behave as ideal independent particles in a mean field and there could exist a clear Fermi surface, *i.e.*, the shell structure. However, when residual interactions are switched on, the correlation between nucleons occurs to form cluster cores at the nuclear surface as a kind of ground-state correlation because of the attractive nuclear forces (see fig. 1). This is nothing but cluster formation, which is often seen in low-lying states of light nuclei. At the stage of the cluster formation in low-lying states, clusters are still largely overlapping with each other and the system has a compact structure with the normal density. However, once clusters are formed in the system, inter-cluster motion can be easily activated with small amount of energy. As a result, spatially developed cluster structures appear in excited states because of excitation of inter-cluster motion, and the system goes to a low-density state.

^{12}C is a typical example of cluster and mean-field coexisting systems (see fig. 2). The ground state of ^{12}C is a mean-field (shell-model–like) state dominated by the $p_{3/2}$-subshell closed configuration with significant mixing of 3α-cluster component. It means that α clusters are partially formed even in the ground state. At approximately 100 MeV, all twelve nucleons in ^{12}C can dissociate, and the system goes to a free nucleon gas state in a low density limit. At approximately 10 MeV, much lower energy than the free nucleon gas, 3α clusters develop spatially in excited states of ^{12}C. This energy for 3α-cluster excitation is much smaller than that of the nuclear gas state, meaning that the mean-field and cluster states coexist in low-energy levels of ^{12}C. Furthermore, as the

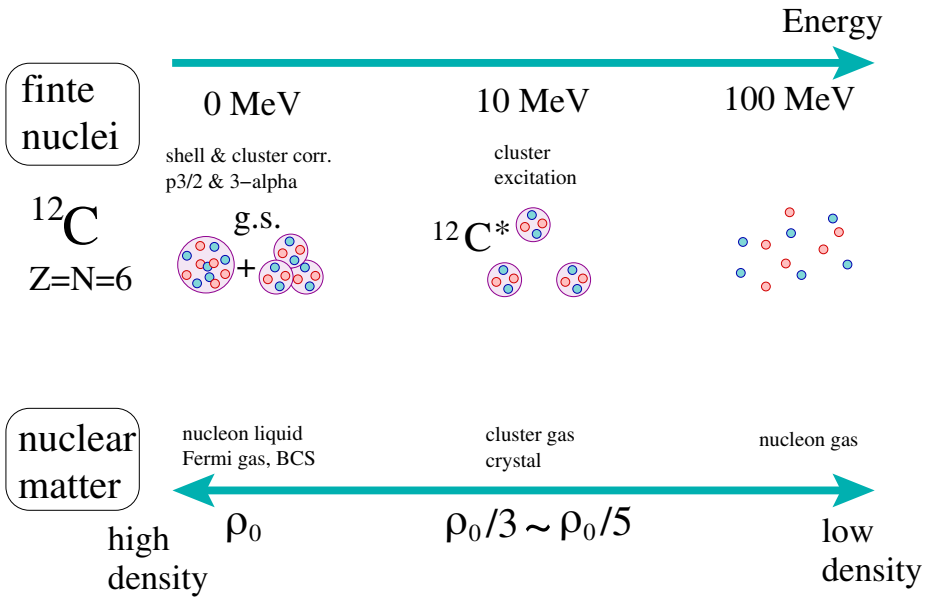

Fig. 2. – Schematic figures for structure changes as a function excitation energy (density).

excitation energy increases from the ground to the excited states, density of the system changes from normal density to low density. In the density changing, remarkable cluster features emerge at a relatively low density region, typically $(1/3)\rho_0 \sim (1/5)\rho_0$. The cluster enhancement at low density is a unique character of nuclear systems and describes the enhanced clustering at nuclear surface, in light-mass nuclei, and excited states.

In order to understand energy systematics of developed cluster states, Ikeda proposed the threshold rule called Ikeda diagram [1]. As shown in fig. 3, the Ikeda diagram describes his prediction that developed cluster structures appear in the energy region near the corresponding cluster-decay threshold energies. For example, appearance of the 2α-cluster, 3α-cluster, and $^{12}\mathrm{C} + \alpha$-cluster structures in ^{8}Be, ^{12}C*, and ^{16}O* can be understood by Ikeda's threshold rule. According to the Ikeda diagram, remarkable cluster structures in various cluster channels are expected (see fig. 3). It also predicts $n\alpha$-cluster states near the α break-up energy in spin-isospin saturated systems with $Z = N = 2n$. The lowest state of a $n\alpha$-cluster system is a α-cluster gas state, in which all α particles are moving in a dilute density as bosonic particles. Such dilute α-cluster gas states have been extensively discussed and attracting a recent interest [2, 3]. Moreover, in the Ikeda diagram, one may consider the α-cluster line just above (several ~ 10 MeV higher than) the ground-state line. Similarly, one can expect the 2α-cluster line at twice higher energy than the α-cluster line, and also the ^{12}C-cluster line in a similar energy region.

Let us turn to cluster aspects in unstable nuclei. In the progress of physics in unstable nuclei in the past decades, a variety of cluster states have been discovered also in unstable nuclei. Experimental and theoretical studies of unstable nuclei have been intensively

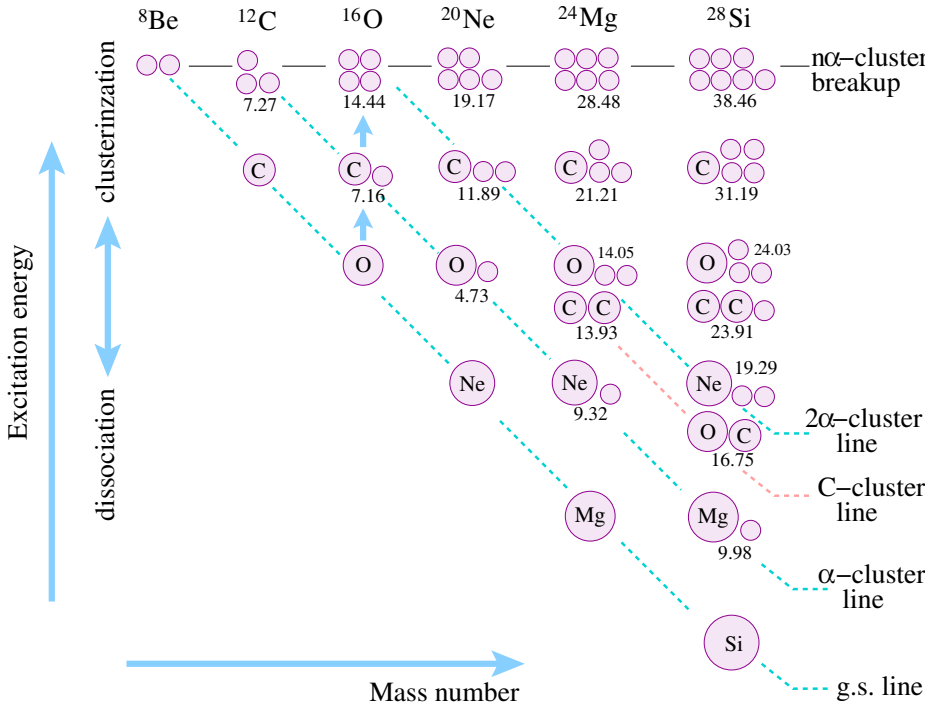

Fig. 3. – Schematic figure for concepts of Ikeda diagram.

performed to discover cluster states, in particular, in neutron-rich nuclei and revealed that excess neutrons play an important role in the cluster states. So, it is natural to expect a new version of the Ikeda diagram extended to cluster structures in unstable nuclei (see ref. [4] and references therein). When valence neutrons are added to known cluster structures in stable nuclei, what happens? A similar threshold rule for developed cluster structures with surrounding valence neutrons is expected to be fulfilled. For instance, developed cluster structures with 2α, 3α, and $^{16}\mathrm{O} + \alpha$ clusters surrounded by valence neutrons are expected in excited states of neutron-rich Be, C, and O isotopes as discussed by von Oertzen *et al.* [4-6].

Fascinating aspects related to cluster feature are seen even in the ground states of unstable nuclei. The ^{8}Be ground state has the developed 2α-cluster structure. Also in ^{12}C, the ground state contains the 3α-cluster component as the ground-state correlation as mentioned above. A question is what happens when valence neutrons are appended to the cluster structures in the ground states. Excess neutrons sometimes weaken the cluster structures, and enhance them in some cases. Figure 4 shows how the ground-state structure changes as the neutron number N increases in light neutron-rich nuclei. In Be isotopes, the cluster structure in the ground states rapidly changes along the isotope chain. The ground state in ^{8}Be is a quasi bound state of 2α particles. The remarkable 2α clustering weakens in ^{10}Be, and it again develops in ^{12}Be because of excess neutrons

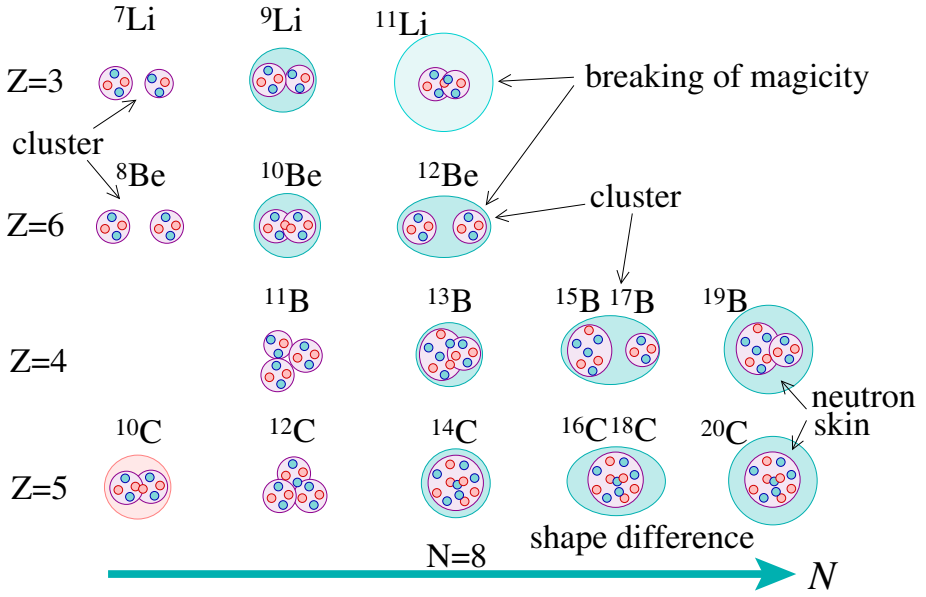

Fig. 4. – Sketches of structure changes as functions of proton and neutron numbers.

around the 2α clustering. As a result of the cluster development, the neutron magic number $N = 8$ disappears in ^{12}Be. That is to say, the ^{12}Be ground state is a largely deformed state with the dominant intruder configuration even though it is a $N = 8$ nucleus. By contrast, the ground states in neutron-rich C isotopes do not show cluster development, but generally have compact proton distribution with an oblate deformation. It means that 3α cluster structure formed in ^{12}C is quenched by excess neutrons around the 3α cluster. This is a brief description of ground-state structures in light neutron-rich nuclei.

Let us now turn to the excited states. In excited states of neutron-rich nuclei, further remarkable cluster structures are found as predicted by the extended Ikeda diagram. In neutron-rich Be isotopes, two kinds of cluster structures exist in excited states. In Be isotopes, 2α cluster cores are formed even in the ground states. The excited state, $^{10}\mathrm{Be}(0_2^+)$, is considered to have a molecular orbital structure, where valence neutrons occupy the longitudinal molecular orbital (MO) called σ-orbital around the 2α and bond two α clusters keeping a certain α-α distance. We call this structure the MO σ-bond structure. Moreover, in highly excited states above the $^{10}\mathrm{Be}(0_2^+)$ state, dinuclear cluster resonances composed of ^{6}He and α clusters have been suggested recently. An important difference between the MO σ-bond structure and the dinuclear cluster resonances is valence neutron motion. In the MO σ-bond structure, valence neutrons are moving around both α clusters bonding two αs, but in the cluster resonances, they are localized around one of α clusters to form a ^{6}He cluster (another cluster is moving around the ^{6}He cluster). Similarly, two types of cluster states, the MO σ-bond structures and dinuclear

resonances, have been predicted also in neutron-rich *sd*-shell nuclei such as Ne, F, O isotopes. For instance, in excited states of ^{22}Ne, von Oertzen *et al.* and Kimura *et al.* predicted MO σ-bond structures with σ-orbital neutrons around the $^{16}\mathrm{O}+\alpha$ core [4,7,8]. In addition, dinuclear resonances of $^{18}\mathrm{O}+\alpha$ clustering were predicted in the higher-energy region than the MO σ-bond structure.

A message is that different kinds of cluster structures, the MO σ-bond structures and dinuclear cluster resonance, coexist in excited states of neutron-rich Be and Ne isotopes. Valence neutrons around the cluster cores play important roles in emergence of these cluster structures in excited states. However, the MO σ-bond structures might be non-general phenomena but special phenomena that can emerge only in the specific case in which molecular orbitals for valence neutrons are formed around cluster cores. On the other hand, cluster resonances may be more general phenomena seen in various nuclei over a wide region of the nuclear chart including stable, unstable, light-mass, and heavy-mass regions, because, as predicted in the (extended) Ikeda diagram, such cluster resonances should generally appear in excited states near the threshold energy. Indeed, recent experiments discovered such cluster resonances in various nuclei. Further studies to search for cluster resonances are in progress.

Another fascinating topic of cluster phenomena in neutron-rich systems is multi-cluster structure such as $n\alpha$ clustering with valence neutrons. Key roles of valence neutrons in $n\alpha$ clustering have been discussed, for instance, stabilization mechanism of linear-chain 3α-cluster structure in excited states of neutron-rich C [9].

A key message is that the clustering is one of the essential features in a wide region of nuclear systems. Systematic investigation of cluster phenomena have revealed that rich cluster phenomena appear as functions of proton and neutron numbers and excitation energy: cluster formation/breaking at the nuclear surface in low-lying states, cluster excitation and resonances in highly excited states, molecular orbital bond structure in neutron-rich Be and Ne, multi-cluster structures such as the cluster gas and the linear chain.

In order to make systematic study of various cluster phenomena for comprehensive understanding of nuclear systems, we need a theoretical framework that can describe various cluster; phenomena including cluster formation/breaking in the ground and excited states in general nuclei. We apply a method of antisymmetrized molecular dynamics called AMD and extended versions [10-12]. In this paper, we discuss some topics of cluster phenomena in light nuclei based on the AMD calculations.

This paper is organized as follows. In the next section, we explain the basic framework of the AMD method. We discuss clustering in neutron-rich Be isotopes in sect. **3** and then describe clustering in ^{12}C and neighboring nuclei in sect. **4**. In sect. **5**, we introduce our recent studies of monopole and dipole excitation in light nuclei focusing on cluster features. Finally, a conclusion is given in sect. **6**.

2. – Antisymmetrized molecular dynamics

The AMD method was originally used for nuclear reaction study [13-15]. Up to now, various versions of the AMD method have been developed for both nuclear reaction and

structure studies. One of the advantages of the AMD is that it can describe cluster and mean-field aspects of nuclear systems. Here we briefly explain the AMD framework for the structure study. For details of the AMD method, the reader is referred to ref. [12] and references therein.

2˙1. *AMD wave function.* – The AMD is a model based on the variational method using effective nuclear forces. A basis wave function of the AMD model is given by a Slater determinant of single-particle Gaussian wave functions as

$$\Phi_{\rm AMD}(\boldsymbol{Z}) = \frac{1}{\sqrt{A!}}\mathcal{A}\{\varphi_1, \varphi_2, \ldots, \varphi_A\}, \tag{1}$$

where the i-th single-particle wave function φ_i is written by a product of spatial, spin, and isospin wave functions as

$$\varphi_i = \phi_{\boldsymbol{Z}_i}\chi_i\tau_i, \tag{2}$$

$$\phi_{\boldsymbol{Z}_i}(\boldsymbol{r}) = \left(\frac{2\nu}{\pi}\right)^{4/3} \exp\left\{-\nu\left(\boldsymbol{r} - \frac{\boldsymbol{Z}_i}{\sqrt{\nu}}\right)^2\right\}, \tag{3}$$

$$\chi_i = \left(\frac{1}{2} + \xi_i\right)\chi_\uparrow + \left(\frac{1}{2} - \xi_i\right)\chi_\downarrow. \tag{4}$$

Here $\phi_{\boldsymbol{Z}_i}$ and χ_i are the spatial and spin functions, respectively, and τ_i is the isospin function fixed to be proton or neutron. The width parameter ν is usually chosen to be an optimized value for each nucleus. Accordingly, an AMD wave function is expressed by a set of variational parameters, $\boldsymbol{Z} \equiv \{\boldsymbol{Z}_1, \ldots, \boldsymbol{Z}_A, \xi_1, \ldots, \xi_A\}$. The Gaussian center position $\boldsymbol{Z}_i$ and the spin orientation χ_i of all nucleons are independently treated as variational parameters.

The model wave function can describe a variety of cluster structure with the spatial configuration of Gaussian center positions because the AMD model space contains the Brink-Bloch cluster wave functions [16]. For example, the Brink-Bloch 2α wave function can be represented with the AMD wave function by choosing Gaussian center parameters $\boldsymbol{Z}_{1,2,3,4}/\sqrt{\nu} = \boldsymbol{D}/2$ and $\boldsymbol{Z}_{5,6,7,8}/\sqrt{\nu} = -\boldsymbol{D}/2$. $\boldsymbol{D}$ is the distance parameter between two α's in the Brink-Bloch wave function. The AMD wave function can also describe mean field states because, if the centers of Gaussian wave packets are located at short distances, the wave function is equivalent to a harmonic oscillator shell-model wave function. Moreover, it can continuously express transition between remarkable cluster and mean-field structures through cluster dissolution/formation. This is a great advantage superior to cluster models and mean-field approaches. Because of the flexibility of the model wave function, the AMD is a powerful approach useful to study cluster and mean-field features in the ground and excited states of general nuclei including exotic nuclei.

An extension of the AMD wave function using triaxially deformed Gaussian wave packets, called the deformed base AMD, was proposed by Kimura *et al.* [17]. The deformed base AMD is efficient in describing coexistence of deformed mean-field and cluster states in *sd*- and *pf*-shell nuclei [12, 18].

It should be commented that, a similar wave function is used for nuclear reaction and structure studies in the fermionic molecular dynamics (FMD) developed by Feldmeier and his collaborators [19-22]. The FMD wave function is also given by a Slater determinant of Gaussian wave packets, but the width parameter ν can be chosen independently for each nucleon as ν_i and treated as variational parameters in the FMD. The flexible ν_i parameters are efficient for loosely bound valence neutron behavior in neutron halo nuclei.

In the AMD framework for structure study, angular-momentum and parity projections and energy variation are performed. For the energy variation, the frictional cooling method is usually applied. For simplicity, we here describe the frictional cooling method for a fixed intrinsic-spin case, but the method can be easily extended to the variational intrinsic-spin case by using the label $\boldsymbol{Z}_i$ for $Z_{i\sigma}$ ($\sigma = 1, 2, 3$) and $Z_{i4} = \xi_i$. We start from the equation of motion for $\boldsymbol{Z}_i$ derived from the time-dependent variational principle as

$$i\hbar \sum_{j\rho} C_{i\sigma,j\rho} \frac{\mathrm{d}Z_{j\rho}}{\mathrm{d}t} = \frac{\partial \mathcal{H}}{\partial Z^*_{i\sigma}}\,, \tag{5}$$

where $\sigma, \rho = x, y, z$ and the expectation value of the Hamiltonian H is expressed as

$$\mathcal{H}(\boldsymbol{Z}, \boldsymbol{Z}^*) = \frac{\langle \Phi_{\mathrm{AMD}}(\boldsymbol{Z})|H|\Phi_{\mathrm{AMD}}(\boldsymbol{Z})\rangle}{\langle \Phi_{\mathrm{AMD}}(\boldsymbol{Z})|\Phi_{\mathrm{AMD}}(\boldsymbol{Z})\rangle}\,. \tag{6}$$

$C_{i\sigma,j\rho} \equiv$ is a positive definite Hermitian matrix

$$C_{i\sigma,j\rho} \equiv \frac{\partial^2}{\partial Z^*_{i\sigma} \partial Z_{j\rho}} \ln\langle \Phi_{\mathrm{AMD}}(\boldsymbol{Z})|\Phi_{\mathrm{AMD}}(\boldsymbol{Z})\rangle. \tag{7}$$

To get the optimum parameter set $\boldsymbol{Z}$ which gives minimum energy state in the AMD model space, the time evolution of the parameters are calculated by the following frictional cooling equation,

$$i\hbar \sum_{j\rho} C_{i\sigma,j\rho} \frac{\mathrm{d}Z_{j\rho}}{\mathrm{d}t} = (\lambda + i\mu) \frac{\partial \mathcal{H}}{\partial Z^*_{i\sigma}}\,. \tag{8}$$

The parameter λ is an arbitrary real number and μ is an arbitrary negative real number. It is easily proved that the energy decreases as time develops because of the frictional term $i\mu$. In the energy variation, the matrix $C_{i\sigma,j\rho}$ can be replaced with $\delta_{ij}\delta_{\sigma\rho}$. In the $\lambda = 0$ case, the frictional cooling method is equivalent to the normal gradient method. After enough cooling time (iteration steps), the optimum set of parameters $\boldsymbol{Z}$ is obtained.

The parity-projected AMD wave function is given as

$$|\Phi^{\pm}_{\mathrm{AMD}}(\boldsymbol{Z})\rangle \equiv P^{\pm}|\Phi_{\mathrm{AMD}}(\boldsymbol{Z})\rangle = \frac{1 \pm P_r}{2}|\Phi_{\mathrm{AMD}}(\boldsymbol{Z})\rangle, \tag{9}$$

where $P^{\pm} = (1 \pm P_r)/2$ is the parity projection operator. The angular-momentum projection is done as

$$|\Phi^J_{MK}\rangle(\boldsymbol{Z}) = P^J_{MK}|\Phi_{\rm AMD}(\boldsymbol{Z})\rangle = \int {\rm d}\Omega D^{J^*}_{MK}(\Omega)\hat{R}(\Omega)|\Phi_{\rm AMD}(\boldsymbol{Z})\rangle. \tag{10}$$

Here $D^J_{MK}(\Omega)$ is the Wigner's D function and $\hat{R}(\Omega)$ is a rotation operator with respect to Euler angle Ω.

In a simplest calculation of the AMD for structure study, the energy variation is usually done with respect to the parity projected AMD wave function by minimizing the energy expectation value

$$\mathcal{H}(\boldsymbol{Z}, \boldsymbol{Z}^*) = \frac{\langle\Phi^{\pm}_{\rm AMD}(\boldsymbol{Z})|H|\Phi^{\pm}_{\rm AMD}(\boldsymbol{Z})\rangle}{\langle\Phi^{\pm}_{\rm AMD}(\boldsymbol{Z})|\Phi^{\pm}_{\rm AMD}(\boldsymbol{Z})\rangle}\,, \tag{11}$$

and the angular momentum projection is performed after the energy variation. In an extended calculation, the energy variation is carried out for the parity and angular momentum projected AMD wave function,

$$\mathcal{H}(\boldsymbol{Z}, \boldsymbol{Z}^*) = \frac{\langle P^J_{MK}\Phi^{\pm}_{\rm AMD}(\boldsymbol{Z})|H|P^J_{MK}\Phi^{\pm}_{\rm AMD}(\boldsymbol{Z})\rangle}{\langle P^J_{MK}\Phi^{\pm}_{\rm AMD}(\boldsymbol{Z})|P^J_{MK}\Phi^{\pm}_{\rm AMD}(\boldsymbol{Z})\rangle}\,. \tag{12}$$

The single AMD wave function obtained by the energy variation is an approximate solution for the ground-state wave function. To improve the wave function, different AMD wave functions are superposed. The superposition is a kind of configuration mixing and it is essential to describe excited states which is orthogonal to the ground state. Let us consider basis wave functions $\Phi_{\rm AMD}(\boldsymbol{Z}^{(k)})$ $(k = 1, \ldots, k_{\rm max})$ to be superposed ($k_{\rm max}$ is the number of considered basis AMD wave functions). The wave function for a $J^{\pm}$ state is given by linear combination of basis wave functions as

$$|\Phi^{J\pm}_n\rangle = \sum_{kK} c_{J^{\pi}_n,K,k}|P^{J\pm}_{MK}\Phi_{\rm AMD}(\boldsymbol{Z}^{(k)})\rangle, \tag{13}$$

where $P^{J\pm}_{MK} \equiv P^J_{MK}P^{\pm}$. Here the coefficients $c_{J^{\pi}_n,K,k}$ are determined by the diagonalization of Hamiltonian and norm matrices.

To efficiently choose basis AMD wave functions for the superposition, the combination of the AMD with the generator coordinate method (AMD+GCM) is useful. In the AMD+GCM method, wave functions for $J^{\pm}$ states are given by linear combination of the AMD wave functions obtained by the energy variation with constraints, which are regarded as generator coordinates. In the β- and $\beta\gamma$-constraint AMD [17,23], the energy variation is done under constraints on deformation parameters β and (β, γ), respectively. In the d-constraint AMD [24], a constraint is imposed for the distance between two (or three) centers of subgroups. After the energy variation with the constraints, the

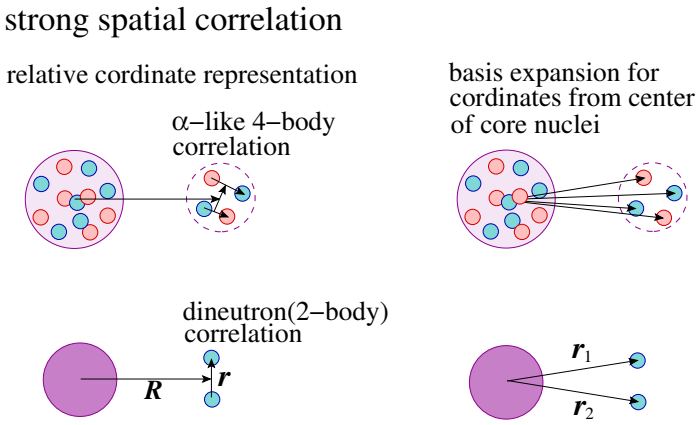

Fig. 5. – Schematic figures for spatially correlated nucleons in cluster structures. Top: α-cluster correlation. Bottom: Dineutron correlation.

obtained AMD wave functions are superposed with the GCM treatment. Namely, coefficients of wave functions are determined by solving the Hill-Wheeler equation, which is equivalent to diagonalizing the norm and Hamiltonian matrices. In the AMD+GCM, large amplitude dynamics along the generator coordinates are taken into account fully microscopically.

2˙2. *Cluster correlation.* – In most cases, spatially developed cluster states are highly correlated states beyond mean-field approximations. Let us consider an α cluster located far from a core nucleus (see fig. 5). The α cluster is a strongly correlated object composed of four nucleons. If one finds a nucleon in the α cluster at a certain position, one should find other three nucleons in the vicinity of the first nucleon. In the harmonic-oscillator basis expansion for such a highly correlated subsystem, a huge number of basis wave functions with extremely high angular momenta are contained in the wave function. The mixing of high-angular-momentum components for the spatially correlated nucleons in the α cluster far from the core can be easily understood by the Heisenberg uncertainty. For simplicity, let us consider two particles with a relative distance r with the mass center at a distance R from the core nucleus. We consider a case of a large R and a small r corresponding to strongly correlating two nucleons with a short distance at far from the core. Because of the Heisenberg uncertainty, the angular momentum l that is needed in the single-particle basis expansion can be roughly estimated to be $l \sim D/r$. It turns out that the strongly correlated two-nucleon system with the larger D and the smaller r inevitably involves mixing of higher angular momentum components, *i.e.*, high shell components in terms of the harmonic-oscillator basis expansion. In fig. 6, we demonstrate how high shell components are mixed in the 0_1^+ and 0_2^+ states of ^{16}O obtained by the ^{12}C(AMD + VAP) + αGCM calculation of ref. [25]. Even in the ground state, higher shell components are significantly contained because of the ground-state correlation of cluster components. The higher shell component mixing is more remarkable in the 0_2^+

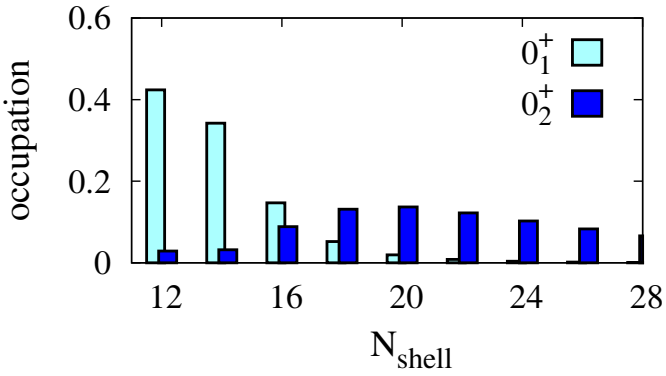

Fig. 6. – Occupation probability of harmonic oscillator shells in $^{16}O(0_1^+)$ and $^{16}O(0_2^+)$ calculated by the $^{12}C(\mathrm{AMD} + \mathrm{VAP}) + \alpha\mathrm{GCM}$. The figure is reproduced from ref. [25].

state, in which the occupation probability of N-shell component is distributed broadly because of the developed $^{12}C + \alpha$ cluster structure. Tiny percents continue toward extremely high shell components, and therefore, it is difficult to describe the $^{12}C + \alpha$ cluster structure in the 0_2^+ state within a truncated model space of mean-field approaches. For such developed cluster states, the one-center basis expansion is not suitable but multi-center-type wave functions like the Brink-Bloch cluster model and the AMD ones are efficient.

3. – Clustering in neutron-rich Be

Cluster structures of neutron-rich Be isotopes have been intensively investigated from both the theoretical and experimental sides (see, for example, refs. [4, 12] and references therein). In ^{10}Be, positive-parity states are classified into the ground, side ($K^\pi = 2^+$), and excited ($K^\pi = 0_2^+$) bands. The AMD+VAP calculation successfully describes experimental spectra of ^{10}Be and shows $2\alpha + 2n$ cluster structures in the ground and excited states [26] (see fig. 7). The remarkable $2\alpha + 2n$ cluster structure produces the $K^\pi = 0_2^+$ band starting from the 0_2^+ state. Experimental observed 2^+ state at 7.54 MeV and a 4^+ state at 10.2 MeV are candidates of the $K^\pi = 0_2^+$ band members [27,28]. This assignment is consistent with the level spacing (the energy slope against $J(J+1)$) of the calculated $K^\pi = 0_2^+$ band and supports a large deformation due to the cluster structure.

Cluster models and also extended models assuming a 2α core describe well low-lying states of neutron-rich Be [5, 29-37]. The validity of the 2α assumption in neutron-rich Be has been checked by the AMD and FMD calculations [10, 12, 38], in which the 2α clustering is actually formed by the cluster correlation in many-nucleon dynamics without model assumptions. The 2α formation has been also found in an *ab initio* calculation using realistic nuclear forces [39]. In order to understand the cluster structures of low-

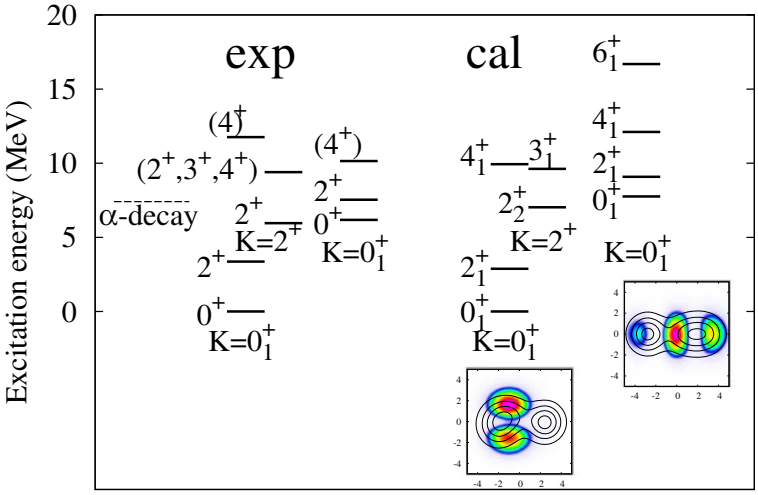

Fig. 7. – Energy spectra of positive-parity states of ^{10}Be obtained by the AMD+VAP using the MV1 force are shown together with experimental data. Matter density and valence neutron density in $^{10}\mathrm{Be}(0^+_{1,2})$ are shown by contour and color mapping, respectively. The figure is taken from ref. [26].

lying states of neutron-rich Be isotopes, the molecular orbit (MO) structure is a useful picture. The MO structure has been proposed for ^{9}Be [40] and extended to further neutron-rich Be isotopes [4, 5, 29, 32]. In the MO picture, valence neutrons in a $2\alpha + Xn$ system occupy molecular orbits constructed around the 2α, which are described by linear combination of p-orbits around α clusters (see fig. 8 for schematic figures of molecular orbits). The negative-parity orbits called "$\pi_{3/2}$-orbit" and "$\pi_{1/2}$-orbit" are the lowest nodal ls-favored and ls-unfavored orbits, which correspond to the $p_{3/2}$ and $p_{1/2}$ orbits in the spherical shell model limit, respectively. The positive-parity orbit denoted by "$\sigma_{1/2}$-orbit" is the longitudinal orbit having two nodes along the α-α direction. A key character of the $\sigma_{1/2}$-orbit is that it has nodes in the stretching direction and therefore it gains the kinetic energy when the 2α cluster develops. As a result, valence neutrons occupying the $\sigma_{1/2}$-orbit enhance the cluster structure. However, those in the $\pi_{3/2,1/2}$-orbits suppress the cluster structure of neutron-rich Be to gain the potential energy. In fig. 9, intrinsic density distributions of band head states having dominantly $\pi^n\sigma^m$ configurations are shown in an $n \times m$ matrix. The density distributions clearly show the enhancement(suppression) of the cluster structure with increase of the number of $\sigma(\pi)$-orbit neutrons.

It is also interesting that, in the developed cluster structure, the $N = 8$ shell gap vanishes because of the lowering mechanism of the $\sigma_{1/2}$-orbit in the well-clusterized 2α system. As a result, intruder $1\hbar\omega$ and $2\hbar\omega$ configurations come down to the low-energy region and almost degenerate with the normal $0\hbar\omega$ configurations in the low-energy

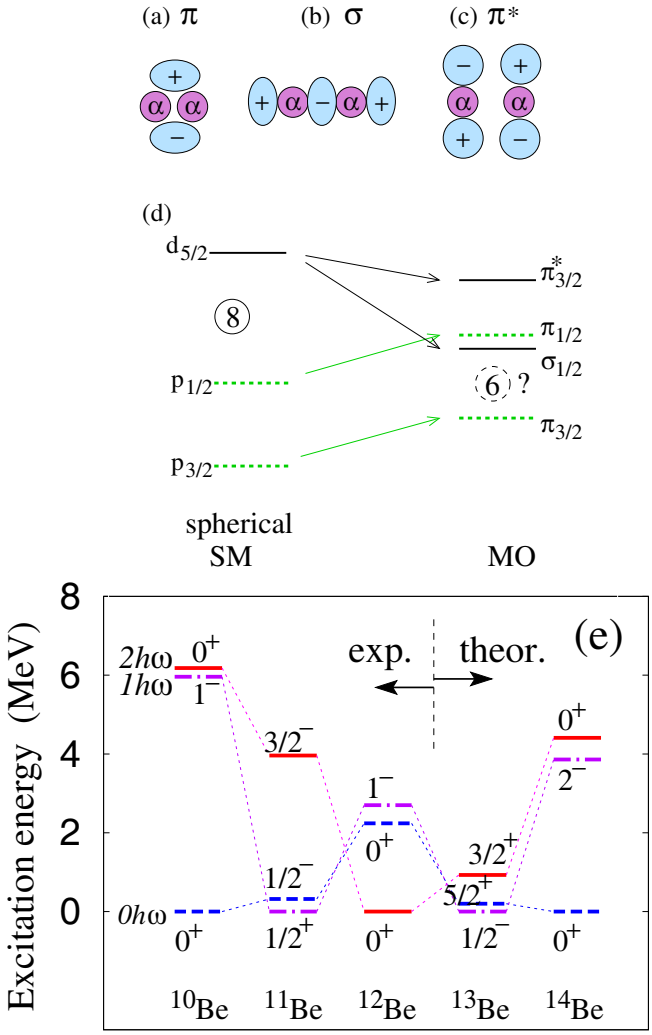

Fig. 8. – (a, b, c) Sketches of molecular orbits around a 2α core in Be. (d) Sketch of single-particle spectra for valence neutrons of spherical shell-model orbits and those of molecular orbits. (e) Experimental energy levels assigned to band-head states in low-lying spectra of ^{10}Be, ^{11}Be, and ^{12}Be, and theoretical predictions for ^{13}Be and ^{14}Be by the AMD+VAP calculations [41,42]. Figures are taken from ref. [41].

spectra of neutron-rich Be (see fig. 8(e)). In ^{11}Be and ^{12}Be, the level inversion between the normal $\pi_{1/2}$-orbit and the intruder $\sigma_{1/2}$-orbit occurs. It means that, the ground states are large deformed states having dominantly the intruder configurations, even though those Be are nuclei near $N = 8$. This feature is known to be breaking of the $N = 8$

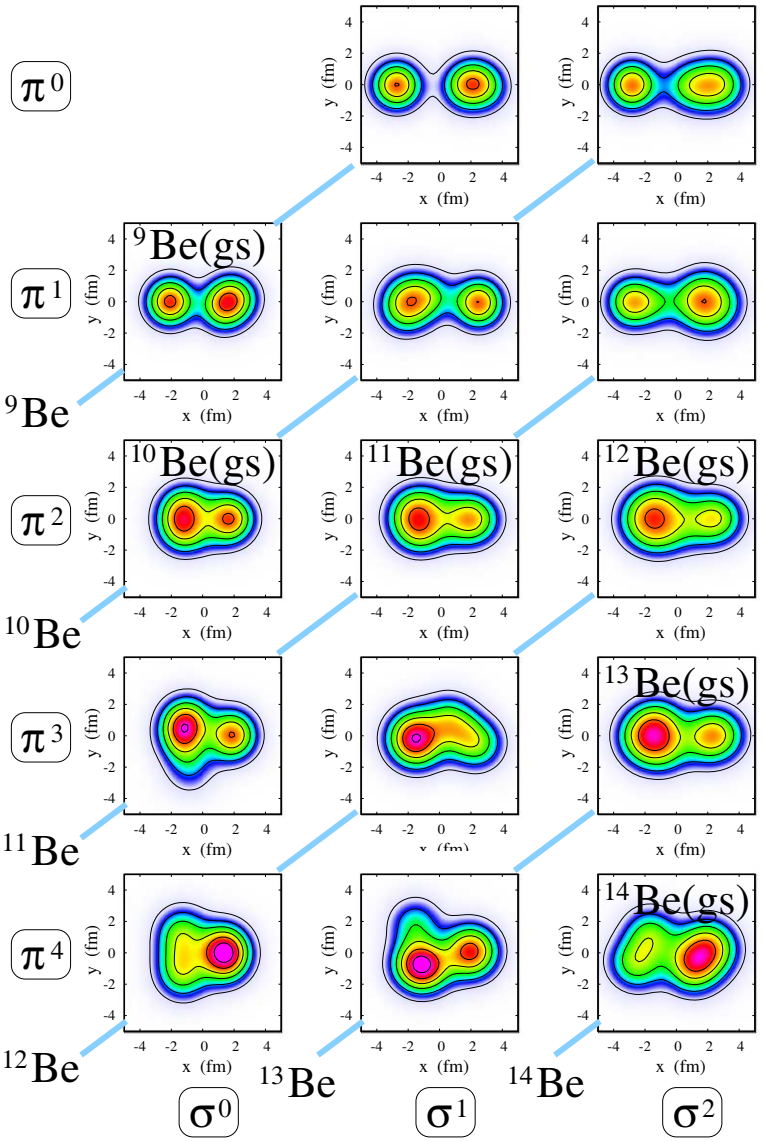

Fig. 9. – Matter density distributions in the band-head states of Be isotopes obtained by the AMD+VAP [26, 41-44]. Figures are aligned in the $n \times m$ matrix according to the classification of molecular orbit configurations $\pi^n \sigma^m$, where n and m are the numbers of π- and σ-orbit neutrons, respectively, around the 2α core.

magicity in neutron-rich Be and has been revealed by various experimental observations such as Gamov-Teller and $E2$ transitions as well as low-lying energy spectra [48-55].

Also for ^{13}Be, the breaking of the neutron magicity has been discussed. If the level inversion occurs, a negative-parity $1/2^-$ state with an intruder configuration should be

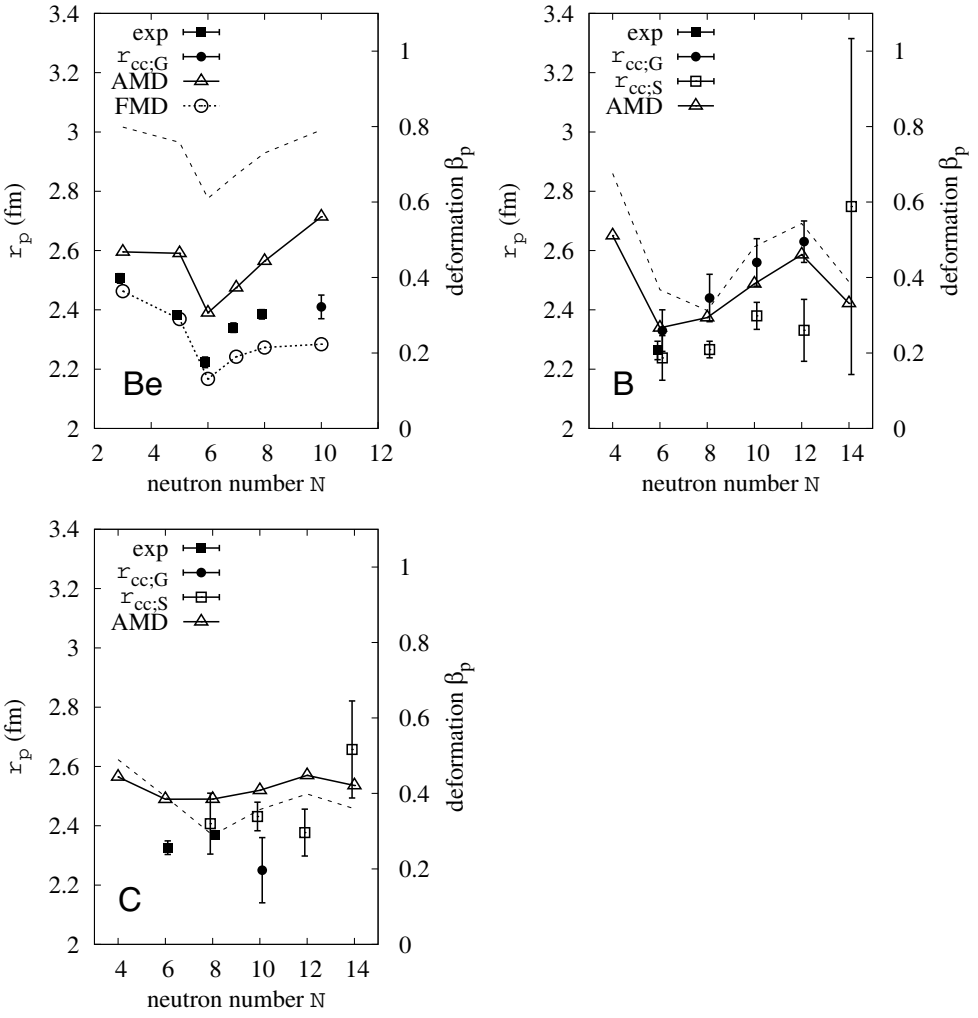

Fig. 10. – Radius and deformation parameter of proton distribution in Be, B, and C isotopes. The theoretical values calculated by the AMD+VAP using the MV1 force [45] are shown. For Be isotopes, compared with the experimental data [46,47] and the FMD results [47]. The proton radii evaluated by charge-changing reactions for B and C isotopes are shown. The figure is taken from ref. [45].

the lowest, but positive-parity states with normal configurations may be higher than the $1/2^-$ state. The AMD calculation predicts the low-lying $1/2^-$ state of ^{13}Be because of the lowering mechanism of the σ-orbit in a developed cluster structure, and suggests the breaking of neutron magicity. Many experiments have been performed to pin down this problem. For ^{13}Be, which is an unbound nucleus, a couple of resonance states have been observed by $1n$ knock-out reaction [56,57]. The latest experiment at RIKEN reported the

existence of a low-lying $1/2^-$ state [57], but ^{13}Be spectra are still controversial between different experiments.

Instead of the broken $N = 8$ shell gap, a possible new magic number at $N = 6$ between the $\pi_{3/2}$- and $\pi_{1/2}\sigma_{1/2}$-shells is indicated in the single-particle spectra of the molecular orbit structure in neutron-rich Be. Reflecting the $\pi_{3/2}$-shell closure feature, the clustering of the ground state is weakest at $N = 6$ for ^{10}Be among neutron-rich Be isotopes as shown in fig. 9. The N dependence of point-proton radii in fig. 10 shows this trend of the $N = 6$ magic number. Namely, the point-proton radius is smallest not at $N = 8$ but at $N = 6$. The AMD and FMD calculations qualitatively describe the N dependence of the point-proton radii in Be isotopes and show kink at $N = 6$ consistently with the experimental data [45, 47].

As discussed previously, the clustering of ground states rapidly changes in Be and B isotopes as a function of the neutron number (see fig. 4). The N dependence of point-proton radii in each isotope chain of Be and B reflects the structure change of clustering. However, for C isotopes, the AMD calculation predicts almost constant point-proton radii independently from the neutron number. The reason is that the proton structure in neutron-rich C isotopes is rather stable against increase of the neutron number and keeps a compact oblate shape. Because of the stable nature of the proton structure, neutron-rich C isotopes have no cluster development resulting in almost no N-dependence of point-proton radii. It is indicated that systematics of point-proton radii provides useful information for cluster structure change of the ground states along an isotope chain. Nowadays, systematic data of proton radii are available for neutron-rich nuclei thanks to precise measurements with the isotope shift technique. Moreover, systematic data of proton radii for B and C isotopes are coming from charge changing cross sections based on Glauber analysis.

4. – Clustering in ^{12}C and neighboring nuclei

4·1. *Cluster structures of* ^{12}C. – In cluster physics, the cluster structure of ^{12}C has been attracting a great interest for a long time. Various 3α cluster structures have been discovered in excited states of ^{12}C by theoretical and experimental works [58, 59]. In the early stage of cluster studies of ^{12}C, possibility of a linear 3α chain structure was proposed for ^{12}C(0_2^+) by Morinaga *et al.* [60, 61], but this idea has been excluded by the large reduced α-decay width [62]. Later, (semi)microscopic and non-microscopic 3α-cluster models have been applied to figure out cluster structures of excited states of ^{12}C [2, 63-74]. In those studies, ^{12}C(0_2^+) has been found to be a weakly bound 3α state, in which α clusters behave as bosonic particles moving freely like a gas in a dilute density. Moreover, the lowest negative-parity state ^{12}C(3_1^-) is understood as the band-head state of the $K^\pi = 3^-$ band produced from an intrinsic structure with a regular triangle 3α configuration.

Despite the success of 3α-cluster models for many excited states ^{12}C, microscopic 3α-cluster models fail to describe the large level spacing between the 0_1^+ and 2_1^+ states and existence of 1^+ states, because α-cluster breaking is not taken into account in the models. The problem of the missing α-cluster breaking has been overcome by the AMD and

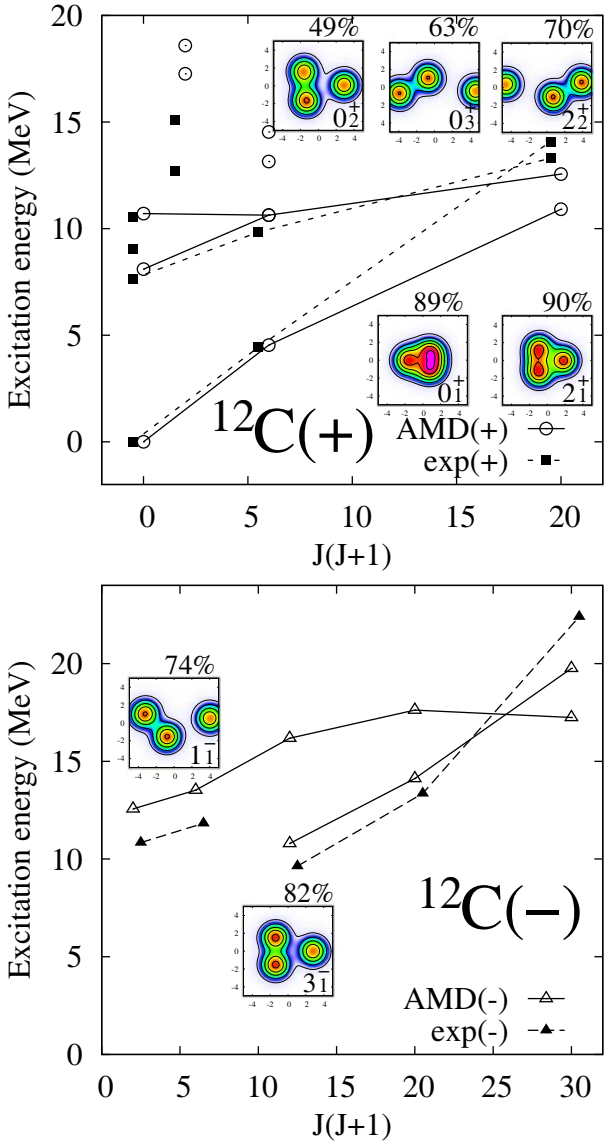

Fig. 11. – Energy levels of ^{12}C. The calculated energies by the AMD+VAP using the MV1 force [75] and experimental data [76-80] are shown. The calculated matter density distribution in the single AMD wave function of the dominant component in each state is shown together with percentages of the dominant component in the final GCM wave function. The upper figure is from ref. [81].

FMD models. The AMD and FMD calculations indicate the 3α-cluster formation in the twelve-nucleon system, ^{12}C, without assuming the existence of α clusters [75,82-84]. The 3α-cluster formation in ^{12}C has been also found in recent *ab initio* calculations [85-87].

The energy levels of ^{12}C obtained by the AMD+VAP [75,82] are shown in fig. 11. The figure also shows intrinsic density distribution of the dominant component in each state. The calculation well reproduces the experimental spectra of the $K^\pi = 0_1^+$, $K^\pi = 0_2^+$, $K^\pi = 3_1^-$, and $K^\pi = 1_1^-$ bands as well as $J^\pi = 1^+$ states. The intrinsic state of the $K^\pi = 0_1^+$ band shows dominantly a compact 3α cluster structure. Note that the band head $^{12}\mathrm{C}(0_1^+)$ is not a simple 3α state but it contains significant cluster-breaking component of the $p_{3/2}$-closed configuration. Because of the mixing of the cluster-breaking component, the $^{12}\mathrm{C}(0_1^+)$ gains extra energy of the spin-orbit interaction, which is essential for the large 0^+-2^+ level spacing. $^{12}\mathrm{C}(0_2^+)$ is described by superposition of various 3α configurations. This is consistent with the cluster gas nature of this state discussed by Funaki *et al.* [67,88]. The experimentally observed 2_2^+ and 4_1^+ states are assigned to the $K^\pi = 0_2^+$ band starting from $^{12}\mathrm{C}(0_2^+)$. However, the strong $E2$ transitions from 2_2^+ to the 0_2^+ and 0_3^+ states are obtained in the AMD+VAP calculation and they indicate rather strong state mixing (or structure change) in the Hoyle band. Detailed discussions will be given later. The $K^\pi = 3_1^-$ band composed of the 3_1^-, 4_1^-, and 5_2^- states is produced by a developed 3α cluster structure. The $K^\pi = 1_1^-$ band has an intrinsic structure of an open triangle 3α configuration.

4·2. *Cluster gas states* ^{12}C *and* ^{11}B *and their rotation.* – In analogy to 3α cluster states in ^{12}C, $2\alpha + t$ cluster states in ^{11}B have been investigated [89-94]. The experimentally measured monopole transition for $^{11}\mathrm{B(g.s.)} \to {}^{11}\mathrm{B}(3/2_3^-)$ is as strong as that for $^{12}\mathrm{C(g.s.)} \to {}^{12}\mathrm{C}(0_2^+)$ suggests a $2\alpha + t$ cluster structure in $^{11}\mathrm{B}(3/2_3^-)$ similar to $^{12}\mathrm{C}(0_2^+)$ as discussed by Kawabata *et al.* [91]. In the AMD+VAP and $\beta\gamma$-constraint AMD calculations, $2\alpha + t$ cluster gas features of $^{11}\mathrm{B}(3/2_3^-)$ have been investigated in detail [92, 94]. Figure 12 shows α and t cluster probabilities around a fixed 2α core in $^{12}\mathrm{C}(0_{1,2,3}^+)$ and $^{11}\mathrm{B}(3/2_{1,3}^-)$, respectively, obtained by the AMD+VAP. In both ^{12}C and ^{11}B, the ground states have large cluster probability at $(X, Y) = (0, 3)$ fm, indicating compact triangle configurations of three clusters. $^{12}\mathrm{C}(0_2^+)$ shows a peak amplitude around $(0, 4)$ fm, but in the outer region ($D \equiv \sqrt{X^2 + Y^2} \sim 6$ fm) far from the 2α core, the α-probability is broadly distributed in the angular mode showing the S-wave feature around the 2α core. It means that $^{12}\mathrm{C}(0_2^+)$ has the cluster gas nature in the outer region, whereas it shows dominantly a triangle configuration in the inner region. The triangle configuration in the inner region of $^{12}\mathrm{C}(0_2^+)$ originates in the Pauli repulsion between α-clusters, and is consistent with an alternative interpretation of the Hoyle state as a vibration mode of the triangle ground band discussed in algebraic cluster models [95].

The t-cluster probability in $^{11}\mathrm{B}(3/2_3^-)$ shows a similar feature to the α probability in $^{12}\mathrm{C}(0_2^+)$. It shows a peak amplitude around $(0, 3-4)$ fm and a broad distribution in the angular mode in the $D \sim 5$ fm region, meaning that $^{11}\mathrm{B}(3/2_3^-)$ also has a cluster gas nature in the outer region and triangle configuration in the inner region. However, quantitatively, the t-cluster distribution is not as broad as the α-cluster distribution in $^{12}\mathrm{C}(0_2^+)$, because the t cluster is moving in the P-wave having a node (zero amplitude) at the X axis around the 2α core instead of the S-wave without nodal structure. It means

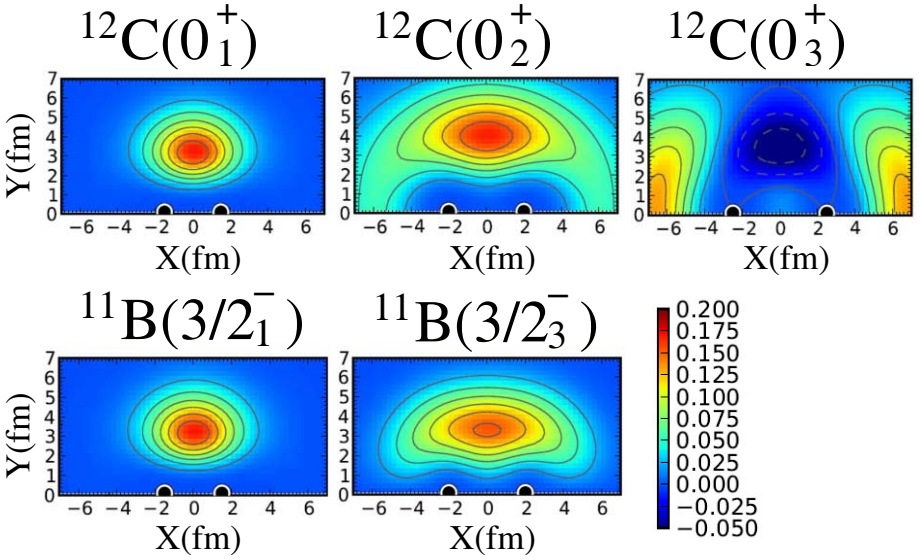

Fig. 12. – α-cluster probability around a 2α core in $^{12}C(0^+_{1,2,3})$ and t-cluster one in $^{11}B(3/2^-_{1,3})$. The center positions of the α's in the 2α core are shown by the filled circles on $Y = 0$ line (the X axis). The figure is taken from ref. [96].

that the gas-like nature of $^{11}B(3/2^-_3)$ is relatively weaker than that of $^{12}C(0^+_2)$. $^{12}C(0^+_3)$ shows a peak around $(7, 0)$ fm with significant angular fluctuation and is regarded as a bent chain-like 3α structure.

Let us turn to band structures starting from the cluster gas states, $^{12}C(0^+_2)$ and $^{11}B(3/2^-_3)$. The question is whether a rotational band is produced by the cluster gas, and if so, what is the physical meaning of rotation of the cluster gas. Rather strong $E2$ transitions are obtained by the AMD+VAP calculation for transitions between $^{12}C(0^+_2)$, $^{12}C(2^+_2)$, and $^{12}C(4^+_2)$. Therefore, these states can be interpreted as band members of the $K^\pi = 0^+_2$ band. However, the calculation shows the stronger $E2$ transition for $2^+_2 \to 0^+_3$ than that for $2^+_2 \to 0^+_2$, and may provide an alternative assignment: $^{12}C(0^+_3)$, $^{12}C(2^+_2)$, and $^{12}C(4^+_2)$ form a $K^\pi = 0^+$ band. In fig. 13, the calculated energy spectra for these bands and corresponding experimental data are plotted as functions of $J(J + 1)$.

Let us discuss intrinsic structures of these states. As mentioned previously, $^{12}C(0^+_2)$ is described by superposition of various 3α configurations showing the cluster gas nature, whereas $^{12}C(2^+_2)$ has 70% overlap with an open triangle configuration similar to $^{12}C(0^+_3)$ (see fig. 11). It indicates that the structure change occurs as J goes up from $^{12}C(0^+_2)$ to $^{12}C(2^+_2)$. As a consequence of the structure change from the cluster gas in $^{12}C(0^+_2)$ to the elongated configuration in $^{12}C(2^+_2)$, the system can rotate and increase its spin towards $J = 4$ with a larger momentum of inertia. Alternatively, considering the similar intrinsic structure of $^{12}C(0^+_3)$, $^{12}C(2^+_2)$, and $^{12}C(4^+_2)$, these states can be interpreted as

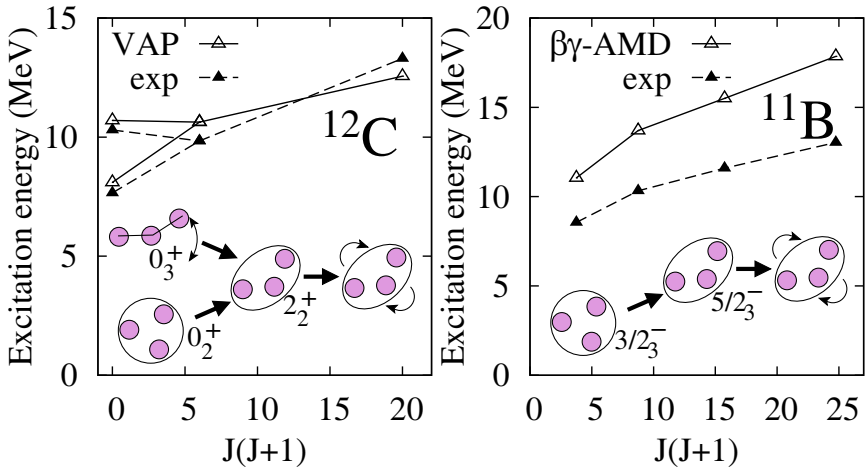

Fig. 13. – Band structures of the cluster gases of ^{12}C and ^{11}B. Theoretical energy spectra of ^{12}C obtained by the AMD+VAP using the MV1 force [75] and those of ^{11}B obtained by the $\beta\gamma$-constraint AMD using the Volkov No. 2 force [94] are shown by open triangles. The corresponding experimental spectra are shown by closed triangles [78, 79, 97].

band members of the open triangle shape, and the band can be described by the rotation of the elongated intrinsic state.

For ^{11}B, the rotational band from the ^{11}B$(3/2^-_3)$ has been discussed by Suhara and Kanada-En'yo based on the $\beta\gamma$-constraint AMD calculation combined with the GCM [94]. In fig. 13, the calculated energy spectra of band members are shown together with the experimental spectra of the candidate states [97]. The calculation reproduces the level spacing in the rotational band, though it somewhat overestimates the band-head energy. Similar to the structure change in ^{12}C$(0^+_2) \rightarrow {}^{12}C(2^+_2)$, the calculation shows the intrinsic structure change from the cluster gas to an elongated structure of $2\alpha+t$ in ^{11}B$(3/2^-_3) \rightarrow {}^{11}B(5/2^-_3)$. The elongated $2\alpha+t$ structure produces the rotational band up to $9/2^-$ with large moment of inertia.

Strictly speaking, the rigid rotor is not a correct picture for these excited states in ^{12}C and ^{11}B because of large quantum fluctuations of cluster positions as well as strong state mixing, *i.e.*, structure change. Consequently, the energy spectra and transition strengths do not show ideal rotational band behavior.

4˙3. *Linear chain structure of* ^{14}C. – A linear-chain $n\alpha$ structure has been a long standing problem. In microscopic 3α-cluster model calculations, the linear α-chain structure in ^{12}C is found to be unstable against the bending motion [65, 98]. Indeed, in the AMD+VAP calculation of ^{12}C, the linear α-chain structure is not obtained, but only the bent chain-like structure is obtained in the 0^+_3 state. However, in neutron-rich C, the linear α-chain structure is expected to be stabilized by excess neutrons surrounding

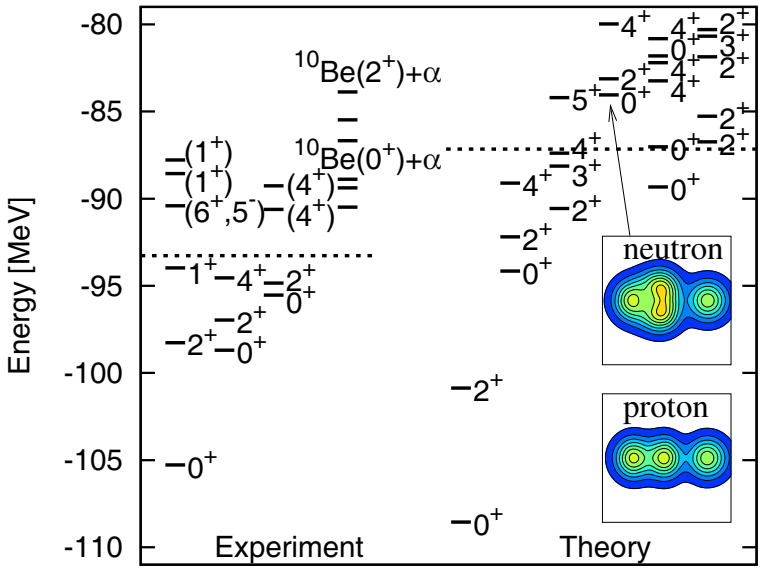

Fig. 14. – Energy spectra of ^{14}C. Theoretical results obtained by the $\beta\gamma$-constraint AMD with the GCM using the Volkov No. 2 force are compared with experimental energy spectra. Intrinsic densities of proton and neutron distributions of the linear-chain band are also shown. Figures are taken from ref. [9].

3α [4, 9, 98-107]. The $\beta\gamma$-constraint AMD with GCM calculation predicted the linear α-chain structure in excited states of ^{14}C [9]. Two valence neutrons play an important role in stabilization of the linear-chain structure. The linear-chain structure produces a $K^\pi = 0^+$ rotational band above the $^{10}\mathrm{Be} + \alpha$ threshold energy (fig. 14). The proton and neutron density distributions shows $^{10}\mathrm{Be} + \alpha$ cluster structure with an α-cluster on the head of the deformed ^{10}Be cluster. Recently, candidate states, 0^+, 2^+, and 4^+, for members of the linear-chain band have been reported by ^{10}Be scattering experiments on α [106, 107]. Also in other neutron-rich C isotopes, linear chain structures are expected to appear in excited states.

5. – Monopole and dipole excitations in light nuclei

5˙1. *Low-energy monopole and dipole excitations*. – In monopole and dipole excitations, significant strengths are known to exist in low-energy regions below higher-energy giant resonances (GR). For example, low-energy isoscalar (IS) monopole excitations for cluster states appear separating from the IS giant monopole resonances (GMR) of the so-called breathing mode. In isovector (IV) dipole ($E1$) excitations, low-energy modes below the IV giant dipole resonances (GDR) are expected to be valence neutron oscil-

lation mode against a core nucleus. The appearance of low-energy strengths separating from the GRs is an evidence of new excitation modes that decouple from the GR modes.

In nuclear excitations, the GRs have been observed as broad bump structure in the high-energy region of strength functions. The GR strength usually exhausts a dominant part of the sum rule value, and it is regarded as an energy eigen mode of collective oscillation of the system. For instance, the IS GMR corresponds to the compressive monopole oscillation called the breathing mode, whereas the IV GDR is the proton-neutron opposite oscillation. The IS GDR is another compressive mode because the ISD operator contains the leading r^3 term. The GRs are small amplitude collective oscillations described by coherent 1p-1h excitations, in which many nucleons participate. The GR energies are related to nuclear matter properties. For example, the ISGMR and IVGDR energies give information of the incompressibility and symmetry energy of a nuclear matter, respectively. The GRs appear in the high-energy region (typical IV GDR energy in a medium-mass region is 20–30 MeV) because nuclear system favors to keep the density and isospin symmetry and feels strong restoring forces in monopole and dipole excitations.

Below the GR strengths, low-energy strengths have been known in IS and IV dipole excitations as well as IS monopole excitations (see refs. [108-111] and references therein). Particularly, low-energy dipole strengths have been intensively and extensively studied by hadronic probes in the past two decades. The history of the measurement of the low-energy $E1$ strengths started in 1960's. The low-energy $E1$ strengths have been measured in ^{208}Pb and named "Pigmy resonance" because they are tiny strengths below the GR. To understand the LE dipole strengths, the idea of neutron skin oscillation against a core has been proposed at the beginning of 1970's with hydro fluid models. The word, Pigmy dipole, is sometimes used for this specific mode of neutron skin oscillation, but one should keep in mind that the low-energy dipole strengths come from not only the neutron-skin oscillation but arises from various origins. In 1980-1990's, in the remarkable progress of physics of unstable nuclei, the soft $E1$ strengths (or soft $E1$ resonances) have attracted a great interest. The soft $E1$ is the $E1$ strength at extremely low energy ($\leq$ 1 MeV) predicted in neutron-halo nuclei, in which weakly bound valence neutrons broadly distributed outward contribute to the strong low-energy $E1$ strengths. The soft $E1$ mode is an phenomenon peculiar to neutron-halo nuclei. In this decade, investigations of the low-energy dipole resonances in general nuclei are revived in experimental and theoretical sides. Major interests of low-energy IVD were its impact to astrophysical r process in photodisintegration and neutron capture rate. It is also discussed to extract information of neutron matter properties.

For the IS channel, the low-energy ISD strengths have been observed by α and ^{6}Li inelastic scattering. In 1980's, it was reported that the low-energy ISD exhausts several percentages of the energy weighted sum rule (EWSR) [112-114]. The question to be answered is why the significant strengths appear in such low-energy region separated from the GR strength. In 1990's and 2000's, more detailed strength functions of the ISD excitation have been measured for various stable nuclei. For the theoretical interpretation

of the low-energy ISD, a torus mode has been proposed by hydro-dynamical models [115, 116]. The torus mode carries nuclear vorticity and also called vortical and toroidal modes. Recently, microscopic calculations based on mean-field approaches have been achieved and the toroidal (vortical) nature of the low-energy dipole resonances have been discussed [108, 117-122]. Thus, in dipole excitations, different modes are expected in low-energy regions, the neutron skin oscillation and toroidal modes.

In light nuclei, cluster modes also contribute to the low-energy excitations, in particular, to isoscalar-type excitations because the isoscalar monopole and dipole operators excite not only the compressive GRs but also the inter-cluster motion. In experimental and theoretical studies of nuclear clustering, isoscalar monopole (ISM) and dipole (ISD) transitions have been investigated to probe cluster modes in various nuclei [91, 123-126]. Yamada *et al.* pointed out two different types of ISM excitations in ^{16}O [124]; the low-energy ISM strengths for excitations into cluster states and the high-energy ISM strengths for the isoscalar giant monopole resonance (ISGMR) corresponding to the collective breathing mode.

Questions to be answered are as follows. Do low-energy strengths appear separating from GR strengths? If so, what are the origins of the low-energy modes? Which operators are sensitive to probe them? What are the roles of cluster structures and excess neutrons in the low-energy modes of light neutron-rich nuclei?

To answer these questions, we need a theoretical framework that can describe both coherent 1p-1h excitations and low-energy cluster modes. For this aim, we constructed a new method, the shifted basis AMD (sAMD) and combined it with the cluster GCM [127-129]. The method sAMD is designed to describe coherent 1p-1h excitations on the ground state, which are essential for giant resonances [127]. On the other hand, the cluster GCM can efficiently describe large amplitude cluster modes which contribute to the low-energy strengths. For details of the sAMD+GCM, the reader is referred to refs. [127-129].

5˙2. *Dipole transition operators.* – The toroidal dipole (TD) operator is useful to measure the nuclear vorticity and its character is much different from the standard compressive dipole (CD) one, which mainly excites the ISGDR corresponding to the normal compressive mode. The TD dominant nature of the low-energy dipole resonances has been demonstrated by toroidal flow in transition current densities [108, 117, 118, 120-122]. To investigate the toroidal nature of dipole excitations, we here use the toroidal dipole operator adopted in ref. [120].

The toroidal and compressive dipole operators are defined as

$$M_{\rm TD}(\mu) = \frac{-i}{2\sqrt{3}c}\int {\rm d}\boldsymbol{r}\boldsymbol{j}(\boldsymbol{r}) \times \left[\frac{\sqrt{2}}{5}r^2\boldsymbol{Y}_{12\mu}(\hat{\boldsymbol{r}}) + r^2\boldsymbol{Y}_{10\mu}(\hat{\boldsymbol{r}})\right], \tag{14}$$

$$M_{\rm CD}(\mu) = \frac{-i}{2\sqrt{3}c}\int {\rm d}\boldsymbol{r}\boldsymbol{j}(\boldsymbol{r}) \left[\frac{2\sqrt{2}}{5}r^2\boldsymbol{Y}_{12\mu}(\hat{\boldsymbol{r}}) - r^2\boldsymbol{Y}_{10\mu}(\hat{\boldsymbol{r}})\right], \tag{15}$$

where $\boldsymbol{j}(\boldsymbol{r})$ is the current density operator and $\boldsymbol{Y}_{\lambda L\mu}$ is the vector spherical harmonics.

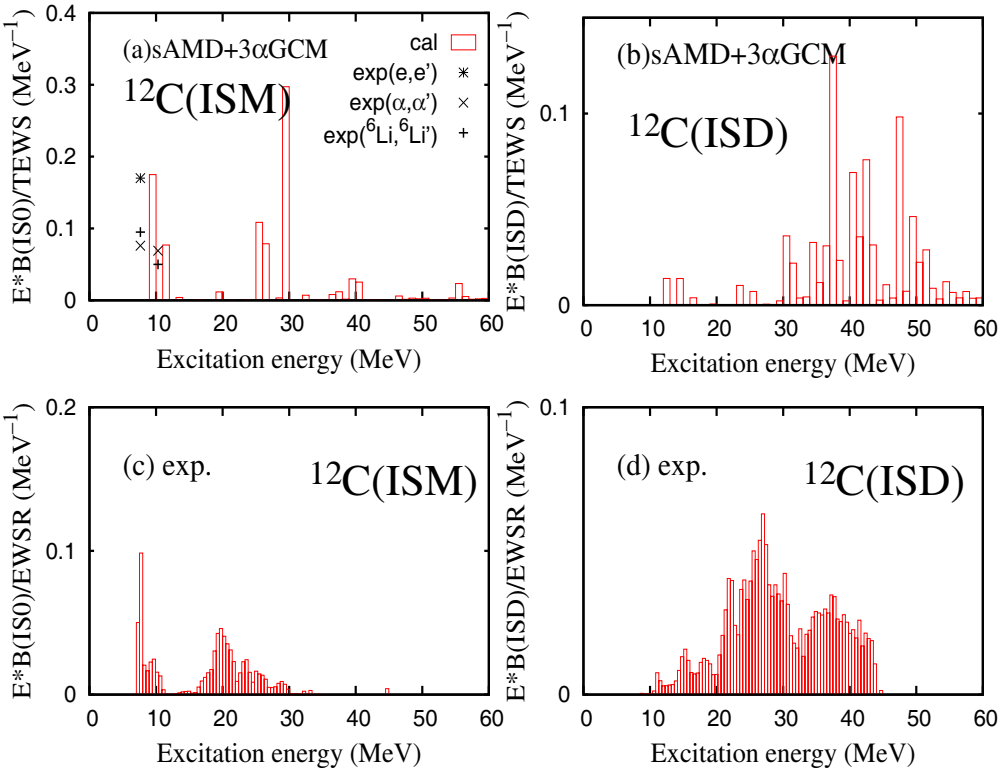

Fig. 15. – The energy weighted ISM and ISD strength distributions calculated by the sAMD+3αGCM and those measured by (α, α') scattering [130]. The data for the 0_2^+ and 0_3^+ states measured by (α, α') [130] and (^{6}Li, ^{6}Li$'$) [132] scattering, and those evaluated by the E0 strengths [133] are also shown by symbols in panel (a). The figure is taken from ref. [125].

The $E1$ operator is written with the IV density operator $\rho^{\mathrm{IV}}(\boldsymbol{r})$ as

$$M_{E1}(\mu) \equiv \int \mathrm{d}\boldsymbol{r}\rho^{\mathrm{IV}}(\boldsymbol{r})rY_{1\mu}(\hat{\boldsymbol{r}}). \tag{16}$$

The transition strength for a dipole operator M_{D} is given as

$$B(\mathrm{D}; 0 \to f) = \frac{1}{2J_0+1}|\langle f|M_{\mathrm{D}}|0\rangle|^2, \tag{17}$$

where J_0 is the angular momentum of the initial state.

By using the continuity equation, the matrix element of the CD operator is easily

transformed into the ordinary IS dipole ($IS1$) matrix element as

$$\langle f|M_{\rm CD}(\mu)|i\rangle = -\frac{1}{10}\frac{E}{\hbar c}\langle f|M_{IS1}(\mu)|i\rangle, \tag{18}$$

$$M_{IS1}(\mu) \equiv \int {\rm d}\boldsymbol{r}\rho(\boldsymbol{r})r^3 Y_{1\mu}(\hat{\boldsymbol{r}}), \tag{19}$$

where E is the excitation energy $E \equiv E_f - E_0$ given with the initial energy (E_0) and final energy (E_f). For convenience, we define scaled strengths of the TD and CD transitions

$$\tilde{B}({\rm TD},{\rm CD}) = \left(\frac{10\hbar c}{E}\right)^2 B({\rm TD},{\rm CD}), \tag{20}$$

so that $\tilde{B}({\rm CD})$ corresponds to the standard ISD strength $B(IS1)$.

5˙3. *Monopole transitions in* ^{12}C. – For ^{12}C, the low-energy ISM and ISD strengths have been experimentally observed below the high-energy GR strengths [130, 134]. In order to clarify the origins of the low-energy strengths, a hybrid model of the shifted basis AMD (sAMD) and 3α-GCM was applied to ^{12}C [125]. The sAMD has been constructed to describe coherent 1p-1h excitations on top of the ground state and proved to be able to describe GR strengths in the high-energy region [127]. On the other hand, the 3α-GCM is essential to describe large amplitude cluster modes which contribute to the low-energy strengths.

In fig. 15, the calculated ISM and ISD strengths in ^{12}C obtained by the sAMD + 3αGCM are shown together with the experimental data [130]. The experimental ISM strengths show that the low-energy strengths appear separately from the high-energy strengths. They exhaust significant percentages of the energy-weighted sum rule (EWSR).

In the sAMD+3αGCM calculation, significant ISM strengths are obtained for cluster states, which contribute to the low-energy ISM strengths. The separation between the low-energy ISM strengths and high-energy ISGMR is described well by the calculation. Also for the ISD strengths, the calculation predicts significant low-energy strengths for 1^- states corresponding to cluster states. The experimentally observed ISD strengths in the $E_x = 10$–15 MeV region are likely to correspond to the predicted low-energy cluster modes.

5˙4. *Dipole excitations in Be.* – As mentioned previously, the ground state of ^{8}Be has the developed 2α cluster structure. In ^{9}Be and ^{10}Be, two α clusters are formed and surrounded by valence neutrons. In the study of dipole excitations in ^{9}Be and ^{10}Be with the sAMD+GCM [128, 131], it was found that the 2α clustering and valence neutrons play important roles in low-lying dipole modes.

Figure 16 shows the calculated $E1$ strengths in ^{8}Be, ^{9}Be, and ^{10}Be. The $E1$ strengths in ^{8}Be show the GDR strengths with a two peak structure. The lower and higher peaks

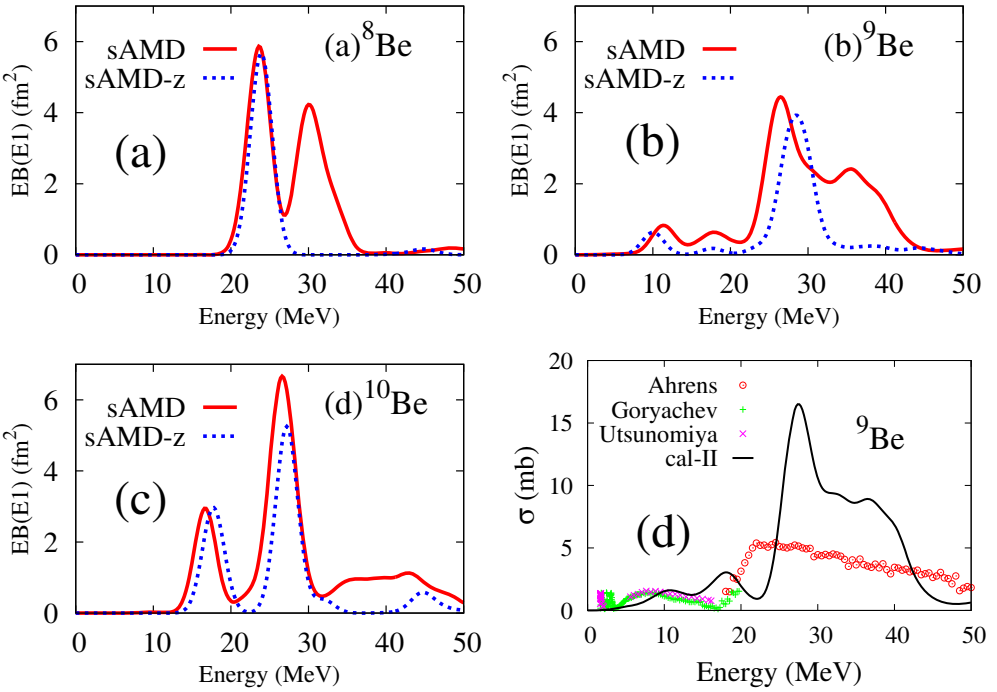

Fig. 16. – Energy-weighted $E1$ strengths in (a)^{8}Be, (b)^{9}Be, and (c)^{10}Be obtained by the sAMD ($\sigma = 1, \ldots, 8$) and the sAMD-z (longitudinal mode: $\sigma = z$) calculations. (d) The calculated $E1$ and experimental photonuclear cross sections in ^{9}Be [135-137]. The calculated $E1$ strengths are smeared with the width $\gamma = 2$ MeV. The figure is taken from ref. [128].

of the GDR originate in the proton-neutron opposite oscillation in the longitudinal and transverse directions in the prolately deformed 2α-cluster structure. The $E1$ strengths in ^{9}Be and ^{10}Be also show the GDR strengths with two-peak structures in the energy region higher than 20 MeV. These GDR strengths come from the proton-neutron opposite oscillation of nucleons inside the 2α core part. The lower peak of the GDR for the longitudinal mode in ^{9}Be and ^{10}Be has almost the same shape as that in ^{8}Be, because valence neutrons sitting in the transverse direction around the 2α core do not disturb the longitudinal vibration of the core. However, the higher peak for the transverse oscillation becomes broader and broader in ^{9}Be and ^{10}Be with increase of valence neutrons, because the transverse mode of the 2α core is strongly affected by the existence of valence neutrons. In the low-energy region of the $E1$ strengths in ^{9}Be and ^{10}Be, we obtain significant $E1$ strengths, which are separated well from the GDRs. The valence neutron motion against the 2-α core contributes to the low-energy $E1$ strengths. In particular, remarkably strong low-energy $E1$ strengths are obtained in ^{10}Be because of coherent two neutron oscillation. It is also interesting that this mode can be regarded as inter-cluster excitation of ^{6}He + α clustering. The experimental photonuclear cross sections in ^{9}Be

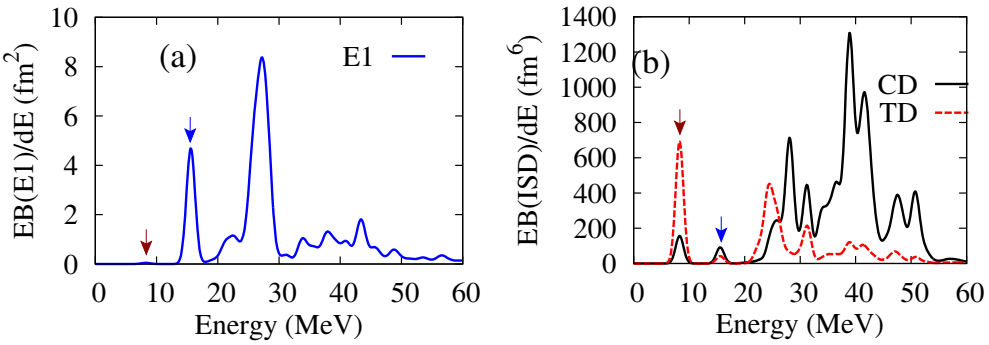

Fig. 17. – Energy-weighted dipole strengths $EB(E1)$, $E\tilde{B}$(CD), and $E\tilde{B}$(TD), for the $E1$, CD, and TD modes of ^{10}Be calculated with the sAMD+αGCM. The smearing width is $\gamma = 1$ MeV. The figure is taken from ref. [131].

clearly show the separation between the low-energy $E1$ strengths and the high-energy GDR [136, 137]. The observed low-energy $E1$ strengths exhaust 10% of the sum rule value. The calculated $E1$ strengths are qualitatively consistent with the experimental data.

Let us discuss the $E1$ and toroidal natures of the dipole excitations in ^{10}Be. Figure 17 shows the calculated CD and TD strengths together with the $E1$ strengths. In the low-energy region, we obtained two kinds of dipole excitations. The $E1$ strength is remarkable for the 1^-_2 around 15 MeV. Below the 1^-_2, we obtain very weak $E1$ strength for the 1^-_1 around 8 MeV. In contrast to the weak $E1$ strength, the 1^-_1 state is excited by the isoscalar compressive dipole operator (CD mode). Moreover, the 1^-_1 state is remarkably excited by the toroidal dipole operator indicating that it is regarded as the toroidal mode. Namely, two different modes exist in low-energy dipole excitations in ^{10}Be, the toroidal dominant 1^-_1 and the $E1$ dominant 1^-_2.

To investigate properties of these two low-energy dipole modes in ^{10}Be, we calculated transition current densities. The calculated transition current densities are shown in fig. 18. The toroidal nature is clearly seen in $0^+_1 \to 1^-_1$. The neutron toroidal current gives significant contribution to the TD strength but it gives no contribution to the $E1$ strength because it does not contain the translational current. On the other hand, the transition current densities for $0^+_1 \to 1^-_2$ show a feature of translational oscillation of valence neutron motion against the 2α core. In this transition, the 2α motion gives no contribution of the IV component, but the surface neutron current simply contributes to the enhancement of the $E1$ strength.

Interestingly, the toroidal and $E1$ natures of these two modes can be understood also in a cluster picture as shown by schematic figures in fig. 18. The 0^+_1, 1^-_1, and 1^-_2 states have cluster structures with the 2α core and two valence neutrons, which can be regarded as the $^6\mathrm{He} + \alpha$ clustering. The $0^+_1 \to 1^-_1$ excitation is interpreted as a rotational mode of the deformed ^{6}He cluster. The toroidal neutron flow is caused by the surface neutron

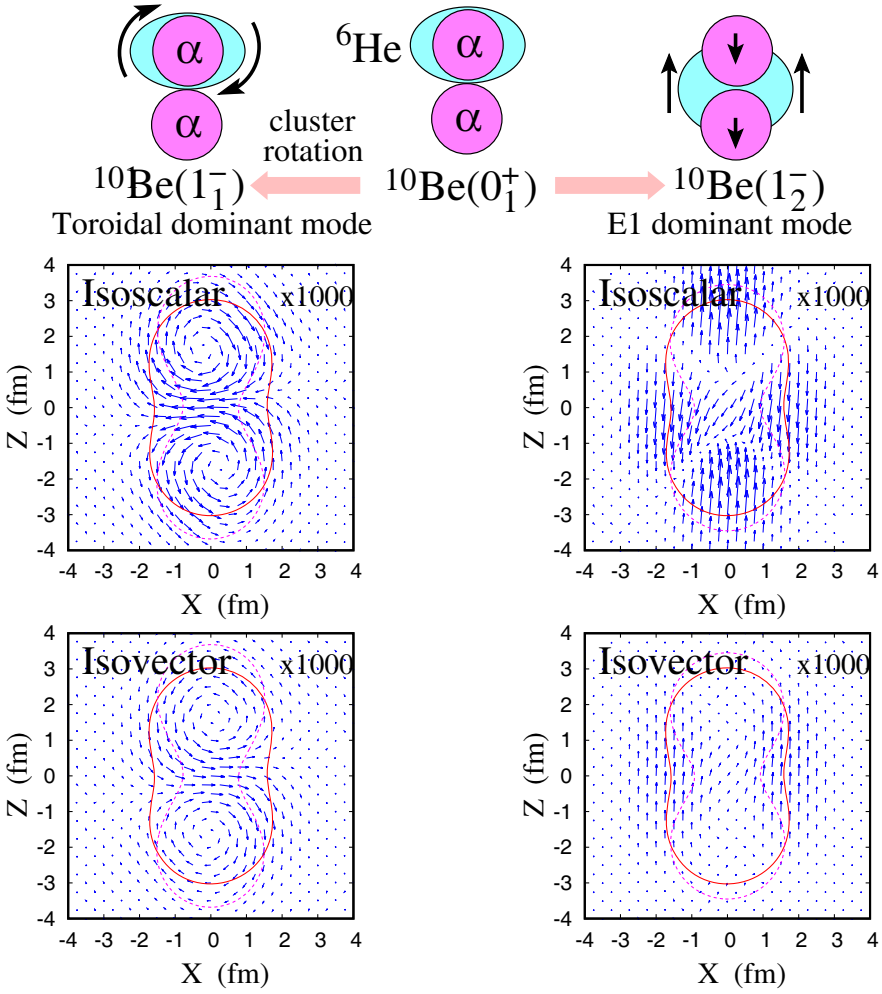

Fig. 18. – Vector plots of the transition current densities for the toroidal mode ($0^+_1 \to 1^-_1$) and the $E1$ mode ($0^+_1 \to 1^-_2$) in ^{10}Be obtained with the sAMD+αGCM. The isoscalar and isovector contributions of the current densities are plotted on the X-Z plane at $Y = 0$ (scaled by a factor of 10^3). Schematic figures for interpretation of the dipole modes in a cluster picture are also shown. The figure is taken from ref. [131].

current around an α cluster induced by the ^{6}He-cluster rotation. On the other hand, in the $0^+_1 \to 1^-_2$ excitation, the translational neutron current is caused by the surface neutron oscillation along the longitudinal directions along the 2α core. In the $^6\mathrm{He} + \alpha$ cluster picture, this mode can be interpreted as the $L = 1$ excitation of the relative motion between ^{6}He and α clusters. It should be stressed again that because of the coherent $2n$ motion, it has strong $E1$ strengths.

6. – Conclusion

Nuclear clustering is one of the essential features of nuclear systems. The coexistence of cluster and mean-field natures brings rich phenomena to nuclear systems depending on proton and neutron numbers and excitation energy. Remarkable clustering appears, in particular, in low-density situations. Examples are cluster formation at nuclear surface and cluster excitation in excited states near the cluster-decay threshold energies. In order to comprehend essential features of nuclear systems, systematic study of cluster and mean-field phenomena in various nuclei is requested. In theoretical study, it is key to describe both the cluster and mean-field aspects of the ground and excited states in a unified manner. We have applied the AMD model and investigated structures of light nuclei. The method is a useful approach to investigate structures of low-lying states and cluster excitations near and above threshold energies. To describe various nuclear excitations in a wide energy region covering low-energy modes and high-energy GRs, the sAMD combined with the cluster GCM has been proved to be a powerful tool, which is suitable to describe coherent 1p-1h excitations and also large amplitude cluster modes. We have discussed cluster phenomena in Be and C isotopes, and also monopole and dipole excitations in neutron-rich Be and ^{12}C. It was found that the 2α and 3α clusterings play an important role in the low-energy monopole and dipole excitations.

* * *

The computational calculations of this work were performed by using the supercomputer in the Yukawa Institute for theoretical physics, Kyoto University. This work was supported by JSPS KAKENHI Grant Number 26400270.

REFERENCES

[1] IKEDA K., HORIUCHI H. and TAKIGAWA N., *Prog. Theor. Phys. Suppl. Extra Number*, **68** (1968) 464.
[2] TOHSAKI A., HORIUCHI H., SCHUCK P. and RÖPKE G., *Phys. Rev. Lett.*, **87** (2001) 192501.
[3] YAMADA T. and SCHUCK P., *Phys. Rev. C*, **69** (2004) 024309.
[4] VON OERTZEN W., FREER M. and KANADA-EN'YO Y., *Phys. Rep.*, **432** (2006) 43.
[5] VON OERTZEN W., *Z. Phys. A*, **354** (1996) 37.
[6] VON OERTZEN W., *Nuovo Cimento*, **110** (1997) 895.
[7] VON OERTZEN W., *Eur. Phys. J. A*, **11** (2001) 403.
[8] KIMURA M., *Phys. Rev. C*, **75** (2007) 034312.
[9] SUHARA T. and KANADA-EN'YO Y., *Phys. Rev. C*, **82** (2010) 044301.
[10] KANADA-ENYO Y., HORIUCHI H. and ONO A., *Phys. Rev. C*, **52** (1995) 628.
[11] KANADA-EN'YO Y. and HORIUCHI H., *Prog. Theor. Phys. Suppl.*, **142** (2001) 205.
[12] KANADA-EN'YO Y., KIMURA M. and ONO A., *Proc. Theor. Exp. Phys.*, **2012** (2012) 01A202.
[13] ONO A., HORIUCHI H., MARUYAMA T. and OHNISHI A., *Phys. Rev. Lett.*, **68** (1992) 2898.

[14] ONO A., HORIUCHI H., MARUYAMA T. and OHNISHI A., *Prog. Theor. Phys.*, **87** (1992) 1185.
[15] ONO A. and HORIUCHI H., *Prog. Part. Nucl. Phys.*, **53** (2004) 501. URL http://www.sciencedirect.com/science/article/pii/S0146641004000936.
[16] BRINK D. M., *Alpha cluster model*, in *Proceedings of the International School of Physics Enrico Fermi, Course 36* (Academic Press) 1966, p. 247.
[17] KIMURA M., *Phys. Rev. C*, **69** (2004) 044319.
[18] KIMURA M., SUHARA T. and KANADA-EN'YO Y., *Eur. Phys. J. A*, **52** (2016) 373.
[19] FELDMEIER H., *Nucl. Phys. A*, **515** (1990) 147.
[20] FELDMEIER H., BIELER K. and SCHNACK J., *Nucl. Phys. A*, **586** (1995) 493.
[21] FELDMEIER H. and SCHNACK J., *Rev. Mod. Phys.*, **72** (2000) 655.
[22] NEFF T. and FELDMEIER H., *Nucl. Phys. A*, **713** (2003) 311.
[23] SUHARA T. and KANADA-EN'YO Y., *Prog. Theor. Phys.*, **123** (2010) 303.
[24] TANIGUCHI Y., KIMURA M. and HORIUCHI H., *Prog. Theor. Phys.*, **112** (2004) 475.
[25] KANADA-EN'YO Y., *Phys. Rev. C*, **96** (2017) 034306.
[26] KANADA-EN'YO Y., HORIUCHI H. and DOTÉ A., *Phys. Rev. C*, **60** (1999) 064304.
[27] MILIN M. *et al.*, *Nucl. Phys. A*, **753** (2005) 263.
[28] FREER M. *et al.*, *Phys. Rev. Lett.*, **96** (2006) 042501.
[29] SEYA M., KOHNO N. and NAGATA S., *Prog. Theor. Phys.*, **65** (1981) 204.
[30] ARAI K., OGAWA Y., SUZUKI Y. and VARGA K., *Phys. Rev. C*, **54** (1996) 132.
[31] OGAWA Y., ARAI K., SUZUKI Y. and VARGA K., *Nucl. Phys. A*, **673** (2000) 122.
[32] ITAGAKI N. and OKABE S., *Phys. Rev. C*, **61** (2000) 044306.
[33] DESCOUVEMONT P. and BAYE D., *Phys. Lett. B*, **505** (2001) 71.
[34] DESCOUVEMONT P., *Nucl. Phys. A*, **699** (2002) 463.
[35] ITO M., KATO K. and IKEDA K., *Phys. Lett. B*, **588** (2004) 43.
[36] ITO M., ITAGAKI N., SAKURAI H. and IKEDA K., *Phys. Rev. Lett.*, **100** (2008) 182502.
[37] DUFOUR M., DESCOUVEMONT P. and NOWACKI F., *Nucl. Phys. A*, **836** (2010) 242.
[38] NEFF T., FELDMEIER H. and ROTH R., *Nucl. Phys. A*, **752** (2005) 321.
[39] YOSHIDA T., SHIMIZU N., ABE T. and OTSUKA T., *J. Phys. Conf. Ser.*, **569** (2014) 012063.
[40] OKABE S., ABE Y. and TANAKA H., *Prog. Theory. Phys.*, **57** (1977) 866.
[41] KANADA-EN'YO Y., *Phys. Rev. C*, **85** (2012) 044320.
[42] KANADA-EN'YO Y., *Phys. Rev. C*, **66** (2002) 011303.
[43] KANADA-EN'YO Y. and HORIUCHI H., *Phys. Rev. C*, **66** (2002) 024305.
[44] KANADA-EN'YO Y. and HORIUCHI H., *Phys. Rev. C*, **68** (2003) 014319.
[45] KANADA-EN'YO Y., *Phys. Rev. C*, **91** (2015) 014315.
[46] NÖRTERSHÄUSER W. *et al.*, *Phys. Rev. Lett.*, **102** (2009) 062503.
[47] KRIEGER A. *et al.*, *Phys. Rev. Lett.*, **108** (2012) 142501.
[48] SUZUKI T. and OTSUKA T., *Phys. Rev. C*, **56** (1997) 847.
[49] IWASAKI H. *et al.*, *Phys. Lett. B*, **481** (2000) 7.
[50] IWASAKI H. *et al.*, *Phys. Lett. B*, **491** (2000) 8.
[51] NAVIN A. *et al.*, *Phys. Rev. Lett.*, **85** (2000) 266.
[52] SHIMOURA S. *et al.*, *Phys. Lett. B*, **560** (2003) 31. URL http://www.sciencedirect.com/science/article/pii/S0370269303003411.
[53] PAIN S. D. *et al.*, *Phys. Rev. Lett.*, **96** (2006) 032502.
[54] IMAI N. *et al.*, *Phys. Lett. B*, **673** (2009) 179.
[55] MEHARCHAND R. *et al.*, *Phys. Rev. Lett.*, **108** (2012) 122501.
[56] SIMON H. *et al.*, *Nucl. Phys. A*, **791** (2007) 267.
[57] KONDO Y. *et al.*, *Phys. Lett. B*, **690** (2010) 245.
[58] FUJIWARA Y. *et al.*, *Prog. Theor. Phys. Suppl.*, **68** (1980) 29.

[59] FREER M. and FYNBO H. O. U., *Prog. Part. Nucl. Phys.*, **78** (2014) 1.
[60] MORINAGA H., *Phys. Rev.*, **101** (1956) 254.
[61] MORINAGA H., *Phys. Lett.*, **21** (1966) 78.
[62] SUZUKI Y., HORIUCHI H. and IKEDA I., *Prog. Theor. Phys.*, **47** (1972) 1517.
[63] FUKUSHIMA Y. and KAMIMURA M., *J. Phys. Soc. Jpn.*, **44** (1978) 225.
[64] KAMIMURA M., *Nucl. Phys. A*, **351** (1981) 456.
[65] UEGAKI E., OKABE S., ABE Y. and TANAKA H., *Prog. Theor. Phys.*, **57** (1977) 1262.
[66] DESCOUVEMONT P. and BAYE D., *Phys. Rev. C*, **36** (1987) 54.
[67] FUNAKI Y., TOHSAKI A., HORIUCHI H., SCHUCK P. and RÖPKE G., *Phys. Rev. C*, **67** (2003) 051306.
[68] FEDOTOV S. I., KARTAVTSEV O. I., KOCHKIN V. I. and MALYKH A. V., *Phys. Rev. C*, **70** (2004) 014006.
[69] KUROKAWA C. and KATŌ K., *Nucl. Phys. A*, **738** (2004) 455.
[70] KUROKAWA C. and KATŌ K., *Phys. Rev. C*, **71** (2005) 021301.
[71] FILIKHIN I., SUSLOV V. M. and VLAHOVIC B., *J. Phys. G*, **31** (2005) 1207.
[72] ARAI K., *Phys. Rev. C*, **74** (2006) 064311.
[73] OHTSUBO S., FUKUSHIMA Y., KAMIMURA M. and HIYAMA E., *Prog. Theor. Exp. Phys.*, **2013** (2013) 073D02.
[74] ISHIKAWA S., *Phys. Rev. C*, **90** (2014) 061604.
[75] KANADA-EN'YO Y., *Prog. Theor. Phys.*, **117** (2007) 655; **121** (2009) 895.
[76] AJZENBERG-SELOVE F. and KELLEY J. H., *Nucl. Phys. A*, **506** (1990) 1.
[77] FREER M. *et al.*, *Phys. Rev. C*, **76** (2007) 034320.
[78] ITOH M. *et al.*, *Phys. Rev. C*, **84** (2011) 054308.
[79] FREER M. *et al.*, *Phys. Rev. C*, **83** (2011) 034314.
[80] MARIN-LAMBARRI D. J., BIJKER R., FREER M., GAI M., KOKALOVA T., PARKER D. J. and WHELDON C., *Phys. Rev. Lett.*, **113** (2014) 012502.
[81] FREER M., HORIUCHI H., KANADA-EN'YO Y., LEE D. and MEISSNER U.-G., *Rev. Mod. Phys.*, (to be published).
[82] KANADA-EN'YO Y., *Phys. Rev. Lett.*, **81** (1998) 5291.
[83] NEFF T. and FELDMEIER H., *Nucl. Phys. A*, **738** (2004) 357.
[84] CHERNYKH M., FELDMEIER H., NEFF T., VON NEUMANN-COSEL P. and RICHTER A., *Phys. Rev. Lett.*, **98** (2007) 032501.
[85] EPELBAUM E., KREBS H., LÄHDE T. A., LEE D. and MEISSNER U.-G., *Phys. Rev. Lett.*, **109** (2012) 252501.
[86] DREYFUSS A. C., LAUNEY K. D., DYTRYCH T., DRAAYER J. P. and BAHRI C., *Phys. Lett. B*, **727** (2013) 511.
[87] CARLSON J., GANDOLFI S., PEDERIVA F., PIEPER S. C., SCHIAVILLA R., SCHMIDT K. E. and WIRINGA R. B., *Rev. Mod. Phys.*, **87** (2015) 1067.
[88] FUNAKI Y., HORIUCHI H., VON OERTZEN W., RÖPKE G., SCHUCK P., TOHSAKI A. and YAMADA T., *Phys. Rev. C*, **80** (2009) 064326.
[89] NISHIOKA H., SAITO S. and YASUNO M., *Prog. Theor. Phys.*, **62** (1979) 424.
[90] DESCOUVEMONT P., *Nucl. Phys. A*, **584** (1995) 532.
[91] KAWABATA T. *et al.*, *Phys. Lett. B*, **646** (2007) 6.
[92] KANADA-EN'YO Y., *Phys. Rev. C*, **75** (2007) 024302.
[93] YAMADA T. and FUNAKI Y., *Phys. Rev. C*, **82** (2010) 064315.
[94] SUHARA T. and KANADA-EN'YO Y., *Phys. Rev. C*, **85** (2012) 054320.
[95] BIJKER R. and IACHELLO F., *Annals Phys.*, **298** (2002) 334.
[96] KANADA-EN'YO Y. and SUHARA T., *Phys. Rev. C*, **91** (2015) 014316.
[97] YAMAGUCHI H., HASHIMOTO T., HAYAKAWA S., BINH D. N., KAHL D., KUBONO S., WAKABAYASHI Y., KAWABATA T. and TERANISHI T., *Phys. Rev. C*, **83** (2011) 034306.

[98] ITAGAKI N., OKABE S., IKEDA K. and TANIHATA I., *Phys. Rev. C*, **64** (2001) 014301.
[99] SOIC N. *et al.*, *Phys. Rev. C*, **68** (2003) 014321.
[100] VON OERTZEN W. *et al.*, *Eur. Phys. J. A*, **21** (2004) 193.
[101] PRICE D. L. *et al.*, *Phys. Rev. C*, **75** (2007) 014305.
[102] HAIGH P. J. *et al.*, *Phys. Rev. C*, **78** (2008) 014319.
[103] MARUHN J. A., LOEBL N., ITAGAKI N. and KIMURA M., *Nucl. Phys. A*, **833** (2010) 1.
[104] FREER M. *et al.*, *Phys. Rev. C*, **90** (2014) 054324.
[105] BABA T., CHIBA Y. and KIMURA M., *Phys. Rev. C*, **90** (2014) 064319.
[106] FRITSCH A. *et al.*, *Phys. Rev. C*, **93** (2016) 014321.
[107] YAMAGUCHI H., KAHL D., HAYAKAWA S., SAKAGUCHI Y., ABE K., NAKAO T., SUHARA T., IWASA N., KIM A., KIM D., CHA S., KWAG M., LEE J., LEE E., CHAE K., WAKABAYASHI Y., IMAI N., KITAMURA N., LEE P., MOON J., LEE K., AKERS C., JUNG H., DUY N., KHIEM L. and LEE C., *Phys. Lett. B*, **766** (2017) 11.
URL `www.sciencedirect.com/science/article/pii/S0370269316307961`.
[108] PAAR N., VRETENAR D., KHAN E. and COLO G., *Rept. Prog. Phys.*, **70** (2007) 691.
[109] AUMANN T. and NAKAMURA T., *Phys. Scr. T*, **152** (2013) 014012.
[110] SAVRAN D., AUMANN T. and ZILGES A., *Prog. Part. Nucl. Phys.*, **70** (2013) 210.
[111] BRACCO A., CRESPI F. C. L. and LANZA E. G., *Eur. Phys. J. A*, **51** (2015) 99.
[112] HARAKEH M. N. and DIEPERINK A. E. L., *Phys. Rev. C*, **23** (1981) 2329.
[113] DECOWSKI P., MORSCH H. P. and BENENSON W., *Phys. Lett. B*, **101** (1981) 147.
[114] POELHEKKEN T. D., HESMONDHALGH S. K. B., HOFMANN H. J., VAN DER WOUDE A. and HARAKEH M. N., *Phys. Lett. B*, **278** (1992) 423.
[115] SEMENKO S. F., *Sov. J. Nucl. Phys.*, **34** (1981) 356.
[116] RAVENHALL D. G. and WAMBACH J., *Nucl. Phys. A*, **475** (1987) 468.
[117] VRETENAR D., PAAR N. and RING P., *Phys. Rev. C*, **65** (2002) 021301.
[118] RYEZAYEVA N., HARTMANN T., KALMYKOV Y., LENSKE H., VON NEUMANN-COSEL P., PONOMAREV V. YU., RICHTER A., SHEVCHENKO A., VOLZ S. and WAMBACH J., *Phys. Rev. Lett.*, **89** (2002) 272502.
[119] PAPAKONSTANTINOU P., PONOMAREV V. YU., ROTH R. and WAMBACH J., *Eur. Phys. J. A*, **47** (2011) 14.
[120] KVASIL J., NESTERENKO V. O., KLEINIG W., REINHARD P. G. and VESELY P., *Phys. Rev. C*, **84** (2011) 034303.
[121] REPKO A., REINHARD P. G., NESTERENKO V. O. and KVASIL J., *Phys. Rev. C*, **87** (2013) 024305.
[122] NESTERENKO V. O., KVASIL J., REPKO A., KLEINIG W. and REINHARD P. G., *Phys. Atom. Nucl.*, **79** (2016) 842.
[123] FUNAKI Y., TOHSAKI A., HORIUCHI H., SCHUCK P. and RÖPKE G., *Eur. Phys. J. A*, **28** (2006) 259.
[124] YAMADA T., FUNAKI Y., MYO T., HORIUCHI H., IKEDA K., RÖPKE G., SCHUCK P. and TOHSAKI A., *Phys. Rev. C*, **85** (2012) 034315.
[125] KANADA-EN'YO Y., *Phys. Rev. C*, **93** (2016) 054307.
[126] CHIBA Y. and KIMURA M., *Phys. Rev. C*, **91** (2015) 061302.
[127] KANADA-EN'YO Y., *Phys. Rev. C*, **89** (2014) 024302.
[128] KANADA-EN'YO Y., *Phys. Rev. C*, **93** (2016) 024322.
[129] KANADA-EN'YO Y., *Phys. Rev. C*, **93** (2016) 054307.
[130] JOHN B., TOKIMOTO Y., LUI Y. W., CLARK H. L., CHEN X. and YOUNGBLOOD D. H., *Phys. Rev. C*, **68** (2003) 014305.
[131] KANADA-EN'YO Y. and SHIKATA Y., *Phys. Rev. C*, **95** (2017) 064319.
[132] EYRICH W., HOFMANN A., LEHMANN A., MUHLDORFER B., SCHLOSSER H., WIRTH H., GILS H. J., REBEL H. and ZAGROMSKI S., *Phys. Rev. C*, **36** (1987) 416.

[133] Chernykh M., Feldmeier H., Neff T., von Neumann-Cosel P. and Richter A., *Phys. Rev. Lett.*, **105** (2010) 022501.
[134] Youngblood D. H., Lui Y. W. and Clark H. L., *Phys. Rev. C*, **57** (1998) 2748.
[135] Ahrens J. *et al.*, *Nucl. Phys. A*, **251** (1975) 479.
[136] Goryachev A., Zalesnyy G., Pozdnev I. and Rossiiskoi I., *Akad. Nauk, Ser.Fiz.*, **56** (1992) 159.
[137] Utsunomiya H., Katayama S., Gheorghe I., Imai S., Yamaguchi H., Kahl D., Sakaguchi Y., Shima T., Takahisa K. and Miyamoto S., *Phys. Rev. C*, **92** (2015) 064323.

This page intentionally left blank

Proceedings of the International School of Physics "Enrico Fermi"
Course 201 "Nuclear Physics with Stable and Radioactive Ion Beams", edited by F. Gramegna,
P. Van Duppen, A. Vitturi and S. Pirrone
(IOS, Amsterdam; SIF, Bologna) 2019
DOI 10.3254/978-1-61499-957-7-95

Density Functional Theory (DFT) for atomic nuclei: A simple introduction

G. Colò

Dipartimento di Fisica, Università degli Studi di Milano,
and INFN, Sezione di Milano
via Celoria 16, 20133 Milano, Italy

Summary. — The present contribution does not aim at replacing the huge and often excellent literature on DFT for atomic nuclei, but tries to provide an updated introduction to this topic. The goal would be, ideally, to help a fresh M.Sc. or Ph.D. student (or a researcher from other fields) to become acquainted with some basic concepts, and then move to the specialized textbooks or papers with some ability for orienteering. We first introduce the basics of DFT, and show the difference with the "naïve" mean-field theory, that is doomed to fail as a model even in the simple case of uniform nuclear matter. We introduce the Energy Density Functionals (EDFs) that are used in nuclear structure, with few examples of their applications. The concepts of symmetry breaking and restoration are briefly discussed. We also include an introduction to the time-dependent extension of DFT that, so far, has been implemented essentially only in the adiabatic approximation and has been applied mainly to the study of nuclear vibrations. With this material, we hope that any reader is able to deal with the texts that go deeper into each of the topics, having understood that DFT is probably the best compromise in nuclear structure theory between simplicity, accuracy, and broad range of applicability.

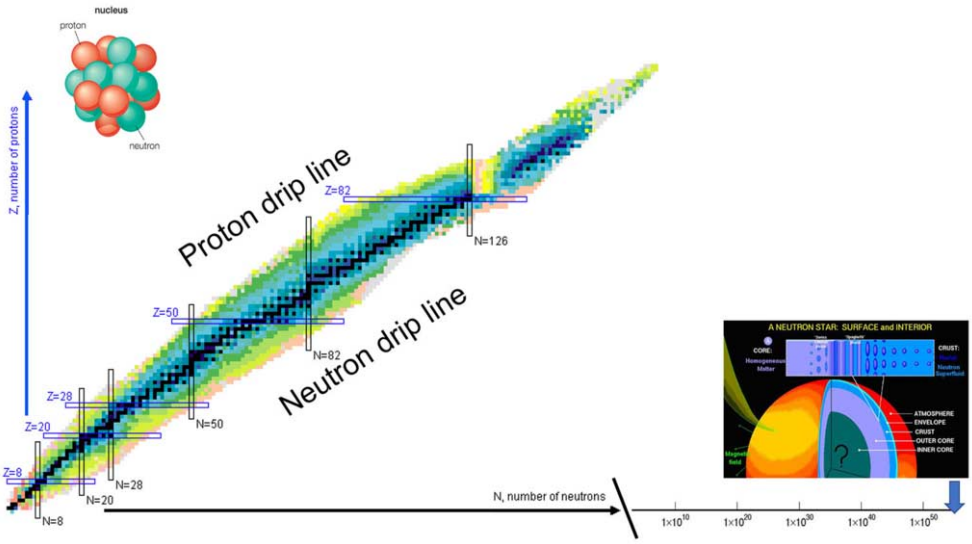

Fig. 1. – Overall view of the nuclear chart. In the right part, a schematic picture of a neutron star (taken from D. Page) is displayed.

1. – Introduction

Atomic nuclei are strongly correlated, self-bound quantum systems that are still capturing the interest of so many scientists, more than a century after their discovery, for a variety of reasons.

The nuclear chart, that is a two-dimensional arrangement of nuclei on a plane where the number of neutrons, N, and the number of protons, Z, are the x- and y-axis, respectively, has still broad territories to be explored. A schematic view from the web (`https://www.nndc.bnl.gov/chart/`) is displayed in fig. 1. Every year, a large number of new nuclei, that amount to $\approx$ 20–30 in the last decade, are being discovered (cf. [1] and references therein). The limit of existence for neutron-rich or neutron-deficient nuclei (so-called drip lines, beyond which nuclei are unbound with respect to neutron and proton emission, respectively), and the search for superheavy elements, are the highlights of this exploration.

At the same time, the nuclear physics and nuclear astrophysics communities are striving to grasp some understanding of compact objects like neutron stars, that are extreme forms of nuclear matter. While ordinary nuclei display densities around the so-called saturation density $\rho_0 = 0.16\,\mathrm{fm}^{-3}$ (see below) and are at, or lie close to, zero temperature, different conditions may be realised in stars. The inner core of neutron stars contains matter in unknown conditions that may also correspond to a quark-deconfined phase, while the crust is made up with nucleons whose density encompasses a broad range from around 1/3 to 10^{-3} times the saturation density [2]. Neutron stars are believed to contain $\approx 10^{55-56}$ neutrons, and as such are displayed in the lower-right corner of fig. 1.

The new input from nuclei with large neutron-proton asymmetry, or superheavy isotopes, or exotic forms of neutron matter in stars, has changed and is still changing our basic understanding of nuclear structure. Consequently, there is certainly a strong need of up-to-date introductions to several topics.

The present lecture has mainly a theoretical content. Nuclear theory is moving ahead quite rapidly in recent years. Many groups are pursuing the idea that the goal should be deriving nuclear properties from (the low-energy limit of) Quantum Chromo Dynamics (QCD). Genuine lattice calculations with explicit quark degrees of freedom have still serious troubles to reproduce basic properties like the binding energy of the few-nucleon systems (two- and three-body systems turn out to be unbound while ^{4}He is severely underbound [3]). A different strategy consists in using an *effective* realization of the QCD Lagrangian, based on chiral symmetry as originally proposed by S. Weinberg [4]. Chiral Effective Field Theory (EFT) gives rise to a family of model Lagrangians, all based on correct symmetries and separation of energy scales, that can be used in connection with many-body methods like lattice simulations, coupled cluster, renormalization group approaches, or Green's function methods. These so-called *ab initio* methods are continuously extending their range of applicability; nonetheless applying them to heavy nuclei, or highly excited states, is still too demanding [5]. More importantly, the quality of the results still depends on the specific Lagrangian [6, 7].

As a summary, deriving nuclear properties directly from QCD is still a long-term project. *Ab initio* is a wording that may be used in connection with many-body methods that are in principle exact, not only in connection with chiral Lagrangians but also when a phenomenological nucleon-nucleon (NN) interaction is employed. In general, the applicability of these approaches has serious limitations in mass number and excitation energy.

In keeping also with the rich variety of the nuclear phenomena, one can easily understand the absence of a nuclear "standard model". In the current volume, the reader can browse through different lectures and judge directly about the pros and cons of models like the nuclear Shell Model, the Cluster Model, and the algebraic approaches; all these models necessarily include a fair amount of phenomenological input. DFT lies somehow in between the purely phenomenological models and those that aim at starting from QCD. It can be said in its own way to be an *ab initio* theory, because it is rooted in the Hohenberg-Kohn theorem (cf. below). There is not, so far, a systematic connection with an underlying theory but many attempts are promising. As we shall argue in this lecture, a reasonable account of experimental data can be achieved in a quite transparent and economic way. Analogies with electronic systems can be traced, having in mind the development of unified methods for many-fermion systems.

The outline of the present contribution is the following. We discuss the basics of DFT, mainly with reference to the electronic systems, in sect. **2**. In the nuclear case, we remind first the reader about the evidences for independent particle motion that may lead to the assumption of the validity of simple HF (sect. **3**), and we then introduce uniform nuclear matter (sect. **4**) and use it as a playground to show the failure of naïve HF (sect. **5**). We advocate the need for density-dependent interactions that are merely

generators of energy functionals, and we discuss the functionals which are currently used in sect. **6**. Few examples of DFT calculations for the ground-state properties are mentioned in sect. **7**. We then move to the concepts of intrinsic density and symmetry breaking in sect. **8** and sect. **9**, respectively. Section **10** is devoted to the extension of DFT to the time-dependent case, with one illustrative example in sect. **11**. Finally, we mention the limitations of DFT in sect. **12**, and we draw some conclusions in sect. **13**.

Many suggestions for further reading are given along the text. Nevertheless, we outline some of them here, for the reader's convenience. There are standard textbooks that constitute a useful starting point for the study of nuclear structure along the line of this paper [8]. If the reader needs a recent, more introductory text, ref. [9] is an option. The literature on DFT in condensed matter is huge, and yet we can single out refs. [10-12]. Recent, and relatively short, papers on the perspectives for electronic DFT can be found [13, 14]. DFT in nuclear physics has been first reviewed in [15], but the reader can also profit from refs. [16, 17]. There are many lectures available on the web, and an ambitious and interesting attempt to introduce the subject of DFT in nuclear physics can be found on the archive [18].

Last but not least, we limit ourselves here to a nonrelativistic treatment. Excellent papers that introduce and explain the relativistic (or covariant) nuclear DFT are available [19, 20].

2. – Basics on DFT for electronic systems

We assume we are concerned with a quantum many-fermion system governed by the Hamiltonian

$$H = \sum_{i=1}^{N} -\frac{\hbar^2}{2m}\nabla_i^2 + \frac{1}{2}\sum_{i\neq j=1}^{N} V(i,j) + \sum_{i=1}^{N} v_{\rm ext}(i), \tag{1}$$

where the first term is the kinetic energy of the N fermions having mass m, the second term is a two-body interaction in which i is a shorthand notation for the space coordinate, $\vec{r}_i$, spin coordinate and any further degree of freedom (*e.g.* isospin), and the last term is a possible external potential. In the case of N electrons interacting with the external field of M ions (labelled by α, and having charge Z_α and associated coordinate $\vec{R}_\alpha$), this Hamiltonian becomes

$$H = \sum_{i=1}^{N} -\frac{\hbar^2}{2m}\nabla_i^2 + \frac{1}{2}\sum_{i\neq j=1}^{N} \frac{e^2}{|\vec{r}_i - \vec{r}_j|} + \sum_{i=1}^{N}\sum_{\alpha=1}^{M} \frac{Z_\alpha e^2}{|\vec{r}_i - \vec{R}_\alpha|}\,, \tag{2}$$

where the interactions between the ions are not written for the sake of simplicity. The many-body problem associated with this Hamiltonian cannot be solved exactly, even if the Coulomb force is well known, and even if one can invoke the Born-Oppenheimer approximation and reduce the whole problem to the electronic problem, for fixed ion positions.

Many strategies have been proposed to solve the many-electron problem. Among them, to the opinion of many, DFT stands out for its conceptual elegance and simplicity (that, most likely, should be a feature of physics as a whole). Its foundation lies in the theorem that bears the name of Hohenberg and Kohn (HK) and that was introduced in their seminal paper [21]. In short, the theorem states that the total energy of the system described by (1), for any external potential $v_{\rm ext}$, can be written as a *functional* of the fermion density $\rho(\vec{r})$:

$$E_{v_{\rm ext}}[\rho] = \langle\Psi|\hat{T} + \hat{V} + \hat{v}_{\rm ext}|\Psi\rangle = F[\rho] + \int {\rm d}^3r\ v_{\rm ext}(\vec{r})\rho(\vec{r}). \tag{3}$$

The first equality is just the definition of total energy, while the second equality defines the functional: the contribution of the external potential is singled out and the *universal functional* F is introduced. The functional E, eq. (3), has a minimum at the exact ground-state density where it becomes equal to the exact energy. It is hard to underestimate the value of eq. (3), because it tells us that the whole information about the ground state of the system is contained in the one-body density ρ that is a real function of three coordinates, and we do not need the whole wave function Ψ, that instead is a complex function of $3N$ coordinates!

The proof of the theorem can be found in the original paper [21]. We advise the reader to go through it; it is quite instructive, although limited to the specific case in which the ground-state is not degenerate. Extensions of the theorem to the case of degenerate ground states, spin-polarized systems, finite temperature etc.([1]), can be found in the literature (see, *e.g.*, [11]).

The real drawback of the HK theorem is that its proof is merely a proof of existence of the universal functional F. It is not a constructive proof, so that the appropriate strategy to build this functional remains an open problem. A step forward in this direction is represented by the Kohn-Sham (KS) scheme [22], in which it is assumed that the density ρ can be represented in terms of so-called auxiliary single-particle wave functions (orbitals) $\phi_j(\vec{r})$, that is

$$\rho(\vec{r}) = \sum_j |\phi_j(\vec{r})|^2. \tag{4}$$

The index j labels the orbitals. The meaning of the word "auxiliary" should be clarified here. The orbitals may be looked at as a formal artifact. This does not exclude that, in specific cases, the orbitals turn out to be a fairly good approximation of the actual single-particle wave functions. Within such framework, the total kinetic energy is written in the usual way,

$$T = \langle\Psi|\hat{T}|\Psi\rangle = \sum_j \langle j|\frac{-\hbar^2}{2m}\nabla^2|j\rangle = \sum_j \int {\rm d}^3r\ \phi_j^*(\vec{r})\left(-\frac{\hbar^2}{2m}\nabla^2\right)\phi_j(\vec{r}), \tag{5}$$

([1]) The list is not exhaustive.

and the direct Coulomb energy (classical, or Hartree, energy) can be also singled out:

$$E_{\rm Hartree} = \frac{e^2}{2} \int {\rm d}^3r \, {\rm d}^3r' \, \frac{\rho(\vec{r})\rho(\vec{r}')}{|\vec{r}-\vec{r}'|} \, . \tag{6}$$

In this way, the functional (3) is re-written as

$$E_{\rm KS} = T + E_{\rm Hartree} + E_{\rm xc} + \int {\rm d}^3r \, v_{\rm ext}(\vec{r})\rho(\vec{r}), \tag{7}$$

where now the part to be built is the so-called "exchange-correlation" part or $E_{\rm xc}$. The minimization of this latter functional with respect to the density should be carried out with the constraint that the orbitals are orthonormal. Therefore, the equations for the orbitals are obtained from

$$\frac{\delta}{\delta\rho(\vec{r})} \left(E_{\rm KS} - \varepsilon \int {\rm d}^3r' \, \phi_j^*(\vec{r}')\phi_j(\vec{r}') \right) = 0, \tag{8}$$

where the usual symbol δ is introduced for the functional derivative. Elementary introductions to functional derivatives can be found in several textbooks (see, *e.g.*, sect. 3.2 of [23]). Equation (8), together with eqs. (7), (5) and (6), leads to the famous Kohn-Sham equations

$$\begin{aligned} &\left(-\frac{\hbar^2}{2m}\nabla^2 + \frac{e^2}{2} \int {\rm d}^3r' \, \frac{\rho(\vec{r}')}{|\vec{r}-\vec{r}'|} + \frac{\delta E_{\rm xc}}{\delta\rho(\vec{r})} + v_{\rm ext}(\vec{r}) \right) \phi_j(\vec{r}) = \\ &\left(-\frac{\hbar^2}{2m}\nabla^2 + v_{\rm KS} \right) \phi_j(\vec{r}) = \varepsilon\phi_j(\vec{r}), \end{aligned} \tag{9}$$

where we have labelled the total effective Kohn-Sham potential by $v_{\rm KS}$, and where the quantities ε are seen to be the energies associated with the auxiliary orbitals. The reader should note that the total energy is *not* the sum of these auxiliary energies (this is left as an exercise). We also wish to stress that the variation with respect to ρ in eq. (8) has in fact been turned into a variation with respect to the orbitals ϕ_j^*.

As for the choice for $E_{\rm xc}$, the simplest possible option is to calculate it in a *uniform* system where translational invariance makes the exact calculation of the total energy feasible. In fact, such a calculation in the limit of high electron densities is analytic and can be found in textbooks (see, *e.g.*, sects. 3 and 12 of [24] or sect. 12.3 of [25]). The total energy per particle $\frac{E}{N}$ reads

$$\frac{E}{N} = \frac{e^2}{2a_0} \left(\frac{2.21}{r_s^2} - \frac{0.916}{r_s} + 0.0622 \ln r_s - 0.094 + \ldots \right) = t + e_{\rm x} + e_{\rm c}. \tag{10}$$

One usually defines $a_0 = \frac{\hbar^2}{me^2}$ as the Bohr radius, r_0 by $\frac{1}{\rho} = \frac{4}{3}\pi r_0^3$ so that it is essentially the interparticle spacing, and $r_s = \frac{r_0}{a_0}$. In the latter equation, the dots represent terms of

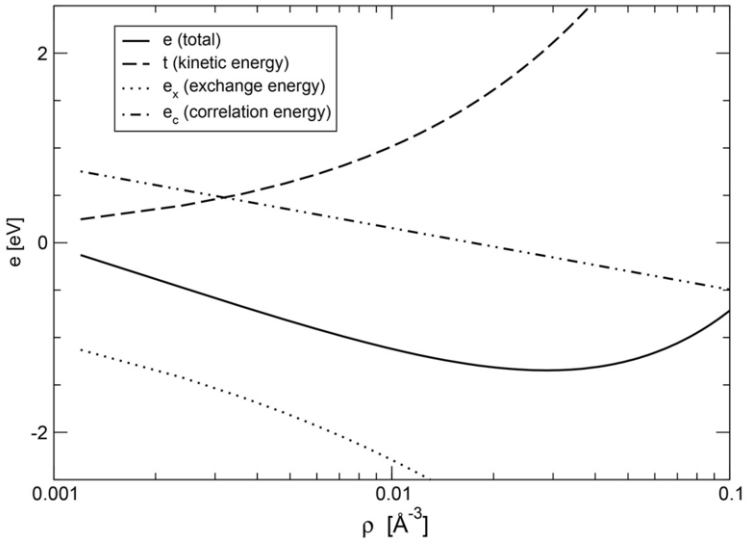

Fig. 2. – Energy per particle of the uniform electron gas as a function of the density, within the LDA as discussed in the main text. The curves correspond to the result of eq. (10) and to the three contributions that appear therein.

the order $O(r_s \ln r_s)$, and other subleading terms that become negligible at high density, that is, small r_s. The first term in brackets in eq. (10) is the kinetic energy per particle t, that goes like $\rho^{2/3}$. In this specific case, the Hartree and external potential contributions cancel exactly([2]). The second term in (10) is the exchange energy $e_{\rm x}$ while the following terms correspond to the correlation energy $e_{\rm c}$. For a two-body potential that goes like $1/r$, it is quite intuitive that interaction terms scale at most like the interparticle spacing, or like $\rho^{1/3}$. The different terms of $\frac{E}{N}$ in eq. (10) are displayed in fig. 2, where $\frac{E}{N}$ is written as e. The total energy has a minimum that mainly results from the balance between the kinetic term that goes like $\rho^{2/3}$ and the exchange term that goes like $\rho^{1/3}$, although the correlation energy plays some role. The minimum corresponds to r_s around 3.8, surprisingly close to the values for real metals that are in the range 3–5. More accurate expressions for the total energy of the uniform electron gas, that are also valid at lower densities, have been derived and are available [26]. Below, we shall compare with the nuclear case.

The so-called Local Density Approximation (LDA) amounts to assuming that, in the vicinity of a given point $\vec{r}$, the exchange-correlation energy of any electron system can be approximated with that of the uniform gas with the same density. In practice, one writes

$$E_{\rm xc} = \int {\rm d}^3 r \, e_{\rm xc}^{\rm hom}[\rho(\vec{r})]\rho(\vec{r}), \tag{11}$$

([2]) Cf. the discussion in sect. 3 of ref. [24].

where we have stressed that the exchange-correlation energy has been taken from the homogeneous gas by means of the superscript. LDA usually produces an overbinding of atoms and molecules, that can be corrected by introducing a dependence of $E_{\rm xc}$ on the gradient of the density, $\nabla\rho$ (Generalized Gradient Approximation, or GGA). At present, increasingly sophisticated functionals that depend also on higher derivatives of the density are discussed and/or start to be built. These various degrees of sophistication are pictorially referred to as a "Jacob's ladder" [27]. As a last rung of the ladder, a possible dependence on the unoccupied quantum states of the system is postulated. We shall come back to these points when discussing the nuclear case.

3. – The nuclear case: the mean-field picture and Hartree-Fock theory

There are analogies but also important differences between the many-electron problem and the many-nucleon problem. In the latter case there is no external potential, that is, nuclei are self-bound objects. In addition, while in eq. (1) we have written only a two-body interaction $V(i,j)$, three-body interactions $V(i,j,k)$ are relevant for nuclei and four-body interactions cannot be completely ruled out. As compared with the Coulomb force, the nuclear interaction is short-ranged (the range is of the order of 1 fm), strongly spin-dependent, and characterised by many terms (central, spin, spin-orbit, tensor) of similar importance.

Electron scattering experiments suggest that ordinary nuclei (except the lightest ones) are characterised in their inner part by an approximately constant density, whose value is $\rho_0 \approx 0.16\,\mathrm{fm}^{-3}$ (saturation density) as it has been mentioned in the introduction. The nuclear surface, although very important for nuclear properties, has a thickness of only $\approx 0.6\,\mathrm{fm}$. As a consequence, the interparticle distance $2r_0$ is $\approx 2.4\,\mathrm{fm}$ and is larger than the range of the nuclear force. In this respect, the nucleus is not a very dense system. Together with the role played by the Pauli exclusion principle, this explains why nucleons do not experience the mutual interaction so often; in fact, it is known experimentally that the nucleon mean free path in nuclei is or the order of, or larger than, the nuclear radius.

Historically, these evidences have led to assuming the validity of mean-field theory, namely of the picture that nucleons move in a one-body potential that results from the average of the interactions with all other nucleons. It has been deemed to be too hard or somehow not so relevant, for many years, trying to deduce the mean field from a complicated NN Hamiltonian. Empirical potentials like the well-known Woods-Saxon have been often taken for granted. Elegant and sophisticated models have been developed by the Copenhagen school [28, 29], or by Landau and Migdal [30], or by Solovev and co-workers [31], based on single-particle and collective excitations on top of the mean field, without daring to ask the question whether this mean field can be derived from an underlying theory, or whether binding energies can be calculated therefrom. This lecture deals instead with a unified picture in which the *effective* mean field can be derived within the DFT framework.

In the 1970s and 1980s, different authors have started to propose effective Hamiltonians with the aim of using them within a microscopic mean-field theory, that is, within

Hartree-Fock (HF). One starts from an Hamiltonian analogous to (1),

$$H = \sum_{i=1}^{N} -\frac{\hbar^2}{2m}\nabla_i^2 + \frac{1}{2}\sum_{i\neq j=1}^{N} V(i,j), \tag{12}$$

where the difference between the neutron and proton mass has been neglected for the sake of simplicity, and defines an energy functional as

$$E_{\mathrm{HF}}[\rho] = \langle\Phi|H|\Phi\rangle, \tag{13}$$

where $|\Phi\rangle$ is the most general Slater determinant made up with single-particle wave functions ϕ_j. The minimization of this functional, with the same constraint as in eq. (8), namely

$$\frac{\delta}{\delta\rho(\vec{r})}\left(E_{\mathrm{HF}} - \varepsilon\int \mathrm{d}^3r'\,\phi_j^*(\vec{r}')\phi_j(\vec{r}')\right) = 0, \tag{14}$$

can be carried out in practice replacing the variation with respect to ρ by the variations with respect to ϕ_j^*, and this leads to the well-known HF equations:

$$-\frac{\hbar^2}{2m}\nabla^2\phi_j(\vec{r}) + \sum_{l=1}^{N}\int \mathrm{d}^3r'\,\phi_l^*(\vec{r}')V(\vec{r},\vec{r}')\left(\phi_l(\vec{r}')\phi_j(\vec{r}) - \phi_l(\vec{r})\phi_l(\vec{r}')\right) = \varepsilon_j\phi_j(\vec{r}), \tag{15}$$

$$\langle j|\frac{-\hbar^2}{2m}\nabla^2|j\rangle + \sum_{l=1}^{N}\langle jl|V\left(1-P_{12}\right)|jl\rangle = \varepsilon_j,$$

where P_{12} exchanges the particles 1 and 2. The total energy reads

$$E_{\mathrm{HF}} = T + \frac{1}{2}\sum_{jl}\int \mathrm{d}^3r\,\mathrm{d}^3r'\,\phi_j^*(\vec{r})\phi_l^*(\vec{r}')V(\vec{r},\vec{r}')\left(\phi_j(\vec{r})\phi_l(\vec{r}') - \phi_l(\vec{r}')\phi_j(\vec{r})\right), \tag{16}$$

where T has the same form as in eq. (5). We are going now to illustrate that a naïve picture of the nuclear mean field is doomed to fail, even in the simple case of uniform nuclear matter that is the analogous system with respect to the electron gas that has been previously discussed. In particular, all attempts to account for the empirical evidence(s) using a *density-independent* effective interaction V, at the HF level, have not been successful.

4. – Uniform nuclear matter

As we have mentioned in the previous section, the inner part of nuclei displays an approximately constant density, ρ_0. In nuclei with $N \approx Z$, proton and neutron densities do not differ too much whereas in nuclei with neutron excess there is a spill-out of the

neutron density but not a large difference in the inside part. Thus, we can picture the inside as similar to an extended system having equal number of protons and neutrons and equilibrium density equal to ρ_0, that is, similar to a piece of symmetric nuclear matter (SNM). The Bethe-Weiszäcker formula for the energy per particle $e \equiv \frac{E}{A}$, namely

$$e(A,Z) = a_V - a_S A^{-1/3} - a_A \left(\frac{A-2Z}{A}\right)^2 - a_C \frac{Z^2}{A^{4/3}}\,, \tag{17}$$

has an associated volume term a_V of about $-16\,\mathrm{MeV}$. If we consider uniform SNM all terms of the mass formula vanish except the volume term. Therefore, it is customary to assume that the energy per particle of this system, at the equilibrium density ρ_0, takes the value $e_0 = -16\,\mathrm{MeV}$. As we have stressed already, this is called the saturation point for SNM.

Around this point, which is a minimum in the energy per particle e, one expand this function as

$$e = e_0 + \frac{1}{2} K_\infty \left(\frac{\rho-\rho_0}{3\rho_0}\right)^2 + \ldots, \tag{18}$$

where K_∞ is called nuclear incompressibility, it is proportional to the second derivative $\frac{\mathrm{d}^2 e}{\mathrm{d}\rho^2}$ and, as such, it is related to the stiffness of nuclear matter under compression. Although this quantity can be only indirectly related to observables, like the properties of the compressional-type vibrations of finite nuclei, some bounds on its values have been established in the last decades (see [32] and references therein).

One can also consider the case of asymmetric matter, in which we expect that the energy per particle must depend both on neutron and proton densities ρ_n and ρ_p. With a simple change of variables, we can use the total density ρ and the local neutron-proton asymmetry, $\beta \equiv \frac{\rho_n - \rho_p}{\rho}$. By making a Taylor expansion in β and retaining only the quadratic term (odd powers of β are obviously forbidden due to isospin symmetry), we can write

$$e(\rho,\beta) = e(\rho,\beta=0) + S(\rho)\beta^2, \tag{19}$$

where the first term on the r.h.s. is the energy per particle of SNM that we have so far discussed, while the second term defines the so-called symmetry energy $S(\rho)$. From the latter equation, the symmetry energy can be easily understood as the energy per particle that is needed to change symmetric matter into neutron matter.

The symmetry energy can, in turn, be expanded as a function of ρ and, as the saturation point of SNM is a useful reference, one usually writes

$$S(\rho) = J + L\left(\frac{\rho-\rho_0}{3\rho_0}\right) + \frac{1}{2} K_{sym} \left(\frac{\rho-\rho_0}{3\rho_0}\right)^2 + \ldots, \tag{20}$$

where J is the value of the symmetry energy at saturation density and the other parameters are related to the first and second derivatives at the same point. In particular, L is often referred to as the "slope parameter". Constraints on the values of J and L have been established by the study of phenomena in which a neutron-proton imbalance is created at different densities, like oscillations where protons and neutrons vibrate out of phase or heavy-ion collisions where projectile and target have different composition; masses as a function of the neutron excess, or observations of neutron stars, can also help in constraining the values of J and L (cf. refs. [33-37]).

5. – Failure of mean field with simple forces and the need for DFT

In SNM the Fermi momentum is given by([3])

$$k_F = \left(\frac{3\pi^2\rho}{2}\right)^{1/3}, \tag{21}$$

and, at saturation density, it takes the value $\approx 1.33\,\mathrm{fm}^{-1}$. The wave functions in a uniform system are plane waves due to translational invariance. This simplifies the calculation of the total energy (16), in keeping with the well-known replacements

$$\begin{aligned} \phi_j(\vec{r}) &\to \frac{1}{\sqrt{\Omega}} e^{i\vec{k}\cdot\vec{r}}, \\ \sum_j &\to \frac{g\Omega}{(2\pi)^3}\int \mathrm{d}^3k, \end{aligned} \tag{22}$$

where $g = 4$ is the degeneracy and Ω is the quantisation volume. The kinetic part T of the total energy can be calculated straighforwardly and re-expressed in terms of the density thanks to eq. (21). The kinetic energy per particle, t, is

$$t = \frac{T}{A} = \frac{2}{\pi^2}\frac{\hbar^2}{2m}\frac{k_F^5}{5}\frac{\Omega}{A} = \frac{3}{5}\left(\frac{3\pi^2}{2}\right)^{2/3}\frac{\hbar^2}{2m}\rho^{2/3}. \tag{23}$$

Now, the question arises under which conditions, within simple HF, an effective force V allows nuclear saturation. In terms of radial dependence, Yukawa functions may constitute a choice as they resemble what is deduced from the Fourier transform of a massive boson propagator. Gaussian functions have also been, and still are, used because they allow an easy calculation of the matrix elements on a harmonic-oscillator basis [38]. From the viewpoint of EFT, if one is interested in nuclear properties at the scale of tens of MeV or less, the details of the radial shape of the force on a scale around 1 fm should

([3]) The presence of two neutrons and two protons for each value of the momentum $\vec{k}$, namely the degeneracy $g = 4$, makes the factor in the next equation different from that of the electronic case.

be unimportant([4]). Intuitively, nuclear saturation should emerge from a balance between some attractive and repulsive mechanisms and we will discuss briefly the minimal number of terms that have to be introduced to this aim, sticking to a nonrelativistic picture as already mentioned([5]).

For a single Gaussian interaction having a range μ,

$$V(\vec{r}_1, \vec{r}_2) = Se^{-\frac{|\vec{r}_1 - \vec{r}_2|^2}{\mu^2}}, \tag{24}$$

the direct and exchange terms of the total energy per particle, v_H and v_x, calculated from eq. (16), read([6])

$$\begin{aligned} v_H &= \frac{S}{2}\mu^3\pi^{3/2}\rho, \\ v_x &= -\frac{S}{2}\frac{1}{\sqrt{\pi}}g(\mu k_F), \end{aligned} \tag{25}$$

where $g(x) = \frac{2}{x^3} - \frac{3}{x} - (\frac{2}{x^3} - \frac{1}{x})e^{-x^2} + \sqrt{\pi}\,\mathrm{erf}(x)$ [40, 41]. One can immediately notice that the direct term goes like ρ, as it must be for a short-range two-body interaction, and in contrast with the case of the electron gas. The exchange term has opposite sign, and a more subtle density dependence that can nevertheless be easily inferred. The force is attractive ($S < 0$), and it turns out by inspection that the repulsion from the exchange term plus the kinetic energy is far too weak to allow saturation. A possible way out, as already suggested long ago by Brink and Boeker [42], is to introduce exchange terms in the interaction. For instance, eq. (24) can be generalised to

$$V(\vec{r}_1, \vec{r}_2) = S(1 - m + mP_M)e^{-\frac{|\vec{r}_1 - \vec{r}_2|^2}{\mu^2}}, \tag{26}$$

where P_M is the operator that exchanges the particles 1 and 2. Then, the potential energies per particle of eq. (25) become

$$\begin{aligned} v_H &= \frac{S}{8}(4 - 5m)\,\mu^3\pi^{3/2}\rho, \\ v_x &= \frac{S}{2}(5m - 1)\,\frac{1}{\sqrt{\pi}}g(\mu k_F). \end{aligned} \tag{27}$$

([4]) The reader should remember that $\hbar c = 197.3\,\mathrm{MeV\,fm}$, and this allows making the equivalence between 1 fm and about 200 MeV. Natural units embed such concepts but will not be used throughout this lecture.

([5]) The mechanism for saturation in a covariant theory (balance between scalar and vector potentials) is discussed in the original paper by Serot and Walecka [39], as well as in the aforementioned refs. [16, 19].

([6]) The calculation is straightforward, although some integrals are not elementary as discussed in the Coulomb case in ref. [24].

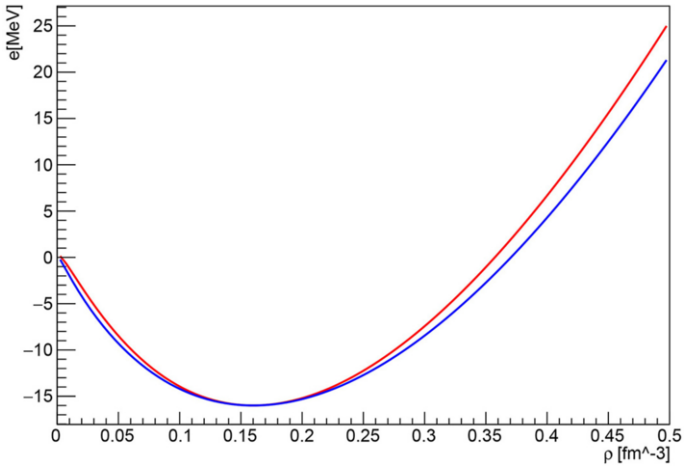

Fig. 3. – Energy per particle in symmetric nuclear matter, calculated either with a force of the type (26) and parameters $S = -429.83\,\text{MeV}$, $m = 1.3218$, $\mu = 0.8343\,\text{fm}$ (blue curve), or with a simplified Skyrme functional of the type (34) and parameters $t_0 = -2552.84\,\text{MeV}\cdot\text{fm}^3$, $t_3 = 16694.7\,\text{MeV}\cdot\text{fm}^{3(\alpha+1)}$, $\alpha = 0.20309$.

In this way, the weight of the different terms is changed, and saturation becomes possible for values of μ that lie approximately in the range $0.5\,\text{fm} < \mu < 1.5\,\text{fm}$ [42]. An example of calculation of the HF energy per particle, performed with a force of this type [41], is shown in fig. 3 and compared with the result of a Skyrme functional that is discussed in the next section. Similar arguments apply in the case of a Yukawa interaction: only exchange terms allow saturation, as it was remarked in sect. 2.3.1 of [43] where one can also find the formulas that are analogous to eq. (27) (cf. also [44]).

The simple forces that we have described earlier in this section do not possess necessarily enough flexibility to reproduce the empirical values of K_∞, J and L. Certainly, one could complicate them and introduce more Gaussian (or Yukawa) terms with different ranges, different exchange operators etc. What seems, so far, impossible to obtain in such naïve mean-field scheme is the empirical value of the effective mass, m^*/m.

In a uniform system, the most general way to write the single-particle dispersion relation, namely the relation between energy and momentum (which is the only available quantum number), reads

$$\varepsilon = \frac{\hbar^2 k^2}{2m} + \Sigma(k,\varepsilon) \equiv \frac{\hbar^2 k^2}{2m^*}\,, \tag{28}$$

where Σ is the single-particle self-energy. The second equality is the definition of the effective mass, and by further elementary steps [45] one can arrive at

$$\frac{m^*}{m} = \left(1 + \frac{m}{\hbar^2 k}\frac{\partial\Sigma}{\partial k}\right)\left(1 - \frac{\partial\Sigma}{\partial\varepsilon}\right)^{-1}. \tag{29}$$

The HF equations of the second line in eq. (15), in the case in which the wave function is a plane wave as in (22), can be easily cast in the form (28). In a simple way, one obtains

$$\Sigma_{\sigma\tau}(k,\varepsilon) = \sum_{\sigma'\tau'} \frac{\Omega}{(2\pi)^3} \int \mathrm{d}^3k' \, \langle \vec{k},\sigma,\tau;\vec{k}',\sigma',\tau'|V\,(1-P_{12})\,|\vec{k},\sigma,\tau;\vec{k}',\sigma',\tau'\rangle, \tag{30}$$

where we have explicitly introduced the sum over the spin and isospin degrees of freedom (τ labels either neutrons or protons). We expect that Σ depends on σ (τ) only in the case of polarized (neutron-proton asymmetric) matter. Once V is given, Σ can be calculated and the effective mass can be extracted therefrom. One can explicitly see that, within HF, Σ does not depend on ε. The non-trivial value of m^*/m is brought by the k-dependence of Σ that comes from exchange terms.

From its definition (28), the effective mass is clearly related to the level density: the larger its value, the smaller the level spacing. In a non-uniform system the picture is less simple, but nevertheless the whole nuclear phenomenology is consistent with a value of the effective mass m^*/m lying in the range ≈ 0.7–1. This has been established for quite a long time (cf. the very comprehensive review paper [45], where also the density and energy dependence of the effective mass is addressed). The simple HF that we have described so far, leads to much smaller values (between 0.2 and 0.4). This problem is discussed in detail in refs. [46-48] (cf. also [41, 44, 49]).

So far, it has *not* been possible to design an effective V that provides a successful description both of the bulk nuclear properties (nuclear saturation and properties of uniform matter around ρ_0, as well as masses and radii of finite nuclei as we discuss below) and of nuclear spectroscopic properties (effective mass, *viz.* level density), without introducing a *density dependence* in the Hamiltonian.

A density-dependent $V[\rho]$ or $H[\rho]$ has, generally speaking, conceptual problems unless one considers it merely as a way to generate an energy functional through eq. (13), that is

$$E[\rho] = \langle\Phi|H[\rho]|\Phi\rangle. \tag{31}$$

In this respect, we can conclude that DFT, and not HF, is a viable theory for nuclei in our current understanding. A similar argument can be found under different forms in the literature [47].

6. – Examples of nuclear EDFs

The finite-range Gogny force [50, 51] is the generalisation of the Brink-Boeker force that we have introduced in the previous Section. It reads

$$\begin{aligned} V_{\mathrm{Gogny}}(\vec{r}_1,\vec{r}_2) = \sum_{j=1}^{2} e^{\frac{|\vec{r}_1-\vec{r}_2|^2}{\mu_j^2}} \, (W_j + B_jP_\sigma - H_jP_\tau - M_jP_\sigma P_\tau) \\ +t_3\,(1+x_0P_\sigma)\,\delta(\vec{r}_1-\vec{r}_2)\rho^\alpha\left(\frac{\vec{r}_1+\vec{r}_2}{2}\right) \\ +iW_{ls}\,(\vec{\sigma}_1+\vec{\sigma}_2)\cdot\vec{k}^\dagger\times\delta(\vec{r}_1-\vec{r}_2)\vec{k}, \end{aligned} \tag{32}$$

where $P_\sigma = \frac{1}{2}(1+\vec{\sigma}_1\cdot\vec{\sigma}_2)$ is the spin-exchange operator, $P_\tau = \frac{1}{2}(1+\vec{\tau}_1\cdot\vec{\tau}_2)$ is the isospin-exchange operator, $\vec{k} = -\frac{i}{2}(\vec{\nabla}_1 - \vec{\nabla}_2)$ is the relative momentum operator acting at right and $\vec{k}^\dagger$ is the adjoint operator acting at left. The interaction is the sum of two Gaussians with exchange operators, a density-dependent term and a spin-orbit term. The density dependent term has been deemed to be essential to obtain a reasonable single-particle level density (cf. our discussion of the effective mass in the last section). This term must be zero-range to avoid ambiguities on the point where the density must be evaluated. The spin-orbit term is also zero-range, for simplicity. This interaction has 14 free parameters to be adjusted.

Another class of successful effective interactions is based on the zero-range, momentum-dependent Skyrme ansatz [52-54]:

$$
\begin{aligned}
V_{\rm Skyrme}(\vec{r}_1,\vec{r}_2) = {} & t_0\,(1+x_0P_\sigma)\,\delta(\vec{r}_1-\vec{r}_2) \\
& +\frac{1}{2}t_1\,(1+x_1P_\sigma)\left(\vec{k}^{\dagger 2}\delta(\vec{r}_1-\vec{r}_2)+\delta(\vec{r}_1-\vec{r}_2)\vec{k}^2\right) \\
& +t_2\,(1+x_2P_\sigma)\,\vec{k}^{\,\dagger}\cdot\delta(\vec{r}_1-\vec{r}_2)\vec{k} \\
& +\frac{1}{6}t_3\,(1+x_3P_\sigma)\,\delta(\vec{r}_1-\vec{r}_2)\rho^\alpha\left(\frac{\vec{r}_1+\vec{r}_2}{2}\right) \\
& +iW_0\,(\vec{\sigma}_1+\vec{\sigma}_2)\cdot\vec{k}^{\,\dagger}\times\delta(\vec{r}_1-\vec{r}_2)\vec{k},
\end{aligned}
\tag{33}
$$

where now there are 10 free parameters to be adjusted. As we have just mentioned, a density-dependent force is just a way to generate an energy functional through eq. (31). It is a good exercise for the reader to show that a simplified Skyrme force without momentum and spin dependence,

$$
V(\vec{r}_1,\vec{r}_2) = t_0\delta(\vec{r}_1-\vec{r}_2)+\frac{1}{6}t_3\,(1+x_3P_\sigma)\,\delta(\vec{r}_1-\vec{r}_2)\rho^\alpha\left(\frac{\vec{r}_1+\vec{r}_2}{2}\right), \tag{34}
$$

generates for even-even systems the functional

$$
\begin{aligned}
E[\rho_n,\rho_p] &= \int \mathrm{d}^3r\,\mathcal{E}[\rho_n,\rho_p], \\
\mathcal{E}[\rho_n,\rho_p] &= \frac{\hbar^2}{2m}\tau+\frac{1}{2}t_0\left[\rho^2-\frac{1}{2}\left(\rho_n^2+\rho_p^2\right)\right]+\frac{1}{12}t_3\left[\rho^{\alpha+2}-\frac{1}{2}\rho^\alpha\left(\rho_n^2+\rho_p^2\right)\right].
\end{aligned}
\tag{35}
$$

In these latter equations, the total energy E is written in terms of the energy density $\mathcal{E}$. Thus, one speaks (in this and all cases to be discussed below) of $\mathcal{E}$ as of an energy density functional (EDF), namely an energy density that depends on functions like ρ_n and ρ_p. Zero-range forces generate local functionals (at variance with the Coulomb case that has been previously discussed). Fractional power dependences like ρ^α cannot come from density-independent two-body, three-body, or many-body forces. In other terms, they mimic many-body effects in a more subtle way. It has been known for many years now that only functionals in which such fractional powers appear, reproduce the empirical

values of K_∞ [43, 32]. The kinetic part of the Hamiltonian introduces the first term appearing in the r.h.s. of eq. (35), that depends on the so-called kinetic energy density,

$$\tau = \sum_j |\vec{\nabla}\phi_j|^2. \tag{36}$$

The whole Skyrme force (33) includes momentum-dependent terms that bring a dependence on τ into the potential energy density as well, together with a dependence on $\vec{\nabla}\rho$. The complete EDF associated with a Skyrme force can be found, for even-even systems, in refs. [53, 54]. More densities appear like the spin-orbit densities $\vec{J}(\vec{r})$. Interestingly, terms that depend on the same kinds of densities that have been introduced for electron systems in [27], characterise the Skyrme EDFs. A finite-range force like the Gogny interaction produces a non-local EDF.

In fact, the very idea that a Hamiltonian including a density-dependent force is *the* tool to generate an EDF has been abandoned by most groups. A functional can be directly parameterized in terms of local densities, without any reference to an underlying interaction. A pioneering step in this direction was taken by Reinhard and Flocard [55] more than twenty years ago, as they wrote the spin-orbit part of their EDFs without reference to a specific form of the force. Later, this has become the customary procedure, *e.g.*, for functionals of the UNEDF family [56].

All possible local densities that can appear in an EDF, have been classified in refs. [57-59, 15] (see also [60]). The nuclear EDF must be invariant with respect to parity, time-reversal, rotational, translational and isospin transformations (details can be found in the quoted works). Time-reversal plays a special role here. Densities can be either time-even or time-odd but the latter vanish in even-even systems. Thus, the EDF can be made up with terms that are bilinear in either types of densities, but the terms that are bilinear in time-odd densities do not vanish only in systems with an odd number of particles. A current open questions for practitioners and not only, is to which extent higher and higher gradients of the density are needed for an EDF in order to satisfactorily account for nuclear properties [61-63].

This discussion is of course not exhaustive. Other forces have been considered as generators of EDFs, for examples semi-realistic forces of Yukawa type with density-dependent terms [64]. Other kinds of functionals have been proposed by Fayans and collaborators [65, 66]. We do not discuss all the attempts to derive functionals from underlying theories like Brückner-Hartree-Fock [67] or chiral forces.

7. – Examples of calculations of ground-state properties

The main observable that one aims at calculating with an EDF, is the total energy which is actually the binding energy of a nucleus and can be compared with very accurate experimental data. The typical errors are of the order of $\approx$ 1–2 MeV. While this accuracy may be thought to be small, at least in comparison with total binding energies that span values like 10^2–10^3 MeV, one should keep in mind that nuclear processes like reactions

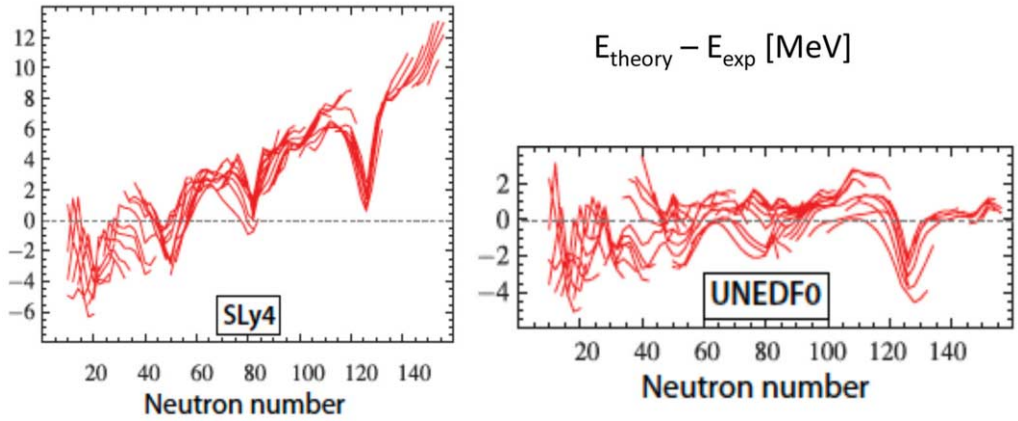

Fig. 4. – Comparison between theoretical and experimental binding energies. Calculations are performed with different EDFs, SLy4 from ref. [54] and UNEDF0 from ref. [70]. Figure taken and adapted from ref. [70].

and decays depend on differences of binding energies, that may be small. This is the motivation for reducing these errors with respect to experiment. Models that include macroscopic ingredients in alternative, or in addition, to the pure implementation of DFT may reach accuracies of the order of hundreds of keV (cf. the review paper [68] or, for more recent advances, [69] and references therein).

In fig. 4 we show examples of comparison between experimental binding energies and the result of DFT calculations. The Skyrme functional SLy4 [54] has been fitted by using masses and charge radii of basically only magic nuclei. This is probably the reason of the archlike behaviour, which is common to many EDFs. Reproducing with similar accuracy closed-shell and open-shell nuclei still represents a challenge. More modern functionals like UNEDF0 [70] seem to behave much better than SLy4, although the trend of the error as a function of the neutron number is not really flat. The reader should be also aware of the significant recent progress in DFT calculations using covariant functionals, not discussed in this contribution: a careful analysis of the mass residuals, and their link(s) with other features of the EDFs, is carried out in ref. [71]. To which extent some correlations that are relevant for nuclear masses cannot be captured by DFT calculations, is still an open question.

EDFs have been applied to predict the limits of nuclear stability, namely the position of the drip lines that we have mentioned in the introduction [72, 73]. Other relevant ground-state observables are radii and density distributions. Charge radii are available for comparison with experiment: EDFs may display errors of the order of 0.02–0.03 fm, typically. As far as isotopic trends of radii are concerned, while in many instances EDFs perform well, there are still specific unresolved issues (cf. fig. 11 of [15]: the isotopic dependence of the charge radii along the Ca chain is a typical case where EDFs fail). Last but not least, there is strong current interest in measuring neutron radii or density

distributions; EDFs provide predictions than span a relatively broad interval for neutron radii, and fixing this observable would be of paramount importance for our understanding of the nuclear symmetry energy (see the discussion in sect. **4**, and the references therein).

8. – Intrinsic density

The biggest difference between DFT in finite electronic systems and nuclei consists in the fact that in the former case, in most instances, the fixed ion positions constrain the shape of the system in the laboratory frame. In nuclei, that are self-bound systems, this is not the case. The usual HK theorem, as has been argued by several authors [74], is irrelevant to the nuclear case because it concerns the laboratory density, while experiments probe the intrinsic density (relative to the nuclear center of mass).

Nonetheless, it has been proven that, at least in principle, given an arbitrary Hermitian operator $\hat{Q}$, one can build an energy functional depending on $Q(\vec{r}) \equiv \langle \hat{Q}(\vec{r}) \rangle$ that is universal in the HK sense and has its minimum at the correct value of Q with the correct energy. In this respect, one can replace the laboratory density with the intrinsic density in the HK theorem [74-76].

A very interesting point is that the intrinisic density appears to break, in many cases, the symmetries associated with the Hamiltonian as we discuss in the next section.

9. – Symmetry breaking and restoration

In general, if the Hamiltonian of a system commutes with a given symmetry operator S,

$$[H, S] = 0, \tag{37}$$

one expects to be able to find eigenstates of the system which are also eigenstates of S. The problem with this statement of principle comes when one is forced to treat strongly correlated systems and to resort to approximations. In that case, a symmetry-conserving solution may be much less realistic, within the approximated framework, than a symmetry-breaking one.

The first example is that of translational symmetry. A very simple example borrowed from [77, 78] will highlight the above statements. Let us consider two particles in 1D, confined in the interval $-L/2 < x < L/2$, interacting through a harmonic potential,

$$H = \frac{p_1^2}{2m} + \frac{p_2^2}{2m} + \frac{C}{L^2}\left(x_1 - x_2\right)^2. \tag{38}$$

By using the center-of-mass and relative coordinates $R = \frac{x_1+x_2}{2}$ and $r = x_1 - x_2$, together with the associated momenta P and p, respectively, this Hamiltonian can be separated into center-of-mass and intrinsic Hamiltonians,

$$H = \frac{P^2}{4m} + \frac{p^2}{m} + \frac{C}{L^2}r^2 = H_{COM} + H_{intr}. \tag{39}$$

This Hamiltonian clearly commutes with the total momentum P, that is, it manifests the translational invariance. The exact wave function is known, namely it is a product of a free particle times a harmonic-oscillator wave function, it is an eigenstate of P, and the associated energy is

$$E_{exact} = \frac{P^2}{4m} + \sqrt{\frac{\hbar^2 C}{mL^2}}\,. \tag{40}$$

Let us now imagine that we restrict ourselves to products of independent wave functions. If the two particles are bosons, or spin 1/2 fermions in a spin-antisymmetric state([7]), the total wave function is

$$\Phi = \phi_1(x_1)\phi_2(x_2). \tag{41}$$

Imposing translational invariance here, would amount to taking the ϕ as plane waves which means $\phi_i(x_i) = \frac{\exp(ip_i x_i/\hbar)}{\sqrt{L}}$. The expectation value,

$$E = \langle \Phi | H | \Phi \rangle, \tag{42}$$

can be easily calculated by using the Hamiltonian in the form (38), and one can verify that its value is significantly different from the exact one of (40). If we use the independent particle ansatz (41) and we give up the requirement of translational invariance, the minimization of (42) produces instead an intrinisic energy given by

$$E_{symm.\ breaking} = 2\sqrt{\frac{\hbar^2 C}{2mL^2}}\,, \tag{43}$$

with an associated wave function that is the product of two localized harmonic oscillators. This energy is relatively close to the intrinsic part of the exact one, that is, the second term at the r.h.s. of eq. (40).

The above example should make clear why the choice of using the variational ansatz with symmetry-breaking wave functions might be preferable to other options. Translational symmetry and its breaking characterises all systems, and it is not of special relevance for the atomic nucleus. On the other hand, rotation and gauge symmetries, that we shall now discuss, are instead associated with the quadrupole and pairing correlations that have been identified as the most important correlations in finite nuclei since several decades.

To make the introduction to rotational symmetry and its breaking as simple as possible, let us pick up another very simple example, by considering several particles in

([7]) We would like to avoid the antisymmetrization of the spatial wave function (41) in order to simplify the pedagogical argument we are developing.

Table I. – *Values of $f(m,m')$ defined in the main text.*

m/m'	-2	-1	0	1	2
-2		0.227	0.227	0.227	0.455
-1	0.227		0.227	0.455	0.227
0	0.227	0.227		0.227	0.227
1	0.227	0.455	0.227		0.227
2	0.455	0.227	0.227	0.227	

a 3D harmonic one-body potential plus a zero-range two-body residual interaction. The corresponding Hamiltonian reads

$$H = \sum_i \frac{\vec{p}_i^2}{2m} + \sum_i \frac{1}{2} m\omega^2 r_i^2 + \frac{1}{2}\sum_{ij} \epsilon\delta(\vec{r}_i - \vec{r}_j), \tag{44}$$

where ϵ is small so that the residual interaction term will be treated as a perturbation of the 3D harmonic oscillator. The particles in this potential have eigenstates $|nlm\rangle$, with associated energies $E_{nl} = \hbar\omega(2n + l - \frac{1}{2})$ and wave functions $\phi_{nlm}(\vec{r}) = \frac{u_{nl}(r)}{r} Y_{lm}(\theta,\phi)$, where the radial part can be explicitly written in terms of Laguerre polynomials. If these particles are fermions, they occupy the states $1s$, $1p$ etc.

If we have a set of orbitals that are filled and we add one particle, this will occupy the lowest unoccupied orbital. The perturbing zero-range interaction (last term in eq. (44)) has been assumed to be weak and, consequently, unable to alter the structure of the orbitals and shells. Nevertheless, if we add a second particle this will produce at lowest order an energy shift ΔE given by

$$\Delta E = \epsilon\langle nlm, nlm'|\delta(\vec{r}_1 - \vec{r}_2)|nlm, nlm'\rangle, \tag{45}$$

where m, m' are the quantum numbers of the two particles in the degenerate levels. This shift can be calculated([8]) and the result reads

$$\Delta E = \epsilon \int \mathrm{d}r \frac{u_{nl}^4(r)}{r^2} \sum_\lambda \frac{2\lambda+1}{4\pi} \langle lm\lambda 0|lm\rangle\langle lm'\lambda 0|lm'\rangle\langle l0\lambda 0|l0\rangle^2, \tag{46}$$

where the sum is limited by the angular momentum selection rules, that are implicit in the Clebsch-Gordan coefficients.

The values of $f(m,m') = \frac{\Delta E}{\epsilon \int \mathrm{d}r u_{nl}^4(r) r^{-2}}$ are displayed in table I for the case of $l = 2$ (d-orbitals). The diagonal values are excluded from the Table because the two particles

([8]) The multipole expansion of the delta function, and the matrix elements of the spherical harmonics, are needed.

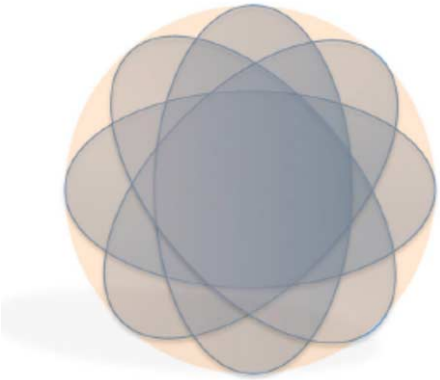

Fig. 5. – Schematic view (in two dimensions) of the deformed nucleus in the intrinsic frame that rotates in the laboratory frame. See the main text for a discussion. Figure adapted from ref. [47].

cannot occupy the same quantum states. The largest values are those with $m' = -m$. This can be intuitively understood in a qualitative way, since the two orbitals with the same absolute value of m have the largest spatial overlap so that a short-range interaction has the largest effect. If such short-range interaction is attractive, two particles will let the system gain energy if the orbitals with $|m| = 2$ are occupied, that is, the system has a non-spherical shape. This deformation is enhanced by polarization effects, namely by the interaction between the particles in the last orbitals and the others. The details of polarization effects go beyond the scope of this lecture. Nevertheless, these effects contribute to make the nucleus deformed as a whole.

Quadrupole deformations are, by far, those dominant along the nuclear chart. Nuclei with quadrupole deformation have been identified by their rotational bands, that is, in keeping with the fact that their spectra correspond to those of a rotor [29]. Also, octupole correlations and octupole deformations have been subject of recent interest and have been now unambiguously proven [79, 80].

If the quadrupole deformed configuration of the system corresponds to a deep minimum of the total energy, that is, the total energy has a stiff behaviour around this minimum, DFT describes well, as a rule, the rotational spectra or at least the lowest sector of the rotational bands [15]. Phenomena that take place when the rotation is fast as the angular momentum is large, or hyperdeformation, are discussed in the literature and also dealt with in the nuclear DFT context (see, *e.g.*, ref. [58]).

As is clear from the previous discussion, deformation occurs in the center-of-mass frame. Thus, we have spontaneous symmetry breaking *in the intrinsic system*. The way in which the symmetry is restored is by means of rotation in the laboratory system, that is, by superimposing different shapes that are produced through a rotation by a set of Euler angles Ω. This is depicted schematically, in 2D, in fig. 5. Since the result of the rotation of a spherical harmonic Y_{lm} by Ω is given by $\sum_{m'} \mathcal{D}^l_{m'm}(\Omega) Y_{lm'}$, where $\mathcal{D}$ is a

Wigner function, the wave function associated with the superposition of states l, m' that are rotated reads

$$|nlm\rangle = \mathcal{N} \int \mathrm{d}\Omega \, \mathcal{D}^l_{m'm}(\Omega) |nlm'\rangle, \tag{47}$$

where $\mathcal{N}$ is a normalization factor. This can be also interpreted as a projection on good angular momentum in the laboratory frame. Superimposing different shapes, and restoring the rotational symmetry by means of this angular-momentum projection, is called multi-reference DFT (MR-DFT) in the context of nuclear EDFs. There is rapid development in recent years concerning MR-DFT, using the Skyrme and Gogny functionals that have been discussed in sect. **6** as well as using the covariant functionals.

A similar, yet more abstract, reasoning holds in the case of the pairing correlations [81]. Open-shell nuclei are characterised by the fact that a fraction of nucleons around the Fermi energy display a superfluid character. Their phenomenology is, as a rule, well described by the BCS (Bardeen-Cooper-Schrieffer) theory. Within this framework, nucleons in time-reversal states form so-called Cooper pairs, and the superfluidity is associated with the coherent behaviour of these fermion pairs that are quasi-bosons. A very economic way to introduce pairs that are made up with fermions in time-reversal states is the BCS ansatz for the many-body wave function, that reads

$$|\Phi\rangle = \Pi_j \left(u_j + v_j a^\dagger_j a^\dagger_{\tilde{j}} \right) |-\rangle, \tag{48}$$

where j labels a set of single-particle orbitals like the ϕ_j that have been previously discussed, a_j and $a^\dagger_j$ are, respectively, the annihilation and creation operators that destroy or add a particle in these orbitals, and the symbol $\tilde{j}$ indicates the time-reversal operation on j.

This wave function is clearly a superposition of components with different number of particles. Within the BCS theory, one determines the orbitals ϕ_j, the parameters u_j and v_j that appear in (48), and other relevant quantities, by minimisation of the total energy (see chapt. 6 of ref. [8]). The most relevant quantity is the pairing gap Δ, that corresponds to the minimal excitation energy of the system and can be interpreted as the binding energy of the Cooper pairs. The results of BCS can be compared with the experimental findings, and the success of the comparison is, in the present context, a further example of a symmetry-breaking wave function that describes nuclei more efficiently than a symmetry-conserving one. The symmetry restoration can be realised in a similar way as in eq. (47), through a rotation in an abstract space by the so-called gauge angle. The reader is advised to consult refs. [8, 81]. The generalisation of BCS, namely the Hartree-Fock-Bogoliubov (HFB) theory, is also described in [8]. Nowadays, the evolution of pairing when going towards the drip lines, or in other dilute systems like the crust of neutron stars, is under discussion. Another subject which is of great interest, but goes beyond the scope of this lecture, is whether pairing between protons and neutron is strong enough to give rise to a condensate [82].

In summary, space deformation and pairing are both characterised by non-vanishing expectation values of operators that correspond to the broken symmetries in the intrinsic system. In the case of quadrupole deformation, the expectation value of the quadrupole moment $\hat{Q}$ shows up. One can of course generalise to other deformations like octupole. In the case of pairing, where the wave function (48) mixes states that differ by two particles, the non-vanishing expectation value is that of $\sum_j a_j a_{\tilde{j}}$ (or its complex conjugate).

From the DFT viewpoint, the breaking of the rotational symmetry implies that the density $\rho(\vec{r})$ can assume an intrinsic non-spherical shape, and the breaking of number symmetry implies that EDFs can also depend on a generalised density that is called abnormal density (or pairing tensor) and reads $\kappa(\vec{r}) = \langle a(\vec{r})a(\vec{r})\rangle$ (where $a(\vec{r})$ is the annihilation operator of a particle at point $\vec{r}$ and $a^\dagger(\vec{r})$ is the corresponding creation operator). We remind the reader that the usual density that we have been dealing with so far reads $\rho(\vec{r}) = \langle a^\dagger(\vec{r})a(\vec{r})\rangle$ in second quantisation.

A full-fledged formulation of DFT with symmetry breaking goes beyond our scope here. The present section can be considered an elementary introduction to specialised lectures on this topic, like ref. [17].

10. – Extension to the time-dependent case

The extension of the HK theorem to the time-dependent case has been proposed by Runge and Gross in ref. [83]. The Runge-Gross theorem guarantees that an exact functional exists, in principle, also for the time-dependent case. More precisely, given a system whose behaviour is governed by an Hamiltonian

$$H' = H + v_{\rm pert}(t), \tag{49}$$

where the second term on the r.h.s. is a perturbing time-dependent potential (whose dependence on all degrees of freedom of the system is implicit), the theorem establishes a one-to-one correspondence between $v_{\rm pert}(t)$ and the time-dependent density $\rho(t)$, that is

$$v_{\rm pert}(\vec{r},t) \quad \Leftrightarrow \quad \rho(\vec{r},t). \tag{50}$$

The proof of the Runge-Gross theorem is more subtle and involved than the proof of the static HK theorem that we have discussed in sect. **2**. This theorem constitutes the basis of time-dependent DFT (TDDFT). For a pedagogical introduction to the subject, the reader can consult chapt. 4 of ref. [84].

TDDFT can also be approached within the Kohn-Sham scheme. In fact, the time-dependent density can be expressed in terms of time-dependent Kohn-Sham orbitals,

$$\rho(\vec{r},t) = \sum_j |\phi_j(\vec{r},t)|^2, \tag{51}$$

and these orbitals must satisfy time-dependent Schrödinger equations of the type

$$i\hbar\frac{\partial}{\partial t}\phi_j(\vec{r},t) = \left[-\frac{\hbar^2}{2m}\nabla^2 + v_{\rm KS}(\vec{r},t) + v_{\rm pert}(\vec{r},t)\right]\phi_j(\vec{r},t). \tag{52}$$

$v_{\rm KS}(\vec{r},t)$ is the sum of three terms. The external potential $v_{\rm ext}(\vec{r},t)$ and the Hartree potential $v_{\rm Hartree}(\vec{r},t)$ are the straightforward generalisation of the first two terms at the l.h.s. of eq. (9), where now the density is taken to be time-dependent. It is much less obvious how to extend the exchange-correlation potential defined in eq. (9) to the time-dependent case, that is, how to determine what must be inserted in eq. (52). Causality arguments play a role when one wishes to design a sensible strategy to build this potential: as pointed out in ref. [85], the potential must not feel at time t the changes that the densities may undergo at later times, that is, at $t' > t$. In fact, the rigorous proof of the Runge-Gross theorem implies a further key point that one should grasp, namely that the mapping (50) holds *for a given initial condition at time* t_0. In other terms, an exact exchange-correlation functional evaluated at time t should have memory of the whole previous history of the system for $t' < t$.

In electronic systems, the construction of exchange-correlation functionals with memory is still in its infancy. Most calculations adopt the simple adiabatic approximation, in which also the exchange-correlation functional has the same form as the static one, eq. (7), but is evaluated making use of the time-dependent density, *viz.*

$$v_{\rm xc}^{\rm (ALDA)}(\vec{r},t) = v_{\rm xc}[\rho(\vec{r},t)], \tag{53}$$

where the label ALDA stays for adiabatic LDA. ALDA is basically the only option that has been so far explored in the nuclear case. Such approximation is expected to work better if the time scale of the perturbation is slow.

Given some assumption for $v_{\rm KS}$, one can solve directly the time-dependent Kohn-Sham equations. A practical way is the following. If $h(t)$ is the sum of $v_{\rm KS}$ plus the kinetic energy, the time evolution of the density can be written as

$$i\hbar\frac{\rm d}{{\rm d}t}\rho(t) = \left[h(t),\rho(t)\right]. \tag{54}$$

Given an initial condition in which $\rho(t = t_0)$ is different from the stationary ground-state density, this latter equation can be solved by defining a time-evolution operator $\hat{U} \equiv e^{-i\frac{\Delta t}{\hbar}\cdot h}$, and by applying it to the density: starting from the density at time t_0, one can in fact write $\rho(t_0 + \Delta t) = \hat{U}\rho(t = t_0)$, where Δt is an appropriate time step. This version of time-dependent DFT has been widely used. A useful introduction can be found in refs. [86, 47], but many applications to nuclear vibrations [87], fusion processes [88], and heavy-ion reactions [89], among others, can be found in the recent literature.

The time-dependent equation (54) can be considered in the case of small external perturbations, namely it can be linearized. This linearization should be appropriate in the case of nuclear vibrations like the so-called giant resonances, and it is called linear

response theory in general, and Random Phase Approximation (RPA) in the nuclear physics context. In this specific case, the adiabatic approximation should make sense as already pointed out in [83]; whether this approximation describes well specific physics cases, is a different and open question.

The derivation of RPA from eq. (54) can be found in standard textbooks (see, *e.g.*, chapt. 8 of [8]). We will not repeat it in detail here, but rather discuss the key ideas. If the perturbation $v_{\rm pert}$ is small, it makes sense to assume it is harmonic,

$$v_{\rm pert}(\vec{r},t) = v_{\rm pert}(\vec{r})e^{i\omega t} + \text{h.c.}, \tag{55}$$

and then the density will display changes $\delta\rho(\vec{r},t)$ that behave similarly as a function of time, that is

$$\begin{aligned} \rho(\vec{r},t) &= \rho(\vec{r}) + \delta\rho(\vec{r},t), \\ \delta\rho(\vec{r},t) &= \delta\rho(\vec{r})e^{i\omega t} + \text{h.c.}, \end{aligned} \tag{56}$$

where $\rho(\vec{r})$ is here the stationary ground-state density. RPA equations can be obtained by inserting (55) and (56) in (54), and retaining only terms that are linear in $\delta\rho$ or in $\delta h \equiv \frac{\delta h}{\delta\rho}\delta\rho$. If we go to limit of vanishing external perturbation, and if the final result is expressed on the basis of the Kohn-Sham orbitals, it reads

$$\begin{pmatrix} A & B \\ -B & -A \end{pmatrix} \begin{pmatrix} X \\ Y \end{pmatrix} = \hbar\omega \begin{pmatrix} X \\ Y \end{pmatrix}. \tag{57}$$

This is an eigenvalue equation, and $\hbar\omega$ are the energies of the small-amplitude vibrations. For each of these modes, we have defined an eigenvector which is made up with the so-called forward-going and backward-going amplitudes X_{mi} and Y_{mi}, respectively([9]). X_{mi} (Y_{mi}) represents the probability amplitude that a transition from the orbital i to m (m to i([10])) contributes to the vibrational mode. The matrix elements that appear in eq. (57) are defined by

$$\begin{aligned} A_{mi,nj} &= \delta_{ij}\delta_{mn}(\varepsilon_m - \varepsilon_i) + \int \mathrm{d}^3r\,\mathrm{d}^3r'\,\phi^*_m(\vec{r})\phi^*_j(\vec{r}')\frac{\delta h(\vec{r})}{\delta\rho(\vec{r}')}\phi_i(\vec{r})\phi_n(\vec{r}'), \\ B_{mi,nj} &= \int \mathrm{d}^3r\,\mathrm{d}^3r'\,\phi^*_m(\vec{r})\phi^*_n(\vec{r}')\frac{\delta h(\vec{r})}{\delta\rho(\vec{r}')}\phi_i(\vec{r})\phi_j(\vec{r}'), \end{aligned} \tag{58}$$

where ε denotes the energies of the Kohn-Sham orbitals that have been introduced in eq. (9). The physical interpretation of $\frac{\delta h(\vec{r})}{\delta\rho(\vec{r}')}$ is pretty intuitive: the changes of the

([9]) Here, i,j are used to label occupied orbitals and m,n are used to label unoccupied orbitals.
([10]) Note that introducing the backward-going amplitudes is consistent with the linearity of the response, but implies relaxing the assumption that the ground state is made up with the auxiliary orbitals filled up to the Fermi energy, and empty above this energy.

density affect the single-particle effective operator h (kinetic energy plus $v_{\rm KS}$) and this, in turn, produces a rearrangement of the system. In other words, the system will perform harmonic oscillations around the ground state that are governed by the residual force

$$V_{\rm res}(\vec{r},\vec{r}\,') \equiv \frac{\delta h(\vec{r})}{\delta\rho(\vec{r}\,')}\,. \tag{59}$$

RPA equations can be also written in real space instead than on a basis. This implementation allows a proper treatment of the continuum, but may become quite demanding if one deals with EDFs with many different terms. In fact, we have only mentioned the total density ρ so far, but, according to the discussion of sect. **6**, realistic EDFs will bring in dependence on τ, $\vec{\nabla}\rho$, $\vec{J}$ etc. Then, the variation of these densities will add new terms to the residual interaction (59), like $\frac{\delta h(\vec{r})}{\delta\tau(\vec{r}\,')}$ and so on.

A multitude of variants and applications of RPA exist in the literature. Part of it is reviewed, *e.g.*, in ref. [15]. We should add, in this context, that recently a new way of implementing RPA has been proposed [90], which is not yet discussed in standard textbooks and review papers. This method, called Finite Amplitude Method (FAM) realizes the above ideas of linear response in a quite straighforward way and has the advantage that the numerical implementation is far easier than those of standard methods.

11. – Examples of RPA calculations

The best example of nuclear collective motion are the giant resonances, as we have already briefly mentioned. They are coherent modes, that dominate the response of nuclei in the energy region around $\approx$ 10–30 MeV. Their properties are consistent with the assumption of an elastic behaviour [91] and, in this respect, their integral properties are well described by RPA. Giant resonances carry different spatial angular momentum L, spin S, and isospin T. The states in which nucleons with opposite spin vibrate in phase (out of phase) are called electric (magnetic) resonances; if nucleons with opposite isospin, *i.e.* neutrons and protons, vibrate in phase (out of phase) one speaks of isoscalar (isovector) resonances.

We will mention only one of the multipoles in what follows. An external electromagnetic field excites the isovector dipole in a practically exclusive way. The response is dominated by the so-called isovector giant dipole resonance (IVGDR) at an energy around $80\,{\rm A}^{-1/3}$: at that energy, the photon wavelength is much larger than the nuclear size and the associated electric field, that acts on the protons, is constant in space and thus consistent with a potential that is linear in the proton coordinates $\vec{r}_p$. It is very easy to check that if we take a potential of the type $e\sum_p \vec{r}_p$, and we transform it to the center-of-mass system, it becomes

$$\hat{O}_{\rm IV\ dipole} = e\frac{N}{A}\sum_p \vec{r}_p - e\frac{Z}{A}\sum_n \vec{r}_n. \tag{60}$$

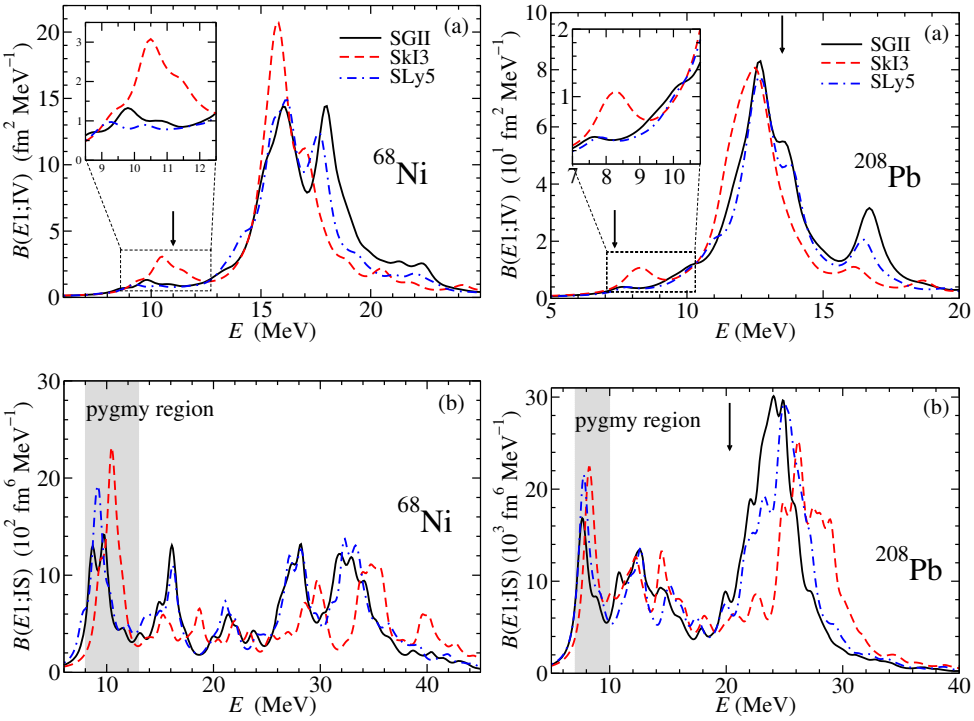

Fig. 6. – Strength functions (61) corresponding to the isovector (a) and isoscalar (b) dipole response of ^{68}Ni (left panels) and ^{208}Pb (right panels) as a function of the excitation energy. The insets display on a larger scale the low-energy, or pygmy, region. The predictions obtained with different Skyrme functionals are depicted (cf. the main text). The results from eq. (61) are averaged with Lorentzian functions having 1 MeV width. Black arrows indicate the experimental results from refs. [92-95]. Figure taken from ref. [96].

In the center-of-mass system, protons and neutrons are displaced in opposite directions and the strong neutron-proton interaction acts as a restoring force.

In fig. 6 we show strength functions resulting from RPA calculations with different Skyrme functionals (SGII from ref. [97], SkI3 from ref. [55] and SLy5 from ref. [54]). Strength functions are defined by

$$S(E) = \sum_n |\langle n|\hat{O}|0\rangle|^2 \delta(E - \hbar\omega_n), \tag{61}$$

where n labels the solutions of eq. (57), namely $\hbar\omega_n$ is an eigenvalue and $|n\rangle$ is the corresponding eigenvector, $|0\rangle$ is the ground-state, and $\hat{O}$ is a generic operator. Panels (a) correspond to the choice of the isovector operator (60), and the main IVGDR peak is compared with the photoabsorbtion result of ref. [92], while the low-lying peak which is sometimes referred to as "pygmy" dipole resonance (PDR) is compared with the experimental findings of refs. [93, 94]. Panels (b) show instead the response to the isoscalar

dipole operator,

$$\hat{O}_{\text{IS dipole}} = \sum_i \left(r_i^3 - \frac{3}{5}\langle r^2 \rangle r_i \right) Y_{1M}(\hat{r}_i). \tag{62}$$

Details for this choice can be found in ref. [96]. The result for the main resonance excited by this operator can be compared with the result of experiments like inelastic (α, α') scattering, as we have done by taking the finding of [95]. The results in the figure seem to indicate that the low-lying dipole response has more isoscalar than isovector character.

Several textbooks have been devoted to the whole subject of nuclear giant resonances and reader can consult refs. [98, 99]. The evolution of collective modes in neutron-rich nuclei is trated in ref. [100].

12. – Limitations of EDFs

There is still debate on which are the intrinsic limitations of DFT in nuclear physics, and which are the practical limitations (due to the specific choices for the form of the EDF, and for the protocol to fit the parameters). Disentangling the two aspects is not easy.

The typical example of such debate is the issue with single-particle states. As we mentioned at the end of sect. **5**, the level density in nuclei is consistent with a value of the effective mass m^*/m that lies around 0.7, but becomes close to 1 in the vicinity of the Fermi surface. Transfer experiments, although subject to a large amount of ambiguities, can provide access to the single-particle strength distributions in nuclei. Qualitatively, these experiments have shown that, close to the Fermi surface, these distributions display dominant peaks, that is, are consistent with the existence of particle-like or hole-like levels; however, far from the Fermi surface, the single-particle strength is very fragmented. These patterns have been known for quite some time, and explained with the coupling between HF single-particle states and nuclear vibrations (particle-vibration coupling or PVC), as discussed at length in ref. [45]. However, there are claims that, although PVC may be needed to explain single-particle fragmentation, the centroids of single-particle states must be obtained through improvements of current EDFs [101].

Even for observables that are the typical focus of nuclear DFT, like masses, we have mentioned in sect. **7** that existing EDFs have errors that are typically around 1–2 MeV. Mass models that are more successful, and reduce this error below 1 MeV, include some terms that go outside the actual DFT philosophy. These terms correspond to vibrational or rotational correlations (cf. [69] and references therein).

There are other open questions that are related to the limits of current DFT implementations. MR-EDF has been shown to be a theory that is mathematically sound, and it has been successful in describing many low-lying nuclear spectra; still, pathologies in the results have shown up, as discussed in [102] and references therein. These pathologies have been associated with density-dependence in the Skyrme EDF, which on the other

hand seems unavoidable if one wants to reconcile bulk properties and the effective mass. This is still a serious concern for practitioners. Another open question exists, regarding the pairing sector of the EDFs. In which way an EDF must depend on the abnormal density $\kappa(\vec{r})$, and possibly on its derivatives etc., is not clear yet. Links with an underlying theory of pairing in nuclei [103, 104] are still not enough. Proton-neutron pairing, as mentioned at the end of sect. **9**, is still not fully understood.

Last but not least, as briefly alluded to in sect. **11**, time-dependent DFT in the RPA implementation is known to be unable to reproduce the width of giant resonances, that is typically from few to several MeV. RPA can reproduce the so-called escape width, associated with particles decaying to the continuum, but not the remaining width, so-called spreading width. This latter is known to be accounted for in calculations that include PVC [105-107]. Whether functionals with memory effect may or not improve on this is a further open question.

Several of these examples hint that vibrational correlations, pairing correlations, or other kinds of dynamical correlations, although in principle should be included in "exact" DFT, in practice are not included in existing EDFs. These limitations also call for a more serious confrontation between DFT and underlying theories, on the one hand, but also between DFT and many-body theories: this is not systematically carried on as it should, in the nuclear structure domain.

13. – Conclusions

We have tried to give the reader a brief survey about DFT, namely about its foundations and about the main specific features of nuclear DFT. Due to the scope of this volume, we have tried to give priority to pedagogical arguments, while we have simply provided references for all those detailed topics that are already well covered in the literature. As has been stressed at the beginning, this contribution is meant to be an advanced, up-to-date introduction that serves mainly as an orientation for those interested in deepening their understanding of the large variety of DFT-related approaches.

The hope is to have been able to convince the reader that DFT has a number of advantages. Its basic principle is very transparent and intuitive: one writes the total energy as a function of the density, and chooses a way to minimise the energy! The HK theorem guarantees, then, that all bulk observables can be obtained: the density determines the shape of the system, the expectation values of relevant one-body operators (like electric quadrupole, or magnetic dipole, or higher multipole operators) as well as the total energy. The main advantage is that the applicability of DFT is very broad. All nuclei are amenable to a DFT description, except perhaps the very light ones. Moreover, there is a natural link with infinite nuclear matter and, thus, with the physics of compact objects like neutron stars.

After discussing DFT in electronic systems, we have, in fact, started our discussion by introducing nuclear DFT in uniform, symmetric nuclear matter. A sensible theory of such prototype system must display a mechanism for saturation; a good reproduction of the saturation point ($\rho_0 = 0.16\,\mathrm{fm}^{-3}$, $e_0 = -16\,\mathrm{MeV}$) is a necessary condition to

describe also finite nuclei in a reasonable way. We have, then, provided arguments why a naïve mean field cannot be, in this respect, a sensible theory while DFT can. Of course, realistic EDFs should not simply provide a mechanism of nuclear saturation but should be flexible enough to account for surface properties, spin and isospin properties, and so on. Accordingly, we have discussed the appearance of different kinds of densities in existing EDFs.

A specific feature of finite nuclei is the appearance of spontaneous symmetry breaking and restoration. Although specialised lectures exist on those topics, we have tried to give here an introduction through simple examples and arguments. In the case of deformed nuclei, the rotational symmetry is broken in the intrinsic reference frame, and rotations in the laboratory frame restore the symmetry. Within DFT, that has necessarily to be formulated in the intrinsic frame, as we have argued in sect. **8**, this implies the appearance of densities that are not rotationally invariant (that is, quadrupole or octupole moments as we have just stressed). A more intriguing example is that of pairing correlations that imply, instead, the appearance of the abnormal density or pairing tensor in the EDFs, breaking the particle number symmetry.

Last but not least, we have discussed the time-dependent case. The time-dependent DFT is still amenable to many improvements. Essentially all groups are using, so far, the adiabatic approximation. While this approximation, that corresponds to RPA in the nuclear structure theory language, has been successful in reproducing the main properties of the nuclear collective motion like the giant resonances, certainly examples of large-amplitude, slow motions exist in the nuclear case and call for more advanced approaches.

There are topics that we have not dealt with in this lecture and/or topics that have not been tackled yet by practitioners. One main issue is that, while in several papers the quest for a universal energy functional is advocated, still many different implementations of EDFs and even more variants based on different parameter sets are available on the market. The situation in the case of electronic systems is, anyway, not much better [13]. Not only this fact makes DFT a domain that is believed to be for experts only but, more importantly, it raises the question if EDFs are systematically improvable or not. EFT has been proposed as a way out to this dilemma. However, a full derivation of DFT from EFT is not available yet.

Another aspect is the confrontation between DFT and many-body theory. The mapping of some many-body approximation into an EDF shoud be pursued more systematically, and is expected also to shed light on the present limitations of nuclear DFT. We have briefly mentioned the fact that DFT cannot describe the fragmentation of single-particle or collective states. This has been traditionally explained, in the nuclear context, by the coupling of single-particle and collective degrees of freedom (vibrations or rotations). Merging this description with up-to-date DFT, still represents a challenging task.

In summary, we may like to quote a saying by W. Kohn, and state that "DFT is an exactification of HF"; however, even though this statement may be true in principle, in practice many steps are still required to make the DFT description of the rich nuclear phenomenology more and more accurate.

* * *

This work is also the result of many collaborations during the last decades. The author would like to thank, for the common work and the beneficial discussions on the topics that are dealt with in this paper, K. Bennaceur, P. F. Bortignon, J. Dobaczewski, T. Duguet, M. Grasso, E. Khan, D. Lacroix, H. Liang, J. Margueron, J. Meyer, Y. Niu, P.-G. Reinhard, P. Ring, X. Roca-Maza, H. Sagawa, N. Van Giai, E. Vigezzi, and D. Vretenar. The author also expresses his thanks to G. Accorto, M. Barani, R. Romano for their reading of the manuscript and help in the preparation of figures. Funding from the European Union's Horizon 2020 research and innovation programme under grant agreement No. 654002 is also acknowledged.

REFERENCES

[1] Thoennessen M., *Int. J. Mod. Phys. E*, **26** (2017) 1730003.
[2] Chamel N. and Haensel P., *Living Rev. Relat.*, **11** (2008) 10.
[3] Inoue T., Aoki S., Doi T., Hatsuda T., Ikeda Y., Ishii N., Murano K., Nemura H. and Sasaki K., *Phys. Rev. Lett.*, **111** (2013) 112503.
[4] Weinberg S., *Physica A: Statistical Mechanics and its Applications*, **96** (1979) 327.
[5] Epelbaum E., Hammer H.-W. and Meissner U.-G., *Rev. Mod. Phys.*, **81** (2009) 1773.
[6] Lynn J. E., Tews I., Carlson J., Gandolfi S., Gezerlis A., Schmidt K. E. and Schwenk A., *Phys. Rev. Lett.*, **116** (2016) 062501.
[7] Simonis J., Stroberg S. R., Hebeler K., Holt J. D. and Schwenk A., *Phys. Rev. C*, **96** (2017) 014303.
[8] Ring P. and Schuck P., *The Nuclear Many-Body Problem* (Springer) 1980.
[9] Bertulani C., *Nuclear Physics in a Nutshell* (Princeton University Press) 2007.
[10] Parr R. G. and Yang W., *Density Functional Theory of Atoms and Molecules* (Oxford University Press) 1989.
[11] Dreizler R. and Gross E., *Density Functional Theory* (Springer) 1990.
[12] Gross E., Dobson J. and Petersilka M., *Density Functional Theory* (Springer) 1996.
[13] Burke K., *J. Chem. Phys.*, **136** (2012) 150901.
[14] Becke A. D., *J. Chem. Phys.*, **140** (2014) 18A301.
[15] Bender M., Heenen P.-H. and Reinhard P.-G., *Rev. Mod. Phys.*, **75** (2003) 121.
[16] Lalazissis G., Ring P. and Vretenar D. (Editors), *Extended Density Functionals in Nuclear Structure Physics*, *Lect. Notes Phys.*, Vol. **641** (Springer) 2004.
[17] Duguet T., *Lect. Notes Phys.*, Vol. **879** (Springer) 2004, p. 293.
[18] Dobaczewski J., *Interactions, symmetry breaking, and effective fields from quarks to nuclei. (A primer in nuclear theory)*, arXiv:nucl-th/0301069 (2003).
[19] Vretenar D., Afanasjev A., Lalazissis G. and Ring P., *Phys. Rep.*, **409** (2005) 101.
[20] Nikšić T., Vretenar D. and Ring P., *Progr. Part. Nucl. Phys.*, **66** (2011) 519.
[21] Hohenberg P. and Kohn W., *Phys. Rev.*, **136** (1964) B864.
[22] Kohn W. and Sham L. J., *Phys. Rev.*, **140** (1965) A1133.
[23] Broglia R. A., Colò G., Onida G. and Roman H. E., *Solid State Physics of Finite Systems* (Springer) 2004.
[24] Fetter A. L. and Walecka J. D., *Quantum Theory of Many-Particle Systems* (McGraw-Hill) 1971.
[25] Mattuck R. D., *A Guide to Feynman Diagrams in the Many-Body Problem* (Dover) 1976.

[26] Perdew J. P. and Zunger A., *Phys. Rev. B*, **23** (1981) 5048.
[27] Perdew J. P. and Schmidt K., *AIP Conf. Proc.*, **577** (2001) 1.
[28] Bohr A. and Mottelson B. R., *Nuclear Structure*, Vol. **I** (Benjamin, New York) 1969.
[29] Bohr A. and Mottelson B. R., *Nuclear Structure*, Vol. **II** (Benjamin, New York) 1975.
[30] Migdal A. B., *Theory of Finite Fermi Systems and Applications to Atomic Nuclei* (Wiley) 1967.
[31] Soloviev V. G., *Theory of Atomic Nuclei: Quasiparticles and Phonons* (Institute of Physics Publishing) 1992.
[32] Garg U. and Colò G., *Prog. Part. Nucl. Phys.*, **101** (2018) 55.
[33] Bao-An Li, Àngels Ramos, Giuseppe Verde and Isaac Vidaña E., *Eur. Phys. J. A*, **50** (2014) 9.
[34] Lattimer J. M. and Lim Y., *Astrophys. J.*, **771** (2013) 51.
[35] Li B.-A. and Han X., *Phys. Lett. B*, **727** (2013) 276.
[36] Oertel M., Hempel M., Klähn T. and Typel S., *Rev. Mod. Phys.*, **89** (2017) 015007.
[37] Horowitz C. J., Brown E. F., Kim Y., Lynch W. G., Michaels R., Ono A., Piekarewicz J., Tsang M. B. and Wolter H. H., *J. Phys. G: Nucl. Part. Phys.*, **41** (2014) 093001.
[38] Gogny D., *Nucl. Phys. A*, **237** (1975) 399.
[39] Serot B. and Walecka J., *Adv. Nucl. Phys.*, **16** (1986) 1.
[40] Sellahewa R. and Rios A., *Phys. Rev. C*, **90** (2014) 054327.
[41] Accorto G., Master's thesis, University of Milano (2015).
[42] Brink D. and Boeker E., *Nucl. Phys. A*, **91** (1967) 1.
[43] Blaizot J. P., *Phys. Rep.*, **64** (1980) 171.
[44] Rancati A., Master's thesis, University of Milano (2016).
[45] Mahaux C., Bortignon P., Broglia R. and Dasso C., *Phys. Rep.*, **120** (1985) 1.
[46] Weisskopf V. F., *Nucl. Phys.*, **3** (1957) 423.
[47] Nakatsukasa T., Matsuyanagi K., Matsuo M. and Yabana K., *Rev. Mod. Phys.*, **88** (2016) 045004.
[48] Davesne D., Navarro J., Meyer J., Bennaceur K. and Pastore A., *Phys. Rev. C*, **97** (2018) 044304.
[49] Romano R., Master's thesis, University of Milano (2015).
[50] Dechargé J. and Gogny D., *Phys. Rev. C*, **21** (1980) 1568.
[51] Berger J., Girod M. and Gogny D., *Comp. Phys. Commun.*, **63** (1991) 365.
[52] Vautherin D. and Brink D. M., *Phys. Rev. C*, **5** (1972) 626.
[53] Chabanat E., Bonche P., Haensel P., Meyer J. and Schaeffer R., *Nucl. Phys. A*, **627** (1997) 710.
[54] Chabanat E., Bonche P., Haensel P., Meyer J. and Schaeffer R., *Nucl. Phys. A*, **635** (1998) 231.
[55] Reinhard P.-G. and Flocard H., *Nucl. Phys. A*, **584** (1995) 467.
[56] Kortelainen M., McDonnell J., Nazarewicz W., Olsen E., Reinhard P.-G., Sarich J., Schunck N., Wild S. M., Davesne D., Erler J. and Pastore A., *Phys. Rev. C*, **89** (2014) 054314.
[57] Engel Y., Brink D., Goeke K., Krieger S. and Vautherin D., *Nucl. Phys. A*, **249** (1975) 215.
[58] Dobaczewski J. and Dudek J., *Phys. Rev. C*, **52** (1995) 1827.
[59] Dobaczewski J. and Dudek J., *Acta Phys. Pol. B*, **27** (1996) 95.
[60] Dobaczewski J. and Dudek J., *Phys. Rev. C*, **55** (1997) 3177.
[61] Raimondi F., Carlsson B. G. and Dobaczewski J., *Phys. Rev. C*, **83** (2011) 054311.
[62] Becker P., Davesne D., Meyer J., Pastore A. and Navarro J., *J. Phys. G: Nucl. Part. Phys.*, **42** (2015) 034001.

[63] Davesne D., Navarro J., Becker P., Jodon R., Meyer J. and Pastore A., *Phys. Rev. C*, **91** (2015) 064303.
[64] Nakada H., *Phys. Rev. C*, **78** (2008) 054301.
[65] Fayans S., Trykov E. and Zawischa D., *Nucl. Phys. A*, **568** (1994) 523.
[66] Fayans S. A., *J. Exp. Theor. Phys. Lett.*, **68** (1998) 169.
[67] Baldo M., Schuck P. and Viñas X., *Phys. Lett. B*, **663** (2008) 390.
[68] Lunney D., Pearson J. M. and Thibault C., *Rev. Mod. Phys.*, **75** (2003) 1021.
[69] Goriely S., Chamel N. and Pearson J. M., *Phys. Rev. C*, **93** (2016) 034337.
[70] Kortelainen M., Lesinski T., Moré J., Nazarewicz W., Sarich J., Schunck N., Stoitsov M. V. and Wild S., *Phys. Rev. C*, **82** (2010) 024313.
[71] Nikšić T., Vretenar D. and Ring P., *Phys. Rev. C*, **78** (2008) 034318.
[72] Erler J., Birge N., Kortelainen M., Nazarewicz W., Olsen E., Perhac A. M. and Stoitsov M., *Nature*, **486** (2012) 509.
[73] Afanasjev A., Agbemava S., Ray D. and Ring P., *Phys. Lett. B*, **726** (2013) 680.
[74] Engel J., *Phys. Rev. C*, **75** (2007) 014306.
[75] Barnea N., *Phys. Rev. C*, **76** (2007) 067302.
[76] Messud J., Bender M. and Suraud E., *Phys. Rev. C*, **80** (2009) 054314.
[77] Goutte H., *Symmetry breaking and symmetry restoration in mean-field based approached*, in *Ecole Joliot Curie*, IN2P3-CNRS (C.E.N.B.G., `http://www.cenbg.in2p3.fr/joliot-curie/`) 2010.
[78] Lacroix D., *Review of mean-field theory*, in *Ecole Joliot Curie*, IN2P3-CNRS (C.E.N.B.G., `http://www.cenbg.in2p3.fr/joliot-curie/`) 2011.
[79] Butler P. A. and Nazarewicz W., *Rev. Mod. Phys.*, **68** (1996) 349.
[80] Gaffney L. P., Butler P. A., Scheck M., Hayes A. B., Wenander F., Albers M., Bastin B., Bauer C., Blazhev A., Bönig S., Bree N., Cederkäll J., Chupp T., Cline D., Cocolios T. E., Davinson T., De Witte H., Diriken J., Grahn T., Herzan A., Huyse M., Jenkins D. G., Joss D. T., Kesteloot N., Konki J., Kowalczyk M., Kröll T., Kwan E., Lutter R., Moschner K., Napiorkowski P., Pakarinen J., Pfeiffer M., Radeck D., Reiter P., Reynders K., Rigby S. V., Robledo L. M., Rudigier M., Sambi S., Seidlitz M., Siebeck B., Stora T., Thoele P., Van Duppen P., Vermeulen M. J., von Schmid M., Voulot D., Warr N., Wimmer K., Wrzosek-Lipska K., Wu C. Y. and Zielinska M., *Nature*, **497** (2013) 199.
[81] Brink D. M. and Broglia R. A., *Nuclear Superfluidity: Pairing in Finite Systems* (Cambridge University Press) 2005.
[82] Sagawa H., Bai C. L. and Colò G., *Phys. Scr.*, **91** (2016) 083011.
[83] Runge E. and Gross E. K. U., *Phys. Rev. Lett.*, **52** (1984) 997.
[84] Fiolhais C., Nogueira F. and Marques M. (Editors), *A primer in Density Functional Theory*, *Lect. Notes Phys.*, Vol. **620** (Springer) 2003.
[85] van Leeuwen R., *Phys. Rev. Lett.*, **80** (1998) 1280.
[86] Reinhard P. and Suraud E., *Introduction to Cluster Dynamics* (Wiley) 2004.
[87] Maruhn J. A., Reinhard P. G., Stevenson P. D., Stone J. R. and Strayer M. R., *Phys. Rev. C*, **71** (2005) 064328.
[88] Simenel C., Keser R., Umar A. S. and Oberacker V. E., *Phys. Rev. C*, **88** (2013) 024617.
[89] Sekizawa K. and Yabana K., *Phys. Rev. C*, **93** (2016) 054616.
[90] Nakatsukasa T., Inakura T. and Yabana K., *Phys. Rev. C*, **76** (2007) 024318.
[91] Bertsch G., *Ann. Phys.*, **86** (1974) 138.
[92] Berman B. L. and Fultz S. C., *Rev. Mod. Phys.*, **47** (1975) 713.

[93] Wieland O., Bracco A., Camera F., Benzoni G., Blasi N., Brambilla S., Crespi F. C. L., Leoni S., Million B., Nicolini R., Maj A., Bednarczyk P., Grebosz J., Kmiecik M., Meczynski W., Styczen J., Aumann T., Banu A., Beck T., Becker F., Caceres L., Doornenbal P., Emling H., Gerl J., Geissel H., Gorska M., Kavatsyuk O., Kavatsyuk M., Kojouharov I., Kurz N., Lozeva R., Saito N., Saito T., Schaffner H., Wollersheim H. J., Jolie J., Reiter P., Warr N., deAngelis G., Gadea A., Napoli D., Lenzi S., Lunardi S., Balabanski D., LoBianco G., Petrache C., Saltarelli A., Castoldi M., Zucchiatti A., Walker J. and Bürger A., *Phys. Rev. Lett.*, **102** (2009) 092502.

[94] Ryezayeva N., Hartmann T., Kalmykov Y., Lenske H., von Neumann-Cosel P., Ponomarev V. Y., Richter A., Shevchenko A., Volz S. and Wambach J., *Phys. Rev. Lett.*, **89** (2002) 272502.

[95] Garg U., *Nucl. Phys. A*, **649** (1999) 66.

[96] Roca-Maza X., Pozzi G., Brenna M., Mizuyama K. and Colò G., *Phys. Rev. C*, **85** (2012) 024601.

[97] Giai N. V. and Sagawa H., *Phys. Lett. B*, **106** (1981) 379.

[98] Harakeh M. N. and van der Woude A., *Giant Resonances Fundamental High-Frequency Modes of Nuclear Excitation* (Oxford University Press, New York) 2001.

[99] Bortignon P. F., Bracco A. and Broglia R. A., *Giant Resonances: Nuclear Structure at Finite Temperature* (Harwood) 1999.

[100] Paar N., Vretenar D., Khan E. and Colò G., *Rep. Progr. Phys.*, **70** (2007) 691.

[101] Tarpanov D., Dobaczewski J., Toivanen J. and Carlsson B. G., *Phys. Rev. Lett.*, **113** (2014) 252501.

[102] Duguet T., Bender M., Bennaceur K., Lacroix D. and Lesinski T., *Phys. Rev. C*, **79** (2009) 044320.

[103] Hebeler K., Duguet T., Lesinski T. and Schwenk A., *Phys. Rev. C*, **80** (2009) 044321.

[104] Idini A., Barranco F. and Vigezzi E., *Phys. Rev. C*, **85** (2012) 014331.

[105] Colò G., Van Giai N., Bortignon P. F. and Broglia R. A., *Phys. Rev. C*, **50** (1994) 1496.

[106] Niu Y. F., Colò G., Vigezzi E., Bai C. L. and Sagawa H., *Phys. Rev. C*, **94** (2016) 064328.

[107] Roca-Maza X., Niu Y. F., Colò G. and Bortignon P. F., *J. Phys. G: Nucl. Part. Phys.*, **44** (2017) 044001.

Proceedings of the International School of Physics "Enrico Fermi"
Course 201 "Nuclear Physics with Stable and Radioactive Ion Beams", edited by F. Gramegna,
P. Van Duppen, A. Vitturi and S. Pirrone
(IOS, Amsterdam; SIF, Bologna) 2019
DOI 10.3254/978-1-61499-957-7-129

Models for nuclear reactions with weakly bound systems

Antonio M. Moro

Departamento de FAMN, Universidad de Sevilla - Apartado 1065, 41080 Sevilla, Spain

Summary. — In this contribution, I present a short overview of the theory of direct nuclear reactions, with special emphasis on the case of reactions induced by weakly bound nuclei. After introducing some general results of quantum scattering theory, I present specific applications to elastic, inelastic, transfer and breakup reactions. For each of them, I first introduce the most standard framework, followed by some alternative models or extensions suitable for the case of weakly bound nuclei. A short discussion on semiclassical theory of Coulomb excitation and its application to breakup of halo nuclei is also provided.

1. – Introduction

Our present knowledge on the properties of atomic nuclei is largely based on the analysis of nuclear reactions. The very existence of the nucleus was inferred by Rutherford in 1905 from his famous α elastic scattering experiment and many features and phenomena, such as the shell structure, the magic numbers, the collective and single-particle degrees of freedom, among others, are investigated using nuclear reactions. Since the 1980s, thanks to the development of radioactive beams, these studies could be extended to regions of the nuclear chart beyond the stability valley.

In the proximity of the proton and neutron driplines, new exotic structures and phenomena were discovered. Prominent examples are the popular halo and Borromean nuclei. It was soon realized that formalisms originally designed to describe the structure and reactions of ordinary nuclei were not well adapted to describe these new phenomena. In particular, in the proximity of the driplines, atomic nuclei are weakly bound. When these fragile systems collide with a stable nucleus they break up easily due to the Coulomb and nuclear forces exerted by a target nucleus. Consequently, reaction theories designed to describe these reactions must incorporate the effect of the strong coupling to the breakup channels.

We enumerate some fingerprints of the weak binding on reaction observables:

- *Large interaction cross sections in nuclear collisions at high energies.* Historically, the first evidence of the unusual properties of halo nuclei came from the pioneering experiments performed by Tanihata and co-workers at Berkeley using very energetic (800 MeV/nucleon) secondary beams of radioactive species [1, 2]. At these high energies, interaction cross sections are approximately proportional to the size of the colliding nuclei. It was found that some exotic isotopes of light isotopes (^{6}He, ^{11}Li, ^{14}Be) presented much higher interaction cross sections than their neighbour isotopes, which was interpreted as an abnormally large radius.
- *Narrow momentum distributions of residues following fast nucleon removal.* Momentum distributions of the residual nucleus following the removal of one or more nucleons of a energetic projectile colliding with a target nucleus are closely related to the momentum distribution of the removed nucleon(s) in the original projectile. Kobayashi *et al.* [3] found that the momentum distributions of ^{9}Li following the fragmentation process $^{11}\mathrm{Li}+^{12}\mathrm{C} \rightarrow {}^{9}\mathrm{Li}+\mathrm{X}$ were abnormally narrow which, according to the Heisenberg's uncertainty principle, suggested a long tail in the density distribution of the ^{11}Li nucleus. This result was later found in other weakly bound nuclei.
- *Abnormal elastic scattering cross sections.* Elastic scattering is affected by the coupling to non-elastic processes. In particular, when coupling to breakup channels is important, elastic scattering cross sections are depleted with respect to the case of tightly bound nuclei. Some other key signatures are the departure of the elastic cross section from the Rutherford cross section at sub-Coulomb energies and the disappearance of the Fresnel peak at near-barrier energies in reactions induced by halo nuclei on heavy targets [4-7].
- *Enhanced near-threshold breakup cross section in Coulomb dissociation experiments of neutron-halo nuclei.* When a neutron-halo nucleus, composed of a charged *core* and one or two weakly bound neutrons (^{11}Be, ^{6}He, ^{11}Li, ...) collides with a high-Z target nucleus, the projectile structure is heavily distorted due to the tidal force originated from the uneven action of the Coulomb interaction on the charged core and the neutrons. This produces a stretching which may eventually break up the loosely bound projectile. This gives rise to a large population of the continuum states close to the breakup threshold.

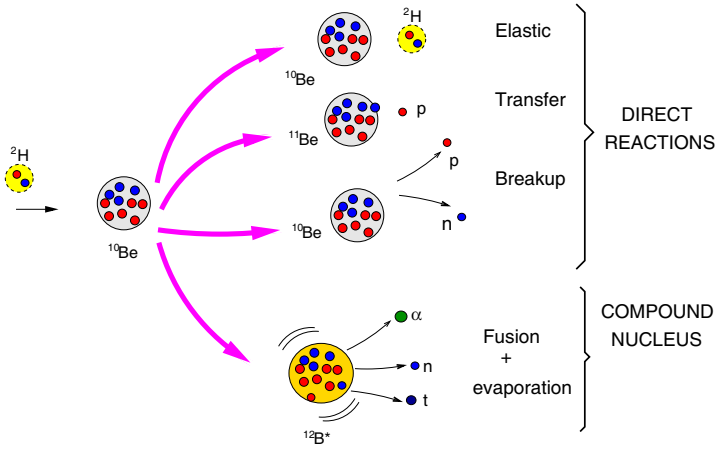

Fig. 1. – Direct and compound nucleus reaction channels taking place in a d + ^{10}Be reaction.

A proper, quantitative understanding of these and other phenomena requires the use of an appropriate reaction theory. But, before we address the features of reactions induced by weakly bound nuclei, we will review some general concepts and results of quantum scattering theory.

A remark on the terminology is in order here. In many cases, the word "exotic" is used as akin to "unstable". Strictly, not all "unstable nuclei" show exotic properties (such as weak binding, haloes, etc.). Conversely, there are also stable nuclei which exhibit some "exotic" (abnormal) features, such as weak binding. This is the case, for instance, of the deuteron system which, albeit not exotic, behaves similarly to halo nuclei due to its relatively small binding energy.

2. – Some general scattering theory

A nuclear collision represents a extremely complicated many-body quantum-mechanical scattering problem, whose rigorous solution is not possible in most cases. Therefore, approximate models, usually tailored to specific types of reactions, are used. These models tend to emphasize specific degrees of freedom, those which are most likely activated during the reaction under study. For example, when low-lying collective states are present in either the projectile or target nucleus, the possibility of exciting and populating these states must be somehow (explicitly or effectively) taken into account. For weakly bound nuclei, such as halo nuclei, the dissociation ("breakup") of the valence nucleon(s) must be considered.

As an example, in fig. 1 we illustrate schematically some of the channels taking place in a d + ^{10}Be reaction. These channels can be divided into two categories, according to the characteristic collision time and degrees of freedom involved. On one side, the *direct reaction channels*, which are relatively fast ($t \sim 10^{-21}$ s) and peripheral processes, usually

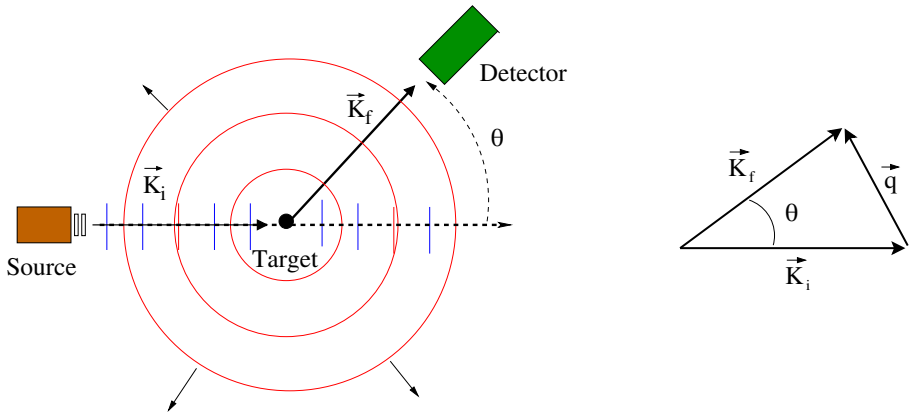

Fig. 2. – Left: schematic representation of a scattering experiment, showing the incident and scattered waves. Right: incident and final momenta, and momentum transfer.

involving a few degrees of freedom and small momentum transfer. This is the case of elastic, inelastic scattering and rearrangement (transfer) processes. Angular distributions of the projectile-like fragment usually peak at forward angles. On the other side, the *compound nucleus* reactions, which take place over a longer time scale ($t \sim 10^{-18}$–10^{-16} s), lead to a significant redistribution of the initial kinetic energy among the nucleons of the collision partners and, hence, a larger number of degrees of freedom involved. The compound nucleus is usually left in a high excited state, which tends to de-excite by particle or gamma-ray emission, whose angular distributions tend to be isotropic in the center-of-mass (CM) frame.

The very different nature of direct and compound nucleus reactions results also in very different formal treatments. The latter are treated using statistical models, first proposed by Bohr [8]. In the remainder of this contribution, only direct reactions will be discussed.

2˙1. *The concept of cross section.* – A typical nuclear reaction experiment (see fig. 2) measures the number of particles, integrated over a given amount of time, of one or more species resulting from a collision between two nuclei, as a function of its scattering angle and/or its energy. This number of particles will depend on the experimental conditions, such as the beam intensity and the target thickness. To compare with the theoretical predictions, it is convenient to introduce the so-called *differential cross section* which is denoted $\mathrm{d}\sigma/\mathrm{d}\Omega$ and is defined as the *flux of scattered particles through the area* $\mathrm{d}A = r^2\mathrm{d}\Omega$ *in the direction* θ*, per unit incident flux, i.e.*

$$\frac{\mathrm{d}\sigma}{\mathrm{d}\Omega} = \frac{\text{flux of scattered particles through } \mathrm{d}A = r^2\mathrm{d}\Omega}{\text{incident flux}}\,, \tag{1}$$

and can be extracted experimentally from the number of recorded events as

$$\Delta I = I_0\, n_t\, \frac{\mathrm{d}\sigma}{\mathrm{d}\Omega}\Delta\Omega, \tag{2}$$

where I_0 is the number of incident particles per unit time, $\Delta\Omega$ is the solid angle subtended by the detector, ΔI is the number of detected particles per unit time in $\Delta\Omega$, and n_t the number of target nuclei per unit surface.

Inspection of eq. (2) shows that the differential cross section has units of area. The differential cross section is *independent* of the experimental conditions, such as the beam intensity, the elapsed time of the measurement and the target thickness. Instead, it depends on the interaction between the projectile and target systems, which is the important quantity that a scattering experiment aims to isolate and probe.

The final goal of the scattering theory is to develop appropriate models to which compare the measured observables, with the aim of extracting information on the structure of the colliding nuclei as well as understanding the dynamics governing these processes. The measured quantities are typically total or partial cross sections with respect to angle and/or energy of the outgoing nuclei. Therefore, the challenge of reaction theory is to obtain these cross sections by solving the dynamical equations of the system (at non-relativistic energies, the Schrödinger equation) with a realistic but manageable structure model of the colliding nuclei.

2˙2. *Model Hamiltonian and scattering wave function.* – The mathematical treatment of a scattering problem requires the solution of the time-dependent or time-independent Schrödinger equation for the system([1]). In the second case, this equation reads

$$[H - E]\Psi = 0. \tag{3}$$

This wave function will be a function of the degrees of freedom (*e.g.* internal coordinates) of the projectile and target, denoted generically as ξ_p and ξ_t, as well as on the relative coordinate between them ($\vec{R}$). Thus, we will express the total wave function as $\Psi(\vec{R}, \xi_p, \xi_t)$. The Hamiltonian of the system is written in the form

$$H = \hat{T}_{\vec{R}} + H_p(\xi_p) + H_t(\xi_t) + V(\vec{R}, \xi_p, \xi_t), \tag{4}$$

where $\hat{T}_{\vec{R}}$ is the kinetic energy operator ($\hat{T} = -\frac{\hbar^2}{2\mu}\nabla^2$), $H_p(\xi_p)$ ($H_t(\xi_t)$) denote the projectile (target) internal Hamiltonian and $V(\vec{R}, \xi_p, \xi_t)$ is the projectile-target interaction. After the collision, the projectile and target may exchange some nucleons, or even break up, so the Hamiltonian (4) corresponds actually to the entrance channel. To distinguish

([1]) For an enlightening discussion on the relation between the time-dependent and time-independent approaches, see chapt. 1 of ref. [9].

between different mass partitions that may arise in a reaction, we will use Greek letters, with α denoting the initial partition. So, the previous Hamiltonian is rewritten as

$$H = \hat{T}_\alpha + H_\alpha(\xi_\alpha) + V_\alpha(\vec{R}_\alpha, \xi_\alpha), \tag{5}$$

where ξ_α denotes the projectile and target internal coordinates in partition α and $H_\alpha(\xi_\alpha) \equiv H_p(\xi_p) + H_t(\xi_t)$. The total energy of the system is given by the sum of the kinetic energy (E_α) and the internal energy (ε_α) of the projectile and target

$$E = E_\alpha + \varepsilon_\alpha = \frac{\hbar^2 {K_\alpha}^2}{2\mu_\alpha} + \varepsilon_\alpha, \tag{6}$$

where $\hbar\vec{K}_\alpha$ is the linear momentum and ε_α is the sum of the projectile and target internal energies.

Equation (3) is a second-order differential equation that must be solved subject to appropriate boundary conditions. The latter must reflect the nature of a scattering process. In our time-independent picture, the incident beam will be represented by a plane wave([2])([3]). After the collision with the target, a set of outgoing spherical waves will be formed. The situation is schematically depicted in fig. 2. So, asymptotically,

$$\Psi^{(+)}_{\vec{K}_\alpha}(\vec{R}, \xi) \to \Phi_\alpha(\xi) e^{i\vec{K}_\alpha \cdot \vec{R}_\alpha} + \text{outgoing spherical waves}, \tag{7}$$

with $\Phi_\alpha(\xi) \equiv \phi_0^{(p)}(\xi_p)\phi_0^{(t)}(\xi_t)$ and where the superscript "+" indicates that this corresponds to the solution with outgoing boundary conditions (mathematically, one may construct also the solution with incoming boundary conditions).

During the collision, the incident wave will be highly distorted due to the interaction with the target nucleus but, after the collision, at sufficiently large distances (that is, when V becomes negligible), the projectile and target will emerge in any of their (kinematically

([2]) This is only true for the case of short-range potentials; in the presence of the Coulomb potential, the incident wavefunction is represented by a Coulomb wave.

([3]) A more realistic description would be in terms of wave packets but the formal treatment is much more complicated. To link both pictures, one can bear in mind that a wave packet can be constructed as a superposition of plane waves.

allowed) states of the projectile and target nuclei. So, asymptotically, we may write([4])

$$\Psi^{(+)}_{\vec{K}_\alpha} \xrightarrow{R_\alpha \gg} \Phi_\alpha(\xi_\alpha) e^{i\vec{K}_\alpha \cdot \vec{R}_\alpha} + \Phi_\alpha(\xi_\alpha) f_{\alpha,\alpha}(\theta) \frac{e^{iK_\alpha R_\alpha}}{R_\alpha} + \sum_{\alpha' \neq \alpha} \Phi_{\alpha'}(\xi_\alpha) f_{\alpha',\alpha}(\theta) \frac{e^{iK_{\alpha'} R_\alpha}}{R_\alpha}\,, \tag{8}$$

$$\Psi^{(+)}_{\vec{K}_\alpha} \xrightarrow{R_\beta \gg} \sum_{\beta \neq \alpha} \Phi_\beta(\xi_\beta) f_{\beta,\alpha}(\theta) \frac{e^{iK_\beta R_\beta}}{R_\beta}\,. \tag{9}$$

The first line corresponds to the elastic and inelastic channels (hence the coordinate R_α), whereas the second line is for rearrangement (*i.e.* transfer) channels. The function $e^{iK_\alpha R_\alpha}/R_\alpha$ represents a spherical outgoing wave. The function multiplying this outgoing wave, $f_{\alpha,\alpha}(\theta)$, is the *scattering amplitude* for elastic scattering. Its argument, θ, is the CM scattering angle, and corresponds to the angle between the incident and final momenta (see fig. 2). Likewise, the coefficients $f_{\alpha',\alpha}$ and $f_{\beta,\alpha}$ correspond to the scattering amplitudes for inelastic and transfer channels, respectively. From the definition of flux given above, it turns out that (see *e.g.* chapt. 3, sect. G of [10])

$$\left(\frac{\mathrm{d}\sigma}{\mathrm{d}\Omega}\right)_{\alpha\to\beta} = \frac{v_\beta}{v_\alpha} \left|f_{\beta,\alpha}(\theta)\right|^2, \tag{10}$$

where v_α and v_β are initial and final asymptotic velocities.

It is customary to define the transition matrix (T-matrix):

$$\mathcal{T}_{\beta\alpha}(\theta) = -\frac{2\pi\hbar^2}{\mu_\beta} f_{\beta\alpha}(\theta), \tag{11}$$

in terms of which

$$\left(\frac{\mathrm{d}\sigma}{\mathrm{d}\Omega}\right)_{\alpha\to\beta} = \frac{\mu_\alpha \mu_\beta}{(2\pi\hbar^2)^2} \frac{K_\beta}{K_\alpha} \left|\mathcal{T}_{\beta\alpha}(\theta)\right|^2. \tag{12}$$

2˙3. *An integral equation for* $f_{\beta,\alpha}(\theta)$. – Consider that we are interested in a particular channel β. The scattering amplitude corresponding to this particular channel can be obtained from the asymptotic form of the total wavefunction, eq. (8), multiplying on the left by the "internal" wavefunction $\Phi^*_\beta(\xi_\beta)$ corresponding the channel of interest, and integrating over the coordinates ξ_β, *i.e.*,

$$\left(\Phi_\beta | \Psi^{(+)}_{\vec{K}_\alpha}\right) \xrightarrow{R \gg} \delta_{\beta,\alpha} e^{i\vec{K}_\alpha \cdot \vec{R}_\alpha} + f_{\beta,\alpha}(\theta) \frac{e^{iK_\beta R_\beta}}{R_\beta}\,, \tag{13}$$

([4]) Note that we distinguish between $\vec{R}_\alpha$ and $\vec{R}_\beta$ since, for a rearrangement process, the coordinates will be different. We will return to this issue later on.

where $(\ldots\rangle$ denotes integration over internal coordinates only. Thus, $(\Phi_\beta|\Psi^{(+)}_{\vec{K}_\alpha}\rangle$ remains a function of $\vec{R}_\beta$, so we may define $X_\beta(\vec{R}_\beta) \equiv (\Phi_\beta|\Psi^{(+)}_{\vec{K}_\alpha}\rangle$. If we know $\Psi^{(+)}_{\vec{K}_\alpha}$ or an approximation to it, we can extract the scattering amplitude from the asymptotics of $X_\beta(\vec{R}_\beta)$. Using this result, it is possible to obtain a formal expression for $f_{\beta,\alpha}(\theta)$. We start by writing the Schrödinger equation, using the form of the Hamiltonian appropriate for the channel β, that is,

$$H = \hat{T}_\beta + H_\beta(\xi_\beta) + V_\beta(\vec{R}_\beta, \xi_\beta). \tag{14}$$

Using this form of the Hamiltonian in the Schrödinger equation, eq. (3), multiplying on the left by $\Phi^*_\beta(\xi_\beta)$ and integrating over the coordinates ξ_β we get the *projected* equation

$$\left[\hat{T}_\beta + \varepsilon_\beta - E\right] X_\beta(\vec{R}_\beta) = -\left(\Phi_\beta|V_\beta|\Psi^{(+)}_{\vec{K}_\alpha}\right\rangle, \tag{15}$$

where we have used $\varepsilon_\beta = \langle\Phi_\beta(\xi_\beta)|H_\beta|\Phi_\beta(\xi_\beta)\rangle$ and the fact that the kinetic energy operator does not depend on the internal coordinates ξ_β. This is a second-order inhomogeneous differential equation for the function X_β. The most general solution is the sum of the solution of the corresponding homogeneous equation, plus a particular solution of the inhomogeneous equation. The homogeneous equation is trivially solved, since it contains only the kinetic energy operator; its solution is just a plane wave with momentum $\vec{K}_\beta$, with modulus $K_\beta = \sqrt{2\mu_\beta(E-\varepsilon_\beta)}/\hbar$. The particular solution of the inhomogeneous equation can be formally obtained using Green's functions techniques (see, for example, [11, 10]) leading to

$$X_\beta(\vec{R}_\beta) = e^{i\vec{K}_\alpha\cdot\vec{R}_\alpha}\delta_{\alpha,\beta} - \frac{\mu_\beta}{2\pi\hbar^2}\int G_\beta\left(\vec{R}_\beta, \vec{R}'_\beta\right)\left(\Phi_\beta|V_\beta\Psi^{(+)}_\alpha\right\rangle \mathrm{d}\vec{R}'_\beta, \tag{16}$$

where G_β is the Green's function in channel β. Explicitly

$$G_\beta\left(\vec{R}_\beta, \vec{R}'_\beta\right) = \frac{e^{iK_\beta|\vec{R}_\beta - \vec{R}'_\beta|}}{|\vec{R}_\beta - \vec{R}'_\beta|}\,. \tag{17}$$

To extract the scattering amplitude, we must take the asymptotic limit, $R_\beta \gg R'_\beta$. In this limit, the Green's function reduces to([5])

$$G_\beta\left(\vec{R}_\beta, \vec{R}'_\beta\right) \to \frac{e^{iK_\beta R_\beta}}{R_\beta} e^{-i\vec{K}_\beta\cdot\vec{R}'_\beta}\,, \tag{18}$$

and the function $X_\beta(\vec{R}_\beta)$ tends to

$$X_\beta(\vec{R}_\beta) \xrightarrow{R_\beta\gg} e^{i\vec{K}_\alpha\cdot\vec{R}_\alpha}\delta_{\alpha,\beta} - \frac{\mu_\beta}{2\pi\hbar^2}\frac{e^{iK_\beta R_\beta}}{R_\beta}\int e^{-i\vec{K}_\beta\cdot\vec{R}'_\beta}\left(\Phi_\beta|V_\beta\Psi^{(+)}_{\vec{K}_\alpha}\right\rangle \mathrm{d}\vec{R}'_\beta. \tag{19}$$

([5]) For $R_\beta \gg R'_\beta$, $|\vec{R}_\beta - \vec{R}'_\beta| \approx R_\beta - \hat{R}_\beta\cdot\vec{R}'_\beta = R_\beta - \hat{K}_\beta\cdot\vec{R}'_\beta$.

Comparing with the asymptotic form (8), and recalling the definition of the scattering amplitude, we have

$$f_{\beta,\alpha}(\theta) = -\frac{\mu_\beta}{2\pi\hbar^2}\left\langle e^{i\vec{K}_\beta\vec{R}_\beta}\Phi_\beta|V_\beta\Psi^{(+)}_{\vec{K}_\alpha}\right\rangle = -\frac{\mu_\beta}{2\pi\hbar^2}\iint e^{-i\vec{K}_\beta\vec{R}_\beta}\Phi^*_\beta(\xi_\beta)V_\beta\left(\vec{R}_\beta,\xi_\beta\right)\Psi^{(+)}_{\vec{K}_\alpha}\left(\vec{R}_\alpha,\xi_\alpha\right)\mathrm{d}\xi_\beta\,\mathrm{d}\vec{R}_\beta. \tag{20}$$

Or, in terms of the T-matrix,

$$\mathcal{T}_{\beta,\alpha} = \iint e^{-i\vec{K}_\beta\vec{R}_\beta}\Phi^*_\beta(\xi_\beta)V_\beta\left(\vec{R}_\beta,\xi_\beta\right)\Psi^{(+)}_{\vec{K}_\alpha}\left(\vec{R}_\alpha,\xi_\alpha\right)\mathrm{d}\xi_\beta\,\mathrm{d}\vec{R}_\beta. \tag{21}$$

2˙4. *Gell-Mann–Goldberger transformation (aka two-potential formula).* – A more general expression for eq. (21) can be obtained introducing an auxiliary (and by now arbitrary) potential $U_\beta(\vec{R}_\beta)$ on both sides of eq. (15),

$$\left[\hat{T}_\beta + U_\beta + \varepsilon_\beta - E\right]X_\beta(\vec{R}_\beta) = -\left(\Phi_\beta|V_\beta - U_\beta|\Psi^{(+)}_{\vec{K}_\alpha}\right). \tag{22}$$

The solution of (22) is given by a general solution of the homogeneous equation, plus a particular solution of the full equation. The homogeneous equation is given by

$$\left[\hat{T}_\beta + U_\beta + \varepsilon_\beta - E\right]\chi^{(+)}_\beta(\vec{R}_\beta) = 0. \tag{23}$$

This equation represents the scattering of the particles in channel β under the potential U_β. The solution is of the form

$$\chi^{(+)}_\beta(\vec{R}_\beta) = e^{i\vec{K}_\beta\cdot\vec{R}_\beta} + \text{outgoing spherical waves.} \tag{24}$$

In the next section, we shall discuss in more detail how this equation is solved in practical situations, making use of the partial wave expansion.

Finally, the full equation (22) is solved adding a particular solution of the inhomogeneous equation. This is done using again Green's functions techniques. Details are given in [9]. The full solution (which generalizes eq. (19)) is given by

$$X_\beta(\vec{R}_\beta) \equiv \left(\Phi_\beta|\Psi^{(+)}_{\vec{K}_\alpha}\right\rangle = \chi^{(+)}_\beta(\vec{R}_\beta)\delta_{\alpha\beta} + \int G^{(+)}_\beta\left(\vec{R}_\beta,\vec{R}'_\beta\right)\left(\Phi_\beta|V_\beta - U_\beta|\Psi^{(+)}_{\vec{K}_\alpha}\right\rangle\mathrm{d}\vec{R}'_\beta. \tag{25}$$

The scattering amplitude (or the T-matrix) is extracted from the asymptotics of the outgoing waves. But note that we have now outgoing waves in both terms of the RHS of the previous equation giving rise also to two contributions to the scattering amplitude,

$$\boxed{\mathcal{T}_{\beta,\alpha} = \mathcal{T}^{(0)}_{\beta,\alpha}\delta_{\alpha\beta} + \iint\chi^{(-)*}_\beta\left(\vec{K}_\beta,\vec{R}_\beta\right)\Phi^*_\beta(\xi_\beta)[V_\beta - U_\beta]\Psi^{(+)}_{\vec{K}_\alpha}\mathrm{d}\xi_\beta\mathrm{d}\vec{R}_\beta.} \tag{26}$$

The first term is the scattering amplitude due to the potential U_β and is present only for $\beta = \alpha$ (*i.e.* elastic scattering). The function $\chi^{(-)}_\beta$ is the time-reversed of $\chi^{(+)}$ and corresponds to the solution of a homogeneous equation consisting on a plane wave with momentum $\vec{K}_\beta$ and ingoing spherical waves. It can be readily obtained from $\chi^{(+)}$ using the relationship $\chi^{(-)*}(\vec{K}, \vec{R}) = \chi^{(+)}(-\vec{K}, \vec{R})$.

The result (26) is known as the *Gell-Mann–Goldberger transformation* or *two-potential formula*. This expression is exact but it cannot be solved as such, since it contains the exact wave function of the system. However, it provides a very useful starting point to derive approximate expressions, as we will see later on.

3. – Defining the modelspace

We have seen that the dynamics of the system in a scattering process is encoded in the full wave function, $\Psi^{(+)}$. Formally, it can be obtained by solving the Schrödinger equation of the system. In our time-independent approach, this wavefunction consists asymptotically on an incident plane, and outgoing spherical waves in all possible channels. Practical calculations require as a first step reducing the full space to a tractable modelspace. This is motivated by two facts: i) the channels of interest to analyze a particular experiment and ii) the numerical/computational complexity of the problem. For example, if we are interested in analyzing some inelastic scattering experiment, our model space might consist in the ground state of the projectile and target, plus the excited states more strongly populated in the experiment.

A formal procedure to reduce the problem from the full space to a selected modelspace was developed by Feshbach [12, 13]. The idea is to separate the full space into two parts, denoted respectively as P and Q. The P space comprises the channels of interest and will therefore be taken into account explicitly in the model wave function $\Psi^{(+)}$. The Q space is composed of the remaining channels. So, following Feshbach (see also [9] and [10], chapt. 8G), we may write $\Psi^{(+)} = \Psi_P + \Psi_Q$. The components Ψ_P and Ψ_Q obey a system coupled equations, with the deceptively simple form

$$(E - H_{PP})\Psi_P = H_{PQ}\Psi_Q, \tag{27}$$

$$(E - H_{QQ})\Psi_Q = H_{QP}\Psi_P, \tag{28}$$

where $H_{PP} = PHP$, $H_{PQ} = PHQ$, and so on. The projected Hamiltonian H_{PP} contains the coupling among the states of the P space, and likewise for H_{QQ}. The terms H_{PQ} and H_{QP} describe couplings between the states of P and those of Q. Since we are interested only in Ψ_P, we eliminate Ψ_Q from the RHS of the first equation, using the second equation([6])

$$\left[E - H_{PP} - H_{PQ}\frac{1}{E - H_{QQ} + i\epsilon}H_{QP}\right]\Psi_P = 0. \tag{29}$$

([6]) The $i\epsilon$ guarantees the outgoing boundary condition. The limit $\epsilon \to 0$ is understood in these expressions.

This equation can be also written as

$$[E - H_\alpha - T_\alpha - \mathcal{V}]\,\Psi_P = 0, \tag{30}$$

with

$$\mathcal{V} = V_{PP} + V_{PQ}\frac{1}{E - H_{QQ} + i\epsilon}V_{QP}. \tag{31}$$

The first term of the RHS (V_{PP}) is the potential operator acting only among the states of the P space, and the second term describes the coupling with the omitted (Q) states. This term is found to be complex, energy-dependent and non-local. Because of the presence of the Q operator, it involves the coupling to all the possible channels and so it cannot be exactly evaluated in practice. Yet, this formal solution provides a useful guidance on how to replace such a complicated object by a more manageable one. Direct reaction theories replace (30) by an approximated one of the form

$$(E - H_{\text{eff}})\Psi_{\text{model}} = 0. \tag{32}$$

where H_{eff} is an effective Hamiltonian which contains an approximation of the complicated object $\mathcal{V}$, usually involving some phenomenological forms.

4. – Single-channel scattering: the optical model

The simplest approximation to the P space is to reduce the physical space to just the ground states of the projectile and target. This gives rise to the optical model formalism. In this case, the effective Hamiltonian acquires the form

$$H_{\text{eff}} = H_\alpha + U_\alpha(\vec{R}), \tag{33}$$

where $U_\alpha(\vec{R})$ is meant to represent the effective potential (31) when P is reduced to the projectile and target ground states. Note that this potential does not contain any explicit dependence on the internal degrees of freedom ξ. Thanks to that, the total wave function of the system can be written in the factorized form([7])

$$\Psi^{(+)}_{\text{model}}(\xi, \vec{R}) = \Phi_0(\xi)\chi^{(+)}_0(\vec{R}). \tag{34}$$

Using the fact that, by construction, $H_\alpha\Phi_0(\xi) = \varepsilon_0\Phi_0(\xi)$, replacement of the previous equation on the Schrödinger (32) gives

$$\left[T_\alpha + U_\alpha(\vec{R}) - E_0\right]\chi^{(+)}_0(\vec{R}) = 0, \tag{35}$$

where $E_0 = E - \varepsilon_0$, *i.e.*, the kinetic energy associated with the relative motion between the projectile and target.

([7]) The subscript α is omitted here when implicitly understood.

If the effective Hamiltonian, $H_{\rm eff}$, is to represent the complicated Feshbach operator, describing not only the interaction in the P space, but also the couplings between the P and Q spaces (all non-elastic channels in this case), then the effective interaction $U_\alpha(\vec{R}\,)$ will be complex, non-local and energy-dependent. The imaginary part accounts for the flux leaving the elastic channel (P space) to the channels not explicitly included (the Q space). The energy dependence is usually taken into account phenomenologically, by parametrizing U with some suitable form and adjusting the parameters to the experimental data over some energy region. Finally, non-locality is rarely taken into account, or it is simply taken into account approximately, by including its effect in the effective local potential [14]. Recently, however, this topic has received renewed attention [15-17]. The effective interaction U_α is referred to as *optical potential*.

4˙1. *Partial wave expansion.* – As an additional simplification, we consider the case in which the spins of the colliding particles are ignored and the optical potential is assumed to be a function only of the projectile-target separation, $R = |\vec{R}|$. In this case, the wave function can be expanded in Legendre polynomials as

$$\chi_0^{(+)}(\vec{K},\vec{R}\,) = \frac{1}{KR}\sum_\ell i^\ell(2\ell+1)\chi_\ell(K,R)P_\ell(\cos\theta), \tag{36}$$

where the constant factors are introduced for convenience. The radial functions $\chi_\ell(K,R)$ are a solution of

$$\left[-\frac{\hbar^2}{2\mu}\frac{\mathrm{d}^2}{\mathrm{d}R^2}+\frac{\hbar^2}{2\mu}\frac{\ell(\ell+1)}{R^2}+U(R)-E_0\right]\chi_\ell(K,R)=0. \tag{37}$$

In the case of $U_\alpha = 0$, the solution $\chi_0^{(+)}(\vec{K},\vec{R}\,)$ must reduce to a plane wave, whose partial wave expansion is known

$$e^{i\vec{K}\cdot\vec{R}} = \frac{4\pi}{KR}\sum_{\ell,m} i^\ell F_\ell(KR)Y_{\ell m}(\hat{R})Y^*_{\ell m}(\hat{K}) = \frac{1}{KR}\sum_\ell i^\ell(2\ell+1)F_\ell(KR)P_\ell(\cos\theta), \tag{38}$$

where $F_\ell(KR) = (KR)j_\ell(K,R)$ with $j_\ell(K,R)$ a spherical Bessel function. Comparing this expression with (36), we see that, in the $U_\alpha = 0$ case, $\chi_\ell(K,R) \to F_\ell(KR)$.

For non-zero potential, we can still say that $\chi_0^{(+)}(\vec{K},\vec{R}\,)$ must verify the following equation at large distances,

$$\left[-\frac{\hbar^2}{2\mu}\frac{\mathrm{d}^2}{\mathrm{d}R^2}+\frac{\hbar^2}{2\mu}\frac{\ell(\ell+1)}{R^2}-E_0\right]\chi_\ell(K,R)=0 \quad \text{(for large } R\text{)}, \tag{39}$$

whose most general solution is a combination of two independent solutions for this equation. One of them can be taken as the regular solution $F_\ell(KR)$. The other can be the irregular solution,

$$G_\ell(KR) = -(KR)n_\ell(KR) \tag{40}$$

or any combination of G and F, that is

$$\chi_\ell(K,R) \xrightarrow{R\gg} AF_\ell(KR) + BG_\ell(KR). \tag{41}$$

The combination appropriate for our purposes is suggested by the known asymptotic behavior of our physical scattering wavefunction, *i.e.*

$$\chi_0^{(+)}(\vec{K},\vec{R}\,) \xrightarrow{R\gg} e^{i\vec{K}\cdot\vec{R}} + f(\theta)\frac{e^{iKR}}{R}\,. \tag{42}$$

The exponential part of the outgoing wave, e^{iKR}, turns out to be just a definite combination of the F and G functions, because

$$G_\ell(\rho) + iF_\ell(\rho) \equiv H_\ell^{(+)}(\rho) \to e^{i(\rho-\ell\pi/2)}. \tag{43}$$

So, returning to the partial wave expansion, the appropriate boundary condition consistent with the behavior (42) is given by

$$\chi_\ell(K,R) \to F_\ell(KR) + T_\ell H_\ell^{(+)}(KR), \tag{44}$$

where the coefficients T_ℓ are to be determined by numerical integration of the differential equation. It is usual to write T_ℓ in terms of the so-called *phase shifts*

$$T_\ell = e^{i\delta_\ell}\sin(\delta_\ell) \tag{45}$$

or, in terms of the *reflection coefficient*, S_ℓ, or *S-matrix*([8])

$$S_\ell = 1 + 2iT_\ell = e^{2i\delta_\ell}. \tag{46}$$

The condition (44) can be also written as

$$\chi_\ell(K,R) \to \frac{i}{2}\Big[H_\ell^{(-)}(KR) - S_\ell H_\ell^{(+)}(KR)\Big], \tag{47}$$

where

$$H_\ell^{(-)}(\rho) = G_\ell(\rho) - iF_\ell(\rho) \to e^{-i(\rho-\ell\pi/2)}. \tag{48}$$

The S-matrix S_ℓ is therefore the coefficient of the outgoing wave ($H_\ell^{(+)}$) for the partial wave ℓ. It reflects the effect of the potential on this particular wave in the

([8]) When these expressions are generalized to the multiple-channel case, the quantity S_ℓ becomes a matrix and is referred to as *scattering or collision matrix* (the name is also used in single-channel case, but the terminology is less obvious).

sense that,

- If no potential is present, there is no outgoing wave. Then, $T_\ell = 0$ or, equivalently, $S_\ell = 1$ and $\delta_\ell = 0$.
- As a consequence of the previous result, for large values of ℓ the centrifugal barrier keeps the projectile well apart from the target, and thus the effect of the (short-ranged) potential U_α will be negligible. Consequently, for $\ell \to \infty \Rightarrow S_\ell \to 1$.
- If the scattering potential is real, the overall outgoing flux for a given partial wave must be conserved, and hence $|S_\ell| = 1$.
- On the other hand, for a complex potential (with negative imaginary part), we have $|S_\ell| < 1$, which reflects the fact that part of the incident flux has left the elastic channel in favor of other channels.

In the accompanying box, we give some basic guidelines on how the wave functions and phase shifts are actually computed (single-channel case).

Numerical calculation of the scattering wave function and phase shifts

For a single-channel case, the wave functions and phase shifts can be computed as follows:

1) Integrate the radial differential equation from the origin outwards, with the initial value $\chi_\ell(K, 0) = 0$ and some finite (arbitrary) slope.
2) At a sufficiently large distance, $R_{\max}$, beyond which the nuclear potentials have become negligible, the numerically obtained solution is matched to the asymptotic form

$$N\chi_\ell(K, R_{\max}) \to F_\ell(\eta, KR_{\max}) + T_\ell H_\ell^{(+)}(\eta, KR_{\max}).$$

3) This equation contains two unknowns, T_ℓ and the normalization N. Thus, it is supplemented with the condition of continuity of the derivative

$$N\chi'_\ell(K, R_{\max}) \to F'_\ell(\eta, KR_{\max}) + T_\ell (H_\ell^{(+)}(\eta, KR_{\max}))'.$$

   From these two conditions, one obtains the T-matrix (or, equivalently, the S-matrix) and the phase shifts.

4) The procedure is repeated for each ℓ, from $\ell = 0$ to $\ell_{\max}$, such that $S_{\ell_{\max}} \approx 1$.

4˙2. *Scattering amplitude.* – To get the scattering amplitude, we substitute the asymptotic radial function $\chi_\ell(K,R)$ from (47) into the full expansion (36):

$$\chi_0^{(+)}(\vec{K},\vec{R}) \to \frac{1}{KR}\sum_\ell i^\ell(2\ell+1)\left\{F_\ell(KR)+T_\ell H_\ell^{(+)}(KR)\right\}P_\ell(\cos\theta) = \tag{49}$$

$$\frac{1}{KR}\sum_\ell i^\ell(2\ell+1)F_\ell(KR)P_\ell(\cos\theta)$$

$$+\frac{1}{K}\sum_\ell i^\ell(2\ell+1)T_\ell\frac{e^{i(KR-\ell\pi/2)}}{R}P_\ell(\cos\theta) =$$

$$e^{i\vec{K}\cdot\vec{R}}+\frac{1}{K}\sum_\ell(2\ell+1)e^{i\delta_\ell}\sin\delta_\ell P_\ell(\cos\theta)\frac{e^{iKR}}{R}\,.$$

The elastic scattering amplitude is the coefficient of e^{iKR}/R in the last line, *i.e.*,

$$f(\theta)=\frac{1}{K}\sum_\ell(2\ell+1)e^{i\delta_\ell}\sin\delta_\ell P_\ell(\cos\theta)=\frac{1}{2iK}\sum_\ell(2\ell+1)(S_\ell-1)P_\ell(\cos\theta). \tag{50}$$

The differential elastic cross section will be given by

$$\frac{\mathrm{d}\sigma}{\mathrm{d}\Omega}=|f(\theta)|^2. \tag{51}$$

In principle, the sum in (50) runs from $\ell=0$ to infinity. However, remember that, for large values of ℓ, the S-matrix tends to 1 so, in practice, the sum can be safely truncated at a maximum value $\ell_{\max}$, determined by some convergence criterion of the cross section.

4˙3. *Coulomb case.* – The Coulomb case deserves a special consideration because the expressions derived in the previous section are strictly applicable to the case of short-range potentials, for which the asymptotic form (42) is appropriate. For a pure Coulomb case, we can perform a partial wave expansion of the scattering wavefunction $\chi_C(\vec{K},\vec{R})$ of the form

$$\chi_C(\vec{K},\vec{R})=\frac{1}{KR}\sum_\ell(2\ell+1)i^\ell\chi_\ell^C(KR)P_\ell(\cos(\theta)), \tag{52}$$

with the radial functions $\chi_\ell^C(KR)$ obeying the equation

$$\left[\frac{\mathrm{d}^2}{\mathrm{d}R^2}+K^2-\frac{2\eta K}{R}+\frac{\ell(\ell+1)}{R^2}\right]\chi_\ell^C(KR)=0, \tag{53}$$

where

$$\eta=\frac{Z_pZ_te^2}{\hbar v}=\frac{Z_pZ_te^2\mu}{\hbar^2K} \tag{54}$$

is the so-called Coulomb or *Sommerfeld parameter.*

The solution of (53) must be regular at the origin. Asymptotically, it behaves as

$$\chi_\ell^C(KR) \xrightarrow{R\gg} e^{i\sigma_\ell} F_\ell(\eta, KR), \tag{55}$$

where $F_\ell(\eta, KR)$ is the regular Coulomb function and σ_ℓ is the Coulomb phase shift for a partial wave ℓ,

$$\sigma_\ell = \arg\Gamma(\ell + 1 + i\eta). \tag{56}$$

The Coulomb function behaves asymptotically as [18]

$$F_\ell(\eta, \rho) \to \sin(\rho - \eta\ln(2\rho) - \ell\pi/2 + \sigma_\ell), \tag{57}$$

which in the case $\eta = 0$ ($\sigma_\ell = 0$) reduces to the regular function $F_\ell(KR)$ introduced in the case of short-range potentials

$$F_\ell(\eta = 0, \rho) = F_\ell(\rho) = \rho j_\ell(\rho). \tag{58}$$

Analogously, an irregular solution of (53) can be found, which reduces to $G_\ell(\rho)$ in the no Coulomb case

$$G_\ell(\eta, \rho) \to \cos(\rho - \eta\ln(2\rho) - \ell\pi/2 + \sigma_\ell) \xrightarrow{\eta=0} G_\ell(\rho) = -\rho n_\ell(\rho), \tag{59}$$

as well as the ingoing and outgoing functions,

$$H_\ell^{(+)}(\eta, \rho) = G_\ell(\eta, \rho) + iF_\ell(\eta, \rho), \tag{60}$$

$$H_\ell^{(-)}(\eta, \rho) = G_\ell(\eta, \rho) - iF_\ell(\eta, \rho). \tag{61}$$

For the pure Coulomb case, the scattering amplitude will be given by

$$f_C(\theta) = \frac{1}{2K}\sum_\ell (2\ell + 1)(e^{2i\sigma_\ell} - 1)P_\ell(\cos\theta). \tag{62}$$

This integral is not convergent (cannot be truncated at a finite ℓ) but the full result is known analytically and is given by

$$f_C(\theta) = -\frac{\eta}{2K\sin^2(\frac{1}{2}\theta)} e^{-i\eta\ln(\sin^2(\frac{1}{2}\theta) + 2i\sigma_0)}. \tag{63}$$

The differential cross section yields the well-known Rutherford formula

$$\frac{\mathrm{d}\sigma_R}{\mathrm{d}\Omega} = |f_C(\theta)|^2 = \frac{\eta^2}{4K^2\sin^4(\frac{1}{2}\theta)} = \left(\frac{Z_p Z_t e^2}{4E}\right)^2 \frac{1}{\sin^4(\frac{1}{2}\theta)}\,. \tag{64}$$

4˙4. *Coulomb plus nuclear case.* – If both Coulomb and nuclear potentials are present, the scattering function $\chi_0^{(+)}(\vec{K},\vec{R}\,)$ will never reach the asymptotic form of a plane wave plus outgoing waves, due to the presence of the $1/R$ term in the Schrödinger equation. Nevertheless, it can be written as

$$\chi_0^{(+)}(\vec{K},\vec{R}\,) \to \chi_C^{(+)}(\vec{K},\vec{R}\,) + \text{outgoing spherical waves}, \tag{65}$$

where the *outgoing waves* are now proportional to the functions $H_\ell^{(+)}(\eta, KR)$. Of course, when only the Coulomb potential is present, this term vanishes, and the scattering wave function reduces to $\chi_C^{(+)}(\vec{K},\vec{R}\,)$.

If we write, as usual, the $\chi_0^{(+)}(\vec{K},\vec{R}\,)$ function as a partial wave expansion, the corresponding radial coefficients $\chi_\ell(K,R)$ verify the asymptotic condition

$$\begin{aligned}\chi_\ell(K,R) \to e^{i\sigma_\ell}\left[F_\ell(\eta,KR) + T_\ell H_\ell^{(+)}(\eta,KR)\right] = \\ e^{i\sigma_\ell}\frac{i}{2}\left[H_\ell^{(-)}(\eta,KR) - S_\ell H_\ell^{(+)}(\eta,KR)\right],\end{aligned} \tag{66}$$

which is very similar to (44) and (47), except for the additional Coulomb phase $e^{i\sigma_\ell}$ and the replacement of the functions $F(KR)$, $H^{(+)}$, etc. by their Coulomb generalizations.

The scattering amplitude results

$$f(\theta) = f_C(\theta) + \frac{1}{2iK}\sum_\ell (2\ell+1)e^{2i\sigma_\ell}(S_\ell - 1)P_\ell(\cos\theta), \tag{67}$$

where the first term corresponds to the pure-Coulomb amplitude, which arises from the outgoing waves in the first term of (65) and the second term is the so-called Coulomb modified nuclear amplitude.

4˙5. *Parametrization of the phenomenological optical potential.* – The effective optical optical potential is usually taken as the sum of Coulomb and nuclear central potentials $U(R) = U_C(R) + U_N(R)$, with the Coulomb part taken as the potential corresponding to a uniform distribution of charge of radius R_c

$$U_C(R) = \begin{cases} \dfrac{Z_p Z_t e^2}{2R_c}\left(3 - \dfrac{R^2}{R_c^2}\right), & \text{if } R \le R_c, \\ \dfrac{Z_p Z_t e^2}{R}, & \text{if } R \ge R_c. \end{cases} \tag{68}$$

As for the nuclear part, it contains in general real and imaginary parts. The most popular parametrization is the so-called Woods-Saxon form

$$U_N(R) = V(R) + iW(R) = -\frac{V_0}{1+\exp(\frac{R-R_0}{a_0})} - i\,\frac{W_0}{1+\exp(\frac{R-R_i}{a_i})}\,. \tag{69}$$

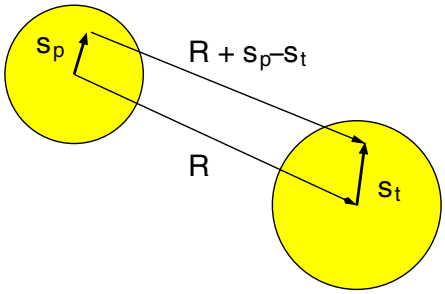

Fig. 3. – Relevant coordinates for nucleus-nucleus folding model calculations.

The parameters V_0, R_0 and a_0 are the depth, radius and diffuseness (likewise for the imaginary part). They are usually determined from the analysis of elastic scattering data so, strictly, this potential might account also for $\lambda > 0$ Coulomb multipoles. The radius R_x is sometimes parametrized using the projectile (A_p) and target (A_t) mass numbers introducing the so-called reduced radius, $R_x = r_x(A_p^{1/3} + A_t^{1/3})$. For ordinary nuclei $r_x \approx 1.1$–$1.3\,\mathrm{fm}$.

If the spin of the projectile (or target) is considered, the potential will contain also spin-dependent terms. The most common one is the spin-orbit term, which is usually parametrized as

$$U_{so}(R) = (V_{so} + iW_{so}) \left(\frac{\hbar}{m_\pi c}\right)^2 \frac{1}{R} \frac{\mathrm{d}f(R, R_{so}, a_{so})}{\mathrm{d}R} (2\ell \cdot \mathbf{s}), \tag{70}$$

where the radial function $f(R, R_{so}, a_{so})$ is again a Woods-Saxon form, and $(\hbar/m_\pi c)^2 = 2\,\mathrm{fm}^2$, is just introduced in order U_{so} has dimensions of energy.

4·6. *Microscopic optical potentials.* – The optical potential or, at least, part of it, can be also calculated microscopically, starting from some effective nucleon-nucleon (NN) interaction. For example, the bare potential can be computed microscopically, by means of a folding procedure in which an effective nucleon-nucleon interaction (JLM, M3Y, etc.) is convoluted with the projectile and target densities (see fig. 3).

$$V_{\mathrm{fold}}(\vec{R}\,) = \int \rho_p(s_p)\rho_t(s_t) v_{NN}\left(\left|\vec{R} + \vec{s}_p - \vec{s}_t\right|\right) \mathrm{d}\vec{s}_p \mathrm{d}\vec{s}_t, \tag{71}$$

where $\rho_p(s_p)$ and $\rho_t(s_t)$ are the projectile and target densities, respectively. Since the latter are g.s. densities, $V_{\mathrm{fold}}(\vec{R}\,)$ accounts only for the bare potential V_{PP} (P-space part) and ignores the effect of non-elastic channels. The remaining part of the effective potential (second term in eq. (31)) must be supplied, using some phenomenological or microscopic prescription.

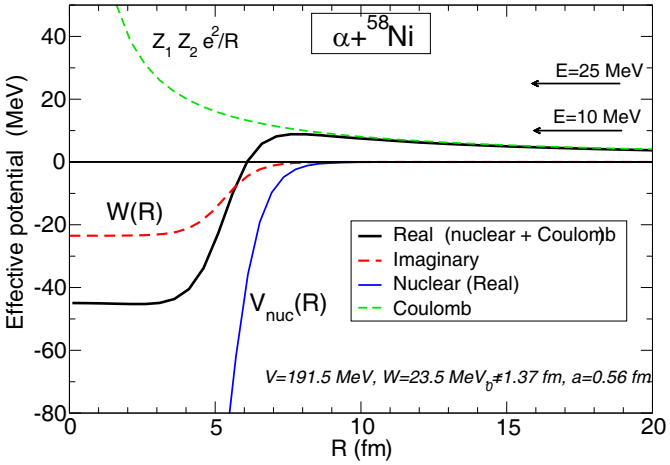

Fig. 4. – Effective potential for a $^{4}\mathrm{He} + {}^{58}\mathrm{Ni}$ system. The labels R_b and V_b indicate the distance and top of the Coulomb barrier.

5. – Elastic scattering phenomenology

5˙1. *Elastic scattering in the presence of strong absorption.* – When the projectile and target nuclei are composite systems, the scattering is largely dominated by the absorptive part of the nucleus-nucleus potential. This means that the effects of the coupling to nonelastic channels is dominant. Absorption introduces quantal effects, such as diffraction, which are analogous to those observed in optical phenomena. Heavy-ion collisions are also characterized by large angular momenta and small de Broglie wavelengths associated to the relative motion, in comparison with the dimensions of the nuclei. In this situation, the projectile-target motion can be interpreted in terms of classical trajectories, which is a useful concept to assist our intuition.

Resorting to this idea of classical trajectories, an important concept in strong-absorption scattering is that of grazing collision, which refers to those trajectories for which the colliding nuclei begin to experience the strong nuclear interaction. Associated to this, one may introduce also the concepts of grazing angle, θ_{gr} (the scattering angle for a grazing collision) and grazing angular momentum ℓ_{gr}. Trajectories with angular momentum $\ell < \ell_{\mathrm{gr}}$ will be strongly absorbed and the corresponding elastic scattering cross section will be largely suppressed.

The specific features of a given reaction in the presence of strong absorption are largely determined by the grazing angular momentum ℓ_{gr} and the Sommerfeld parameter (η). In particular, for large values of ℓ_{gr}, where many partial waves are involved, one observes characteristic diffraction patterns analogous to the Fresnel and Fraunhofer patterns encountered in optics.

Recalling the definition of the Sommerfeld parameter, it can be regarded as a measurement of the energy of the system relative to the Coulomb barrier. The latter is

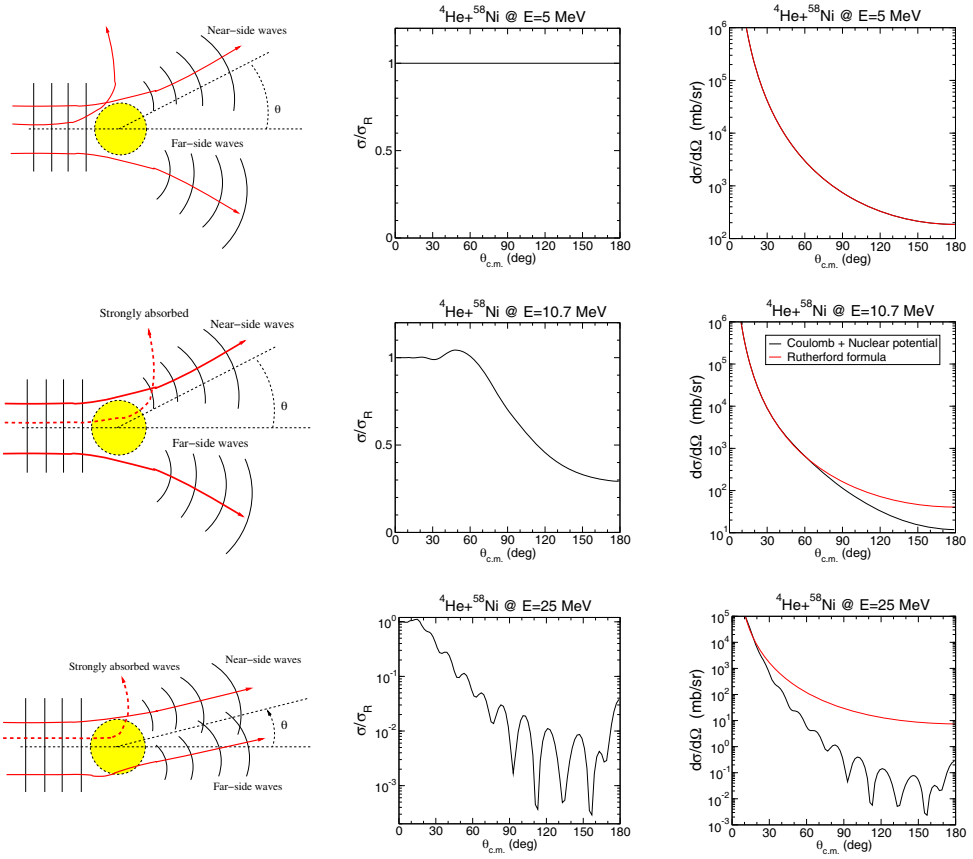

Fig. 5. – Three characteristic regimes encountered in reactions dominated by strong absorption, illustrated for the reaction $^4\mathrm{He} + {}^{58}\mathrm{Ni}$ at $E = 5\,\mathrm{MeV}$ (top panels), 10.7 MeV (middle) and 25 MeV (bottom). On the left panels, a pictorial representation in terms of classical trajectories. Dashed trajectories get inside the nuclear range and are likely to be absorbed (*i.e.* leave the elastic channel).

defined as the top of the real (nuclear+Coulomb) potential. This is exemplified in fig. 4 for the $^4\mathrm{He} + {}^{58}\mathrm{Ni}$ system, whose Coulomb barrier is about 10 MeV.

Depending on the values of η and $\ell_{\rm gr}$, we may distinguish three distinct regimes:

– *Rutherford scattering:* When the CM energy is well below the Coulomb barrier, the colliding partners feel only the Coulomb interaction. In absence of strong $\lambda > 0$ Coulomb couplings, the projectile-target motion is dictated by the monopole term $Z_p Z_t e^2/R$, and the differential cross sections follow the Rutherford formula. These situations are characterized by large Sommerfeld parameters ($\eta \ggg 1$). In terms of classical trajectories (see LHS of the first row of fig. 5), the repulsive Coulomb interaction acts as a diverging lens, preventing the trajectories from entering into the inner region (dominated by the nuclear interaction).

– *Fraunhofer scattering:* A very different scenario occurs when the incident energy is much higher than the Coulomb barrier. The nuclear potential gains importance with respect to the Coulomb potential ($\eta \lesssim 1$) which affects in two ways. First, due to its attractive character, far-side orbits (orbits scattered on the opposite side with respect the incoming projectile) are deflected inward and are allowed to interfere with *near-side* trajectories scattered at the same angle (see bottom panels of fig. 5). This produces a characteristic oscillatory pattern in the angular distribution, with maxima and minima corresponding to the constructive and destructive interference. Second, due to absorption, some of the trajectories entering into the range of the nuclear potential will be absorbed (*i.e.* will be removed from the elastic channel due to non-elastic processes). This produces an overall reduction of the elastic cross section with respect to the Rutherford formula.

– *Fresnel scattering:* Fresnel scattering takes place at incident energies slightly above the top of the Coulomb barrier and so it can be considered an intermediate situation between Rutherford and Fraunhofer scattering. Distant trajectories (as the one labeled as 1 in the middle panel of fig. 5) are scattered by the Coulomb potential and hence undergo pure Rutherford scattering. However, closer trajectories experience grazing collisions with the target. Some of them, like the one labeled as 2, can be scattered at the same scattering angle as some more distant Coulomb trajectories. These accumulation of trajectories entering within a narrow range of impact parameters and exiting at about the same scattering angle are responsible for the prominent peak observed in the middle panel, and characteristic of Fresnel scattering. These grazing trajectories divide the angular range into two regions, usually called "illuminated" and "shadow" regions. The former, corresponding to trajectories more distant than the grazing ones, do not feel the nuclear potential and hence do not experience absorption. Conversely, trajectories entering with impact parameters smaller than the grazing ones will experience strong absorption. These are the trajectories with larger deflections and, hence, for scattering angles larger than the grazing ones, a drastic reduction of the elastic cross section is found, as seen in the middle panel in the second row of fig. 5.

The three scenarios described in this section (Rutherford, Fresnel and Fraunhofer) are typical of ordinary, tighly bound nuclei. In the following sections, we will see how these features are modified in the case of weakly bound nuclei.

5˙2. *Elastic scattering of weakly bound nuclei.* – We have stressed that the elastic scattering is affected by the coupling with non-elastic channels (inelastic, transfer, breakup, fusion, ...). The relative importance of these channels will depend on the participant nuclei as well as on the energy regime. In the case of weakly bound projectiles, which is the core topic of this contribution, we have to pay particular attention to the role of the breakup channels since the weak binding usually translates into a large dissociation probability. What modifications should we expect in the optical potential, as compared to *normal* nuclei?

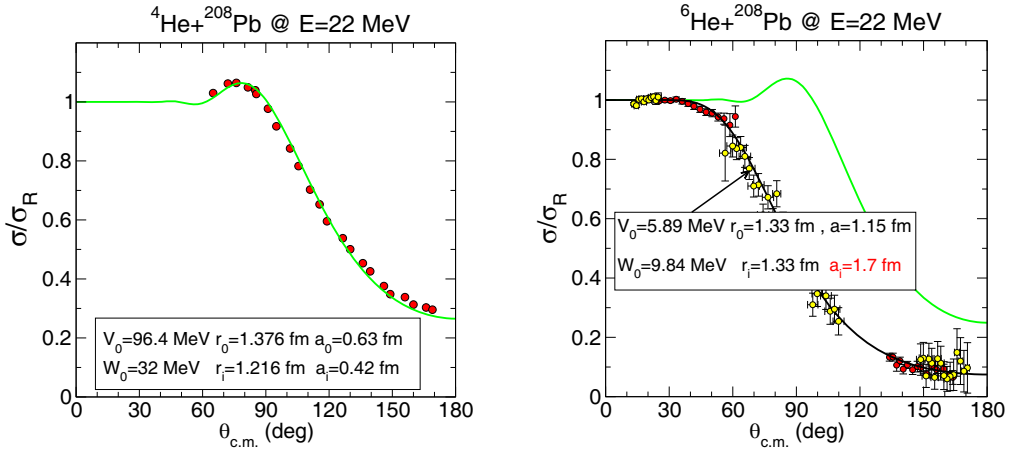

Fig. 6. – Elastic scattering of ^{4,6}He + ^{208}Pb at $E_{\rm lab} = 22\,$MeV. The ^{4}He and ^{6}He data are, respectively, from refs. [19] and [4, 20].

Let us consider as examples the ^{4,6}He + ^{208}Pb reactions at $E_{\rm lab} = 22\,$MeV (see fig. 6). In the ^{4}He case, the measured differential cross section shows a typical Fresnel pattern, with a maximum around the grazing angle and a rapid decrease at larger angles. The ^{6}He case is markedly different. The cross section is largely suppressed with respect to the Rutherford formula and the Fresnel peak is completely absent. The reduction with respect to the Rutherford cross section starts at relatively small angles which, classically, correspond to large impact parameters (*i.e.* distant trajectories). This suggests the existence of a long-range non-elastic mechanism, which removes a significant part of the flux from the elastic channel. Since ^{6}He is bound by only $\sim 1\,$MeV, a natural candidate is of course the breakup of the projectile but, other mechanisms, such as neutron transfer, can contribute as well. These features can be also seen in the optical model potentials describing these data. The curves shown in fig. 6 are optical model calculations using phenomenological WS forms (eq. (69)). In the case of the ^{4}He projectile, the radius and diffuseness parameters of the real and imaginary parts follow closely the densities of normal, well-bound nuclei ($a \sim 0.56\,$fm). If this potential is used for the ^{6}He + ^{208}Pb case (scaling the radii according to the mass number of A or, equivalently, using the same reduced radii), we get the green line of the right panel in which, as can be seen, the Fresnel behaviour persists, in clear disagreement with the data. If the potential parameters are varied to reproduce the data (keeping the radii $r_0 = r_i = 1.33\,$fm to reduce the number of free parameters) one obtains the values listed in the figure, and the corresponding differential cross section (black solid line). Its more salient feature is the large value of the real and imaginary diffuseness parameters ($a_i > 1\,$fm). This is a clear indication of the influence of the non-elastic channels (possibly transfer and breakup) which, in the Feshbach formalism, would be embedded in the polarization potential (cf. eq. (31)).

Understanding and disentangling the nature of these non-elastic channels requires going beyond the optical model. This can be done, for example, using approximate

forms of the polarization potential or within the coupled-channels method, described below.

5˙3. *Coulomb dipole polarization potentials.* – The effect of Coulomb dipole polarizability (CDP) on the elastic scattering can be included by means of a polarization potential. From physical arguments, we may expect this potential to be complex, and its real and imaginary parts can be understood as follows:

1) The strong Coulomb field will produce a polarization ("stretching") of the projectile, giving rise to a dipole contribution on the *real* potential.

2) The weakly bound nucleus can eventually break up, leading to a loss of flux of the elastic channel, which corresponds to the imaginary part of the polarization potential.

The CDP acquires a particularly simple form in the so-called adiabatic limit, in which one assumes that the excitation energies are high enough so the characteristic time for a transition to a state n ($\tau_{\rm ex} \approx \hbar/(\varepsilon_n - \varepsilon_0)$) is small compared to the characteristic time for the collision ($\tau_{\rm coll} \approx a_0/v$, where a_0 is the distance of closest approach in a head-on collision and v is the projectile velocity). Applying second-order perturbation theory, one gets the following expression for this adiabatic dipole polarization potential [21]:

$$V_{\rm ad}(R) = -\sum_{n=1} \frac{|\langle n|V_{\rm dip}|0\rangle|^2}{\varepsilon_n - \varepsilon_0} = -\alpha \frac{(Z_t e)^2}{R^4}\,, \tag{72}$$

where α is the *dipole polarizability parameter*, defined as

$$\alpha = \frac{8\pi}{9} \frac{B(E1; gs \to n)}{\varepsilon_n - \varepsilon_0}\,,$$

with $B(E1; gs \to n)$ the dipole strength for the coupling to the dipole excited state $|n\rangle$.

We see that the adiabatic polarization potential is purely real and does not depend on the collision energy. When the average excitation energies are small, as it is the case of weakly bound nuclei (such as halo nuclei), the adiabatic approximation is questionable. A expression for a non-adiabatic CDP will be presented in sect. **8** in the context of the semiclassical theory of Alder and Winther.

6. – Inelastic scattering: the coupled-channels method

Nuclei are not inert or *frozen* objects; they do have an internal structure of protons and neutrons that can be modified (excited), for example, in collisions with other nuclei. In fact, an important and common process that may occur in a collision between two nuclei is the excitation of one (or both) of the nuclei. Inelastic scattering is an example of *direct reaction* and, as such, the colliding nuclei preserve their identity after the collision.

The energy required to excite a nucleus is *taken* from the kinetic energy of the projectile-target relative motion. This means that, if one of the colliding nuclei is excited,

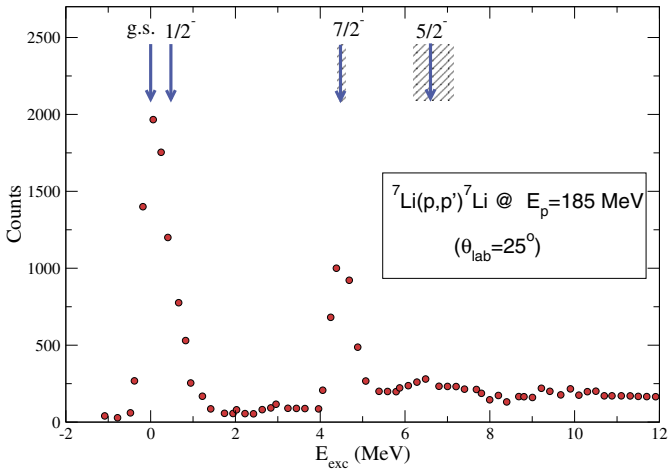

Fig. 7. – Energy spectrum of detected outgoing protons of 185 MeV scattered from a ^{7}Li target. The vertical arrows indicate the position of the ^{7}Li bound states and two lowest resonances. Experimental data are from ref. [22].

the final kinetic energy of the system is reduced by an amount equal to the excitation energy of the excited state populated in the reaction. So, by measuring the kinetic energy of the outgoing fragments, one can infer the excitation energy of the projectile and target. This has been indeed a common technique to measure and identify such excited states.

As an example, let us consider the scattering of a proton beam off a ^{7}Li target. Figure 7 shows the experimental excitation energy spectrum inferred from the energy of the outgoing protons detected at an scattering angle of 25°, for a proton incident energy of 185 MeV [22]. We have superimposed the position of the low-lying levels of ^{7}Li to highlight the correspondence between the observed peaks and these states. The peak at $E_x = 0$ (corresponding to $Q = 0$) corresponds to the ^{7}Li ground state. Thus, it is just elastic scattering. At $E_x = 0.48$ MeV, we should see a second peak corresponding to the first excited state of ^{7}Li. However, due to the energy resolution, this peak is not resolved in these data from the elastic peak. At $E_x = 4.6$ MeV there is a prominent peak corresponding to a $7/2^-$ state in ^{7}Li. This state is above the $^4\mathrm{He} + {}^3\mathrm{H}$ threshold placed at 2.47 MeV and does actually correspond to a continuum resonance. This threshold corresponds to the energy necessary to dissociate the ^{7}Li nucleus into $\alpha + t$. Therefore, for excitation energies above this value, we have a continuum of accessible energies, rather than a discrete spectrum, and any value of E_x is possible. This explains the *background* observed at these excitation energies.

Note that the information provided by these data is not enough to determine other properties of the energy spectrum, such as as the spin/parity assignment or their collective/single-particle character. Further information can be obtained from the shape

and magnitude of the angular distribution of the emitted ejectile. To do that, one needs to compare the data with a suitable reaction calculation, as we will see in the next section.

6˙1. *Formal treatment of inelastic reactions.*

6˙1.1. The coupled-channels (CC) method. Remember from sect. **3** that any practical solution of the scattering problem starts with a reduction of the full physical space into P and Q subspaces, the former corresponding to the channels that are to be explicitly included. In an inelastic process, this P space will comprise the elastic channel, plus some excited states of the projectile and/or target, those more strongly coupled in the process or, at least, those that will be compared with the experimental data.

Let us consider the scattering of a projectile a by a target A, and let us assume for simplicity that only the projectile is excited during the process, the target remaining in its ground state. We denote this mass partition by the index α, *i.e.*, $\alpha \equiv a + A$. Our model Hamiltonian will describe a set of states of the projectile and possible couplings between them during the collision. This model Hamiltonian will be expressed as (cf. eq. (5)):

$$H = -\frac{\hbar^2}{2\mu}\nabla^2_{\vec{R}} + H_a(\xi) + V_\alpha(\xi, \vec{R}\,), \tag{73}$$

where $H_a(\xi)$ is the projectile internal Hamiltonian and ξ its internal coordinates.

Let us denote by $\{\phi_n(\xi)\}$ the internal states of the projectile. These will be the eigenstates of the Hamiltonian $H_a(\xi)$: $H_a\phi_n = \varepsilon_n\phi_n$. The idea of the CC method is to expand the total wave function of the system in the set of internal states $\{\phi_n(\xi)\}$,

$$\Psi^{(+)}(\vec{R}, \xi) = \phi_0(\xi)\chi_0(\vec{R}\,) + \sum_{n>0}^{N} \phi_n(\xi)\chi_n(\vec{R}\,), \tag{74}$$

with $\phi_0(\xi)$ representing the ground-state wave function and N the number of excited states included.

The unknown coefficients $\chi_n(\vec{R}\,)$ describe the relative motion between the projectile and target in the corresponding internal states. They tell us the relative "probability", as a function of $\vec{R}$, for the projectile being in state n. The different possibilities for n are frequently referred to as "channels". The total wave function $\Psi(\vec{R}, \xi)$ verifies the Schrödinger equation: $[E - H]\Psi^{(+)}(\vec{R}, \xi) = 0$. We now proceed as follows: i) insert the expansion (74) and the Hamiltonian (73) in this equation; ii) multiply on the left by each of the basis functions $\phi^*_n(\xi)$, and iii) integrate over the internal coordinates ξ. For each n, we get a differential equation of the form

$$\left[E - \varepsilon_n - \hat{T}_{\vec{R}} - V_{n,n}(\vec{R}\,)\right] \chi_n(\vec{R}\,) = \sum_{n' \neq n} V_{n,n'}(\vec{R}\,)\chi_{n'}(\vec{R}\,), \tag{75}$$

where $V_{n,n'}$ are the so called *coupling potentials*, defined as

$$V_{n,n'}(\mathbf{R}) = \int \mathrm{d}\xi \phi_n^*(\xi) V(\xi, \vec{R}) \phi_{n'}(\xi). \tag{76}$$

So, for example, $V_{0,m}$ is the potential responsible for the excitation from the ground state ($n = 0$) to a given final state m. We have not yet defined the form of the effective potential $V(\xi, \vec{R})$ and the internal states ϕ_n, that is, the model Hamiltonian. These potentials are constructed within a certain model, as we will see later.

Note that the equation associated with a given value of n contains not only the unknown $\chi_n(\vec{R})$, but also $\chi_{n'}(\vec{R})$ with $n' \neq n$. Consequently, eq. (75) represents a set of coupled differential equations for the set of functions $\{\chi_n(\vec{R})\}$.

6˙1.2. Boundary conditions. Similarly to the OM case, the CC equations must be solved with appropriate boundary conditions. These boundary conditions correspond to the physical situation in which the projectile is initially in the ground state (ϕ_0) and impinges with momentum $\vec{K}_0$. The projectile-target relative motion is represented by a plane wave with momentum $\vec{K}_0$. As a result of the collision with the target, a series of outgoing spherical waves is created (fig. 2). Recalling the general asymptotic behaviour of the total wave function, eq. (8), for the case of inelastic scattering we will have

$$\Psi^{(+)}_{\vec{K}_0}(\vec{R}, \xi) \xrightarrow{R\gg} \left\{ e^{i\vec{K}_0 \cdot \vec{R}} + f_{0,0}(\theta) \frac{e^{iK_0 R}}{R} \right\} \phi_0(\xi) + \sum_{n>0}^{N} f_{n,0}(\theta) \frac{e^{iK_n R}}{R} \phi_n(\xi). \tag{77}$$

Comparing with (74) we see that the functions $\chi_n(\vec{R})$ must verify the following boundary conditions:

$$\chi_0^{(+)}(\vec{K}_0, \vec{R}) \to e^{i\vec{K}_0 \cdot \vec{R}} + f_{0,0}(\theta) \frac{e^{iK_0 R}}{R}, \quad n = 0 \quad \text{(elastic)}, \tag{78}$$

$$\chi_n^{(+)}(\vec{K}_n, \vec{R}) \to f_{n,0}(\theta) \frac{e^{iK_n R}}{R}, \quad n \neq 0 \quad \text{(non-elastic)}, \tag{79}$$

from which the elastic and inelastic differential cross sections are to be obtained from the coefficient of the corresponding outgoing wave

$$\left(\frac{\mathrm{d}\sigma(\theta)}{\mathrm{d}\Omega} \right)_{0 \to n} = \frac{K_n}{K_0} |f_{n,0}(\theta)|^2. \tag{80}$$

Note that:

– Plane waves are present only in the χ_0 component (that is, the elastic component) but outgoing waves appear in all components.

– The scattering angle in the CM frame, θ, is determined by the direction of the momenta $\vec{K}_0$ and $\vec{K}_n$. Defining the *momentum transfer* as $\vec{q} = \vec{K}_n - \vec{K}_0$, we have (see fig. 2)

$$q^2 = K_0^2 + K_n^2 - 2K_0K_n\cos(\theta). \tag{81}$$

– The modulus of $\vec{K}_n$ is obtained from energy conservation([9])

$$E = \varepsilon_0 + \frac{\hbar^2 K_0^2}{2\mu} = \varepsilon_n + \frac{\hbar^2 K_n^2}{2\mu}\,. \tag{82}$$

6˙1.3. The DWBA method for inelastic scattering. If the number of states is large, the solution of the coupled equations can be a difficult task. In many situations, however, some of the excited states are very weakly coupled to the ground state and can be treated perturbatively. In this case, the set of equations (75) can be solved iteratively, starting from the elastic channel equation, and setting to zero the source term (the RHS of the equation). This allows the calculation of the distorted wave $\chi_0(\vec{K}_0, \vec{R}\,)$. This solution is then inserted into the equation corresponding to an excited state n, thus providing a first order approximation for $\chi_n(\vec{K}_0, \vec{R}\,)$. If the process is stopped here, then the method is referred to as *distorted wave Born approximation* (DWBA).

We provide here an alternative derivation of the DWBA method, which leads to a more direct connection with the scattering amplitude. We make use of the *exact* scattering amplitude (26) derived in subsect. **2**˙4 using the Gell-Mann–Goldberger transformation. To particularize this general result to our case, we consider a transition between an initial state i (typically, the g.s.) and a final state f. Since these states belong to the same partition (α) we do not need to specify explicitly the subscripts α and β. Then, the general amplitude (26) reduces to

$$\mathcal{T}_{f,i} = \iint \chi_f^{(-)*}(\vec{K}_f, \vec{R}\,)\phi_f^*(\xi)[V_f - U_f]\Psi^{(+)}_{\vec{K}_i}\mathrm{d}\xi\,\mathrm{d}\vec{R}, \tag{83}$$

where, within the CC method, $\Psi^{(+)}_{\vec{K}_i}$ is given by the expansion (74). Recall that, in this expression, $\chi_f^{(-)}(\vec{K}_f, \vec{R}\,)$ is the time reversal of $\chi_f^{(+)}(\vec{K}_f, \vec{R}\,)$, which is a solution of

$$\left[\hat{T}_{\vec{R}} + U_f(\vec{R}\,) + \varepsilon_f - E\right]\chi_f^{(+)}(\vec{K}_f, \vec{R}\,) = 0, \tag{84}$$

for some auxiliary potential $U_f(\vec{R}\,)$. Typically, $U_f(\vec{R}\,)$ is chosen as a phenomenological potential that describes the elastic scattering of the $a + A$ system at the energy of the exit channel ($E_f = E - \varepsilon_f$).

([9]) For $\varepsilon_n > E$, the kinetic energy is negative and the corresponding momentum K_n becomes imaginary. Consequently, the asymptotic solutions χ_n of eq. (78) vanish exponentially and then these channels do not contribute to the outgoing flux.

The DWBA formula is obtained by approximating the total wave function $\Psi^{(+)}_{\vec{K}_i}$ by the factorized form

$$\Psi^{(+)}(\vec{R},\xi) \simeq \chi_i^{(+)}(\vec{K}_i,\vec{R})\phi_i(\xi), \tag{85}$$

where $\chi_i^{(+)}(\vec{K},\vec{R}\,)$ is the distorted wave describing the projectile-target motion in the entrance channel,

$$\left[\hat{T}_{\vec{R}} + U_i(\vec{R}\,) + \varepsilon_i - E\right] \chi_i^{(+)}(\vec{K}_i,\vec{R}\,) = 0, \tag{86}$$

where $U_i(\vec{R}\,)$ is the average potential in the initial channel, and is usually taken as the potential that describes the elastic scattering in this channel. With this choice, one hopes to include effectively some of the effects of the neglected channels.

In DWBA, the scattering amplitude corresponding to the inelastic excitation of the projectile from the initial state $\phi_i(\xi)$ and momentum $\vec{K}_i$ to a final state $\phi_f(\xi)$ and momentum $\vec{K}_f$ is given by

$$f_{f,i}^{\mathrm{DWBA}}(\theta) = -\frac{\mu}{2\pi\hbar^2}\int \mathrm{d}\vec{R}\,\chi_f^{(-)*}(\vec{K}_f,\vec{R})W_{if}(\vec{R})\chi_i^{(+)}(\vec{K}_i,\vec{R}\,), \tag{87}$$

where $W_{if}(\vec{R}\,)$ is the coupling potential

$$W_{if}(\vec{R}\,) \equiv \langle\phi_f|V_f - U_f|\phi_i\rangle = \int \mathrm{d}\xi\,\phi_f^*(\xi)(V_f - U_f)\phi_i(\xi). \tag{88}$$

In actual calculations, the internal states have definite angular momentum (spin) so, we may introduce this dependence explicitly using the following notation:

$$\phi_i(\xi) = |I_i M_i\rangle \quad \text{and} \quad \phi_f(\xi) = |I_f M_f\rangle.$$

To exploit this property, one usually expands the projectile-target interaction in multipoles

$$V(\vec{R},\xi) = \sqrt{4\pi}\sum_{\lambda,\mu} V_{\lambda\mu}(R,\xi)Y_{\lambda\mu}(\hat{R}). \tag{89}$$

DWBA calculations require the matrix elements

$$\langle I_f M_f|V(\vec{R},\xi)|I_i M_i\rangle = \sqrt{4\pi}\sum_{\lambda,\mu}\langle I_f M_f|V_{\lambda\mu}(R,\xi)|I_i M_i\rangle Y_{\lambda\mu}(\hat{R}). \tag{90}$$

The dependence on the spin projection can be singled out using the *Wigner-Eckart theorem*([10])

$$\langle I_f M_f | V_{\lambda\mu}(R,\xi) | I_i M_i \rangle = (2I_f+1)^{-1/2} \langle I_f M_f | I_i M_i \lambda\mu \rangle \langle I_f \| V_\lambda(R,\xi) \| I_i \rangle, \tag{91}$$

where the quantities $\langle I_f \| V_\lambda(R,\xi) \| I_i \rangle$ are called *reduced matrix elements*. These are independent of the spin projections, as the notation implies.

Actual applications of the DWBA amplitude (87) require the specification of the structure model (that will determine the functions $\phi_i(\xi)$) as well as the projectile-target interaction V_f. We give some examples in the following section.

6˙2. *Specific models for inelastic scattering.*

6˙2.1. Macroscopic (collective) models. Ignoring spin-dependent forces, the nuclear interaction between spherical, static nuclei is a function of the distance between the nuclear surfaces of the colliding nuclei ($V_N = V_N(R-R_0)$, with $R_0 \simeq R_p + R_t$). However, if one (or both) of the colliding nuclei is deformed (rotor) the nucleus-nucleus interaction will depend on the orientation of the deformed nucleus in space (because, depending on this orientation, the distance between the surfaces will vary accordingly). This introduces a dependence on the angles of the relative coordinate, and the nucleus-nucleus potential will not be central any more. A similar situation occurs when one of the nuclei undergoes surface vibrations.

If the deviation from the spherical shape is small, one may use a Taylor expansion of the potential around this spherical shape

$$V_N(\vec{R},\xi) = V_N(R-R_0) - \sum_{\lambda,\mu} \hat{\delta}_{\lambda\mu} \frac{\mathrm{d}V(R-R_0)}{\mathrm{d}R} Y_{\lambda\mu}(\theta,\phi) + \ldots, \tag{92}$$

where $\hat{\delta}_{\lambda,\mu}$ are the so-called *deformation length operators*. For a nucleus with a permanent deformation (rotor) they are related to the intrinsic shape of the nucleus. For a spherical vibrational nucleus, a formally analogous expression can be obtained, but in this case the operators $\hat{\delta}_{\lambda,\mu}$ are to be understood as dynamical quantities, which produce surface vibrational excitations under the action of the potential exerted by the other nucleus.

Similarly, for the Coulomb interaction, we make use of the multipole expansion of the electrostatic interaction between the charge distribution of the projectile nucleus and that for the target (assumed here to be represented by a point-charge $Z_t e$ for simplicity)

$$V_C(\vec{R},\xi) = \frac{Z_t Z_p e^2}{R} + \sum_{\lambda>0,\mu} \frac{4\pi}{2\lambda+1} \frac{Z_t e}{R^{\lambda+1}} \mathcal{M}(E\lambda,\mu) Y_{\lambda\mu}(\hat{R}), \tag{93}$$

([10]) We assume thoroughout this contribution the Bohr and Mottelson convention of reduced matrix elements [23].

where $\mathcal{M}(E\lambda,\mu) \equiv e\sum_i^{Z_p} r_i^\lambda Y^*_{\lambda\mu}(\hat{r}_i)$ is the *electric multipole operator*.

We include in the auxiliary potentials U_i and U_f the monopole parts of the nuclear and Coulomb interactions (those which cannot excite the nuclei), *i.e.*

$$U_i = U_f = V_N(R-R_0) + \frac{Z_t Z_p e^2}{R}\,,$$

and incorporate the $\lambda > 0$ terms in the residual interaction $W = V_f - U_f$. The transition potentials for the nuclear and Coulomb parts of this residual interaction are, respectively,

$$W^N_{if}(\vec{R}\,) = -\frac{\mathrm{d}V_N(R-R_0)}{\mathrm{d}R}\sum_{\lambda>0,\mu}\langle f;I_fM_f|\hat{\delta}_{\lambda\mu}|i;I_iM_i\rangle Y_{\lambda\mu}(\hat{R}), \tag{94}$$

and

$$W^C_{if}(\vec{R}\,) = \sum_{\lambda>0,\mu}\frac{4\pi}{2\lambda+1}\frac{Z_t e}{R^{\lambda+1}}\langle f;I_fM_f|\mathcal{M}(E\lambda,\mu)|i;I_iM_i\rangle Y_{\lambda\mu}(\hat{R}). \tag{95}$$

The dependence on the spin projections of the structure matrix elements can be singled out using the Wigner-Eckart theorem. For example, for the Coulomb matrix element

$$\langle f;I_fM_f|\mathcal{M}(E\lambda,\mu)|i;I_iM_i\rangle = (2I_f+1)^{-1/2}\langle I_iM_i\lambda\mu|I_fM_f\rangle\langle f;I_f\|\mathcal{M}(E\lambda)\|i;I_i\rangle, \tag{96}$$

and the reduced matrix element is related to the electric reduced probabilities

$$B(E\lambda;I_i\to I_f) = (2I_i+1)^{-1}\,|\langle f;I_f\|\mathcal{M}(E\lambda,\mu)\|i;I_i\rangle|^2 \quad (I_i\neq I_f). \tag{97}$$

Likewise, for the nuclear matrix elements

$$\langle f;I_fM_f|\delta_{\lambda\mu}|i;I_iM_i\rangle = (2I_f+1)^{-1/2}\langle I_iM_i\lambda\mu|I_fM_f\rangle\langle f;I_f\|\delta_\lambda\|i;I_i\rangle, \tag{98}$$

which are proportional to the reduced matrix elements of the deformation length operator. For a $I_i = 0 \to I_f$ transition in a even-even nucleus characterized by a deformation parameter β_λ, this reduced matrix element is simply given by $\langle f;I_f\|\delta_\lambda\|i;I_i\rangle = \beta_\lambda R_0$, where R_0 is the average radius.

For a purely nuclear excitation process, with multipolarity λ, the DWBA amplitude is

$$f^N_{f,i}(\theta) = \frac{\mu}{2\pi\hbar^2}\langle f;I_fM_f|\hat{\delta}_{\lambda\mu}|i;I_iM_i\rangle\int \mathrm{d}\vec{R}\,\chi^{(-)*}_f(\vec{K}_f,\vec{R}\,)\frac{\mathrm{d}V_N}{\mathrm{d}R}Y_{\lambda\mu}\left(\hat{R}\right)\chi^{(+)}_i(\vec{K}_i,\vec{R}\,), \tag{99}$$

whereas for a purely Coulomb excitation, also of multipolarity λ,

$$\begin{aligned} f^C_{f,i}(\theta) = &-\frac{\mu}{2\pi\hbar^2}\frac{4\pi Z_t e}{2\lambda+1}\langle f;I_fM_f|\mathcal{M}(E\lambda,\mu)|i;I_iM_i\rangle \\ &\times\int \mathrm{d}\vec{R}\,\chi^{(-)*}_f(\vec{K}_f,\vec{R}\,)\frac{1}{R^{\lambda+1}}Y_{\lambda\mu}\left(\hat{R}\right)\chi^{(+)}_i(\vec{K}_i,\vec{R}\,). \end{aligned} \tag{100}$$

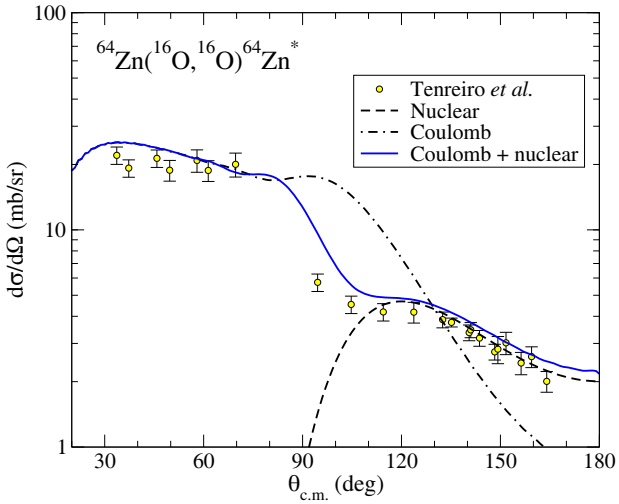

Fig. 8. – Differential inelastic cross section for the excitation of the first excited state of ^{64}Zn ($E_x = 0.992\,\text{MeV}$, $I = 2^+$) in the reaction $^{16}\text{O}+^{64}\text{Zn}$ at $E = 44\,\text{MeV}$. The data from ref. [24] are compared with DWBA calculations based on a collective model of the target nucleus including nuclear, Coulomb and nuclear+Coulomb couplings. The structure parameters and potentials are those from [24].

In general, both the nuclear and Coulomb potentials may contribute to the excitation mechanism and so the total scattering amplitude will be the coherent sum of both amplitudes and the differential cross section will be([11])

$$\left(\frac{\mathrm{d}\sigma(\theta)}{\mathrm{d}\Omega}\right)_{i\to f} = \frac{K_f}{K_i}\left|f^N_{f,i} + f^C_{f,i}\right|^2 . \tag{101}$$

This means that interference effects will arise at those angles for which the nuclear and Coulomb amplitudes are of the same order. These interference effects are illustrated in fig. 8 for the ^{64}Zn(^{16}O,^{16}O)^{64}Zn* reaction at $E = 44\,\text{MeV}$, where a clear destructive interference between the Coulomb and nuclear couplings is observed around 90°.

6˙2.2. Few-body model. Some nuclei exhibit a marked cluster structure. This is trivially the case of the deuteron ($d = p+n$) but also of other nuclei, particularly in the light region of the nuclear chart. Some examples are $^6\text{Li} = \alpha + d$, $^7\text{Li} = \alpha + t$ and $^9\text{Be} = \alpha + \alpha + \text{n}$, among many others.

If the separation energy between the clusters is small compared to the cluster excitation energies, it is plausible to treat these clusters as inert objects and consider only

([11]) Note that this expression corresponds to definite initial and final spin projections. For unpolarized projectile and target, the actual cross section would correspond to a sum over the spin projections of the final nuclei, and an average over the initial ones [10].

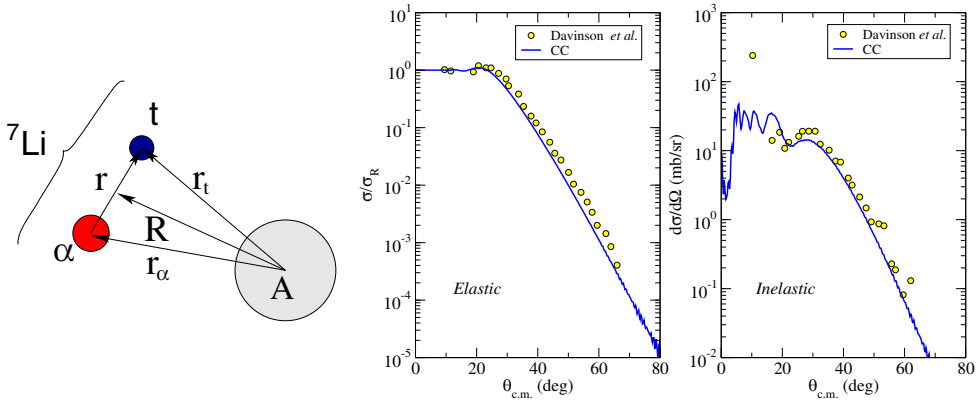

Fig. 9. – Left: relevant coordinates for a $^7\mathrm{Li} + A$ reaction, using a two-body cluster model of $^7\mathrm{Li}(\alpha{+}t)$. Right: application of the CC formalism to the $^7\mathrm{Li}{+}^{208}\mathrm{Pb}$ reaction at $E_{\mathrm{lab}} = 68\,\mathrm{MeV}$, the two-body cluster model for $^7\mathrm{Li}$. The left and right cross sections are for the elastic and inelastic (excitation of $1/2^-$ excited state of $^7\mathrm{Li}$) differential cross sections. Experimental data are from ref. [25].

possible excitations between them. Using the Feshbach terminology, we include in the P space only the inter-cluster excitations. In this way, we convert the many-body structure (and reaction) problem into a few-body problem. In this Feshbach reduction, cluster-target interactions are described by effective potentials (complex in general) evaluated at the corresponding energy per nucleon. Additionally, the inter-cluster interaction is described with an effective potential tuned to describe the known properties of the projectile, such as the separation energy, spin-parity, rms radius, etc.

Considering as an example the case of a two-body projectile, the projectile-target interaction will be described by the effective potential

$$V(\vec{R},\xi) \equiv V(\vec{R},\vec{r}) = U_1(\vec{r}_1) + U_2(\vec{r}_2), \tag{102}$$

where $\vec{r}$ is the inter-cluster coordinate and $\vec{r}_i$ the cluster-target coordinates. Note that, in this model, the internal variables ξ are represented by the relative coordinate $\vec{r}$.

To apply the CC or DWBA methods we need to evaluate the coupling potentials

$$V_{n,n'}(\vec{R}\,) = \int \mathrm{d}\vec{r}\,\phi^*_n(\vec{r}\,)\,[U_1(\vec{r}_1) + U_2(\vec{r}_2)]\,\phi_{n'}(\vec{r}\,). \tag{103}$$

As an example, consider the scattering of $^7\mathrm{Li}$, treated as $\alpha + t$, by a target A (see fig. 9). In this model, the $^7\mathrm{Li}$ ground-state $(3/2^-)$ can be interpreted assuming that the α (0^+) and t $(1/2^+)$ clusters are in a $\ell = 1$ state of relative motion. Analogously, the first excited state $(1/2^-)$ can be interpreted also assuming a $\ell = 1$ configuration and so it would correspond to a spin-orbit partner of the ground-state level. The wave functions

for these states would be obtained from a single-channel Schrödinger equation

$$\left[\hat{T}_{\vec{r}} + V_{\alpha-t}(\vec{r}) - \varepsilon_n\right] \phi_n(\vec{r}) = 0, \tag{104}$$

where, for the ground-state ($n = 0$), $\varepsilon_0 = -2.47\,\mathrm{MeV}$.

A successful application of such a model to elastic and inelastic scattering of $^7\mathrm{Li} + ^{208}\mathrm{Pb}$ at 68 MeV is shown in fig. 9, where the calculations are compared with the data from ref. [25]. In this case, the model space was restricted to the two bound states of ^{7}Li. In fact, the application of the CC method to unbound states (resonant or non-resonant) requires appropriate extensions of the method, as explained in the following section.

7. – Breakup reactions I: quantum-mechanical approach

7˙1. *The CDCC method.* – If one of the colliding partners is weakly bound and is excited above its breakup threshold, the system will become unbound and will eventually dissociate into two or more fragments (recall the $^7\mathrm{Li}(p, p')$ example of fig. 7). This will be the case of halo nuclei, an example of which is the ^{6}He nucleus already discussed. If we are interested in the description of these breakup channels, our modelspace must be augmented to include, at least, part of them. A way of doing that is by means of the coupled-channels (CC) method. However, direct application of this method, as introduced in the previous section, is not possible because i) the breakup states are continuous in energy, thereby leading to an infinite number of states and ii) the positive-energy wave functions, unlike those for bound states, do not vanish at large distances, presenting an oscillatory asymptotic behaviour. Consequently, they can not be normalized. Coupling potentials calculated with this kind of functions will also oscillate at large distances, posing severe problems to the standard methods of solution of the coupled equations.

These difficulties motivated the development of the continuum-discretized coupled-channels (CDCC) method. This method was originally introduced by G. Rawitscher [26] and later refined by the Pittsburgh-Kyushu collaboration [27, 28] to describe the effect of the breakup channels on the elastic scattering of deuterons. Denoting the reaction by $a + A$, with $a = b + x$ (referred hereafter as the *core* and *valence* particles, respectively), the method assumes the effective three-body Hamiltonian

$$H = H_{\mathrm{proj}} + \hat{T}_{\vec{R}} + U_{bA}(\vec{r}_{bA}) + U_{xA}(\vec{r}_{xA}), \tag{105}$$

with $H_{\mathrm{proj}} = T_{\vec{r}} + V_{bx}$ the projectile internal Hamiltonian, $\hat{T}_{\vec{r}}$ and $\hat{T}_{\vec{R}}$ are kinetic energy operators, V_{bx} the inter-cluster interaction and U_{bA} and U_{xA} are the core-target and valence-target optical potentials (complex in general) describing the elastic scattering of the corresponding $b + A$ and $x + A$ sub-systems, at the same energy per nucleon of the incident projectile. In the CDCC method the three-body wave function of the system is expanded in terms of the eigenstates of the Hamiltonian H_{proj} including both

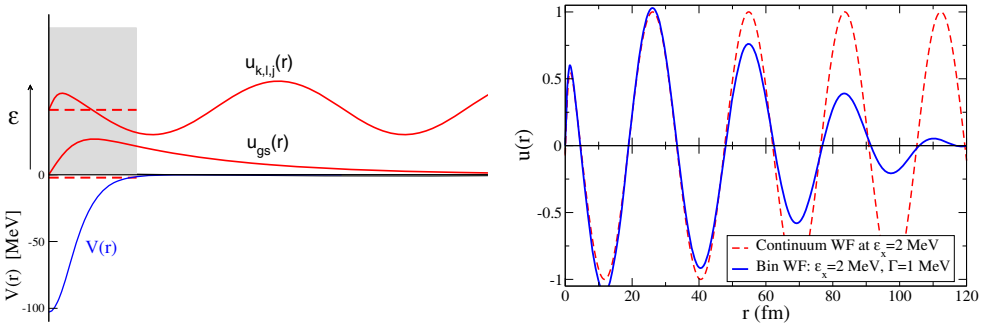

Fig. 10. – Left: the p-n potential showing the bound state wave function (deuteron) and an unbound state wave function. Right: comparison of a scattering state with a *bin* wave packet centered around the same nominal energy and with a width of 1 MeV.

bound and unbound states. Since the latter form a continuum, a procedure of discretization is applied, consisting in representing this continuum by a finite and discrete set of square-integrable functions. In actual calculations, this continuum must be truncated in excitation energy and limited to a finite number of partial waves ℓ associated to the relative co-ordinate $\vec{r}$. Normalizable states representing the continuum should be obtained for each ℓ, j values. Two main methods are used for this purpose:

– *The pseudo-state method*, in which the $b+x$ Hamiltonian is diagonalized in a basis of square-integrable functions, such as Gaussians [29] or transformed harmonic oscillator functions [30]. Negative eigenvalues correspond to the bound states of the systems, whereas positive eigenvalues are regarded as a finite representation of the continuum.

– *The binning method*, in which normalizable states are obtained by constructing a wave packet (*bin*) by linear superposition of the actual continuum states over a certain energy interval [28].

We describe this latter method in some more detail. Assuming for simplicity a spinless core, these discretized functions are denoted as

$$\phi_i(\vec{r}) = \frac{u_i(r)}{r}[Y_{\ell_i}(\hat{r}) \otimes \chi_s]_{j_i m_i}, \tag{106}$$

where $i \equiv \{[k_i, k_{i+1}]\ell_i s j_i m_i\}$ specifies the i-th bin, with $[k_i, k_{i+1}]$ the wave number interval of the bin, ℓ the valence-core orbital angular momentum, s the valence spin, and $\vec{j} = \vec{\ell} + \vec{s}$ the total angular momentum. The symbol $\otimes$ denotes angular momentum coupling. The radial part of the bin is obtained as a linear combination (*i.e.* a wave packet) of scattering states as

$$u_i(r) = \sqrt{\frac{2}{\pi N_i}} \int_{k_i}^{k_{i+1}} w_i(k) u_{k,\ell_i s j_i}(r) \mathrm{d}k, \tag{107}$$

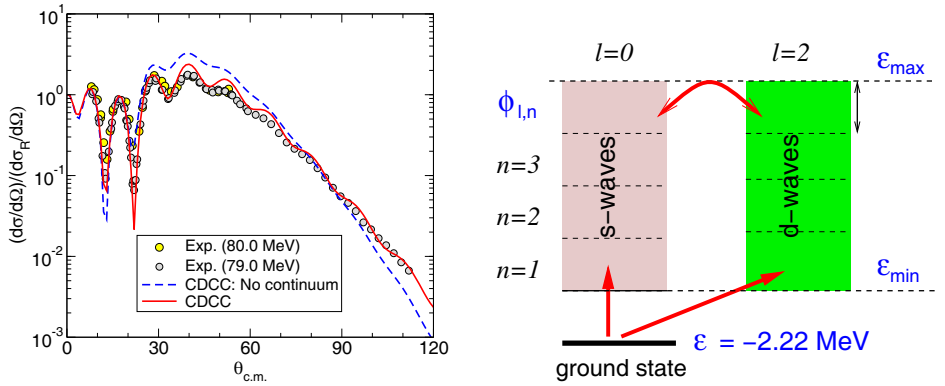

Fig. 11. – Left: application of the CDCC method to $\mathrm{d} + {}^{58}\mathrm{Ni}$ elastic scattering at $E_d = 80\,\mathrm{MeV}$. The solid line is the full CDCC calculation. The dashed line is the calculation omitting the breakup channels. The calculations were performed ignoring the internal spins of the proton and neutron and so $\ell = j$. Right: illustration of continuum discretization for the same problem.

where $w_i(k)$ is a weight function (for non-resonant continuum $w(k)$ is usually taken as $e^{i\delta_{\ell_i}}$ where δ_{ℓ_i} are the phase shifts of the scattering states within the bin) and N_i is a normalization constant. The effect of this averaging is to damp the oscillations at large distances, making the bin wave function normalizable (see fig. 10).

Assuming a single bound state for simplicity, the CDCC wave function reads

$$\Psi^{\mathrm{CDCC}}(\vec{R},\vec{r}) = \chi_0^{(+)}(\vec{R})\phi_0(\vec{r}) + \sum_{i=1}^{N} \chi_i^{(+)}(\vec{R})\phi_i(\vec{r}), \tag{108}$$

where the index $i = 0$ denotes the ground state of the $b + x$ system.

This model wave function must verify the Schrödinger equation: $[H - E]\Psi^{\mathrm{CDCC}}(\vec{R},\vec{r}) = 0$. This gives rise to a set of coupled differential equations similar to that of eq. (75) with the coupling potentials given by

$$U_{ij}(\vec{R}) = \int \mathrm{d}\vec{r}\,\phi_i^*(\vec{r})\,[U_{bA} + U_{xA}]\,\phi_j(\vec{r}). \tag{109}$$

An example of the application of the CDCC method to deuteron elastic scattering is depicted in fig. 11.

The standard CDCC method is based on a strict three-body model of the reaction $(b + x + A)$, and has proven rather successful to describe elastic and breakup cross sections of deuterons and other weakly bound two-body nuclei, such as ${}^{6,7}\mathrm{Li}$ and ${}^{11}\mathrm{Be}$ (see fig. 12). However, it has limitations. The assumption of inert bodies is not always justified, since excitations of the projectile constituents (b and x) and of the target (A) may take place along with the projectile dissociation. Furthermore, the two-body picture may be inadequate for some nuclei as, for example, in the case of the Borromean systems

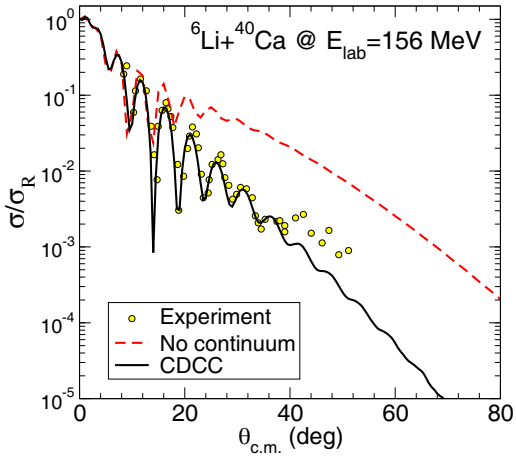

Fig. 12. – Application of the CDCC method to $^6\mathrm{Li} + {}^{40}\mathrm{Ca}$ elastic scattering at 156 MeV. Experimental data are from ref. [31].

(*e.g.* ^{6}He, ^{11}Li). Some extensions of the CDCC method to deal with the these situations are outlined below.

7˙1.1. Inclusion of core and target excitations. Excitations of the projectile constituents (b and x in our case) may take place concomitantly with the projectile breakup. This mechanism is not included explicitly in the standard formulation of the CDCC method. For example, for the scattering of halo nuclei, collective excitations of the core b may be important. These core excitations will affect both the structure of the projectile as well as the reaction dynamics. In the inert core picture, the projectile states will correspond to pure single-particle or cluster states but, if the core is allowed to excite, these states will contain in general admixtures of core-excited components. Additionally, the interaction of the core with the target will produce excitations and deexcitations of the former during the collision, and this will modify the reaction observables to some extent. These two effects (structural and dynamical) have been recently investigated within extended versions of the DWBA and CDCC methods [32-35]. For example, considering only possible excitations of b, the effective three-body Hamiltonian is generalized as follows:

$$H = H_{\mathrm{proj}}(\vec{r}, \xi_b) + \hat{T}_{\vec{R}} + U_{bA}(\vec{r}_{bA}, \xi_b) + U_{xA}(\vec{r}_{xA}). \tag{110}$$

The potential $U_{bA}(\vec{r}_{bA}, \xi_b)$ is meant to describe both elastic and inelastic scattering of the $b + A$ system (for example, it could be represented by a deformed potential as discussed in the context of inelastic scattering with collective models). Note that the core degrees of freedom (ξ_b) appear in the projectile Hamiltonian (structure effect) as well as in the core-target interaction (dynamic effect).

In the weak-coupling limit, the projectile Hamiltonian can be written more explicitly

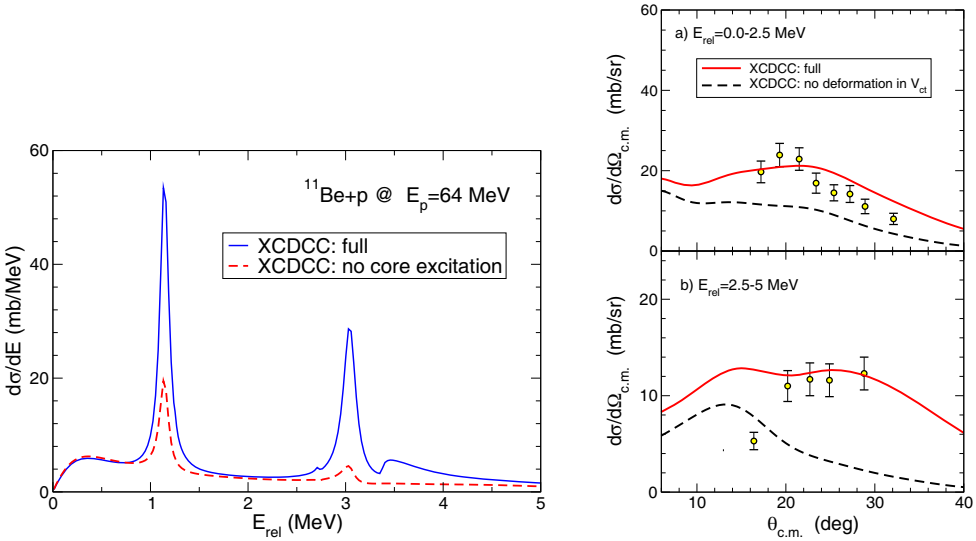

Fig. 13. – Left: differential breakup cross sections, with respect to the n-^{10}Be relative energy, for the breakup of ^{11}Be on protons at 63.7 MeV/nucleon. Right: breakup angular distributions for the relative-energy cuts indicated in the labels.

as

$$H_{\rm proj} = \hat{T}_{\vec{r}} + V_{bx}(\vec{r}, \xi_b) + h_{\rm core}(\xi_b), \tag{111}$$

where $h_{\rm core}(\xi_b)$ is the internal Hamiltonian of the core. The eigenstates of this Hamiltonian are of the form

$$\phi_i(\xi) \equiv \sum_\alpha \left[\varphi_\alpha(\vec{r}) \otimes \Phi_I(\xi_b)\right]_{j_p m_p}, \tag{112}$$

where i is an index labeling the states with angular momentum $j_p m_p$, $\xi \equiv \{\xi_b, \vec{r}\}$, $\alpha \equiv \{\ell, s, j, I\}$, with I the core intrinsic spin, $\vec{j} = \vec{\ell} + \vec{s}$ and $\vec{j}_p = \vec{j} + \vec{I}$. The functions $\Phi_I(\xi_b)$ and $\varphi_\alpha(\vec{r})$ describe, respectively, the core states and the valence-core relative motion. For continuum states, a procedure of continuum discretization is used.

Once the projectile states (112) have been calculated, the three-body wave function is expanded in a basis of such states, as in the standard CDCC method. Early calculations using this extended CDCC method (XCDCC) were first performed by Summers *et al.* [34, 36] for ^{11}Be and ^{17}C on ^{9}Be and ^{11}Be + p, finding a very little core excitation effect in all these cases. However, later calculations for the ^{11}Be + p reaction based on a alternative implementation of the XCDCC method using a pseudo-state representation of the projectile states [35] suggested much larger effects. The discrepancy was found to be due to an inconsistency in the numerical implementation of the XCDCC formalism presented in ref. [34], as clarified in [37]. For heavier targets, such as ^{64}Zn or ^{208}Pb,

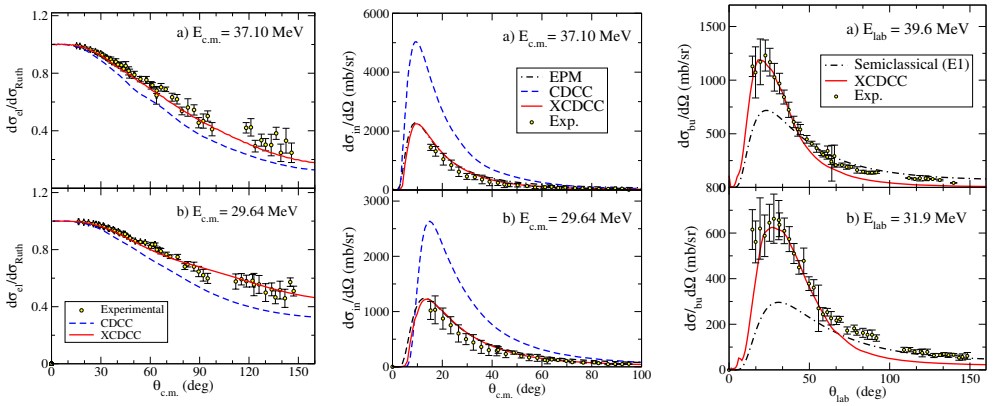

Fig. 14. – Elastic (left), inelastic (middle) and breakup (right) cross sections for the reaction ^{11}Be + ^{197}Au at near barrier energies ($V_b \sim 40$ MeV). Experimental data are compared with CDCC, CDCC and first-order semiclassical pure $E1$ calculations (labeled EPM). Adapted from ref. [7].

the calculations of [35] suggest that the core excitation mechanism plays a minor role, although its effect on the structure of the projectile is still important.

As an example of these XCDCC calculations we show in the left panel of fig. 13 the differential breakup cross section, as a function of the n-^{10}Be relative energy, for the reaction $^{11}\mathrm{Be} + p$ at 63.7 MeV/nucleon. Details of the structure model and potentials as given in ref. [35]. Continuum states with angular momentum/parity $j_p = 1/2^{\pm}$, $3/2^{\pm}$ and $5/2^{+}$ were included using a pseudostate representation in terms of transformed harmonic oscillator (THO) functions [38]. To get a smooth function of the energy, the calculated differential cross sections were then convoluted with the *actual* scattering states of H_{proj}. The two peaks at $\varepsilon = 1.2$ and 3.2 MeV correspond to $5/2^{+}$ and $3/2^{+}$ resonances, respectively. The solid line is the full XCDCC calculation, including the ^{10}Be deformation in the structure of the projectile as well as in the projectile-target dynamics. The dashed line is the XCDCC calculation omitting the effect of the core-target excitation mechanism. It is clearly seen that the inclusion of this mechanism increases significantly the breakup cross sections, particularly in the region of the $3/2^{+}$ resonance, owing to the dominant $^{10}\mathrm{Be}(2^{+}) \otimes 2s_{1/2}$ configuration of this resonance [32, 33, 38]. The right graph shows two angular distributions, corresponding to the relative-energy intervals indicated in the labels, compared with the XCDCC calculations with (solid) and without (dashed) core excitations.

The importance of the deformation on the structure of the projectile is clearly evidenced in the elastic and inelastic scattering of ^{11}Be on ^{197}Au at energies around and below the Coulomb barrier [7], shown in fig. 14. XCDCC calculations based on the particle-plus-rotor model (solid lines) are able to reproduce simultaneously the elastic, inelastic and breakup angular distributions. By contrast, standard CDCC calculations using single-particle wave functions fail to describe the elastic and inelastic data, even describing well the breakup. This is due to the overestimation of the $B(E1)$ connecting the ground state with the bound excited state, as shown in fig. 21.

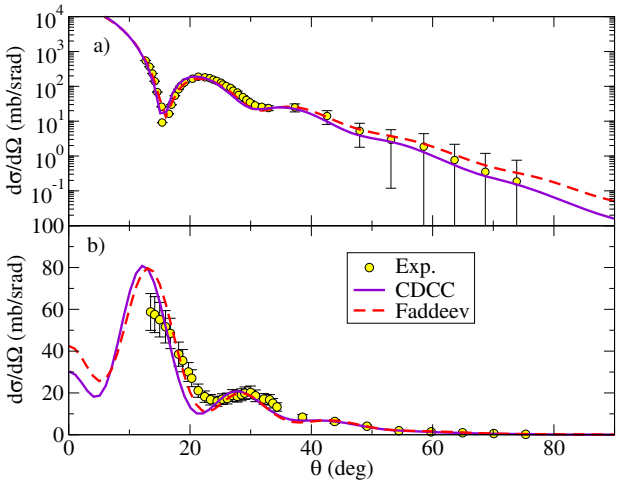

Fig. 15. – Elastic (upper) and ^{24}Mg(2^+) excitation (lower) differential angular cross sections for d + ^{24}Mg $E_d = 70$ MeV. CDCC calculations are compared with Faddeev calculations from ref. [43] and with the data of ref. [42]. The calculations employ CH89 [44] parameterization for the $p + {}^{24}$Mg and $n + {}^{24}$Mg potentials and treat the target excitation with a collective model, assuming a deformation of $\beta = 0.5$ for the ^{24}Mg nucleus. The plot is adapted from ref. [41].

A simpler DWBA, no-recoil version of the formalism (XDWBA) has been also proposed in refs. [32, 33]. An application of this formalism to the ^{11}Be + ^{12}C reaction at 69 MeV/u showed that the core excitation mechanism may interfere with the single-particle excitation mechanism, producing a conspicuous effect on the interference pattern of the resonant breakup angular distributions [39].

In addition to the excitations of the projectile constituents, excitations of the target nucleus may also take place and compete with the projectile breakup mechanism. Note that, within CDCC, the projectile breakup is treated as an inelastic excitation of the projectile to its continuum states and, thus, inclusion of target excitation amounts to including, simultaneously, projectile plus target excitations so their relative importance, and mutual influence, can be assessed. These target excitations can be treated with the collective models mentioned in sect. **6**˙2. It is worth noting that, within this three-body reaction model, target excitation arises from the non-central part of the valence-target and core-target interactions. To incorporate this effect, the effective Hamiltonian, eq. (105), must be now generalized as

$$H = \hat{T}_{\vec{r}} + \hat{T}_{\vec{R}} + V_{bx} + U_{bA}(\vec{r}_{bA}, \xi_t) + U_{xA}(\vec{r}_{xA}, \xi_t), \tag{113}$$

in which the $b - A$ and $x - A$ interactions depend now, in addition to the corresponding relative coordinate, on the target degrees of freedom (denoted as ξ_t). Ideally, these U_{xA} and U_{bA} potentials should reproduce simultaneously the elastic and inelastic scattering for the $x + A$ and $b + A$ reactions, respectively.

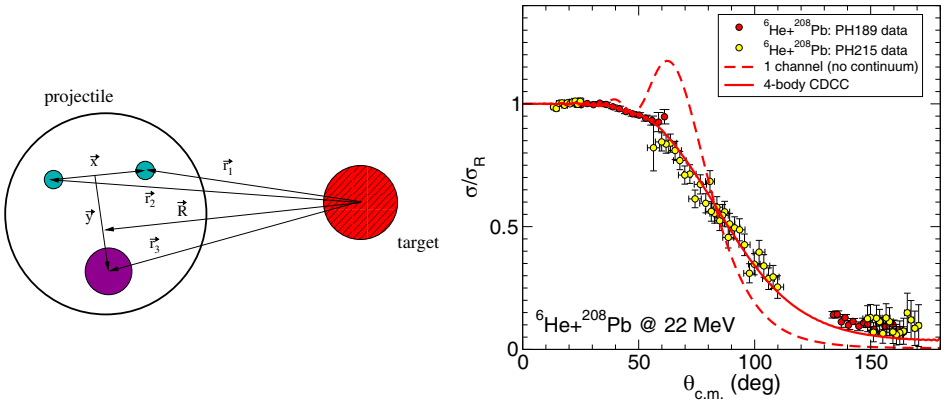

Fig. 16. – Left: relevant coordinates of the four-body scattering problem. Right: differential elastic cross section, relative to Rutherford, for the $^6\mathrm{He}+^{208}\mathrm{Pb}$ reaction at $E_{\mathrm{lab}} = 22\,\mathrm{MeV}$. The solid (dashed) line is the four-body CDCC calculation including (excluding) ^{6}He continuum states. Experimental data are from refs. [4, 20] and the CDCC calculations from ref. [47].

The explicit inclusion of target excitation was first done by the Kyushu group in the 1980s [27], which considered the case of deuteron scattering. The motivation was to compare the roles of target-excitation and deuteron breakup in the elastic and inelastic scattering of deuterons. They applied the formalism to the $\mathrm{d}+^{58}\mathrm{Ni}$ reaction at $E_d = 22$ and 80 MeV, including the ground state and the first excited state of ^{58}Ni (2^+) and finding that, in this case, the deuteron breakup process is more important than the target-excitation.

Recently, the problem has been also addressed by some authors [40, 41], also in the context of deuteron elastic and inelastic scattering. A recent application of the formalism is shown in fig. 15, which corresponds to the reaction $^{24}\mathrm{Mg}(d,d)^{24}\mathrm{Mg}^*$ at $E_d = 70\,\mathrm{MeV}$, including the ground and first excited states of ^{24}Mg, in addition to the deuteron breakup. The data are from ref. [42]. The target excitation was treated within the collective model, using a quadrupole deformation parameter of $\beta_2 = 0.5$. Also included are Faddeev calculations performed by A. Deltuva [43]. Both calculations reproduce equally well the elastic differential cross section. The calculated inelastic angular distributions are slightly out of phase with the data, but they agree well with each other, pointing to some inadequacy of the structure or potential inputs. Although these inelastic cross sections can be also well reproduced with standard DWBA calculations based on a deformed deuteron-target potential, it was shown in [43] that the extracted deformation parameter obtained with the three-body approach is more consistent with that derived from nucleon-nucleus inelastic scattering.

7˙1.2. Extension to three-body projectiles. To study the scattering of three-body projectiles, such as Borromean nuclei, the Hamiltonian (105) must be generalized in order to take into account the three-body structure of the projectile. For example, for a two-neutron Borromean system with a structure of the form $a = b + n + n$, one may use the

Hamiltonian

$$H = H_{\rm proj}(\vec{x},\vec{y}) + \hat{T}_{\vec{R}} + U_{nA}(\vec{r}_1) + U_{nA}(\vec{r}_2) + U_{bA}(\vec{r}_3), \tag{114}$$

where $H_{\rm proj}(\vec{x},\vec{y})$ is the projectile (three-body) Hamiltonian, depending now on two relative coordinates (for example, the Jacobi coordinates shown in the cartoon of fig. 16), and $U_{nA}(\vec{r}_i)$ the valence-target effective interactions. Clearly, the calculation of the projectile states will be much more involved than in the two-body case. In general, a given projectile state with angular momentum j_p, m_p will consist in a superposition of many configurations involving the internal orbital angular momenta and spins of the constituents,

$$\phi_i(\xi) = \sum_\alpha \left[\varphi_\alpha(\vec{x},\vec{y})\right]_{j_p m_p}, \tag{115}$$

where $\xi \equiv \{\vec{x},\vec{y}\}$ are the internal coordinates of the three-body system. The label α denotes the set of quantum numbers $\{\ell_1,\ell_2,s_1,s_2,\ldots\}$, required to characterize the three-body state, which may vary depending on the three-body approach used. Note that $\phi_i(\xi)$ is an (approximate) eigenstate of the projectile three-body Hamiltonian, with a given energy and angular momentum.

Once the internal states are obtained, coupling potentials are computed using a generalized form of eq. (109)

$$V_{i;i'}(\vec{R}) = \int {\rm d}\vec{r}\, \phi_i^*(\vec{x},\vec{y})\left[U_{nA}(\vec{r}_1) + U_{nA}(\vec{r}_2) + U_{\alpha A}(\vec{r}_3)\right]\phi_{i'}(\vec{x},\vec{y}). \tag{116}$$

The formulation and first applications of this four-body CDCC method can be found in refs. [45] and [46]. As an illustrative example, we show in fig. 16 the elastic scattering of ^{6}He on ^{208}Pb at 22 MeV [47]. The solid line represents the four-body CDCC calculation, whereas the dashed line is the calculation omitting the breakup channels. The full calculation shows a very good agreement with the data from refs. [4,20]. We finally see that the disappearance of the Fresnel peak, already discussed in the context of the phenomenological OM, can be understood as a consequence of the strong coupling to the breakup channels.

From a coupled-channel calculation, one may infer an effective polarization potential, also called *trivial equivalent local polarization potential* (TELP). This is done rewriting the elastic channel equation as

$$\left[E - \varepsilon_0 - \hat{T}_{\vec{R}} - V_{0,0}(\vec{R})\right]\chi_0(\vec{R}) = \sum_{i\neq 0} V_{i,0}(\vec{R})\chi_i(\vec{R}) \equiv U_{\rm TELP}(R)\chi_0(\vec{R}). \tag{117}$$

In an angular momentum representation, in which actual calculations are standardly performed, one has an independent set of equations of each total angular momentum of the system (J). Each of these sets defines an angular-momentum-dependent TELP, $U^J_{\rm TELP}(R)$. An approximate TELP can be obtained by averaging the $U^J_{\rm TELP}(R)$ potentials

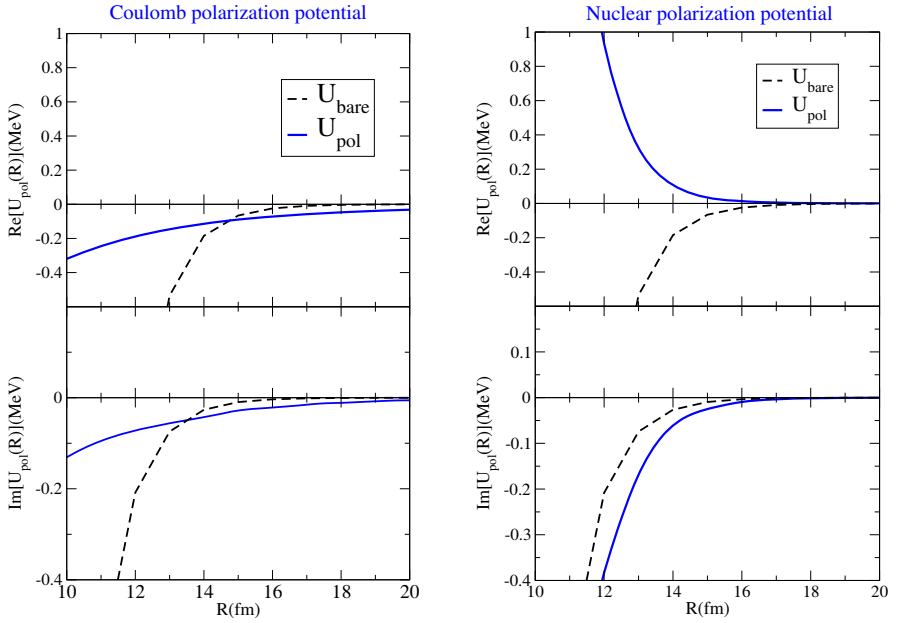

Fig. 17. – Coulomb (left) and nuclear (right) polarization potentials extracted from the ^{6}He + ^{208}Pb CDCC calculations of fig. 16. The *bare* potential corresponds to the ground-state diagonal potential. Adapted from ref. [49].

using as weights the cross sections for each J [48]. The result of such angular-momentum-averaged TELP extracted from the aforementioned CDCC calculation for ^{6}He + ^{208}Pb at 22 MeV is displayed in fig. 17. To isolate the Coulomb and nuclear effects two different calculations were performed, one including only Coulomb breakup couplings and the other including only nuclear breakup. The corresponding TELPs are shown in the left and right panels of this figure, respectively. The bare potential (dashed line) is represented in this case by the ground-state diagonal potential $V_{0,0}$. The most noticeable feature of the Coulomb polarization potential is its long range, with respect to the bare potential. This is consistent with the behaviour of the phenomenological optical potential discussed in sect. **5**˙2. Note also the different character of the Coulomb and nuclear real parts: the former is attractive (*i.e.*, negative; recall the adiabatic limit, eq. (72)), whereas the latter is strongly repulsive. The nuclear polarization potential is also found to be of long range.

7˙1.3. Connection with the Faddeev formalism. The CDCC method was originally devised as a physically sound and numerically appealing *ansatz* for the three-body wave function, rather than as a formally rigorous solution of the three-body problem. This rigorous solution was provided by Faddeev in the '60s [50], who showed that this solution can be obtained from a system of coupled-differential equations, named the Faddeev equations after him. The numerical solution of these equations is very involved but, recently, it has been possible to solve them for a number of situations [51, 52], thus providing a valuable benchmark for more approximate models. These comparative studies

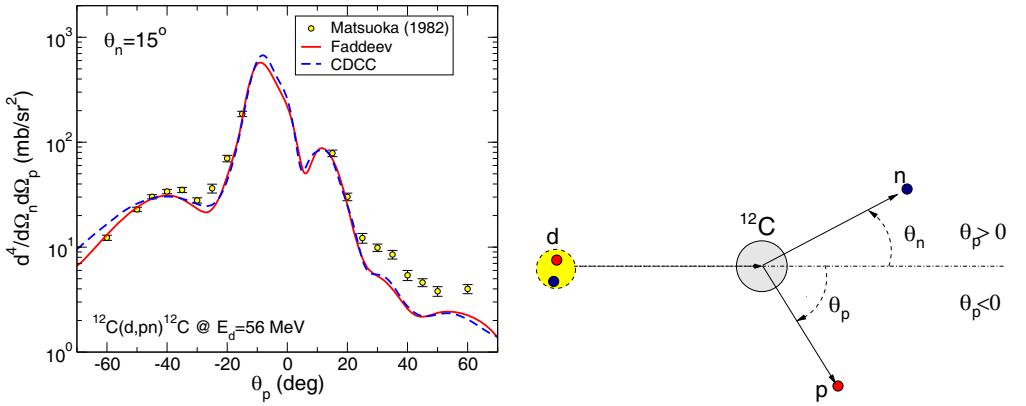

Fig. 18. – Breakup differential cross section for $^{12}\mathrm{C}(p,pn)^{12}\mathrm{C}$ at $E_d = 56\,\mathrm{MeV}$, as a function of the proton scattering angle and for a fixed neutron detection angle of 15°. The Faddeev and CDCC calculations are given by the solid and dashed lines, respectively. The circles are the data from ref. [53]. From ref. [51].

have shown that the elastic and breakup observables calculated with the CDCC method agree in general very well with the Faddeev solution (see fig. 18). However, there are also kinematical situations and observables [52] for which differences appear. This result calls for additional studies and, possibly, for extensions and improvements of the CDCC formalism.

7˙1.4. Microscopic CDCC. The standard CDCC method assumes a cluster (two-body or three-body) description of the projectile nucleus. This simplification has of course limitations and drawbacks. For example: i) it requires cluster-target optical potentials, which are not always well determined; ii) the extension to more than three bodies is very challenging and currently not available; iii) excitations of the fragments are ignored altogether or, at most, approximately included with some collective model. To overcome these problems, a microscopic version of the CDCC method (MCDCC) has been proposed by Descouvemont and co-workers [54, 55]. The method uses a many-body description of the projectile states, based on a cluster approximation, known as resonating group method (RGM). In the RGM, an eigenstate of the projectile Hamiltonian is written as an antisymmetric product of cluster wave functions. For example, for a ^{7}Li projectile, described as $\alpha + t$, the RGM wave function is expressed as

$$\phi_i(\xi_p) = \mathcal{A}\left[[\phi_\alpha \otimes \phi_t]^{1/2} \otimes Y_\ell(\Omega_\rho)\right]^{jm} g_i^{\ell j}(\rho), \tag{118}$$

where ϕ_α and ϕ_α are shell model wave functions of the α and t clusters, ℓ their relative orbital angular momentum and j the total spin. In eq. (118), $\vec{\rho}$ is the relative coordinate (see fig. 19), and $\mathcal{A}$ is the 7-body antisymmetrization operator which takes into account the Pauli principle among the 7 nucleons of the projectile. The function $g_i^{\ell j}(\rho)$ is determined from a Schrödinger equation associated with the projectile Hamil-

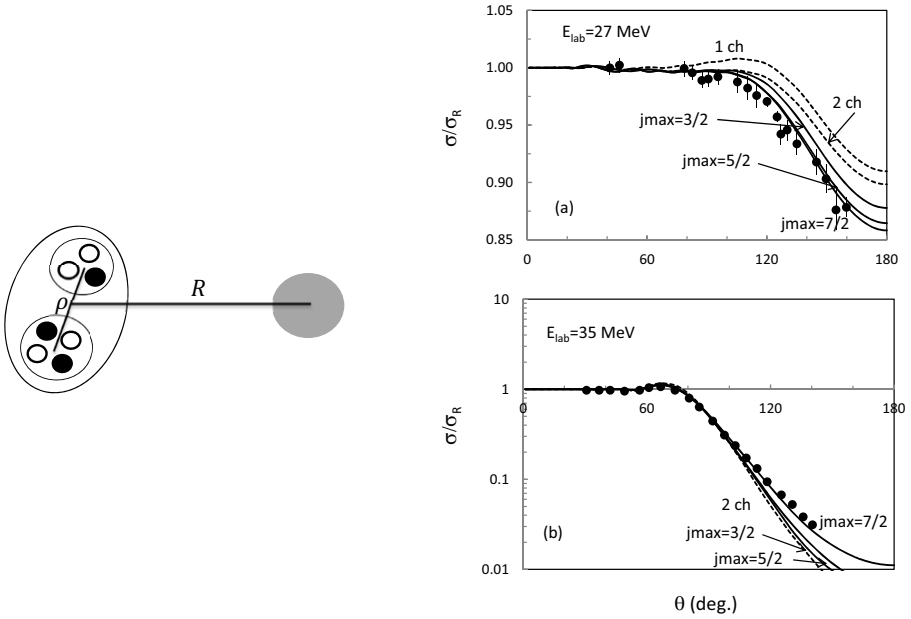

Fig. 19. – Left: schematic picture of the projectile-target system, with a microscopic cluster structure of the projectile. Right: $^7\mathrm{Li} + {}^{208}\mathrm{Pb}$ elastic cross section [56], relative to Rutherford, compared with microscopic CDCC calculations. Dotted lines represent the calculations without breakup channels and the solid lines are the full calculations with increasing $\alpha + t$ maximum angular momentum j_p. Taken from [54].

tonian. Continuum states are included using a pseudo-state basis. The projectile-target interaction is given by the sum of nucleon-nucleus interactions (instead of cluster-target interactions), for which reliable parametrizations are available.

Figure 19 shows an application of the method to the reaction $^7\mathrm{Li} + {}^{208}\mathrm{Pb}$ at near-barrier energies. Experimental data are compared with a one-channel calculation (only ^{7}Li g.s.), two-channels calculations (ground plus first excited state) and several CDCC calculations including continuum states up to a certain projectile angular momentum. It is seen that a good description of the data is achieved when a sufficiently large number of continuum states is included.

7˙2. *Exploring the continuum with breakup reactions.*

7˙2.1. Coulomb breakup. Breakup observables, which provide valuable information about the dissociated nucleus, can be computed within the CDCC formalism. An example is shown in fig. 20 for the reaction $^{11}\mathrm{Be} + {}^{208}\mathrm{Pb} \to n + {}^{10}\mathrm{Be} + {}^{208}\mathrm{Pb}$ at $E_{\mathrm{lab}} = 69\,\mathrm{MeV/u}$, measured at RIKEN [57]. The left panel is the angular distribution, with respect to the center of mass of the outgoing system $n + {}^{10}$Be. The different lines are the contributions coming from different continuum states of ^{11}Be ($j_p^\pi = 1/2^\pm$, $3/2^\pm$ and $5/2^\pm$), obtained from a XCDCC calculation [35]. The thick dashed line is the total contribution which, after convoluting with the experimental angular resolution, yields the

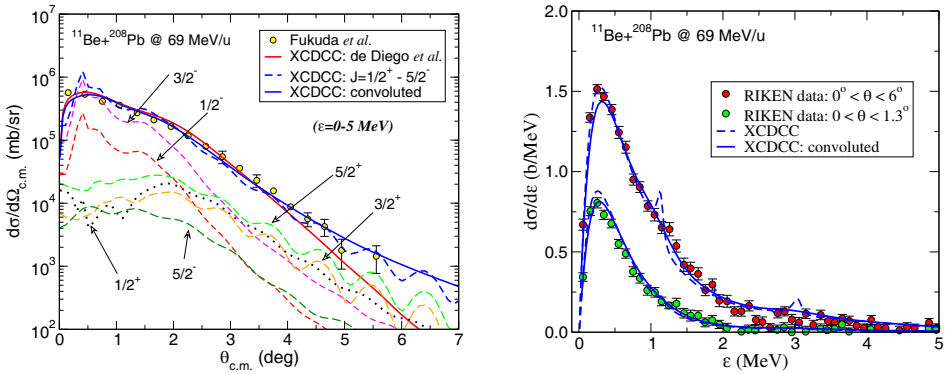

Fig. 20. – Left: experimental [57] and calculated (XCDCC) breakup angular distributions for the $^{11}\mathrm{Be} + {}^{208}\mathrm{Pb}$ reaction at 69 MeV/u. The separate contributions of the different continuum angular momenta are shown, as indicated by the labels. Right: measured and calculated angle-integrated relative-energy distribution for the outgoing n-^{10}Be system.

thick solid line. This is found to reproduce very well the data. Moreover, it is seen that the main contributions come from the $3/2^-$ and, to a lesser extent, the $1/2^-$ waves. Since the g.s. has $j_p = 1/2^+$ these correspond to dipole ($\lambda = 1$) transitions. At these very small scattering angles, the nuclear contribution is very small so the breakup is mostly due to the Coulomb interaction. The right panel shows the breakup cross section as a function of the relative energy of the n and ^{10}Be fragments, and integrated up to $\theta_{\mathrm{c.m.}} = 1.3°$ and $\theta_{\mathrm{c.m.}} = 6°$. The most notable feature is the enhanced breakup cross section near the breakup threshold which, in turn, is a consequence of the large $B(E1)$ strength at these energies. The dipole strength distribution is given by

$$\frac{\mathrm{d}B}{\mathrm{d}\varepsilon} = \frac{3}{4\pi}(Z_{\mathrm{eff}}e^2)\langle \ell 010|\ell' 0\rangle^2 \left| \int \mathrm{d}r\, r^3\, u^*_{k,\ell',s,j'}(r) u_\ell(r) \right|^2 , \tag{119}$$

where Z_{eff} is the effective charge ($Z_{\mathrm{eff}} = -Z/A$ for a neutron halo nucleus), and $u_\ell(r)$ and $u_{k,\ell',s,j'}(r)$ are the radial parts of the ground and scattering states with orbital angular momenta ℓ and ℓ', respectively. For weakly bound nuclei, the integral is dominated by the asymptotic region, which allows to replace the bound state by its asymptotic form and the scattering state by a plane wave. For a s to p transition, as it is the case of ^{11}Be, this yields [58]

$$\frac{\mathrm{d}B}{\mathrm{d}\varepsilon}(s \to p) = \frac{3\hbar^2}{\pi^2 \mu}(Z_{\mathrm{eff}}e)^2 \frac{\sqrt{\varepsilon_b}\varepsilon^{3/2}}{(\varepsilon + \varepsilon_b)^4} , \tag{120}$$

where ε_b is the separation energy. This distribution has a maximum at $\varepsilon = 3/5\varepsilon_b$. Hence, the smaller the binding energy, the closer this peak to the breakup threshold.

Figure 21 shows some $\mathrm{d}B/\mathrm{d}E_x$ distributions for the ^{11}Be nucleus extracted from Coulomb dissociation experiments [57,59], compared with two theoretical predictions, one

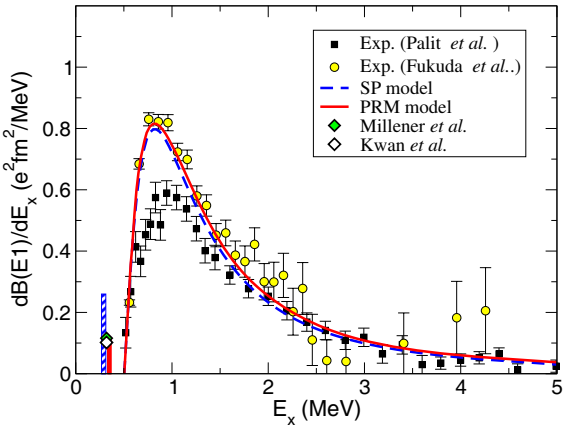

Fig. 21. – Experimental and calculated $B(E1)$ strength distributions for ^{11}Be as a function of the excitation energy $E_x = \varepsilon_b + \varepsilon$. The experimental distributions are from the Coulomb dissociation experiments of Palit *et al.* [59] and Fukuda *et al.* [57]. The filled diamond and the vertical bars represent the experimental and calculated $B(E1; 1/2^+ \to 1/2^-)$ value (in units of e^2fm^2) between the bound states of ^{11}Be [60, 61]. The theoretical distributions correspond to the single-particle model of ref. [62] and the particle-plus-rotor model of ref. [63].

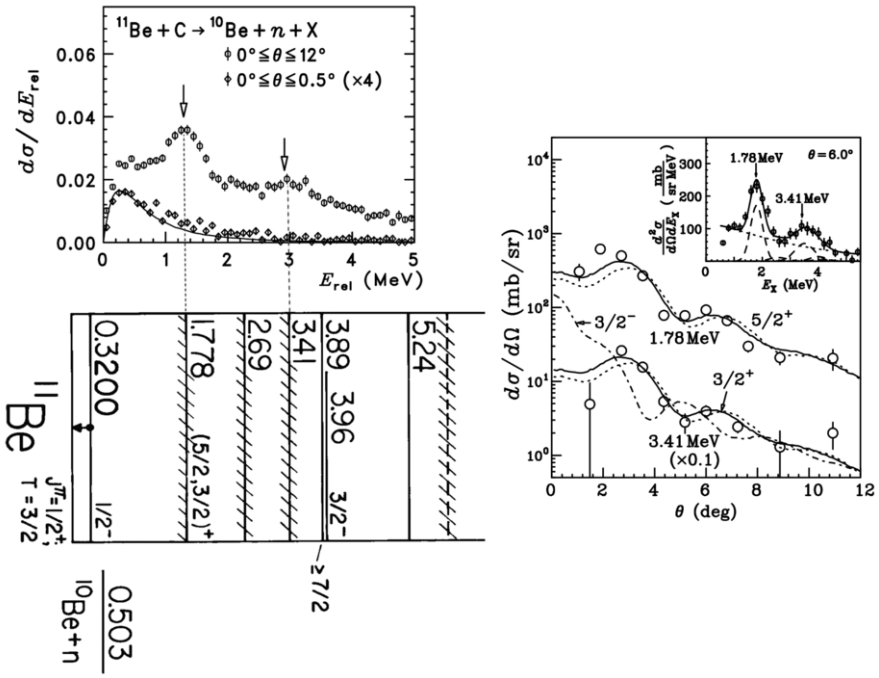

Fig. 22. – Left: experimental breakup cross section for ^{11}Be + ^{12}C at 69 MeV/u from ref. [57] (top) and ^{11}Be low-lying spectrum (bottom). Right: comparison of the angular distribution of the resonant peaks with DWBA calculations based on a collective model of ^{11}Be. Adapted from ref. [57].

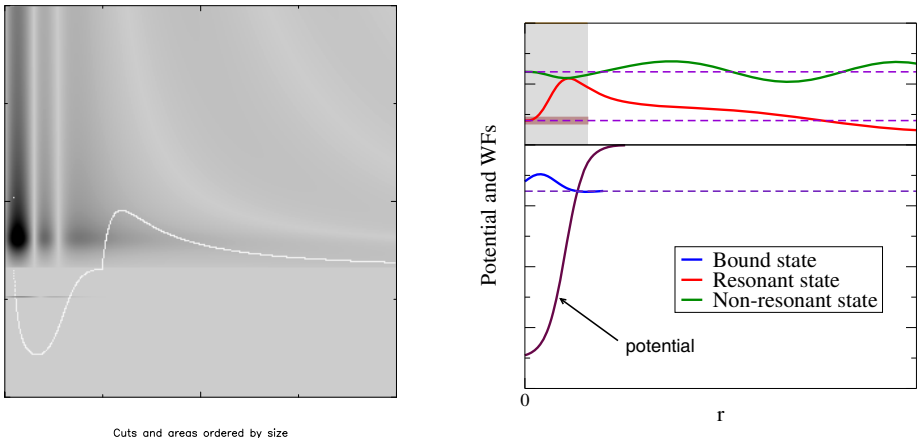

Fig. 23. – Left panel: potential well and density probabilities (square of wave functions). Courtesy of C.H. Dasso. Right panel: wave functions for a bound state, a non-resonant state and a resonant state.

based on a single-particle (SP) model of ^{11}Be and the other on a particle-plus-deformed-core (PRM). The large concentration of strength near threshold can be attributed to the low separation energy ($\varepsilon_b = 0.5\,\mathrm{MeV}$), according to the simple model just presented.

7˙2.2. Resonant nuclear breakup. The scattering of a weakly bound nucleus with a heavy target emphasizes the electric response of this nucleus, which can be quantified in terms of the electric reduced probability $\mathrm{d}B/\mathrm{d}E$. Conversely, when the nucleus scatters by a light target, such as ^{9}Be or ^{12}C, Coulomb breakup will be less important and nuclear breakup will gain importance. This kind of measurements are helpful to probe low-lying resonances which would be otherwise hindered by the dipole strength. An example of this is depicted in fig. 22, corresponding to the data for the $^{11}\mathrm{Be} + {}^{12}\mathrm{C}$ breakup reaction at 69 MeV/u. The upper panel shows the experimental data from ref. [57]. Superimposed on a smooth structure, one can see two peaks which, according to the energies shown in the spectrum of the bottom panel, correspond to low-lying resonances of ^{11}Be with spin-parity assignment $5/2^+$ and $3/2^+$.

Before addressing the problem of the theoretical analysis of these reactions, let us briefly recall the origin and meaning of continuum resonances. The simplest case is that of a potential resonance, illustrated in fig. 23. The left panel shows a potential well consisting on an attractive potential and a repulsive one (the latter can be due to the Coulomb interaction, the centrifugal barrier, $\hbar^2\ell(\ell+1)/2\mu r^2$, or the combination of both). In general, the potential will contain a finite number of bound states at negative energies and a infinite, and continuous, number of unbound states at positive energies. A particle moving in this well would remain confined in the case of bound states, but it would scape for the case of unbound states. However, due to the presence of the potential barrier, the system exhibits also quasi-bound structures (or resonances) at positive energies. For an infinitely high barrier, these states would be also permanently confined but, for a finite barrier, they will eventually decay by means of barrier penetration. If the resonant

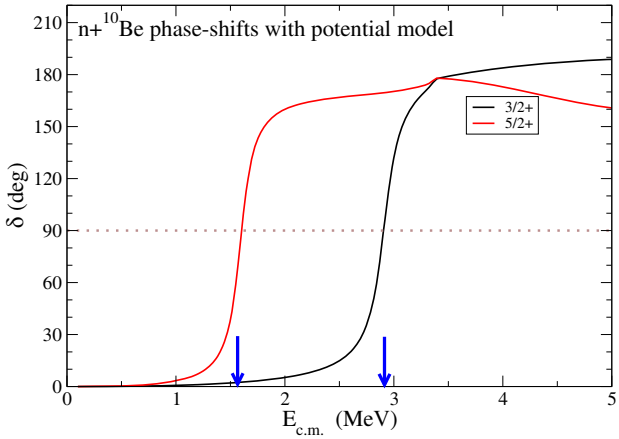

Fig. 24. – Elastic phase shifts for the $5/2^+$ and $3/2^+$ waves in $n + {}^{10}$Be elastic scattering using a deformed potential, which includes the coupling to the ^{10}Be(2^+) excited state. The vertical arrows indicate the nominal position of the resonances, defined as the energies for which the phase shift jumps over $\pi/2$.

region extends over an energy range Γ, the system will "survive" in this state over a period $\tau \approx \hbar/\Gamma$ (the lifetime of the resonance). In terms of their wave functions, these quasi-bound regions, or resonances, have therefore a higher presence probability. This is depicted in fig. 23 using a gray scale, with the darker regions corresponding to larger probabilities (given by the modulus squared of the wave function). One can observe a bound state and a resonant continuum region, with the node structure of the wave functions. The right panel of this figure shows three wave functions: a bound state wave function, a non-resonant continuum wave function, and a resonant wave function. It is seen that the resonant wave function presents a much larger probability inside the range of the potential as compared to the non-resonant one.

The resonant character is also apparent in the S-matrix and phase shifts (recall sect. **4**). For a potential resonance, the phase shift displays a rapid increase as a function of the continuum energy, when crossing the nominal energy of the resonance. This is shown in fig. 24 for the $n + {}^{10}$Be phase shifts, where the jumps at the position of the $5/2^+$ and $3/2^+$ resonances are clearly seen.

Whereas the energy differential cross section gives information on the position of resonances, the angular momentum assignment can be inferred from the shape of the angular distribution. These calculations have been performed using different formalisms: DWBA with collective form factors [57], semiclassical models [62], CDCC [64] and, more recently, also the generalized CDCC method with inclusion of ^{10}Be excitations, XCDCC [33]. In the right panel of fig. 22 we show the experimental angular distributions of the resonances (after subtracting the non-resonant background) compared with DWBA calculations based on a collective model of the ^{11}Be nucleus. From this analysis, the authors of ref. [57] concluded that these resonances were populated by $\lambda = 2$ transitions, which led the authors to propose the spin-parity assignments $5/2^+$ and $3/2^+$, respectively.

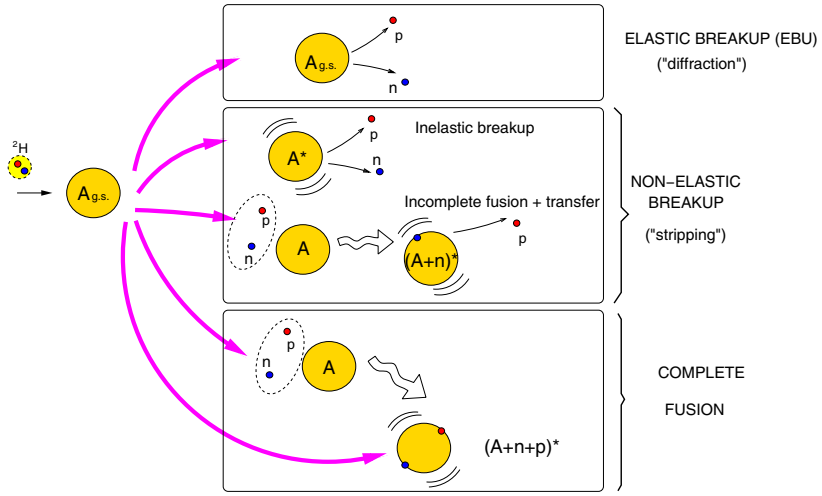

Fig. 25. – Pictorial representation of elastic and non-elastic breakup channels for a $d+A$ reaction.

7˙3. *The problem of inclusive breakup*. – In previous sections, we have considered only exclusive breakup processes in which the three fragments (b, x and A) survive after the collision and are observed in a definite internal state. In particular, when all fragments end up in their ground state, the process is called *elastic breakup* (EBU). In many experiments, however, the final state of one or more fragments is not determined in the final state. This is the case, for example, of reactions of the form $A(a,b)X$, in which only one of the projectile constituents (b in this case) is observed. The angular and energy distributions of the b fragments will contain contributions from all possible final states of the $x+A$ system. This includes the EBU channel, in which x and A remain in their ground state, but also x transfer, breakup accompanied by excitations of A, and $x+A$ fusion (named *incomplete fusion* (ICF)). These processes are schematically depicted in fig. 25 for a deuteron-induced reaction. These non-elastic breakup components (NEB) must be added to the EBU component to give the total inclusive breakup. Whereas the EBU contribution can be accurately calculated within the CDCC method and other approaches, the evaluation of NEB is more involved due to the large number of accessible states.

7˙3.1. The IAV model for inclusive breakup. The problem of inclusive breakup was addressed in the 1980s by several groups, which developed formal techniques to reduce the sum over final states to a closed form. We cite here the theory developed by Ichimura, Austern and Vincent (IAV) [28, 65, 66], in which the double differential cross section for NEB with respect to the angle and energy of the b fragments is given by

$$\left.\frac{\mathrm{d}^2\sigma}{\mathrm{d}E_b\mathrm{d}\Omega_b}\right|_{\mathrm{NEB}} = -\frac{2}{\hbar v_a}\rho_b(E_b)\langle\varphi_x(\vec{k}_b)|\,\mathrm{Im}[U_{xA}]|\varphi_x(\vec{k}_b)\rangle, \tag{121}$$

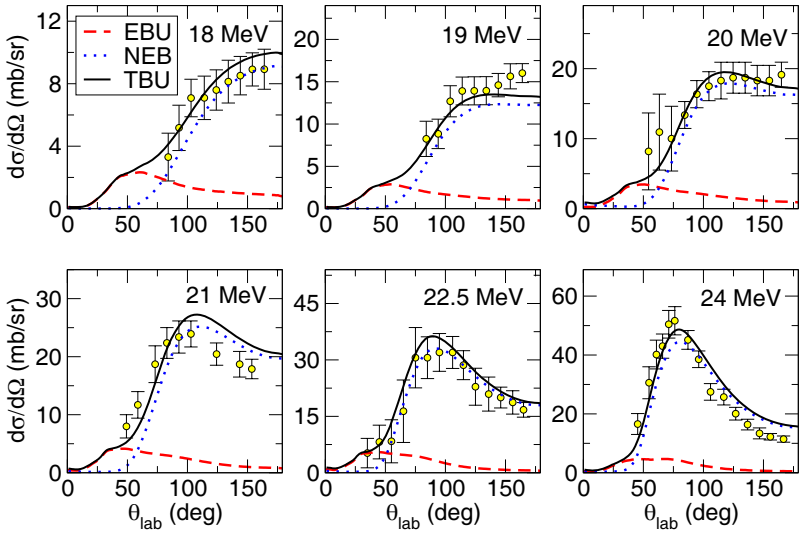

Fig. 26. – Energy distribution of α particles produced in the reaction ^{118}Sn(^{6}Li, α)X at the incident energies indicated by the labels. The dashed and dotted lines are the EBU and NEB contributions, and the solid line is their incoherent sum (TBU).

where $\rho_b(E_b) = k_b\mu_b/[(2\pi)^3\hbar^2]$, U_{xA} is the optical potential describing $x + A$ elastic scattering, and $\varphi_x(\vec{k}_b, \vec{r}_{xA})$ is the wave function describing the evolution of the x particle after dissociating from the projectile, when the core is scattered with momentum $\vec{k}_b$ and the target remains in its ground state. This function is obtained by solving the inhomogeneous equation

$$\left(E_x^+ - \hat{T}_x - U_{xA}\right)\varphi_x(\vec{k}_b, \vec{r}_{xA}) = \left(\chi_b^{(-)}(\vec{k}_b)|V_{\rm post}|\Psi^{3b}\right\rangle, \tag{122}$$

where $E_x = E - E_b$, $\chi_b^{(-)}(\vec{k}_b, \vec{r}_{bB})$ is the distorted wave describing the scattering of the outgoing b fragment with respect to the $B \equiv x + A$ system, obtained with some optical potential U_{bB}, and $V_{\rm post} \equiv V_{xb} + U_{bA} - U_{bB}$ is the post-form transition operator. This equation is to be solved with outgoing boundary conditions.

Although IAV suggested approximating the three-body wave function appearing in the source term of eq. (122), Ψ^{3b}, by the CDCC one, a simpler choice is to use the DWBA approximation $\psi^{3b} \approx \chi_a^{(+)}(\vec{R})\phi_a(\vec{r})$, where $\chi_a^{(+)}$ is a distorted wave describing $a + A$ elastic scattering, obtained with some optical potential, and ϕ_a is the projectile ground state wave function.

This DWBA version of the IAV model has been recently revisited by some groups, and applied to several deuteron [67-69] and ^{6}Li-induced reactions [69, 70], showing in most cases a very promising agreement with the existing data. Further applications and developments are in progress.

As an example, in fig. 26 we show the experimental and calculated energy distribution of α particles emitted in the reaction induced by ^{6}Li on ^{118}Sn at the incident energies indicated by the labels (adapted from ref. [70]). The EBU contribution (dashed line) was evaluated with the CDCC method whereas the NEB part (dotted line) was obtained with the IAV method, in its DWBA form. Interestingly, one can see that the inclusive α-yield is largely dominated by the NEB mechanism. The EBU is only important at small scattering angles (distant collissions, in a classical picture).

7˙3.2. Eikonal approximation to inclusive breakup. At sufficiently high energies, inclusive breakup is usually assumed to proceed via a one-step mechanism in which a portion of the projectile (a nucleon, for instance) is suddenly removed, without disturbing the rest of the system. So, for a reaction of the form $a+A \to b+X$, one assumes that the observed states of b are already contained in the ground state of the a system. The probability for the production of a given b state is therefore proportional to the parentage with the initial projectile. This parentage, that will be addressed also in sect. **9**, is directly linked to the normalization of the overlap function between the projectile wave function (a) and that of the core (b). For that, one can use the so-called *fractional parentage decomposition* (see *e.g.*, chapt. 7 of [10]), which is a technique to expand a given antisymmetrized many-body wave function in terms of antisymmetrized wave functions of two of its constituents. For the present purposes, it refers to the expansion of the a wave function in terms of wave functions of the b subsystem (the *core*). This expansion will contain, in general, one term (or more than one) involving exactly the state $\phi_b(\xi)$ observed in the experiment, plus additional terms containing other b states. Assuming for simplicity a single contribution we may write

$$\sqrt{a}\,\phi_a^*(\xi,\vec{r}) = \phi_b(\xi)\varphi_{bx}(\vec{r}) + \{\text{other } b \text{ states}\}, \tag{123}$$

where the factor $\sqrt{a}$ accounts for the fact that there are "a" identical nucleons that can be "isolated" from the rest "$a-1$" nucleons. Note that, for simplicity, we have omitted Clebsch-Gordan coefficients (needed to ensure conservation of angular momentum). This expansion defines the overlap function $\varphi_{bx}(\vec{r})$. From the previous equation

$$\sqrt{a}\int \mathrm{d}\xi\,\phi_a^*(\xi,\vec{r})\phi_b(\xi) \equiv \varphi_{bx}(\vec{r}). \tag{124}$$

The normalization of this overlap is known as *spectroscopic factor* (denoted hereafter as S),

$$S_{bx}^{a} = \int \mathrm{d}\vec{r}\,|\varphi_{bx}(\vec{r})|^2. \tag{125}$$

The evaluation of the overlap integrals (124) represents a difficult problem, because they require the knowledge of the many-body wave functions of a and b. For that reason, in

many practical applications, it is customary to approximate $\varphi_{bx}(\vec{r})$ by a single-particle wave function of x relative to the core b

$$\varphi_{bx}(\vec{r}) \to C^a_{bx}\tilde{\varphi}^{n\ell jI}_{bx}(\vec{r}), \tag{126}$$

where I is the spin of the core b, ℓ the orbital angular momentum and $\vec{j} = \vec{\ell} + \vec{s}$, with $\vec{s}$ the intrinsic spin of x. The single-particle wave function is obtained as a solution of a one-body equation of the form

$$\left[\hat{T}_{bx} + V_{bx} - \varepsilon_{\ell jI}\right]\tilde{\varphi}^{n\ell jI}_{bx}(\vec{r}) = 0, \tag{127}$$

where $\varepsilon_{\ell jI}$ is the effective separation energy of the particle x in the system a, when the core is left in the state I, and V_{bx} some mean-field potential, for example, of Woods-Saxon type. By definition, the solution $\tilde{\varphi}^{n\ell jI}_{bx}(\vec{r})$ is normalized to unity.

The coefficient C^a_{bx} is called spectroscopic amplitude and, according to (125), $|C^a_{bx}|^2 = S^a_{bx}$. The spectroscopic factor can be understood as the occupation number of the orbital ℓsj with the core in a given state I (of course, other quantum numbers may be required, but we use a loose notation here assuming that the core states are fully characterized by I). Clearly, the solution of eq. (127) will depend on the choice of the mean-field potential V_{bx}. Consequently, the spectroscopic amplitudes (and the corresponding spectroscopic factors), defined according to eq. (126), will depend on this choice. This model dependence leads to some ambiguity in the determination of spectroscopic factors([12]).

Returning to the evaluation of the inclusive breakup cross section, the nucleon removal inclusive cross section is then expressed as [72]:

$$\sigma_b = \sum_{n\ell j} S^a_{bx}(I; n\ell j)\sigma_{\rm sp}(I; n\ell j), \tag{128}$$

where $\sigma_{\rm sp}(I; n\ell j)$ is the single-particle cross section for the removal of a nucleon from the $n\ell j$ configuration, leaving the core in the state I. The sum extends over all allowed configurations $n\ell j$. Owing to the inclusive character of this reaction, $\sigma_{\rm sp}(I; n\ell j)$ contains contributions from elastic and non-elastic breakup mechanisms which, in the context of this intermediate-energy reactions, are referred to as *diffraction* and *stripping contributions*, respectively. Thus, we may write $\sigma_{\rm sp} = \sigma^{\rm str}_{\rm sp} + \sigma^{\rm diff}_{\rm sp}$.

([12]) Strictly speaking, the occupation probability of a single-particle orbital and its associated energies are not physical observables. This is because these single-particle states are solutions of a given mean-field potential, but the latter is model-dependent since there is an infinite number of ways of splitting the full many-body Hamiltonian into mean-field plus residual Hamiltonians. Still, for some standard mean-field potential (*e.g.* Hartree-Fock, Woods-Saxon with some "standard" parameters) they provide useful quantities for the interpretation of experimental data. A more formal discussion about the non-observability of spectroscopic factors can be found in ref. [71].

Hussein and McVoy [73] showed that a simple expression for the stripping contribution can be obtained using the so-called eikonal limit, in which one assumes that the projectile constituents move along straight-line trajectories, characterized by their asymptotic velocity and impact parameter ($\vec{b}$). In this limit, known as Glauber optical limit approximation, the distorted waves describing the scattering by an optical potential $U(\vec{R})$ can be expressed as

$$\chi(\vec{K},\vec{R}) = e^{i\vec{K}\cdot\vec{R}} \exp\left[-\frac{i}{2\hbar v}\int_{-\infty}^{z} \mathrm{d}z' U(b,z')\right], \tag{129}$$

where z is the component of the vector $\vec{R}$ along the z-axis. The quantity

$$S(b) = \exp\left[-\frac{i}{\hbar v}\int_{-\infty}^{\infty} \mathrm{d}z' U(b,z')\right] \tag{130}$$

is the so-called profile function, which is nothing but the elastic S-matrix as a function of the continuous parameter b.

In terms of these S-matrices, the stripping single-particle cross section can be written as

$$\sigma_{\mathrm{sp}}^{\mathrm{str}} = 2\pi \int b\,\mathrm{d}b \int \mathrm{d}\vec{r}\,|\varphi_{bx}(\vec{r})|^2 (1-|S_{xA}(b_x)|)^2 |S_{bA}(b_b)|^2, \tag{131}$$

where b_x and b_b are the impact parameters of the valence and core, respectively. This equation has an appealing and intuitive form: the integrand contains the product of the probabilities for the core being elastically scattered by the target, $|S_{bA}(b_b)|^2$, times the probability of the valence particle being absorbed, $(1-|S_{xA}(b_x)|)^2$. These probabilities are weighted by the projectile wave function squared, and integrated over all possible impact parameters.

Likewise, for the diffraction contribution, one obtains

$$\sigma_{\mathrm{sp}}^{\mathrm{diff}} = 2\pi \int b\,\mathrm{d}b\,\left[\langle\varphi_{bx}|\,|S_b S_x|^2|\varphi_{bx}\rangle - |\langle\varphi_{bx}|S_b S_x|\varphi_{bx}\rangle|^2\right]. \tag{132}$$

Comparison of knockout absolute cross sections with the eikonal model permits in principle the extraction of information about the spectroscopic factors. A recent compilation of these results can be found in ref. [74]. Usually, these analyses start from some theoretical spectroscopic factors, such as those obtained from truncated-space shell-model calculations, and compute the ratio $R_s = \sigma_b^{\mathrm{exp}}/\sigma_b^{\mathrm{theo}}$. Typically, one obtains $R_s < 1$, which has been interpreted as an effect of additional correlations not present in small-scale shell-model calculations, and which lead to a larger fragmentation of single-particle strengths (and the subsequent reduction of spectroscopic factors). Moreover, these studies have found a systematic dependence of this ratio on the separation energy of the removed nucleon, with R_s becoming smaller and smaller as the separation energy becomes larger (see right panel of fig. 27). Some authors have interpreted this result as an

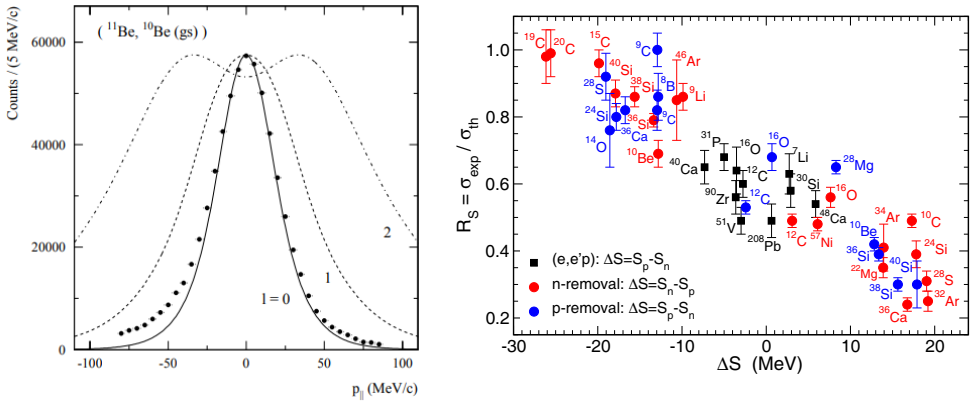

Fig. 27. – Left panel: longitudinal momentum distribution of the ^{10}Be fragments, in the rest frame of the projectile, from the knockout reaction ^{9}Be(^{11}Be,^{10} Be) at 60 MeV/u. The curves are eikonal calculations assuming a nucleon knockout from s, p, and d states. Quoted from ref. [75]. Right: compilation of the computed ratios R_s of the experimental and theoretical inclusive one-nucleon-removal cross sections for each of the projectile nuclei indicated, as a function of the parameter $\Delta S = \pm(S_p - S_n)$, used as a measure of the asymmetry of the neutron and proton Fermi surfaces. The red points are for neutron removal cases and the blue points those for proton removal. Taken from ref. [74].

indication of additional correlations (coming from tensor and short-range portion of the nucleon-nucleon interaction) [74]. However, this interpretation has been recently questioned by other authors, because this trend is apparently not observed in other reactions, such as transfer and (p, pN) reactions, to be discussed below. These results are still under debate.

Knockout reactions provide also valuable information about the angular momentum content of the struck nucleon. Assuming a sudden removal of a nucleon, momentum conservation in the projectile rest frame gives

$$\vec{k}_x = \frac{A-1}{A}\vec{k}_a - \vec{k}_b, \tag{133}$$

where $\vec{k}_x$ is the momentum of the struck particle. This expression shows that the latter can be directly inferred from the momentum of the observed residue b. Normally, either the component of the momentum along the beam direction (longitudinal momentum) or that perpendicular to it (transverse momentum) is used for this purpose. An example is shown in the left panel of fig. 27, corresponding to the longitudinal momentum of the ^{10}Be(g.s.) fragments produced in the ^{9}Be(^{11}Be,^{10} Be) reaction at 60 MeV/u, taken from ref. [75]. The calculations, based on the eikonal model, clearly support a dominance of the $\ell = 0$ component, as confirmed indeed by other experiments.

7˙4. *Quasi-free* (p, pN) *reactions*. – Breakup experiments of the form $A(p, pn)C$ and $A(p, 2p)C$ were used extensively in the 1970s as a tool to extract spectroscopic information

on proton-hole and neutron-hole states in nuclei, such as separation energies, spin-parity assignments, and occupation probabilities. In these reactions, an energetic proton beam ($E > 100\,\mathrm{MeV}$) collides with a stable target nucleus, removing one or more nucleons, and leaving a residual nucleus (C), either in its ground state, or in an excited state.

Theoretical analyses of (p, pN) reactions with stable nuclei have traditionally relied on the distorted-wave impulse approximation (DWIA) [76,77], which assumes that the binding potential of the removed particle can be neglected in comparison with the projectile-target kinetic energy. At sufficiently high energies (several hundreds of MeV per nucleon) this approximation is expected to be well justified.

In the DWIA formalism, the transition amplitude for a $A(p, pN)C$ reaction (with $A = C + N$ and $N = \{n, p\}$) is given by

$$\mathcal{T}_{if} = \left\langle \chi_p^{(-)}(\vec{r}_p)\chi_N^{(-)}(\vec{r}_N)|t_{pN}|\varphi_a\chi_{pA}^{(+)}\right\rangle, \tag{134}$$

where φ_a is the wave function of the removed nucleon relative to the "core" nucleus C and

$$t_{pN}(E) = V_{pN} + V_{pN}\frac{1}{E^+ - \hat{K}_r - \hat{K}_R - U_{pC} - U_{NC} - V_{pN}}V_{pN}, \tag{135}$$

which is the T-matrix describing the scattering of the incident proton with the struck nucleon in the presence of the interactions with the core. This is to be compared with the *free* p-N transition amplitude, *i.e.*,

$$t_{pN}^f(E_{pN}) = V_{pN} + V_{pN}\frac{1}{E_{pN}^+ - \hat{K}_r - V_{pN}}V_{pN}. \tag{136}$$

They are formally related by

$$t_{pN}(E) = t_{pN}^f(E - K_R - U_{pC} - U_{NC}). \tag{137}$$

At sufficiently high incident energies, one may neglect U_{pC} and U_{NC} in the propagator of eq. (135), thus resulting

$$\mathcal{T}_{if} = \left\langle \chi_p^{(-)}(\vec{r}_p)\chi_N^{(-)}(\vec{r}_N)|t_{pN}^f(E - \hat{K}_R)|\varphi_a\chi_{pA}^{(+)}\right\rangle. \tag{138}$$

This corresponds to the distorted-wave impulse approximation (DWIA). The amplitude t_{pN}^f is difficult to evaluate because it contains the operator $\hat{K}_R$. A simple approach to overcome this difficulty is by making the approximation $\hat{K}_R \approx \frac{1}{2}E$, so that $t_{pN}(E) \approx t_{pN}^f(\frac{1}{2}E)$. This approximation has been used, for example, in the context of proton inelastic scattering [78]. Another common approximation in (p, pN) analyses is the assumption that the T-matrix entering (138) varies sufficiently slowly with momenta, so that its arguments may be replaced by their asymptotic values. In this case, the matrix elements of this T-matrix between these asymptotic momenta can be singled out

from the integral, giving rise to a factorized expression for the scattering amplitude, and to cross sections which are proportional to the free NN cross section. Furthermore, if one describes the motion of the initial and outgoing nuclei by plane waves, one gets the plane wave impulse approximation (PWIA)

$$\mathcal{T}_{if}^{\mathrm{PWIA}} = t_{pN}\left(\vec{k}'_{pN}, \vec{k}_{pN}; E\right) F(\vec{Q}) \tag{139}$$

with the structure form factor $F(\vec{Q}) = \int \mathrm{d}\vec{r} e^{-i\vec{Q}\vec{r}} \varphi_a(\vec{r})$, where $\vec{Q} = \vec{k}'_p - \vec{k}_N - \frac{A}{A-1}\vec{k}_p$ is the so-called missing momentum. Expression (139) shows very clearly the connection between the (p, pN) cross section and the transferred momentum. Although formally appealing, the PWIA approximation is not expected to describe correctly the magnitude of the experimental cross sections because the distortion and absorption effects, arising from the interaction of the core with the incoming proton and with the outgoing nucleons, can be rarely neglected. In DWIA, these distortion effects are taken into account by the (complex) optical potentials used to generate the distorted waves.

In recent years, (p, pN) reactions have experienced a renewed interest because of the possibility of performing these measurements with unstable nuclei, using inverse kinematics, *i.e.*, bombarding a hydrogen target with an energetic radioactive beam. This technique is analogous to the knockout experiments with composite targets discussed in sect. **7**˙3.2, but it is expected to be sensitive to deeper regions of the nuclear density because of the larger penetrability of the proton probe. In addition to the DWIA method (*e.g.* [79]), some other approaches are being developed and applied to these reactions, such as the so-called transfer to the continuum method, which is based on the CDCC method [80], and the Faddeev formalism [81, 82].

While *normal* kinematics experiments $A(p, pN)C$ provide typically exclusive observables corresponding to specific outgoing angles of the emitted nucleons, in inverse kinematics experiments the measured observables usually correspond to parallel or longitudinal momentum distributions of the residual nucleus C. As we have seen in the case of knockout reactions between composite nuclei, the shape of these momentum distributions carries information on the orbital angular momentum of the struck nucleon. Moreover, their magnitude is proportional to the occupation probability of the orbital from which this nucleon has been removed (spectroscopic factor). Therefore, the comparison of the measured distributions with a suitable reaction framework provides useful spectroscopic information.

8. – Breakup reactions II: semiclassical methods

When the de Broglie wavelength of the projectile is small compared to some characteristic distance of the collision process one may describe its motion in terms of classical trajectories. This provides a more intuitive and, normally, mathematically simpler description of the reaction. This approximation cannot be done to the internal motion of the nucleons inside the nucleus because their typical wavelength is of the same order as the size of the nucleus and hence quantum effects are important (for example, for a

typical energy of 30 MeV, $v \sim c/5$ and so $\lambda\!\!\!^{-} = \hbar/p \approx 1\,\mathrm{fm}$). The methods in which the internal excitations are treated quantum-mechanically, while the projectile-target relative motion is treated classically, are called semiclassical methods. There exists in the literature a large variety of such models [62, 83-87]. As an example, we discuss here the one developed by Alder and Winther and its application to Coulomb excitation experiments.

8˙1. *The semiclassical formalism of Alder and Winther.* – In its simplest form, the theory of Alder and Winther [21] assumes that the projectile moves along a classical trajectory, which is not much affected by the internal excitations of the colliding nuclei. This means that

$$\frac{\Delta\ell}{\ell} \ll 1 \qquad \text{and} \qquad \frac{\Delta\varepsilon_n}{E} \ll 1.$$

The projectile-target interaction is assumed to consist of two terms: $V(\vec{R},\xi) = V_0(\vec{R}) + V_{\mathrm{coup}}(\vec{R},\xi)$, where $V_0(\vec{R})$ is independent of the internal coordinates and determines the classical trajectory $\vec{R}(t)$. The time evolution of the total wave function of the system verifies the Schrödinger equation

$$i\hbar\frac{\mathrm{d}\Psi(\xi,\theta,t)}{\mathrm{d}t} = \Big[V(\vec{R}(\theta,t),\xi) + H_p(\xi)\Big]\,\Psi(\xi,\theta,t), \tag{140}$$

subject to the initial condition $|\Psi(-\infty)\rangle = |0\rangle$.

In the spirit of the coupled-channels method, the total wave function is expanded in the internal states of the projectile Hamiltonian $[H_p(\xi) - \varepsilon_n]\phi_n(\xi) = 0$

$$\Psi(\xi,\theta,t) = \sum_{n=0} c_n(\theta,t)e^{-i\varepsilon_n t/\hbar}\phi_n(\xi), \tag{141}$$

which, when inserted in (140), gives rise to the following set of coupled equations for the expansion coefficients:

$$i\hbar\frac{\mathrm{d}c_n(\theta,t)}{\mathrm{d}t} = \sum_m e^{-i(\varepsilon_m-\varepsilon_n)t/\hbar}V_{nm}(\theta,t)c_m(\theta,t), \tag{142}$$

with the initial condition $c_n(\theta,-\infty) = \delta_{n0}$. The time-dependent coupling potentials $V_{nm}(\theta,t)$ are given by

$$V_{nm}(\theta,t) = \int \mathrm{d}\xi\phi_n^*(\xi)V(\vec{R}(\theta,t),\xi)\phi_m(\xi). \tag{143}$$

Once the coefficients are obtained, the excitation probability for a $0 \to n$ transition is given by

$$P_n(\theta) = |c_n(\theta,\infty)|^2,$$

and the differential cross section

$$\left(\frac{\mathrm{d}\sigma}{\mathrm{d}\Omega}\right)_{0\to n} = \left(\frac{\mathrm{d}\sigma}{\mathrm{d}\Omega}\right)_{\mathrm{clas}} P_n(\theta),$$

where $(\mathrm{d}\sigma/\mathrm{d}\Omega)_{\mathrm{clas}}$ is the classical differential elastic cross section which, for a pure Coulomb case, coincides with the Rutherford cross section.

Due to the conservation of the total probability (flux), one has

$$\sum_n P_n(t) = \sum_n |c_n(t)|^2 = 1.$$

When the couplings are weak, one may solve (142) perturbatively, assuming that $c_0 \approx 1$ and $c_n \ll 1$ for $n > 0$. This gives the first-order solution

$$c_n(\theta) \equiv c_n(\theta, \infty) \simeq \frac{1}{i\hbar} \int_{-\infty}^{\infty} e^{-i(\varepsilon_0 - \varepsilon_n)t/\hbar} V_{n0}(\theta, t)\mathrm{d}t. \tag{144}$$

In the important case of pure Coulomb scattering, which was the case studied in detail by Alder and Winther [21], one finds analytical expressions for the excitation probabilities. In particular, the first-order excitation probability for a $0 \to n$ transition, due to the electric Coulomb operator $E\lambda$, results

$$\left(\frac{\mathrm{d}\sigma}{\mathrm{d}\Omega}\right)_{0\to n} = \left(\frac{Z_t e^2}{\hbar v}\right)^2 \frac{B(E\lambda, 0 \to n)}{e^2 a_0^{2\lambda-2}} f_\lambda(\theta, \xi), \quad (\theta < \theta_{\mathrm{gr}}), \tag{145}$$

which is valid only for angles smaller than the grazing one (θ_{gr}) and where a_0 is half of the distance of closest approach in a head-on collision, $\xi_{0\to n} = \frac{(\varepsilon_n - \varepsilon_0)}{\hbar} \frac{a_0}{v}$ is the adiabaticity parameter and $f_\lambda(\theta, \xi)$ is an analytic function, depending on the kinematical conditions, but independent of the structure of the projectile.

For weakly bound nuclei, the excitation occurs to unbound (continuum) states. The previous formula can be generalized to

$$\frac{\mathrm{d}\sigma(E\lambda)}{\mathrm{d}\Omega\,\mathrm{d}\varepsilon} = \left(\frac{Z_t e^2}{\hbar v}\right)^2 \frac{1}{e^2 a_0^{2\lambda-2}} \frac{\mathrm{d}B(E\lambda)}{\mathrm{d}\varepsilon} \frac{\mathrm{d}f_\lambda(\theta, \xi)}{\mathrm{d}\Omega}, \quad (\theta < \theta_{\mathrm{gr}}), \tag{146}$$

where $\mathrm{d}f_\lambda(\theta, \xi)/\mathrm{d}\Omega$ is also a well-defined analytic function and $\mathrm{d}B(E\lambda)/\mathrm{d}\varepsilon$ is the electric reduced probability to the continuum states.

An appealing feature of these formulas is that they provide a neat separation between the structure of the projectile (through $B(E\lambda)$) and the reaction dynamics. This separation allows in principle to extract the $\mathrm{d}B(E\lambda)/\mathrm{d}\varepsilon$ distribution from the analysis of small-angle Coulomb dissociation data. For that, one can integrate the double differential

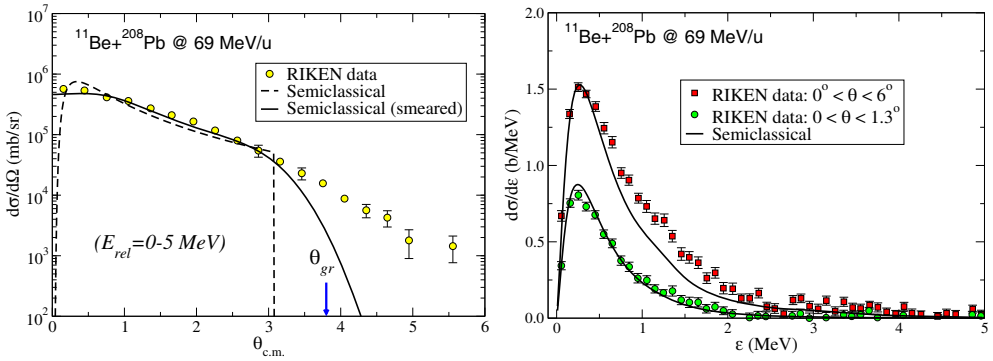

Fig. 28. – Left: angular distribution of the c.m. of the outgoing $n + {}^{10}$Be system, following the breakup of ^{11}Be on ^{208}Pb at 69 MeV/u. Right: relative energy distribution between the $n + {}^{10}$Be fragments, integrated up to two different maximum angles, as indicated by the labels. The curves are semiclassical calculations based on the theory of Alder and Winther and smeared with the experimental resolution.

cross section (146) up to a maximum angle ($\theta_{\max}$) such that for $\theta < \theta_{\max}$ the breakup can be assumed to be purely Coulomb and hence (146) is valid ($\theta_{\max} < \theta_{\rm gr}$). This gives

$$\frac{\mathrm{d}\sigma}{\mathrm{d}\varepsilon}(\theta < \theta_{\max}) = \int_0^{\theta_{\max}} \frac{\mathrm{d}\sigma(E\lambda)}{\mathrm{d}\Omega\,\mathrm{d}\varepsilon}\mathrm{d}\Omega \propto \frac{\mathrm{d}B(E\lambda)}{\mathrm{d}\varepsilon}\,. \tag{147}$$

An application of this method to the $^{11}\mathrm{Be} + {}^{208}\mathrm{Pb}$ reaction discussed above is shown in fig. 28. The curves are the result of semiclassical calculations, convoluted with the experimental energy and angular resolutions. In the left panel, it is apparent that the semiclassical calculation reproduces well the data up to $\theta_{\rm c.m.} \sim 3°$. For larger angles, the assumption of pure Coulomb scattering is no longer accurate (the grazing angle is estimated to be $\theta_{\rm gr} = 3.8°$). In the right panel, the corresponding relative-energy distributions are compared with the data, for two angular cuts. It is seen that, for the wider angular range ($\theta_{\rm c.m.} < 6°$), there is some underestimation of the data, which may be attributed to the omission of nuclear effects and higher Coulomb multipoles.

The assumption of pure Coulomb trajectories can be relaxed, at the expense of losing some of the simplicity of the method. A compelling application is shown in fig. 29 (taken from [88]) where semiclassical coupled-channels calculations, using trajectories modified by the nuclear interaction, are compared with CDCC calculations for the breakup angular distribution of the $^{8}\mathrm{B} + {}^{58}\mathrm{Ni}$ reaction at the near-barrier energy of 26 MeV.

8˙2. *Dynamic Coulomb polarization potential from the AW theory.* – We have seen in sect. **5˙3** that the effect of the coupling to the breakup channels due to the dipole Coulomb interaction is given in the adiabatic limit by a simple analytical form. The resultant expression (eq. (72)) is purely real, and depends on the structure of the dissociated nucleus through the so-called polarizability parameter.

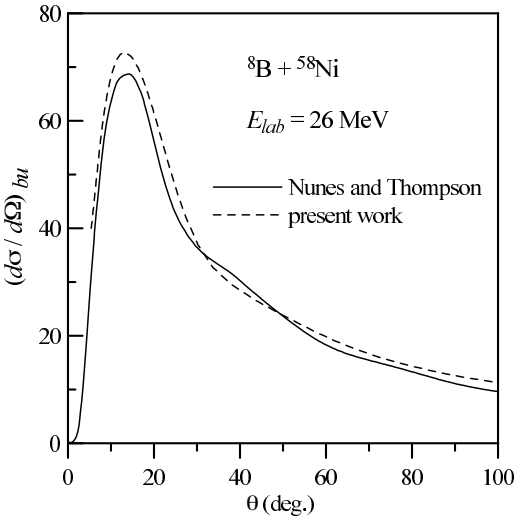

Fig. 29. – Breakup of $^8\mathrm{B} \to {}^7\mathrm{Be} + p$ on a ^{58}Ni target at 26 MeV. Coupled-channel semiclassical calculations, using Coulomb+nuclear trajectories, are compared with CDCC calculations, which include also nuclear and Coulomb couplings. Quoted from [88].

This adiabatic expression assumes that the excitation energies are large and, therefore, is not applicable to the Coulomb breakup of very weakly bound nuclei, for which the average excitation energies are typically small (of the order of 1 MeV or less).

A non-adiabatic (also called *dynamic*) polarization potential can be derived from the Alder and Winther theory [89, 90]. For that, we consider the second-order process in which the projectile is excited to a continuum state due to the dipole Coulomb interaction ($V_1(t)$) and then de-excites, returning to the ground state. The situation is schematically

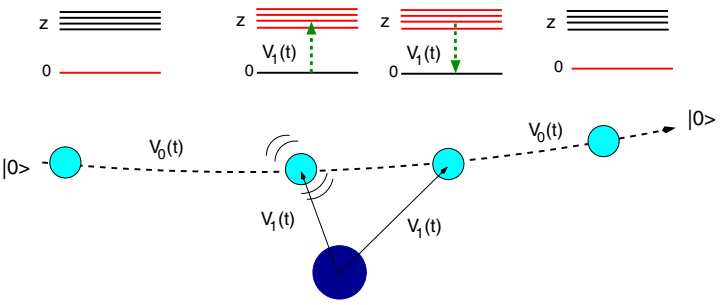

Fig. 30. – Second-order process describing the excitation and de-excitation of a nucleus moving along a classical trajectory determined by the potential $V_0(t)$, due to the action of the potential $V_1(t)$.

depicted in fig. 30. The amplitude probability for this process is given by

$$c_n^{(2)} = \sum_z \left(\frac{-i}{\hbar}\right)^2 \int_{-\infty}^{+\infty} \mathrm{d}t \langle n|V_1(t)|z\rangle \exp\left\{\frac{i}{\hbar}(\varepsilon_n - \varepsilon_z)t\right\} \times \int_{-\infty}^{t} \mathrm{d}t' \langle z|V_1(t')|0\rangle \exp\left\{\frac{i}{\hbar}(\varepsilon_z - \varepsilon_0)t'\right\}, \tag{148}$$

where $|z\rangle$ denotes the intermediate states populated during the reaction. Then, one requires that this second-order amplitude coincides with the first-order amplitude associated with the polarization potential for all classical trajectories corresponding to a given scattering energy. This gives rise to

$$U_{\mathrm{pol}}(R) = -\frac{4\pi}{9}\frac{Z_t^2 e^2}{\hbar v}\frac{1}{(R-a_o)^2 R} \times \int_0^\infty \mathrm{d}\varepsilon \frac{\mathrm{d}B(E1,\varepsilon)}{\mathrm{d}\varepsilon}\left[g\left(\frac{R}{a_o}-1,\xi\right) + if\left(\frac{R}{a_o}-1,\xi\right)\right], \tag{149}$$

where g and f are analytic functions defined as

$$f(z,\xi) = 4\xi^2 z^2 \exp(-\pi\xi) K''_{2i\xi}(2\xi z), \tag{150}$$

$$g(z,\xi) = \frac{P}{\pi}\int_{-\infty}^{\infty} \frac{f(z,\xi')}{\xi - \xi'}\mathrm{d}\xi', \tag{151}$$

and ξ is the Coulomb adiabaticity parameter corresponding to the excitation to the continuum energy ε of the nucleus. An important feature of this potential is that when the breakup energy ε_b is large enough, the purely real adiabatic dipole potential is reobtained. In the opposite limit, for small breakup energies, $f(\frac{R}{a_o}-1,\xi) \to 1$ and $g(\frac{R}{a_o}-1,\xi) \to 0$, and the polarization potential becomes purely imaginary, depending on R as $1/[(R-a_o)^2 R]$.

As an example, we show in the left part of fig. 31 the elastic scattering data for ^{6}He + ^{208}Pb at 22 MeV compared with the optical model calculations obtained with a bare potential alone (dashed) and with the bare plus the Coulomb dipole polarization (CDP) potential (solid line). For the bare interaction we have used an optical potential for the nearby projectile ^{6}Li, which has a similar structure to that of ^{6}He but which does not exhibit the strong dipole excitation mechanism. The elastic cross section predicted by the bare potential presents a Fresnel-like diffraction pattern, not observed in the data. The inclusion of the CDP reduces significantly the elastic cross section and suppresses the Fresnel peak. On the right, the real and imaginary parts of the bare and CDP potentials are shown. Their most remarkable feature is their long range, which was anticipated from the optical model analysis of fig. 6, and is associated with the long range of the dipole Coulomb couplings, as we have already discussed in the context of the CDCC method.

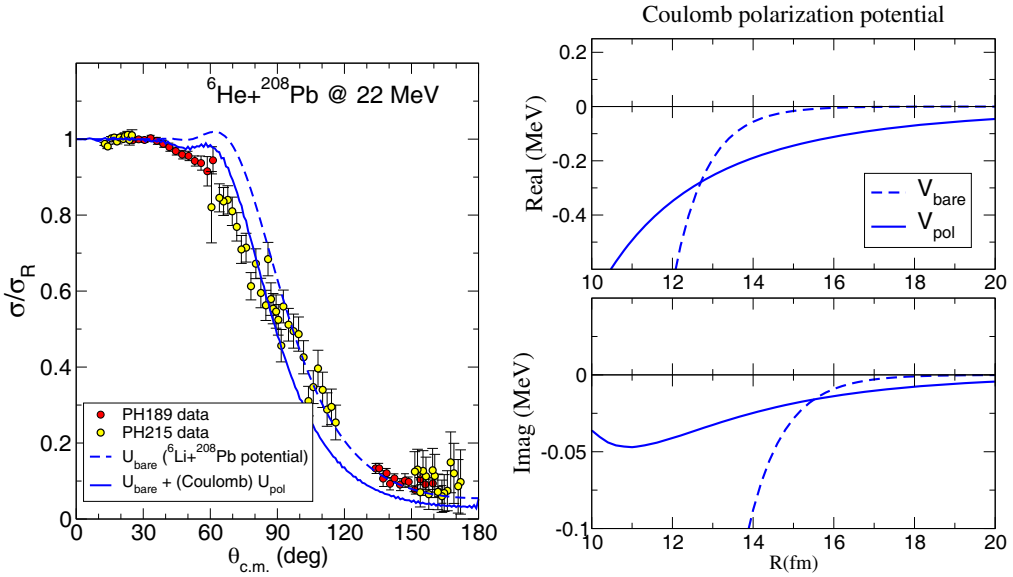

Fig. 31. – Left: elastic scattering differential cross section for $^6\mathrm{He} + {}^{208}\mathrm{Pb}$ at $E_{\mathrm{lab}} = 22\,\mathrm{MeV}$. The dashed line is a single-channel calculation performed with a *bare* potential, given by a $^6\mathrm{Li} + {}^{208}\mathrm{Pb}$ optical potential. The solid line is the optical model calculation obtained with the bare plus dynamic Coulomb polarization potential of eq. (149). Right: real and imaginary parts of the bare and CDP potentials.

9. – Transfer reactions

Another example of direct reaction is that of transfer reactions. In this kind of processes, the projectile and target exchange one or more nucleons. Compared to inelastic scattering, the modeling of transfer reactions has the added difficulty that the initial and final nuclei are different so one has to deal with two different mass partitions (see fig. 32). The analysis of transfer reactions has been traditionally performed using the DWBA method. In the next section, we derive the DWBA formula from the exact transition amplitude.

9˙1. *An exact expression for the transfer amplitude.* – Following the notation introduced in the introductory section, the initial and final partitions will be denoted as α and β, respectively. Accordingly, the full Hamiltonian can be written in two different forms, depending on whether we choose the coordinates of the initial (left part of fig. 32) or the final (right part) configuration. For example, if we choose the final (*post*) representation, it reads

$$H = \hat{T}_{\vec{R}'} + H_\beta(\xi_\beta) + V_\beta(\vec{R}', \vec{r}') = \hat{T}_{\vec{R}'} + \underbrace{H_B(\xi', \vec{r}') + H_b(\xi)}_{H_\beta(\xi_\beta)} + \underbrace{V_{bx} + U_{bA}}_{V_\beta(\vec{R}', \vec{r}')}, \tag{152}$$

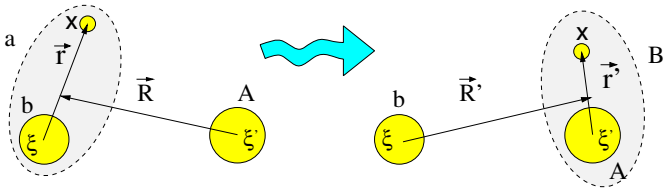

Fig. 32. – Schematic representation of a transfer reaction, showing the relevant coordinates for the initial and final states.

where we have used the notation $\xi_\beta = \{\xi, \xi', \vec{r}'\}$ to denote the set of internal coordinates.

The total wave function, which must contain at least the incident (elastic) and the transfer channel of interest, must behave asymptotically according to eq. (8). To obtain the transfer scattering amplitude ($f_{\beta,\alpha}(\theta)$ in that equation), we could proceed as in the coupled-channels method, by writing an *ansatz* for $\Psi^{(+)}_{\vec{K}}(\vec{R}, \xi_\alpha)$ which includes the desired transfer channels β. This procedure gives rise to a set of coupled integro-differential equations involving non-local couplings. This is the so-called Coupled Reaction Channels (CRC) method [91, 92]. This is in fact the procedure followed by some computer codes, such as the popular code `FRESCO` [93]. From the formal point of view, a more straightforward derivation of the scattering amplitude can be obtained making use of the general expression (26) for the transition amplitude, which we rewrite as

$$\mathcal{T}^{\text{post}}_{\beta,\alpha} = \iint \chi^{(-)*}_\beta(\vec{K}', \vec{R}')\Phi^*_\beta(\xi_\beta)(V_\beta - U_\beta)\Psi^{(+)}_{\vec{K}}(\vec{R}, \xi_\alpha)\mathrm{d}\xi_\beta \mathrm{d}\vec{R}', \tag{153}$$

where $\Psi^{(+)}_{\vec{K}}(\vec{R}, \xi_\alpha)$ is the exact wave function and $\Phi_\beta(\xi_\beta)$ represents the internal state of the final nuclei, which are eigensolutions of the internal Hamiltonian H_β

$$H_\beta \Phi_\beta(\xi_\beta) = \varepsilon_\beta \Phi_\beta(\xi_\beta), \quad \text{with } \Phi_\beta(\xi_\beta) = \phi_b(\xi)\phi_B(\xi', \vec{r}'),$$

where ε_β represents the sum of the internal energies of the outgoing nuclei. Finally, $\chi^{(-)}_\beta$ is the time-reversal of $\chi^{(+)}_\beta$, which is the distorted wave generated by the auxiliary potential U_β

$$\left[E - \varepsilon_\beta - \hat{T}_{\vec{R}'} - U_\beta(\vec{R}')\right] \chi^{(+)}_\beta(\vec{K}', \vec{R}') = 0. \tag{154}$$

9˙2. *The DWBA approximation.* – The transition amplitude (153) can not be directly evaluated because it contains the exact scattering of the many-body problem ($\Psi^{(+)}_{\vec{K}}$). A solvable formula can be obtained making the approximation

$$\Psi^{(+)}_{\vec{K}}(\vec{R}, \xi_\alpha) \approx \chi^{(+)}_\alpha(\vec{K}, \vec{R})\Phi_\alpha(\xi_\alpha), \tag{155}$$

where $\Phi_\alpha(\xi_\alpha) = \phi_a(\xi, \vec{r})\phi_A(\xi')$ and where the distorted wave $\chi^{(+)}_\alpha$, which describes the projectile-target relative motion in the entrance channel, is generated with some potential

U_α, that is

$$\left[E - \varepsilon_\alpha - \hat{T}_{\vec{R}} - U_\alpha(\vec{R}\,)\right] \chi_\alpha^{(+)}(\vec{K}, \vec{R}\,) = 0. \tag{156}$$

Typically, U_α is chosen so as to reproduce the elastic scattering differential cross section. This approximation gives rise to the DWBA scattering amplitude

$$\mathcal{T}_{\beta,\alpha}^{\rm DWBA} = \iint \chi_\beta^{(-)*}(\vec{K}', \vec{R}')\Phi_\beta^*(\xi_\beta)(V_\beta - U_\beta)\chi_\alpha^{(+)}(\vec{K}, \vec{R}\,)\Phi_\alpha(\xi_\alpha)\mathrm{d}\xi_\beta\,\mathrm{d}\vec{R}'. \tag{157}$$

Let us consider for simplicity the important (d,p) case. The post-form interaction V_β is given by $V_\beta = V_{pn} + U_{pA}$. Moreover, the internal states and internal coordinates are given in this case by

$$\Phi_\alpha(\xi_\alpha) = \varphi_d(\vec{r}\,)\phi_A(\xi'), \qquad \xi_\alpha = \{\xi', \vec{r}\,\}, \tag{158}$$

$$\Phi_\beta(\xi_\beta) = \Phi_B(\xi', \vec{r}\,'), \qquad \xi_\beta = \{\xi', \vec{r}\,'\}, \tag{159}$$

where $\vec{r}$ is the proton-neutron relative coordinate and $\vec{r}\,'$ that of the transferred neutron relative to the target nucleus (cf. fig. 32). Moreover, for not very light targets, we can further approximate: $U_{pA} \approx U_{pB} \Rightarrow V_{pn} + U_{pA} - U_{pB} \approx V_{pn}(\vec{r}\,)$. The amplitude is then dominated by the V_{pn} interaction and hence by small p-n separations. Then, (157) becomes in the (d,p) case

$$\mathcal{T}_{d,p}^{\rm DWBA} = \iint \chi_p^{(-),*}(\vec{K}_p, \vec{R}')\Phi_B^*(\xi', \vec{r}\,')V_{pn}(\vec{r}\,)\chi_d^{(+)}(\vec{K}_d, \vec{R}\,)\varphi_d(\vec{r}\,)\phi_A(\xi')\mathrm{d}\xi_\beta\mathrm{d}\vec{R}'. \tag{160}$$

The integral in the target coordinates ξ involves the overlap function between the target A and the residual nucleus B wave functions. Resorting to eqs. (124), (125) and (126) we end up with the transition amplitude

$$\mathcal{T}_{d,p}^{\rm DWBA} = C_{An}^B \iint \chi_p^{(-)*}(\vec{K}_p, \vec{R}')\tilde{\varphi}_{An}^{\ell jI}(\vec{r}\,')^*\, V_{pn}(\vec{r}\,)\, \chi_d^{(+)}(\vec{K}_d, \vec{R}\,)\, \varphi_d(\vec{r}\,)\mathrm{d}\vec{r}\,'\mathrm{d}\vec{R}', \tag{161}$$

and the corresponding differential cross section

$$\left(\frac{\mathrm{d}\sigma}{\mathrm{d}\Omega}\right)_{\beta,\alpha} = \frac{\mu_\alpha\mu_\beta}{(2\pi\hbar^2)^2} S_{An}^B \times \left| \iint \chi_p^{(-)*}(\vec{K}_p, \vec{R}'\,)\, \tilde{\varphi}_{An}^{\ell jI}(\vec{r}\,')^*\, V_{pn}(\vec{r}\,)\, \chi_d^{(+)}(\vec{K}_d, \vec{R}\,)\, \varphi_d(\vec{r}\,)\mathrm{d}\vec{r}\,'\mathrm{d}\vec{R}' \right|^2. \tag{162}$$

The presence of the overlap function $S_{An}^B\tilde{\varphi}_{An}^{\ell jI}(\vec{r}\,')$ tells us that the transfer cross section contains information about the single-particle content of a given state of the residual nucleus. States with a strong single-particle character (large spectroscopic factor) will

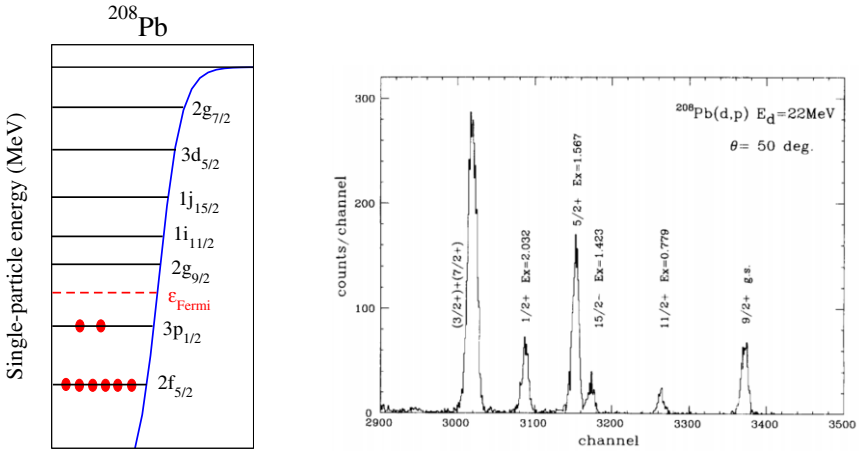

Fig. 33. – Left: single-particle orbitals for ^{208}Pb. Right: experimental energy spectrum of protons for the ^{208}Pb(d,p) reaction at $E_d = 22$ MeV at 50°. Quoted from ref. [94] with permission from Elsevier.

be strongly populated. An extreme case is that of a single nucleon outside a closed-shell core, such as in the ^{208}Pb$(d,p)^{209}$Pb reaction. This is shown in fig. 33. Low-lying states above the Fermi level in ^{209}Pb are populated and this allows for a natural spin assignment according to a simple shell-model picture.

In a more general case, the determination of the angular momentum of the populated states is done with the assistance of the angular distribution of these states. This stems from the fact that the angular dependence of eq. (162) is strongly dependent on the

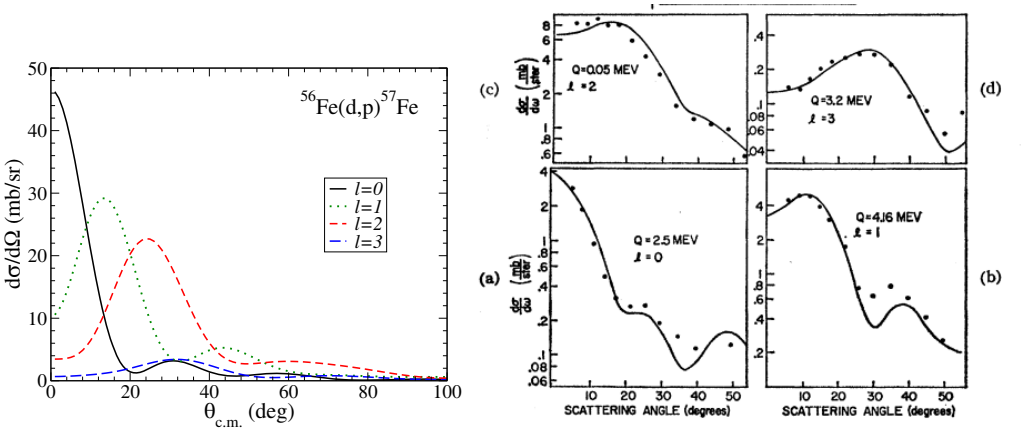

Fig. 34. – Left: DWBA calculations for ^{56}Fe$(d,p)^{57}$Fe reaction at $E_d = 15$ MeV assuming several values of the orbital angular momentum of the transferred neutron in the final nucleus. Right: Comparison with experimental data. From Cohen *et al.* [95].

orbital angular momentum ℓ so, upon comparison with experiment, the value of ℓ can be determined. An example is shown in fig. 34, corresponding to the ^{56}Fe$(d,p)^{57}$Fe reaction at $E_d = 15\,$MeV. The left panel shows DWBA model calculations for a hypothetical final state in ^{57}Fe with different values of ℓ. It is seen that, the larger the value of ℓ, the larger the value of the angle corresponding to the first peak. In particular, for $\ell = 0$ the distribution peaks at $\theta = 0$. The right panel shows the comparison of experimental data for this reaction with DWBA calculations [95], where the sensitivity of the angular distributions on ℓ is clearly seen.

Finally, under the assumption of the validity of the DWBA approximation, the absolute magnitude of the spectroscopic factor for the decomposition $B \to A + n$ can be determined by comparing the magnitude of the experimental and calculated cross sections.

9˙3. *Influence of breakup channels on transfer: the ADWA method.* – In the DWBA method, the three-body wave function appearing in the transition amplitude (153) is approximated by the elastic component ($\Psi^{(+)} \approx \chi_d^{(+)}(\vec{K}_d, \vec{R}\,)\varphi_d(\vec{r}\,)$). This approximation is motivated by the assumption that the elastic channel dominates the reaction. However, this choice, albeit intuitively plausible, deserves some caution. First, the phenomenological DWBA approach relies on the use of optical potentials, usually taken as local, angular-momentum-independent potentials, chosen to reproduce elastic scattering. This only means that the optical potentials will reasonably reproduce the phase shifts, for all partial waves, in the elastic channel. In other words, the standard DWBA approach reproduces the elastic wave function asymptotically, at large projectile-target distances. It is not obvious that this elastic wave function reproduces correctly the elastic component of the wave function in the radial range relevant for the transfer T-matrix elements. Second, the preponderance of the elastic cross section means that the elastic channel dominates the full wave function asymptotically, but this does not necessarily imply that the elastic channel is also dominant at shorter distances, where the transfer process takes place. Inspection of eq. (160) shows that the transfer cross section is dominated by small p-n separations (for which V_{pn} is non-negligible). Consequently, an accurate evaluation of (160) requires a good approximation of $\Psi^{(+)}(\vec{r}, \vec{R}\,)$ within the range of V_{pn}. This includes not only elastic channel component (*i.e.* with p-n forming a deuteron) but also excited components, in which the p-n system is unbound. Stated otherwise, this requires an approximation of $\Psi^{(+)}$ including the deuteron breakup channels.

The problem has been addressed at length by R.C. Johnson and co-workers, who have provided some practical solutions within the so-called *adiabatic approximation*. The simpler of these solutions, proposed by Johnson and Soper [96], was originally formulated for (d,p), or (d,n) reactions, although it can be applied to other weakly bound composite systems. It is based on the fact that the composite projectile has a relatively low binding energy (2.22 MeV in the case of the deuteron), and so, if the collision energy is relatively high, we can expect that, during the collision process, the relative proton-neutron coordinate does not change significantly; it is "frozen".

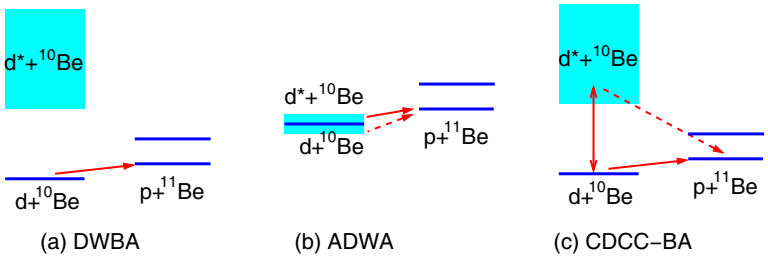

Fig. 35. – Schematic representation of DWBA, ADWA and CDCC-BA approaches for a (d, p) transfer reaction.

Note that, even if the p-n wave function $\varphi_d(\vec{r})$ has a relatively long range (which is also the case of halo nuclei), $V_{pn}(r)$ has a much shorter range. Therefore, for the purpose of evaluating the transfer matrix element, one can calculate the adiabatic wave function using the potential evaluated at $\vec{r} = 0$. This leads to the Johnson-Soper approximation [96], in which

$$\Psi^{(+)}(\vec{R}, \vec{r}) \simeq \chi_{JS}^{(+)}(\vec{R})\varphi_d(\vec{r}), \tag{163}$$

where $\chi_{JS}^{(+)}(\vec{R})$ is the solution of a two-body scattering problem, on the coordinate $\vec{R}$, in which the interaction is given by

$$U_{JS}(R) = U_{pA}(R) + U_{nA}(R). \tag{164}$$

We see that, in this limit, the adiabatic theory of the transfer amplitude adopts a form akin to that found in the DWBA theory, but this analogy is misleading because the function $\chi_{JS}^{(+)}(\vec{R})$ includes contributions from breakup and the potential $U_{JS}(R)$ may have little to do with the optical potential describing the deuteron elastic scattering. Due to the adiabatic approximation, the JT theory is not expected to be accurate at low incident energies.

The adiabatic approximation is equivalent to neglecting the excitation energy of the states of the projectile [96]. The adiabatic wave function takes into account the excitation to breakup channels, assuming that these states are degenerate in energy with the projectile ground state, as illustrated in fig. 35(b). Therefore, the ADWA approach takes into account, approximately, the effect of deuteron breakup on the transfer cross section, within the adiabatic approximation. So, it should be well suited to describe deuteron scattering at high energies, around 100 MeV per nucleon. Systematic studies [97-99] have shown that ADWA is superior to standard DWBA for (d, p) scattering at these relatively high energies.

Although the zero-range adiabatic model of Johnson and Soper provides a systematic improvement over the conventional DWBA, there are situations in which the former fails to reproduce the experimental data [100, 101]. Models which go beyond the zero-range

and adiabatic approximations are therefore needed. One of such models is the Weinberg expansion method of Johnson and Tandy [102]. The idea is to expand $\Psi^{(+)}$ in terms of a set of functions which are complete within the range of V_{pn}. A convenient choice is the set of Weinberg states (also called Sturmians),

$$\Psi^{(+)}(\vec{R},\vec{r}) = \sum_{i=0}^{N} \phi_i^W(\vec{r})\chi_i^W(\vec{R}), \tag{165}$$

where $\phi_i^W(\xi)$ are the Weinberg states, which are solutions of the eigenvalue equation

$$[\hat{T}_{\vec{r}} + \alpha_i V_{pn}]\phi_i^W(\vec{r}) = -\varepsilon_d \phi_i^W(\vec{r}), \tag{166}$$

where $\varepsilon_d = 2.225\,\text{MeV}$ is the deuteron binding energy and where α_i are the eigenvalues, to be determined along with the eigenfunctions. Beyond the range of the potential all the Weinberg states decay exponentially, like the deuteron ground-state wave function. For $i = 0$, $\alpha_0 = 1$ and so $\phi_0^W(\vec{r})$ is just proportional to the deuteron ground state. As i and α_i increase, they oscillate more and more rapidly at short distances. The Weinberg states form a complete set of functions of $\vec{r}$ inside the range of the potential V_{pn}. They are well suited to expand $\Psi^{(+)}$ in this region, as it is required by the amplitude (160). They do not satisfy the usual orthonormality relation but the less conventional one

$$\left\langle \phi_i^W | V_{pn} | \phi_j^W \right\rangle = -\delta_{ij}. \tag{167}$$

If we retain in (165) only the leading term, $\Psi^{(+)}(\vec{R},\vec{r}) \approx \phi_0^W \chi_0^W(\vec{R})$, one finds [102] that χ_0^W verifies the single-channel equation

$$\left[\hat{T}_{\vec{R}} + U_{JT}(\vec{R}) - E_d\right] \chi_0^W(\vec{R}) = 0, \tag{168}$$

with $E_d = E - \varepsilon_d$ and where the potential U_{JT} is given by

$$U_{JT}(R) = \frac{\langle \varphi_{pn}(\vec{r}) | V_{pn}(U_{nA} + U_{pA}) | \varphi_{pn}(\vec{r}) \rangle}{\langle \phi_{pn}(\vec{r}) | V_{pn} | \phi_{pn}(\vec{r}) \rangle}\,. \tag{169}$$

The bra and ket in this equation mean integration over $\vec{r}$, with fixed $\vec{R}$. Interestingly, in the zero-range limit, $U^{JT}(R)$ reduces to the JS potential, eq. (164). Therefore, the zero-order result given by eq. (169) can be regarded as a finite-range version of the adiabatic (JS) potential. These two models are globally referred to as Adiabatic Distorted Wave Approximation (ADWA). However, it is worth noting that the full Weinberg expansion makes no reference to the incident energy and, as such, does not involve the adiabatic approximation. This suggests that a stripping theory based on this Weinberg expansion can be used at low energies, where the adiabatic condition is not well satisfied. The inclusion of higher-order terms ($i > 0$) in the Weinberg expansion has been investigated in refs. [103, 104].

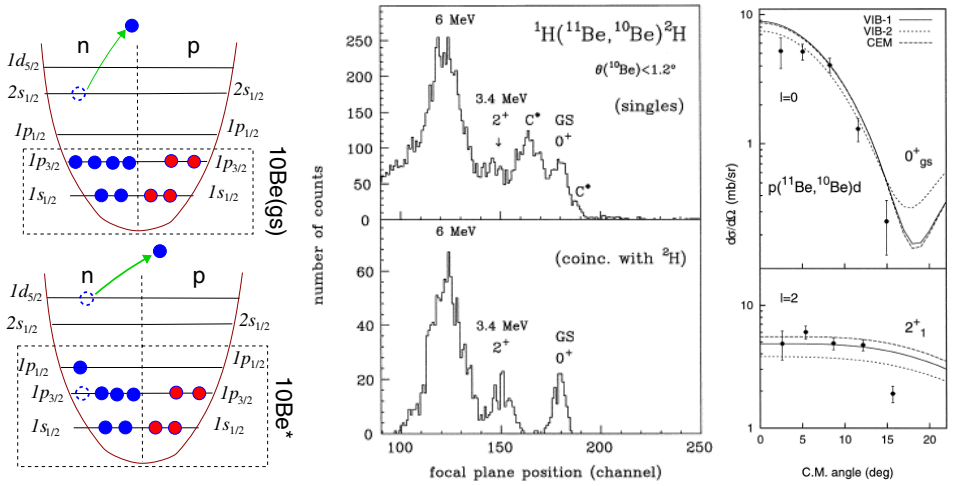

Fig. 36. – Application of the ADWA method to the ^{11}Be$(p,d)^{10}$Be reaction. The left panels show a shell-model picture of the ^{11}Be nucleus. The middle panels show the data from Fortier *et al.* [106], displaying the excitation energy function of ^{10}Be events, where one can distinguish the peaks corresponding to the ground state and the first excited state (2^+, $E_x = 3.367$ MeV). The rightmost panels show the angular distributions corresponding to these two peaks compared with ADWA calculations, assuming that they correspond to the neutron removal from the $2s_{1/2}$ and $1d_{5/2}$ single-particle configurations in ^{11}Be, respectively.

An appealing feature of the ADWA is that its ingredients are completely determined by experiments. These ingredients are the proton-target and neutron-target optical potentials, evaluated at half of the deuteron incident energy, as well as the well-known proton-neutron interaction. On the negative side, the ADWA approach does not consistently describe elastic scattering and nucleon transfer. Although, physically, elastic scattering, transfer and breakup should be closely related, so that the increase of flux in one channel should reduce the flux in the others, this connection is not present in ADWA. Furthermore, the arguments leading to ADWA are strongly associated with the assumption that the transfer is governed by a short-range operator. So, it is not obvious that the approximations remain valid for other weakly bound systems, like ^{11}Be. Even in the case of (d,p) scattering, the transfer matrix element is determined not only by the n-p interaction, but also by the proton-target and neutron-target interactions, that define the *remnant* term. The role of these terms, that would have contributions of three-body configurations in which proton and neutron are not so close together, is not clear *a priori*. An alternative method, that avoids the presence of these remnant terms, has been proposed by Timofeyuk and Johnson [105].

As an example of the application of the ADWA model, we consider the reaction ^{1}H(^{11}Be,^{10}Be)^{2}H measured at GANIL [106, 107]. Considering the nucleus ^{11}Be as a neutron outside a ^{10}Be core, we may write for the ^{11}Be ground state

$$|^{11}\mathrm{Be}\rangle_{\mathrm{g.s.}} = \alpha|^{10}\mathrm{Be}(0^+)\otimes\nu 2s_{1/2}\rangle + \beta|^{10}\mathrm{Be}(2^+)\otimes\nu 1d_{5/2}\rangle + \ldots, \tag{170}$$

where only the two dominant configurations ($2s_{1/2}$ and $1d_{5/2}$) are indicated explicitly. By comparing with (123), the α and β coefficients are the spectroscopic amplitudes for these two configurations, respectively. The left cartoons in fig. 36 illustrate these two configurations of ^{11}Be, using a simple independent-particle-model picture. The $2s_{1/2}$ configuration is associated with the ^{10}Be(g.s.). Thus, removing a neutron from the $2s_{1/2}$ orbital will produce ^{10}Be in its ground state. Conversely, if the neutron is removed from the $1d_{5/2}$ orbital, the ^{10}Be nucleus will be produced in the first excited state ($E_x = 3.4\,\text{MeV}$). Note that these arguments assume that the reaction occurs in one-step, which is a reasonable approximation at this energy. The middle panel in fig. 36 shows the experimental yields of these ^{10}Be states. In addition to the two peaks corresponding to the ^{10}Be g.s. and first excited state, an even more prominent peak is observed for excitation energies of $\approx 6\,\text{MeV}$, which is due to the stripping of neutrons from the $1p_{3/2}$ shell. The rightmost panels in fig. 36 show the comparison of the angular distributions of the two first states of ^{10}Be with ADWA calculations. This comparison allowed for a confirmation of the ℓ assignment, as well as a determination of the corresponding spectroscopic factors α^2 and β^2 [106, 107].

9˙4. *Continuum Discretized Coupled Channels Born Approximation CDCC-BA.* – An alternative choice for the three-body wave function $\Psi^{(+)}$ to be used in the transfer amplitude (153) is the CDCC expansion, eq. (108). When inserted into the transition amplitude we get, for the (d,p) case,

$$\mathcal{T}_{d,p}^{\text{CDCC-BA}} = C_{An}^{B}\left\langle \chi_p^{(-)}(\vec{K}_p,\vec{R}')\tilde{\varphi}_{An}^{\ell jI}(\vec{r}')\,V_{pn}(\vec{r})\,\chi_0^{(+)}(\vec{K}_d,\vec{R})\varphi_d(\vec{r})\right\rangle + C_{An}^{B}\sum_{i=1}^{N}\left\langle \chi_p^{(-)}(\vec{K}_p,\vec{R}')\tilde{\varphi}_{An}^{\ell jI}(\vec{r}')\,V_{pn}(\vec{r})\,\chi_i^{(+)}(\vec{K}_d,\vec{R})\varphi_{pn}^{i}(\vec{r})\right\rangle . \tag{171}$$

The first term in this expression corresponds to the *direct transfer*, in which the neutron is transferred directly from the deuteron ground state, whereas the second term accounts for the *multi-step* transfer occurring via the breakup states of the p-n system. These two types of processes correspond, respectively, to the solid and dashed lines in fig. 35(c) for the $^{10}\text{Be}(d,p)^{11}\text{Be}$ case. Clearly, the multi-step processes going through the breakup channels are omitted in the DWBA calculation. At most, the DWBA considers the effect of these channels on the elastic scattering if a suitable choice of the entrance optical potential is made. The adiabatic approximation includes in principle both mechanisms, but under the assumption that the excited (breakup) channels of the projectile are degenerate with the ground state (fig. 35(b)). The advantage of the CDCC-BA approach is that all relevant bound and continuum states in the $b+x$ system are explicitly included in the calculation.

Some early comparisons between these three methods can be found in refs. [29, 108-110] and the main results are also summarized in refs. [28, 111]. Due to numerical limitations, these first studies where done using a zero-range approximation of the V_{bx} potential. Overall, it was found that the ADWA model describes well the direct transfer contribution. However, the multi-step contributions, which are completely absent in

DWBA, are described very inaccurately by the adiabatic approximation. At low energies ($E_d < 20\,\mathrm{MeV}$) the discrepancy between the zero-range ADWA and CDCC-BA calculations can be understood because at these energies the adiabatic approximation itself is questionable. However, even at medium energies ($E_d \approx 80\,\mathrm{MeV}$) there are situations in which transfer through breakup channels is found to be very significant, and therefore the ADWA method does not work well either. In these situations, the CDCC-BA or the Weinberg expansion should be better used instead. The disadvantage of the CDCC-BA calculations is that, in principle, a large basis of internal states has to be included, making this approach much more demanding numerically.

Finite-range effects have been studied within the adiabatic approximation in refs. [103, 112] and were found to be small ($< 10\%$) at energies below 20–30 MeV/u but become more and more important as the incident energy increases. This limitation should be also taken into account in the analysis of experimental data.

Along with deuteron breakup, target excitations may affect the (d, p) and (p, d) transfer cross sections. The problem has been recently tackled in several ways. Deltuva *et al.* [113] used a formulation of the momentum space Faddeev equations including *core* excitations, and studied the effect of ^{10}Be excitations in the $^{10}\mathrm{Be}(d, p)^{11}\mathrm{Be}$ reaction. It is found that the cross sections are no longer proportional to the spectroscopic factor and the departure from this proportionality increases with increasing incident energies, reaching a maximum at a deuteron energy of $E_d \approx 60\,\mathrm{MeV}$. Similar results and conclusions were achieved in [114] using two alternative methods. One uses an extended ADWA model, with a deformed adiabatic potential. The other uses the extended version of the CDCC method including target excitations discussed in sect. **7**˙1.1, which is then used in the transfer transition amplitude (26). These works conclude that the main deviation from the pure three-body calculation with inert bodies originates from the destructive interference of the direct one-step transfer and the two-step transfer following target excitation.

9˙5. *Transfer reactions populating unbound states.* – So far, we have considered transfer reactions as a tool to investigate bound states of a given nucleus. However, in a rearrangement process, the transferred particle can populate also unbound states of the final nucleus. This opens the possibility of studying and characterizing structures in the continuum, such as resonances or virtual states.

As in the case of transfer to bound states, the simplest formalism to analyze these processes is the DWBA method. In this case, the bound wave function $\varphi_{An}^{\ell j I}(\vec{r}')$ appearing in the final state in eq. (162) should be replaced by a positive-energy wave function describing the state of the transferred particle n with respect to the core A. In principle, for this purpose one could use a scattering state of the $n + A$ system at the appropriate relative energy. However, this procedure tends to give numerical difficulties in the evaluation of the transfer amplitude due to the oscillatory behaviour of both the final distorted wave and the wave function $\varphi_{An}^{\ell j I}(\vec{r}')$. To overcome this problem, several alternative methods have been attempted. We enumerate here some of them:

i) The bound state approximation [115]. In the case of transfer to a resonant state, this method replaces the scattering state $\varphi_{An}^{\ell j I}(\vec{r}')$ by a weakly bound wave function

with the same quantum numbers ℓ and j. In practice, this can be achieved by starting with the potential that generates a resonance at the desired energy and increasing progressively the depth of the central potential until the state becomes bound.

ii) Huby and Mines [116] use a scattering state for $\varphi_{An}^{\ell jI}(\vec{r}')$, but it is multiplied by a convergence factor $e^{-\alpha r'}$ (with α a positive real number), which artificially eliminates its contribution to the integral coming from large r' values, and then extrapolate numerically to the limit $\alpha \to 0$. The convergence factor can be physically justified taking into account that the incident and outgoing fragments are not characterized by well-defined linear momenta, but correspond instead to wave packets. Thus, physical results depend on energy averages of stationary-state scattering amplitudes which, in the case of three-body breakup, destroy the asymptotic oscillations of the integrand in the same manner as the convergence factor [9].

iii) Vincent and Fortune [117] questioned the bound state approximation arguing that, in general, the bound state and resonant form factors can be very different and, even in those cases in which the fictitious form factor gives the correct shape, they can lead to very different absolute cross sections. They suggest using the actual scattering state, but choosing an integration contour along the complex plane in such a way that the oscillatory integrand is transformed into an exponential decay, thus improving the convergence and numerical stability of the calculation.

iv) In a real transfer experiment leading to positive-energy states, one does not have access to a definite final energy, but to a certain region of the continuum. That is to say, the extracted observables, such as energy differential cross sections, are integrated over some energy range which, at least, is of the order of the energy resolution of the experiment. This suggests a method of dealing with the unbound states consisting in discretizing the continuum states in energy bins, as in the CDCC approximation.

An advantage of the method iv) is that it can be equally applied to both resonant and non-resonant continuum final states. An example is shown in fig. 37, which corresponds to the differential cross section, as a function of the n-^{9}Li relative energy, for the reaction ^{2}H(^{9}Li, p)^{10}Li* at 2.36 MeV/u measured at REX-ISOLDE [118]. The lines are the results of CDCC-BA calculations, including the transfer to ^{10}Li* continuum states, showing the separate contribution of the s-wave ($\ell = 0$) continuum and p-wave ($\ell = 1$) continuum. The strength of the measured cross section close to zero energy is due to the presence of a virtual state in the ^{10}Li* system, whereas the peak around 0.4 MeV is due to a $p_{1/2}$ resonance. This is an example of how the use of transfer reactions can provide information on the continuum structure of weakly bound or even unbound systems.

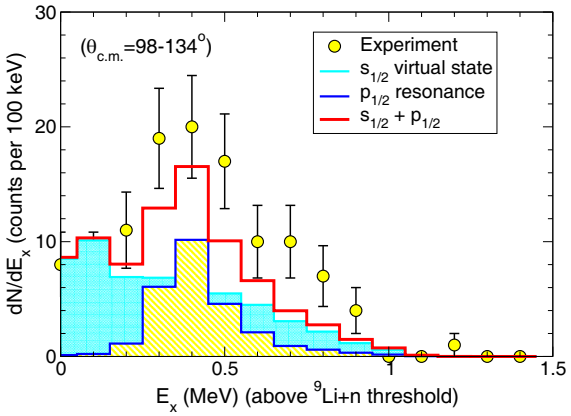

Fig. 37. – Experimental yield for the population of ^{10}Li states for the reaction ^{2}H(^{9}Li, p)^{10}Li* as a function of the $n+^{9}$Li relative energy. The calculations consider the transfer of a neutron from the deuteron to a set of final states of the ^{10}Li system, using a binning discretization method. Adapted from ref. [118].

10. – Final remarks

We have reviewed the current status of the theoretical description of nuclear reactions, with emphasis on the case of reactions involving by weakly bound nuclei. Although formal quantum-mechanical scattering theory provides exact solutions to compute the scattering amplitudes and their associated cross sections for a general scattering problem, we have seen that important approximations must be applied in practice. These approximations try to reduce the extremely complicated many-body scattering problem into a simplified, numerically tractable one. These approximations are usually tailored to specific types of reactions, giving rise to a large variety of models. Although we have reexamined the most common ones, the models presented here do not exhaust the variety of approaches available in the literature. Some of the omitted topics are the following (again, the list is not exhaustive):

– *Two-particle transfer reactions.* In the case of transfer reactions, we have restricted ourselves to the case of one-particle transfers, and have omitted altogether the important case of two-particle transfer. These are perfect tools to study the so-called pairing rotations and vibrations, collective modes associated with a field (the pairing field) which changes the number of particles by two. The formal description of two-particle transfer reactions dates back to the seminal works of Glendenning [119] and Baynman [120] and has received renewed attention in recent years [121, 122].

– *Charge-exchange reactions.* The nucleon-nucleon interaction contains spin- and isospin-dependent terms which are able to induce spin and isospin changing transitions such as those triggered by the weak interaction in β-decay. For example, the

presence of $\sigma\tau$ terms in the strong interaction gives rises to spin-flip, isospin-flip processes analogous to the Gamow-Teller (GT) transitions. In fact, charge-exchange (CE) reactions, such as the (p, n) or $(^3\mathrm{He}, t)$ reactions at intermediate beam energies can selectively excite GT states up to high excitation energies in the final nucleus. It has been found empirically that there is a close proportionality between the cross-sections at 0° and the transition strengths $B(GT)$ in these CE reactions. Therefore, CE reactions are useful tools to study the relative values of $B(GT)$ strengths up to high excitation energies (see [123] for a comprehensive review). Most recently, double charge-exchange reactions have been put forward as a promising tool to constrain the nuclear matrix elements involved in neutrino-less double-beta decay with potential access on the nature of the neutrino (Majorana *versus* Dirac) [124].

– *Ab initio methods.* Our discussion has been mostly confined to macroscopic and few-body models. Much work is being done in recent years in the field of the so-called *ab initio* approaches, whose final goal is to describe both the structure and dynamics of nuclei starting from the nucleon-nucleon interaction. One of the most promising tools is the *no-core shell model* which enables to study bound and scattering states of many-body systems (see [125] for a recent review). Due to the complexity of these calculations, applications have been restricted to light systems. Promising results have been obtained for a number of reactions, such as $^4\mathrm{He}(n, n)^4\mathrm{He}$ [125], $^3\mathrm{H}(d, n)^4\mathrm{He}$, $^3\mathrm{He}(d, p)^4\mathrm{He}$ [126], $^7\mathrm{Be}(p, \gamma)^8\mathrm{B}$, $^{10}\mathrm{C}(p, p)^{10}\mathrm{C}$, among others.

The curious reader is encouraged to go through the recommended references to discover by him/herself these and other recent developments and advances in the field of nuclear reaction modeling.

* * *

This paper is based on the lectures given during the Course "Nuclear Physics with Stable and Radioactive Ion Beams" within the International School of Physics "Enrico Fermi", held at Varenna, Italy, Summer 2017. I am deeply grateful to the organizers for giving me the opportunity to enjoy such a stimulating environment with other lecturers and attendants. This work is partially supported by the Spanish Ministerio de Economía y Competitividad and FEDER funds under project FIS2014-53448-C2-1-P and by the European Union's Horizon 2020 research and innovation program under grant agreement No. 654002.

REFERENCES

[1] TANIHATA I., HAMAGAKI H., HASHIMOTO O., NAGAMIYA S., SHIDA Y., YOSHIKAWA N., YAMAKAWA O., SUGIMOTO K., KOBAYASHI T., GREINER D. *et al.*, *Phys. Lett. B*, **160** (1985) 380.
[2] TANIHATA I. *et al.*, *Phys. Rev. Lett.*, **55** (1985) 2676.
[3] KOBAYASHI T., YAMAKAWA O., OMATA K., SUGIMOTO K., SHIMODA T., TAKAHASHI N. and TANIHATA I., *Phys. Rev. Lett.*, **60** (1988) 2599.
URL `https://link.aps.org/doi/10.1103/PhysRevLett.60.2599`

[4] SÁNCHEZ-BENÍTEZ A., ESCRIG D., ÁLVAREZ M., ANDRÉS M., ANGULO C., BORGE M., CABRERA J., CHERUBINI S., DEMARET P., ESPINO J. *et al.*, *Nucl. Phys. A*, **803** (2008) 30.
[5] DI PIETRO A. *et al.*, *Phys. Rev. C*, **85** (2012) 054607.
[6] CUBERO M. *et al.*, *Phys. Rev. Lett.*, **109** (2012) 262701.
[7] PESUDO V. *et al.*, *Phys. Rev. Lett.*, **118** (2017) 152502.
URL https://link.aps.org/doi/10.1103/PhysRevLett.118.152502
[8] BOHR N., *Nature*, **137** (1936) 344.
[9] AUSTERN N., *Direct Nuclear Reaction Theories* (John Wiley & Sons, New York) 1970.
[10] GLENDENNING N. K., *Direct Nuclear Reactions* (Academic Press, Inc.) 1983.
[11] MESSIAH A., *Quantum Mechanics*, Vol. **2** in *Quantum Mechanics* (North-Holland) 1981.
[12] FESHBACH H., *Ann. Phys.*, **5** (1958) 357.
[13] FESHBACH H., *Ann. Phys.*, **19** (1962) 287.
[14] PEREY F. and BUCK B., *Nucl. Phys.*, **32** (1962) 353.
URL http://www.sciencedirect.com/science/article/pii/0029558262903450
[15] TITUS L. J. and NUNES F. M., *Phys. Rev. C*, **89** (2014) 034609.
URL https://link.aps.org/doi/10.1103/PhysRevC.89.034609
[16] TIAN Y., PANG D.-Y. and MA Z.-Y., *Int. J. Mod. Phys. E*, **24** (2015) 1550006.
[17] LOVELL A. E., BACQ P.-L., CAPEL P., NUNES F. M. and TITUS L. J., *Phys. Rev. C*, **96** (2017) 051601.
URL https://link.aps.org/doi/10.1103/PhysRevC.96.051601
[18] ABRAMOWITZ M. and STEGUN I., *Handbook of Mathematical Functions* (Dover Pub., New York) 1972.
[19] BARNETT A. and LILLEY J., *Phys. Rev. C*, **9** (1974) 2010.
[20] ACOSTA L., SÁNCHEZ-BENÍTEZ A., GÓMEZ M., MARTEL I., PÉREZ-BERNAL F., PIZARRO F., RODRÍGUEZ-QUINTERO J., RUSEK K., ALVAREZ M., ANDRÉS M. *et al.*, *Phys. Rev. C*, **84** (2011) 044604.
[21] ALDER K. and WINTHER A., *Electromagnetic excitation: Theory of Coulomb excitation with heavy ions* (North-Holland, Amsterdam) 1975.
[22] HASSELGREN D., RENBERG P., SUNDBERG O. and TIBELL G., *Nucl. Phys.*, **69** (1965) 81.
[23] BOHR A. and MOTTELSON B., *Nuclear Structure*, Vol. **1** (World Scientific) 1998.
[24] TENREIRO C., ACQUADRO J. C., FREITAS P. A. B., LIGUORI NETO R., RAMIREZ G., CUEVAS N., GOMES P. R. S., CABEZAS R., ANJOS R. M. and COPNELL J., *Phys. Rev. C*, **53** (1996) 2870.
URL https://link.aps.org/doi/10.1103/PhysRevC.53.2870
[25] DAVINSON T., RAPP V., SHOTTER A. C., BRANFORD D., NAGARAJAN M. A., THOMPSON I. J. and SANDERSON N. E., *Phys. Lett.*, **139B** (1984) 150.
[26] RAWITSCHER G. H., *Phys. Rev. C*, **9** (1974) 2210.
URL https://link.aps.org/doi/10.1103/PhysRevC.9.2210
[27] YAHIRO M., ISERI Y., KAMEYAMA H., KAMIMURA M. and KAWAI M., *Prog. Theor. Phys. Suppl.*, **89** (1986) 32.
[28] AUSTERN N., ISERI Y., KAMIMURA M., KAWAI M., RAWITSCHER G. and YAHIRO M., *Phys. Rep.*, **154** (1987) 125.
[29] KAWAI M., *Prog. Theor. Phys. Suppl.*, **89** (1986) 11.
[30] MORO A., ARIAS J., GÓMEZ-CAMACHO J. and PÉREZ-BERNAL F., *Phys. Rev. C*, **80** (2009) 054605.
[31] MAJKA Z., GILS H. J. and REBEL H., *Z. Phys. A*, **288** (1978) 139.
URL https://doi.org/10.1007/BF01408643
[32] CRESPO R., DELTUVA A. and MORO A. M., *Phys. Rev. C*, **83** (2011) 044622.

[33] MORO A. M. and CRESPO R., *Phys. Rev. C*, **85** (2012) 054613.
[34] SUMMERS N. C. *et al.*, *Phys. Rev. C*, **74** (2006) 014606.
[35] DE DIEGO R., ARIAS J. M., LAY J. A. and MORO A. M., *Phys. Rev. C*, **89** (2014) 064609.
[36] SUMMERS N. C. and NUNES F. M., *Phys. Rev. C*, **76** (2007) 014611.
[37] SUMMERS N. C., NUNES F. M. and THOMPSON I. J., *Phys. Rev. C*, **89** (2014) 069901.
URL http://link.aps.org/doi/10.1103/PhysRevC.89.069901
[38] LAY J. A., MORO A. M., ARIAS J. M. and GÓMEZ-CAMACHO J., *Phys. Rev. C*, **85** (2012) 054618.
URL http://link.aps.org/doi/10.1103/PhysRevC.85.054618
[39] MORO A. M. and LAY J. A., *Phys. Rev. Lett.*, **109** (2012) 232502.
URL https://link.aps.org/doi/10.1103/PhysRevLett.109.232502
[40] CHAU HUU-TAI P., *J. Phys.: Conf. Series*, **312** (2011) 082018.
[41] GÓMEZ-RAMOS M. and MORO A. M., *Phys. Rev. C*, **95** (2017) 034609.
URL https://link.aps.org/doi/10.1103/PhysRevC.95.034609
[42] KISS A., ASPELUND O., HREHUSS G., KNPFLE K., ROGGE M., SCHWINN U., SERES Z., TUREK P. and MAYER-BRICKE C., *Nucl. Phys. A*, **262** (1976) 1.
URL http://www.sciencedirect.com/science/article/pii/0375947476904371
[43] DELTUVA A., *Nucl. Phys. A*, **947** (2016) 173.
[44] VARNER R., THOMPSON W., MCABEE T., LUDWIG E. and CLEGG T., *Phys. Rep.*, **201** (1991) 57.
[45] MATSUMOTO T., HIYAMA E., YAHIRO M., OGATA K., ISERI Y. and KAMIMURA M., *Nucl. Phys. A*, **738** (2004) 471.
[46] RODRÍGUEZ-GALLARDO M. *et al.*, *Phys. Rev. C*, **77** (2008) 064609.
[47] RODRÍGUEZ-GALLARDO M., ARIAS J. M., GÓMEZ-CAMACHO J., MORO A. M., THOMPSON I. J. and TOSTEVIN J. A., *Phys. Rev. C*, **80** (2009) 051601.
URL https://link.aps.org/doi/10.1103/PhysRevC.80.051601
[48] THOMPSON I. J., NAGARAJAN M. A., LILLEY J. S. and SMITHSON M. J., *Nucl. Phys. A*, **505** (1989) 84.
[49] FERNÁNDEZ-GARCÍA J., RODRIGUEZ-GALLARDO M., ALVAREZ M. and MORO A., *Nucl. Phys. A*, **840** (2010) 19.
[50] FADDEEV L. D., *Zh. Eksp. Teor. Fiz.*, **39** (1960) 1459.
[51] DELTUVA A., MORO A. M., CRAVO E., NUNES F. M. and FONSECA A. C., *Phys. Rev. C*, **76** (2007) 064602.
[52] UPADHYAY N. J., DELTUVA A. and NUNES F. M., *Phys. Rev. C*, **85** (2012) 054621.
[53] MATSUOKA N., HATANAKA K., SAITO T., ITAHASHI T., HOSONO K., SHIMIZU A., KONDO M., OHTANI F. and CYNSHI O., *Nucl. Phys. A*, **391** (1982) 357.
[54] DESCOUVEMONT P. and HUSSEIN M. S., *Phys. Rev. Lett.*, **111** (2013) 082701.
URL https://link.aps.org/doi/10.1103/PhysRevLett.111.082701
[55] DESCOUVEMONT P. and ITAGAKI N., *Phys. Rev. C*, **97** (2018) 014612.
URL https://link.aps.org/doi/10.1103/PhysRevC.97.014612
[56] MARTEL I., GMEZ-CAMACHO J., RUSEK K. and TUNGATE G., *Nucl. Phys. A*, **605** (1996) 417.
URL http://www.sciencedirect.com/science/article/pii/0375947496001728
[57] FUKUDA N. *et al.*, *Phys. Rev. C*, **70** (2004) 054606.
[58] NAGARAJAN M., LENZI S. and VITTURI A., *Eur. Phys. J. A*, **24** (2005) 63.
[59] PALIT R. *et al.*, *Phys. Rev. C*, **68** (2003) 034318.
URL https://0-link.aps.org.fama.us.es/doi/10.1103/PhysRevC.68.034318

[60] MILLENER D. J., OLNESS J. W., WARBURTON E. K. and HANNA S. S., *Phys. Rev. C*, **28** (1983) 497.
URL https://link.aps.org/doi/10.1103/PhysRevC.28.497
[61] KWAN E., WU C., SUMMERS N., HACKMAN G., DRAKE T., ANDREOIU C., ASHLEY R., BALL G., BENDER P., BOSTON A. *et al.*, *Phys. Lett. B*, **732** (2014) 210.
[62] CAPEL P., GOLDSTEIN G. and BAYE D., *Phys. Rev. C*, **70** (2004) 064605.
URL https://0-link.aps.org.fama.us.es/doi/10.1103/PhysRevC.70.064605
[63] TARUTINA T., CHAMON L. C. and HUSSEIN M. S., *Phys. Rev. C*, **67** (2003) 044605.
URL https://0-link.aps.org.fama.us.es/doi/10.1103/PhysRevC.67.044605
[64] HOWELL D., TOSTEVIN J. and AL-KHALILI J., *J. Phys. G: Nucl. Part. Phys.*, **31** (2005) S1881.
[65] AUSTERN N. and VINCENT C. M., *Phys. Rev. C*, **23** (1981) 1847.
[66] ICHIMURA M., AUSTERN N. and VINCENT C. M., *Phys. Rev. C*, **32** (1985) 431.
[67] POTEL G., NUNES F. M. and THOMPSON I. J., *Phys. Rev. C*, **92** (2015) 034611.
URL http://0-link.aps.org.fama.us.es/doi/10.1103/PhysRevC.92.034611
[68] CARLSON B. V., CAPOTE R. and SIN M., *Few-Body Syst.*, **57** (2016) 307.
URL http://dx.doi.org/10.1007/s00601-016-1054-8
[69] LEI J. and MORO A. M., *Phys. Rev. C*, **92** (2015) 044616.
[70] LEI J. and MORO A. M., *Phys. Rev. C*, **95** (2017) 044605.
URL https://link.aps.org/doi/10.1103/PhysRevC.95.044605
[71] DUGUET T., HERGERT H., HOLT J. D. and SOMÀ V., *Phys. Rev. C*, **92** (2015) 034313.
URL https://link.aps.org/doi/10.1103/PhysRevC.92.034313
[72] TOSTEVIN J., *Nucl. Phys. A*, **682** (2001) 320.
URL http://www.sciencedirect.com/science/article/pii/S0375947400006564
[73] HUSSEIN M. and MCVOY K., *Nucl. Phys. A*, **445** (1985) 124.
[74] TOSTEVIN J. A. and GADE A., *Phys. Rev. C*, **90** (2014) 057602.
URL https://link.aps.org/doi/10.1103/PhysRevC.90.057602
[75] AUMANN T. *et al.*, *Phys. Rev. Lett.*, **84** (2000) 35.
[76] JACOB G. and MARIS T. A., *Rev. Mod. Phys.*, **38** (1966) 121.
[77] JACOB G. and MARIS T. A., *Rev. Mod. Phys.*, **45** (1973) 6.
[78] AMAKAWA H., MORI A. and YAZAKI K., *Nucl. Phys. A*, **340** (1980) 125.
[79] OGATA K., YOSHIDA K. and MINOMO K., *Phys. Rev. C*, **92** (2015) 034616.
URL https://link.aps.org/doi/10.1103/PhysRevC.92.034616
[80] MORO A. M., *Phys. Rev. C*, **92** (2015) 044605.
URL http://link.aps.org/doi/10.1103/PhysRevC.92.044605
[81] CRESPO R., DELTUVA A. and CRAVO E., *Phys. Rev. C*, **90** (2014) 044606.
URL https://link.aps.org/doi/10.1103/PhysRevC.90.044606
[82] CRAVO E., CRESPO R. and DELTUVA A., *Phys. Rev. C*, **93** (2016) 054612.
URL https://link.aps.org/doi/10.1103/PhysRevC.93.054612
[83] TYPEL S. and BAUR G., *Phys. Rev. C*, **50** (1994) 2104.
[84] ESBENSEN H. and BERTSCH G. F., *Nucl. Phys. A*, **600** (1996) 37.
[85] KIDO T., YABANA K. and SUZUKI Y., *Phys. Rev. C*, **50** (1994) R1276.
[86] TYPEL S. and BAUR G., *Phys. Rev. C*, **64** (2001) 024601.
[87] GARCÍA-CAMACHO A., BONACCORSO A. and BRINK D. M., *Nucl. Phys. A*, **776** (2006) 118.
[88] MARTA H., CANTO L., DONANGELO R. and LOTTI P., *Phys. Rev. C*, **66** (2002) 024605.
[89] ANDRÉS M., GÓMEZ-CAMACHO J. and NAGARAJAN M., *Nucl. Phys. A*, **579** (1994) 273.
[90] ANDRÉS M., GÓMEZ-CAMACHO J. and NAGARAJAN M., *Nucl. Phys. A*, **583** (1995) 817.
[91] SATCHLER G., *Direct Nuclear Reactions* (Oxford University Press, New York) 1983.

[92] THOMPSON I. J. and NUNES F. M., in *Nuclear Reactions for Astrophysics*, edited by IAN J. THOMPSON and FILOMENA M. NUNES, Vol. **1** (Cambridge University Press, Cambridge) 2009.
[93] THOMPSON I. J., *Comput. Phys. Rep.*, **7** (1988) 167.
[94] HIROTA K., AOKI Y., OKUMURA N. and TAGISHI Y., *Nucl. Phys. A*, **628** (1998) 547. URL http://www.sciencedirect.com/science/article/pii/S0375947497006416
[95] COHEN B. L., FULMER R. H. and MCCARTHY A. L., *Phys. Rev.*, **126** (1962) 698. URL https://link.aps.org/doi/10.1103/PhysRev.126.698
[96] JOHNSON R. C. and SOPER P. J. R., *Phys. Rev. C*, **1** (1970) 976.
[97] HARVEY J. D. and JOHNSON R. C., *Phys. Rev. C*, **3** (1971) 636.
[98] SATCHLER G. R., *Phys. Rev. C*, **4** (1971) 1485.
[99] WALES G. L. and JOHNSON R. C., *Nucl. Phys. A*, **274** (1976) 168.
[100] STEPHENSON E., JOHNSON R., TOSTEVIN J., CUPPS V., BROWN J., FOSTER C., GERING J., JONES W., LOW D., MILLER D., NANN H., OLMER C., OPPER A., SCHWANDT P., SEUBERT J. and WISSINK S., *Phys. Lett. B*, **171** (1986) 358. URL http://www.sciencedirect.com/science/article/pii/0370269386914206
[101] JOHNSON R., STEPHENSON E. and TOSTEVIN J., *Nucl. Phys. A*, **505** (1989) 26. URL http://www.sciencedirect.com/science/article/pii/0375947489904156
[102] JOHNSON R. C. and TANDY P. C., *Nucl. Phys. A*, **235** (1974) 56.
[103] LAID A., TOSTEVIN J. A. and JOHNSON R. C., *Phys. Rev. C*, **48** (1993) 1307.
[104] PANG D., TIMOFEYUK N., JOHNSON R. and TOSTEVIN J., *Phys. Rev. C*, **87** (2013) 064613.
[105] TIMOFEYUK N. K. and JOHNSON R. C., *Phys. Rev. C*, **59** (1999) 1545.
[106] FORTIER S. *et al.*, *Phys. Lett. B*, **461** (1999) 22.
[107] WINFIELD J. S. *et al.*, *Nucl. Phys. A*, **683** (2001) 48.
[108] RAWITSCHER G. H., *Phys. Rev. C*, **11** (1975) 1152.
[109] ISERI Y., YAHIRO M. and NAKANO M., *Prog. Theor. Phys.*, **69** (1983) 1038.
[110] AMAKAWA H. and AUSTERN N., *Phys. Rev. C*, **27** (1983) 922.
[111] GÓMEZ CAMACHO J. and MORO A. M., *A pedestrian approach to the theory of transfer reactions: Application to weakly-bound and unbound exotic nuclei*, in *The Euroschool on Exotic Beams*, Vol. **IV**, edited by SCHEIDENBERGER C. and PFTZNER M., *Lecture Notes in Physics*, Vol. **879** (Springer Berlin Heidelberg) 2014, pp. 39–66.
[112] NGUYEN N. B., NUNES F. M. and JOHNSON R. C., *Phys. Rev. C*, **82** (2010) 014611.
[113] DELTUVA A., ROSS A., NORVAIŠAS E. and NUNES F. M., *Phys. Rev. C*, **94** (2016) 044613. URL https://link.aps.org/doi/10.1103/PhysRevC.94.044613
[114] GOMEZ-RAMOS M. and MORO A. M., *Phys. Rev. C*, **95** (2017) 044612. URL https://link.aps.org/doi/10.1103/PhysRevC.95.044612
[115] COKER W. R., *Phys. Rev. C*, **9** (1974) 784.
[116] HUBY R. and MINES J. R., *Rev. Mod. Phys.*, **37** (1965) 406.
[117] VINCENT C. M. and FORTUNE H. T., *Phys. Rev. C*, **2** (1970) 782.
[118] JEPPESEN H. B. *et al.*, *Phys. Lett. B*, **642** (2006) 449.
[119] GLENDENNING N. K., *Phys. Rev.*, **137** (1965) B102. URL https://link.aps.org/doi/10.1103/PhysRev.137.B102
[120] BAYMAN B. F. and HINTZ N. M., *Phys. Rev.*, **172** (1968) 1113. URL https://link.aps.org/doi/10.1103/PhysRev.172.1113
[121] POTEL G., IDINI A., BARRANCO F., VIGEZZI E. and BROGLIA R. A., *Phys. Rev. C*, **87** (2013) 054321. URL https://link.aps.org/doi/10.1103/PhysRevC.87.054321

[122] POTEL G., IDINI A., BARRANCO F., VIGEZZI E. and BROGLIA R. A., *Rep. Prog. Phys.*, **76** (2013) 106301.
URL http://stacks.iop.org/0034-4885/76/i=10/a=106301
[123] FUJITA Y., RUBIO B. and GELLETLY W., *Prog. Part. Nucl. Phys.*, **66** (2011) 549.
URL http://www.sciencedirect.com/science/article/pii/S0146641011000573
[124] CAPPUZZELLO F., CAVALLARO M., AGODI C., BONDÌ M., CARBONE D., CUNSOLO A. and FOTI A., *Eur. Phys. J. A*, **51** (2015) 145.
[125] NAVRÁTIL P., QUAGLIONI S., HUPIN G., ROMERO-REDONDO C. and CALCI A., *Phys. Scr.*, **91** (2016) 053002.
URL http://stacks.iop.org/1402-4896/91/i=5/a=053002
[126] NAVRÁTIL P. and QUAGLIONI S., *Phys. Rev. Lett.*, **108** (2012) 042503.
URL https://link.aps.org/doi/10.1103/PhysRevLett.108.042503

This page intentionally left blank

Proceedings of the International School of Physics "Enrico Fermi"
Course 201 "Nuclear Physics with Stable and Radioactive Ion Beams", edited by F. Gramegna,
P. Van Duppen, A. Vitturi and S. Pirrone
(IOS, Amsterdam; SIF, Bologna) 2019
DOI 10.3254/978-1-61499-957-7-209

Nucleon-transfer reactions with radioactive ion beams

R. Raabe

KU Leuven, Instituut voor Kern-en Stralingsfysica - 3001 Leuven, Belgium

Summary. — These notes summarise the lectures given at the International School of Physics "Enrico Fermi", in July 2017 at Varenna (Italy), about the use of transfer reactions to extract spectroscopic information on nuclei far from the valley of stability. Transfer reactions as a probe of nuclear structure have re-gained importance in the last 20 years with the development of good-quality beams of unstable nuclei, and thus the possibility of carrying out reaction studies in inverse kinematics. After a short introduction about the general properties of nuclear reactions and transfer reactions in particular, the notes discuss the experimental challenges related to the use of radioactive ion beams. The main part is then dedicated to the presentation of a number of selected experimental studies. The focus lies on the impact of those studies on our understanding of the nuclear structure and the features of the underlying nucleon-nucleon interaction. The topics touched upon are: shell evolution in light nuclei at $N = 8$, the disappearance of the $N = 20$ shell closure and the emergence of another shell gap at $N = 16$; the spin-orbit term of the nucleon-nucleon interaction and the changes in its strength in exotic nuclei; the microscopic origin of shape coexistence in low-lying 0^+ states, in the neutron rich Mg and Ni regions. We conclude with a brief reflection on the present developments and challenges for experiments and theory in this field.

1. – Introduction

The topic of nuclear reactions is a broad and complex one. In these lecture notes, we will limit ourselves to a well-defined subject: the use of reactions, in particular nucleon-transfer reactions, for the study of nuclei far from stability. This implies the use of radioactive ion beams (RIBs), which brings along a number of issues, both experimental and theoretical.

The notes are organised as follows: after a short introduction of the characteristics of nuclear reactions in general (sect. **2**˙1), we will motivate the use of direct reactions as a powerful probe of nuclear structure (sects. **2**˙2 to **2**˙5). Then (sects. **3**˙1 and **3**˙2) we will briefly review the challenges of performing studies with RIBs. Finally, we will present some cases from literature (sect. **4**), lead by the main questions that are presently driving the research on nuclear structure. A brief outlook (sect. **5**) concludes the notes.

As general references for the matter presented here we recommend the book of Satchler [1] for a general introduction on nuclear reactions; the text of Thompson and Nunes [2] for a formal treatment; and the articles of the Nobel Symposium 152 [3] for a review of the physics with radioactive ion beams.

2. – Characteristics of nuclear reactions

In a very general way, a nuclear reaction can be defined as a collision between a nucleus X and a probe a (which can be a particle, or a γ-ray), in which the reactants may exchange energy, momentum and possibly mass. The result is a product nucleus Y and some outgoing radiation b (again, a particle or electromagnetic radiation). The following notations are used:

$$a + X \rightarrow b + Y, \tag{1}$$

or the shorthand form

$$X(a, b)Y. \tag{2}$$

The second notation puts the accent on the process (a, b), which has specific characteristics that do not depend much on the nucleus X. It is used to refer to a class of reactions that share similar features: for example, the nucleon-transfer reaction (d, p).

The mechanism of nuclear reactions is a vast and interesting topic on its own. Here, however, we consider reactions as a mere tool to access information on nuclear structure. In this cases, usually X is the complex nucleus to be studied; the probe a, on the other hand, is mostly chosen with a simple and well-known structure, to constrain the complexity of the problem.

2˙1. *Classification.* – Reactions can be classified according to different criteria. Two important definitions used in this context are those of *(mass) partition*: the combination of particles at the beginning or at the end of a reaction process, and of *reaction*

channel: the combination of particles with their specific excitation states and radiation emitted. For example, based on the reaction channel, we have:

- *elastic scattering* $X(a,a)X$ when the exit channel is the same as the entrance one: same particles in the same states (usually the ground state). For example: $^{12}\mathrm{C}(p,p)^{12}\mathrm{C}$; $^{208}\mathrm{Pb}(n,n)^{208}\mathrm{Pb}$. An important remark is that elastic scattering is always present in a nuclear collision, while all the other channels may or not be present ("open") according to conservation and selection rules;

- *inelastic scattering* $X(a,a')X^*$ when one of the particles (or both) are left in an excited state. For example: $^{12}\mathrm{C}(\alpha,\alpha')^{12}\mathrm{C}^*$;

- *rearrangement reactions* when the mass partition changes. Among these are *transfer* reactions, when one or more nucleons c are transferred from the probe to the nucleus X or vice-versa. The first case is that of *stripping*: $X((b+c),b)(X+c)$, for example $^{12}\mathrm{C}(d,p)^{13}\mathrm{C}$; the second is *pick-up*: $(Y+c)(a,(a+c))Y$, for example $^{13}\mathrm{C}(p,d)^{12}\mathrm{C}$.

  Another class is that of *knockout* reactions $X(a,ac)Y$; the probe survives and literally knocks out one or more nucleons from the nucleus X. For example $^{12}\mathrm{C}(p,2p)^{11}\mathrm{B}$.

- *photo-disintegration* $X(\gamma,a)Y$ occurs when a nucleus is excited and splits following the absorption of a γ-ray. For example $^{16}\mathrm{O}(\gamma,\alpha)^{12}\mathrm{C}$. The inverse is a *capture* reaction $X(a,\gamma)Y$, for example $^{14}\mathrm{N}(\alpha,\gamma)^{18}\mathrm{F}$. These reactions are especially important in nuclear astrophysics.

Reactions can also be classified according to their *mechanism*, *i.e.* the model which is used to describe the reaction process that leads to a given outcome. Some of the parameters involved in the description are reaction timescales, proximity of the reacting particles, energy and spatial distribution of the products. This classification is not rigorous; the differences are sometimes blurred.

- In *compound-nucleus* reactions, all the nucleons from the initial nuclei *fuse*, forming a highly-excited compound. In the process there is time for the excess energy to be distributed among all the nucleons (tipically $t \approx 10^{-22}$ s, which is the time that a nucleon takes to traverse a nucleus). The system is in a superposition of many states with a given energy and different spins. Statistically, if the energy balance allows, one or more nucleons may acquire enough energy to escape the nucleus. The compound nucleus thus de-excite through nucleon *evaporation* and γ-ray emission, leaving behind a *residue*. This latter process is purely statistical and only depends upon the energy of the compound system; in other words, there is no memory of the entrance channel. The probability of such a process to occur increases if the collision is central (head-on).

- In *direct* reactions, at the opposite, only few nucleons participate in the process. The collision is fast ($t \ll 10^{-22}$ s) and peripheral: the nuclei do not deviate much

from the original trajectories, such that the products are observed preferentially at forward centre-of-mass angles. Clearly, the products have a large overlap with the particles in the entrance channel. Nucleon-transfer reactions are modelled as direct processes.

– *Resonance reactions* are similar to compound-nucleus reactions, but the product is formed in a well-defined excited state with given energy and spin, that can decay only through few channels with probabilities that depend on the spectroscopic structure of the state.

– *Deep-inelastic* reactions (also called *multi-nucleon transfers*) are in between direct and compound-nucleus reactions, and share characteristics of both. They are also mostly binary (two particles in the outgoing channel) with products that differ only by a few nucleons from the initial nuclei. However, a large fraction of the kinetic energy is converted into excitation energy of the products (from which the alternative name of *damped* collisions). Deep inelastic processes are typical of heavy-ion reactions (the initial nuclei are both heavier than an α-particle) at energies slightly above that of the Coulomb barrier between the nuclei.

It is important to realise that, when measuring a reaction (thus a given entrance channel at a given centre-of-mass energy), we may observe products corresponding to all the different processes listed above. Even for a selected outgoing channel (through the identification of the products), different processes can contribute: for example, proton emitted in a collision with deuterons may be produced in a direct (d, p) reaction or through the statistical evaporation from the compound nucleus.

2˙2. *Importance of transfer reactions*. – As mentioned above, transfer reactions only involve a few nucleons, the most peripheral ones. For a particular nucleon transfer to occur, matching conditions have to be fulfilled concerning the relative linear and angular momenta of the nucleon in the initial and final nucleus, so that, for example, the nucleon would conserve its momentum in the direction of the collision [4]. Furthermore, we expect that a state in the final nucleus will be populated if it has some probability of having a structure similar to the initial nucleus plus one nucleon (or hole) with given quantum numbers, dictated by the (shell-model) binding potential. This is called a *single-particle* configuration, and can be more or less pronounced in a state (remember that a state can contain different configurations as long as they have the same spin). This way, the validity of the predictions of a model can be directly tested.

Experimentally, specific pieces of information are related to observables: a) the energy balance, measured as the difference in kinetic energy between initial and final nuclei, allows to determine the excitation energy of the populated state; b) the conservation of angular momentum imposes a relation between the initial and final spins of the nuclei and the transferred angular momentum, where the latter can be measured; c) the probability of a reaction to occur (its *cross section*), and thus the number of observed events, is proportional to the weight of the single-particle configuration corresponding to the initial

nucleus plus one nucleon (or hole) with quantum numbers determined by the selected channel. We will look now at each of these features in detail.

2˙3. *Conservation of energy.* – We can write the conservation of energy in the following way:

$$E_{\mathrm{k,i}} + M_{\mathrm{i}}c^2 = E_{\mathrm{k,f}} + M_{\mathrm{f}}c^2, \tag{3}$$

where $E_{\mathrm{k,i}}$, $E_{\mathrm{k,f}}$ are the (initial and final) kinetic energies and $M_{\mathrm{i,f}}$ is the sum of the masses of the particles in the entrance and exit channels; in this notation the masses also include the excitation energies.

The relation obviously holds both in the centre-of-mass and laboratory reference frames. In the former (where we denote quantities with a prime, *i.e.* E') we have

$$E'_{\mathrm{k,i}} + (M_{\mathrm{i}}c^2 - M_{\mathrm{f}}c^2) = E'_{\mathrm{k,f}}. \tag{4}$$

Since $E'_{\mathrm{k,f}}$ must be positive, relation (4) represents a condition (*threshold*) on the minimum initial kinetic energy, necessary for the channel (i,f) to be open. By defining the *Q-value* of the reaction as

$$Q = M_{\mathrm{i}}c^2 - M_{\mathrm{f}}c^2, \tag{5}$$

the condition becomes

$$E'_{\mathrm{k,i}} > -Q. \tag{6}$$

The Q-value is usually calculated through the mass excess $\Delta = (M - A)c^2$, which is tabulated in the mass tables. The centre-of-mass kinetic energy is related to the laboratory (beam) energy by $E'_{\mathrm{k,i}} = E_{\mathrm{k,i}} \frac{A_{\mathrm{t}}}{A_{\mathrm{t}}+A_{\mathrm{p}}}$, where A_{t} and A_{p} are, respectively, the mass numbers of target and projectile.

As an example, consider the reaction $^{41}\mathrm{Ca}(p,d)^{40}\mathrm{Ca}$. The mass excesses are $\Delta_{^{41}\mathrm{Ca}} = -35138\,\mathrm{keV}$, $\Delta_{^{40}\mathrm{Ca}} = -34846\,\mathrm{keV}$, $\Delta_p = 7289\,\mathrm{keV}$, $\Delta_d = 13136\,\mathrm{keV}$. The Q-value is $Q = -6139\,\mathrm{keV}$; the energy threshold for the (proton) beam to populate the ground state of $^{40}\mathrm{Ca}$ is thus $E_{\mathrm{k,i}} > 6.289\,\mathrm{MeV}$; for excited states, the excitation energy should be added to $M_{\mathrm{f}}c^2$, *i.e.* subtracted from the Q-value.

If we write the conservation of energy in the laboratory system, we see that

$$Q = E_{\mathrm{k,f}} - E_{\mathrm{k,i}}. \tag{7}$$

By measuring the kinetic energy of the outgoing particles we can thus calculate the Q-value of the event and determine the corresponding reaction channel (excitation energy of the product nucleus).

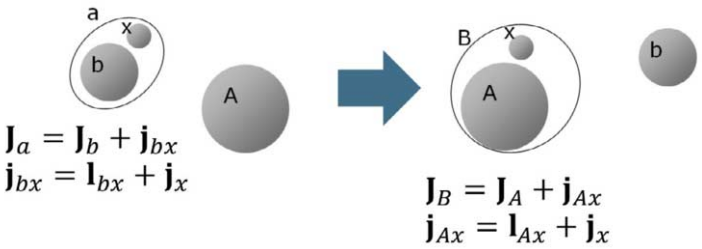

Fig. 1. – Schematic representation of a stripping reaction. Orbital angular momenta $\mathbf{l}$ and angular momenta $\mathbf{j}$ compose to total spins $\mathbf{J}$ as indicated.

2˙4. *Conservation of angular momentum.* – We consider the reaction $a + A \to b + B$; we indicate with $\mathbf{J}$ the total spin of each particle, and with $\vec{\ell}$ the angular momentum between the two particles in the entrance (α) and exit (β) channels. The conservation of angular momentum is then written as

$$\mathbf{J}_a + \mathbf{J}_A + \vec{\ell}_\alpha = \mathbf{J}_b + \mathbf{J}_B + \vec{\ell}_\beta. \tag{8}$$

We defined the *transferred angular momentum* as the additional spin that we find in the outgoing particles:

$$\mathbf{l} = (\mathbf{J}_b + \mathbf{J}_B) - (\mathbf{J}_a + \mathbf{J}_A) = \vec{\ell}_\alpha - \vec{\ell}_\beta. \tag{9}$$

We refer now to fig. 1 and consider, for simplicity, a stripping reaction in which the particle x is transferred from the projectile $a = b + x$ to the target A. From the composition of angular momenta to the total spins we can easily derive

$$\mathbf{l} = (\mathbf{J}_b + \mathbf{J}_B) - (\mathbf{J}_a + \mathbf{J}_A) = \mathbf{j}_{Ax} - \mathbf{j}_{bx} = \mathbf{l}_{Ax} - \mathbf{l}_{bx}. \tag{10}$$

In other words, the transferred angular momentum is constrained by the binding orbital angular momenta of the particle x in the initial $a = b + x$ and final $B = A + x$ systems([1]). For nucleon transfers, these are simply the angular momenta (s, p, d, g, f ...) given by the shell-model orbitals occupied by x in the two systems. We already see from this picture that only few values of l can contribute to the transfer.

We now show how this transferred angular momentum can be measured experimentally. This argument is based on a semi-classical picture, illustrated in fig. 2. We assume that the reaction takes place on the surface of the target nucleus at a distance $\mathbf{R}$ from its centre. The transferred angular momentum is then $\mathbf{l} = \mathbf{q} \times \mathbf{R}$, where $\mathbf{q} = \mathbf{k}_\alpha - \mathbf{k}_\beta$

([1]) The interactions at work in nuclear reactions also conserve parity, thus it must be: $\pi_a \pi_A \pi_b \pi_B = (-1)^l = (-1)^{l_{Ax}+l_{bx}}$. This means that either only even or only odd values of l are allowed.

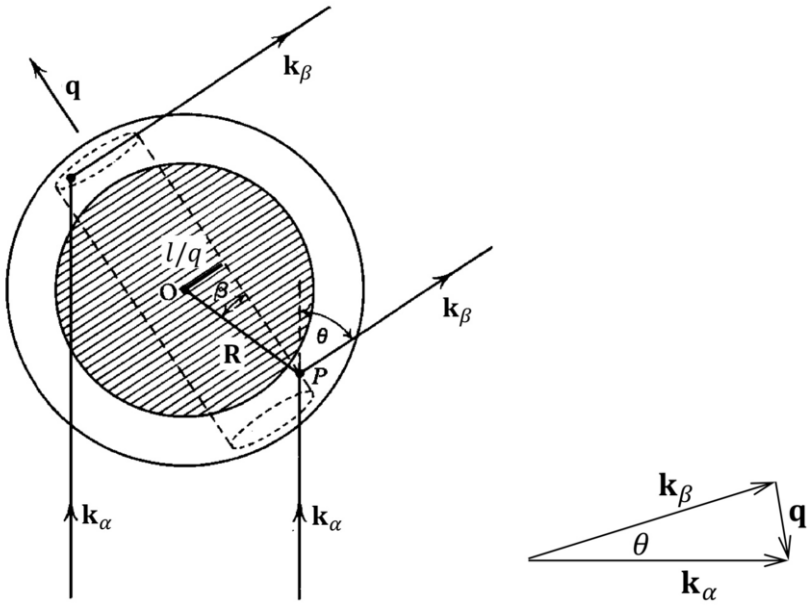

Fig. 2. – Left: illustration, in a classical picture, of the rings of radius l/q from which particles observed at an angle θ may originate. Right: relation between the linear momenta $\mathbf{k}$ in the entrance and exit channels, the transferred momentum $\mathbf{q}$ and the angle θ.

is the transferred linear momentum. We consider a transfer reaction leading to a state of a given energy: the transferred linear momentum $\mathbf{q}$ is then fixed in magnitude. For an observation angle θ, additionally, $\mathbf{k}_\beta$ is fixed in direction. This implies that the angle β between $\mathbf{q}$ and $\mathbf{R}$ is also fixed, and thus also the ratio l/q. The latter is the radius of two similar circles, located on the opposite sides of the surface of the target nucleus, where the reaction may take place. Finally, if we assume that the incoming and outgoing linear momenta do not differ much in direction and magnitude (which is reasonable for a peripheral transfer of one nucleon), we have $q \approx \bar{k}\theta$, see fig. 2 right, where can define an average momentum $k = (k_\alpha + k_\beta)/2$ or, alternatively, $k = \sqrt{k_\alpha k_\beta}$.

We now impose that the circles remain on the surface: $l/q \leq R$. With the expression for q as a function of the scattering angle, the condition can be rewritten as $\theta \geq l/(\bar{k}R)$: classically, we expect to observe products from the transfer reaction only at angles θ larger than $l/(\bar{k}R)$. Also, we may expect interference between the waves emitted from the two circles at opposite sides. We will have constructive interference for a difference in path (if the circles are small) $\delta x \approx 2R\theta$ equal to an integer number of wavelengths $\lambda = 2\pi/\bar{k}$, which leads to $\theta = n\pi/(\bar{k}R)$. Quantistically, maxima and minima will be smoothed out, also because of the uncertainty in the location of the nuclear surface. In conclusion, if we measure the number of events (cross section) as a function of the centre-of-mass emission angle with respect to the beam direction (*angular distributions*) we observe a pattern

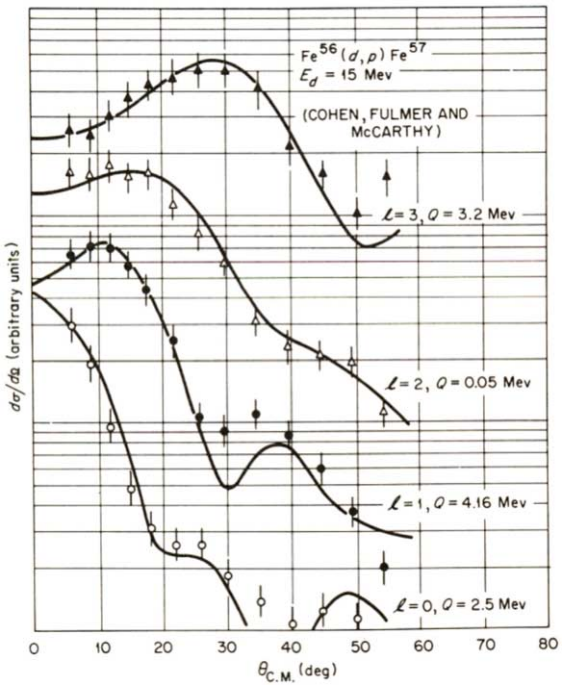

Fig. 3. – Angular distributions observed in the reaction $^{56}\mathrm{Fe}(d,p)^{57}\mathrm{Fe}$. Each curve corresponds to the transfer to a specific state in ^{57}Fe, with the given Q-values. The first maximum of the distribution is in $\theta = 0$ for $l = 0$, and moves to the right for increasing values of l. The maxima on each curve are separated by $\Delta\theta = \pi/(\bar{k}R)$. Figure modified from ref. [5].

as those shown in fig. 3. From the location of the first maximum, knowing the average momentum $\bar{k}$ and the interaction radius R (usually taken $\approx 3\,\mathrm{fm}$ larger than the sum of the nuclear radii), we can extract the transferred angular momentum l. The spin of the populated state is then obtained by a (vector) sum with the spin of the transferred particle, see for example eq. (9). For the simple, but recurring, case of the transfer of one nucleon onto an even-even target (in its 0^+ ground state), the final spin is constrained to the two values $J_B = l \pm 1/2$ (except for $l = 0$, for which $J_B = +1/2$).

The same conclusions can be derived from an analysis of the quantistic expression of the cross section as calculated in the framework of a model for transfer reactions (for example the Born Approximation BA, or the Distorted-Wave Born Approximation DWBA). For the extraction of l from experimental data, usually the cross section is calculated in one of these models and fitted to the data, with l and an overall normalisation (see further) as free parameters. We refer to ref. [1] for a full illustration.

2˙5. *Spectroscopic factors*. – Expressions for the cross section of a transfer reaction (probability of the process to occur) can be derived in various ways. For our purposes, we can refer to fundamental concepts such as Fermi's golden rule for the transition rate

between two states. The key quantity in the expression, as in all other expressions for a cross section, is the *transition matrix element*, which in our case can be written as

$$U(\mathbf{r}) = \int \phi_a^* \phi_A^* V(\mathbf{r}) \phi_b \phi_B \, \mathrm{d}\tau, \tag{11}$$

where ϕ are the wave functions for the internal states of the respective particles, $V(\mathbf{r})$ is some interaction potential and the integral extends to all internal degrees of freedom of the nuclei a A, b, B involved in the process. With a smart choice of the probe a, this usually reduces to a factor times the overlap between the wave functions of the complex nuclei ϕ_A and ϕ_B, which is expressed by the *spectroscopic factor*.

Various definitions of the spectroscopic factor exist, either incorporating or not statistical factors for the spin and isospin. Very generally, we may understand its meaning by considering a stripping reaction and writing the wave function of B as $\phi_B = (\phi_A \phi_x)_{(l_{Ax} j_{Ax}) J_B}$, *i.e.* the combination of A and the transferred particle x in a given orbital angular momentum and total spin. The cross section will then be proportional to the square of ϕ_x in that state and statistical factors, which together form the spectroscopic factor $S_{(l_{Ax} j_{Ax}) J_B}$.

In practice, one usually assumes $|\phi_x|^2 = 1$, *i.e.* a *pure single particle configuration*, in the calculation of the expected cross section. This calculated value is then compared([2]) to the experimental one to extract the *experimental spectroscopic factor*:

$$S_{\mathrm{exp}} = \left(\frac{\mathrm{d}\sigma}{\mathrm{d}\Omega}\right)_{\mathrm{exp}} \Big/ \left(\frac{\mathrm{d}\sigma}{\mathrm{d}\Omega}\right)_{\mathrm{cal}}, \tag{12}$$

which is essentially a measure of how much the populated state contains that specific single-particle configuration([3]). As an example see fig. 4, where the measured fractions of $^{90}\mathrm{Zr} + n$ single-particle configuration in the low-lying states of $^{91}\mathrm{Zr}$, populated in the $^{90}\mathrm{Zr}(d,p)^{91}\mathrm{Zr}$ reactions, are shown.

Spectroscopic factors (SFs) should be used with caution. The absolute values of the theoretical SFs depend upon several factors, like the model (approximation) used for the description of the reaction mechanism, and the potentials describing the interaction between nuclei (optical potentials) and the binding of the particles. The possible choices are countless, leading to SF values that may differ significantly. For this reason, very often *relative* SFs, calculated with respect to the SF of a state which is argued to have a rather pure single-particle configuration, are used to derive conclusions about the structure of the different populated states in a nucleus.

Transfer reactions are potentially very useful in the determination of the energy gap between orbitals. Simplifying, if a nucleon transfer populates two pure single-particle

([2]) A fit of the experimental angular distribution with the calculated model provides the transferred angular momentum l and the normalisation factor.

([3]) This assumes that the initial nucleus A is in a well-defined configuration (negligible mixing with excited configurations). Otherwise, all combinations have to be taken into account.

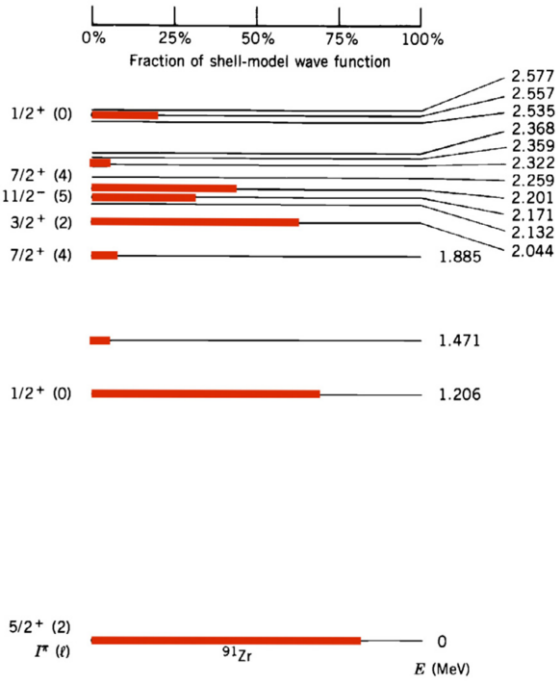

Fig. 4. – Level scheme (with spins and l-values) and fractions of single-particle wave functions deduced from the measurement of the $^{90}\mathrm{Zr}(d,p)^{91}\mathrm{Zr}$ stripping reaction. Figure adapted from ref. [6].

states, their difference in energy corresponds to the gap between the orbitals occupied by the nucleon in the two configurations. If the states are not pure and the *strength* of a configuration is spread over different states, an energy *centroid* can be found, by weighing the energy of each state by its SF. This procedure, however, relies on the detection of the full strength of a configuration; this is not obvious, because a significant fraction may lie in states at high excitation energies, outside the limit of detection (remember the condition for the threshold energy of the incoming beam). An example is the $^{40}\mathrm{Ca}(d,p)^{41}\mathrm{Ca}$ reaction, for which two $l=1$ excited states at $E^*=1.95\,\mathrm{MeV}$ and $E^*=2.47\,\mathrm{MeV}$ are observed: a hurried interpretation would be that of the transfer of a neutron to the $p_{3/2}$ and $p_{1/2}$ orbitals, respectively. The expected ratio of SFs for pure single-particle states (thus $2J+1$ statistical factors only) would give a ratio of $4/2$ in the cross section; a factor of three is observed, possibly leading to the erroneous conclusion of rather pure states and thus a very small spin-orbit splitting of $\approx 500\,\mathrm{keV}$. However, a measurement extended to higher excitation energies would reveal several other $l=1$ states with significant SFs: we now know that both the states mentioned above contain components of the $p_{3/2}$ configuration, while the $p_{1/2}$ strength is found mainly in a state at $E^*=4\,\mathrm{MeV}$ and is fragmented in many states above, with a centroid at about $4.5\,\mathrm{MeV}$. The derived spin-orbit splitting is about $2\,\mathrm{MeV}$.

3. – Transfer reactions with nuclei far from stability

We have shown how transfer reactions can be a powerful spectroscopic tool for the study of the nuclear structure. These studies have become very relevant in recent years on nuclei far from the valley of stability, since the discovery of changes in the shell structure in such systems. The reason lies in the excess number of neutron or protons, which leads to an enhancement of particular parts of the underlying nucleon-nucleon interaction [7,8]: spin-orbit force, tensor part of the interaction, three-nucleon forces, are some examples. It is thus not a surprise that the whole international community of nuclear-structure physicists is strongly investing in the research on nuclei far from stability, with the realisation of new facilities where more detailed studies will be possible.

The use of nuclear reactions to study unstable nuclei, however, carries severe experimental challenges.

3˙1. *Inverse kinematics*. – A conventional arrangement for nuclear reaction studies would consist in a beam of light ions (p, d, α particles) impinging on a thin target (a foil) of the nuclei of interest, with charged-particle detectors placed at defined angles to record the scattered particles. Unstable nuclei, however, have short half lives that do not allow making them into targets: such species are only available as beams of radioactive ions (RIBs) at dedicated facilities. Experiments have to be conducted in *inverse kinematics*, with a heavier beam impinging on a light target.

The inverse-kinematic arrangement has various implications, that can be understood by looking at the kinematical relationships of the collision; we have presented them in the appendix. We consider eq. (A.2), which shows that the characteristics of inverse-kinematic binary reactions are essentially determined by the ratio of the masses of the light target and light ejectile (see discussion in the appendix). We then expect similar kinematics regardless of the target and the beam energy (as long as the Q-value is small with respect to the centre-of-mass energy). This is shown in fig. 5, where the energy of the light particle is plotted against the emission angle in the laboratory frame for a number of reactions induced by a ^{16}C (top) and a ^{74}Kr beam (bottom). We see that the kinematic lines are similar for (p,d), (p,t), (d,t), $(p,{}^3\mathrm{He})$ on one side (at forward angles), and (d,p) on the other (at backward angles).

3˙2. *Detection setup*. – Figure 6 shows a schematic, generic setup that is used in reaction studies in inverse kinematics. Key characteristics are a good efficiency, to counter the weak intensities of the RIBs; good position resolution and energy resolution.

The target, usually a foil of material containing a light nucleus or a thin gas target, is surrounded in close geometry (within the reaction chamber) by an array of charged-particle detectors. This array catches the light products of the reactions; it has to be finely segmented to provide position information — the scattering angles of the outgoing particles — together with energy and particle identification. A good resolution is crucial (see further), but it is in conflict with the requirement of a close geometry.

Outside the reaction chamber, an array of γ-ray detectors may be present, to measure the prompt radiation emitted by the reaction products. Mostly, γ-rays are emitted by

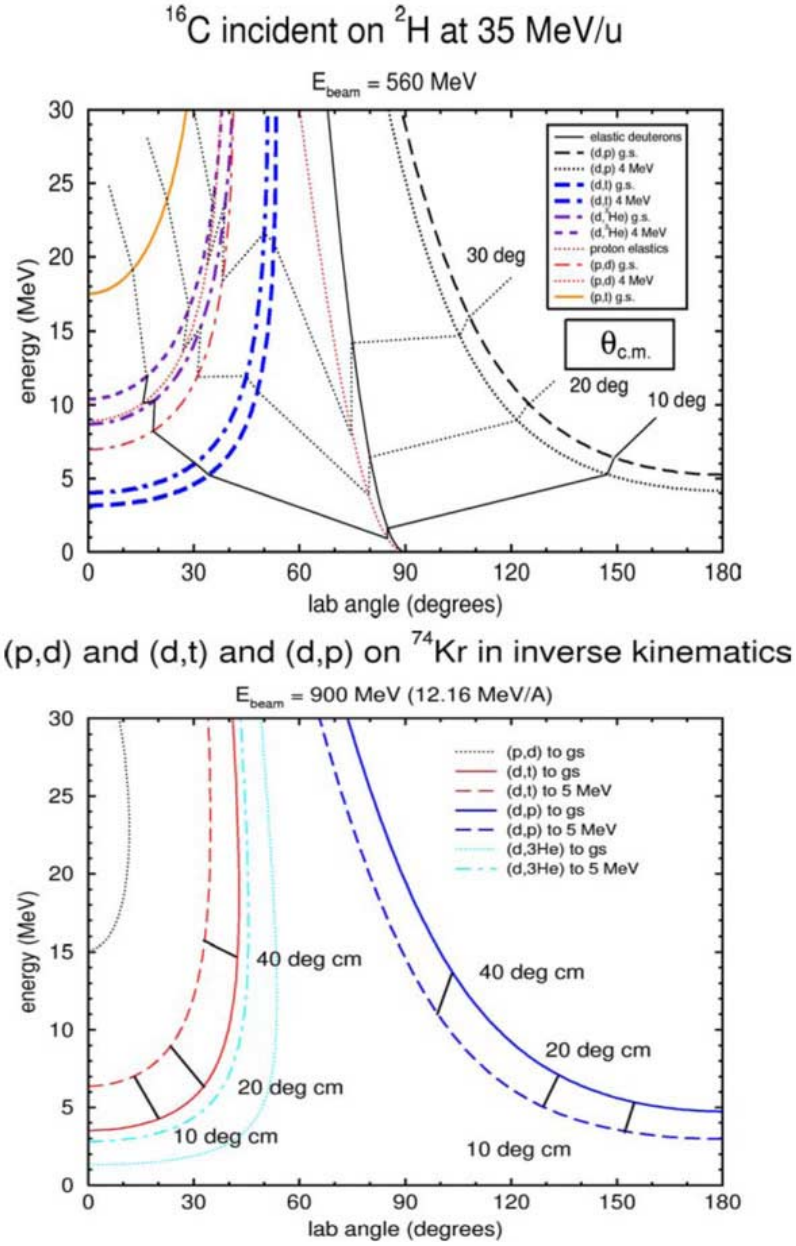

Fig. 5. – Laboratory energies and angles of the light particle emitted in reactions in inverse kinematics, induced by ^{16}C at 560 MeV (top) and ^{74}Kr at 900 MeV (bottom). Figure adapted from ref. [9].

the heavy beam-like nucleus, travelling forward at about the beam velocity, a measurable fraction of the speed of light (for example, 5 MeV/nucleon corresponds to 10% of c). The emitted γ-ray will then be Doppler-shifted, and knowledge of the emission angle is

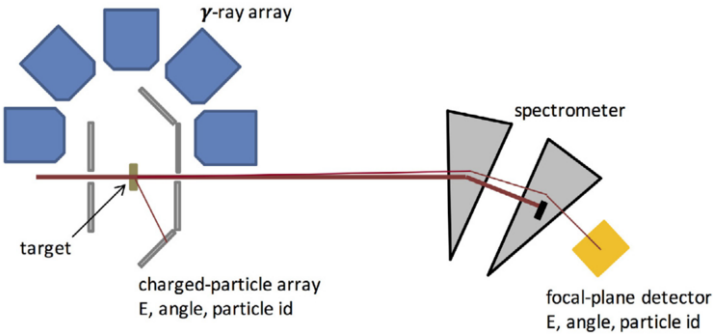

Fig. 6. – Schematic view of a generic setup for the study of reactions in inverse kinematics.

necessary for a correction. For this reason, the γ-ray array also needs to be segmented.

In the forward direction, the unreacted beam particles and the reaction products travel with very little spatial separation. A *magnetic spectrometer* may be used to separate the species, identify the reaction products and measure their momentum. This is a challenging task, and with present devices it can be achieved with good efficiency only if the mass of the incoming beam does not exceed $A \approx 50$. With larger masses the kinematics is very forward focused and a spectrometer will have to employ slits, inevitably reducing its acceptance and thus the overall efficiency of the detection setup. For this reason, in many cases a spectrometer is not used.

By studying fig. 5 in detail we can derive some important properties of the charged-particle detection setup surrounding the target.

– *A universal setup*

We notice that the energies of all particles emitted for small centre-of-mass angles (where the cross sections are largest and most structured) are rather low, around 5 MeV, and do not exceed 30 MeV in the full angular range of interest. This feature suggests that the array of charged-particle detectors surrounding the target may be built in a rather "universal" way, and used in a wide range of reaction studies.

– *Kinematical compression*

We turn now our attention to the energy difference between the light particles when reactions produce nuclei either in their ground state or in an excited state. Such differences are only a fraction of the excitation energies of the product, see for example the backward protons in $^{16}\mathrm{C}(d,p)$ or the forward tritons in $^{16}\mathrm{C}(d,t)$, in the regions were the kinematic lines are "horizontal" (small centre-of-mass angles). This is the so-called *kinematical compression* of the energies of the detected ions. As a consequence, the resolution in the Q-value of the detected event, and thus in the excitation energy of the populated state, is only a fraction of the energy resolution that is achieved in the detector itself. This is clearly a problem when the density of states in the populated nucleus is high.

– *Angular resolution*

Finally, consider the regions where the kinematic lines become more "vertical", beyond 30 degrees in the centre of mass for (d, p) reactions and beyond 20 degrees for the others. There, a small uncertainty in the detected scattering angle translates in a very large uncertainties in the Q-value and the centre-of-mass angle of the detected event. In these regions, the construction of the angular distributions of the cross sections for each excited state becomes very difficult.

The problems discussed above are aggravated by the weak intensities of RIBs. To attain the luminosity required to perform the measurement in a reasonable time (typically a week), one could increase the target thickness. This way, however, the incoming heavy ions would lose a sizeable amount of energy in the target. Since the reaction may take place at any point in the target, there is an uncertainty on the energy available at the reaction vertex. As a result, the energy of the light particle, outgoing at a given angle, is broadened, with a direct effect on the determination of the Q-value of the reaction, worsened by the kinematical compression. In practice, it is difficult to achieve resolutions in excitation energy better than about 150 keV; resolutions of the order of 500 keV or worse are often encountered.

The coincident detection of γ-rays from the decay of the heavy excited product can potentially provide a much better resolution, of the order of a few keV, on the energy of the excited states (only if, of course, γ rays are emitted in the process: for reactions populating the ground state this is not the case). However, the efficiency of γ-ray arrays is low, of the order of 10%. It is then necessary to use much thicker targets to achieve sufficient yields, with consequences on the resolution of the light charged particles. In recent measurements this has been the trend, see for example refs. [10, 11]. "Clean" angular distributions of the light particles for a populated state can be constructed by requiring a coincidence with a γ-ray from the de-excitation of the state.

Detection of the full momentum (angle and energy) of one of the reaction products is in principle sufficient to reconstruct the full kinematics of the binary reaction. Nevertheless, the use of a spectrometer for the detection of the heavy beam-like product (see fig. 6) may help alleviating the problems illustrated for the detection of the light particles and improve the resolution, but only in certain cases. To measure the momentum of the nuclei, magnetic and electric fields are used to bend their trajectories. Gaseous detectors are then used to measure the ion position (bending angle) at different locations on the track, complemented by arrays of solid-state detectors to measure the energy. Different configurations of fields are used, according to the aim of the setup, that could be oriented towards high resolution or towards a high acceptance.

In ref. [12], the authors considered some examples of neutron-transfer reactions in inverse kinematics, and calculated the effect of various contributions to the final resolution of the measurement. Their results show that a spectrometer is useful when the incoming beam nuclei are not too heavy, for example in the $^{12}\mathrm{Be}(p, d)^{11}\mathrm{Be}$ reaction in inverse kinematics. In such case, the uncertainty in the resolution of the Q-value when calculated from the momentum of the light particle is dominated by the uncertainties on

the energy loss of the beam ion (and light ejectile) in the target. The resolution on the Q-value improves (by a factor 3 or 4) if the momentum of the heavy ion is measured in a spectrometer. However, when the incoming beam particle is heavier (the authors of ref. [12] considered ^{76,77}Kr on deuterons and protons), the differences in angle between the forward-focused heavy products become too small, and the uncertainty on their determination in the spectrometer are large. In that case, the detection of the light ejectile, even with the associated large uncertainties, is preferable.

4. – Case studies

We now turn to a short selection of recent measurements of nucleon-transfer reactions with radioactive ion beams. We will only briefly touch on the experimental aspects, focusing rather on the motivations and the conclusions derived from the results, which concern aspects of the nucleon-nucleon interaction and their effect on the shell evolution.

4˙1. *Light nuclei*. – The unexpected results on the structure of light exotic nuclei — diffuse matter distributions (halos), strong clustering, states with structures reminiscent of those found in molecules — were among the main triggers for the development of the field of radioactive ion beam research.

Here we focus on the magic number $N = 8$. At stability, the sequence of the neutron orbitals predicted by the shell model is $1p_{1/2}$ below $N = 8$, $1d_{5/2}$ and $2s_{1/2}$ above. The shell closure is indeed well established in oxygen isotopes: ^{17}O has the expected $J^\pi = 5/2^+$ ground state and a $1/2^+$ excited state at 871 keV. Both states exhaust most of the strength of the single-particle configurations, so that the energy difference is a good indication of the distance between the $\nu 1d_{5/2}$ and $\nu 2s_{1/2}$ orbitals. The $N = 8$ gap can be estimated from the position of the $\nu 1p_{1/2}$ hole strength, which is mostly found in the $1/2^-$ second excited state at 3.055 MeV.

Already in ^{15}C, however, two protons below, we find a $1/2^+$ ground state and a $5/2^+$ excited state at 740 keV, indication of an inversion of the two orbitals. Part of the $\nu p_{1/2}$ hole strength is in a state at 3.103 MeV, but experimental information is scarce. The $N = 7$ ^{13}C isotope has the predicted $1/2^-$ ground state and a $1/2^+$ state at 3.089 MeV; the $d_{5/2}$ strength is in states at higher excitation energy.

The collapse of the $N = 8$ shell appears suddenly in ^{11}Be: instead of the expected $1/2^-$, the spin-parity of the ground state is $1/2^+$. This is an indication of the lowering of the $\nu 2s_{1/2}$ orbital below the $\nu 1p_{1/2}$, see fig. 7. The $1/2^-$ state is observed at 320 keV, close to the neutron separation energy at 502 keV.

A $1/2^+$ state could also be formed by the coupling of a neutron in $d_{5/2}$ with a 2^+ excited ^{10}Be core (a 2^+ state in ^{10}Be is located at 3.37 MeV). In order to probe the structure of the ^{10}Be core in the ^{11}Be ground state, a measurement was performed at the GANIL facility in Caen (France) [13, 14]. The reaction employed for this study was the neutron removal ^{11}Be$(p, d)^{10}$Be, with the aim of measuring the final state of ^{10}Be and correlate it to the probability of existing as such in the original ^{11}Be nucleus. The ^{11}Be

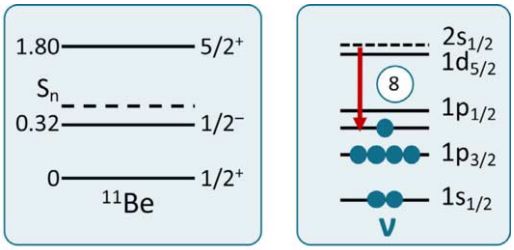

Fig. 7. – Level scheme and sequence of the neutron orbitals in ^{11}Be. The lowering of the positive-parity $2s_{1/2}$ into the negative-parity $1p$ shell is indicated.

beam was obtained by fragmentation of a primary ^{15}N beam at 65 MeV/nucleon. The final ^{11}Be beam had an energy of 35.3 MeV/nucleon and an average intensity of 3×10^4 particles per second (pps). The outgoing deuterons were identified in the CHARISSA silicon detectors, fig. 8(a), while the momentum of the residual ^{10}Be nuclei was measured in the SPEG magnetic spectrometer.

The spectrum of events as function of the focal plane position, which corresponds to the energy of the ^{10}Be nuclei, is shown in fig. 8(b). The resolution is about 700 keV. A group corresponding to the 0^+ ground state is observed, coming from the $[0^+ \otimes 2s]_{1/2^+}$ component in the ground state of ^{11}Be. As well, the events where the ^{10}Be is left in its 2^+ state are a measure of the $[2^+ \otimes 1d]_{1/2^+}$ component. The fit of the angular distributions shown in fig. 8(c) was made assuming a DWBA model for the transfer; from the normalisation, the spectroscopic factors were extracted. Different optical-model potentials (corresponding to the different curves) provided rather dissimilar absolute SFs; however, the ratio of the SF for the 2^+ state to the total $\mathrm{SF}(0^+) + \mathrm{SF}(2^+)$ was shown to be rather constant, with a minimum value set at 30% [13].

Besides the uncertainties in the interaction potential, as we mentioned in sect. **2**˙5, attention should be given to the way one builds the composite configurations $[0^+ \otimes 2s]_{1/2^+}$ and $[2^+ \otimes 1d]_{1/2^+}$. In [14], a new analysis was performed by taking into account the large deformation in the 2^+ state of ^{10}Be and recalculating the corresponding ^{11}Be wave functions and spectroscopic factors. The new results pointed to a dominant (84%) $[0^+ \otimes 2s]_{1/2^+}$ component in the ground state of ^{11}Be, with only about 16% of the $[2^+ \otimes 1d]_{1/2^+}$ core-excitation admixture.

Another transfer reaction measurement in this region used the ^{11}Be$(d, p)^{12}$Be neutron stripping to investigate the structure of the 0^+ states in ^{12}Be [15]. Because of the small difference in energy between the $s_{1/2}$ and $p_{1/2}$ orbitals, it is expected that the two configurations, with a pair of neutrons in one or the other orbital, may generate two 0^+ states with mixed contents. Indeed, besides the ground state, a 0^+ excited state is observed at 2.24 MeV, see fig. 9(a). The neutron transfer to the ground state of ^{11}Be (which already has a neutron in $s_{1/2}$) would populate only the $\nu(s_{1/2})^2$ configuration — two neutrons in the $s_{1/2}$ orbital — in each 0^+ state.

The experiment was performed at TRIUMF (Vancouver, Canada) with a ^{11}Be beam (produced using the Isotope-Separation On-Line method) at 5 MeV/nucleon. Segmented

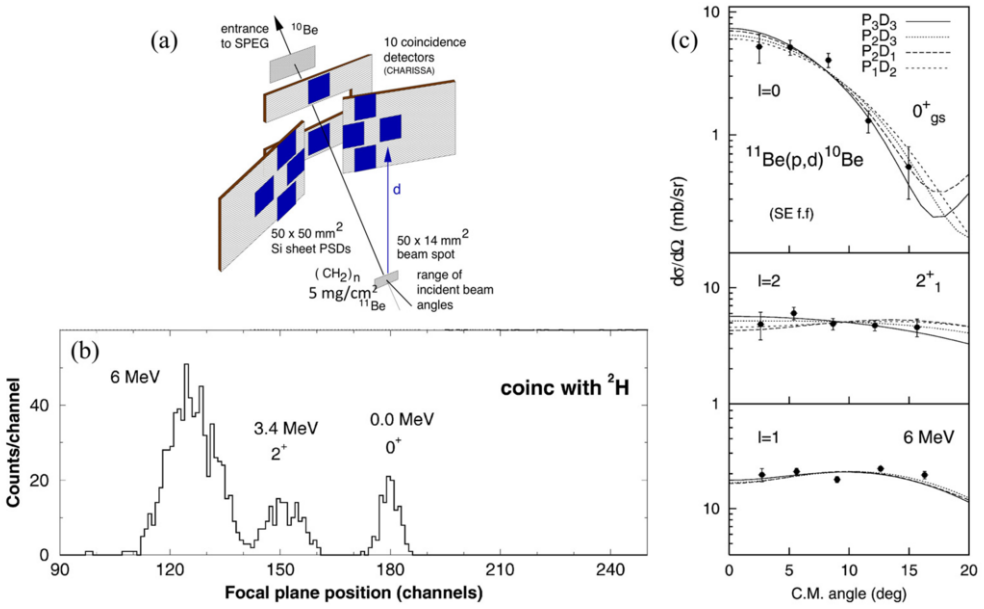

Fig. 8. – The ^{11}Be$(p,d)^{10}$Be measurement [14]. (a) Schematic view of the CHARISSA detector array. (b) Focal-plane spectrum of ^{10}Be events, in coincidence with deuterons identified in CHARISSA. (c) Angular distributions (number of events as function of the detection angle) for the three observed peaks, with fits based on a DWBA model (the curves are calculated for different optical model potentials). Figure adapted from ref. [14].

charged-particle detectors were employed to measure the protons, emitted in the backward hemisphere, in coincidence with the ^{12}Be nuclei identified in the forward hemisphere. All bound states in ^{12}Be were populated in the reaction: the 0^+ states with a neutron transfer to the $2s_{1/2}$ orbital, the 2^+ state through a transfer to the $1d_{5/2}$ orbital and the 1^- state with a neutron transfer to the $1p_{1/2}$ orbital (negative parity). The excited 0^+ state could not be separated from the closely-lying 2^+ state, fig. 9(b), and the corresponding angular distribution had to be fitted with a sum of the predicted cross sections for the two states (fig. 9(c), middle panel). The extracted spectroscopic factors for the $\nu(s_{1/2})^2$ configuration were $0.28^{+0.03}_{-0.07}$ for the ground state and $0.73^{+0.27}_{-0.40}$ for the 0^+ excited state.

While this result may lead to think that the natural order $1p_{1/2}$-$2s_{1/2}$ is restored in ^{12}Be, a recent measurement of the same reaction [16] has shown that the dominant configuration in the ground-state of ^{12}Be is in fact the intruder $\nu(d_{5/2})^2$. While an evolution of the sequence of neutron orbitals is observed when going from ^{11}Be to ^{12}Be, the collapse of the $N = 8$ shell closure persists.

4˙2. *The emergence of* $N = 16$. – Figure 10 shows the portion of the chart of nuclei that we will discuss in this section. The collapse of the $N = 20$ neutron shell closure,

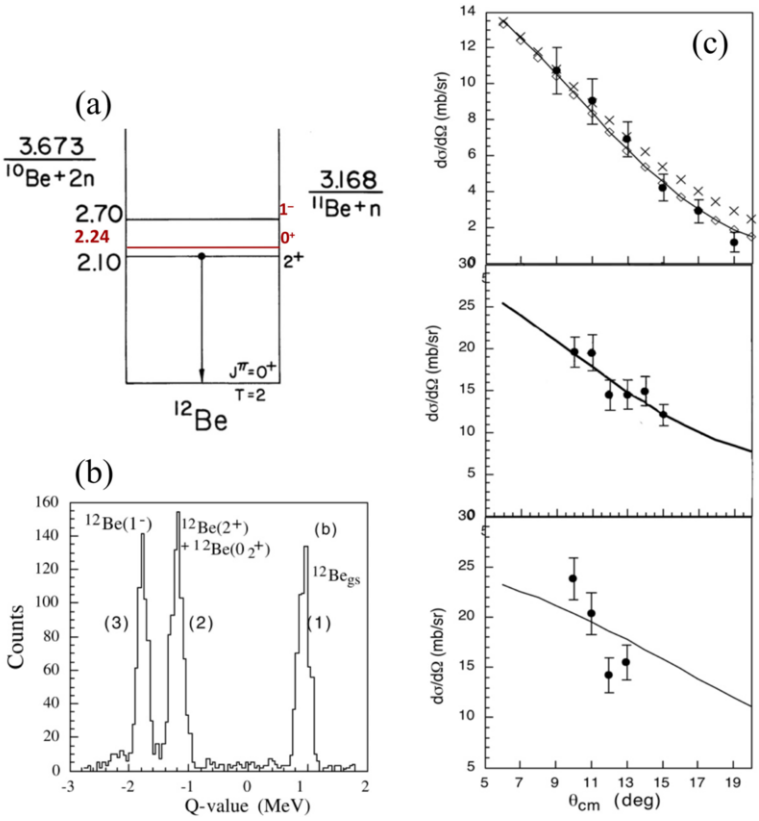

Fig. 9. – The ^{11}Be$(d,p)^{12}$Be measurement [15]. (a) Low-lying (bound) energy levels in ^{12}Be. (b) Proton spectra, detected in coincidence with ^{12}Be nuclei, plotted as function of the reaction Q-value. (c) Top: angular distribution for the transfer to the ground state, peak (1) in panel (b): the black circles are the experimental data, other markers and the line are DWBA calculations using different potentials; middle, angular distribution and best fit for the 2^+-0^+ doublet, peak (2) in panel (b); bottom, angular distribution and best fit for the 1^- state, peak (3) in panel (b). Figure partly adapted from ref. [15].

when descending from stability (^{38}Ar and ^{36}S) towards ^{32}Mg was the first identification of shell evolution far from stability in the mid-1970s. This was eventually explained in terms of the underlying nucleon-nucleon interaction, which in this region is dominated by the force between the protons in $\pi d_{5/2}$ (full in Si at $Z = 14$) and the neutrons in the $\nu d_{3/2}$ orbital (full at $N = 20$). When the $\pi d_{5/2}$ empties, the $\nu d_{3/2}$ becomes rapidly less bound, thus closing the gap at $N = 20$, see fig. 11. Two-particle two-holes (2p-2h) excitations across the gap become possible, as the necessary energy is compensated by the gain in quadrupole correlation that drive the ^{32}Mg nucleus to deformation.

At the same time, fig. 11 shows that, below the $\nu d_{3/2}$ orbital, a new gap at $N = 16$ develops. This gap becomes very large (about 4 MeV) in oxygen at $Z = 8$, where the

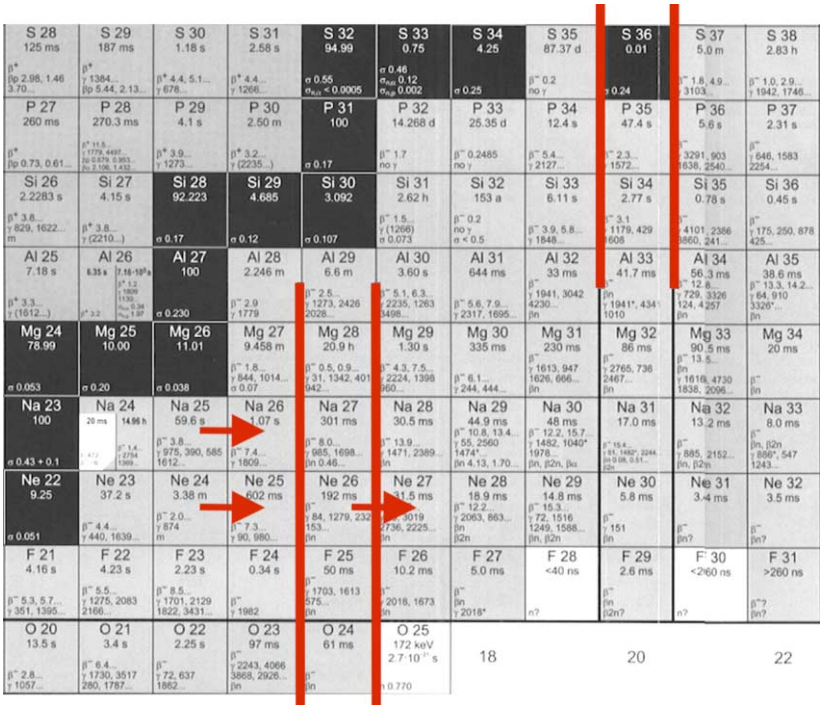

Fig. 10. – Portion of the chart of nuclei showing the disappearing shell closure at $N = 20$ and the emerging one at $N = 16$. Arrows indicate the nuclei involved in the (d, p) reactions discussed in this section.

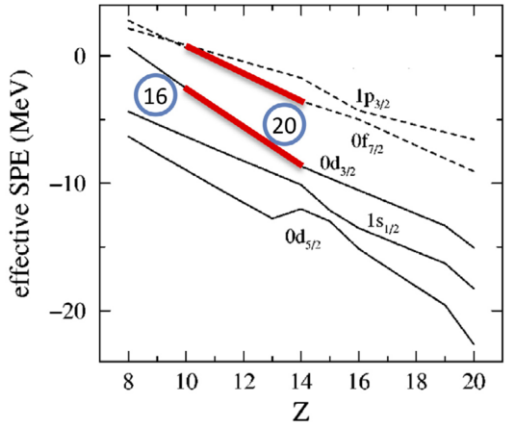

Fig. 11. – Effective single-particle energies for $N = 20$ isotones as a function of the proton number. The figure shows the narrowing of the gap at $N = 20$ and the appearance of a gap at $N = 16$ when the proton number decreases from 14 to 8. Figure adapted from ref. [17].

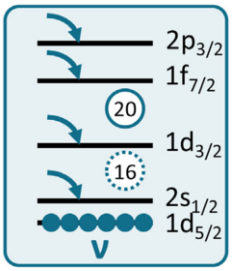

Fig. 12. – Orbitals above $N = 14$ that can be populated in the neutron-transfer reactions ^{24}Ne$(d,p)^{25}$Ne, ^{26}Ne$(d,p)^{27}$Ne and ^{25}Na$(d,p)^{26}$Na.

$\nu d_{3/2}$ is unbound by about 1.5 MeV. The attractive neutron-neutron interaction that appears when adding neutrons to this orbital in ^{26}O is not any more sufficient to bind the nucleus: the neutron drip line suddenly appears, 6 neutrons earlier than in the flourine isotopic chain. Recent works by Otsuka *et al.* [18] also highlight the essential role of three-nucleon forces in the evolution of the $\nu d_{3/2}$ orbital.

We discuss now three nucleon-transfer measurements, performed to investigate the $N = 16$ gap in the Na and Ne isotopic chains (see fig. 10): ^{24}Ne$(d,p)^{25}$Ne, ^{26}Ne$(d,p)^{27}$Ne and ^{25}Na$(d,p)^{26}$Na [11, 19, 20]. The measurements were performed at GANIL (on the Ne isotopes) and TRIUMF (with the ^{25}Na beam) using very similar setups: a very efficient array of charged-particle detectors surrounding the target in closed geometry (TIARA at GANIL, SHARC at TRIUMF), an array of high-resolution germanium γ-ray detectors (EXOGAM in France, TIGRESS in Canada) and a zero-degree device for the detection of the beam-like particles: the VAMOS magnetic spectrometer in GANIL, the TRIFOIL scintillation detector in TRIUMF. While the plastic scintillator was only used to separate the products of direction-reaction events from residues of fusion-evaporation reactions through their different time-of-flight from the target to the detector, the VAMOS spectrometer provided an identification of the particles and a measurement of their momentum. The detection of de-excitation γ rays allowed to resolve the excited states populated in the transfer, otherwise overlapping in the poorly-resolved particle spectra. By selecting events with charged-particles energies in a narrow region around that of a coincident γ-ray, charged-particle angular distributions of transfers to the different states were obtained.

The orbitals that can be populated by the transferred neutron in the reactions mentioned above are shown in fig. 12.

Figure 13 summarises the results for the ^{24}Ne$(d,p)^{25}$Ne reaction [19]. Panel (a) shows example of proton spectra measured at different angles, as a function of the excitation energy in ^{25}Ne. States, which are not resolved in the spectra, are identified through the coincidence with γ-rays, which are shown in panel (b). The deduced level scheme and observed γ-rays are reported in panel (c), while the angular distributions (as a function of the laboratory angle) are shown in panel (d), labeled by the excitation energy

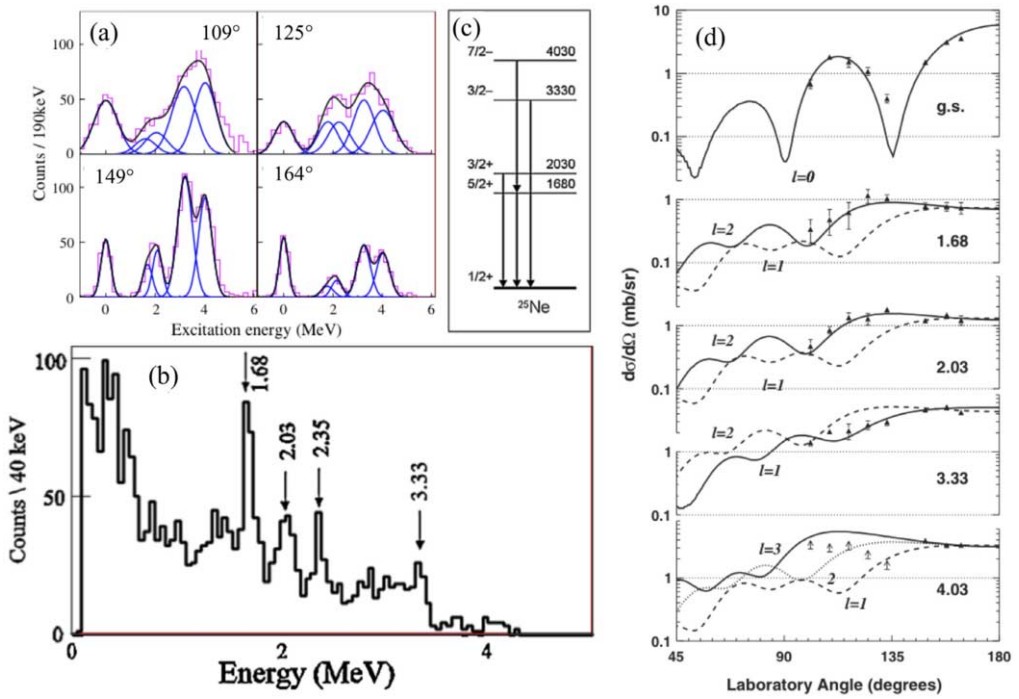

Fig. 13. – Results for the ^{24}Ne$(d,p)^{25}$Ne reaction [19]. (a) Proton yields at various laboratory angles, fitted with states as deduced from the γ-ray analysis. (b) Doppler-corrected γ-ray spectrum in coincidence with all protons. (c) Deduced level scheme and γ-decay pattern of ^{25}Ne. (d) Angular distributions for the different populated states compared to normalised ADWA calculations. Adapted from ref. [19].

and compared with (normalised) ADWA calculations. The extraction of the transferred angular momenta l, together with considerations on the γ-decay pattern, led to the spin assignment of panel (c). The $l = 2$ state at 1.68 MeV is assigned spin $5/2^+$ on the basis of the decay pattern and because it is much less populated than the other $l = 2$ state at 2.03 MeV; this is because the $5/2^+$ is a hole state that can only be populated through admixtures of excited configurations in the ground state of ^{24}Ne. The state at 2.03 MeV is the $3/2^+$ (neutron in $1d_{3/2}$), which is raised about 1 MeV with respect to the $5/2^+$ when compared to ^{27}Mg. On the other hand, the distance between the $1/2^+$ ground state and the $5/2^+$ excited state remains about the same in the two nuclei: this points to an increase of the $N = 16$ gap between $\nu 2s_{1/2}$ and $\nu 1d_{3/2}$. The simultaneous observation of the intruder negative-parity $3/2^-$ and $7/2^-$ states (at about the same energy as in ^{27}Mg) confirms the erosion of the $N = 20$ gap. Notice that a discussion on the actual energy of the orbitals (single-particle energies) should be nuanced depending on the single-particle character of the states, as determined by the measured spectroscopic factors; however, if we assume that the character of the states is similar for the nuclei that are directly compared, here ^{25}Ne and ^{27}Mg, the conclusions remain essentially valid.

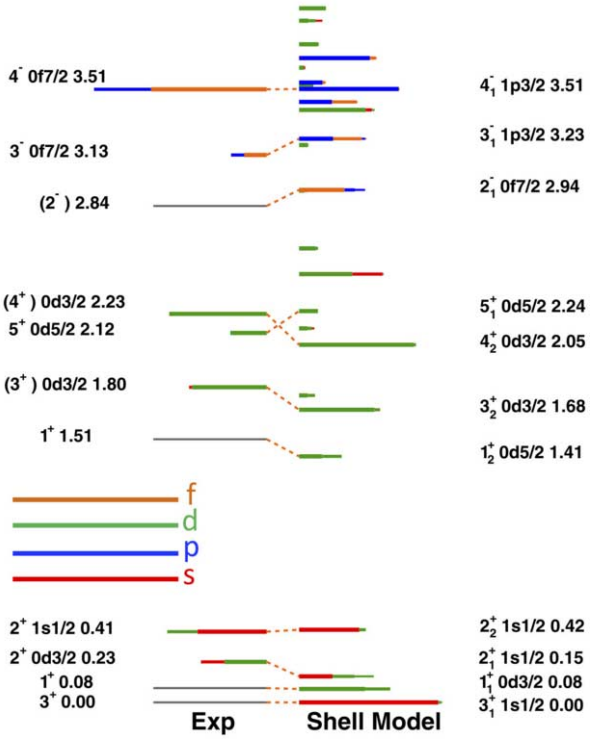

Fig. 14. – States populated in the ^{25}Na$(d,p)^{26}$Na, with spin assignments and strength of the neutron configurations as deduced from the spectroscopic factors extracted from the measurement, compared to shell-model predictions. Adapted from ref. [11].

The ^{25}Na$(d,p)^{26}$Na reaction [11] populates states in the odd-odd nucleus ^{26}Na. Typically, the density of states is higher and their structure is difficult to interpret as they result from the coupling of the odd proton (normally in the $\pi 1d_{5/2}$) with the odd neutron. Figure 14 shows the states populated in the measurement, where possible with the spin assignment and the strengths of the various configurations as determined by the spectroscopic factors. They are compared to shell-model calculations performed in a complete *sp-sdfp* basis and incorporating an *ad hoc* reduction of the $N = 20$ shell gap by 0.7 MeV. The overall agreement is good; the remarkable feature is the presence of rather low-lying negative-parity states, due to the neutron sitting in the $1f_{7/2}$ and $2p_{3/2}$ orbitals. The trend observed in the neighbouring nuclei (narrowing of the $N = 20$ gap) is confirmed in ^{26}Na, with an important role played by the $2p_{3/2}$ orbital that comes down in energy with respect to the ^{28}Al isotone.

In the ^{26}Ne$(d,p)^{27}$Ne reaction [20] we start from a $N = 16$ nucleus, thus we expect to transfer the neutron to the orbitals above the $2s_{1/2}$ (fig. 12). This measurement was the most challenging to perform, with a beam intensity of only ≈ 2500 pps. The weak intensity forced the use of a rather thick target (1.2 mg/cm^2), resulting in a very poor

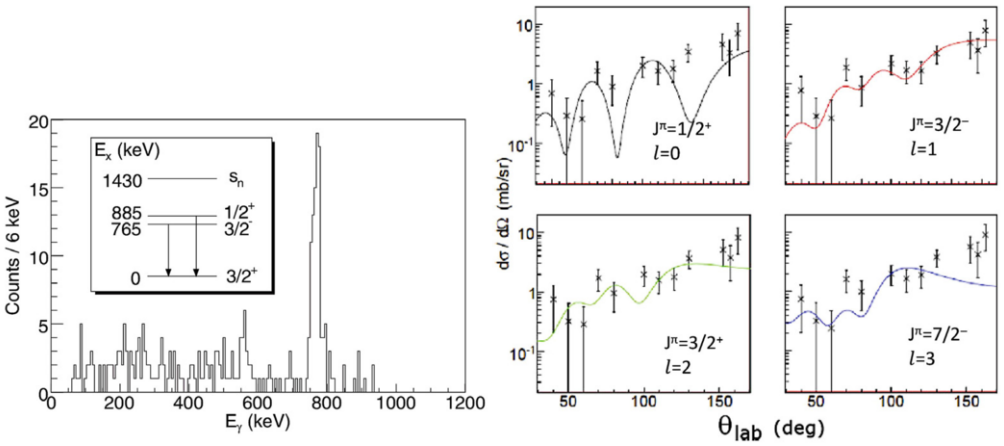

Fig. 15. – Results for the ^{26}Ne$(d,p)^{27}$Ne reaction [20]. Left, the Doppler-corrected γ-ray spectrum in coincidence with ^{27}Ne identified in VAMOS, with, in the insert, the decay pattern in ^{27}Ne. The presence of a state at 885 keV is known from previous measurements. Right, angular distribution for the state at 765 keV (charged-particle – γ-ray coincidences) compared to calculations for different values of l. A value $l = 1$ is preferred. Adapted from ref. [20].

Q-value resolution from the charged-particle spectra (630 keV FWHM). Once again, the coincidence with γ-rays was crucial to identify the populated states, for which the energy was already known from a previous measurement [21]. The result are shown in fig. 15. On the left, the γ-ray spectrum in coincidence with ^{27}Ne ions identified in VAMOS (thus for transfers to bound states in ^{27}Ne) clearly shows only one of the two known states at 765 keV and 885 keV. The higher in energy is very poorly populated (confirming the previous measurement), which is expected if the spin-parity is $1/2^+$: this states results from a hole in the $\nu 2s_{1/2}$ orbital, a configuration which is only weakly present in the ground state of ^{26}Ne. The angular distribution of the 765 keV state, shown on the right([4]), is best fitted by a calculation for $l = 1$ leading to an assignment of $3/2^-$ with a spectroscopic factor $\mathrm{SF}(3/2^-) = 0.64(33)$. For the ground state (not shown in the figure) the authors obtained $\mathrm{SF}(3/2^-) = 0.42(22)$. The uncertainties are large; however, the lowering of the $3/2^-$ state to less than 1 MeV from the $5/2^+$ is a clear sign of the collapse of the $N = 20$ shell gap (see fig. 12).

What about the $f_{7/2}$ strength? Clearly, there is an inversion, already observed in ^{25}Ne, with the $p_{1/2}$ orbital as compared to the sequence at stability. Its measurement in

([4]) Since the angular distributions are built from proton-γ coincidence events, one needs to consider the combined detection efficiency for a given spin. Except for $l = 0$, there is an angular correlation between the directions of the charged particle and γ ray. The correlation changes with the value of l, thus a correction for the coincident detection efficiency must be introduced each time. The four angular distributions on the right of fig. 15 are from the same state, but they differ slightly.

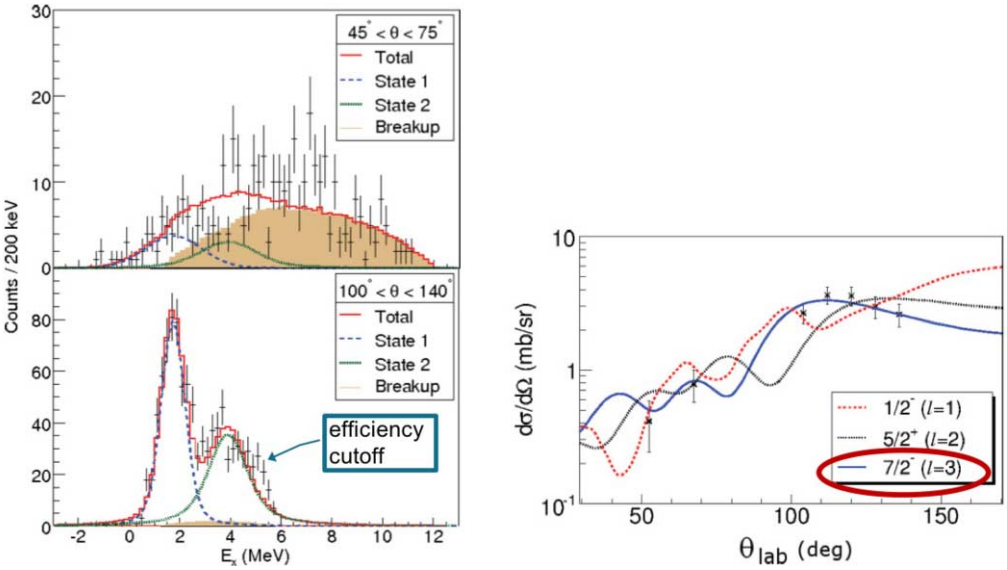

Fig. 16. – Left, reconstructed excitation energy for the coincident detection of a proton and a ^{26}Ne nucleus from the $^{26}\mathrm{Ne}(d,p)^{27}\mathrm{Ne}^{*} \rightarrow {}^{26}\mathrm{Ne} + \mathrm{n}$ process. The two panels correspond to different detection angles for the protons. Right, angular distribution of the observed peak at 1.74 MeV, best fit by a calculation for an $l = 3$ transfer. Adapted from ref. [20].

^{27}Ne, however, is complicated by the low neutron separation energy: the $f_{7/2}$ strength lies in the continuum. When such a state (resonance) is populated, it mainly decays via neutron emission instead of γ. Experimentally, these events were selected by requiring a coincidence of a proton at backward angles (from the (d,p) reaction) with a ^{26}Ne nucleus (from the breakup of ^{27}Ne) in the VAMOS spectrometer. Possible background events come mostly from the direct breakup of the deuteron into a proton and a neutron. The spectrum is shown in fig. 16 (left) for two different angular domains. The background from the deuteron breakup has known energy distribution and shape (obtained from simulations). It is fitted to the spectrum in order to maximise its contribution and derive a minimum number of events for the population of the $f_{7/2}$ states. As expected, the background is only pronounced at forward angles, where, on the other hand, the cross section for transfer should be small. The spectra show two peaks, one at 1.74 MeV and one higher; the latter could be the result of detection cutoff in the spectrum at backward angles (where the energy of the protons is low), but it appears to be an actual resonance in the forward-angle spectrum. The width of the 1.74 MeV resonance, once the experimental resolution is unfolded, is consistent with $\Gamma = 0$ and has a 2σ limit $\Gamma < 0.46$ MeV. The angular distribution, shown on the right in fig. 16, agrees with an $l = 3$ transfer and thus a $7/2^{-}$ assignment. Notice that the calculation of the cross section of a nucleon-transfer reaction to a state in the continuum is a non-trivial problem, essentially because the scattering wave function is not integrable; different clever tricks

can be used, but at present there is no consensus on the best way to model the process.

Coming back to the measurement, the same shell-model calculation used for ^{26}Na, with the a lowering of 0.7 MeV for the fp shell above $N = 20$, reproduces the state sequence and energies in ^{27}Ne remarkably well. Once more, this is a confirmation of the strong decrease of the $N = 20$ gap also in this region, accompanied by a lowering of the $2p_{1/2}$ strength.

4˙3. *The spin-orbit term.* – The (central) spin-orbit (SO) term in the nucleon-nucleon interaction is often parametrised by the expression

$$V_{ls}(r) = \frac{1}{r}\frac{\mathrm{d}\rho}{\mathrm{d}r}\,\mathbf{l}\cdot\mathbf{s} \tag{13}$$

which contains the derivative of the matter distribution as a coefficient. The strength of the interaction is thus maximum at the surface. This has an intuitive explanation, as a nucleon moving in the interior of a nucleus through uniform nuclear matter would not experience a SO force, because there would be no preferred reference point for the definition of **l**.

For nuclei far from stability, for example with a large excess of neutrons, it is expected that the matter distribution would become more diffuse, with less sharp edges. This reduction of the density gradient would cause a decrease of the SO force. Conversely, if a nucleus has a depletion of the density in its interior, the SO force could also decrease there (the derivative has the opposite sign with respect to the one at the surface). These ideas are illustrated in fig. 17.

The ^{46}Ar$(d,p)^{47}$Ar transfer measurement was performed at GANIL with the aim of measuring the SO splitting between the $\nu 2p_{3/2}$ and $\nu 2p_{1/2}$ orbitals above the $N = 28$ shell closure [22]. The experimental setup consisted in the MUST array of charged-particle telescope detectors around the target and the SPEG magnetic spectrometer, which was only used to identify the ^{47}Ar nuclei in coincidence with protons to reduce the background (from the deuteron breakup and the C nuclei in the plastic target). The beam was delivered by the SPIRAL facility (ISOL production method) at 11 MeV/nucleon and a mean intensity of 2×10^4 pps.

Figure 18 shows the neutron orbitals that can be populated with a transfer on ^{46}Ar ($Z = 18$, $N = 28$). The results of the measurements are summarised in fig. 19. We notice how, without an array of γ-ray detectors, one has to cope with the poor resolution of the particle spectrum alone, panel (a). The angular distributions, panel (b), are nevertheless rather well characterised, providing the l values reported in panel (c). As usual, the fit to DWBA calculations also provides the spectroscopic factors. The identification of the peaks and the spin assignment relies partially on the prediction of the shell model. The ground state and the one at 1.13 MeV, both populated with $l = 1$ transfers, are assigned the spins $3/2^-$ and $1/2^-$, respectively. They both contain a good fraction of the respective single-particle strength (especially the excited state). A state at 1.74 MeV (hardly resolved in the figure, but with a different angular distribution than the peak at 1.13 MeV) is identified as an $l = 3$, $7/2^-$ state predicted by the shell model. This hole

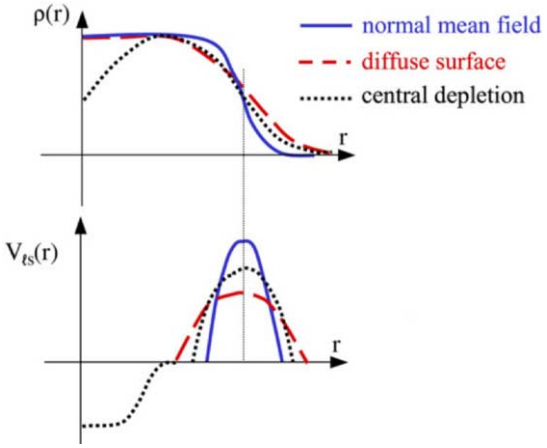

Fig. 17. – Top, density distributions for normal nuclei (blue continuous line), nuclei with a diffuse surface (red dashed line) and with a central density depletion (black dotted line). Bottom, corresponding strengths of the SO interaction. Adapted from ref. [7].

state is not much populated; its presence, however, points to a partial occupancy of the $\nu p_{3/2}$ orbital already in ^{46}Ar, providing a partial explanation for the missing strength in the ground state of ^{47}Ar. Finally, the group of non-fully resolved states from ≈ 2.6 MeV up to ≈ 4 MeV is assigned to the $f_{5/2}$ strength.

Conclusions are drawn from the comparison with the neighbouring isotone ^{49}Ca. With respect to the latter, in ^{47}Ar the $N = 28$ gap is reduced by about 330 keV; the $f_{7/2}$-$f_{5/2}$ SO (f SO) splitting is reduced by 875 keV, while the $p_{3/2}$-$p_{1/2}$ SO (p SO) splitting decreases by 890 keV (45% of its value in ^{49}Ca). This latter reduction was then revised and brought to a smaller value of 270 keV in a subsequent work by the same authors, to account for correlation energies and missing strengths in the configurations.

What is the reason for these reductions? The authors point out that no difference is expected in the matter diffuseness at the surface of ^{49}Ca and ^{47}Ar. Instead, the difference should be looked for in the removal of two protons from the $\pi 1d_{3/2}$ orbital

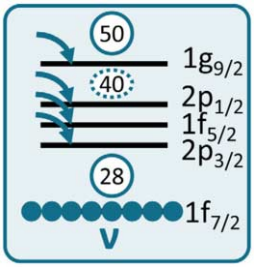

Fig. 18. – Orbitals above $N = 28$ that can be populated in the neutron-transfer reactions $^{46}\mathrm{Ar}(d,p)^{46}\mathrm{Ar}$.

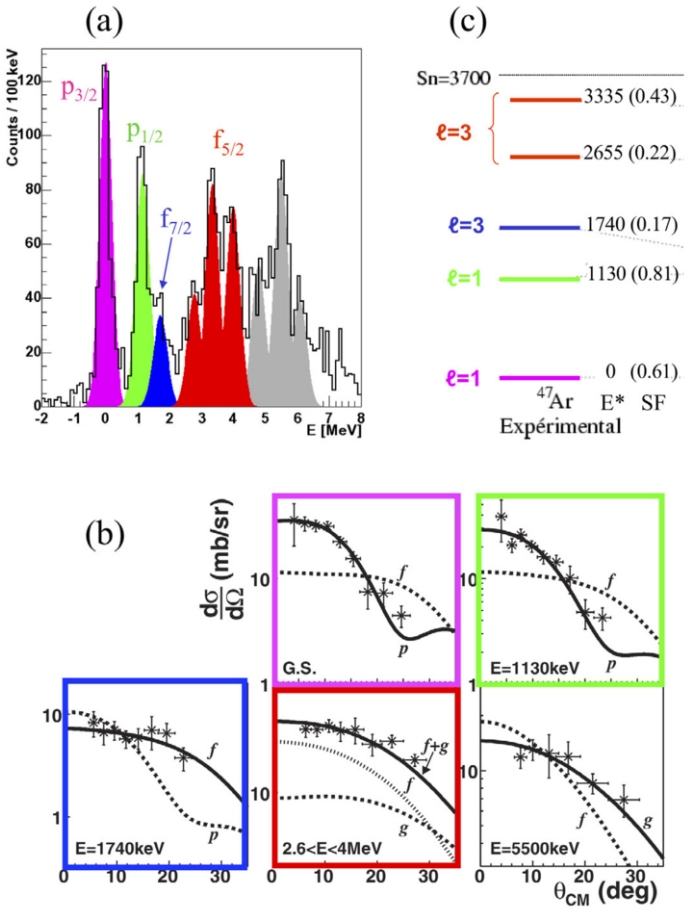

Fig. 19. – Results of the $^{46}\mathrm{Ar}(d,p)^{47}\mathrm{Ar}$ measurement [22]. Counterclockwise from top left: (a) proton spectrum as function the reconstructed excitation energy in ^{47}Ar. (b) Angular distributions for the populated states along with DWBA calculations assuming transfers with $l = 1$, 3, 4. The colours correspond to the peaks identified in the proton spectrum. (c) Derived spectrum of ^{47}Ar with excitation energies and spectroscopic factors for the populated states. Adapted from ref. [22].

(and partially from the $\pi 2s_{1/2}$ orbital, which is quasi-degenerate with the $\pi 1d_{3/2}$ in ^{48}Ca). The proton-neutron tensor force [23] has opposite signs between protons in $\pi d_{3/2}$ and neutrons in $\nu f_{7/2}$ (attractive), and the same protons with the neutrons in $\nu f_{5/2}$ (repulsive); its calculated value explains well the change in the f SO splitting. This force, however, is balanced by other components when we consider the global effect of the $\pi d_{3/2}$ protons on the $\nu p_{3/2}$ and $\nu p_{1/2}$ orbitals. The change in the p SO splitting is to be found, according to the authors, entirely in the removal of the $\pi s_{1/2}$ proton strength, which causes a depletion of the density in the inner part of the nucleus.

The conclusion from the work above implies that an even stronger p SO reduction should be observed when *all* the protons are removed from the $\pi s_{1/2}$ orbital, *i.e.* for the Si isotopes at $Z = 14$. This is best probed at a neutron shell closure, where single-particle strengths are concentrated in a few states: at $N = 28$ around ^{42}Si or at $N = 20$ around ^{34}Si. The measurement of the ^{34}Si$(d, p)^{35}$Si reaction [24] was aimed precisely at this goal.

The experiment was performed at the LISE in-flight separation facility of GANIL, with a 20 MeV/nucleon ^{34}Si beam at an average intensity of 10^5 pps. The array of charged-particle detectors around the target was MUST2, composed of $10 \times 10\,\mathrm{cm}^2$ finely-segmented telescopes with different detection stages for particle identification. A rather thick CD_2 target ($2.6\,\mathrm{mg/cm}^2$) was used, but the populated states could be resolved thanks to the γ-rays detected in the EXOGAM array. Downstream from the target, the beam-like particles were identified by means of their energy loss in an ionisation chamber; an additional plastic detector allowed the separation of direct-reaction events from fusion residues through their time-of-flight from the target.

The orbitals that can be populated in the neutron transfer onto ^{34}Si are those above $N = 20$: the same as in fig. 18, with the addition of the empty $1f_{7/2}$ orbital. The results are summarised in fig. 20. Some states were already observed in previous measurements, in particular a bound state at 910 keV (negative parity, tentative assignment 3/2) and a 6 ns isomer at 973 keV (tentative assignment $3/2^+$) seen in the β-decay of ^{35}Al. The breakup threshold is at $S_n = 2.47$ MeV. Knowledge of those states guided the selection of the peaks in the proton spectrum, fig. 20(a), fitted with "rectangular" functions that took into account the energy loss of the beam in the target. From the number of γ-rays from the de-excitation of the 910 keV state, panel (b), the number of protons in the structure at ≈ 950 keV is consistent with a pure population of the 910 keV state, with no yield from the 973 keV state. The structure at ≈ 2 MeV is confirmed as a state by the observation of the 1134 keV γ-ray of the de-excitation to the 910 keV state. Angular distributions, panel (c), provided the l assignment and the spectroscopic factors. These are compared to those of the neighbouring heavier isotones in panel (d).

The main conclusion from this work is a sizeable reduction of the splitting between the $3/2^-$ and $1/2^-$ states, that carry most of the strength of the p SO partners orbitals (while the difference between the f SO partners remains about constant). After unfolding the contribution of correlations (with the help of shell-model calculations), the actual reduction of the p SO splitting was calculated to be ≈ 380 keV. This value was argued to be due *entirely* to the monopole SO interaction between the protons removed from the $\pi 2s_{1/2}$ orbital and the neutrons in the p orbitals. Since the $\pi 2s_{1/2}$ occupancy goes from 1.7 in ^{37}S (measured value) to 0.19 in ^{35}Si (calculated value), the proton-neutron s-p SO interaction is calculated to be ≈ 260 keV. This would be thus a first clean experimental determination of the two-body SO interaction in nuclei.

The results from [24] rely on shell-model calculations for the $\pi 2s_{1/2}$ occupancy in ^{35}Si. A recent measurement, however, has tried to check this number experimentally. The probability of proton removal from ^{34}Si was measured in a knock-out reaction at the NSCL facility (MSU, Michigan, USA) [25]. A fast (beyond a hundred MeV/nucleon) beam of ^{34}Si was sent on a ^{9}Be target; after the removal of a proton, the residue ^{33}Al ions

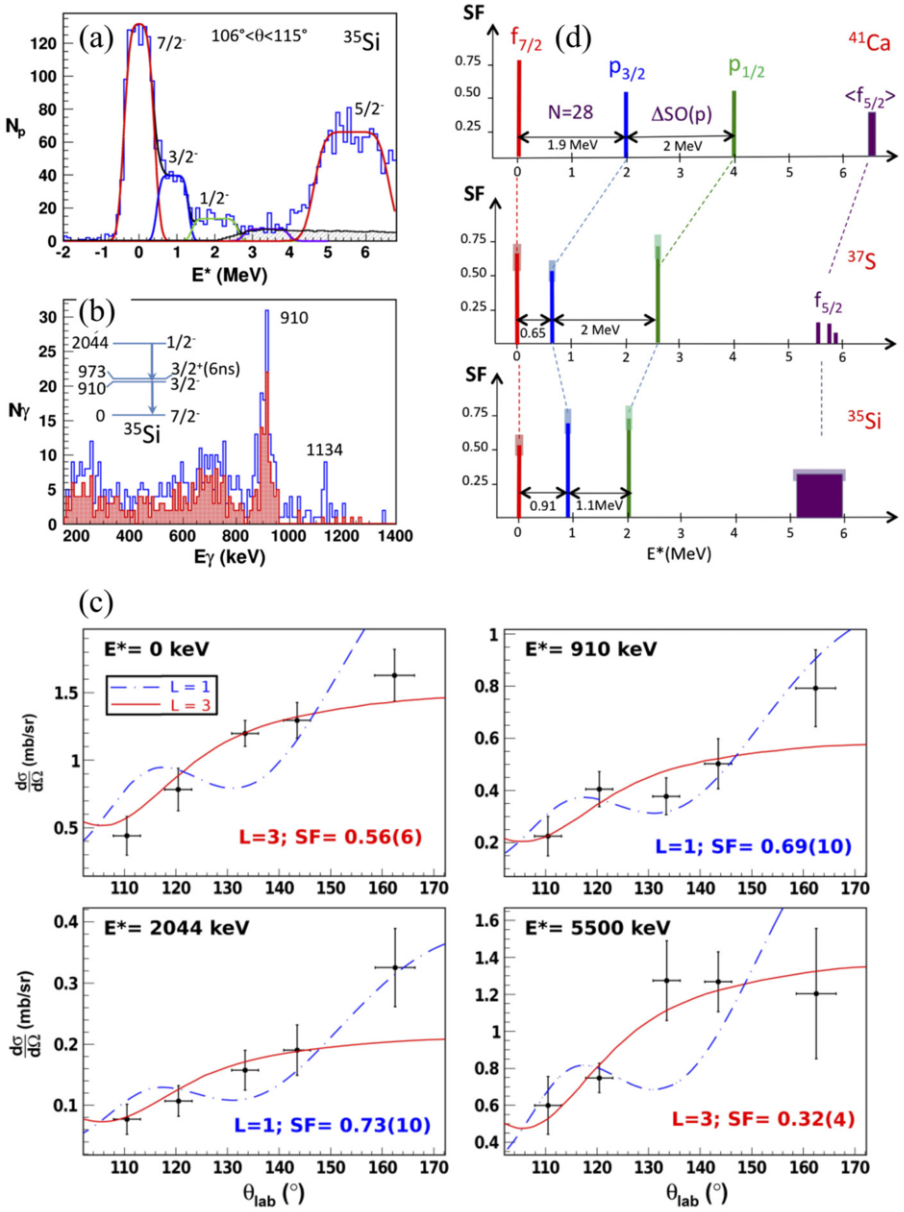

Fig. 20. – Results of the ^{34}Si$(d,p)^{35}$Si measurement [24]. Counterclockwise from top left: (a) proton spectrum as function of the reconstructed excitation energy in ^{35}S. (b) Doppler-corrected γ-ray energy spectrum. The inset shows the decay pattern in ^{35}S. (c) Angular distributions for the selected peaks and ADWA calculations for $l = 1, 3$. (d) Single-particle strengths in ^{41}Ca, ^{37}S and ^{35}Si. Adapted from ref. [24].

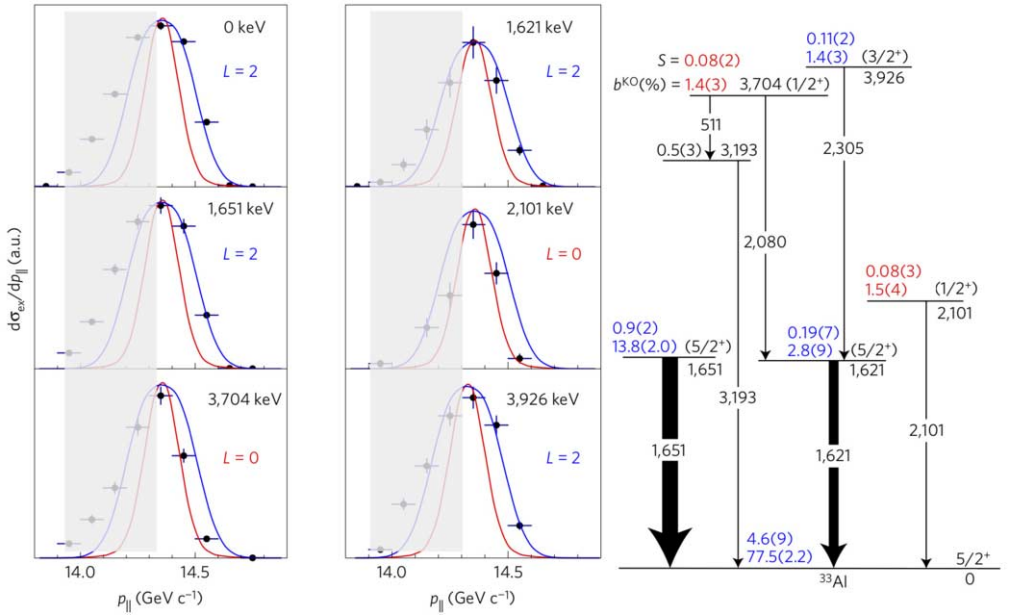

Fig. 21. – Results of the ^{34}Si proton-knockout measurement [25]. Left, distribution of the longitudinal momenta of the ^{33}Al fragments for the populated states in ^{33}Al, selected by requiring a coincidence with the corresponding γ ray. The curves are fit for $l = 0$ (in red) and $l = 2$ (blue), based only on the non-shaded high-momentum part of the distributions. Right, level scheme deduced from the γ-rays detected in coincidence with an identified ^{33}Al fragment. Each level reports the (normalised) spectroscopic factor S, the branching ratio b^{KO}, the (tentative) assigned spin and the excitation energy. Only states with $b^{\mathrm{KO}} \geq 0.5\%$ are shown. Modified from ref. [25].

were identified and their longitudinal momenta were measured in the S800 spectrograph. The γ-ray array GRETINA was used to identify the states populated in ^{33}Al. There were no charged-particle detectors for the measurement of the removed proton; as this is not a binary reaction, some of the features differ from those of nucleon-transfer reactions. The angular-momentum conservation principles, however, still hold: the spin of the final nucleus can be deduced from the transferred angular momentum. The latter is obtained from the distribution of the longitudinal momenta of the ^{33}Al residues, rather than from the angular distributions of the removed protons.

The fit of the distributions, for the states most strongly populated in the knockout, are shown on the left of fig. 21. The fit is only based on the high-momentum part of the distributions because significant background from dissipative reactions may be present in the lower-momentum part. The fit provides, as usual, the values of l and the spectroscopic factors S. Protons can be removed in ^{34}Si mainly from the $\pi 1d_{5/2}$ orbital, which should be fully occupied by 6 protons. The populated states in ^{33}Al, shown in the level scheme deduced from the γ-ray spectra on the right of fig. 21, are indeed mainly $l = 2$, with a total normalised spectroscopic factor $S(d_{5/2}) = 5.7(10)$. The spectroscopic

factor for the $l = 0$ transfers, corresponding to the $\pi 2s_{1/2}$ occupancy in ^{34}Si, is only $S(s_{1/2}) = 0.17(3)$: the orbitals are almost completely empty. We recall that a 1.7(4) occupancy (thus almost full) was measured in a similar experiment on ^{36}S, two proton more than ^{34}Si.

The wave functions of the s orbitals, because of their $l = 0$ angular momentum, extend through the nuclear interior up to the centre, while higher-l orbitals are excluded from the central region. The empty $2s$ orbital in ^{34}Si implies a depletion of the nuclear density in the central region of the nucleus, a sort of a "bubble" structure that, as we have seen, may have important effects on the SO part of the nuclear interaction. The depletion, predicted by some models but refused by others, is here for the first time supported by an experimental observation.

4˙4. *The structure of* 0^+ *states*. – Among the very interesting features of atomic nuclei is the possibility of gaining energy by deformations. It is quite unique that the scale of these gains is the same as the energy gaps that are present between single-particle orbitals. The situation is completely different, for example, in molecules, where the two degrees of freedom (geometrical arrangements and bonds between the constituents) are entirely decoupled. In nuclear physics, on the other hand, a special effort has to be made to reconcile the (macroscopic) *collective* and (microscopic) single-particle pictures, that are both used to explain the presence of excited states with very different properties in the low-lying spectra of nuclei.

When spherical and deformed states appear with similar energies at low excitation energy and low spin we speak of *shape coexistence*. The phenomenon was initially thought of as an exception, occurring in "islands" of the chart of nuclei, but has slowly evolved to a very diffuse phenomenon observed over the whole chart. Reference reviews are found in refs. [26, 27].

An interesting case is that of 0^+ states with different shapes found in single- and doubly-closed shell nuclei. They are understood as originating from multiple particle-hole (p-h) excitations across shells, which are possible because of the large gain in binding energy (mainly from proton-neutron correlations and pairing). These configurations give rise to collective excitations and deformed bands, that appear together with states in which the nucleus still mainly behaves as a closed-shell system. At times, it is possible to observe an inversion in energy of the configuration with multiple p-h excitations with respect to the 0p-0h closed-shell configuration. Such *islands of inversion* are present, for example, in neutron-rich nuclei at $N = 20$ and 28.

The situation at $N = 20$ was already briefly touched upon in sect. **4**˙2: the neutron shell gap collapses because of the rise in energy of the $\nu d_{3/2}$ orbital, with respect to the fp shell lying above, when protons are removed from the $\pi d_{5/2}$ orbital (fig. 11). The evolution of the monopole and correlation energies can also be followed in Mg isotopes, see panels (a) and (b) in fig. 22: while the monopole gap has a minimum in $N = 20$, the difference in correlation energy between the 0p-0h and the 2p-2h configurations has there a maximum. The promotion of neutrons to the fp shell becomes energetically favourable, and the ground state of ^{32}Mg is deformed.

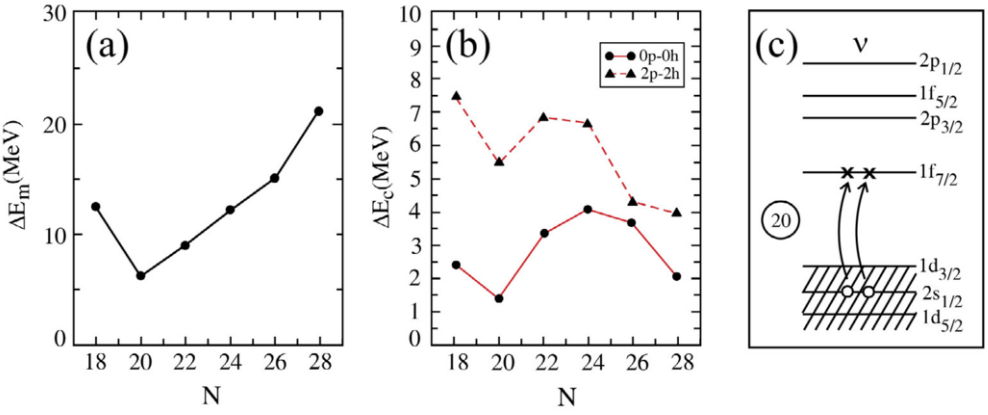

Fig. 22. – (a) Calculated monopole gaps in Mg isotopes ($Z = 12$) as a function of the neutron number. (b) Calculated correlation energies for the 0p-0h and 2p-2h configurations. (c) Schematic view of the 2p-2h neutron excitations into the fp shell ^{32}Mg. Panels (a) and (b) adapted from ref. [28], panel (c) adapted from ref. [26].

Above the ground state, the spherical 0^+ state should be present in the spectrum at low excitation energy. In fact, the two configurations (and possibly others, like 4p-4h) may mix and be present with different weights in the two (and probably more) low-lying 0^+ states. How can we experimentally access those 0^+ states and probe their single-particle configurations? One possibility is to use transfer reactions. The one-neutron addition to the ground state of ^{31}Mg is at present just out of experimental reach; also, the population of one or other of the 0^+ states would depend on the unknown weights of the configurations in the ground state of ^{31}Mg. A viable alternative is the transfer of *two* neutrons in a (t, p) reaction to the ground state of ^{30}Mg, which is known to have a spherical ground state with only a small mixing from the intruder configuration (mostly present in an excited 0^+ state at 1.8 MeV). Naively, if the two neutrons are transferred as a cluster in a relative $l = 0$ state, the observed angular distributions should just provide the spin of the populated state; however, the possibility of more complicated mechanisms, like a sequential transfer, has to be assessed carefully in order to derive reliable information from the measurement. Instead of spectroscopic factors, *two-neutron amplitudes* are used in the calculation of the cross sections. They can be derived from the wave functions of the configurations, thus probing their weight in a given populated state.

The experiment was performed at the post-accelerated ion beam facility of ISOLDE-CERN (Switzerland) [29]. The 1.8 MeV/nucleon ^{30}Mg beam (average intensity $\approx 5 \times 10^4$ pps) was sent onto a tritium-loaded Ti foil, surrounded by the T-REX array of charged-particle detectors and the Miniball array of γ-ray detectors. Results are shown in fig. 23: the protons, as function of the excitation energy in ^{32}Mg, form two distinct groups corresponding to the population of the ground state and an excited state at $E^* \approx 1.8$ MeV. The angular distributions, fig. 23(b), are both well fitted assuming

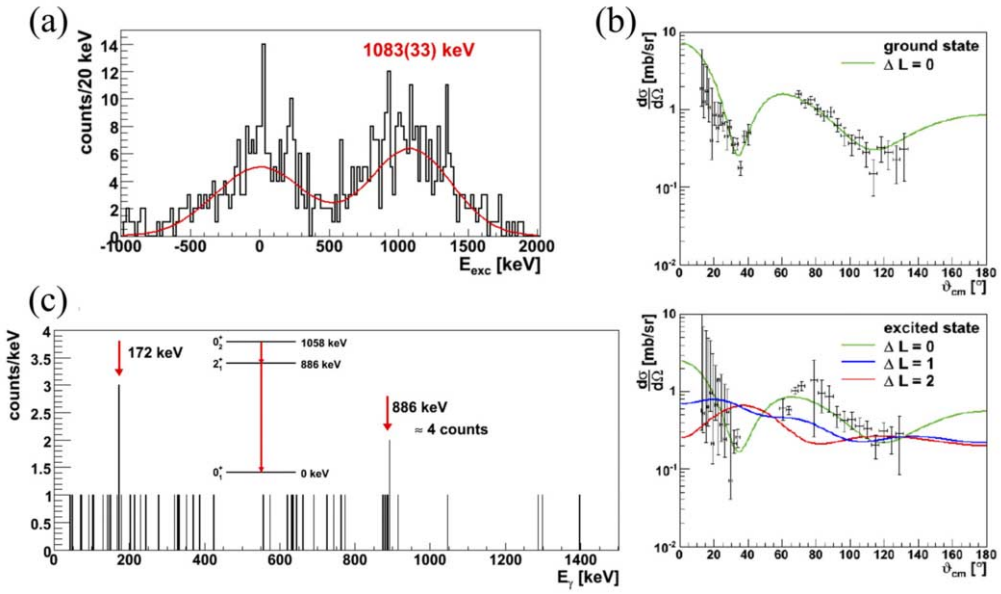

Fig. 23. – Results of the ^{30}Mg$(t,p)^{32}$Mg experiment [29]. Clockwise from top left: (a) proton spectra as a function of the reconstructed excitation energy in ^{32}Mg. (b) Angular distributions of the two proton groups, fitted with DWBA calculations for different values of the transferred angular momentum. (c) γ-ray spectrum detected in coincidence with the proton group of the excited state. In the insert, decay scheme in ^{32}Mg. Figures adapted from ref. [29].

an $l = 0$ transfer. The possibility that the second proton group could contain events due to the transfer to the known excited 2^+ state at 886 keV is ruled out by the small number of observed γ rays from that state, fig. 23(c). All the 886 keV events, together with the observed 172 keV events, can be attributed to the sequential decay from the populated 0^+ excited state through the 2^+ state and eventually to the ground state. The γ-ray spectrum also allows a better determination of the energy of the excited 0^+ state at 1058 keV. The small number of events in the γ-ray spectrum indicates that the half life of the excited state should exceed 10 ns.

The analysis of the cross-section data assumed a one-step process. Wave functions for the two 0^+ states were built with various weights for the 0p-0h and 2p-2h configurations. The interesting result was that any combination of the "natural" $\nu(d_{3/2})^2$ and intruder $\nu(f_{3/2})^2$ configurations does not succeed in reproducing the large observed yields; in both cases it is necessary to add a strong component of the $\nu(p_{3/2})^2$ configuration. For the ground state the best result is obtained for $\approx 50\%$ $\nu(p_{3/2})^2$ and $\nu(f_{7/2})^2$; in the excited state, a $\approx 30\%$ mixing of the $\nu(p_{3/2})^2$ has to be included next to the $\nu(d_{3/2})^2$. These results point to a rather complex picture where several orbitals play a role. Experimental indications of the presence of the $\nu(p_{3/2})^2$ component have been actually found in one-neutron knock-out reactions from the ground state of both ^{32}Mg and ^{30}Mg.

We now move to the region of neutron-rich semi-magic (proton shell closure at $Z = 28$) Ni nuclei. The ^{68}Ni nucleus has 40 neutrons, corresponding to the harmonic-oscillator shell closure. After initial experimental hints towards a doubly-magic nature (large energy of the first 2^+ state, small $B(E2)$ transition probability), it was shown that in fact the shell gap above $N = 40$ is not large and excitation are only hindered by the change in parity of the orbitals above. Additionally, the $\Delta L = 2$ sequence of positive-parity orbitals $\nu g_{9/2}\, d_{5/2}\, s_{1/2}$ above $N = 40$ are known to induce strong quadrupole collectivity in the Fe and Cr isotopes below the nickel region, a feature that could extend to ^{68}Ni.

Three 0^+ states (and two 2^+ states) are known experimentally in ^{68}Ni below 2.8 MeV, see fig. 24(a). Both Large-Scale shell model and Monte Carlo shell model calculations predict similar structures for the states: a mixed character for the ground state $(0^+_1)$and first excited 0^+ (0^+_2), with a prevalence of the 0p-0h component in the ground state and the neutron 2p-2h component in the 0^+_2; the 0^+ state at 2511 keV (0^+_3) should have a complex proton 2p-2h neutron 4p-4h configuration. The proton and neutron occupation numbers for the three 0^+ states predicted by the Monte Carlo shell model are also shown in panel (b) of fig. 24. In the Monte Carlo shell model, under certain assumptions, a deformation can be connected to each basis wave function; by studying the weights of those functions in a state, a dominant deformation can be inferred for the state. In this picture, the shape of the 0^+_1 ground state should be spherical, the 0^+_2 state should be oblate and the 2.5 MeV 0^+_3 state should be prolate [31].

As for ^{32}Mg, the ^{66}Ni(t, p) two-neutron transfer reactions was employed to study the states in ^{68}Ni. The available orbitals are shown in fig. 24(c). The measurement was performed at ISOLDE [32] with the same setup described above for ^{32}Mg. The results are shown in fig. 25. Below 3 MeV, panel (a), the transfer populates the ground state, the 0^+_2 and the first-excited 2^+ state, while an upper limit can be set for the transfer to the 0^+_3, the second 2^+ and the 5^- in the region 2.5–2.8 MeV. Coincidence with γ-rays are absent for the 0^+_2 state as the decay can only proceed via an $E0$ transition; also, because of its long half life, most decays take place far beyond the target position. The angular distributions for the transfer to the first two 0^+ states are fitted in panel (b) with DWBA calculations using transfer amplitudes from a shell-model calculation in the neutron $f_{5/2}p_{3/2}p_{1/2}g_{9/2}$ model space. The DWBA calculations include both direct and sequential transfer of the two neutrons.

It is shown in ref. [32] that a combination of the full fpg space is necessary to reproduce the measured cross sections. The dominant amplitude for the transfer is, as expected, the $(p_{1/2})^2$; however, this component alone cannot reproduce the large cross section to the ground state, and an admixture with the $(f_{5/2})^2$ and $(p_{3/2})^2$ is necessary, with a small contribution even from the $(g_{9/2})^2$ beyond $N = 40$. This is reflected in panel (c), which shows the differences in neutron occupation numbers between the 0^+ states in ^{68}Ni and the ground state of ^{66}Ni: for the 0^+_1 state about 1.6 neutrons are transferred to the fp shell. The cross section for the 0^+_2 state is much lower, as it contains very little p strength; the dominant strength is the $(g_{9/2})^2$, which is much weaker than the p amplitudes but it is especially present at small centre-of-mass angles where the data are recorded. From panel (c) we see that, for the 0^+_2 state, neutrons are mainly transferred to the $g_{9/2}$ orbital

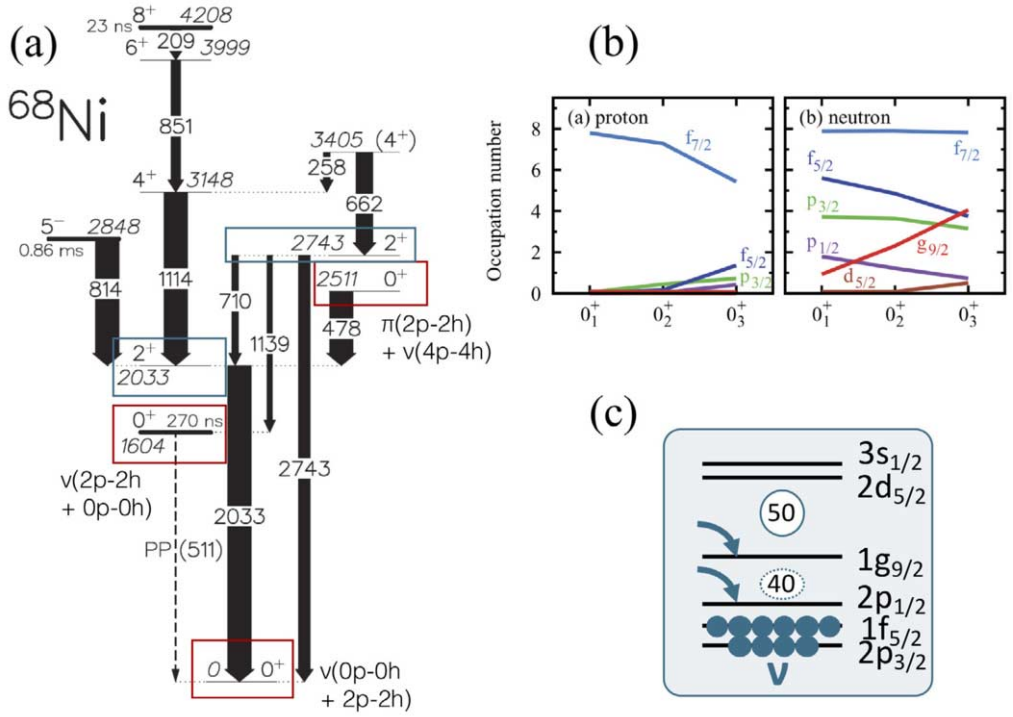

Fig. 24. – (a) Level scheme and γ-ray transitions in ^{68}Ni. Calculated leading configurations in the 0^+ states are shown. (b) Proton and neutron occupation numbers in the three 0^+ states in ^{68}Ni as predicted by the Monte Carlo shell model. (c) Neutron orbitals above $N = 38$ that can be populated in the two-neutron transfer reactions ^{66}Ni$(t, p)^{68}$Ni. Panel (a) adapted from ref. [30], panel (b) adapted from ref. [31].

(≈ 1.4 neutrons) beyond $N = 40$. The 0^+_3 state is not observed: this is in line with the prediction of the shell model, which describes it as due to *proton* 2p-2h excitations above $Z = 28$ (and neutron 4p-4h), that cannot be realised in a two-neutron transfer.

These results give an experimental confirmation of the recent shell-model calculations in this region, thus supporting the microscopic picture of the origin of shape coexistence in ^{68}Ni. An important ingredient in these calculation is the role of the tensor force when the orbital occupancy changes *within* a nucleus [31]. For example, when the proton 2p-2h excitation in the 0^+_3 state in ^{68}Ni partially empties the $\pi f_{7/2}$ orbital: the (repulsive) tensor interaction with the neutrons in $\nu g_{9/2}$ becomes weaker, the orbital comes down in energy and feeds additional neutron excitations. This "type-II" shell evolution forms a solid base to interpret the phenomena of shape coexistence observed in neighbouring nuclei, and can be possibly extended to other regions. Very interesting, but still very challenging both experimentally and theoretically, is the region of neutron-deficient Pb isotopes, where shape coexistence was first identified and where we find the showcase of three 0^+ states with different shapes as the lowest states in the energy spec-

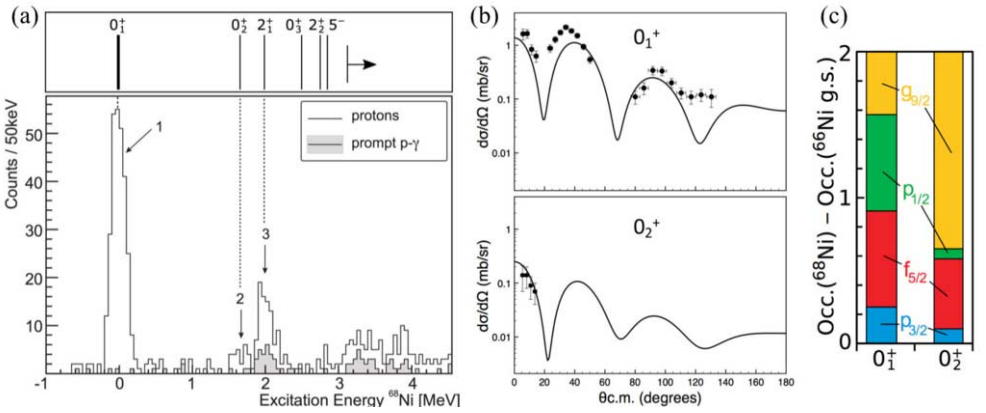

Fig. 25. – Results of the ^{68}Ni$(t,p)^{68}$Ni measurement. (a) Spectrum of protons emitted at backward angles (beyond 150 degrees in the laboratory frame) as function of the reconstructed excitation energy in ^{68}Ni. The numbers indicate feeding to (1) the 0^+_1 ground state, (2) the 0^+_2 state and (3) the first excited 2^+ state. The non-shaded area of the figure shows all detected protons, the light grey area shows the protons that were detected in prompt coincidence with a γ ray. The known states are indicated above the spectrum. (b) Angular distributions of the transfer events to the ground and the first excited 0^+ states, fitted with DWBA calculations (including direct and sequential transfer) using two-neutron amplitudes provided by shell-model calculations. (c) Differences in occupation numbers of indicated neutron orbitals between 0^+ states in ^{68}Ni and the ^{66}Ni ground state.

trum of ^{186}Pb [33]. An analog orbital arrangement as in the Ni case, with the $\pi h_{11/2}$ below the $Z = 82$ shell closure and the $\nu i_{13/2}$ orbital above the $N = 102$ harmonic shell, could trigger the same mechanism observed in the neutron-rich Ni nuclei. The recently-commissioned HIE-ISOLDE post-accelerator, that increases the energy of RIBs at ISOLDE to 10 MeV/nucleon, together with the latest developments of the Monte Carlo shell model, may soon bring this region in the range for transfer reaction and microscopic single-particle spectroscopic studies.

5. – Present and future developments

We discussed in sect. **3**˙2 the issues arising from performing measurements in inverse kinematics with RIBs. Some methods have been devised to solve or mitigate those problems.

The *solenoidal spectrometer* approach uses a large magnet of the MRI type to create a strong, uniform magnetic field, up to 3 tesla, around the target (see fig. 26). The charged particles emitted from the target are confined within the magnet by the Lorentz force, designing helicoidal trajectories and eventually coming back to the beam axis at a distance z from the target. The distance z is related to the scattering angle. The interesting feature of the configuration is that, for a given Q-value, the energy of the detected particle has a linear dependence upon z; and a change in Q-value produces a

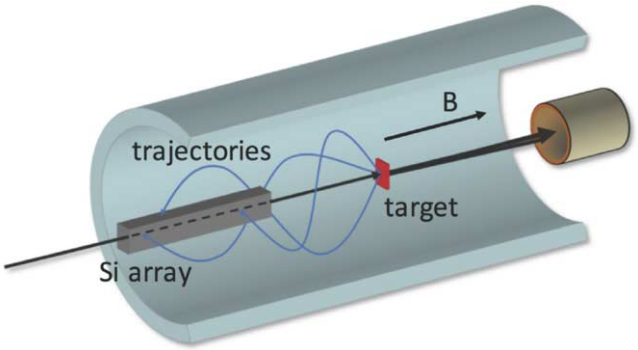

Fig. 26. – Schematic view of the working principle of a solenoidal spectrometer (adapted from ref. [34]).

shift of the same value in the particle energy. In other words, the detector resolution is preserved when the Q-value is calculated from the particle energy, avoiding the problem of the kinematical compression due to the inverse kinematics. Solenoidal spectrometers are in use at the Argonne National Laboratory (USA) and at ISOLDE-CERN.

The solenoidal spectrometer does not solve the worsening of the resolution due to the energy loss of the beam and products in a thick target. To lift this problem, it would be necessary to determine the interaction point within the target: this is the idea motivating the construction of *active target* detectors. Active targets, fig. 27, are time-projection chamber detectors, where the nuclei of the detection gas also play the role of targets for

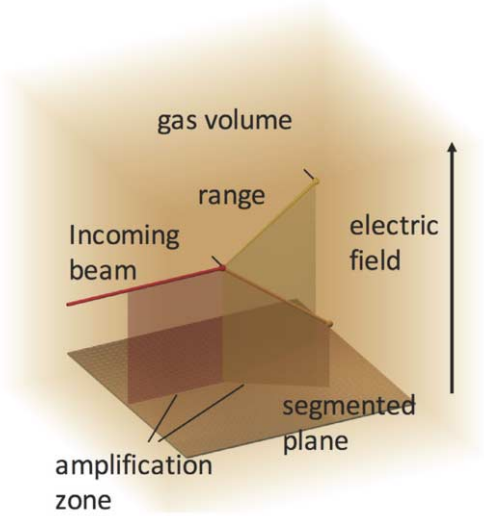

Fig. 27. – Arrangement and working principle of an active target detector.

the reactions of interest. By reconstructing the tracks of all particles in the gas volume, the reaction vertex is found and the energy of the beam particle at that position can be calculated from energy loss relations. With pressures of hydrogen or helium gases of the order of 1 bar, a resolution of 1 mm on the position translate in an energy uncertainty ten times smaller than by using a solid foil of $100\,\mu g\,cm^{-2}$; at the same time, the total target thickness for a length of the active volume of 20 cm is 20 times larger, with a large gain in luminosity. The use of an active target has to deal with the problems of gaseous detectors, in particular the dynamic range of the signals, and the very large amount of data when a plane of several thousands pads is used. A new generation of these novel detectors has recently come into operation, with very promising results.

In parallel, theoretical efforts should be made to cope with the problems of measuring reactions with nuclei far from stability. While nuclear structure calculations are progressing in an almost spectacular way in the last years, nuclear reaction models are struggling to incorporate the new features. The following challenges should be addressed:

- When dealing with weakly-bound nuclei, what is the effect of extended matter distributions on the reaction probability? What are the effects of the continuum on the reaction mechanism? How do we parametrise the continuum and take into account the couplings?

- In reactions where a transfer to states in the continuum is measured, how do we define the spectroscopic factors?

- Multi-step, sequential processes: how can we include them in the reaction model in a consistent way?

It is clear that these issues will become more pressing as the experimental progress brings us to more exotic systems, if we want to continue to use nuclear reactions to derive spectroscopic information about the structure of nuclei.

Appendix

Two-body kinematics

We consider a reaction of the type $1 + 2 \rightarrow 3 + 4$, with a Q-value Q. Particle 1 is the beam ion, 2 is the target, 3 is typically the light ejectile. The masses of the particles are m_i, $i = 1$ to 4, with $m_1 + m_2 = m_3 + m_4$. We assume $m_3 < m_4$. Quantities in the laboratory system are the kinetic energy (before the reaction) E_k, the velocities $v_1 \ldots$, the momenta $p_1 = m_1 v_1 \ldots$, and so on. Quantities in the centre-of-mass system are denoted with a prime: E'_k, v'_1, $p'_1 = m_1 v'_1$, and so on.

The velocity and momentum *of the centre-of mass in the laboratory system* are

$$v_\mathrm{CM} = v_1 m_1/(m_1 + m_2) \text{ (because } v_2 = 0), \text{ and}$$
$$p_\mathrm{CM} = p_1.$$

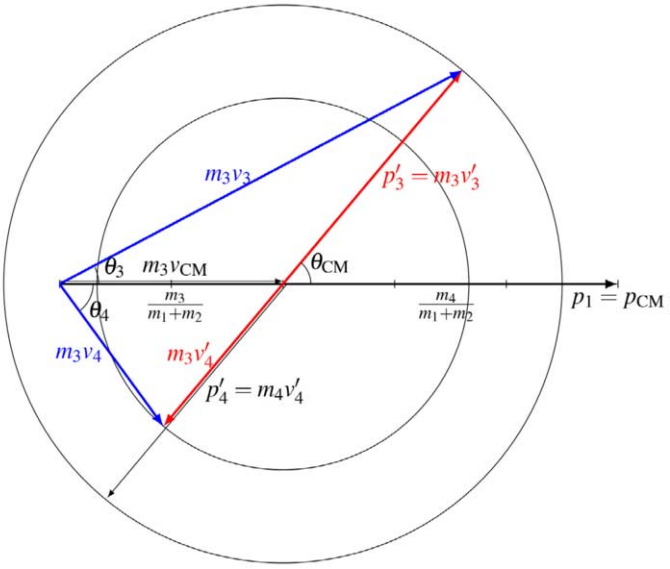

Fig. 28. – Kinematic diagram of a binary nuclear reaction. Here $m_3/m_4 = 2/3$.

The conservation of energy in the centre-of-mass system can be written as

$$\frac{1}{2}m_1v_1'^2 + \frac{1}{2}m_2v_2'^2 + Q = \frac{1}{2}m_3v_3'^2 + \frac{1}{2}m_4v_4'^2,$$
$$\frac{1}{2}m_1(v_1 - v_{CM})^2 + \frac{1}{2}m_2v_{CM}^2 + Q = \frac{1}{2}m_3v_3'^2 + \frac{1}{2}m_4v_4'^2.$$

By using the expression for v_{CM} and the conservation of momentum in the centre of mass: $p'_3 = p'_4$, with some algebra one finds

$$\frac{m_2}{2m_1(m_1+m_2)}p_1^2 + Q = \frac{m_3+m_4}{2m_3m_4}p_3'^2$$

or

$$p_3'^2 = 2\frac{m_3m_4}{m_3+m_4} \times \underbrace{\left[\underbrace{\frac{p_1^2}{2m_1}}_{E_k}\frac{m_2}{m_1+m_2} + Q\right]}_{E'_k}, \tag{A.1}$$

which is just the momentum available in the centre of mass: $p_3'^2 = 2\mu E_{tot}$ (μ is the reduced mass).

We can build a *kinematic diagram* (see fig. 28) by starting with a segment representing the initial momentum in the laboratory $p_1 = \sqrt{2m_1E_k} = p_{CM}$. We divide it in $m_1 + m_2$

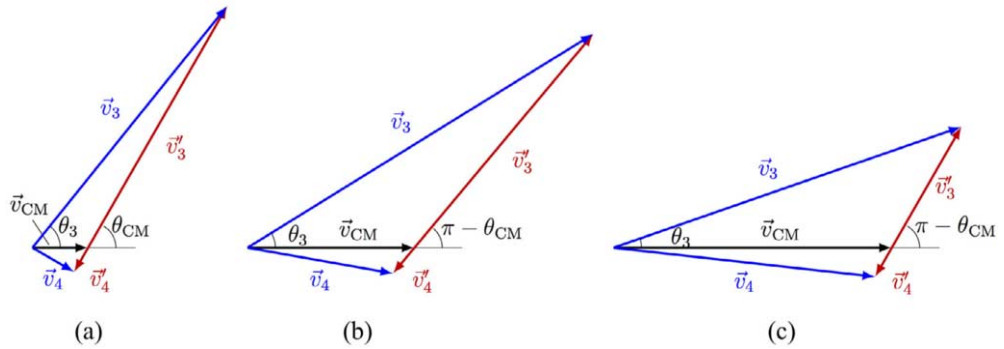

Fig. 29. – Kinematics of binary reactions: velocity vectors of outgoing particles in the centre-of-mass system (in red, denoted with a prime) and in the laboratory system. (a) Direct kinematics. (b) Inverse kinematics, with the mass of the recoil light ion m_3 lighter than the mass of the light target m_2. (c) Inverse kinematics, with $m_3 > m_2$. For all cases we chose $m_3 < m_4$. The centre-of-mass scattering angle is measured from the beam-like particle, thus, in inverse kinematics, from the vector v'_4.

parts and we take the segment proportional to m_3. This segment represents

$$\frac{m_3}{m_1+m_2} p_{\rm CM} = m_3 v_{\rm CM}.$$

The other vectors can now be thought of as representing velocities, *all scaled to* m_3. From the end of the $m_3 v_{\rm CM}$ vector we draw a vector $m_3 v'_3 = p'_3$ at a freely chosen angle $\theta_{\rm CM}$. The length of this vector with respect to the $m_3 v_{\rm CM}$ vector can be calculated from the reaction parameters using eq. (A.1):

$$\text{(A.2)} \qquad \frac{p'_3}{m_3 v_{\rm CM}} = \frac{\left[2\frac{m_3 m_4}{m_3+m_4} \times \left(\frac{p_1^2}{2m_1}\frac{m_2}{m_1+m_2} + Q\right)\right]^{1/2}}{\frac{m_3}{m_1+m_2}\sqrt{2m_1 E_{\rm k}}} \xrightarrow[Q \ll E_{\rm tot}]{} \approx \sqrt{\frac{m_2 m_4}{m_1 m_3}}\,.$$

The velocity of particle 3 in the laboratory system is now just $v_3 = v'_3 + v_{\rm CM}$ (all scaled to m_3). For particle 4 we draw a vector $p'_4 = -p'_3$; the velocity is found by scaling: $m_3 v'_4 = p'_4\, m_3/m_4$. We recognise the scattering angles in the laboratory frame θ_3 and θ_4.

Figure 28 shows the diagram for a ratio $m_3/m_4 = 2/3$. By varying the centre-of-mass angle $\theta_{\rm CM}$ one can find out how the velocity vectors for particles 3 and 4 are directed, thus where particles are emitted in the laboratory frame.

As shown in eq. (A.2), when the Q-value is small with respect to the total centre-of-mass energy the kinematics is essentially determined by the ratio of the masses. In direct kinematics, fig. 29(a), it is $m_1 < m_2$, $m_3 < m_4$; the vector v'_3 is longer than $v_{\rm CM}$ and the light ejectiles (particle 3) are always emitted in all directions in the laboratory frame (and $\theta_3 \approx \theta_{\rm CM}$). In inverse kinematics it is $m_1 \approx m_4$, thus the determining factor is $\sqrt{m_2/m_3}$: for example, in a (p,d) reaction, fig. 29(c), v'_3 is shorter than $v_{\rm CM}$, θ_3 has a limiting maximum value and deuterons are only emitted in a forward cone. In a (d,p) reaction, fig. 29(b), conversely, protons are emitted at all angles. Notice

that, in inverse kinematics, the centre-of-mass angle should refer to the beam-like heavy particle 4. Figure 28 should thus be modified with the substitution $\theta_{\rm CM} \rightarrow \pi - \theta_{\rm CM}$. We see how, in a (d, p) reaction, for small centre-of mass angles protons are emitted at backward angles.

REFERENCES

[1] SATCHLER G. R., *Introduction to nuclear reactions*, 2nd edition (MacMillan Education Ltd., London) 1990.

[2] THOMPSON I. J. and NUNES F. M., *Nuclear reactions for astrophysics: principles, calculation and applications of low-energy reactions* (Cambridge Univeristy Press, Cambridge) 2009.

[3] FAHLANDER C. and JONSON B. (Editors), *Nobel Symposium 152: Physics with Radioactive Beams*, *Phys. Scr.*, **2013** (2013) T152.

[4] BRINK D. M., *Phys. Lett. B*, **40** (1972) 37.

[5] COHEN B. L., FULMER R. H. and MCCARTHY A. L., *Phys. Rev.*, **126** (1962) 698.

[6] KRANE K. S., *Introductory Nuclear Physics* (Wiley, New York) 1988.

[7] SORLIN O. and PORQUET M. G., *Prog. Part. Nucl. Phys.*, **61** (2008) 602.

[8] OTSUKA T., *Phys. Scr.*, **2013** (2013) 014007.

[9] CATFORD W. N., *The Euroschool Lectures on Physics with Exotic Beams, Vol. IV* (Springer, Berlin and Heidelberg) 2014, Ch. What Can We Learn from Transfer, and How Is Best to Do It?, p. 67.

[10] DIRIKEN J., PATRONIS N., ANDREYEV A. N., ANTALIC S., BILDSTEIN V., BLAZHEV A., DARBY I. G., DE WITTE H., EBERTH J., ELSEVIERS J., FEDOSSEEV V. N., FLAVIGNY F., FRANSEN C., GEORGIEV G., GERNHAUSER R., HESS H., HUYSE M., JOLIE J., KROELL T., KRUECKEN R., LUTTER R., MARSH B. A., MERTZIMEKIS T., MUECHER D., NOWACKI F., ORLANDI R., PAKOU A., RAABE R., RANDISI G., REITER P., ROGER T., SEIDLITZ M., SELIVERSTOV M., SIEJA K., SOTTY C., TORNQVIST H., VAN DE WALLE J., VAN DUPPEN P., VOULOT D., WARR N., WENANDER F. and WIMMER K., *Phys. Lett. B*, **736** (2014) 533.

[11] WILSON G. L., CATFORD W. N., ORR N. A., DIGET C. A., MATTA A., HACKMAN G., WILLIAMS S. J., CELIK I. C., ACHOURI N. L., AL FALOU H., ASHLEY R., AUSTIN R. A. E., BALL G. C., BLACKMON J. C., BOSTON A. J., BOSTON H. C., BROWN S. M., CROSS D. S., DJONGOLOV M., DRAKE T. E., HAGER U., FOX S. P., FULTON B. R., GALINSKI N., GARNSWORTHY A. B., JAMIESON D., KANUNGO R., LEACH K. G., ORCE J. N., PEARSON C. J., PORTER-PEDEN M., SARAZIN F., SIMPSON E. C., SJUE S., SMALLEY D., SUMITHRARACHCHI C., TRIAMBAK S., UNSWORTH C. and WADSWORTH R., *Phys. Lett. B*, **759** (2016) 417.

[12] WINFIELD J. S., CATFORD W. N. and N. A. O., *Nucl. Instrum. Methods Phys. Res. A*, **396** (1997) 147.

[13] FORTIER S., PITA S., WINFIELD J. S., CATFORD W. N., ORR N. A., VAN DE WIELE J., BLUMENFELD Y., CHAPMAN R., CHAPPELL S. P. G., CLARKE N. M., CURTIS N., FREER M., GALES S., JONES K. L., LANGEVIN-JOLIOT H., LAURENT H., LHENRY I., MAISON J. M., ROUSSEL-CHOMAZ P., SHAWCROSS M., SMITH M., SPOHR K., SUOMIJARVI T. and DE VISMES A., *Phys. Lett. B*, **461** (1999) 22.

[14] WINFIELD J. S., FORTIER S., CATFORD W. N., PITA S., ORR N. A., VAN DE WIELE J., BLUMENFELD Y., CHAPMAN R., CHAPPELL S. P. G., CLARKE N. M., CURTIS N., FREER M., GALES S., LANGEVIN-JOLIOT H., LAURENT H., LHENRY I., MAISON J. M.,

ROUSSEL-CHOMAZ P., SHAWCROSS M., SPOHR K., SUOMIJARVI T. and DE VISMES A., *Nucl. Phys. A*, **683** (2001) 48.

[15] KANUNGO R., GALLANT A. T., UCHIDA M., ANDREOIU C., AUSTIN R. A. E., BANDYOPADHYAY D., BALL G. C., BECKER J. A., BOSTON A. J., BOSTON H. C., BROWN B. A., BUCHMANN L., COLOSIMO S. J., CLARK R. M., CLINE D., CROSS D. S., DARE H., DAVIDS B., DRAKE T. E., DJONGOLOV M., FINLAY P., GALINSKI N., GARRETT P. E., GARNSWORTHY A. B., GREEN K. L., GRIST S., HACKMAN G., HARKNESS L. J., HAYES A. B., HOWELL D., HURST A. M., JEPPESEN H. B., LEACH K. G., MACCHIAVELLI A. O., OXLEY D., PEARSON C. J., PIETRAS B., PHILLIPS A. A., RIGBY S. V., RUIZ C., RUPRECHT G., SARAZIN F., SCHUMAKER M. A., SHOTTER A. C., SUMITHARACHCHI C. S., SVENSSON C. E., TANIHATA I., TRIAMBAK S., UNSWORTH C., WILLIAMS S. J., WALDEN P., WONG J. and WU C. Y., *Phys. Lett. B*, **682** (2010) 391.

[16] CHEN J., LOU J. L., YE Y. L., LI Z. H., PANG D. Y., YUAN C. X., GE Y. C., LI Q. T., HUA H., JIANG D. X., YANG X. F., XU F. R., PEI J. C., LI J., JIANG W., SUN Y. L., ZANG H. L., ZHANG Y., AOI N., IDEGUCHI E., ONG H. J., LEE J., WU J., LIU H. N., WEN C., AYYAD Y., HATANAKA K., TRAN D. T., YAMAMOTO T., TANAKA M. and SUZUKI T., *Phys. Lett. B*, **781** (2018) 412.

[17] UTSUNO Y., OTSUKA T., MIZUSAKI T. and HONMA M., *Phys. Rev. C*, **60** (1999) 054315.

[18] OTSUKA T., SUZUKI T., HOLT J. D., SCHWENK A. and AKAISHI Y., *Phys. Rev. Lett.*, **105** (2010) 032501.

[19] CATFORD W. N., TIMIS C. N., LEMMON R. C., LABICHE M., ORR N. A., FERNÁNDEZ-DOMÍNGUEZ B., CHAPMAN R., FREER M., CHARTIER M., SAVAJOLS H., REJMUND M., ACHOURI N. L., AMZAL N., ASHWOOD N. I., BALDWIN T. D., BURNS M., CABALLERO L., CASADJIAN J. M., CURTIS N., DE FRANCE G., GELLETLY W., LIANG X., PAIN S. D., PUCKNELL V. P. E., RUBIO B., SORLIN O., SPOHR K., THEISEN C. and WARNER D. D., *Phys. Rev. Lett.*, **104** (2010) 192501.

[20] BROWN S. M., CATFORD W. N., THOMAS J. S., FERNÁNDEZ-DOMÍNGUEZ B., ORR N. A., LABICHE M., REJMUND M., ACHOURI N. L., AL FALOU H., ASHWOOD N. I., BEAUMEL D., BLUMENFELD Y., BROWN B. A., CHAPMAN R., CHARTIER M., CURTIS N., DE FRANCE G., DE SEREVILLE N., DELAUNAY F., DROUART A., FORCE C., FRANCHOO S., GUILLOT J., HAIGH P., HAMMACHE F., LAPOUX V., LEMMON R. C., LEPRINCE A., MARÉCHAL F., MOUGEOT X., MOUGINOT B., NALPAS L., NAVIN A., PATTERSON N. P., PIETRAS B., POLLACCO E. C., RAMUS A., SCARPACI J. A., STEFAN I. and WILSON G. L., *Phys. Rev. C*, **85** (2012) 011302.

[21] OBERTELLI A., GILLIBERT A., ALAMANOS N., ALVAREZ M., AUGER F., DAYRAS R., DROUART A., DE FRANCE G., JURADO B., KEELEY N., LAPOUX V., MITTIG W., MOUGEOT X., NALPAS L., PAKOU A., PATRONIS N., POLLACCO E. C., REJMUND F., REJMUND M., ROUSSEL-CHOMAZ P., SAVAJOLS H., SKAZA F. and THEISEN C., *Phys. Lett. B*, **633** (2006) 33.

[22] GAUDEFROY L., SORLIN O., BEAUMEL D., BLUMENFELD Y., DOMBRADI Z., FORTIER S., FRANCHOO S., GELIN M., GIBELIN J., GREVY S., HAMMACHE F., IBRAHIM F., KEMPER K. W., KRATZ K.-L., LUKYANOV S. M., MONROZEAU C., NALPAS L., NOWACKI F., OSTROWSKI A. N., OTSUKA T., PENIONZHKEVICH Y.-E., PIEKAREWICZ J., POLLACCO E. C., ROUSSEL-CHOMAZ P., RICH E., SCARPACI J. A., ST. LAURENT M. G., SOHLER D., STANOIU M., SUZUKI T., TRYGGESTAD E. and VERNEY D., *Phys. Rev. Lett.*, **97** (2006) 092501.

[23] OTSUKA T., SUZUKI T., FUJIMOTO R., GRAWE H. and AKAISHI Y., *Phys. Rev. Lett.*, **95** (2005) 232502.

[24] BURGUNDER G., SORLIN O., NOWACKI F., GIRON S., HAMMACHE F., MOUKADDAM M., DE SÉRÉVILLE N., BEAUMEL D., CÀCERES L., CLÉMENT E., DUCHÊNE G., EBRAN J. P.,

FERNANDEZ-DOMINGUEZ B., FLAVIGNY F., FRANCHOO S., GIBELIN J., GILLIBERT A., GRÉVY S., GUILLOT J., LEPAILLEUR A., MATEA I., MATTA A., NALPAS L., OBERTELLI A., OTSUKA T., PANCIN J., POVES A., RAABE R., SCARPACI J. A., STEFAN I., STODEL C., SUZUKI T. and THOMAS J. C., *Phys. Rev. Lett.*, **112** (2014) 042502.

[25] MUTSCHLER A., LEMASSON A., SORLIN O., BAZIN D., BORCEA C., BORCEA R., DOMBRÁDI Z., EBRAN J.-P., GADE A., IWASAKI H., KHAN E., LEPAILLEUR A., RECCHIA F., ROGER T., ROTARU F., SOHLER D., STANOIU M., STROBERG S. R., TOSTEVIN J. A., VANDEBROUCK M., WEISSHAAR D. and WIMMER K., *Nat. Phys.*, **13** (2017) 152.

[26] HEYDE K. and WOOD J. L., *Rev. Mod. Phys.*, **83** (2011) 1467.

[27] WOOD J. L. and HEYDE K. (Editors), *A focus on shape coexistence in nuclei*, *J. Phys. G: Nucl. Part. Phys.*, **43** (2016) no. 2.

[28] CAURIER E., NOWACKI F., POVES A. and RETAMOSA J., *Phys. Rev. C*, **58** (1998) 2033.

[29] WIMMER K., KROLL T., KRUCKEN R., BILDSTEIN V., GERNHAUSER R., BASTIN B., BREE N., DIRIKEN J., VAN DUPPEN P., HUYSE M., PATRONIS N., VERMAELEN P., VOULOT D., VAN DE WALLE J., WENANDER F., FRAILE L. M., CHAPMAN R., HADINIA B., ORLANDI R., SMITH J. F., LUTTER R., THIROLF P. G., LABICHE M., BLAZHEV A., KALKUHLER M., REITER P., SEIDLITZ M., WARR N., MACCHIAVELLI A. O., JEPPESEN H. B., FIORI E., GEORGIEV G., SCHRIEDER G., DAS GUPTA S., LO BIANCO G., NARDELLI S., BUTTERWORTH J., JOHANSEN J. and RIISAGER K., *Phys. Rev. Lett.*, **105** (2010) 252501.

[30] RECCHIA F., CHIARA C. J., JANSSENS R. V. F., WEISSHAAR D., GADE A., WALTERS W. B., ALBERS M., ALCORTA M., BADER V. M., BAUGHER T., BAZIN D., BERRYMAN J. S., BERTONE P. F., BROWN B. A., CAMPBELL C. M., CARPENTER M. P., CHEN J., CRAWFORD H. L., DAVID H. M., DOHERTY D. T., HOFFMAN C. R., KONDEV F. G., KORICHI A., LANGER C., LARSON N., LAURITSEN T., LIDDICK S. N., LUNDERBERG E., MACCHIAVELLI A. O., NOJI S., PROKOP C., ROGERS A. M., SEWERYNIAK D., STROBERG S. R., SUCHYTA S., WILLIAMS S., WIMMER K. and ZHU S., *Phys. Rev. C*, **88** (2013) 041302.

[31] TSUNODA Y., OTSUKA T., SHIMIZU N., HONMA M. and UTSUNO Y., *Phys. Rev. C*, **89** (2014) 031301.

[32] ELSEVIERS J., *Probing the Semi-Magicity of* ^{68}Ni *via the* ^{66}Ni$(t,p)^{68}$Ni *Two-Neutron Transfer Reaction in Inverse Kinematics*, PhD Thesis, KU Leuven (2014). https://fys.kuleuven.be/iks/ns/files/thesis/thesis-jytte-finaal.pdf.

[33] ANDREYEV A. N., HUYSE M., VAN DUPPEN P., WEISSMAN L., ACKERMANN D., GERL J., HESSBERGER F. P., HOFMANN S., KLEINBOHL A., MUNZENBERG G., RESHITKO S., SCHLEGEL C., SCHAFFNER H., CAGARDA P., MATOS M., SARO S., KEENAN A., MOORE C., O'LEARY C. D., PAGE R. D., TAYLOR M., KETTUNEN H., LEINO M., LAVRENTIEV A., WYSS R. and HEYDE K., *Nature (London)*, **405** (2000) 430.

[34] WUOSMAA A. H., SCHIFFER J. P., BACK B. B., LISTER C. J. and REHM K. E., *Nucl. Instrum. Methods Phys. Res. A*, **580** (2007) 1290.

This page intentionally left blank

Proceedings of the International School of Physics "Enrico Fermi"
Course 201 "Nuclear Physics with Stable and Radioactive Ion Beams", edited by F. Gramegna,
P. Van Duppen, A. Vitturi and S. Pirrone
(IOS, Amsterdam; SIF, Bologna) 2019
DOI 10.3254/978-1-61499-957-7-253

β decay studies of the most exotic nuclei

G. Benzoni

INFN, Sezione di Milano - Milano, Italy

Summary. — Radioactive decay occurs in unstable nuclei, being β decay the dominant process. The exotic nuclei encountered when going further away from the valley of stability are useful test benches for nuclear models at the limits of the existence of the nucleus. The properties of these exotic systems are of fundamental importance when describing the formation of the elements in the universe through stellar nucleosynthesis processes. The most recent techniques to study β decays in exotic systems and an overview of their specific properties are discussed in these lecture notes.

1. – Introduction

In nature we can find 288 nuclei, which are either stable or have a lifetime comparable to or longer than the Earth age. Other nuclear systems can be produced artificially in laboratory, which, even if not stable, can be accessed experimentally. Recent estimates by theoretical models predict the existence of 7000(500) bound nuclei.

The collection of the nuclei as a function of their neutron and proton content is given in the Segrè chart, where stable nuclei (usually marked with black boxes) follow the so-called valley of stability. This line, also named β stability line, is located at the $N = Z$ locus for the lightest species, bending, above Fe, towards a richer content of neutrons.

Nuclei lying above the valley of stability are characterised by $Z > N$, and are therefore defined as proton-rich (p-rich) or neutron deficient. They extend few units away from the valley of the stability in an isotopic chain, until reaching the proton drip line, where the proton separation energy becomes null and the nuclei are no more bound. Nuclei characterised by $N > Z$ lie, instead, below the valley of stability and are named neutron-rich (n-rich). The neutron drip line is situated further away from the valley of stability, allowing for accommodation of tens of additional neutrons. Its exact location is still under debate, in particular for heavy systems.

Unstable nuclei can be accessed by various reactions, which occur in a limited time-frame, after which the resulting residual nuclei are let decay. Properties of the unstable nuclei can be accessed via specifically studied experiments, which can reveal both macroscopic, in terms of shape and collectivity, and microscopic, in terms of single-particle orbitals, features of the nucleus under analysis.

Exotic nuclei can be produced with different type of reactions where the final production rate depends on the cross section, beam intensity and the target thickness. If direct reactions allow the population of nuclei close to the beam and or target species, fusion-evaporation or deep-inelastic reactions populate nuclei which are formed by the sum of the single constituents of both the projectile and target nuclei. These reactions, however, do not help reaching very far away from the valley of stability, owing mainly to the charge-equilibration mechanism. Exotic species can also be produced in either spontaneous or neutron-induced fission of trans-uranium elements. The cross section for producing exotic species is quickly dropping going towards the tails of the fission fragments distribution.

In order to access exotic systems, both p- and n-rich, more energetic reactions are exploited. The reactions can be induced by light particles (protons or deuterons) accelerated up to few GeV/nucleon on targets of heavy systems up to U, or by energetic beams of heavy elements impinged onto light targets, such as Be. In both cases, these very energetic reactions strip and evaporate a large number of nucleons, populating regions in the Segré chart far away from the initial partners. In the first type of reactions thick targets, several layers of materials, are used to increase the final number of nuclei produced, and the resulting species are extracted from the bulk material via physical and chemical processes defined by the properties of the materials and temperatures used. This type of production mechanism is at the basis of the Isotope Separation On-Line method (ISOL). In the second process the targets are smaller, few g/cm^2, and the resulting nuclei keep a forward momentum, and can be transported into magnetic separators. This is at the basis of the in-flight methods. Both techniques allow for the use of thick targets, thus compensating for the small production cross-sections. Additional details on the two techniques for the production of radioactive ion beams are found in ref. [1].

The non-stable nuclei decay via emission of α-particles, dominated by the interplay of the strong and electromagnetic force, via β-decay, which is mediated by the weak force, or by spontaneous fission. Moving further away from the stability valley new exotic decay modes are encountered, such as proton or neutron emission, and β-delayed emission of particles or fission. Most of the α emitters are artificial isotopes heavier than Pb, while the most popular decay mode is the β-decay.

The study of its β-decay is usually the first mean to access a newly produced nucleus, since it does not require post-acceleration or reactions.

The study of exotic nuclei has a great impact on defining the evolution of nuclear structure properties away from the valley of stability and in assessing the robustness of theoretical models describing the nuclear medium. In addition, the knowledge of β-decay rates and properties is important for our understanding of the creation of the heavier elements in explosive stellar processes.

A number of everyday applications of β-decaying sources can be found, for instance, in nuclear medicine, such as the use of unstable isotopes for Positron Emission Tomography imaging, and in nuclear safety related to decay heat evaluation in nuclear power plants.

Experimental campaigns aiming at accessing the most exotic species are pursued worldwide, and new facilities to produce very intense radioactive beams are being built in key laboratories in Europe, USA, Asia and South Africa.

In this contribution basic properties of β-decay will be revised in order to be used, then, to detail the properties of the most exotic nuclei, in particular on the neutron-rich side, in relation to nuclear structure and nuclear astrophysics studies.

The paper is organised as follows: in sect. **2** the basic properties of β decay are recalled, while in sect. **3** basic techniques and experimental set-ups to measure the β decay of exotic nuclei are described. Section **4** discusses the link between gross properties of the β-decay and stellar nucleosynthesis, while sect. **5** highlights the peculiarities of the decay of very neutron-rich nuclei, together with examples from recent studies.

2. – Properties of β-decay

When talking about *radioactive decay* we describe a phenomenon in which an initial nuclear species, ${}^{A}_{Z}\mathrm{X}_{N}$, disappears, transforming itself into a new nucleus, whose $A' = Z' + N'$ is defined by the decay process. The initial nucleus is usually referred to as *parent, mother* or *precursor*, while the final nucleus is the *daughter* or *successor*. The decay process has a statistical behaviour and is described by the *law of the radioactive decay*:

$$N(t) = N_0 e^{-\lambda t}, \tag{1}$$

being N_0 the initial number of parent nuclei present in the sample, and λ the decay constant. It is often useful to write eq. (1) as a function of the *meanlife* (τ) or the *half-life* ($T_{1/2}$), which is the time required for half of the initial nuclei to decay. These quantities are related to the decay constant by

$$T_{1/2} = \frac{\ln 2}{\lambda} \approx 0.693\tau. \tag{2}$$

The energy available for a decay is given by the Q-*value*, difference in neutral atomic mass between the initial and final decay products:

$$Q = M_{initial} - M_{final}. \tag{3}$$

The decay of a nucleus can occur via many competing processes, and one can define a *branching ratio* as the probability of each decay path.

α and β decays usually occur from the mother nucleus's ground state, but excited states can also de-excite via the emission of particles. In addition, the decay does not always populate directly the ground state of the final nucleus, and can feed excited states which then de-excite via internal γ decay.

If the daughter nucleus is itself radioactive, it also decays with a specific half-life. To describe this chain of decays, we have to use a set of equations, the so-called *Bateman equations*, describing abundances and activities in a decay chain as a function of time. If at a time t, there are $N_i(t)$ atoms of the i-th isotope which decay into the $(i+1)$-th nucleus with a decay rate λ_i, the amounts of isotopes in the k-th step of the decay chain evolves as

$$\begin{aligned} \frac{\mathrm{d}N_1(t)}{\mathrm{d}t} &= -\lambda_1 N_1(t), \\ \frac{\mathrm{d}N_i(t)}{\mathrm{d}t} &= -\lambda_i N_i(t) + \lambda_{i-1} N_{i-1}(t), \\ \frac{\mathrm{d}N_k(t)}{\mathrm{d}t} &= \lambda_{k-1} N_{k-1}(t). \end{aligned} \tag{4}$$

A detailed description of the Bateman equations can be found in ref. [2].

If one of the species has a much shorter half-life than its precursor nucleus there is a time at which all activities are equal, that is to say that the rates of accumulation and decay compensate. This condition is defined as *secular equilibrium*.

In general when studying a radioactive decay, one can get access to properties of both the mother and daughter nuclei: by the identification of the emitted particles, we define the decay modes and decay rates of the mother nucleus, while studying the populated levels and internal de-excitations we can describe the structure of the daughter nucleus.

The largest number of non-stable nuclei decay via β-decay. β-decay refers to three different processes:

– β^--decay:

$$\mathrm{n} \to \mathrm{p} + \mathrm{e}^- + \bar{\nu}_e,$$

which describes the decay of a neutron into a proton with the production of an electron and an electric antineutrino. The β^--decay process in the nucleus corresponds to

$$(Z, N) \to (Z+1, N-1) + \mathrm{e}^- + \bar{\nu}_e.$$

The Q-value for β^--decay equals, in terms of nuclear masses,

$$Q_{\beta^-} = m({}^A_Z X)c^2 - m({}^A_{Z+1} X')c^2 - m_e c^2. \tag{5}$$

In terms of atomic masses, neglecting the differences in electron binding energy, eq. (5) translates into

$$Q_{\beta^-} = M(^A_Z X)c^2 - M(^A_{Z+1}X')c^2. \tag{6}$$

This decay is allowed by the mass difference between the neutron and the proton, assuming the antineutrino and neutrino have a very small rest mass, close to zero.

– β^+-decay:

$$\mathrm{p} \rightarrow \mathrm{n} + \mathrm{e}^+ + \nu_e,$$

which describes the decay of a proton into a neutron with the emission of a positron and an electric neutrino. The corresponding nuclear decay is

$$(Z, N) \rightarrow (Z - 1, N + 1) + \mathrm{e}^+ + \nu_e$$

and its Q-value equals

$$Q_{\beta^+} = m(^A_Z X)c^2 - m(^A_{Z-1}X')c^2 - m_e c^2, \tag{7}$$

which translates, in terms of atomic masses, into

$$Q_{\beta^+} = M(^A_Z X)c^2 - M(^A_{Z-1}X')c^2 - 2m_e c^2. \tag{8}$$

For a β^+-decay to occur the atomic mass difference needs to be larger than $2m_e = 1.022\,\mathrm{MeV}$.

– Electron capture (EC):

$$\mathrm{p} + \mathrm{e}^- \rightarrow \mathrm{n} + \nu_e,$$

where a proton captures an electron and converts it into a neutron and an electric neutrino. The electron is captured by one atomic orbital, usually an s-wave electron, having a larger orbital overlap in the region of the nucleus.

The corresponding nuclear decay:

$$(Z, N) + \mathrm{e}^- \rightarrow (Z - 1, N + 1) + \nu_e$$

has a Q-value of

$$Q_{EC} = m(^A_Z X)c^2 + m_e c^2 - m(^A_{Z-1}X')c^2. \tag{9}$$

In the case of EC, when writing eq. (9) using atomic masses, one has to include the binding energy of the n-th shell captured electron, B_n, resulting in

$$Q_{EC} = M(^{A}_{Z}X)c^2 - M(^{A}_{Z-1}X')c^2 - B_n. \tag{10}$$

These three decay processes occur within isobars, nuclei with the same mass number: in the first case the atomic number Z is increased by one unit, while in the second and third cases it is instead decreased by one unit. Usually neutron-rich nuclei decay through a β^--decay, while proton-rich ones can undergo β^+ or EC. There are, however, examples of nuclei which undergo all the three processes.

For the lightest nuclei the Q-values are, for a given mass number, slightly higher on the proton-rich side than on the neutron-rich side of beta-stability line and, consequently, half-lives are systematically shorter on the proton-rich side. The asymmetry is enhanced by the contribution from the IAS (isobaric analogue state) transition in nuclei with $N < Z$. For masses above 100 the situation is reversed: experimentally the half-lives for nuclei more than 3–4 nucleons away from the beta-stability line are systematically shorter on the neutron-rich side than on the proton-rich side.

Because of the parabolic mass surface term in the mass formula, the Q-value increases as one moves away from the beta-stability line, which, by itself, enhances β-decay rates. Empirically, the β-decay half-lives fall off approximately exponentially away from stability [3].

Being a 3-body process, the energy spectrum of the electrons (positrons) can assume all values ranging from 0 to the decay Q-value. There is a wide range of variations of this quantity, being it equal to 2.6 keV for the decay of ^{187}Re [4] and up to 20 MeV for exotic neutron-rich nuclei. Also the half-lives for β-decay show a large variation, ranging within 10^{-2} s to 10^{17} years. Only three nuclei are known to exhibit very long half-lives: ^{115}In (10^{14} y), ^{113}Cd (10^{15} y) and ^{50}V (10^{17} y).

β-decay is not only governed by energy considerations, while it obeys to selection rules based on the Pauli principle and angular-momentum conservation. This is at the basis of the classification of β-decays into allowed and forbidden transitions.

In order to describe the β-decay process we will make the following assumptions, which are at the basis of the *Fermi theory of β-decay*: electron (positron) and antineutrino (neutrino) do not exist in the nucleus at the moment of the decay, they are created when the neutron converts into a proton (or viceversa the proton into a neutron). In the case of β^--decay, the neutron is depicted as an excited state of the nucleon which decays to the ground state, the proton, with the emission of an electron-antineutrino couple. The Coulomb interaction between the electron and the nucleus is here neglected. This approximation holds in particular for light nuclei with $Z < 10$.

The mass of the electron being $m_e \ll M_{nucleus}$, and under the assumption that the neutrino is massless, the recoil of the nucleus is considered null. The last assumption made in this description is that the electron and the neutrino share the available energy in all possible ways.

β decay is the result of the interaction of the nucleons with the field produced by the electron-antineutrino couple. At variance from α-decay, peculiarity of the β-decays is that the electron and neutrino do not exist before the decay process, and one needs to account for their formation. The Fermi theory is based on the hypothesis that the transition probability caused by the interaction is weak compared to the interaction that forms the quasi-stationary states. The interaction which causes the weak decay is treated as a perturbation, and follows the Fermi's Golden Rule:

$$\lambda = \frac{2\pi}{\hbar}|V_{fi}|\rho(E_f), \tag{11}$$

where the matrix element, V_{fi} connects the quasi-stationary initial and final states of the system, and the factor $\rho(E_f)$ accounts for the density of the final states. The final state has to include the wave function of the nucleus and those of the electron and neutrino. The density of the states determines, to the lowest order, the shape of the β-energy spectrum, which, after a proper derivation, can be represented by a bell-shaped function obeying the relation

$$N(p) = \frac{C}{c^2}p^2(Q - T_e)^2, \tag{12}$$

where Q is the Q-value of the reaction and T_e is the kinetic energy of the electron. The spectrum vanishes at zero momenta, $p = 0$, and has an endpoint for $T_e = Q$.

Equation (12) well describes the high-energy part of the spectrum. At low energies the electron feels the Coulomb field of the daughter nucleus, and the spectrum shape is influenced by the number of final states. This can be accounted for including a statistical factor and a *Fermi function* $F(Z', p)$ which describes the influence of the Coulomb field of the daughter nucleus.

If we stand in the allowed approximation, where the nuclear matrix element M_{fi} is considered to be independent of the specific nucleus, we can write the quantity

$$(Q - T_e) \propto \sqrt{\frac{N(p)}{p^2F(Z', p)}}, \tag{13}$$

and plotting this quantity against T_e we obtain a straight line, known as *Kurie plot*. This plot resembles experimental data very well, with small deviations at low energies, owing to scattering of low-energy electrons.

From the Fermi golden rule one can extract the total decay rate λ:

$$\lambda = \frac{g^2|M_{fi}|^2}{2\pi^3\hbar^7c^3}\int_0^{p_{max}} F(Z', p)p^2(Q - T_e)^2\mathrm{d}p. \tag{14}$$

The constants and the dependence on the electron energy can be grouped into a

factor, known as *Fermi integral*, $f(Z', E_0)$:

$$f(Z', E_0) = \frac{1}{(m_e c)^3 (m_e c^2)^2} \int_0^{p_{max}} F(Z', p) p^2 (E_0 - E_e)^2 \mathrm{d}p \tag{15}$$

which depends on Z' and on the maximum electron total energy E_0. Converting the decay rate into the half-life $t_{1/2}$ via eq. (2), one finds the relation

$$ft_{1/2} = 0.693 \frac{2\pi^3 \hbar^7}{g^2 m_e^5 c^4 |M_{fi}|^2}\,, \tag{16}$$

which is known as *comparative half-life* (ft): the differences in ft are related to differences in the matrix elements, and thus to the nuclear wave functions.

Owing to the large variations found in β decays, with ft values ranging between 10^3 to 10^{20} s, the quantity $\log_{10}(ft)$, also known as $\log ft$, is usually calculated, and can be used to classify the decays.

In summary, the electron (positron) and the antineutrino (neutrino) in the final state influence the β-decay transition rate in three ways, namely:

i) For a given energy released in the decay there is a density of possible final states for both the electron and antineutrino.

ii) The β-particle will feel the Coulomb field created by the protons in the nucleus. In other words the wave functions of the electron (positron) are enhanced (suppressed) close to the nucleus.

iii) The possible angular momentum and parity in the final state. The product of the electron and neutrino wave functions has parity $(-1)^L$, where L is the orbital angular momentum carried away by the electron.

The first two effects can be calculated and the combination of the two is the Fermi Integral of eq. (15).

By definition, in an *allowed* $\beta^{\pm}$-decay the final-state leptons, electron (positron) and neutrino (antineutrino), are emitted in an s state ($l = 0$) relative to the nucleus. Similarly in the *allowed electron capture* the initial electron is removed from an s shell and the final neutrino is in an s-state relative to the nucleus.

In addition to any orbital angular momentum, each of the leptons has spin $s = 1/2$. Thus in $\beta^{\pm}$ decays the final-state leptons can couple to total spin $S = 0$ or $S = 1$. In electron capture, the initial proton and electron can couple to $j \pm 1/2$ and the final neutron and neutrino can couple to $j \pm 1/2$ or $j \mp 1/2$, with coherent sign. Therefore in allowed β transitions the leptons can change the total angular momentum J by 0 or 1 unit.

Selection rules for the allowed decays and their classification in *Fermi transitions*, if electron and neutrino are coupled to spin $S = 0$, or *Gamow-Teller*, if they are coupled to $S = 1$, are shown in table I.

TABLE I. – *Classification of β-decays as a function of exchanged angular momentum. Selection rules for allowed and forbidden β-decay transitions are reported. Here J_i and J_f are the angular momentum in the initial and final nuclear states. π_i and π_f the corresponding parities.*

Type of transition	$\Delta J = \lvert J_f - J_i \rvert$	$\pi_i \pi_f$
allowed	$0, 1$	$+1$
Fermi	0	
Gamow-Teller	1 ($J_i = 0$ or $J_f = 0$)	
Gamow-Teller	$0, 1$ ($J_i > 0, J_f > 0$)	
first-forbidden	$1, 2$	-1
second-forbidden	$2, 3$	$+1$
third-forbidden	$3, 4$	-1
...	...	...

TABLE II. – *Classification of β-decay transitions according to their* $\log ft$ *values.*

Type of transition	$\log ft$
superallowed	2.9–3.7
unfavoured allowed	3.8–6.0
l-forbidden allowed	≥ 5.0
first-forbidden unique	8–10
first-forbidden non-unique	6–9
second-forbidden	11–13
third-forbidden	17–19
fourth-forbidden	> 22

Additionally, there is another selection rule pertaining the change in the number of radial nodes in the wave function (the principal quantum number n), which implies that $\Delta n = 0$, since the radial overlap integral vanishes [5]. This selection rule commands only a limited number of decays, for instance in the region of n-rich Tl isotopes: ^{209}Tl ground state is identified as a 3 $s_{1/2}$ proton hole and can only decay towards the $1/2^-$ state at 2.15 MeV in ^{209}Pb, even if there exists a lower-lying $1/2^+$ state at 2.03 MeV. This decay is, in fact, hindered since it involves a transformation of the 3 $s_{1/2}$ proton hole into a 4 $s_{1/2}$ neutron state at 2.03 MeV. This branching has been measured to be lower than 10% [6, 7].

Forbidden decays involve higher values of lepton angular momenta. They are not actually forbidden while retarded (hindered) compared to the allowed transitions. This can be easily accounted for if we consider that the wave functions superposition is minimal for these transitions. The classification of forbidden transitions is also given in table I.

β-decay rates vary largely, as mentioned earlier in this section. This is only partially accounted for by a mismatch in the nuclear wave functions of the initial and final states.

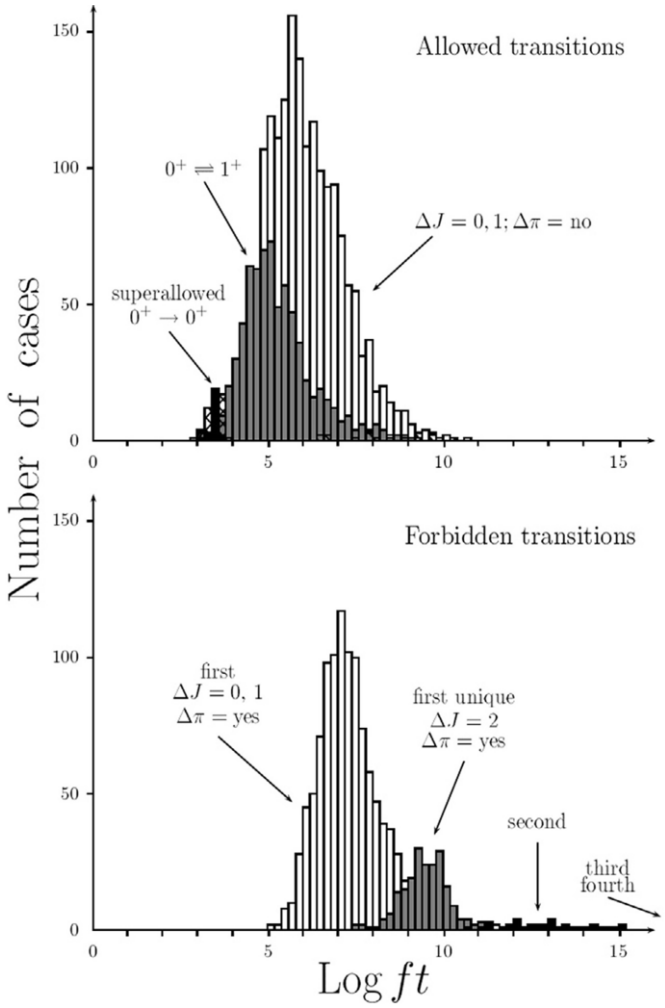

Fig. 1. – Log ft values for allowed (upper panel) and forbidden (lower panel) decays. (Reprinted with permission from B. Singh *et al.*, *Nuclear Data Sheet*, **84** (1998) 487, © 1998 Elsevier, DOI:10.1006/ndsh.1998.0015.)

The large variation is to be attributed to the great difficulty for a β-particle–neutrino couple to be formed in a $l > 0$ state.

We can relate the degree of forbiddenness to the experimental log ft values, and we see that decays of the same kind group around similar values. This is visible in table II and in fig. 1.

Superallowed transitions occur in nuclei where the proton and neutron Fermi surfaces are roughly at the same position, allowing for maximal overlap between initial and final nuclear wave functions. Usually these transitions are of a single-particle type and yield the maximum values for Fermi and Gamow-Teller matrix elements.

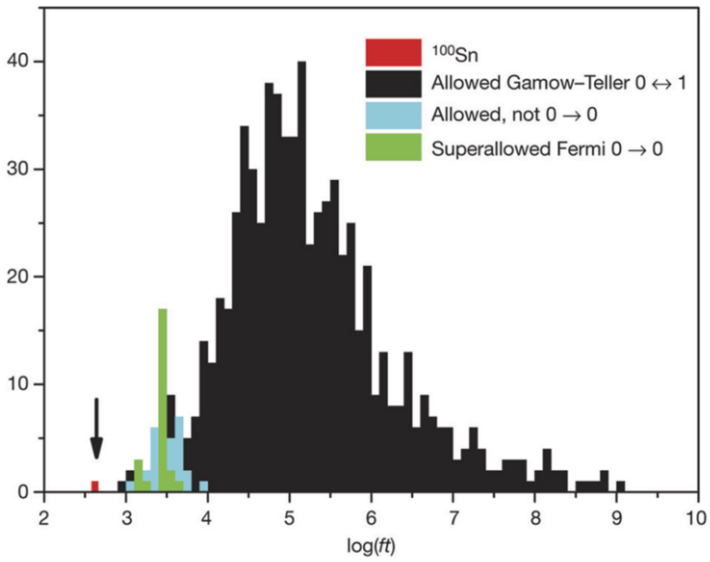

Fig. 2. – Similar to the upper panel of fig. 1, distribution of log ft values for allowed transitions. The arrow indicates the value measured for the *superallowed Gamow-Teller* decay of ^{100}Sn. (Reprinted by permission from C. B. Hinke *et al.*, *Nature*, **486** (2012) 341 © 2012, Springer Nature, DOI:10.1038/nature11116.)

Transitions named *l-forbidden allowed* occur in cases where the simple single-particle transition, in the mean-field shell model picture, is forbidden by the $\Delta l = 0$ selection rule, while rules on nuclear angular momentum and parity are satisfied. The wave function can be described introducing a residual interaction mixing the single-particle states. The decay is however hindered and log ft values are usually not lower than 5.

Unfavoured allowed transitions do not belong to either of the two cases described above: they are allowed transitions since there is no l-forbiddenness, but the single-particle transitions are not pure but diluted in the final and initial many-nucleon wave functions.

Forbidden unique transitions involve the maximum possible angular momentum difference between initial and final states. They relate to leptons emitted with high angular momentum, which is reflected in the degree of forbiddenness. The maximum change in angular momentum for a K-th–order forbidden transition is given by $\Delta L = K + 1$.

Parity conservation alternates with successive degrees of forbiddenness, being satisfied in the even cases.

One particular case is that of ^{100}Sn, whose Gamow-Teller transitions has been recently measured to have the lowest log ft ever extracted: in this very challenging experiment it was possible to extract, with high precision, the half-life for the decay and to define the end-point energy spectrum of the β decay. The extracted log ft value is the lowest measured so far and classifies this decay as a *superallowed Gamow-Teller* transition.

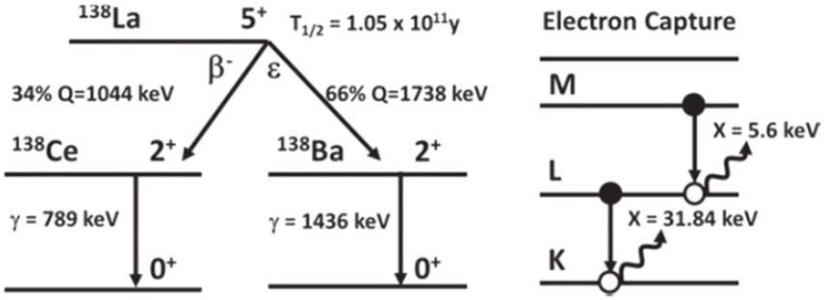

Fig. 3. – In the left panel the decay scheme of ^{138}La is shown, while in the right panel the electron capture shell refilling is sketched. (Reprinted with permission from A. Giaz *et al.*, *EPL*, **110** (2015) 42002, © 2015 EPLA, DOI:10.1209/0295-5075/110/42002.)

Figure 2 shows the measured $\log ft$ compared to known transitions. Additional details on the experiment and analysis can be found in [8].

An example of a highly forbidden decay is that of ^{138}La decay: ^{138}La decays by electron capture into an excited state of ^{138}Ba with 66.4% probability and the remaining 33.6% by β^--decay into an excited state of ^{138}Ce. In both cases, ^{138}La decays into an excited state of the daughter nucleus with the consequent emission of one γ-ray, as shown in fig. 3. In particular, in the electron capture decay, one γ-ray of 1436 keV is emitted while in the β^--decay process, one γ-ray of 789 keV is registered. Both the ^{138}La β^--decay and electron capture are 2-nd–order unique forbidden transitions, since, in both cases the decay connects a 5^+ state to a 2^+ state. The limited energy windows available for the decays, $Q_{EC} = 1742(3)$ keV, and $Q_{\beta^-} = 1052(4)$ keV, does not allow for the population of other states in the final nuclei, therefore this decay is highly-forbidden, occurring with a half-life of 1.05×10^{11} years. The β^- decay towards the 788.7 keV level in ^{138}Ce has a $\log ft$ value of 18.05(4), while the one corresponding to the decay towards the 1435.8 keV level in ^{138}Ba is 17.24(3).

Additional details can be found in [9, 7, 10].

The decay rate for allowed β^+ or β^- decays can be transformed to give a known expression for the ft value:

$$ft = \frac{K}{g_V^2 B_F + g_A^2 B_{GT}}, \tag{17}$$

where t is the partial half-life of the transition, K/g_V^2 equals to 6144.2(1.6) s, and $g_A/g_V = -1.2694(28)$ [11]. B_F and B_{GT} are the reduced matrix elements squared for the Fermi and Gamow-Teller parts. Nuclear electron capture will also contribute, but it is sizeable only for low decay energies in heavy elements.

The reduced transition probabilities, B_F and B_{GT}, can be related to the nuclear

matrix element as

$$B_F = \frac{g_V^2}{2J_i + 1}|M_F| \tag{18}$$

and

$$B_{GT} = \frac{g_A^2}{2J_i + 1}|M_{GT}| \tag{19}$$

where J_i is the angular momentum of the initial state and M the matrix elements already defined previously. The quantity g_V is the *vector coupling constant* of the weak interaction, which is determined to be equal to 1 in the Conserved Vector Coupling (CVC) hypothesis of the standard model; g_A is the *axial-vector coupling constant* of the weak interaction and it is instead calculated to be equal to 1.25 under the partially conserved axial-vector current hypothesis. These values correspond to the free-nucleon approximation, while, for a number of applications in nuclei, they can be affected by many-nucleon correlations.

The phase-space factor can be approximated roughly by $f = (1 + Q/m_e c^2)^5/30$, as function of the decay Q-value.

There are only few β decays where most of the β strength is energetically accessible in the decay energy window: the Fermi strength is concentrated around the isobaric analog state (IAS) and the summed strength fulfils the following sum rule:

$$\Sigma B_F^+ - \Sigma B_F^- = Z - N. \tag{20}$$

The Gamow-Teller decay strength obeys the Ikeda sum rule:

$$\Sigma B_{GT}^- - \Sigma B_{GT}^+ = 3(N - Z). \tag{21}$$

Most part of the Gamow-Teller strength is collected in the so-called Gamow-Teller Giant Resonance (GTGR) state, while β decays only probe the weak low-energy tail of this distribution.

A complementary approach to study the GT strength function is that of using nuclear reactions, in particular charge exchange reaction (CE). CE reactions can be classified as β^--type such as $(\mathrm{p,n})$, $(^3\mathrm{He,t})$, $(^6\mathrm{Li},^6\mathrm{He})$ and $(^{12}\mathrm{C},^{12}\mathrm{B})$ and β^+-type, such as $(\mathrm{n,p})$, $(\mathrm{d},^2\mathrm{He})$, $(\mathrm{t},^3\mathrm{He})$, $(^7\mathrm{Li},^7\mathrm{Be})$, $(^{12}\mathrm{C},^{12}\mathrm{N})$. These reactions allow the measurement of the high-energy part of the GTGR extending to excitation energies $E_x \sim 20$–$30\,\mathrm{MeV}$.

Charge-exchange reactions performed at intermediate beam energies ($E > 100\,\mathrm{MeV/A}$) measured at 0° are shown to exhibit a proportionality between the measured differential cross section and the $B(GT)$, via a unity factor, which can be derived if the $B(GT)$ for a mass A is known from β-decay studies.

It is not, however, possible to make a direct comparison between the two measurements, since the reaction mechanisms differ in several aspects. First of all, CE reactions

are sensitive mainly to the surface part of the radial wave function, while β-decays are insensitive to the radial part of the wave function and can occur at any point in the nucleus. Being CE reactions mediated by the strong interaction, the amount of transferred momentum is always finite, even if measured at 0°, and the p $\leftrightarrow$ n conversion can occur in two-steps, or higher-order, processes. This is at variance from β-decays which are mediated by the weak interaction only, and for which the p $\leftrightarrow$ n conversion is a one-step process involving the conversion of a u $\leftrightarrow$ d quark.

Further discussion on the extraction of the $B(GT)$ can be found in literature, in the review paper [12] and in the Euroschool lecture notes [13].

3. – Measuring β-decays properties, half-lives and $\log ft$

Depending on the half-life, a β-decay can be studied in different ways: the common idea is to identify the emitted β-particles and to correlate them with additional information. Here we classify the decays in two groups depending on their half-lives: long-lived species, with half-lives longer than tens of seconds, and short-lived species, characterised by shorter half-lives.

Long-lived species can be studied off-line, by producing the radioactive sample, moving it to a measuring station and then letting it decay. A standard experimental equipment for these studies is a moving tape station: the samples are collected over a definite amount of time, calculated on the basis of the expected decay rate and aiming at reaching a secular equilibrium, and then moved away to the measuring point. The measuring point is usually equipped with a plastic scintillator to detect the β-particles and ancillary detectors to measure the delayed emission of particles, either γ rays, neutrons or protons.

The time correlation between the sample collection and the measurement of the β-particles defines the decay curve from which one extracts the decay half-life, using eq. (1). The presence of an array to detect γ rays helps disentangling between decay products, in case competition with other decay modes is open, and the decay of successors.

If the half-life of the nucleus of interest is expected to be in the ms to s range, this technique cannot be applied: the implantation and detection points need to coincide. In case of exotic nuclei produced in an ISOL facility, where the outgoing exotic beams are accelerated to 40–60 keV, the species of interest are implanted onto a moving tape, surrounded by the same equipment described before. After letting the nucleus decay, the tape is moved away from the implantation point, in order to minimise background contributions originating from decay successors, or coming from long-lived species present as contaminants of the beam, and a fresh piece of tape is presented to a new implantation.

In this type of measurements, one can follow the growth and decay of the activity. The decay spectrum of ^{83}Ga ($T_{1/2} = 0.31(1)$ s), measured at the BEDO decay station in ALTO (Orsay, Paris) [14], is shown in fig. 4 as a typical example. The experimental set-up is shown in the upper panels, where we see the moving tape coming from the top of the picture and the direction of the radioactive beam sketched by the red arrow. Mass-selected ^{83}Ga nuclei are implanted on the mylar tape for a period of ~ 3 s, until a saturation is reached. When this is achieved the implantation is stopped and the

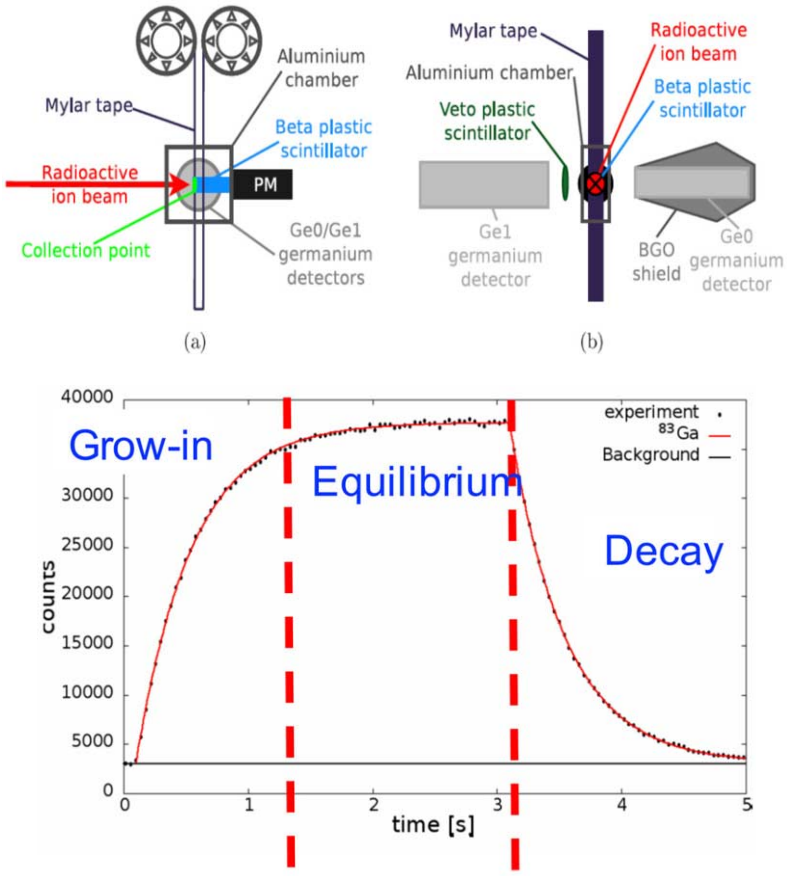

Fig. 4. – Top panels: Schematic representation of the BEDO array at ALTO, Orsay (Fr). In the left panel the moving tape comes from the top of the figure, while the radioactive beam is represented by the red arrow coming from the left-hand side. In the right panel the location of β and γ detectors is instead depicted. The decay curve collected over 5 s for the decay ^{83}Ga $\rightarrow$ ^{83}Ge is shown in the bottom panel. The three components, accumulation (grow-in), equilibration and decay, are clearly seen. A constant background is included in the fit. (Adapted from Master Thesis in ref. [15].)

accumulated nuclei are let to decay. The total decay curve, showing the three different steps of the process, accumulation of the nuclei, saturation and decay are visibile in the decay spectrum shown in the bottom panel of fig. 4. The shown decay curve is collected when a constant production rate during implantation is achieved. The fit to the decay curve has to comprise all these elements, and is represented by a red continuous line in the plot. A constant background owing to uncorrelated decays is also assumed and shown by the grey straight line.

In case the short-lived nuclei of interest are produced following fragmentation or fission of relativistic beams a different technique is employed. The cocktail beam of nuclides

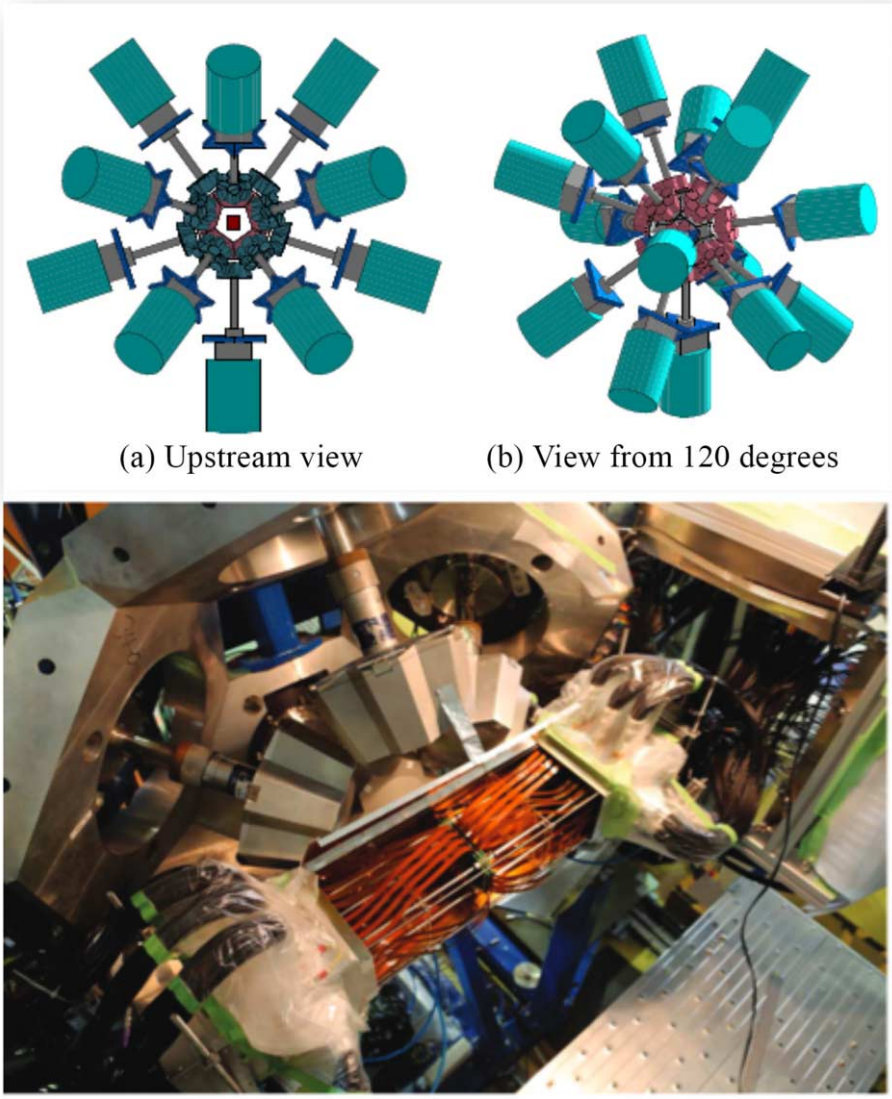

Fig. 5. – Top row: CAD drawings of the EURICA set-up at Riken(J). The 12 seven-fold HPGe cluster detectors, shown in light blue, surround the implantation chamber. To maximise the efficiency of the set-up the BGO anti-Compton shields were removed. Bottom row: detail of the WAS3ABI array consisting of several layers of DSSSD, located in the center of the EURICA HPGe detectors. (Adapted from [16].)

produced in the primary target, after selection and transport in a spectrometer, has an energy of tens to hundreds of MeV/A and is slowed down and finally stopped at the measuring point. The decay station for these measurements is equipped with an active

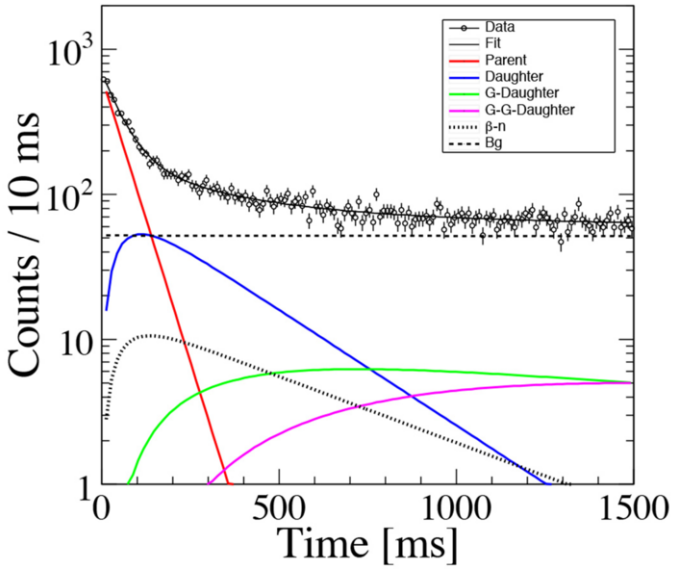

Fig. 6. – Decay curve of ^{68}Mn $\rightarrow$ ^{68}Fe measured from the time of detection of the β signal in the DSSSD WAS3ABI array of EURICA. The data points, shown in black symbols are fitted to the Bateman equations including contributions from the main decay (red line), decay of the daughter nucleus, ^{68}Fe $\rightarrow$ ^{68}Co (blue line), of the granddaughter, ^{68}Co $\rightarrow$ ^{68}Ni (green line), of the great granddaughter, ^{68}Ni $\rightarrow$ ^{68}Cu (pink line) and of the β-n channel, ^{68}Mn $\rightarrow$ ^{67}Fe (dotted black line). A linear background owing to random decays is also included in the fit (dashed line). The overall fitting function is represented by the black continuous line.

stopper, usually consisting of layers of Double-Sided Silicon Stripped Detectors (DSSSD), which register both the implanted nucleus and its subsequent β- or α-decay. A cocktail beam is composed of many decaying species, therefore correlations in space and time are requested to assign each recorded decay to the correct parent implanted nucleus. Low implantation rates, of the order of 100 Hz, avoid double implantation events in the same pixel. Also in this case, the implantation area is surrounded by γ-ray detectors. In fig. 5 the realization of such a set-up, the EURICA array, is shown: in the central part of the figure the detailed view of the DSSSD array is shown, while the drawing of the HPGe array surrounding the decay chamber is presented in the top panels. A variable number of silicon layers, ranging from 3 to 7, have been used during the experimental campaign [16, 17].

In an in-flight facility, it is possible to produce the most exotic species, which are characterised by very short half-lives. In order to correctly account for the measured decay curve one needs to include also subsequent decays, comprising daughter, granddaughter and —even— great granddaughter decays. An example of such studies is given in fig. 6, where the decay curve for ^{68}Mn $\rightarrow$ ^{68}Fe, occurring in 40(3) ms, is shown. The contributions coming from the decay of the daughter, ^{68}Fe $\rightarrow$ ^{68}Co ($T_{1/2}$ = 188(4) ms), of the granddaughter, ^{68}Co $\rightarrow$ ^{68}Ni ($T_{1/2}$ = 1.6(3) s), and of the great granddaughter,

$^{68}\mathrm{Ni} \rightarrow {}^{68}\mathrm{Cu}$ ($T_{1/2} = 29(2)\,\mathrm{s}$) are also considered in order to correctly fit the decay spectrum. These contributions are evaluated on the basis the Batemann equations described in sect. **2**, and are depicted in the figure. Also the β-delayed neutron-emission channel, accounting for a sizeable fraction of the decay ($P_n = 18(10)\%$) has been included in the evaluation. The definition of the probability for delayed emission of neutrons, indicated by the P_n value is discussed in details in sect. **5**. A constant background accounts for random contributions. Further details on this analysis can be found in ref. [18].

As mentioned above, typical set-ups for measuring β-decays comprise HPGe detectors, to measure the internal de-excitation in the daughter nucleus. Such arrays are characterised by high resolution and granularity, which help in the reconstruction of decay schemes and in describing the decay towards the daughter's states. By evaluating the intensity of γ transitions feeding and depopulating each level, one can evaluate how the primary β decay feeds each individual state, the so-called β feeding, I_β. The determination of β feeding to the states, once the relative half-life is taken into account, can be used to extract the $\log ft$ value and, therefore, to classify the decay. If the spin and parity of the initial state are known, assumptions on the J^π of populated states can then be proposed.

The measurement of the feeding fraction of the decay directly populating the ground state has to follow a different approach, since all transitions in the decay scheme finally feed this level, and, in parallel, no direct information on its de-excitation is given. If we can measure the number of implanted ions and the number of registered β decays, we can extract this value from the missing feeding once the contribution measured by γ transitions has been subtracted. In case these numbers cannot be accessed, such as in studies performed at ISOL facilities, a typical approach is to follow the decay down to granddaughters or great granddaughters, which, lying closer to the stability, are usually studied in previous experiments. The relative population of granddaughter ground state returns information on the decays coming directly from the daughter ground state.

Measurements performed at ISOL facilities often have problems in accessing very short half-lives and in determining absolute activities, owing to delay losses in the extraction of the species from the target ion source, whereas experiments at in-flight facilities have to define special procedures to correct from the decay of non-relevant species. If the advantage of the ISOL technique is that of having an almost mono-isotopical beam, in the case of experiments performed at in-flight facilities it is possible to measure very short half-lives of nuclei populated with little statistics.

Examples of tape-moving decay stations are found in almost all ISOL facilities, such as ISOLDE at CERN (Switzerland) [19], ALTO at Orsay (France) [14], TRIUMF (Canada) [20], and projects to build new ones are being proposed for the future facilities, such as SPIRAL2 (France) [21] and SPES (Italy) [22]. Dedicated campaigns to study β-decay of exotic nuclei are instead carried on at in-flight facilities such as GSI-FAIR (Germany) [23], RIKEN (Japan) [16] and MSU (USA) [24].

The increasing Q_β window of n-rich nuclei allows access to a large fraction of the GT strength. This however implies also a stronger impact of the so-called *Pandemonium effect* [25].

The Pandemonium effect is a consequence of the use of HPGe detectors in the study of β-decay: HPGe detectors are typically characterised by optimum energy resolutions ($\approx$ 2 keV for 1.3 MeV γ rays), associated to low efficiency for energetic γ rays. The large Q_β window characteristic of the decay of exotic nuclei, opens the possibility of the emission of energetic γ rays, which might escape detection in a HPGe detector. As a consequence, the β feeding to each state is not correctly accounted for. This adds up to the decrease of the decay strength, which varies as $(Q_\beta - E_{ex})^5$, diminishing at increasing excitation energy (E_{ex}).

To overcome this problem, a different technique is used, based on *Total Absorption Spectrometers* (TAS), arrays composed of high-efficiency scintillator detectors aiming at covering —ideally— the full solid angle. A TAS can be made out of single bulky crystals (such as the case of the Lucrecia TAS operating at CERN [26] or the SuN array in MSU [27]), or of modular segments combined in honeycomb structures around the implantation point, such as the MTAS array used at HRIBF in Oak Ridge [28].

As a consequence of the poor energy resolution of the scintillator materials employed, either BaF_2 or NaI, a TAS cannot resolve the single transitions, while it acts as a calorimeter and sums the released γ rays. In this respect this is a complementary technique to that of high-resolution β-decay studies, since the detailed measured de-excitation scheme is used as input to extract the multiplicity of emitted γ rays and correctly reconstruct the sum energy.

In general the analysis of data acquired with a TAS is complicated and requires to solve the inverse problem

$$d = R(B)f, \tag{22}$$

being d the measured data and f the feeding function. R is the response matrix of the detector, which depends on the structural characteristic of the detector (geometry and material composition) and varies as a function of measured γ energy and multiplicity. This needs to be evaluated using *ad hoc* simulations and then validated by calibration sources. The analysis of the results is helped by a GEANT4 simulation of the experiment. This complex simulation takes into account the efficiency and response function of the array, both as function of the energy and of the multiplicity of emitted γ-rays. The experimental level scheme, comprising the measured β feeding to the states, is also fed to the simulation.

Detailed descriptions of the analysis with a TAS spectrometer can be found in ref. [29].

4. – β-decay and astrophysics

β-decay studies are directly linked to element nucleosynthesis, in particular for n-rich nuclei. Half of the elements beyond Fe are assumed to be produced in the rapid neutron-capture process known as *r process*, which spreads out towards the heaviest radioactive heavy actinide elements present on Earth, such as Th and U.

The r-process starts around seed nuclei and occurs via a sequence of near-equilibrium rapid neutron capture and photo-neutron emission reactions, populating neutron-rich nuclei far away from the valley of stability. The equilibrium is established with an abundance peaked around one or two isotopes [30, 31].

The r-process pattern is extracted from the solar system abundances after the contributions coming from the slow-neutron capture (*s-process*) and proton-capture process (*p-process*) are subtracted [32]. The resulting pattern is characterised by three main abundance peaks for $A \sim 80, 130, 195$, that can be linked to neutron shell closures, and a high plateaux for the rare-earth deformed nuclei. This latter peak is predicted to generate in a different stage of the process, either during freeze-out or following fission recycling.

A crucial parameter which defines the evolution of element formation is the neutron flux. Three different scenarios can be identified: in environments where few neutron captures per seed occur (n/s ~ 50) the r-process can proceed up to nuclei with $A \sim 125$. This is the weak component of the r-process, taking place in the neutrino-driven wind of core-collapse supernovae. In environments with increasing neutron fluxes, allowing for enough neutron captures per seed (n/s ~ 100), the r-process can produce the two abundance peaks $A = 130$ and 195. This is the so-called main component and it can occur in outflow of neutron-rich material via magnetic turbulence driven jets in core-collapse supernovae. If the neutron flux is even larger, of the order of thousands n-captures per seed nucleus, the r-process can proceed all the way up to fissile nuclei ($A \sim 300$), where β- or n-induced fission terminates the process. The two fission fragments experience the neutron flux and enter again in the r-process cycle. After a few cycles the abundances are dominated by the distribution of fission fragments rather than by the β-decay flow near closed shells, therefore fission recycling produce an r-process abundance pattern between the second and third r-process peaks that is relatively insensitive to variations in the initial conditions. In addition, fission introduces a new flux of neutrons which can induce neutron-capture events. For a recent description of the impact of fission recycling see ref. [33].

The recent historical measurement of gravitational waves detected by the LIGO-VIRGO collaboration [34] provided new insight in the astrophysical site for the r-process: within hours from the measurement of the binary neutron star merger emission of gravitational waves and associated γ-ray burst, ground- and space-based telescopes registered an electromagnetic transient, called *kilonova*, which is associated to the synthesis of heavy elements in the r-process. It is estimated that about 0.05 solar masses of r-process elements were created in this single event [35, 36]. A new era of multimessenger astronomy is starting where astronomy, cosmology, nuclear physics, astrophysics, atomic physics, chemistry come together and join forces to solve the puzzle of the creation of elements in the universe.

The relative abundance is determined by β-decay rates along the r-process path, and is described by the Nuclear Statistical Equilibrium equation (NSE), expressed in terms

of number density for the isotope ${}^{A}Z$, $n(Z,A)$ [37]:

$$\frac{n(Z,A)}{n(Z,A+1)} = \frac{1}{n_n}\left(\frac{2\pi\mu kT}{h^2}\right)^{3/2} \times \frac{G_A G_n}{G_{A+1}} e^{\frac{Q_n}{kT}}, \tag{23}$$

where μ is the reduced mass of the ${}^{A}Z$ nucleus and the neutron, h Planck's constant, k the Boltzmann constant and T the temperature. G_A is the partition function of the nucleus ${}^{A}Z$, Q_n the neutron separation energy for the ${}^{A+1}Z$ nucleus.

This equation results in the presence of sharp peaks in the abundances for one —or few— isotopes within one isotopic chain. The flow of β-decays along these peaks define the r-process path. The location of the path is given by the assumption that [30]

$$\frac{n(Z,A+1)}{n(Z,A)} \leq 1. \tag{24}$$

The elemental abundances $n(Z,A)$ along this path are determined by the β-decay flow:

$$\frac{\mathrm{d}n(Z,A)}{\mathrm{d}t} = \lambda_{Z-1} n(Z,A-1) - \lambda_Z n(Z,A), \tag{25}$$

where the total β-decay rate of each element is given by the weighted sum of β-decay rates for each isotope:

$$\lambda_Z = \sum_A n(Z,A)\lambda_\beta(Z,A). \tag{26}$$

This description is able to reproduce, at a typical r-process temperature $T_9 \sim 1$, the experimentally measured three principal abundance peaks, for $A = 80$, $A = 130$, $A = 195$, corresponding to the neutron closed-shell waiting points ^{80}Zn, ^{130}Cd and ^{195}Tm.

Another important parameter which determines the r-process path is the neutron density: at the beginning neutron densities are high, shifting the r-process path towards neutron-rich species. With time the number of available neutrons decreases, reaching the so-called *freeze out* condition when they are exhausted. At this moment the process moves towards the line of stability via successive β decays.

At this later stage the condition for nuclear statistical equilibrium is no more met,

and the evaluation of the abundances have to take into account a full reaction network:

$$\begin{aligned}\frac{\mathrm{d}n(Z,A)}{\mathrm{d}t} = & \, n(Z,A-1)\phi_n\sigma_{n,\gamma}(Z,A-1) \\ & +n(Z,A+1)\phi_\gamma\sigma_{\gamma,n}(Z,A+1) \\ & +n(Z-1,A)\lambda_\beta(Z-1,A) \\ & +(n,p),(n,\alpha),(p,\gamma),(\alpha,\gamma), \\ & +(n,\text{fission}),(\beta,n)(\beta,\text{fission}),\ \text{etc.} \\ & -n(Z,A)[\phi_n\sigma_{n,\gamma}(Z,A)+\lambda_\beta(Z,A) \\ & +\phi_\gamma\sigma_{\gamma,n}(Z,A)+\ldots],\end{aligned}$$

where ϕ_n and ϕ_γ are the time-dependent neutron and γ fluxes.

The measurement of the β-decay rates and the determination of possible branches, either to competing decay mechanisms (α-decay or fission) or leading to emission of secondary neutrons, is the most important input for network calculations to defining the r-process path and aiming at reproducing measured solar-system abundances.

R-process calculations rely on a network of inputs, some of which are not presently available. Therefore the need for reliable calculations which can, on the one hand, accurately reproduce experimental values and, on the other hand, extrapolate towards the most exotic species.

Two main approaches are usually followed: the macroscopic approach of gross theory and the microscopic approach of large scale shell models. A number of in-between global models are also effectively used.

Gross Theory models [38] aim at describing the behaviour of the β-strength distribution in a statistical manner, where allowed and first-forbidden (ff) transitions are built from one-particle strength functions folded using paring. Newly refined versions of Gross-Theory models (2nd-generation Gross Theory) have been developed recently. Despite the simplicity of the approach, Gross Theory models show a remarkable predictive power throughout the nuclide chart, in particular when large Q_β windows are involved, as in the case of neutron-rich nuclei [39, 40].

Large-scale shell-model calculations may aim at successfully describing the β-decay matrix elements or strength distribution, via the use of realistic effective interactions. The limit of these calculations is the exploding number of Slater determinants that need to be calculated when leaving close shells. A truncation of the model space is usually required, thus hampering the reproduction of properties on large scale. The present advance in computational power is quickly changing the situation, with the possibility of performing heavy load calculations [41].

In between these two approaches, various semi-microscopic models have been developed, based on effective nucleon-nucleon interactions which allow particle-hole excitations of the charge-exchange collective mode. Random-Phase Approximation (RPA) and

microscopic-macroscopic application of the Quasi-particle Random Phase Approximation (QRPA) [42] are the basic ones. In the QRPA approach the β strength, containing the nuclear matrix elements for the Gamow-Teller, Fermi, and first-forbidden decays, is calculated using a folded-Yukawa single-particle potential to which pairing and Gamow-Teller residual interactions are added.

It is remarkable to note that these calculations are used to reproduce data over the whole nuclide chart: the QRPA-FRDM approach has been applied to predict gross properties (mass, $T_{1/2}$ and P_n) over a broad range of nuclei, including more than 8000 species above ^{16}O [43]. Even if they may not account for the half-lives locally in specific mass regions, they have a strong predictive power on the entire nuclide chart.

Extended description of the above-described models are given in refs. [45, 44].

There are currently many active programs to measure β-decay rates for nuclei in the vicinity of the r-process path. If some regions are most accessible, like the two lightest abundances peaks at $N = 50$ or $N = 82$, scarce information is still available for half-lives around the third peak at $N = 126$ and for the rare-earth nuclei.

A very recent successful campaign provided the measurement of a large number of unknown half-lives. The experiments have been performed at Riken laboratory using the EURICA set-up, already described earlier on in these proceedings. The high intensity of the ^{238}U beam allowed the study of very exotic nuclei [46, 47]. Examples of the transported and identified cocktail beams produced in two experiments are reported in fig. 7, where we see that hundreds of nuclei could be addressed at the same time. Nuclei lying on the right side of the red line have been studied for the first time. The red circles highlight newly produced species.

Such a systematic study of β-delayed half-lives led to the measurement of more than 200 decay rates, concentrating on nuclei in the rare-earth peak and around the $N = 82$ abundance peak.

The effect of these new measurements is visible in a fully dynamic reaction-network calculation study, that simulated a spherically symmetric out-flow from a neutron-rich stellar environment without specific assumptions on the astrophysics site, in order to highlight the impact of the new experimental nuclear physics data. Starting from the same assumptions, two sets of calculations were performed, including or not the newly measured half-lives. The comparison to measured solar abundances (data points) [32] is shown in fig. 8: panel (a) shows, with a red continuous line the abundances calculated excluding the latest measured decay rates, while they are included in panel (b). The impact of these new rates is clearly visible in the rare-earth peak which is well accounted for in panel (b) at variance from panel (a). These network calculations point also to the fact that these nuclei are most probably populated during the freeze-out of a $(\mathrm{n}, \gamma) \rightleftharpoons (\gamma, \mathrm{n})$ equilibrium. Further details on this analysis can be found in ref. [46].

As mentioned earlier on, the region around the third abundance peak has been scarcely investigated. Isotopes belonging to this region can be accessed by different reactions: nuclei north-east of ^{208}Pb can be accessed by fragmentation reactions induced on ^{238}U or heavier elements at beam energies around 1 GeV/A. Such reactions can be studied at the FRS fragmentation facility at GSI-FAIR [23]. To populate nuclei south of ^{208}Pb one can

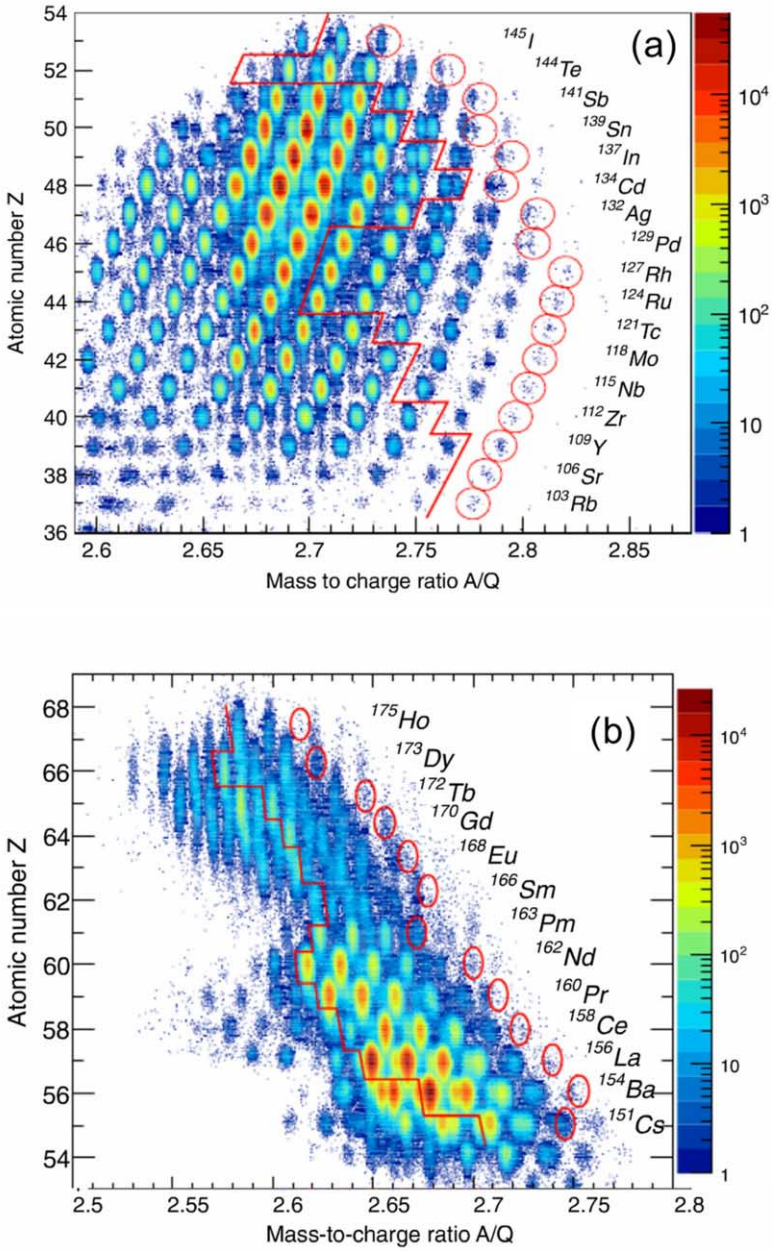

Fig. 7. – Z *vs.* A/Q identification plots representing the nuclei produced in a fission reaction of ^{238}U at 345 MeV/u on a ^{9}Be target for two different settings of the Big-RIPS separator. Newly measured lifetimes were measured for nuclei to the right side of the red lines, while newly produced species are surrounded by red circles. (Reprinted figure with permission from G. Lorusso *et al.*, *Phys. Rev. Lett.*, **114** (2015) 192501. © 2015 by the American Physical Society. Reprinted with permission from J. Wu *et al.*, *Phys. Rev. Lett.*, **118** (2017) 072701, © 2017 by the American Physical Society.)

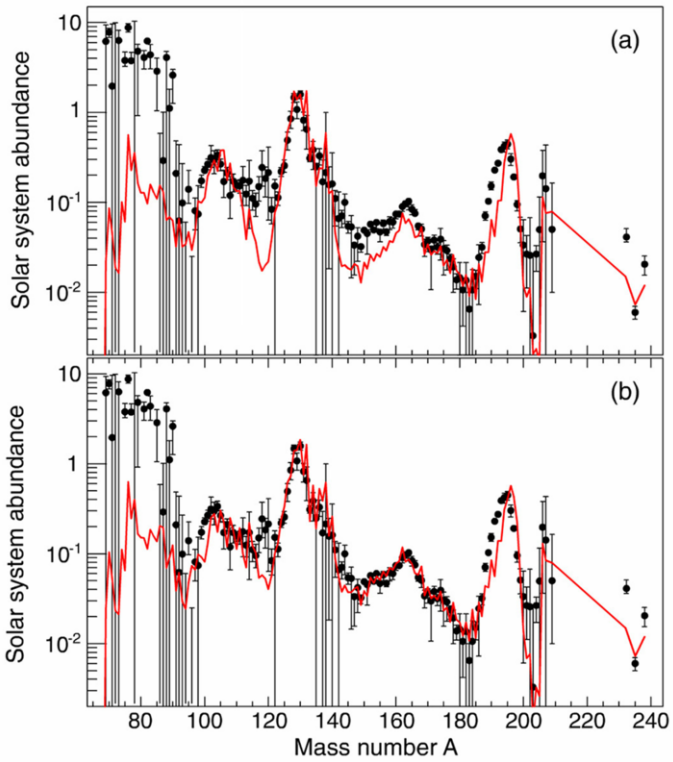

Fig. 8. – Comparison between the r-process Solar-System abundance pattern [32] and the abundances calculated (a) without and (b) with newly measured half-lives from ref. [46]. Calculations make use of masses calculated by the KTUY mass model [39] and reaction rates extracted from the ReaclibV1 library [52]. The half-lives, other than the ones we measured, are from the FRDM-QRPA model [42]. (Reprinted figure with permission from G. Lorusso *et al.*, *Phys. Rev. Lett.*, **114** (2015) 192501, © 2015 by the American Physical Society.)

perform cold-fragmentation reactions on a ^{208}Pb beam, where the fragmentation process removes few protons from the primary beam [48]. Recently, an alternative approach employing Multi-Nucleon-Transfer (MNT) reactions of heavy species, such as ^{136}Xe on ^{198}Pt, has been employed to populate this mass region with sizeable cross sections. The original idea dates back to the '90s [49], and has been recently experimentally verified in Ganil, using the VAMOS variable mode mass spectrometer [50]. This new approach is at the basis of the KISS isotope separator set-up aiming at measuring masses and rates in nuclei around the third abundance peak [51].

The work performed in the past decade at the GSI fragmentation facility already conveyed first experimental insight in nuclei at and beyond $N = 126$. Numerous experiments have been performed, mainly using the RISING set-up in its stopped-beam configuration, which is based on the same detectors used for EURICA. The results are collected in fig. 9 for various isotopic chains ranging from Re ($Z = 75$) to Bi ($Z = 83$) [53-57].

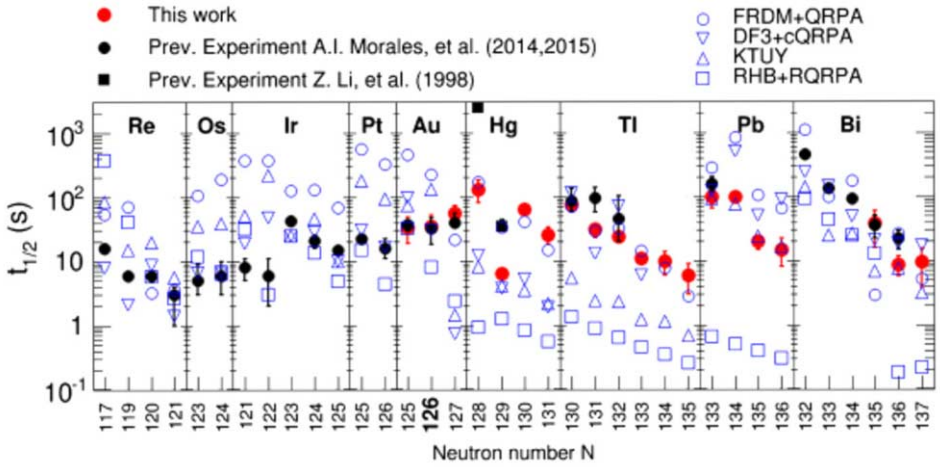

Fig. 9. – Experimental half-life values (solid symbols) on both sides of $N = 126$ from previous experiments [53-57] (bold circles and bold squares), and from the work of Caballero-Folch and coauthors [59]. Open circles show published theoretical half-lives with different models (see legend). (Reprinted from R. Caballero-Folch *et al.*, *Phys. Rev. Lett.*, **117** (2016) 012501, under the terms of the *Creative Commons Attribution 3.0 License* for DOI:10.1103/PhysRevLett.117.012501).

Shell model [41], FRDM-QRPA [42], DF3+cQRPA [58] calculations reproduce very well data around the $N = 82$ abundance peak, while the situation around the third abundance peak, $N = 126$, is more complicated, and predictions by different approaches vary wildly, as it is seen in fig. 9, where theoretical models tend to overestimate the results for nuclei with $N < 126$ while they instead underestimate the rates for those having $N > 126$. This may be an effect of the less accurate single-particle energy reproduction in nuclei near shell closures, given by the fact that at low Q_β values the decay is dominated by few transitions and it is, therefore, more sensitive to the share of FF and GT transitions. Indeed, first-forbidden transitions are expected to play a major role in this mass region suppressing the half-lives. They are included in the framework of Gross Theory in FRDM+QRPA calculations, while they are instead treated on the same footing by the DF3+cQRPA.

The review paper by Mumpower *et al.* [44] compares the measured half-lives tabulated reported in the literature [7] compared to predictions obtained using QRPA calculations in the FRDM-QRPA framework and using the KTUY. The comparison of data is performed in three different ways: as function of the neutron number, highlighting the exoticity, for increasing $T_{1/2}$ and as function of the β-decay Q value. Even if the discrepancy between theoretical and experimental values is large, spanning 6 orders of magnitude, a close look shows that the largest contribution to this mismatch comes from decays characterised by long lifetimes and small Q_β values, thus corresponding to nuclei close to the stability valley. In fact, decays with narrow Q_β windows have a small number of available states to decay to, as is the case of the region around $N \sim 126$. Deviations for exotic nuclei are indeed small, covering only two decades.

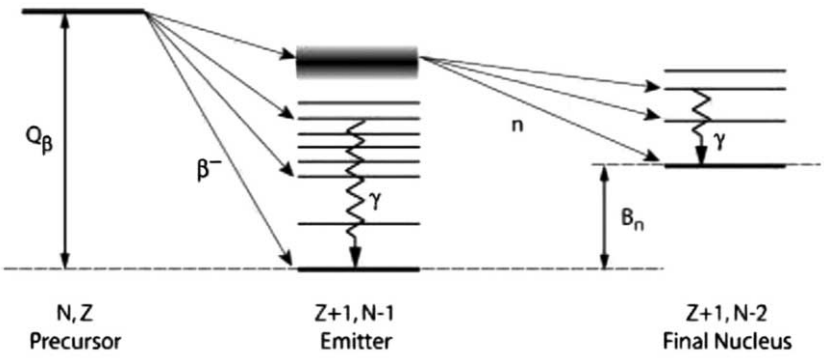

Fig. 10. – Sketch of the β-delayed neutron emission mechanism: the Q_β window allowed for the decay of the precursor nucleus, is larger that the neutron separation energy, therefore the decay can populate, together with discrete states in the daughter-emitter nucleus, also high-lying resonances. These resonant states can decay by the emission of one neutron, therefore populating states in a different final nucleus.

5. – β-decay in exotic neutron-rich nuclei

Neutron-rich nuclei, going away from the valley of stability, are characterised by increasing Q_β values and decreasing values for neutron-separation energies (S_n). Given these conditions, the delayed emission of neutrons becomes a dominant decay channel, leading to the formation of different successor nuclei.

In fig. 10 a schematic representation of the process is given: the precursor nucleus, on the left side of the figure, decays towards the daughter nucleus, also called emitter. As the Q_β window gets large, part of the flux does not end in low-lying states of the daughter nucleus, while feeds unbound states, which decay, primarily, by the emission of neutrons. The decay, thus, populates two different nuclear species: the intermediate emitter $(Z+1, N-1)$ and the final successor nucleus $(Z+1, N-2)$. In cases where the Q_β window is large enough, we can observe the emission of more than one neutron.

This exotic decay mode is a powerful tool to access the β strength function above the neutron separation energy, allowing access to the structure of discrete states and resonances.

Moreover, β-delayed neutron emission alters the final abundances by shifting the decay path toward lower masses and providing neutrons reactivating the r-process after freeze-out. The impact of β-delayed neutron emission is, therefore, two-fold: from one side it provides additional source of neutrons that feed the capture process, even after neutron exhaustion, and, on the other, it is important to finalise the details of the isotopic abundances, which are shifted towards lower mass distributions.

The probability for emission of a neutron following a β decay can be expressed in terms of

$$P_{xn} = \frac{\sum_{i,E_i=S_{xn}}^{Q_\beta} \lambda_i}{\sum_i \lambda_i} = \frac{\sum_{E_i=S_{xn}}^{Q_\beta} S_\beta(E_i) \cdot f(Q_\beta - E_i)}{\sum_{E_i=0}^{Q_\beta} S_\beta(E_i) \cdot f(Q_\beta - E_i)}, \tag{27}$$

where the assumption is that the nucleus emits as many neutrons as energetically possible, overestimating the number of emitted neutrons. The competition between neutron emission and γ decay from these excited states, expressed in terms of decay widths Γ_n and Γ_γ, has to be taken into account, leading to a more refined —and operative— formulation as

$$P_n = \frac{C}{\lambda_\beta} \int_{-Q_\beta+S_n}^{0} |M(E)|^2 f(Z,-E) \frac{\Gamma_n}{\Gamma_n+\Gamma_\gamma} \mathrm{d}E, \tag{28}$$

where C includes all coefficients outside the integral in eq. (15).

Experiments in neutron-rich nuclei focus both on the measurement of the probability of emission of delayed neutrons, by measuring the number of emitted neutrons, and on the decay mechanism itself, with the measurement of the neutron energy spectrum.

The determination of the probability of delayed emission of neutrons can be performed even without the direct measurement of the emitted particles: the study of the internal deexcitation of the successor, based on the missing flux estimated from a detailed knowledge of the I_β branching ratios to each states, including the ground state, conveys the wanted information. Good efficiency and angular coverage are demanded.

Neutrons can be measured using detectors based on ^{3}He tubes, which detect neutrons after their energy has been moderated in paraffin or polyethylene matrix, or using scintillator detectors for Time-of-Flight measurements.

The capture of thermal neutrons by ^{3}He results in the reaction

$$^3\mathrm{He} + \mathrm{n} \rightarrow {}^3\mathrm{H} + {}^1\mathrm{H} + \gamma, \tag{29}$$

where the emitted γ-ray has a typical energy of 765 keV. The measurement of this specific γ transition is therefore an indication of the detection of a neutron.

This detection technique is employed in many set-ups, such as, for example, BELEN [60], in use in GSI-FAIR and Jyväskylä, by the TETRA array [61] at ALTO-Orsay, 3Hen [62] in HRIBF-Oak Ridge, and in the BRiken set-up [63] in Riken.

Time of Flight (TOF) techniques are instead pursued using long bars of scintillator material, read to the sides by photomultiplier tubes. Different dimensions and distances from the emitting source are used to detect neutrons of different energy and cover a large solid angle. The TOF is calculated with respect to a start signal coming from a β detector (either a plastic scintillator or a Si detector). The TOF techniques enables the measurement of the energy spectrum of the emitted neutrons, which maps the $B(GT)$ above the neutron separation energy.

An example of such array is the VANDLE array [64], successfully used in many campaign at HRIBF-Oak Ridge, ISOLDE-CERN and Riken.

Recent successful determination of P_n values in Hg and Tl has been achieved in GSI [59]. The measurement of β-delayed neutron emission probability in such heavy systems, even if not directly lying on the r-process path, are instrumental also to discern theorectical models aiming at describing the β-decay strength function.

The same theoretical approaches used to predict decay rates are employed for the probability of emission of delayed neutrons. The reliability of such approaches in extracting this quantity is however very limited, suggesting that the given description of the mechanism is too simplistic: we will see later that a Q_β value greater than the neutron separation energy is not a sufficient condition for the emission of delayed neutrons, and that the competition with energetic γ decay is stronger than expected. Moreover, the shape and deformation of the parent nucleus is expected to influence the probability of emission of particles.

The increasing Q_β window of n-rich nuclei allows access to a large fraction of the GT strength. This however implies also a stronger impact of the *Pandemonium effect*, described in sect. **3**.

We report here the comparison of two experiments aiming at the study of the decay ^{70}Co $\rightarrow$ ^{70}Ni performed with two different approaches: the first one employing a standard set-up comprising HPGe detectors (high resolution), while the second one using a total absorption spectrometer (low resolution). The decay ^{70}Co $\rightarrow$ ^{70}Ni is characterised by the presence of two β-decaying states: the high-spin ground state $(6^-, 7^-)$ and a low-spin $(1^+, 2^+)$ isomeric state, decaying with similar half-lives ($T_{1/2} = 112(7)$ ms and $T_{1/2} = 508(7)$ ms respectively). This decay has a large Q_β window of 12.3(3) MeV, with a low probability for delayed-neutron emission [65, 66, 7].

The high-resolution experiment has been performed at Riken, using the EURICA set-up [17], composed of a combination of 15 7-crystal HPGe detectors and 5 layers of DSSSD from the WAS3ABI array, to study the cocktail beam produced by relativistic fission of a primary ^{238}U beam at 345 MeV/u on a ^{9}Be target. A picture of the experimental set-up is given in fig. 6. The fission products were transported and identified into the Big-RIPS and ZeroDegree spectrometers, and implanted in the DSSSD detectors to study their decay. The high resolution and granularity of the EURICA γ array allows to reconstruct, via the analysis of γ-γ coincidences, the complicated level scheme following the decay under analysis. This allows to disentangle the decays coming from the two β-decaying states: the fission reaction at relativistic energies, in fact, populates the β-decaying isomeric state with a probability of 45%, while the remaining ^{70}Co nuclei are produced in their ground state.

An example of the discrimination of two closely lying transitions, at 681 and 683 keV, is shown in fig. 11. The two transitions are not well resolved in the total $\beta\gamma$ coincidence spectrum (panel (a)), and they can be distinguished requiring higher-level coincidences, as shown in panels (b) and (c). The two transition arise from the decay of the ground state decay of ^{70}Co, and were located as the $7^- \rightarrow 5^-$ transition (681 keV) and as the $5^- \rightarrow 4^+$ transition (683 keV), as shown in the decay scheme in the middle of fig. 11.

The level schemes following the two decay paths, from the ground state and from the isomer, are shown in the right side of fig. 11. The two decays populate states of different spins, according to β-decay selection rules.

This experiment conveyed new experimental information, extending the known decay scheme up to $\sim$ 6.2 MeV, very close to the neutron separation energy $S_n = 7.3(1)$ MeV [67]. The proposed I_β, extracted for both decay paths, extracted in this

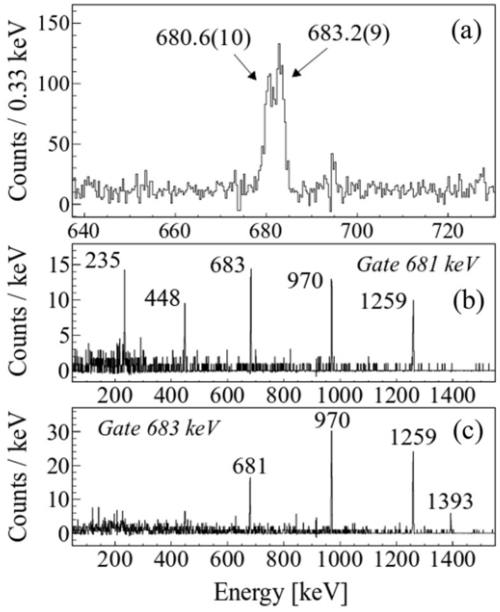

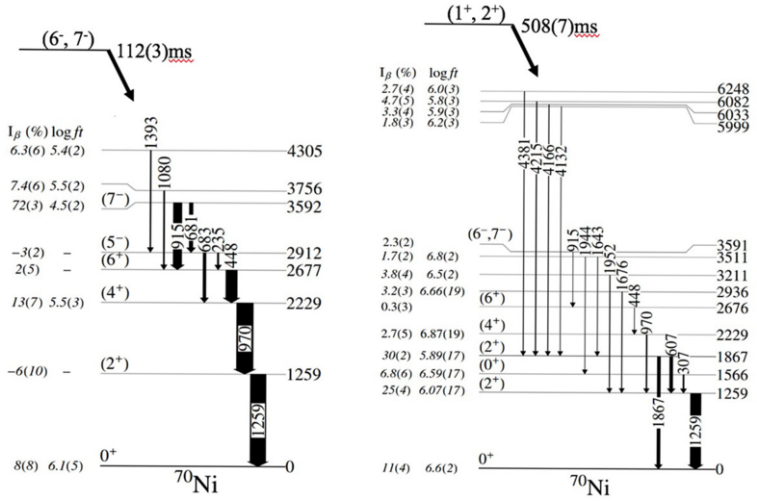

Fig. 11. – Panels (a-c): $\beta\gamma$ and $\beta\gamma\gamma$ coincidence spectra for the decay ^{70}Co $\rightarrow$ ^{70}Ni showing the presence of two closely lying transitions. The two transitions belong to different de-excitation schemes, one occurring from the $(6^-, 7^-)$ ground state and from the $(1^+, 2^+)$ β-decaying isomer. The detailed level schemes from these two decays are reported in the lower panels of the figure.

detailed study helped confirming the proposed J^π in the daughter nucleus, which can then be compared to state-of-the-art Shell Model calculations for a correct interpretation of their origin: they provide first evidence of strongly prolate-deformed shapes for the low-lying levels and the ground state of in ^{70}Co, which preferentially decays towards similarly

deformed structures in ^{70}Ni. This decay path can be clearly distinguished from the one passing through nearly spherical levels following the decay of the high-spin state of ^{70}Co

Additional details on the experiment and the experimental set-up can be found in refs. [18, 65].

A complementary approach to the study of the same decay is that employed in the second experiment. This TAS experiment has been performed at NSCL, employing the SuN (Summing NaI) detector to study the decay of the parent nucleus, populated by a fragmentation of a ^{86}Kr beam at 140 MeV/u on a ^{9}Be target. The TAS SuN is composed of eight optically isolated segments created in a single large NaI crystal. Details on this measurement can be found in ref. [66].

In order to extract the β-decay intensity one should compare different spectra: the event-by-event spectrum given by the sum of the energy collected in the segments (panel (a) of fig. 12), the spectrum coming from each single segment (panel (b)) and the segment multiplicity (panel (c)). Each of them conveys a different piece of information: the spectra extracted from each single segment is sensitive to the individual transitions in the de-excitation cascade, while the energy sum of all segments returns the initial excitation energy of the decay. The segment multiplicity can be unfolded to return the number of emitted γ rays in each event. A randomly correlated background has been subtracted to the spectra.

The peaks seen in the single-segment spectrum correspond to the strongest transitions at 449, 683, 970 and 1260 keV, which have been identified to follow the decay from the high-spin ground state of ^{70}Co (see fig. 11). The observation of these peaks rule out the possibility of seeing the decay coming from the isomeric state, which could, in principle, be populated in fragmentation reactions at this energy, as was observed in a previous experiment [68].

A prominent feature of the summed spectrum is that of showing a strong population of the level at 3592 keV, in accordance with the results from the high-resolution experiment, which extracted a $I_\beta = 72(3)\%$ for this state. This large fraction of feeding suggests an allowed GT transition of $\nu 0f_{5/2}$ into $\pi 0f_{7/2}$. Another interesting property of the summed spectrum is that of presenting sizeable γ-ray emission above the 7.3 MeV neutron separation energy (indicated by the arrow in the spectrum in panel (a)).

As explained in sect. **3**, the analysis of the TAS spectra is helped by the comparison with simulations accounting for the efficiency and response function of the array. The experimental level scheme, comprising the measured β feeding to the states, is also fed to the simulation. Since the level scheme is known only up to ~ 4 MeV, levels above this energy are artificially created by a statistical model code. The spreading of these levels reflects the energy resolution of the array.

The simulation populates spectra similar to the experimental ones, following randomly chosen de-excitation paths. Examples of such spectra are compared, via a χ^2 minimisation procedure, to the experimental data in fig. 12 (black dashed lines in panels (a), (b), (c) of fig. 12).

The experimental I_β decay intensity was used, via the evaluation of the $\log ft$, to extract the Gamow-Teller cumulative strength distribution, $B(GT)$, which is shown in

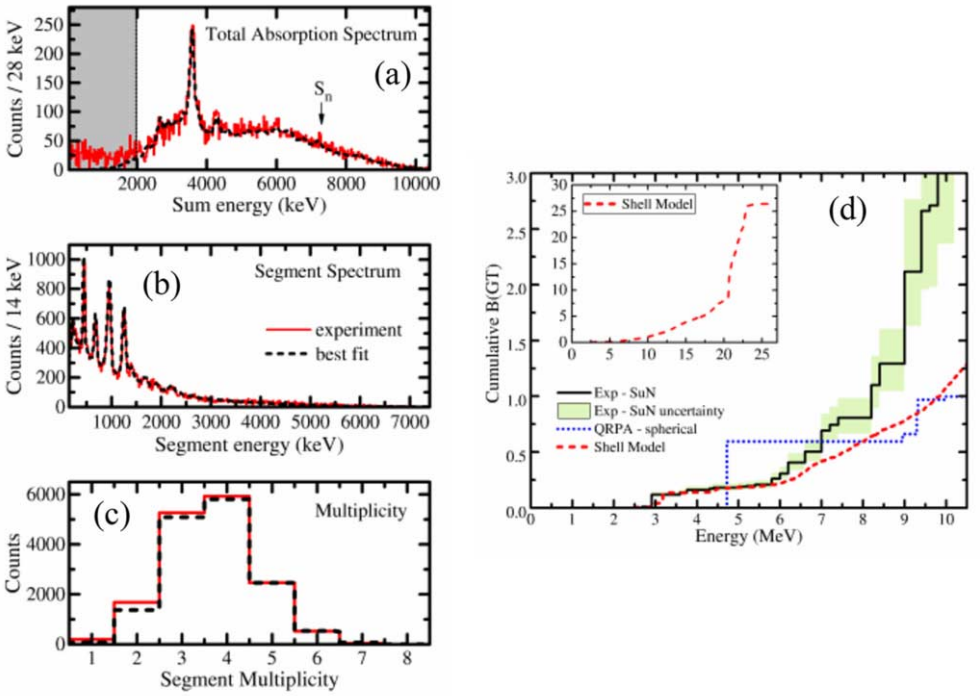

Fig. 12. – TAS spectra for the decay ^{70}Co $\rightarrow$ ^{70}Ni (solid red line) together with the best fit of the χ^2 minimization analysis procedure (dashed black line). Panel (a) shows the total TAS spectrum, sum of the single segments, panel (b) the segment spectrum and panel (c) the multiplicity. Panel (d) shows the cumulative β-decay intensity as function of excitation energy of the final states in ^{70}Ni. The solid black line and green-shaded area are the experimental results with uncertainties. A comparison with shell-model calculation is shown with the dashed red line, while the thick dotted blue line is a QRPA calculation under the assumption of spherical shape (Reprinted with permission from A. Spyrou *et al.*, *Phys. Rev. Lett.*, **117** (2016) 142701, © 2016 by the American Physical Society.)

panel (d) of fig. 12. The experimental results, shown with a continuous black line are compared to shell-model calculations (dashed line) and QRPA calculations (dotted line) in the folded-Yukawa QRPA model [43] under the assumption of spherical shape [69]. This assumption is corroborated by the analysis of high-resolution data, which is consistent with the quasi-spherical structure of the ground-state of ^{70}Co, which, in turns, feeds levels of similar deformation in the daughter nucleus ^{70}Ni.

Shell-model calculation are carried out in the $0f_{7/2}$, $0_{f5/2}$, $1p_{3/2}$, $1p_{1/2}$, $0g_{9/2}$, $0g_{7/2}$, $1p_{1/2}$, $0g_{9/2}$, $0g_{7/2}$ model space, where the GPFX1A Hamiltonian [70] was used for the $0f$-$1p$ part of the space, while the part of the Hamiltonian involving the $0g$ orbitals was obtained from the N^{3}LO interaction [71] renormalized using the V_{low-k} approach into six major oscillator shells and then renormalized up to second order perturbation theory into the model space [72].

The experimental distribution shows that a sizeable fraction of strength at high energy is not reproduced by the two models. The Gamow-Teller strength around 3 MeV is dominated by the $\nu 0f_{5/2} \rightarrow \pi 0f_{7/2}$ transition, while the gradual rise in strength above 5 MeV can be referred to $\nu 0p$ to $\pi 0p$, $\nu 0f_{5/2}$ to $\pi 0f_{7/2}$, $\nu g_{9/2}$ to $\pi 0g_{9/2}$ transitions.

The strength measured above 6 MeV can be related to the spreading width of the higher state coming from $2p$-$2h$ configurations. A contribution coming from first-forbidden transitions may also partly explain the missing strength.

The presence of a sizeable strength above the neutron separation energy has been observed in neutron-rich nuclei in several mass regions. One recent example is the measurement of an excess of strength in the decay of very exotic ^{83}Ga $\rightarrow$ ^{83}Ge.

In order to highlight this effect one can compare the $\beta\gamma$ coincidence spectra measured in a $LaBr_3$(Ce) scintillator detector for the two decays ^{80}Ga $\rightarrow$ ^{80}Ge and ^{83}Ga $\rightarrow$ ^{83}Ge. The first decay, ^{80}Ga $\rightarrow$ ^{80}Ge, has a $Q_\beta = 10.3$ MeV and a $S_n = 8.1$ MeV, while the second decay, involving a more exotic isotope, is characterised by a slightly larger decay window ($Q_\beta = 11.7$ MeV), and a sizeable neutron emission probability, between 56–87%, being the $S_n = 3.6$ MeV in this case.

Given the low-lying neutron separation energy, one would expect the γ-ray spectrum in coincidence with the decay of ^{83}Ge to reach slightly above 4 MeV. Surprisingly the spectrum extends to much higher energies, with no changes in slopes above the S_n. This is shown in panel (a) of fig. 13, where we can compare the spectra from the two decays.

This unexpected high-energy γ-ray emission can only be linked to fast, possibly collective, $E1$ transitions, which can compete with neutron emission from levels in this energy range. Other parity-changing electromagnetic transition, like $M2$ or $E3$, are suppressed by at least three orders of magnitude due to their higher multipolarity.

In order to understand the possible origin of this excess of strength the data are compared to fully microscopic QRPA calculations based on the Gogny D1M interaction. The calculated GT ($B(GT)$) and $E1$ spectra ($B(E1)$) are also presented in panel (b) of fig. 13 for the two nuclei under analysis. No quenching is included in the calculation of any of these strengths. In the case of ^{83}Ge both the $B(GT)$ and the $B(E1)$ show an accumulation of strength at 5–7 MeV and then again above 8 MeV, in good agreement with the experimental γ-ray spectrum. Typical timescales of 10^{-17} s can be attributed to the $E1$ decay, which can therefore compete with the neutron emission lifetimes of 10^{-16}–10^{-19} s, Consequently, microscopic calculations support the hypothesis that the states populated by the GT decay have strong $E1$ transitions to the low-lying and ground states in the daughter nuclei. A different behaviour is instead seen in the case of ^{80}Ge, for which a suppressed GT and $E1$ strength are expected in the region of interest, being shifted towards higher energies, in agreement with the measured spectrum.

In order to help describing the experimental spectra, fully microscopic Quasi particle Random Phase Approximation (QRPA) calculations with no free parameters, based on the effective nucleon-nucleon Gogny D1M interaction, were performed. The resulting spectra are shown in panel (b) of fig. 13. In the case of ^{83}Ge, the $B(GT)$ and $E1$ distributions show an accumulation of strength in the region between 5 and 7 MeV, and then again beyond 8 MeV, in good agreement with the measured spectrum in panel (a).

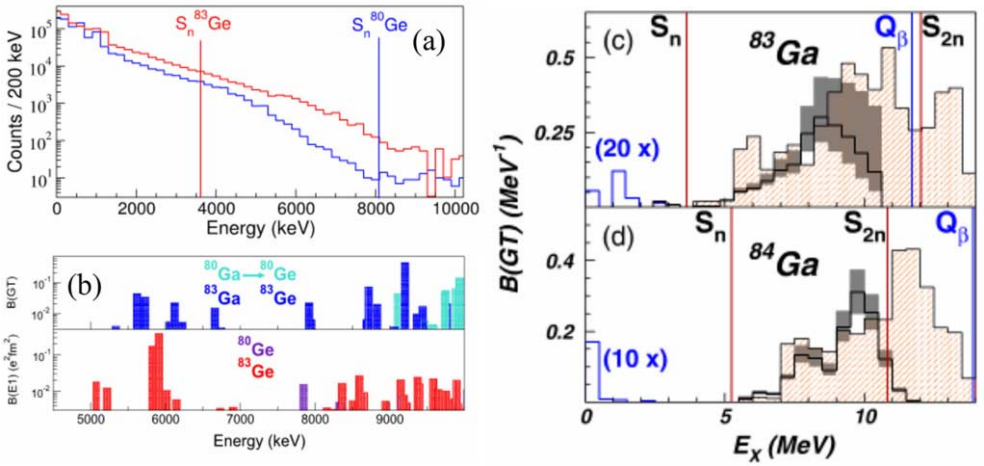

Fig. 13. – Panel (a): $\beta\gamma$ coincidence spectra for the decay of ^{80,83}Ga, blue and red line respectively. The vertical line shows the location of the neutron separation energies of the daughter nuclei ^{80,83}Ge. The two spectra are normalized to the same number of β-decay events. The corresponding GT β-decay $E1$ strength distributions calculated with a microscopic Gogny-QRPA model are reported in panel (b) for comparison. Panel (c) and (d) show the GTstrength distribution above the neutron separation energy in the decay of ^{83}Ga (c) and ^{84}Ga (d). The data are shown in a solid black line and the grey shaded parts of the histogram indicate the uncertainties of the strength distribution. The strength distributions extracted from $\beta\gamma$ spectroscopy are shown by blue lines, enhanced by factors of 20 and 10 for ^{83}Ga and ^{84}Ga. (Adapted from A. Gottardo *et al.*, *Phys. Lett. B*, **772** (2017) 359, under the CC BY license (`http://creativecommons.org/licenses/by/4.0/`). Funded by SCOAP^3, for DOI: `http://dx.doi.org/10.1016/j.physletb.2017.06.050`, and from M. Madurga *et al.*, *Phys. Rev. Lett.*, **117** (2016) 092502, under the terms of the *Creative Commons Attribution 3.0 License* for DOI: 10.1103/PhysRevLett.117.092502.)

This justifies the existence of a significant γ-decay branch from neutron-unbound states. In parallel the calculations do not show such β-delayed γ-ray strength in ^{80}Ge with respect to ^{83}Ge.

Further details on the experiment and analysis can be found in ref. [73].

An independent measurement of the same decay, $^{83\text{–}84}$Ga $\rightarrow$ $^{83\text{–}84}$Ge, has been reported by Madurga *et al.* in ref. [74]. In this paper the authors analyse the decays in terms of the competition between the β and βn channels. The Time-Of-Flight (TOF) neutron-detection array VANDLE was employed to study the decay above the neutron separation energy, extracting the $B(GT)$ distribution shown in the panels (c-d) of fig. 13. This distributions shows again an extra strength above 6–7 MeV, which indicates that the decay above the neutron separation energy is dominated by allowed Gamow-Teller transitions.

The large Q_β windows also allow for the study of low-lying components of giant resonances, the so-called *Pygmy* states. In several neutron-rich nuclei an additional

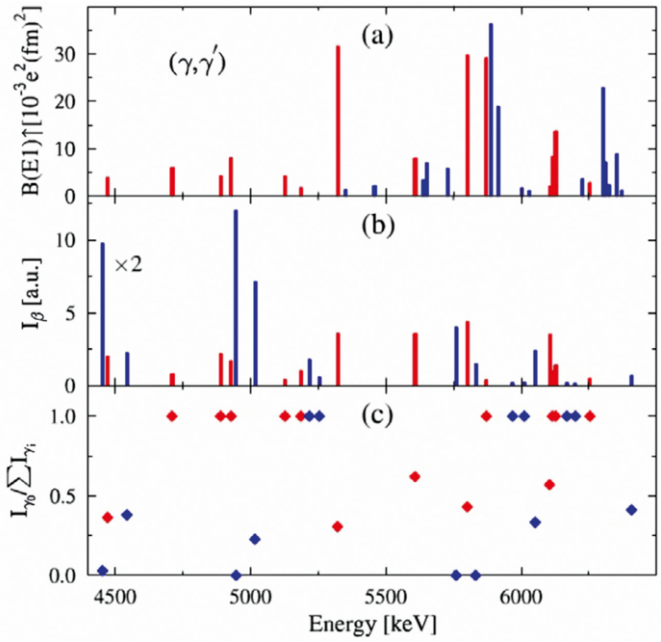

Fig. 14. – Candidates for 1^- levels in ^{136}Xe populated by (γ, γ') reactions (panel (a)) and by the decay $^{136}\mathrm{I} \rightarrow {}^{136}\mathrm{Xe}$ in panel (b). Levels represented by red bars are seen in both methods. Panel (c) shows the ground-state branching ratios extracted from β decay (Reprinted with permission from M. Scheck *et al.*, *Phys. Rev. Lett.*, **116** (2016) 132501, © 2016 by the American Physical Society.)

structure in the $E1$-strength distribution of atomic nuclei has been identified near the particle-separation thresholds. It appears as a resonance-like accumulation of 1 levels on top of the low-energy tail of the isovector giant dipole resonance (GDR) and is denoted as the pygmy dipole resonance (PDR) [75]. While the GDR exhausts 100% or even more of the $E1$ strength predicted by the Thomas-Reiche-Kuhn sum rule, the $E1$ strength of the PDR is typically of the order of a few percent or even less [76]. If the character of such states has not been well defined yet, it has a strong impact in neutron-capture rates in astrophysical calculations [77-79].

The possibility of populating these states following β decay of exotic nuclei, has been demonstrated by the work of Scheck and collaborators [80] studying the decay $^{136}\mathrm{I} \rightarrow {}^{136}\mathrm{Xe}$.

Figure 14 shows the comparison of states populated in a (γ, γ') experiment (panel (a)) compared to states populated in β decay (panel (b)). Red bars indicate levels populated in both reactions. Even if a considerable number of states is populated exclusively by one of the two mechanisms, this study shows a different experimental approach which can highlight the presence of the low-lying components of the resonances. This is particularly attractive being decay spectra comparably background free, and allowing to perform $\gamma\gamma$-coincidence studies.

The possibility to access a larger fraction of the GT strength has a large impact not only for basic research, but also for the evaluation of decay heat in nuclear power plants. In 2007 the Nuclear Energy Agency (NEA) of the Organisation for Economic Cooperation and Development provided an assessment in which it asked for a systematic revision of β-decay data regarding abundant fission products present in nuclear reactors, aiming at removing systematic errors and biases mainly related to the use of low-efficiency detectors [81].

Approximately 8% of the total energy generated in by fission arises from energy released by the decay of elements created during the process. Once the fission is ended, because of a reactor shutdown or because of discharge of the fuel, the radioactive decay is the source for the remaining heating. The decay heat varies as a function of time and the power function can be extracted by the available nuclear data:

$$f(t) = \sum_i (\overline{E}_{\beta,i} + \overline{E}_{\gamma,i} + \overline{E}_{\alpha,i})\lambda_i N_i(t), \tag{30}$$

being $\overline{E}_i$ is the mean decay energy of the i-th decay for the various components, α, β, γ. λ_i is the decay constant for the nuclide i and $N_i(t)$ is the number of nuclides i at time t.

A recent revision of the data available in literature showed a substantial discrepancy between measured and calculated fraction of the γ-decay heat, in particular for cooling times ranging between 300 and 3000 s. This lead to a compilation of a priority list of contributors whose properties are known with low accuracy.

If half-lives are usually known with high accuracy, the incorrect evaluation of the β feeding due to the Pandemonium effect, implying an under-estimation of the decay mean energy, is the main responsible for such discrepancy.

High-precision measurements with TAS techniques are being carried out [82] and will help gaining the requested accuracy in these calculations, which result in increased security and reduced cost when employing fission power plants.

The relative population of nuclear levels in decays of exotic fission fragments is determined by the competition between allowed Gamow-Teller (GT) and first forbidden (ff) transitions. This is due to the asymmetry of the neutron and proton Fermi energies and the large β energy window (over 10 MeV), particularly in heavy nuclei. As the decay window opens up for nuclei further away from stability, the fraction of the GT transition strength contained within the decay energy window dominates the decay probabilities. The ff decays, with small transition matrix elements, are nevertheless amplified by the phase space factor, due to large decay energy and compete with the GT decays [42, 58]. The resulting distribution of β intensity is complex, with low-energy, well-separated states populated by ff transitions and a high-level density of γ-ray emitting states near the neutron separation energy (S_n). One- and two-neutron emission from the states populated by GT transitions above the S_{1n} and S_{2n} adds to the complexity of decay paths.

Only a combination of detection techniques, including high-resolution γ-ray spectroscopy, neutron detection, and total absorption γ-ray studies can yield a true picture of the beta decay of neutron-rich nuclei and illuminate the underlying nuclear struc-

ture. The importance of decay studies of fission fragments goes well beyond nuclear structure and is critical to the understanding of the astrophysical r-process and its scenarios [44]. The decay properties of reactor-produced fission fragments are relevant for the understanding of the nuclear fuel cycle, in particular for safety issues related to nuclear power [81].

6. – Conclusions and outlook

The properties of exotic systems are of fundamental importance when describing the formation of the elements in the universe through stellar nucleosynthesis processes. Radioactive decay of the unstable nuclei conveys inputs, such as decay rates and decay branching ratios, instrumental for a detailed description of the properties of the nuclear interaction with unbalanced number of protons and neutrons.

The study of exotic nuclei has a great impact on defining the evolution of nuclear structure properties away from the valley of stability and in assessing the robustness of theoretical models describing the nuclear medium.

The large Q_β window, characteristic of the decay of n-rich species, allows access to a large fraction of the decay strength function, with increasing interplay between GT and ff decay modes.

After a quick reminder of the basic properties of β-decay, key features of neutron-rich system have been presented, together with a description of the most common techniques to study β-decays in exotic systems, have been addressed in these proceedings. The impact of the measurement of β-decay rates and branching in nuclear models for stellar nucleosynthesis and on the study of nuclear structure has been also highlighted through examples of state-of-the-art experiments.

The current experimental program, carried out worldwide, will be greatly pushed forward by the advent of second-generation radioactive beam facilities, such as SPIRAL2, SPES, HIE-ISOLDE, FAIR, FRIB, which will extend further out the reach of exotic species. The use of new beam purification methods, such as MR-TOF or Penning traps, in addition to high-resolution spectrometers, is also instrumental in increasing the precision of these studies.

REFERENCES

[1] Raabe R., *Eur. Phys. J. Plus*, **131** (2016) 362.
[2] Bateman H., *Proc. Cambridge Philos. Soc.*, **IS** (1910) 423.
[3] Zhang X. *et al.*, *J. Phys. G*, **34** (2007) 2611.
[4] Cattadori C. M. *et al.*, *Nucl. Phys. A*, **748** (2005) 333.
[5] Lawson B. D., in *Proceedings of the International Conference on Nuclear Structure and Spectroscopy*, edited by Blok H. P. and Dieperink A. E. L., Vol. **2** (Scholar's Press, Amsterdam) 1974, p. 464.
[6] Datar V. M., *Phys. Rev. C*, **22** (1980) 1787.
[7] Nuclear Wallet Cards and Evaluated Nuclear Structure Data File (ENSDF), available from `http://www.nndc.bnl.gov`.

[8] HINKE C. B. *et al.*, *Nature*, **486** (2012) 341.
[9] FIRESTONE J. R. B. *et al.* (Editors), *Table of Isotopes*, 8th edition (Wiley-VCH) 1999, available from `http://ie.lbl.gov/toi.html`.
[10] GIAZ A. *et al.*, *EPL*, **110** (2015) 42002.
[11] TOWNER I. S. and HARDY J. C., *Rep. Prog. Phys.*, **73** (2010) 04630.
[12] FUJITA Y. *et al.*, *Progr. Part. Nucl. Phys.*, **66** (2011) 549.
[13] RUBIO B. and GELLETLY W., *Beta Decay of Exotic Nuclei*, edited by AL-KHALILI J. and ROECKL E. in *The Euroschool Lectures on Physics with Exotic Beams*, Vol. **III**, *Lect. Notes Phys.*, Vol. **764** (Springer, Berlin, Heidelberg) 2009.
[14] `http://ipnwww.in2p3.fr/Installation-ALTO,5?lang=fr`.
[15] GERMOGLI G., Master Thesis, Università degli Studi di Padova (I) (2012).
[16] `https://ribf.riken.jp/EURICA/`.
[17] SÖDERSTRÖM P. A. *et al.*, *Nucl. Instrum. Methods B*, **317** (2013) 649.
[18] BENZONI G. *et al.*, *Phys. Lett. B*, **751** (2015) 107.
[19] `http://isolde.web.cern.ch/experiments/isolde-decay-station-ids`.
[20] `https://www.physics.uoguelph.ca/Nucweb/griffin.html`.
[21] `http://www.cenbg.in2p3.fr/desir/`.
[22] `https://web.infn.it/spes/`.
[23] `https://web-docs.gsi.de/~wolle/EB_at_GSI/RISING/rising.htm`; `https://fair-center.eu/public/experiment-program/nustar-physics/despechispec.html`.
[24] `http://www.nscl.msu.edu/users/equipment.html#bcs`.
[25] HARDY J. C. *et al.*, *Phys. Lett. B*, **71** (1977) 307.
[26] RUBIO B. *et al.*, *J. Phys. G, Nucl. Part. Phys.*, **31** (2005) S1477.
[27] SIMON A., QUINN S. and SPYROU A. *et al.*, *Nucl. Instrum. Methods Phys. Res. A*, **703** (2013) 16.
[28] KARNY M. and RYKACZEWSKI K. P. *et al.*, *Nucl. Instrum. Methods A*, **836** (2016) 83; RASCO B. C. *et al.*, *Instrum. Methods A*, **788** (2015) 137; RASCO B. C. *et al.*, *JPS Conf. Proc.*, **6** (2015) 030018.
[29] RUBIO B. *et al.*, *J. Phys. G: Nucl. Part. Phys.*, **31** (2005) S1477.
[30] BURBIDGE E. M. *et al.*, *Rev. Mod. Phys.*, **29** (1957) 547.
[31] MATHEWS G. J. and WARD R. A., *Rep. Prog. Phys.*, **48** (1985) 1371.
[32] GORIELY S., *Astron. Astrophys.*, **342** (1999) 881.
[33] SHIBAGAKI S. *et al.*, *Astroph. J.*, **816** (2016) 79.
[34] ABBOTT B. P.*et al.*, *Phys. Rev. Lett.*, **119** (2017) 161101.
[35] FATTOYEV F. J., PIEKAREWICZ J. and HOROWITZ C. J., *Phys. Rev. Lett.*, **120** (2018) 172702.
[36] DROUT M. R. *et al.*, *Science*, **358** (2017) 1570.
[37] CLIFFORD F. and TAYLER R., *Mem. R. Astron. Soc.*, **69** (1965) 2.
[38] TAKAHASHI K. and YAMADA M., *Progr. Theor. Phys.*, **41** (1969) 1470; KOYAMA S., TAKAHASHI K. and YAMADA M., *Progr. Theor. Phys.*, **44** (1970) 663; TAKAHASHI K., *Progr. Theor. Phys.*, **45** (1971) 1466.
[39] KOURA H. *et al.*, *Prog. Theor. Phys.*, **113** (2005) 305.
[40] TACHIBANA T. *et al.*, *Prog. Theor. Phys.*, **84** (1990) 641.
[41] ZHI Q., CAURIER E., CUENCA-GARCA J. J., LANGANKE K. H., MARTNEZ-PINEDO G. and SIEJA K., *Phys. Rev. C*, **87** (2013) 025803.
[42] MÖLLER P., PFEIFFER B. and KRATZ K.-L., *Phys. Rev. C*, **67** (2003) 055802.
[43] MÖLLER P., NIX J. R. and KRATZ K.-L., *At. Data Nucl. Data Tables*, **66** (1997) 131.
[44] MUMPOWER M. R. *et al.*, *Progr. Part. Nucl. Phys.*, **86** (2016) 86.
[45] ARNOULD M., GORIELY S. and TAKAHASHI K., *Phys. Rep.*, **450** (2007) 97.
[46] LORUSSO G. *et al.*, *Phys. Rev. Lett.*, **114** (2015) 192501.

[47] Wu J. *et al.*, *Phys. Rev. Lett.*, **118** (2017) 072701.
[48] Kurtukian-Nieto T. *et al.*, *Phys. Rev. C*, **89** (2014) 024616.
[49] Dasso C. H., Pollarolo G. and Winther A., *Phys. Rev. Lett.*, **73** (1994) 1907.
[50] Watanabe Y. X. *et al.*, *Phys. Rev. Lett.*, **115** (2015) 172503.
[51] Hirayama Y. *et al.*, *Nucl. Instrum. Methods B*, **353** (2015) 4.
[52] Cyburt R. H. *et al.*, *Astrophys. J. Suppl. Ser.*, **189** (2010) 240.
[53] Morales A. I. *et al.*, *Phys. Rev. Lett.*, **113** (2014) 022702.
[54] Morales A. I. *et al.*, *Phys. Rev. C*, **89** (2014) 014324.
[55] Morales A. I. *et al.*, *EPL*, **111** (2015) 52001.
[56] Li Z. *et al.*, *Phys. Rev. C*, **58** (1998) 156.
[57] Benzoni G. *et al.*, *Phys. Lett. B*, **715** (2012) 293.
[58] Borzov I. N., *Phys. Rev. C*, **67** (2003) 025802.
[59] Caballero-Folch R. *et al.*, *Phys. Rev. Lett.*, **117** (2016) 012501.
[60] Caballero-Folch R., Phd Thesis, Universitat Politècnica de Catalunya, Barcelona (E) (2015); Torner A. *et al.*, Technical Design Report of the Beta-Delayed Neutron Detector (BELEN) for NUSTAR (DESPEC), Universitat Politécnica de Catalunya, Barcelona (E), (2014); Gómez-Hornillos M. B. *et al.*, *J. Phys.: Conf. Ser.*, **312** (2011) 052008.
[61] `http://ipnwww.in2p3.fr/TETRA?lang=en`; Testov D. *et al.*, *JINST*, **10** (2015) P09011.
[62] Grzywacz R. and Rykaczewski K. P. *et al.*, *Acta Phys. Pol. B*, **45** (2014) 217.
[63] Tarifeño-Saldivia A. *et al.*, *JINST*, **12** (2017) P04006.
[64] Peters W. A. *et al.*, *Nucl. Instrum. Methods A*, **836** (2016) 122.
[65] Morales A. I. *et al.*, *Phys. Lett. B*, **765** (2017) 328.
[66] Spyrou A. *et al.*, *Phys. Rev. Lett.*, **117** (2016) 142701.
[67] Wang M. *et al.*, *Chin. Phys. C*, **36** (2012) 1603.
[68] Prokop C. *et al.*, *Phys. Rev. C*, **92** (2015) 061302(R).
[69] Möller P., Sierk A., Ichikawa T. and Sagawa H., *At. Data Nucl. Data Tables*, **109-110** (2016) 1.
[70] Honma M., Otsuka T., Brown B. A. and Mizusaki T., *Phys. Rev. C*, **69** (2004) 034335.
[71] Entem D. R. and Machleidt R., *Phys. Rev. C*, **68** (2003) 041001(R).
[72] `https://github.com/ManyBodyPhysics/CENS`.
[73] Gottardo A. *et al.*, *Phys. Lett. B*, **772** (2017) 359.
[74] Madurga M. *et al.*, *Phys. Rev. Lett.*, **117** (2016) 092502.
[75] Savran D., Aumann T. and Zilges A., *Prog. Part. Nucl. Phys.*, **70** (2013) 210.
[76] Bracco A., Crespi F. C. L. and Lanza E. G., *Eur. Phys. J. A*, **51** (2015) 99.
[77] Goriely S., *Phys. Lett. B*, **436** (1998) 10.
[78] Goriely S., Khan E. and Samyn M., *Nucl. Phys. A*, **739** (2004) 331.
[79] Tsoneva N., Goriely S., Lenske H. and Schwengner R., *Phys. Rev. C*, **91** (2015) 044318.
[80] Scheck M. *et al.*, *Phys. Rev. Lett.*, **116** (2016) 132501.
[81] Yoshida T. and Nichols A. L., *Assessment of Fission Product Decay Data for Decay Heat Calculations: A Report by the Working Party on International Evaluation Co-operation of the Nuclear Energy Agency Nuclear Science Committee* (Nuclear Energy Agency, Organization for Economic Cooperation and Development, Paris, France) 2007.
[82] Algora A. *et al.*, *Phys. Rev. Lett.*, **105** (2010) 202501.

This page intentionally left blank

Proceedings of the International School of Physics "Enrico Fermi"
Course 201 "Nuclear Physics with Stable and Radioactive Ion Beams", edited by F. Gramegna,
P. Van Duppen, A. Vitturi and S. Pirrone
(IOS, Amsterdam; SIF, Bologna) 2019
DOI 10.3254/978-1-61499-957-7-293

New developments in laser spectroscopy for RIBs

W. Nörtershäuser

Institut für Kernphysik, Technische Universität Darmstadt
Schlossgartenstr. 9, 64289 Darmstadt, Germany

Summary. — The optical spectrum of ions and atoms exhibits a nuclear fingerprint. With sufficient resolution and the choice of appropriate atomic transitions, nuclear properties like the spin, nuclear magnetic dipole moments, electric quadrupole moments and the change in the mean-square charge radius can be determined. During the last decade, progress in this field towards higher sensitivity and accuracy has allowed to study new regions of the nuclear chart.

1. – Introduction

Precision spectroscopy of ions and atoms is an important source of information about the microscopic world. The spectrum of hydrogen has been a cornerstone for the development of quantum theory, the fine structure has provided evidence for the existence of the electron spin and its magnetic moment and the hyperfine structure is due to the finite size and electromagnetic properties of the nucleus. The existence of the Lamb shift gave rise to the development of quantum electrodynamics and even the weak interaction leaves traces in the atomic spectrum that can be observed by studying parity-forbidden transitions. Soon after its invention, the laser was applied for spectroscopy and has been an invaluable tool ever since. Starting in the late seventies of the last century, lasers were applied for the investigation of short-lived isotopes. Charge radii and nuclear moments

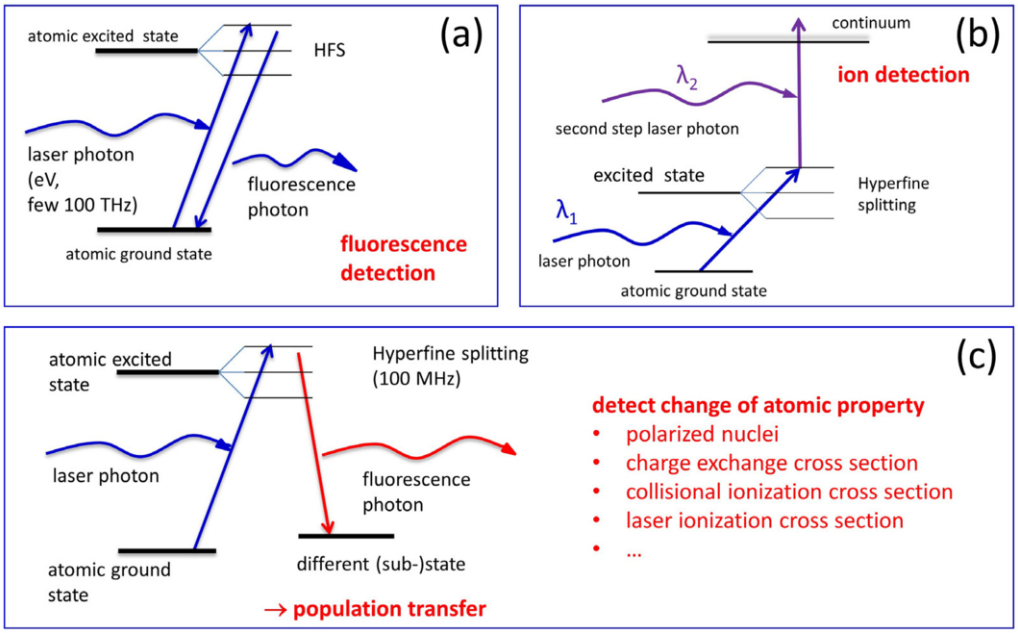

Fig. 1. – Detection principles for on-line laser spectroscopy: (a) Classical fluorescence spectroscopy. Photons that are resonantly scattered are detected (perpendicularly to the laser direction). (b) Resonance ionization: Atoms are excited in a resonant transition and subsequently ionized by the absorption of one or more additional photons. (c) Decay after resonant excitation can populate other states or substates (*e.g.* m-levels) that are not (or weaker) populated without resonant excitation. If these states have properties different from the original starting level, this can be used for detection. Examples are listed to the right.

are obtained from high-resolution measurements of atomic spectral lines which exhibit hyperfine structure and isotope shift caused by the interaction of the shell electrons with the nucleus [1]. It was particularly the technique of collinear laser spectroscopy [2], developed for the purpose of on-line investigations, that has delivered a large amount of nuclear data of isotopes far from the valley of β-stability. Standard collinear spectroscopy is based on resonant excitation and detection of the fluorescence decay from the excited level as it is shown in fig. 1(a). However, optical fluorescence detection is rather inefficient and suffers from background photons due to the scattered laser light. The signal-to-noise ratio limits such experiments to isotopes produced at rates of typically more than 10^6 ions/s. This has been improved in recent times by accumulation and bunching of ion beams [3]. In a few very favourable cases this now allows studies of isotopes that are produced with rates of about 100 ions/s.

The excited state of the atom can usually also decay to a different state than the one from which excitation occurred as is depicted in fig. 1(c). While this limits in many cases the efficiency of fluorescence detection because excitation and spontaneous emission

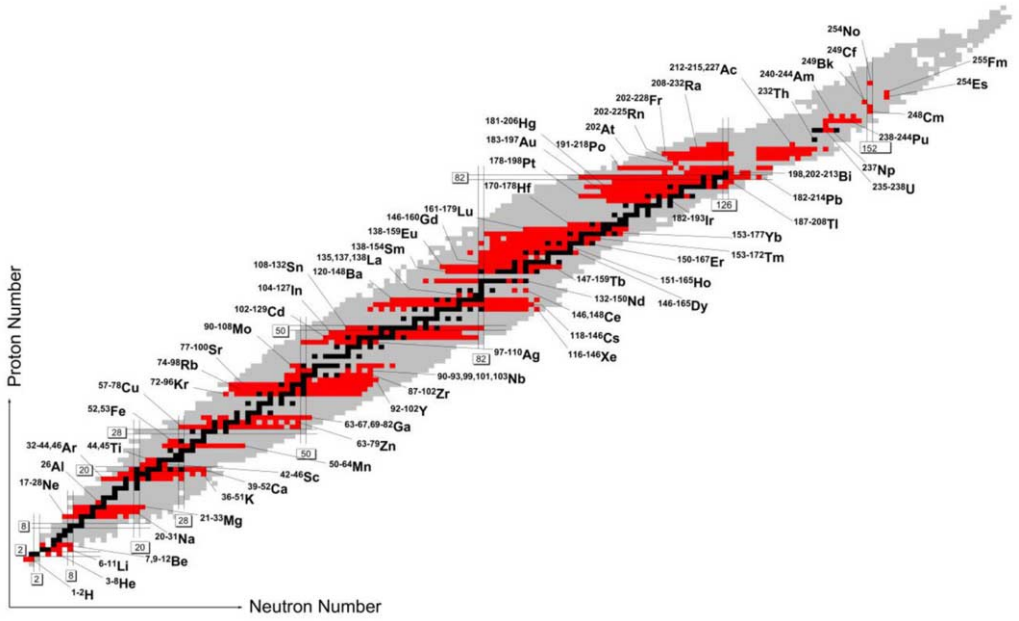

Fig. 2. – Regions of the nuclear chart in which on-line laser spectroscopy of short-lived isotopes was performed so far. All isotopes that have been addressed are marked in red. Black are the stable isotopes and depicted in grey are those isotopes that are known to exist. An up-to-date version of this chart, links to all references and a table with the applied techniques and extracted nuclear observables is available on-line [5].

cannot be repeated arbitrarily often, it can be used to provide more efficient detection techniques to study even more exotic isotopes that are produced at lower rates. A variety of particle- or radiation-detection techniques based on this laser optical pumping have been applied. These schemes provide higher efficiency and less background, which considerably enhances the sensitivity. Beams with rates down to 10^3 ions/s, in favourable cases even somewhat below 100 ions/s [4], are usually sufficient for an experiment.

A second technique that became very popular for on-line studies is resonance ionization spectroscopy (RIS). In this case, resonance excitation is followed by absorption of another photon that removes the electron from the excited atoms, leaving a singly charge ion behind as shown in 1(b). This ion can then be detected very efficiently since charged particles can be collected by the use of electric and magnetic fields and guided towards sensitive detectors. Sometimes two or even three resonant steps are used before ionization is performed. When pulsed lasers are used, high excitation and ionization efficiency is reached at the cost of resolution. However, especially in the high-Z region, hyperfine splittings and isotopes shifts are huge and the resolution offered by pulsed RIS is sufficient to obtain accurate nuclear information. Resolution can be increased by applying continuous-wave (cw) lasers or cw-seeded pulsed lasers.

These techniques provided a wealth of nuclear structure information as indicated in the nuclear chart shown in fig. 2. Isotopes indicated in red have been investigated by on-line laser spectroscopy (in a very few cases experiments were performed off-line after on-line production). In this contribution recent progress in laser spectroscopy of radioactive isotopes is discussed. In specific examples, the way of extracting nuclear information from the optical spectrum is presented as well as the conclusions about the nuclear structure that can be drawn from the observables. The field of laser spectroscopy on beams of radioactive isotopes has been treated more generally in several recent review articles [6-8].

2. – Nuclear signatures in the optical spectrum

All contributions to the energy levels of an atom beyond the description of the solutions of the relativistic Dirac equation assuming a structureless point-like infinitely heavy source of charge in the atom's center are summarized under the term "Hyperfine Structure". These include the contribution of the nuclear recoil, the finite nuclear size and the intrinsic charge distribution, effects of the magnetic field of a nucleus possessing a nuclear spin, nuclear deformations and last but not least corrections by quantum electrodynamics (Lamb shift). In the following, we will shortly summarize the effect of these terms.

2˙1. *Finite nuclear size and the isotope shift.* – The finite mass and size of the atomic nucleus has a small but distinct influence on the optical spectrum of an isotope. Comparing the transition frequencies ν^A of a specific electronic transition for different isotopes with mass numbers A and A', a small difference

$$\delta\nu^{AA'} = \nu^{A'} - \nu^{A} \tag{1}$$

is observed and called the isotope shift. An example is shown in fig. 3(a). According to its twofold origin, it is divided into the finite nuclear-mass shift (MS) and the nuclear volume or field shift (FS)

$$\delta\nu_{\mathrm{IS}}^{AA'} = \delta\nu_{\mathrm{MS}}^{AA'} + \delta\nu_{\mathrm{FS}}^{AA'}. \tag{2}$$

The mass shift is related to the fact that the center-of-mass (cm) of the atom does not coincide with the center-of-mass of the nucleus and therefore there is a center-of-mass motion of the present nucleus that also contributes to the internal energy of the atom. The size of this effect changes from isotope to isotope since they differ in nuclear mass. In a nonrelativistic approach, this can be taken into account writing

$$\delta\nu_{\mathrm{MS}}^{AA'} = \frac{M_{A'} - M_A}{M_A\, M_{A'}} \left(K_{\mathrm{NMS}} + K_{\mathrm{SMS}}\right). \tag{3}$$

The so-called "normal mass shift" (NMS) is the part of the shift that is expected for a one-electron system, whereas the "specific mass shift" (SMS) arises from the correlation

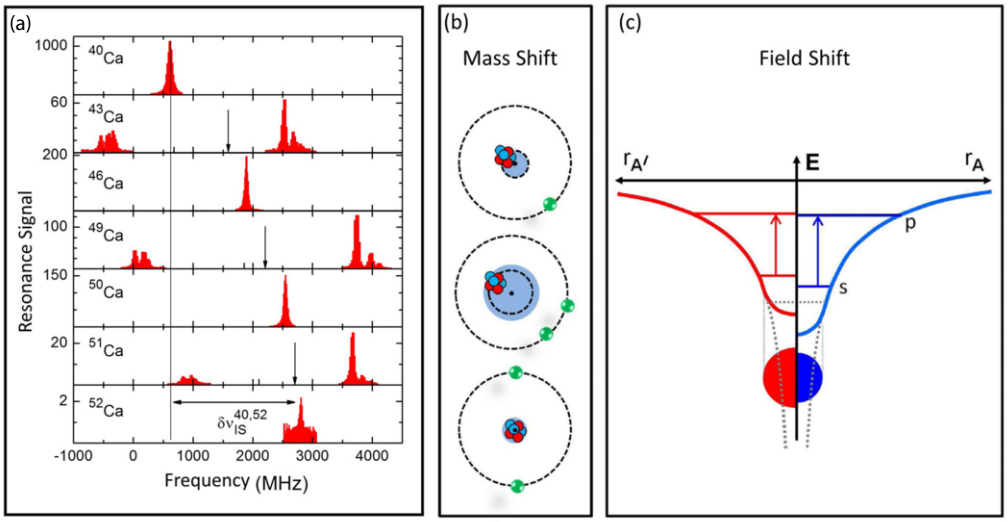

$$\delta\nu_{\mathrm{IS}}^{AA'} = K_{\mathrm{MS}} \cdot \frac{M_{A'} - M_A}{M_A M_{A'}} + F\,\delta\left\langle r_c^2 \right\rangle^{AA'}.$$

Fig. 3. – (a) Optical resonance signals along the chain of calcium isotopes. The isotope shift is clearly visible by the shift of the resonances of the even isotopes. For the odd isotopes, the centre-of-gravity of the hyperfine structure has to be taken, which is indicated by the arrow in the respective spectrum. (b) Representation of the normal mass shift (NMS, top) in a one-electron system and the specific mass shift (SMS) in a two-electron system. If the correlation of the electrons is such that they are preferably close in space, the nuclear center-of-mass motion is large, whereas it is much smaller if the electrons prefer to be far apart and on opposite sides of the nucleus as shown on the bottom. (c) Origin of the field shift. With increasing size of the nucleus, the electrostatic potential deviates already at larger r from the Coulomb potential of a point-like charge (dotted line). Thus, the level energies of the bound electrons change and this change is particularly large for s-electrons having a finite probability for being inside the nucleus. The dotted horizontal line represents the level energy of the s-electron for a point-like nucleus, which is lifted in the two isotopes with mass numbers A (right) and A' (left). The field shift is represented by the different length of the blue and the red arrow.

of electron momenta as indicated in fig. 3(b). The NMS can be easily calculated by replacing the electron mass m_{e} with the reduced mass of the system. This leads to

$$K_{\mathrm{NMS}} = m_{\mathrm{e}}\nu. \tag{4}$$

The specific mass shift constant K_{SMS} can only be approximated numerically by solving electron-correlation integrals that are extremely difficult to evaluate. This is already a challenge in a two-electron system and has so far been solved accurately and in full detail only for up to five electrons.

The second part of the isotope shift is much more interesting from nuclear-physics point of view: it is related to the finite nuclear size. For a point-like nucleus, the electrons

experience a $1/r$ Coulomb potential which has a negative pole at the nuclear site. However, for an extended nucleus, the potential deviates from the $1/r$-law within the nuclear volume and acquires a finite value at the nuclear center. This is visualized in fig. 3(c). Electrons with a finite probability density $|\Psi(0)|^2 \neq 0$ inside the nuclear volume, *i.e.*, especially s electrons, will experience this reduced potential. The contribution of the FNS effect to the transition frequency arises from the difference of the electron density at the nucleus $|\Psi(0)|^2$ between the initial (i) and the final (f) state of the transition

$$\delta\nu_{\mathrm{FNS,i\to f}} = \frac{Ze^2}{6h\varepsilon_0} \left\langle r_{\mathrm{c}}^2 \right\rangle \left(\Delta|\Psi(0)|^2\right)_{\mathrm{i\to f}} \tag{5}$$

with

$$\left(\Delta|\Psi(0)|^2\right)_{\mathrm{i\to f}} = |\Psi_{\mathrm{f}}(0)|^2 - |\Psi_{\mathrm{i}}(0)|^2 \,. \tag{6}$$

The nuclear mean-square charge radius $\langle r_{\mathrm{c}}^2 \rangle$ is defined as

$$\left\langle r_{\mathrm{c}}^2 \right\rangle = \frac{1}{Ze} \int \rho_{\mathrm{c}}(r)\, r^2 \,\mathrm{d}V \tag{7}$$

with the nuclear charge density $\rho_{\mathrm{c}}(r)$. This effect contributes to the isotope shift if the two isotopes A and A' have different charge radii

$$\delta\nu_{\mathrm{FS}}^{AA'} = \frac{Ze^2}{6h\varepsilon_0} \Delta|\Psi(0)|^2 \left(\left\langle r_{\mathrm{c}}^2 \right\rangle^{A'} - \left\langle r_{\mathrm{c}}^2 \right\rangle^{A} \right) \tag{8}$$

$$= \frac{Ze^2}{6h\varepsilon_0} \Delta|\Psi(0)|^2\, \delta \left\langle r^2 \right\rangle^{AA'} = F\, \delta \left\langle r_{\mathrm{c}}^2 \right\rangle^{AA'} , \tag{9}$$

where the index of the corresponding atomic transition i $\to$ f is dropped and the field shift constant F is introduced.

While the mass shift is roughly proportional to $1/M^2$, the field shift increases approximately by $Z^2/\sqrt[3]{A}$. The dependency is represented in fig. 4(c): The mass shift by far dominates the field shift for light elements. Figure 4(a) shows a spectrum of the stable lithium isotopes ^{6,7}Li in the $2s \to 3s$ two-photon transition [9]. The huge isotope shift of about 12 GHz is almost exclusively caused by the mass shift. Figure 4(b) shows the resonance transition in strontium isotopes without mass separation and for ^{84}Sr and ^{87}Sr with mass separation [10]. Here the isotope shift is very small, only a few 10 MHz for neighboring isotopes. Even techniques with high resolution cannot easily resolve the isotopes. The odd isotope ^{87}Sr is covered by the wings of the resonance line of ^{88}Sr but can be isolated using mass separation. The small isotope shifts are caused by the opposite trends of the two contributions: The (normal) mass shift leads to an increase of binding energy for the heavier nucleus while the increasing size weakens the binding. This leads to a vanishing isotope shift around the crossing point in fig. 4(d). For heavier nuclei the field shift supersedes the mass shift and the isotope shift shown for polonium isotopes [11]

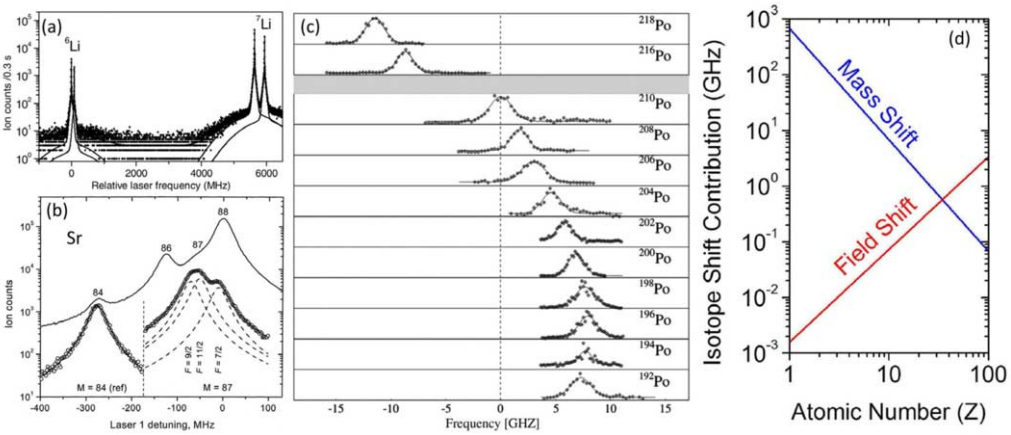

Fig. 4. – Isotope shift examples from three mass regions: (a) Lithium ^{6,7}Li ($Z = 3$) in the $2s \rightarrow 3s$ two-photon transition. Please note the logarithmic scale and that the isotope shift is twice as large as indicated by the frequency axis since two photons are absorbed simultaneously in this transition. Figure reprinted with permission from Bushaw B.A. *et al.*, Phys. Rev. Lett. **91**, 043004. © 2003 by the American Physical Society [9]. (b) Strontium $^{84,86-88}$Sr ($Z = 38$) in the $5s^2\,{}^1S_0 \rightarrow 5s5p\,{}^1P_1$ transition [10], please note the logarithmic scale on the y-axis. Figure reprinted with permission from Bushaw B.A. and Nörtershäuser W. from Spectrochimica Acta Part B **55**, 1679. © 2000, by Elsevier. (c) Even isotopes of polonium $^{192-218}$Po ($Z = 84$) in the $6p^37s\,{}^5S_2 \rightarrow 6p^37p\,{}^5P_2$ transition (here linear scale). Reprinted with permission from T.E. Cocolios *et al.*, Phys. Rev. Lett. **106** 052503. © 2011 by American Physical Society [11]. (d) Schematic of the contribution of field shift and mass shift in GHz (logarithmic scale) to the overall isotopic shift, drawn as a function of the atomic number. For details see text.

shown in fig. 4(c) can be determined even with moderate resolution caused by a linewidth of 2–3 GHz originating from the Doppler broadening in a hot atomic ensemble.

Finally it should be noted that the electron density cannot be assumed to be constant across the whole nucleus for heavy elements. Therefore higher radial moments and relativistic contributions to the wave function of the electron have to be considered (see for example [12]).

2˙2. *Nuclear moments and the hyperfine splitting.* – The hyperfine structure is usually dominated by the magnetic interaction between the nucleus and the shell electrons, which gives access to the magnetic moments of nuclei. Nuclear spins can often be directly obtained from the hyperfine structure pattern, *i.e.* the number of components, their splittings and their intensity ratio. The interaction of the nuclear quadrupole moment with the electric field gradient produced by the electrons is in most cases smaller. With the small quadrupole moments of light nuclei it tends to fall below the natural linewidth limit which is of the order of 10 MHz for sufficiently strong optical transitions. However, in heavy and strongly deformed nuclei it can have considerable influence on the spectra.

2˙2.1. Magnetic hyperfine structure. The magnetic interaction of an atomic nucleus with spin $\mathbf{I} \neq 0$ and the electron shell can be approximated in first order as that of a point magnetic dipole interacting with the magnetic field that is produced by the electrons at the center of the nucleus $\mathbf{B}_e(0)$. It leads to a coupling of the total angular momentum $\mathbf{J}$ of the electron shell and the nuclear spin $\mathbf{I}$ to the atomic total angular momentum $\mathbf{F} = \mathbf{J} + \mathbf{I}$. According to the angular momentum coupling rules, the quantum number F can take any value between $I + J$ and $|I - J|$ and the energy of the corresponding level is proportional to the scalar product $\mathbf{I} \cdot \mathbf{J}$, which can be written

$$\Delta E = a\,\mathbf{I} \cdot \mathbf{J} = a\frac{1}{2}\left(F^2 - I^2 - J^2\right) \tag{10}$$

and leads to a hyperfine splitting energy

$$\Delta\nu_{\mathrm{mag}} = \frac{A}{2}C = \frac{A}{2}\left[F(F+1) - J(J+1) - I(I+1)\right] \tag{11}$$

with

$$A = \frac{\mu_I B_e(0)}{hIJ}\,. \tag{12}$$

The magnetic interaction is dominated by the contact term, *i.e.*, the interaction of the electron's intrinsic magnetic moment with the magnetic moment of the nucleus. Since this term contributes only if there is a non-vanishing electron-spin density inside the nucleus, it is largest for s-electrons.

The ratio of the A factors of different levels is — besides the "trivial" dependence on the quantum numbers I and J — governed by the ratio of the magnetic field at the nucleus. If we look at the A factors of different isotopes along a chain, it is obvious that — at first order — the ratios should be determined by the ratios of the magnetic moments. We obtain for the ratio of the magnetic dipole hyperfine structure constant in two electronic levels i and f for two isotopes 1 and 2 the relation

$$\frac{A_1^f}{A_1^i} = \frac{A_2^f}{A_2^j}\,, \tag{13}$$

which is often used as a constraint in fitting spectra with low statistics. Similarly, the unknown nuclear moment of one isotope can be connected to the known moment of a reference isotope via

$$\mu = \frac{A}{A_{\mathrm{Ref}}}\frac{I}{I_{\mathrm{Ref}}}\mu_{\mathrm{Ref}}. \tag{14}$$

These relations neglect finite-size contributions of the nucleus, which arise from the change of the electron wave function due to the spatial extension, the distribution of

the nuclear charge (Breit-Rosenthal effect, BR) and the distribution of the nuclear magnetic moment inside the nucleus (Bohr-Weisskopf effect, BW). Such modifications from the point-like nucleus give rise to the so-called hyperfine structure anomaly in the ratio of the A factors between two isotopes

$$\frac{A_1}{A_2} \approx \frac{g_I(1)}{g_I(2)} \left(1 + {}^1\Delta^2\right), \tag{15}$$

where g_I is the nuclear gyromagnetic ratio $\mu_I = g_I \mu_N I$ and ${}^1\Delta^2$ the differential hyperfine structure anomaly. In extreme cases, ${}^1\Delta^2$ can be of the order of a few percent but in most cases it is on the 10^{-4} level or even smaller.

2˙2.2. Electric hyperfine structure. A non-spherical nucleus with spin posseses also higher electromagnetic multipole moments up to the order $2I$. Besides the monopole term — accounted for by the Coulomb term — the quadrupole moment is the next possible higher order of an electric moment. It arises from the energy of the orientation of the nuclear charge distribution in the inhomogeneous electric field of the electron shell and is given by

$$\Delta\nu_{\mathrm{el}} = B \frac{\frac{3}{4}C(C+1) - I(I+1)J(J+1)}{2I(2I-1)J(2J-1)}, \tag{16}$$

where

$$B = \frac{eQ_s}{h} \left.\frac{\partial^2 V}{\partial z^2}\right|_{r=0}, \tag{17}$$

with Q_s being the spectroscopic quadrupole moment of the nucleus, and $V_{zz}(0)$ the electric field gradient at the nucleus. The electric hyperfine structure appears only for nuclei and electronic states with $I > 1/2$ and $J > 1/2$, respectively. It shifts the magnetic hyperfine levels in a characteristic way, depending on the prolate or oblate shape of the nucleus.

The observation of the atomic hyperfine structure allows us to determine also the spin of a nucleus if it is unknown. As long as $I < J$, the spin can directly and unambiguously be determined from the number of observed hyperfine components. Otherwise, the relative distances between the hyperfine components as well as the relative intensities are signatures of the spin. The theoretical line strength $S_{FF'}$ of a hyperfine transition between the hyperfine levels F and F' arising from the fine structure levels with total angular momentum J and J' are related to the line strength in the underlying fine-structure transition $S_{JJ'}$ by

$$S_{FF'} = (2F+1)(2F'+1) \begin{Bmatrix} F & F' & 1 \\ J' & J & I \end{Bmatrix}^2 S_{JJ'}, \tag{18}$$

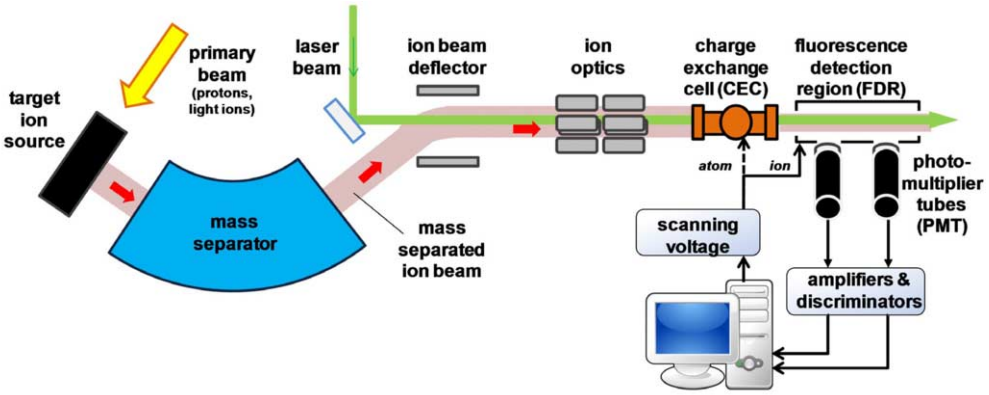

Fig. 5. – Principle of classical CLS. Radioactive isotopes are produced by bombardment of a target with a high-energy primary beam. After extraction and mass separation the ion beam is superimposed with a collimated laser beam using electrostatic deflector plates. Additional ion optical systems match the ion beam profile for maximum overlap with the laser beam. The ions are either neutralized in a charge exchange cell (CEC) or directly studied in the fluorescence detection region (FDR). When the scanning voltage applied to the CEC or the FDR results in a beam velocity that fulfills the resonance condition of an atomic transition with the Doppler-shifted light, the laser induced fluorescence in the FDR is detected by photomultiplier tubes (PMTs) and recorded after signal processing in the data acquisition system. Figure reprinted with permission from *Lecture Notes in Physics*, Vol. 879, chapter *Nuclear Charge Radii of Light Elements and Recent Developments in Collinear Laser Spectroscopy* by Nörtershäuser W. and Geppert C. (2014), pp. 233–292 © 2014, Springer.

where $\{\cdots\}$ denotes the 6-j coefficient that can be taken from standard books on angular momentum theory. However, these intensities must be handled with care since they are only correct for the excitation with unpolarized light and isotropic detection efficiency. Otherwise the detection geometry and the intensity distribution must be taken into account. Moreover, optical pumping can significantly alter the intensity ratios and lineshapes. In such cases, detailled studies of the lineshape have to be carried out.

3. – Techniques of on-line laser spectroscopy

3˙1. *Collinear laser spectroscopy*. – Hyperfine splittings of the order of 10–1000 MHz and ionic (atomic) transitions in the visible frequency range ($\sim 10^{15}$ Hz) require very high spectroscopic resolution, better than 10^{-7}–10^{-8}. Collinear laser spectroscopy (CLS) was developed in order to meet these demands and to perform high-resolution laser spectroscopy on short-lived isotopes. At ISOL (isotope separation on-line) facilities like ISOLDE/CERN, mass-separated beams with low emittance and beam energies of typically 30–60 keV are available. In CLS, such ion beams are superimposed with a laser beam in copropagating (collinear) or counterpropagating (anticollinear) geometry. A typical experimental setup at an ISOL facility is depicted in fig. 5. It consists of an ion source,

where the short-lived isotopes are produced and ionized by various processes. Surface ionization, electron-impact ionization in plasmas as well as resonance laser ionization (see below) are usually applied. The ion source is at a high positive potential (typically 30–60 keV), such that the ions extracted are accelerated towards ground potential. The ions are then mass-separated in a magnetic sector field and transported to the collinear laser spectroscopy beamline, where an electrostatic deflector is used to superimpose the ion beam with a laser beam.

The electrostatic acceleration has two consequences for laser spectroscopy: First, it leads to a large Doppler shift of the resonance frequency ν_0 of the ion

$$\nu = \nu_0 \frac{\sqrt{1-\beta^2}}{1-\beta\cos\theta} \tag{19}$$

with the ion velocity in terms of the speed of light $\beta = v/c$ and the angle between the ion beam and the laser beam direction θ. For an exact copropagating or counterpropagating geometry, this simplifies to

$$\nu_\pm = \nu_0 \sqrt{\frac{1\pm\beta}{1\mp\beta}}, \tag{20}$$

where + refers to the collinear ($\theta = 0$) and − to the anticollinear ($\theta = \pi$) case. The laser frequency in the laboratory must therefore be blue-shifted for collinear $\nu_{\text{coll}} = \nu_+$ and red-shifted for anticollinear $\nu_{\text{anticoll}} = \nu_-$ excitation. The second effect of the static acceleration is the longitudinal kinematic compression during the acceleration: the potential energy eU is gained by all ions starting in the source. Hence the kinetic energy distribution δE must stay constant. Using the derivative expression $\delta E = mv\,\delta v = \text{const}$ clearly shows that the velocity spread δv must decrease with increasing velocity v. In practice, residual Doppler widths on the order of 50–100 MHz are usually obtained in CLS. Consequently, high sensitivity is reached since a Doppler width matching the natural linewidth means that optical resonance occurs simultaneously for all ions in the beam.

Fluorescence spectroscopy can be performed on ions or on atoms. The latter offer usually more convenient transition wavelengths in the visible spectrum while ions require in most cases UV light. Neutralization of the ions is performed in a so-called charge-exchange cell (CEC) [13], in which alkaline vapor is generated by heating a small amount of solid alkaline metal. The ion beam passing through the vapor is then neutralized by electron transfer. To perform spectroscopy on ions, the CEC is either removed or it is not heated. Subsequently, the atoms or ions enter the fluorescence detection region (FDR).

Another elegant feature of CLS is that the laser can be fixed in frequency, while scanning across the resonance profile is performed by the so-called "Doppler tuning". This requires an additional tunable acceleration voltage applied to either the fluorescence detection region (for ions) or the CEC (for atoms). Varying this voltage will change the ion velocity and the Doppler effect changes the laser frequency in the rest frame of the ion.

3˙2. *Resonance ionization spectroscopy (RIS).* – Resonance ionization spectroscopy (RIS) combines the large cross section of resonant optical excitation with the very sensitive charged-particle detection. This is achieved by stepwise excitation of a valence electron in a neutral atom along dipole-allowed transitions until it is finally detached from the atom and a singly charged ion is left behind. Either the electron, the ion, or both are detected to provide evidence of the process. There is a multitude of arrangements for RIS. Efficient excitation at medium to low resolution can be obtained using pulsed lasers with bandwidths adjusted to the Doppler width of the atomic ensemble that has to be ionized. It has been first applied for nuclear charge radii measurements of short-lived isotopes at Gatchina [14]. Here, RIS was applied to thermal atomic beams [15]. The concept of a hot-cavity laser ion source for on-line use was suggested by Kluge *et al.* [16] as well as by Andreev *et al.* [17] and first realized at Gatchina [18]. In this modification it is now widely used as an ion source for element selective ionization. At ISOLDE the Resonant Laser Ion Source (RILIS) [19] is chosen for more than 50% of all beamtimes.

A laser ion source based on a gas cell has been proposed by Van Duppen and coworkers [20] and demonstrated at the Leuven Isotope Separator on-line (LISOL) [21, 22]. A development of an on-line gas-cell laser ion source is going on at Jyväskylä [23] and is also foreseen at RIKEN (Rikagaku Kenkyusho, Institute of Physical and Chemical Research, Japan) [24].

Resonance ionization spectroscopy is also being used to measure nuclear moments and charge radii: It has been applied combined with collinear laser spectroscopy [25-27], in a gas cell [28], after deposition and laser ablation from a beam catcher [29], or directly inside the hot-source. The examples are listed in order of decreasing resolution. While the last method offers the lowest resolution it is extremely sensitive and the resolution often still sufficient for the heavy isotopes that exhibit large field shifts (see fig. 4(c)) and large hyperfine splittings. A recent review on RIS for nuclear physics has been given by Fedoseev, Kudryatsev and Mishin [30].

It should be noted that the technique can also provide ultrahigh isotopic selectivity if cw lasers and a multi-step excitation scheme is used. This approach has been chosen for the trace detection of many ultra-low abundant or radiotoxic isotopes, for example ^{41}Ca, ^{89,90}Sr, ^{135,137}Cs [31,32]. Continuous-wave resonance ionization mass spectrometry (cw-RIMS) was also used for the investigation of the charge radii of the lithium isotopes as discussed below.

4. – Examples

In this section we present a number of recent highlights. They have been chosen to cover different regions of the nuclear chart, to demonstrate the specific strengths of the applied technique and to illustrate the way in which the nuclear structure information is extracted from the spectra. They are ordered by increasing atomic number (from beryllium to nobelium) and for each element one typical nuclear-structure theme is discussed.

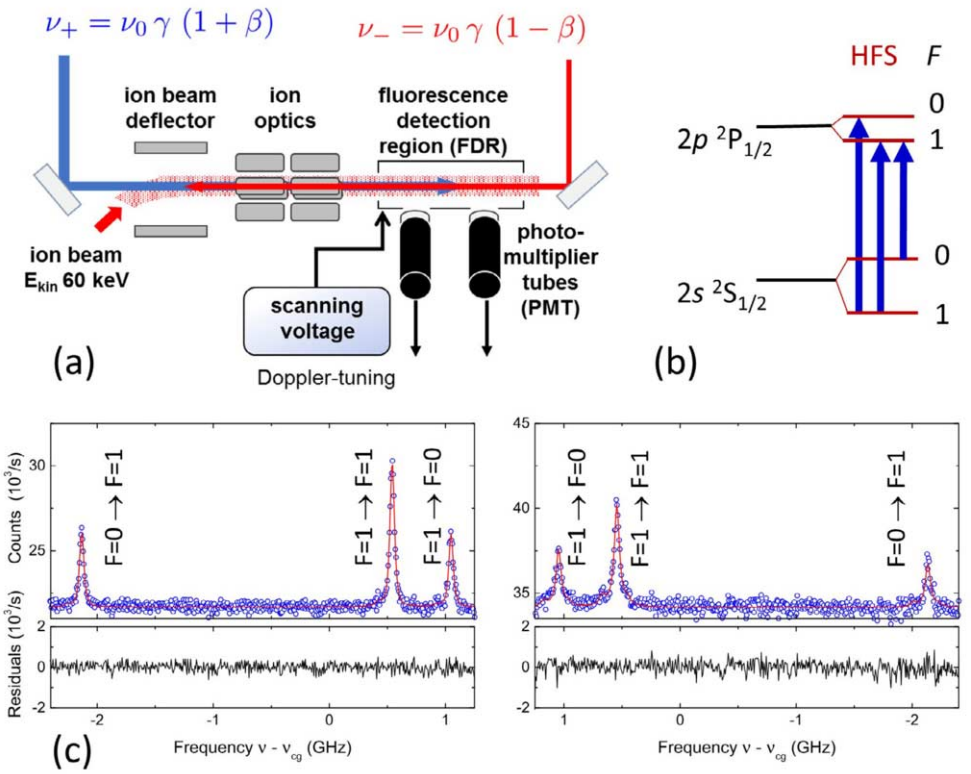

Fig. 6. – (a) Principle of the isotope shift measurement of Be isotopes. Resonance spectra are recorded with lasers copropagating and counterpropagating to the ion beam. (b) Level scheme including hyperfine structure for ^{11}Be. (c) Spectra of ^{11}Be in copropagating (left) and counterpropagating (right) geometry. Production rate was approximately 10^6 ions/proton pulse with a pulse repetition time of roughly 2.4 s.

4˙1. *Beryllium — Halos and vanishing shell closures.* – Isotope shift measurements of light isotopes with $Z < 10$ with collinear laser spectroscopy have not been possible until recently because of large uncertainties induced by the limited knowledge of the exact starting potential of the ions inside the ion source. The ion source potential, is typically known with about 10^{-4} relative uncertainty. The corresponding uncertainty in the ion velocity leads to a systematic error of about 15 MHz for the isotope shift between ^{9}Be$^+$ and ^{11}Be$^+$ in the $2s \rightarrow 2p$ resonance lines of these ions, which has to be compared with the expected field-shift contribution of approximately 5 MHz. In order to address this chain of isotopes, a technique that combined collinear laser spectroscopy using counterpropagating and copropagating lasers with frequency-comb technology was developed [33]. As indicated in fig. 6(a), it is based on measuring the total transition frequencies in the laboratory frame for both directions ($\nu_\pm$) with a precision of $\delta\nu/\nu < 10^{-10}$. These are

related to the rest-frame frequency ν_0 according to

$$\nu_\pm = \nu_0\gamma(1 \pm \beta). \tag{21}$$

The time dilation factor $\gamma = (1-\beta^2)^{-1/2}$ as well as the velocity of the ions $\beta = v/c$ depend on the acceleration voltage but if both Doppler-shifted transition frequencies $\nu_\pm$ are precisely measured in the laboratory frame, both variables can be completely eliminated

$$\nu_+ \cdot \nu_- = \nu_0^2\gamma^2(1+\beta)(1-\beta) = \nu_0^2. \tag{22}$$

Hence, the rest-frame transition frequency $\nu_0 = \sqrt{\nu_+ \cdot \nu_-}$ can be extracted without additional knowledge of the ion velocity or the acceleration voltage. An example of such a pair of spectra is shown for the halo isotope ^{11}Be in fig. 6(c). The left one is taken in copropagating ν_+ and the right one in counterpropagating ν_- geometry. In each spectrum the total angular momenta of the initial and the final hyperfine state are indicated according to the level scheme shown in fig. 6(b).

The spectrum features only three peaks, which immediately leads to the conclusion that ^{11}Be has a nuclear spin of $I = 1/2$. Hence, there is no contribution of electric hfs and the peak positions are determined by eq. (11). In order to extract the isotope shift, the center of gravity (cg) has to be determined. In fig. 6(c), the frequency scale offset is chosen such that 0 indicates the cg. Please note that spectra taken with co- and counterpropagating laser beams look like mirror images. This is an additional asset of this technique since small inaccuracies in the modelling of the lineshape are largely cured because they shift the peak centre into opposite directions in the two scans. Consequently, the respective shift is largely compensated when taking the geometric average.

The separation of the small field shift contribution from the dominant mass shift, requires additional theoretical input. Therefore, the isotope shifts of all isotopes with respect to ^{9}Be $\delta\nu^{9,A}_{\mathrm{IS,exp}} = \nu^A - \nu^9$ as obtained in the measurements were combined with state-of-the-art *ab initio* atomic structure calculations [34-36] of the three-electron system. These calculations can provide the mass shift $\delta\nu^{A,A'}_{\mathrm{MS,theory}}$ and the field shift factor F with very high accuracy needed to extract the change in the mean-square nuclear charge radius

$$\delta\langle r_c^2\rangle^{9,A} = \frac{\delta\nu^{9,A}_{\mathrm{IS,exp}} - \delta\nu^{9,A}_{\mathrm{MS,theory}}}{F}\,. \tag{23}$$

Total charge radii were then obtained by combining $\delta\langle r_c^2\rangle^{9,A}$ with the known charge radius of the stable isotope ^{9}Be determined using elastic electron scattering [38]. Results are shown in fig. 7 and depict a characteristic trend with a minimum at ^{10}Be and a strong increase for ^{11}Be. This can be explained by the clustered structure of these light nuclei (see also the contribution by Y. Kanada-Enyo in this volume). The effect is visualized in a very simplified picture in the small panels below the graph, starting with ^{7}Be, which can

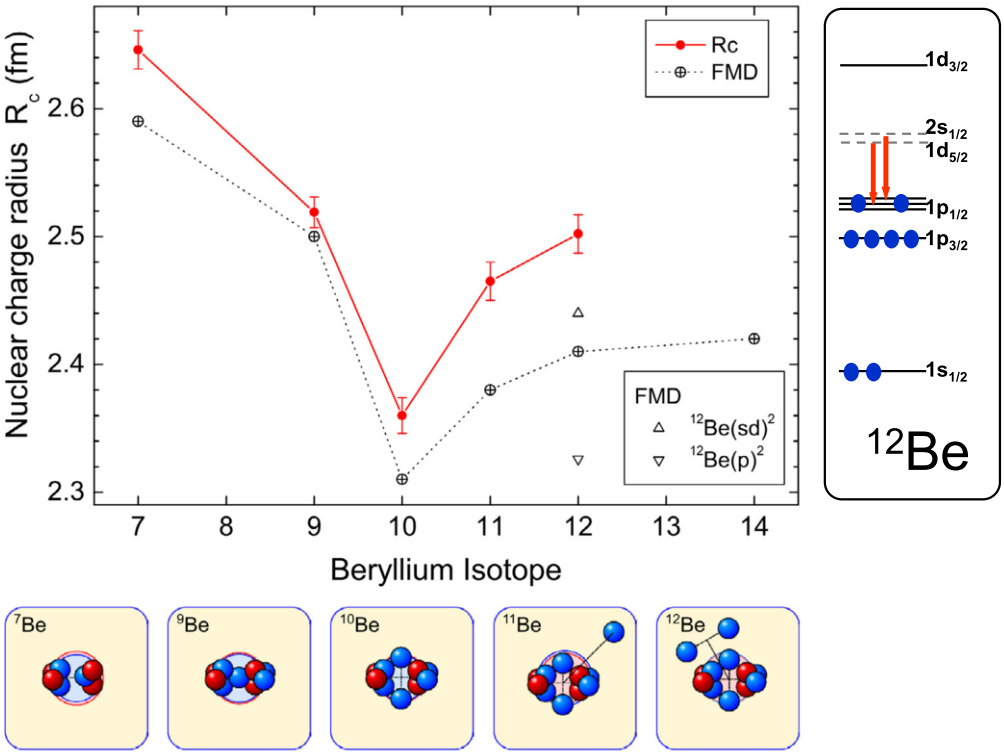

Fig. 7. – Nuclear charge radii along the beryllium isotopic chain. The red bullets (•) represent the experimental results with error bars dominated by the uncertainty of the reference charge radius of ^{9}Be [38]. Additionally shown are results of Fermionic Molecular Dynamic (FMD) calculations [41], which reproduce the trend along the isotopic chain very well. The bottom row shows a simplified structure of the isotopes interpreted in a cluster picture and the very simplified level scheme in the nuclear-shell-model picture on the right visualizes the disappearance of the $N = 8$ shell gap due to the lowering of the single-particle energies of the *sd* shell. A more detailed discussion of the nuclear physics aspects in the beryllium chain can be found in the contributions by T. Otsuka, and Y. Kanada-Enyo in this volume. Figure slightly modified from [37].

be regarded as a two-body cluster $\alpha + {}^3$He. The center-of-mass (CM) motion blurs the proton distribution and leads to a comparably large charge radius. The stable isotope ^{9}Be has an $\alpha+\alpha+n$ structure and is less extended than ^{7}Be due to the compactness of the α particles and the binding strength of the additional neutron. This effect is even enhanced with the second neutron added in ^{10}Be. The sudden upward trend to ^{11}Be is attributed to the one-neutron halo character of ^{11}Be which can be disentangled into a ^{10}Be core and a loosely bound neutron. This halo character increases the matter radius and also affects the charge radius due to the CM motion of the core. The further increase towards ^{12}Be is attributed to a strongly mixed $(sd)^2$ character of the two outermost neutrons. Results of Fermionic Molecular Dynamics (FMD) calculations are plotted for comparison. They

reproduce the general trend along the isotopic chain quite well but are generally slightly too small. For ^{12}Be three results are shown: The two triangles represent charge radii calculated under the assumption of a pure p^2 or a pure $(sd)^2$ configuration, as expected for a strong shell closure or a diminishing shell closure at $N = 8$, respectively. The full FMD calculation that fits roughly to the experimentally observed trend, predicts an $(sd)^2$ admixture of about 70% for this nucleus, being a clear indication for the disappearance of the classical $N = 8$ shell closure as indicated on the right in fig. 7. For a more detailed discussion of the nuclear charge radii, the comparison with *ab initio* microscopic nuclear structure calculations and the conclusions about the shell closure see refs. [39-41].

4˙2. *Magnesium — The island of inversion.* – The so-called island of inversion around the $N = 20$ shell closure of the isotopes of Ne, Na, Mg and Al has now been investigated for more than 35 years after the observation of anomalous ground-state properties of ^{31}Na: An unusual increase in binding energy was seen for $N = 20, 21$ (^{31,32}Na) instead of the normal behavior of a sudden drop after a shell has been completed [42]. It was from the beginning interpreted as being a sign of the sudden onset of deformation, which is unusual for a magic nucleus. For the prominent $N = 20$ nucleus ^{32}Mg strong deformation was postulated from the large $B(E2; 2^+ \rightarrow 0^+)$ value [43]. Laser spectroscopic studies of the sodium isotopes supported this picture by finding a spin of $I = 3/2$ for ^{31}Na instead of the expected $I = 5/2$ for a $d_{5/2}$ proton and isotope shift measurements also indicated an additional volume effect by a prolate deformed nucleus [44]. This all motivated laser spectroscopic studies along the isotopic chain of Mg. However, production rates beyond ^{30}Mg are too small for standard CLS.

For magnesium as well as for some other light short-lived isotopes this problem of sensitivity can be addressed by optically polarising the nuclei and detecting the asymmetry in the angular distribution of β-decay electrons or positrons, which is asymmetric with respect to the nuclear spin direction. A setup of this technique with the illustration of the pumping process is shown in fig. 8. The standard CLS is extended by a puming zone with a weak longitudinal magnetic field (guiding field) and a β-detection setup inside a strong magnetic field at the end of the beamline. Along the beamline circularly polarized laser light ($\sigma^{\pm}$) is used to transfer angular momentum to the atom with each absorbed photon. The atomic scheme is indicated for a $^2S_{1/2} \rightarrow {}^2P_{3/2}$ transition. σ^+ light induces transitions with the selection rule $\Delta m = +1$. Consecutive spontaneous decay can happen with $\Delta m = 0, \pm 1$ and, hence, on average $1\,\hbar$ of angular momentum is transferred to the atom per absorption/emission cycle. While the atoms entering the beamline are equally distributed in all magnetic substates of the electronic ground level, the population is gradually transferred into the state with the largest projection along the magnetic guiding field by repeated excitation as is visualized in the center part of the figure. In the best case, all population is finally in the maximum m_F state, the ensemble is polarized and the total angular momentum F precesses around the weak guiding field. In the β-decay station a strong magnetic field is oriented perpendicularly to the beamline. In the guiding field, the atomic state is affected by the Zeeman effect, *i.e.* the total angular momentum F is still a good quantum number and the nuclear spin

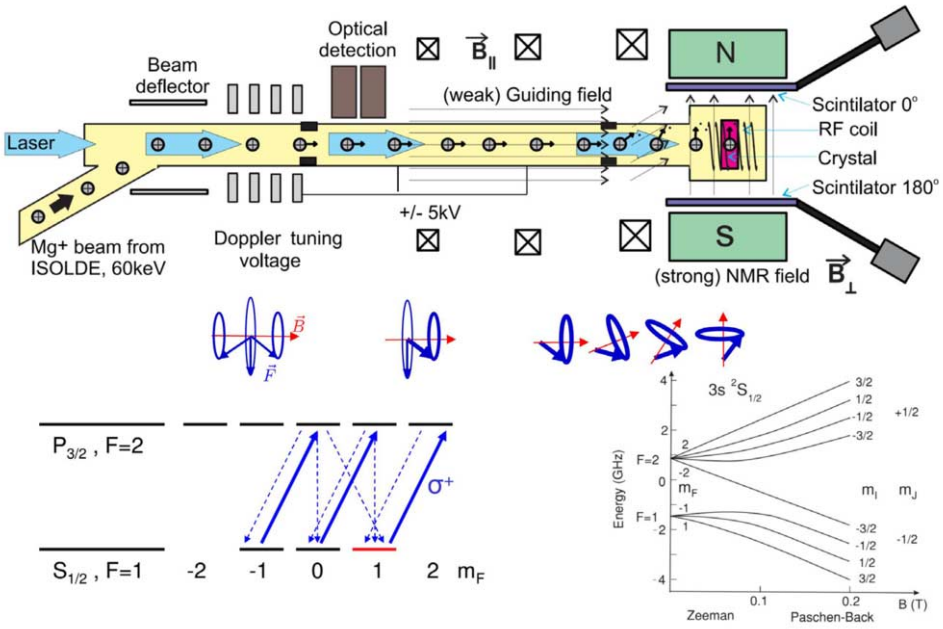

Fig. 8. – Setup for charge radii measurements of magnesium isotopes. Top: Collinear laser spectroscopy adapted with magnetic guiding fields for the magnetic moment and extended with a β-asymmetry detection setup to the right. Middle: Schematic representation of the orientation distribution of F-vectors for the case $F = 1$ during the pumping process along the beamline and the transfer from longitudinal to transversal polarization in the transition region to the strong NMR field. The thickness of the arrow represents the population. The precession of the vector around the magnetic field direction (red) is also indicated and must be much faster than the change in the magnetic field direction in the ions frame. Bottom: m_F level scheme for optical pumping (left) and energies of the m_F states in the weak guiding field (Zeeman region) and the strong NMR field (Paschen-Back region).

is coupled to the electron angular momentum. This changes when entering the strong field (typically $\approx 0.3\,\mathrm{T}$). Here, the electronic angular momentum is decoupled from the nuclear spin (Paschen-Back regime) as is shown in the diagram in the lower right part of fig. 8. Before this can happen, an additional field is required to adiabatically rotate the magnetic moment of the atoms from longitudinal polarization into the transversal direction of the strong field. This is also indicated in the middle plane of fig. 8, where the magnetic field direction (red) is slowly transferred from horizontal to the vertical direction and the total angular momentum (blue) quickly precesses around the direction and therefore follows the field direction. Finally the ion is implanted into a suitable host crystal. The implanted unstable nucleus will eventually undergo β-decay and emit positrons or electrons. The β-particles are detected with a pair of scintillators above and below the crystal. Due to parity violation, the β-emission occurs preferentially along

or against the nuclear spin direction. The corresponding asymmetry in the number of events within the two scintillators can serve as a detector for optical excitation, since polarized nuclei are only produced if the laser is in resonance with the ions. The implantation of the beam into a suitable host crystal lattice offers an alternative access to the nuclear moments, which is based on nuclear magnetic resonance (NMR) detected by the influence of radiofrequency on the β-decay asymmetry (β-NMR). Therefore the laser is fixed on resonance, where it produces the largest polarization, *i.e.*, the population is transferred into the $m_I = \pm I$ substate for $\sigma^{\pm}$ pumping, respectively. The polarization can then be destroyed by inducing transitions between neighboring magnetic substates with the Larmor frequency

$$\omega_L = \frac{g_I \mu_N I}{\hbar} B_0 \tag{24}$$

which is directly connected to the nuclear g-factor provided that the magnetic field is known. The latter is usually calibrated using a second species with a well-known nuclear magnetic moment like, *e.g.*, ^{8}Li.

While the magnetic moments of nuclei interact with a static magnetic field, the quadrupole moments interact with an electric field gradient produced at their lattice site in a non-cubic crystal. Hence, β-NMR can also be used to measure nuclear quadrupole moments. The latter is particularly important for light atomic systems where the quadrupole interaction is too small to be resolved in the hyperfine structure of spectral lines and has been applied, *e.g.*, for ^{9,11}Li [46].

The Mg isotopes $^{21-33}$Mg were investigated at ISOLDE using a combination of all techniques described so far: For the longer-lived isotopes closer to stability, information on the radii and moments was obtained from conventional CLS measurements. Detection of the resonances of ^{21,31,33}Mg was only possible applying the β-asymmetry detection. These nuclei appeared to be ideal candidates for β-NMR because of their short half-lifes of a few 100 ms and a still abundant production of more than 10^5 ions/s and 2500 ions/s for ^{31}Mg and ^{33}Mg, respectively.

The β-asymmetry spectrum as a function of the laser frequency is shown in fig. 9 [45] and exhibits only three resonances. The vertical lines along the peaks guide the eye to the respective transition in the level scheme depicted below the spectrum. The observation of only three lines is already a clear signature for an $I = 1/2$ nucleus since any other half-integer spin would result in six allowed transitions. A *direct spin measurement* was also performed by an independent determination of the magnetic moment from the optical spectrum and the g-factor from the β-NMR measurement. The ground-state splitting obtained in the optical spectrum in a $^2S_{1/2}$ state is $\Delta E = A(I + 1/2)$ with $A = \frac{g_I \mu_N B_0}{IJ}$ while the Larmor frequency measured in β-NMR is $\Delta\nu_L = g_I \mu_N B_0$. If the ratio A/g_I is known from a reference isotope, the only unknown is the spin I which can then be unambigiously determined. In this way the spin $I = 1/2$ was determined for ^{31}Mg and similarly the ground-state spin of ^{33}Mg was determined to be $I = 3/2$.

The spin $I = 1/2$ with a positive parity and the magnetic moment of the $N = 19$ nucleus ^{31}Mg came as a great surprise [47]. It was in conflict with all expectations

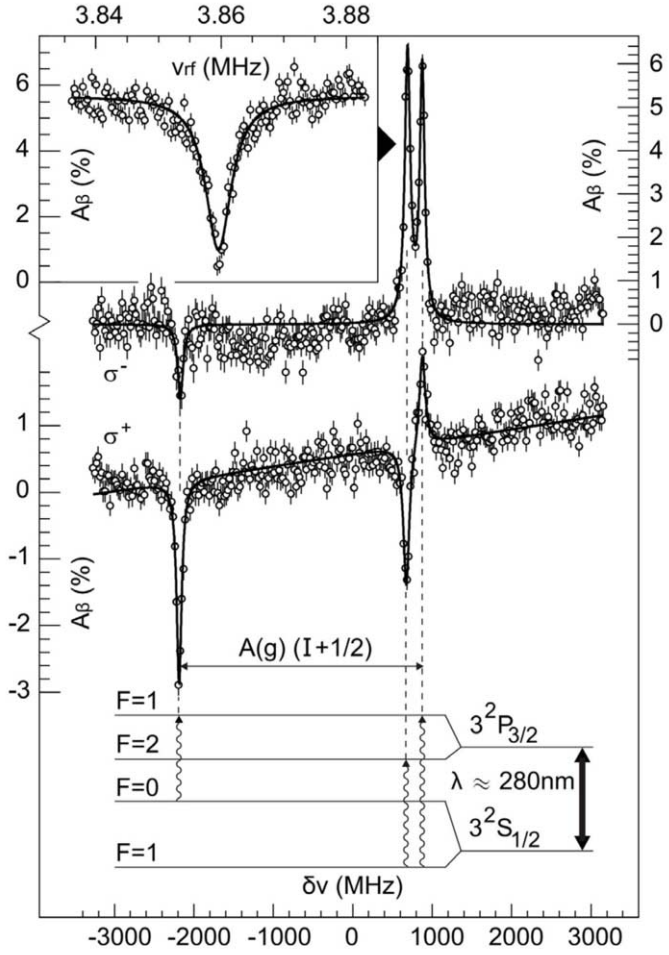

Fig. 9. – Hyperfine spectrum of ^{31}Mg in the D2 line detected using β-asymmetry detection recorded as a function of Doppler-tuned laser frequency [45]. The respective transitions are indicated on the level scheme below the resonances. The inset on the top shows the β-NMR signal as a function of the applied radiofrequency after optical pumping with σ^- on the transition with the highest β-asymmetry ($F = 1 \rightarrow F = 2$).

from systematics and from shell-model calculations. This puzzling result initiated some theoretical effort [48] that succeeded to reproduce the level assignments based on the measured ground state spin and confirmed a ground state wave function being dominated by neutron two-particle–two-hole (2p-2h) intruder configurations as inferred already from the magnetic moment [47]. The result for ^{33}Mg yielding $I = 3/2$ combined with a magnetic moment that was consistent only with a negative parity [49,50] initiated further controversy with conclusions from nuclear spectroscopy and shell-model theory. The

^{33}Mg ground state was shown to have a nearly pure 2p-2h intruder nature, contrary to the earlier suggested 1p-1h configuration and in agreement with the structure of other isotopes in the "island".

While magnetic moments and quadrupole moments can be readily accessed from β-asymmetry spectra, the determination of the isotope shift from such spectra has been unsuccessful for a long time due to an insufficient description of the peak shape and the line intensities in the β-asymmetry spectrum. It can only be obtained with a quantitative model based on rate equations of the optical pumping process along the path of flight. However, different magnetic fields are required along the beam path for defining the orientation axis, rotating the atomic total angular momentum and for decoupling the electron and nuclear spins as discussed above. This goes along with a variable Zeeman effect and a change in the relative strengths of transitions between the Zeeman levels of the hyperfine structure. For a beam of neutral atoms the final nuclear polarization results from the interaction of the atoms with the laser light all along the beam. Once the atoms are generated in the charge exchange cell, their velocity cannot be varied anymore by applying varying potentials. But a realistic description of the resonance line shapes is possible if optical pumping is performed in ions for which the interaction with the light can be switched on and off by the Doppler effect and the resonance condition is established only in a well-defined low-magnetic-field region. This approach was developed for Mg^+ ions and excellent agreement was found [51] between the experimental and the simulated spectra.

The quantitative simulation of the resonance line shape of the ^{31}Mg β-asymmetry spectrum is included in fig. 9 as an example. It was the basis for the determination of the isotope shift of ^{21,31}Mg reported in [52]. The conventional method of optical resonance detection was used for odd-A isotopes of magnesium close to stability and on even-even isotopes. The weak signal of ^{32}Mg could still be observed by counting photons in coincidence with ions.

4˙3. *Calcium — Mystery beyond the $N = 28$ shell closure.* – A variety of spectroscopy experiments on neutron-rich isotopes with $Z \geq 20$ suggested the appearance of a new magic number at $N = 32$ [53-56]. Recent mass measurements up to ^{54}Ca confirmed that result and reported that they "unambiguously" establish a prominent shell closure at neutron number $N = 32$ [57]. The trend of charge radii usually exhibits a pronounced kink when crossing magic neutron numbers and is therefore a strong indicator for magicity. Therefore, the mean square charge radii of the Ca isotopes from $N = 20$ up to $N = 32$ were investigated by resonance fluorescence CLS. These measurements were facilitated by the ISCOOL cooler and buncher [58]. ISCOOL is a radiofrequency quadrupole (RFQ) device filled with helium buffer gas at low pressure (typically 10^{-2} mbar). The principle of such an RFQ structure is shown in fig. 10. It consists of four cylindrical rods to which a radiofrequency (RF) of typically about 0.2–1 MHz is applied in such a way that opposing rods have the same amplitude and sign of the AC electrical signal (a few 100 V). Due to the quickly oscillating potential, ions inside the rods experience on average a confining harmonic potential so that they are transversely trapped. The rods are additionally

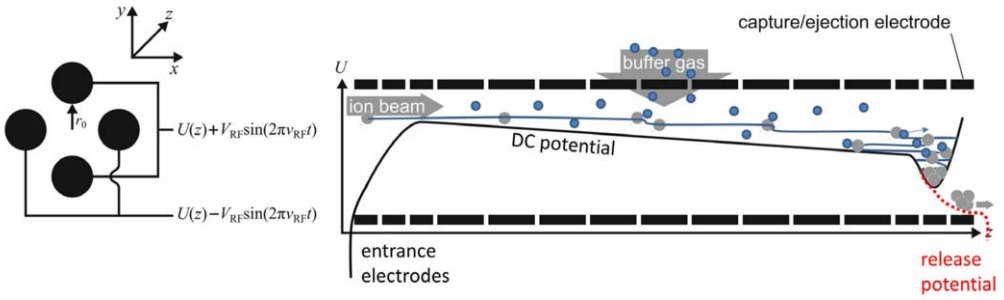

Fig. 10. – Principle of the RFQ operation as an ion cooler and buncher. Left: Sketch of the rods and their supply voltages along the symmetry axis. Right: Schematic side view of the segmented rods. The DC potential along the z-axis is drawn in between the rods. The black line represents the potential during ion accumulation. The effect of cooling is indicated by the collisions with the buffer gas (blue) which leads to a stepwise decrease of the ion energy. The ions are reflected between the potential walls, collide repeatedly with the ions and are finally accumulated in the deep potential well close to the exit. After accumulation times of typically a few 10 ms, an ion bunch is released by turning down the potential at the exit segment as indicated by the red dotted line.

segmented in longitudinal (z) direction and different DC potentials can also be applied, such that a trapping potential can be created along the axis. The potential at the RFQ exit is chosen to create a potential wall of typically a few 10 V such that the ions cannot leave the RFQ. At the entrance, the potential is slightly less so that ions delivered from the on-line ion source — mass separator combination have just sufficient energy to climb that potential and enter the RFQ. Once inside, they quickly loose some energy in buffer gas collisions so that they cannot overcome the entrance potential anymore. In subsequent collisions they loose more and more energy until they are cooled down to the bottom of the potential well. After some sampling and cooling time, chosen according to the experimental condidtions and the properties of the isotope of interest (lifetime, beam intensity etc.) the potential wall at the RFQ exit is pulsed down and the ions can leave the RFQ as a short bunch with typical bunch width of a few μs.

The advantage of such a short ion pulse is that the main background in standard CLS can be effectively suppressed. This background originates from scattered laser light that is produced at apertures along the beamline or at the entrance and exit windows. After some reflections inside the beamline it may end up at the photomultiplier tube and cannot be discriminated against fluorescence light produced by the ions. The background is clearly visible for example in fig. 6(c), where the signal height is only a small portion of the background. Typical background rates are on the order of a few kHz and lead to a considerable noise that can bury weak signals.

If the ions are delivered as short bunches, the bunch-transition time in front of the photomultipliers can be determined from the release trigger of the RFQ and signal detection is restricted to these intervalls. In the typical case of 50 ms bunching time and 5 μs bunch length, the continuous laser-scatter background is reduced by a factor of 10^4. The

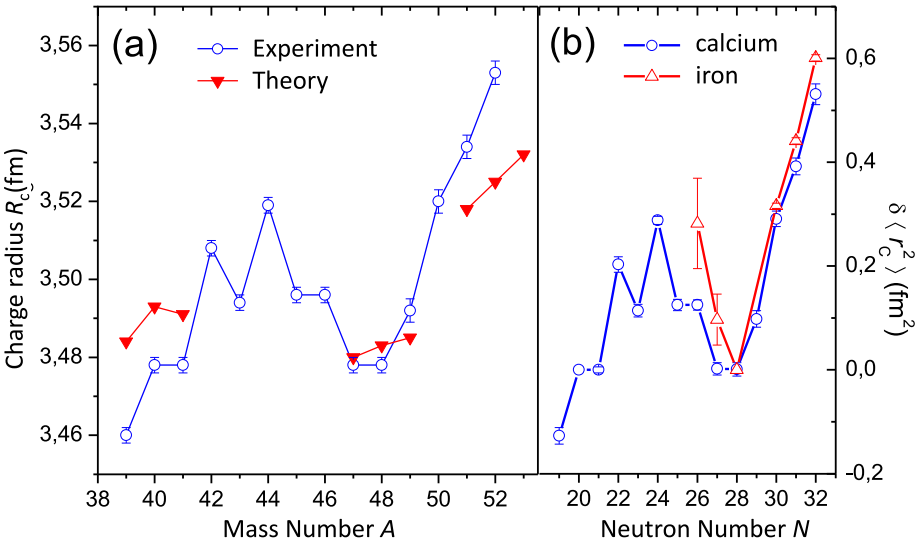

Fig. 11. – (a) Total charge radii of calcium isotopes from experiment and theory. (b) Change in the mean-square charge radius along the isotopic chains of calcium and iron.

corresponding noise reduction is about two orders of magnitude. In the case of calcium isotopes, this allowed to record a fluorescence signal of ^{52}Ca at a production rate of the order of only 100 ions/s. The resonance signals are depicted in fig. 3(a). Please note that there is very little background in these spectra.

The charge radii extracted for the calcium isotopes are plotted in fig. 11. In fig. 11(a) absolute radii of all calcium isotopes are depicted. Between ^{40}Ca and ^{48}Ca the radii show the famous and well-known parabolic behaviour, which results in almost equal charge radii of the two doubly magic isotopes ^{40}Ca and ^{48}Ca. Additionally the radii exhibit a remarkably strong odd-even staggering. In red, results from coupled-cluster calculations performed with realistic potentials based on chiral effective field theory are included. Compared to all previous theoretical attempts, the prediction of the total nuclear charge radius is excellent. However, the increase between ^{48}Ca and ^{52}Ca is much steeper in experiment than in theory. In fig. 11(b) the change in the mean square charge radius around $N = 28$ is compared for calcium and iron. The increase is similar for the magic-Z isotopes of Ca and the open-shell nuclei of Fe and no signature of a shell effect at $N = 32$ is seen [59]. A flattening towards $N = 32$, as would be expected for a magic shell gap, is also not observed in potassium isotopes. Additionally, also from the magnetic moments of the odd-A Ca isotopes no signature for a shell closure at $N = 32$ is observed [60]. Indeed, the observed magnetic moment of ^{51}Ca, with 31 neutrons, requires excitations of neutrons across $N = 32$ in the higher pf-orbits, to reproduce the observed value. These results illustrate that more experimental studies on the single-particle nature of the ground-state wave functions of Ca isotopes, such as transfer reaction experiments, are needed to further investigate this ambiguity.

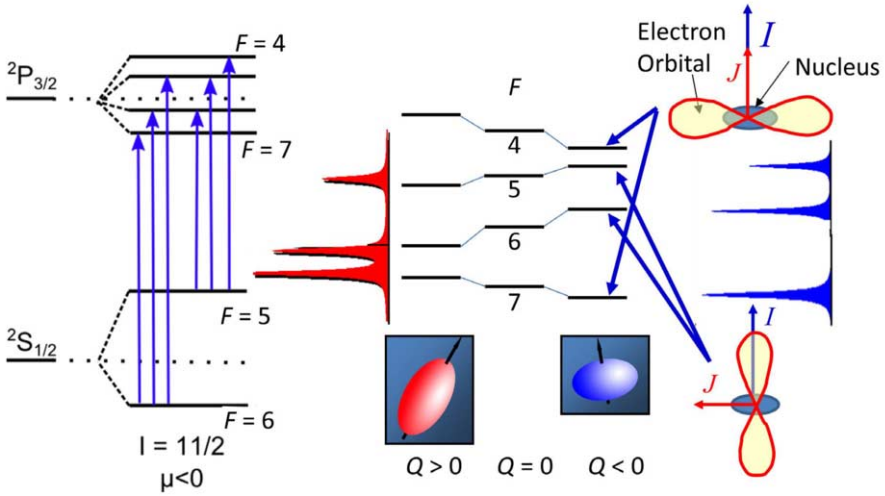

Fig. 12. – Left: Electronic level scheme of the hyperfine structure of a $11/2^-$ isomer. Right: Influence of the nuclear quadrupole moment on the energies of the excited $5p\,^2P_{3/2}$ level and the observed resonance pattern. For details see text.

4˙4. *Cadmium — Simple structure in complex nuclei.* – Spectroscopy of cadmium at COLLAPS was originally motivated by nuclear astrophysics: The neutron-rich isotopes were expected to shed light on a shell-quenching hypothesis at $N = 82$ and its consequences for the duration of the r-process along the waiting-point nuclei below ^{130}Cd, whereas the neutron-deficient ones should elucidate the role of the cadmium isotopes in the rp-process for rapidly accreting neutron stars [61]. Surprisingly, the properties of the $11/2^-$ isomers in the range of $^{111-129}$Cd turned out to behave in an extremely predictable manner and are a textbook example of nuclear quadrupole moments. While this can be partially understood in the conventional interpretation of the nuclear shell model, a full description must clearly go beyond this picture. The spectra are also clear enough to elucidate the influence of the quadrupole moment on the atomic spectra.

Laser spectroscopy studies were performed on Cd^+ in the $5s\,^2S_{1/2} \rightarrow 5p\,^2P_{3/2}$ transition. The level scheme for one of the $I = 11/2$ isomers is depicted in the left part of fig. 12. The magnetic dipole moment of an $\nu\, h_{11/2}$ state is negative and therefore the F level scheme is inverted. For all isotopes with $I \geq 3/2$ (all odd Cd isotopes have half-integer nuclear spin) we expect two triplets in the hyperfine structure, while for $I = 1/2$ a doublet and a singlet appears, which are in both cases separated by the hyperfine splitting in the $5s\,^2S_{1/2}$ electronic ground state. This splitting is not affected by the quadrupole moment since a state with $J = 1/2$ is spherical and does not exhibit an electric field gradient at the nucleus. The distance between the two multiplets is therefore proportional to the nuclear magnetic moment. Contrary, in the $5p\,^2P_{3/2}$ excited level, the splitting depends on the nuclear magnetic moment and the nuclear quadrupole moment. The influence of the latter on the level scheme is depicted in the middle part of fig. 12. The enlarged

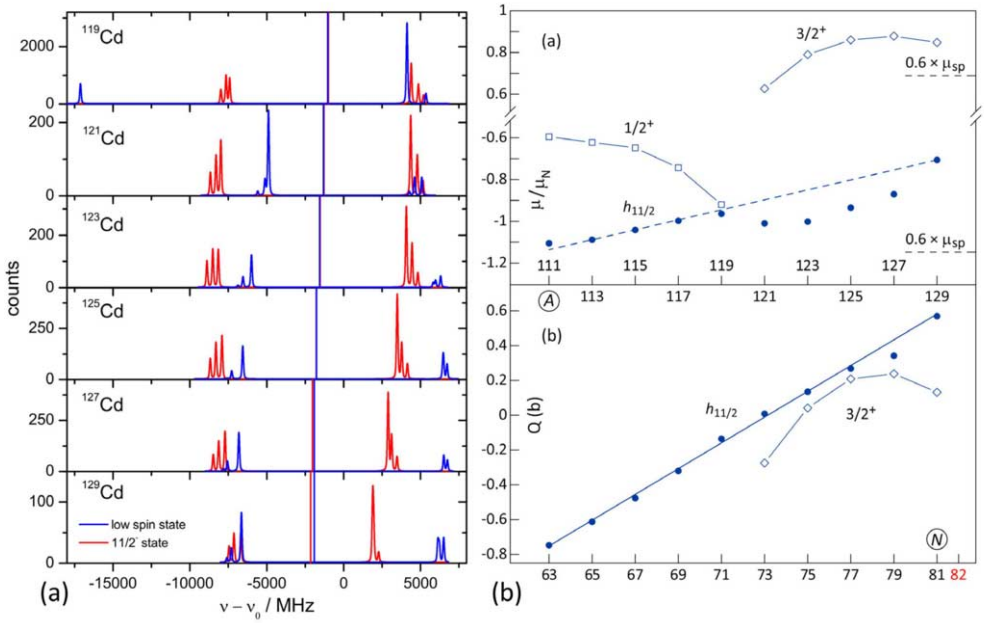

Fig. 13. – (a) Hyperfine structure pattern of the nuclear ground state (blue) and the $11/2^-$ isomers of Cd. (b) Magnetic moments (top) and spectroscopic quadrupole moment of various Cd isotopes and isomers. For details see text. Figure (b) reprinted with permission from D.T. Yordanov *et al.*, Phys. Rev. Lett. **110**, 192501 [62]. © 2013 by the American Physical Society.

level scheme of the $^2P_{3/2}$ state is shown for three cases: a spherical nucleus ($Q = 0$, middle), a prolate nucleus ($Q > 0$, left), and a nucleus with oblate deformation ($Q < 0$, right). While the pure magnetic hyperfine structure exhibits the well-known interval rule (splitting is proportional to the upper state F value), the quadrupole interaction violates this rule. The reason for the energy shift is schematically depicted in the figure for a prolate nucleus. If the electron total angular momentum and the nuclear momentum are close to be parallel to each other (for $F_{\max}$ and $F_{\min}$), the overlap of the electronic wave function with the nucleus is increased compared to a spherical nucleus and, thus, the level energy drops. Contrary, the level energy rises if $\vec{I}$ and $\vec{J}$ are almost perpendicular to each other, since the overlap of the two charge distributions is then reduced. Within the two triplets, a prominent change in the resonance pattern is visible with varying nuclear deformation. This is readily observed in the spectral structure of the odd-mass isotopes $^{119–129}$Cd depicted in fig. 13(a). It is immediately visible that there are too many (more than 6) resonances for a single nuclide. Hence, the spectrum indicates that there is an (11/2) isomer besides the (low spin) nuclear ground state admixed to the delivered ion beam. In the figure the first one is plotted in red, while the structure of the ground state is plotted in blue. While ^{119}Cd has a ground state of spin $I = 1/2$ (only three peaks), ^{121}Cd has spin $I = 5/2$ and exhibits two triplets similar to the isomeric state.

If we now concentrate on the regular structure of the isomer, we can immediately see how the magnitude of the magnetic moment evolves along the chain: it increases from ^{119m}Cd to ^{121m}Cd, stays approximately constant from ^{121m}Cd to ^{123m}Cd and gradually decreases towards ^{129m}Cd. The structure of the left and the right triplet is close to the one expected for a spherical nucleus and turns then into an increasing (slightly) prolate deformation. The blue and red vertical lines in the middle of each spectrum represents the center-of-gravity of the ground-state hyperfine structure and the isomer hyperfine structure, respectively. The frequency difference between them is called the isomer shift and almost exclusively due to the differences in field shift since the mass difference between the two states is very small. Hence, it is a direct measure of $\delta\langle r^2\rangle$ between the ground state and the isomer.

Overall, the isotopes from ^{100}Cd up to the shell-closure at ^{130}Cd were studied and nuclear magnetic moments and electric quadrupole moments were extracted from the spectra using reference dipole moments and calculated electric field gradients, respectively [62]. The moments are shown in fig. 13(b). The quadrupole moments of the $11/2^-$ isomers exhibit an extremely linear behaviour. This is exactly what was predicted for the filling of a (proton) shell in the basis of the independent particle model. For a nucleus of odd-A and a single proton in a state of angular momentum j, the single-particle quadrupole moment is

$$Q_{\mathrm{sp}} = -\left\langle r^2\right\rangle \frac{2j-1}{2(j+1)}\,. \tag{25}$$

The negative sign corresponds to the fact that the charge distribution of a single proton outside a spherical closed shell with $m_j = j$ represents an oblate spheroid. With increasing number (λ) of protons in the state j and normal coupling to $J = j$ for an odd number λ of protons, it can be shown that the quadrupole moments develop as

$$Q_\lambda = Q_{\mathrm{sp}}\left(1 - \frac{2(\lambda-1)}{2j-1}\right). \tag{26}$$

The quadrupole moment is negative ($Q_{\mathrm{sp}} < 0$) as long as $\lambda < (2j+1)/2$, *i.e.* for a less than half-filled level and positive for large occupation and reaches the magnitude of the single-particle value (but opposite sign) for one remaining hole in the level $\lambda = 2j$. The quadrupole moment vanishes for a half-filled level. In the case of Cd, where a neutron level is filled, the neutron is attributed an effective charge. This can be understood by the interaction of the neutrons with the protons, which leads to a polarization of the core.

While this simple structure is at first sight reflected by the quadrupole moments, a second look reveals considerable differences from this model: The number of 10 odd-mass isomers is 4 more than the expected number for solely filling the $h_{11/2}$ shell and the zero-crossing is not exactly at mid-shell. In [62], a degeneracy of the $h_{11/2}$ and some of the neighbouring $s_{1/2}$, $d_{3/2}$, and $d_{5/2}$ orbitals has been suggested to explain these observations, giving rise to a kind of a "super-shell" that is shared by the $I = 0$ neutron pairs. With this assumption, a single-particle quadrupole moment of $Q_{\mathrm{sp}} = -667(31)$ mbarn

and a constant core deformation with $Q_{\text{const}} = -85(8)$ mbarn can be extracted. This implies a rather huge effective neutron charge of $q_{\text{eff},n} = 2.5e$. Later it was shown that these assumptions can indeed be used to explain also the isomer shift between the respective ground state and the isomer, which were found to follow a distinct parabolic dependence as a function of the atomic mass number [63]. Even though the nuclear shape is very close to spherical all along the isotopic chain and never exceeds a deformation parameter of 0.07, this unique regularity in the isomeric shift can be understood as a manifestation of nuclear deformation.

4˙5. *CRIS — Collinear resonance ionization spectroscopy.* – The collinear resonance ionization spectroscopy (CRIS) experiment at ISOLDE combines collinear laser spectroscopy with the technique of resonance ionization spectroscopy (RIS) discussed already in sect. **3˙2**. This was already demonstrated at ISOLDE in 1991 [25] but suffered at that time from limitations due to the short temporal overlap of the continuous ion beam and the pulsed laser used for ionization. The implementation of the RFQ cooler and buncher offered decisive advantages for this type of experiments: The pulsed ionization lasers are synchronized with bunches delivered from ISCOOL and, hence, all atoms delivered from ISOLDE can interact with the pulsed laser light and the full duty cycle is available for excitation and subsequent ionization. Pulsed beam collinear resonance ionization was demonstrated at the IGISOL facility [64, 65]. This stimulated the development of a new dedicated beam line with an UHV interaction region, for efficient bunched-beam collinear resonance ionization spectroscopy (CRIS) at ISOLDE. The detection of ions is very efficient and quasi background-free, since ultra-high vacuum (UHV) in the interaction region highly reduces the background which originates from collisional ionization of isobaric beam contaminants.

The stepwise resonance ionization scheme (using pulsed lasers) is also used for low-resolution in-source laser spectroscopy experiments [66], where high efficiency and selectivity allow experiments on beams with rates of less than 1 ion/s and in some cases even 0.01 ions/s [67].

A scheme of the CRIS technique is shown in fig. 14: Bunched ions from ISOLDE are transported to a charge-exchange cell filled with a load of potassium and operated at about 150 °C to provide a sufficiently dense potassium vapor for neutralization of the ion beam. Remaining ions are deflected out of the beam by an electrostatic deflector plate, positioned within a differential pumping region after the charge-exchange cell. The bunch of neutral atoms enters a region of ultra-high vacuum (to avoid collisional excitation or re-ionization) where it is collinearly overlapped with two or more laser beams, depending on the resonance ionization scheme used. In the simplest configuration, a cw laser is used for resonant excitation which is then followed by non-resonant ionization using a short and intense pulse of a second laser. The resonantly produced ions are then deflected from the remaining atoms into a charged-particle detector (MCP) or transported to a decay spectroscopy station [68].

This simple scheme has the disadvantage that the appearance of the high-intensity laser pulse leads to shifts and broadening of the atomic level energies caused by the AC

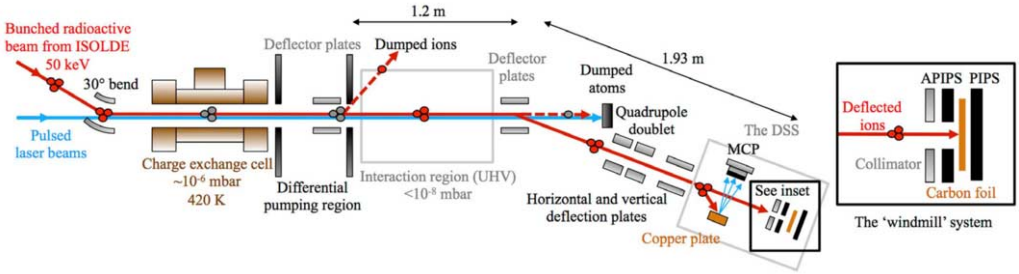

Fig. 14. – Principle of collinear resonance ionization spectroscopy (CRIS) (taken from [69]). For details see text.

Stark effect. Therefore, the cw laser can be chopped or pulse amplified to avoid such systematic variations by temporarly separating the interaction with the resonant and the ionization lasers.

Another asset of CRIS is the possibility to combine it with decay spectroscopy in order to either study the nuclear decay of clean samples or to use the decay to separate and identify the signals of isomeric states that are delivered from ISOLDE in the same beam. This is indicated in the inset of fig. 14.

First on-line measurements with CRIS were performed on the francium isotope chain and were motivated by evidence for shape coexistence in the neutron-deficient isotopes and isomers [70]. The neutron-rich isotopes were studied to gain better knowledge around the region of reflection asymmetry. The CRIS measurements delivered additional data for about 5 more mass numbers in each direction towards neutron-rich and neutron-deficient isotopes. This demonstrated the high selectivity of the CRIS technique.

4˙6. *In-source resonance ionization spectroscopy: Studies in the Pb region.* – Atoms enclosed in a small hot cavity can be efficiently ionized with pulsed resonance ionization spectroscopy. A cylindrical geometry with relatively small diameter (a few mm, adapted to the size of the laser beams) but sufficient length (typically a few 10 mm, adapted to the flight path of an atom between two laser pulses) provides confinement of atoms during the time interval between consecutive laser pulses. A high temperature is required to prevent the atoms from sticking on the cavity walls. This temperature can be reached, *e.g.*, by direct heating with a high current applied along the tubus or by bombardement with high-energy electrons. Stepwise resonance ionization and ionization is performed with two to four lasers. At ISOLDE, the RILIS (resonance ionization laser ion source) is by now required for more than 75% of all beamtimes. The advantage of RIS compared to surface or plasma ionization is the elemental selectivity that is provided since the ionization scheme is unique to a single element. Hence, isobaric contaminations can be suppressed. However, one still might have to cope with isobars that are easily surface ionized, *e.g.*, alkaline elements. The frequency bandwidth of pulsed lasers is well adapted to the Doppler linewidth of atomic transitions in a hot cavity since it is usually on the order of a few GHz as long as no special measures are taken to further reduce it.

The resonant interaction of the lasers with the atoms inside the cavity can also be used for spectroscopy. In this case, one of the resonant lasers is scanned across the resonance transition and the production rate is measured as a funtion of the laser frequency. Similar as discussed above for CRIS, the detection can be combined with decay spectroscopy to avoid also non-resonant ionization background in the detection by gating to a specific decay branch. In-source RIS is the most sensitive technique for on-line laser spectroscopy at ISOL facilities and has been applied to isotopes with production rates down to 0.01 atoms/s [67].

4˙7. *Gas-cell resonance ionization spectroscopy: Studying superheavy elements.* – Resonance ionization spectroscopy can also be applied in a buffer gas cell. This is particularly useful to address species that are created in flight and stopped in a gas cell. This method was developed at KU Leuven [22] and has been regularly used at the Leuven Isotope Separator On-Line (LISOL) facility at Louvain-La-Neuve (Belgium). More recently, it was implemented at the IGISOL facility (Finland) [23] and in RIKEN (Japan). The application of this technique for studies of the heaviest elements was developed at Mainz University [71, 72] and has lead recently to the first studies of the superheavy element nobelium (No) at the GSI Helmholtz Centre at Darmstadt [73]. Here, the isotope ^{254}No was produced in a fusion-evaporation reaction ($^{48}\mathrm{Ca} + {}^{208}\mathrm{Pb} \rightarrow {}^{254}\mathrm{No} + 3\mathrm{n}$). The fusion products, emerging from the thin ^{208}Pb target, were separated in-flight from the intense ^{48}Ca primary beam by the Separator for Heavy Ion reaction Products (SHIP). In the focal plane of SHIP a buffer-gas stopping cell was located, in which approximately 4 ions per second were stopped. After thermalization, the ions were dragged with electric fields to a tantalum catcher filament, for neutralization and accumulation over a period of 25 s. Afterwards, the incoming flux of ^{254}No was turned off for 5 s to perform laser spectroscopy. During this period the adsorbed nobelium atoms were evaporated from the filament by briefly heating it to a temperature of about 1350 K and firing the lasers for resonance ionization. The first laser was supposed to resonantly excite the nobelium atoms in the $5f^{14}7s^2\,{}^1S_0$ atomic ground state to the $5f^{14}7s7p\,{}^1P_1$ state. The second laser further excited the electron into the continuum beyond the ionization potential. Ions produced by this process are subsequently guided by electrostatic fields to a silicon detector where the characteristic α decay of ^{254}No was detected.

The inherent limited spectral resolution of in-gas cell laser ionization spectroscopy because of pressure and Doppler broadening (rising up to a few GHz), can be reduced by an order of magnitude using in-gas jet laser ionization spectroscopy [74]. In this method, the radioactive atoms are embedded in a homogeneous, cold gas jet created by a "de Lavale" nozzle and are ionized by overlapping the laser light with the gas jet. Photo ions are subsequently captured in an RF ion guide and transported to a detection station.

It should be noted that laser spectroscopy on superheavy elements lacks information on available atomic transitions since optical spectroscopy was never before applied to such atoms. Hence, the experiments are based on level-scheme predictions from theoretical atomic physics, applied to systems with more than 100 bound electrons. Large wavelength regions must therefore be covered in such experiments for the search of adequate

transitions. Once a resonance transition is located, the wavelength of the ionization laser can be varied to determine the ionization potential of the species, another important fundamental quantity for an element and its physical behavior. Once such a transition is identified, it can then be used to study other isotopes of this element to extract spins, charge radii, magnetic dipole moments and spectroscopic quadrupole moments.

5. – Summary

The determination of nuclear ground-state properties along isotopic chains from laser spectroscopy is meanwhile indispensable in nuclear physics research with radioactive beams. The success of this method can best be seen by the fact that almost all radioactive beam facilities in the world have now an active or planned program for laser spectroscopy, including all future facilities. Despite the tremendous progress made in this field over the past decades, large unexplored regions still remain in the nuclear chart that have not yet been investigated with laser spectroscopy partly because of a lack of accessible transitions/wavelengths or a lack of yield and there is always the quest for higher sensitivity and efficiency in order to reach more and more exotic species which are produced in less and less quantities.

* * *

The author acknowledges support from the German Federal Ministry for Education and Research (BMBF), the German Research Foundation (DFG) and the Helmholtz International Centre for FAIR (HIC for FAIR). He is also grateful to all colleagues with whom he had productive collaborations for many years. Special thanks to Dr. R. Sánchez, GSI, for preparing figures.

REFERENCES

[1] Kopfermann H., *Nuclear Moments* (Academic Press Inc, New York) 1958.
[2] Kaufman S., *Opt. Commun.*, **17** (1976) 309.
[3] Nieminen A. *et al.*, *Phys. Rev. Lett.*, **88** (2002) 094801.
[4] Marinova K. *et al.*, *Phys. Rev. C*, **84** (2011) 034313.
[5] `http://www.ikp.tu-darmstadt.de/gruppen_ikp/ag_noertershaeuser/research_wn/exotic_nuclei_wn/uebersicht_2/laserspectroscopy_survey.de.jsp`
[6] Campbell P., Moore I. and Pearson M., *Prog. Part. Nucl. Phys.*, **86** (2016) 127.
[7] Blaum K., Dilling J. and Nörtershäuser W., *Phys. Scr.*, **T152** (2013) 014017.
[8] Cheal B. and Flanagan K. T., *J. Phys. G*, **37** (2010) 113101.
[9] Bushaw B. A., Nörtershäuer W., Ewald G., Dax A. and Drake G. W. F., *Phys. Rev. Lett.*, **91** (2003) 043004.
[10] Bushaw B. A. and Nörtershäuer W., *Spectrochim. Acta B*, **55** (2000) 1679.
[11] Cocolios T. E. *et al.*, *Phys. Rev. Lett.*, **106** (2011) 052503.
[12] Otten E. W., *Nuclear radii and moments of unstable isotopes*, in *Treatise on Heavy-Ion Science*, edited by Bromley D. A. (Plenum, New York) 1989, pp. 517–638.
[13] Klose A. *et al.*, *Nucl. Instrum. Methods Phys. Res. A*, **678** (2012) 114.
[14] Alkhazov G. D. *et al.*, *JETP Lett.*, **37** (1983) 274.

[15] FEDOSEYEV V. N. *et al.*, *Opt. Commun.*, **52** (1984) 24.
[16] KLUGE H. J., AMES F., RUSTER W. and WALLMEROTH K., in *Proceedings of the Accelerated Radioactive Beams Workshop* 1985, Parksville, Canada.
[17] ANDREEV S. V., MISHIN V. I. and LETOKHOV V. S., *Opt. Commun.*, **57** (1986) 317.
[18] ALKHAZOV G. D., BERLOVICH E. Y. and PANTELEYEV V. N., *Nucl. Instrum. Methods Phys. Res. A*, **280** (1989) 141.
[19] MARSH B. A. *et al.*, *Hyperf. Interact.*, **196** (2010) 129.
[20] VAN DUPPEN P. *et al.*, *Hyperf. Interact.*, **74** (1992) 193.
[21] VERMEEREN L. *et al.*, *Phys. Rev. Lett.*, **73** (1994) 1935.
[22] KUDRYAVTSEV Y. *et al.*, *Nucl. Instrum. Methods Phys. Res. B*, **114** (1996) 350.
[23] MOORE I. D. *et al.*, *Nucl. Instrum. Methods Phys. Res. B*, **268** (2010) 657.
[24] WADA M. *et al.*, *Hyperf. Interact.*, **196** (2010) 43.
[25] SCHULZ C. *et al.*, *J. Phys. B*, **24** (1991) 4831.
[26] PROCTER T. J. *et al.*, *J. Phys. Conf. Ser.*, **381** (2012) 012070.
[27] LYNCH K. M. *et al.*, *J. Phys. Conf. Ser.*, **381** (2012) 012071.
[28] LAUTH W. *et al.*, *Phys. Rev. Lett.*, **68** (1992) 1675.
[29] SAUVAGE J. *et al.*, *Hyperf. Interact.*, **129** (2000) 303.
[30] FEDOSSEEV N., KUDRYAVTSEV YU. and MISHIN V. I., *Phys. Scripta*, **85** (2005) 058104.
[31] WENDT K. *et al.*, *Fresenius J. Anal. Chem.*, **364** (1999) 471.
[32] LU Z.-T. and WENDT K., *Rev. Sci. Instrum.*, **74** (2003) 1169.
[33] KRIEGER A. *et al.*, *Appl. Phys. B*, **123** (2017) 15.
[34] YAN Z.-C. and DRAKE G. W. F., *Phys. Rev. A*, **61** (2000) 022504.
[35] PUCHALSKI M. and PACHUCKI K., *Phys. Rev. A*, **78** (2008) 052511.
[36] YAN Z.-C., NÖRTERSHÄUSER W. and DRAKE G. W. F., *Phys. Rev. Lett.*, **100** (2008) 243002.
[37] NEUGART R. *et al.*, *J. Phys. G*, **44** (2017) 064002.
[38] JANSEN J., PEERDEMAN R. and VRIES C. D., *Nucl. Phys. A*, **188** (1972) 337.
[39] NÖRTERSHÄUSER W. *et al.*, *Phys. Rev. Lett.*, **102** (2009) 062503.
[40] ŽÁKOVÁ M. *et al.*, *J. Phys. G*, **37** (2010) 055107.
[41] KRIEGER A. *et al.*, *Phys. Rev. Lett.*, **108** (2012) 142501.
[42] THIBAULT C. *et al.*, *Phys. Rev. C*, **12** (1975) 644.
[43] MOTOBAYASH T. *et al.*, *Phys. Lett. B*, **346** (1995) 9.
[44] HUBER G. *et al.*, *Phys. Rev. C*, **18** (1978) 2342.
[45] YORDANOV D., *From ^{27}Mg to ^{33}Mg: transition to the Island of inversion*, Dissertation, 2007, KU Leuven.
[46] NEUGART R. *et al.*, *Phys. Rev. Lett.*, **101** (2008) 132502.
[47] NEYENS G. *et al.*, *Phys. Rev. Lett.*, **94** (2005) 022501.
[48] MARÉCHAL F. *et al.*, *Phys. Rev. C*, **72** (2005) 044314.
[49] YORDANOV D. T. *et al.*, *Phys. Rev. Lett.*, **99** (2007) 212501.
[50] YORDANOV D. T. *et al.*, *Phys. Rev. Lett.*, **104** (2010) 129201.
[51] KOWALSKA M. *et al.*, *Phys. Rev. C*, **77** (2008) 034307.
[52] YORDANOV D. T. *et al.*, *Phys. Rev. Lett.*, **108** (2012) 042504.
[53] HUCK A. *et al.*, *Phys. Rev. C*, **31** (1985) 2226.
[54] JANSSENS R. *et al.*, *Phys. Lett. B*, **546** (2002) 55.
[55] FORNAL B. *et al.*, *Phys. Rev. C*, **70** (2004) 064304.
[56] GADE A. *et al.*, *Phys. Rev. C*, **74** (2006) 021302.
[57] WIENHOLTZ F. *et al.*, *Nature*, **498** (2013) 346.
[58] FRÅNBERG H. *et al.*, *Nucl. Instrum. Methods Phys. Res. B*, **266** (2008) 4502.
[59] GARCIA RUIZ R. F. *et al.*, *Nat. Phys.*, **12** (2016) 594.
[60] GARCIA RUIZ R. F. *et al.*, *Phys. Rev. C*, **91** (2015) 041304.

[61] Atanasov D. *et al.*, *Phys. Rev. Lett.*, **115** (2015) 232501.
[62] Yordanov D. T. *et al.*, *Phys. Rev. Lett.*, **110** (2013) 192501.
[63] Yordanov D. T. *et al.*, *Phys. Rev. Lett.*, **116** (2016) 032501.
[64] Flanagan K. T., PhD Thesis, University of Manchester, UK, 2004.
[65] Campbell P. *et al.*, *Eur. Phys. J. A*, **15** (2002) 45.
[66] Marsh B. *et al.*, *Nucl. Instrum. Methods Phys. Res. B*, **317** (2013) 550.
[67] Seliverstov M. D. *et al.*, *Phys. Lett. B*, **719** (2013) 362.
[68] Rajabali M. *et al.*, *Nucl. Instrum. Methods Phys. Res. A*, **707** (2013) 35.
[69] Lynch K. M. *et al.*, *Phys. Rev. X*, **4** (2014) 011055.
[70] Uusitalo J. *et al.*, *Phys. Rev. C*, **71** (2005) 024306.
[71] Backe H. *et al.*, *Nucl. Instrum. Methods Phys. Res. B*, **126** (1997) 406.
[72] Backe H. *et al.*, *Eur. Phys. J. D*, **45** (2007) 99.
[73] Laatiaoui M. *et al.*, *Nature*, **538** (2016) 495.
[74] Ferrer R. *et al.*, *Nat. Commun.*, **8** (2017) 14520.

This page intentionally left blank

Session on the occasion of the 90th birthday of Prof. Renato Angelo Ricci celebrating his fundamental and seminal contributions and achievements in the field of nuclear physics during the last 65 years.

Proceedings of the International School of Physics "Enrico Fermi"
Course 201 "Nuclear Physics with Stable and Radioactive Ion Beams", edited by F. Gramegna,
P. Van Duppen, A. Vitturi and S. Pirrone
(IOS, Amsterdam; SIF, Bologna) 2019
DOI 10.3254/978-1-61499-957-7-327

The electric dipole excitation in nuclei: From zero to finite temperature

Angela Bracco(*)

Dipartimento di Fisica, Università di Milano - Milano, Italy

INFN, Sezione di Milano - Milano, Italy

Summary. — The gamma decay of the giant dipole resonance (including its low-energy tail region) is an important tool to probe the properties of these states, and thus to test in detail the existing predictions. This paper focuses on two main aspects concerning the electric dipole excitation in nuclei. One is the study of the isospin character of the low-energy tail of the Giant Dipole Resonance (GDR), the so-called pygmy resonance, and the other is the isospin mixing of nuclear systems at finite temperature. In the first case, the pygmy resonance was populated using the inelastic-scattering reaction induced by ^{17}O beams at 20 MeV/u. Comparison is made with data obtained with $(\alpha, \alpha'\gamma)$ and (γ, γ') reactions. In the second case, the gamma decay of the GDR in thermalized nuclear systems, formed in fusion-evaporation reactions, was used to investigate the isospin mixing in ^{80}Zr. For this work the reactions ^{40}Ca + ^{40}Ca at 3.4 MeV/u and ^{37}Cl + ^{44}Ca at 2.6 MeV/u were employed.

(*) E-mail: angela.bracco@mi.infn.it

1. – Introduction

The gamma decay of the high-lying electric dipole states up to the region of the giant dipole resonance is an important tool to address relevant questions related to nuclear collectivity and isospin effects.

This paper focuses on results of experiments addressing two different specific problems. The first is the isospin character of the low-lying part of the dipole response, commonly denoted as the pygmy resonance, due to the much smaller size of its strength in comparison with the Giant Dipole Resonance (GDR). In recent years, experimental and theoretical investigations, on both stable and radioactive nuclei, revealed that the presence of the pygmy resonance is a common phenomenon in a large number of atomic nuclei (see refs. [1] and [17] for a review). The hydrodynamical model describes this pygmy strength as associated to the vibration of the neutron skin. Details of the dipole strength distribution of the nuclei involved in the r-process will play a role and influence the abundance pattern [2].

The second topic concerns the investigation of isospin mixing at finite temperature by measuring the gamma decay of the GDR excitation. The $E1$ decay from excited states of $N = Z$ nuclei is forbidden by the isospin selection rules. Because of the small size of the isospin mixing responsible of $E1$ decay, the best case to study isospin effects is the de-excitation of the GDR where most of the strength is concentrated. Here the isospin mixing is studied at finite temperature using fusion-evaporation reactions. The temperature dependence of the isospin mixing was obtained and the zero-temperature value was then deduced. The isospin-symmetry-breaking correction used for the Fermi superallowed transitions was extracted and found to be consistent with β-decay data.

2. – Pygmy states populated with inelastic scattering of isoscalar probes

Although the general properties of the Giant Dipole Resonance (GDR) have been extensively studied during the past decades there is presently great attention to the electric dipole response in the region around the particle binding energy ($< 10\,\mathrm{MeV}$). In that region an additional concentration of $E1$ strength exceeding the Lorentzian shape of the GDR was identified in many nuclei, particularly the neutron rich ones. This $E1$ strength is denoted as Pygmy Dipole Resonance (PDR) and within the hydrodynamical model is described as due to oscillations of neutrons forming a skin outside a core made out of the other neutrons and protons occupying the same nuclear orbitals.

The study of the PDR is very interesting because this excitation mode affects considerably the reaction rates in astrophysical scenarios, where photodisintegration reactions are important [2]. In addition, the precise knowledge of the $E1$ strength is expected to provide information on the neutron skin and thus on the symmetry energy of the equation of state (see, *e.g.*, refs. [3-9]).

A key question concerning pygmy states is the understanding of their nature and for that one needs to excite them not only with the Coulomb field but also using the nuclear

interaction of isoscaler and isovector types. While in the isovector oscillation proton and neutrons moves out of phase, the isoscalar strength of dipole type, the Isoscalar Giant Dipole Resonance (ISGDR) is due to a squeezing mode in the nucleus. This paper focuses on the isospin character of pygmy states and discusses selected experimental and theoretical results related to this aspect.

The use of inelastic scattering of light and medium heavy ions at bombarding energy in the interval 20–35 MeV/u is a good tool to be employed to understand the nature of nuclear collective excitations. In addition, if one measures the subsequent gamma decay it is possible to select states of 2^+ and 1^- since the gamma transitions of $E1$ and $E2$ types are the dominant ones.

The existing studies for the excitation of pygmy states via the reactions $(\alpha, \alpha'\gamma)$ at 35 MeV/u and $(^{17}\mathrm{O},^{17}\mathrm{O}'\gamma)$ at 20 MeV/u [10-21] have provided valuable information on the nature of the discrete 1^- states. An interesting feature of the pygmy states has been observed by comparing results of photon-scattering and ^{17}O scattering experiments. In particular, it has been found that one group of states is excited in both types of reactions, while another group of states at higher energies is only excited in the (γ, γ) case.

The comparison of the measured cross sections with (γ, γ') and $(\alpha, \alpha'\gamma)$ and $(^{17}\mathrm{O},^{17}\mathrm{O}'\gamma)$ results for the ^{124}Sn and ^{140}Ce nuclei are shown in figs. 1 and 2. In the experiments using the $(^{17}\mathrm{O},^{17}\mathrm{O}'\gamma)$ reaction the detection of gamma rays was performed with the AGATA (Advanced Gamma Tracking Array) Demonstrator. At the time of these experiments the AGATA Demonstrator [25-27] consisted of three to five triple clusters of HPGe detectors and was placed 13.5 cm from the target covering an angular range in theta from 100° to 150° (relative to the beam direction). The segmentation of the HPGe detectors allowed the direction of the gamma-ray emission to be determined with a precision of 1 degree. The AGATA detection efficiency was deduced from measurements with radioactive γ-ray sources and by simulations including the geometrical configuration of these particular experiments. A system of telescopes of Si detectors was used for the identification and measurement of the kinetic energy of the scattered ions [24].

In the case of ^{124}Sn data, for each 100 keV bin two cross sections are shown in fig. 1: one corresponding to the counts in the known discrete peaks (full coloured bars) and the other to the total measured counts denoted as unresolved strength (dashed grey bars). From these figures one sees clearly the presence of the splitting of the PDR states in two regions. The low-lying part of the $E1$ strength appears to be characterised by isoscalar transition densities that are peaked on the surface which lead to an enhancement in the isoscalar $E1$ response, while the higher-lying states can be interpreted as transitions towards the GDR and, thus, are suppressed in the isoscalar channel [16].

The splitting of the PDR region becomes even more evident if we integrate the strength in the discrete peaks into two regions, 5–7 and 7–9 MeV (insets of fig. 1). From here one sees clearly that the strengths in the two regions measured in the (γ, γ') experiment are almost equal while this is not the case for $(^{17}\mathrm{O},^{17}\mathrm{O}'\gamma)$ and $(\alpha, \alpha'\gamma)$ experiments. The small relative difference between $(\alpha, \alpha'\gamma)$ and $(^{17}\mathrm{O},^{17}\mathrm{O}'\gamma)$ in the population cross sections of some states might be related to the nature of these states and to the different Coulomb and nuclear contributions of the used reactions.

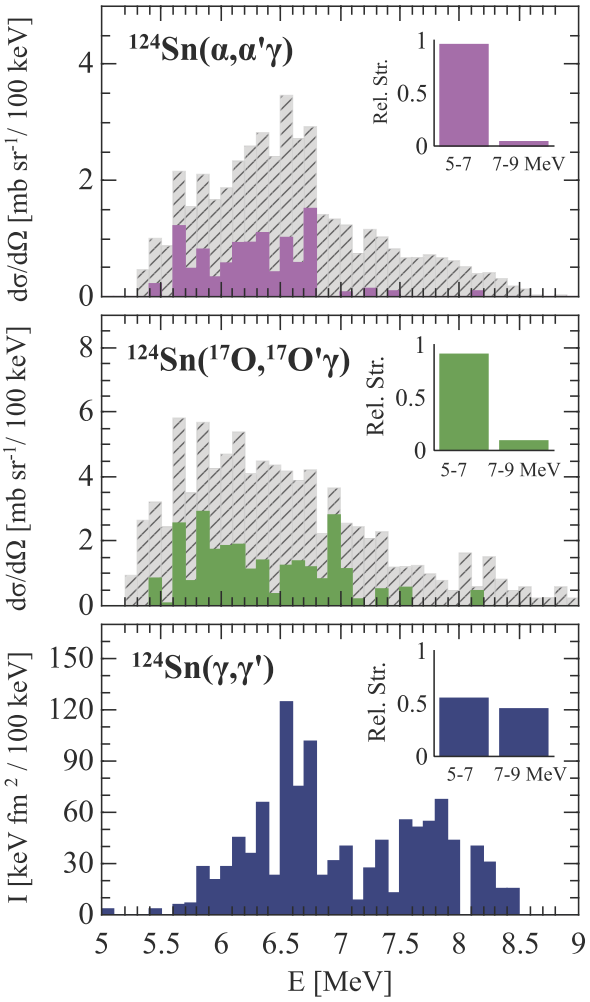

Fig. 1. – Differential cross sections measured in ^{124}Sn(^{17}O,^{17}O$'\gamma$) experiment, in bins of 100 keV (central panel). The unresolved strength, corresponding to the total binned counts in the measured spectra, is depicted in grey. For comparison, the strengths measured in α-scattering (top panel) [16] and photon-scattering (bottom panel) [23] are reported. In each panel, the inset gives the relative intensity corresponding to the measured cross sections in the discrete lines integrated in two regions (5–7 and 7–9 MeV). Adapted from [19].

These experimental findings are in qualitative agreement with different phonon models, which predict a low-lying isoscalar component dominated by neutron-skin oscillations and a higher-lying group of states with a stronger isovector character associated to the tail of the giant dipole resonance.

Predictions obtained using the form factors based on microscopic calculations of the transition densities are shown in comparison with the data in fig. 3 (red solid lines).

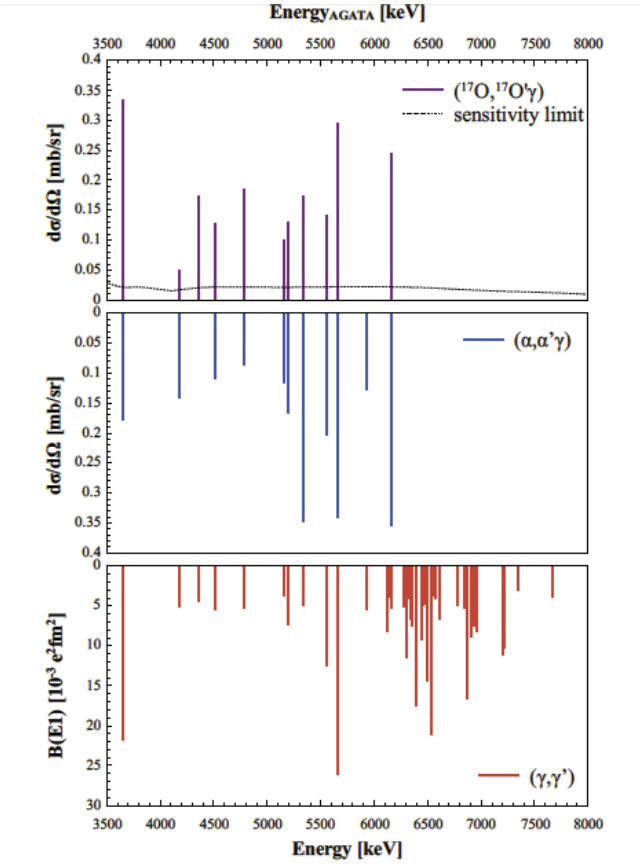

Fig. 2. – Differential cross sections measured in ^{140}Ce(^{17}O,^{17} O′γ) experiment (top panel). For comparison, the strengths measured in α-scattering (central panel) [15] and photon-scattering (bottom panel) [22] are reported. Adapted from [20].

The calculation of the cross section was made using the Distorted Wave Born Approximation (DWBA) including the microscopic form factor. The form factor was obtained with the double folding method using the M3Y nucleon-nucleon interaction [28, 29]. As expected for these states, the dominant contribution to the form factor comes from the isoscalar part of the nucleon-nucleon interaction component. The form factor calculation uses as input the proton and neutron transition densities. The latter were obtained using the fully consistent relativistic quasiparticle random phase approximation (RQRPA) model [30]. They are shown in the bottom panel of fig. 3. To be noted that these transition densities show the typical features of the PDR states: neutron and proton transition densities are in phase in the interior and there is a strong surface contribution due only to neutrons.

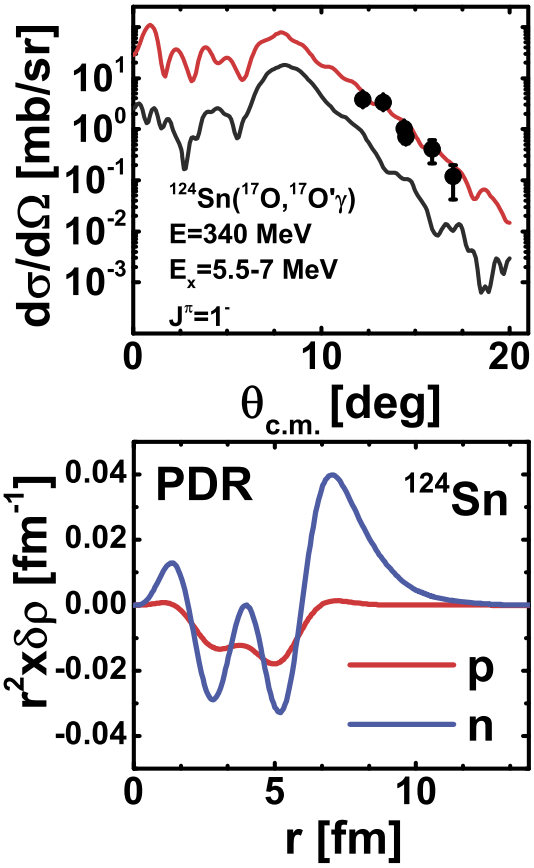

Fig. 3. – Top: Inelastic scattering cross section ^{124}Sn(^{17}O,^{17} O′γ)^{124}Sn* at 340 MeV for the 1^{-} states between 5.5 and 7 MeV. The error bars are the statistical errors. The lines show DWBA calculations. The black solid curve represents the calculations with the standard phenomenological form factor. The red solid line includes the nuclear contribution calculated with the microscopic form factor derived using the transition density shown in the bottom panel. Adapted from [19].

The calculations were fitted to the data to extract the value of the Isoscaler Energy Weighted Sum Rule (ISEWSR) strength. In particular, it has been assumed that the cross section is a sum of two parts, one being the Coulomb and the other the nuclear (isoscalar) contribution. For the Coulomb contribution we fixed the value corresponding to the known $B(E1)$ measurements. For the nuclear contribution to fit the data the starting value was that associated to the microscopic form factor used corresponding to a specific fraction of the ISEWSR strength. The extracted values for ^{124}Sn of the fraction of the ISEWSR $E1$ strength is 1.5(2)%. In general the deduced values are consistent with the results for the isoscalar giant dipole resonance and they are ranging from 1 to 9% of the ISEWSR (see references for details [17] and [20]). In addition it is

E_x (MeV)	J_n^π	ISD EWSR (%)	$B(E\lambda)\uparrow$ $(e^2\,\mathrm{fm}^{2\lambda})$
4.07(4)	2_2^+		28.8 ± 6.6
5.36(5)	1_1^-	2.70(32)	$3.57(20) \times 10^{-2}$
5.62(5)	(3^-)		$1.19(10) \times 10^{3}$
6.84(7)	1_2^-	0.67(12)	$3.79(26) \times 10^{-2}$

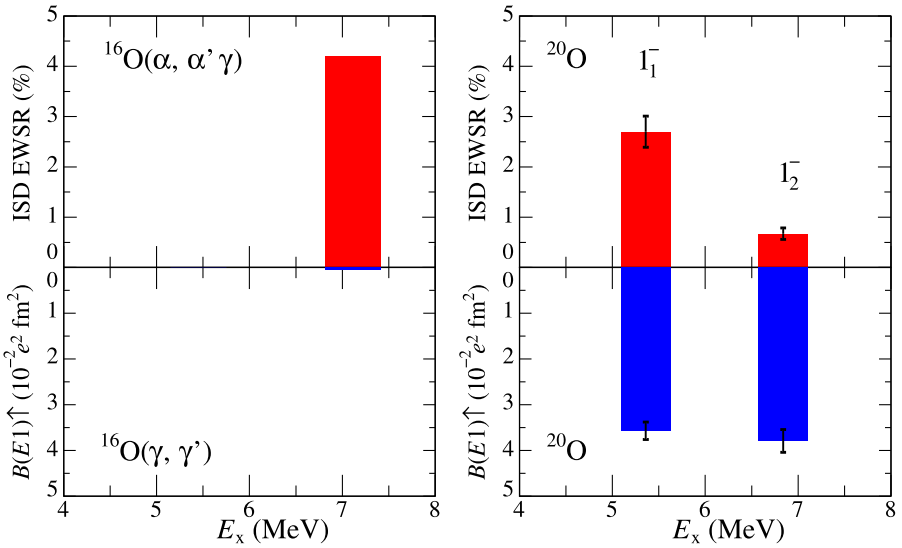

Fig. 4. – Measured ISD EWSR (top) and $B(E1)\uparrow$ (bottom) strength in ^{20}O (right panel), in comparison with ^{16}O (left panel). The top table gives the properties of known states in ^{20}O. Adapted from [33].

worth noticing that the good reproduction of the data with these calculations, shown in fig. 3, supports the picture that these pygmy states are excitation of the neutron skin. Also for light neutron nuclei it is interesting to investigate the isospin character of the low-energy dipole excitations because there, with only few nucleons at work, the nature of the excitation could be different and not so much related to colletive effects. Recently the gamma decay from states in ^{20}O, populated selectively via Coulomb and nuclear exitation, was investigated [33]. The ^{20}O nucleus has four neutrons added on the doubly magic core of ^{16}O which are expected to be involved in the its excitation. In addition, this nucleus is known to have significantly strong dipole excitations at energies below the neutron threshold [34, 35]. Measuring the isoscalar dipole strength of these states is particularly imporant, since several theories based on collective models [36, 37] predict that these states have strong isoscalar dipole strength [37].

The experiment to study $E1$ strength in ^{20}O was performed at the Radioactive Isotope Beam Factory (RIBF) of the Nishina Center of RIKEN [31]. A ^{48}Ca primary beam was accelerated at 345 MeV/A with an average intensity of 250 pnA. A secondary ^{20}O beam

impinged on two different reaction targets, a gold target and liquid-helium target. Decay γ-rays from the reaction products were detected by a large-volume LaBr3:Ce scintillator array located at a laboratory angle of 30°.

The isoscaler dipole EWSR fractions and $B(E1)\uparrow$ strengths deduced from the data of ^{20}O are plotted in fig. 4 (right panel), along with the ^{16}O values (left panel) in the same energy region. The ^{16}O ISD EWSR fraction is from ref. [38] and the $B(E1)\uparrow$ strength is from ref. [39]. There is a significant difference in $B(E1)\uparrow$ strength between ^{16}O, the doubly magic nucleus in the oxygen chain, and ^{20}O.

The $B(E1)\uparrow$ strength integral over the two states is increased from $0.492\times10^{-2}\,\mathrm{e^2fm^2}$ in ^{16}O to $7.36(33)\times10^{-2}\,\mathrm{e^2fm^2}$ in ^{20}O. More interestingly, the integrated ISD EWSR fraction does not show much variation: 4.2% in ^{16}O and 3.37(34)% in ^{20}O. In the case of ^{16}O, because it is $N = Z$, the isovector dipole strength is strongly suppressed. This explains the almost purely isoscalar nature of the state referred to as the macroscopic squeezing mode [38], but the present results indicate that low-energy dipole excitations in ^{20}O exhibit a dual character, suggesting that these states have different underlying structures.

A new set of data for several stable nuclei from experiments recently performed at RCNP Osaka is presently being analysed. These experiments used beams of alpha particles and protons, at bombarding energy of 130 MeV and 80 MeV, respectively. The high-resolution spectrometer Grand Raiden (GR) was used coupled to the CAGRA array consisting of 12 clover HpGe detectors and with four LaBr3:Ce scintillators (crystal dimensions 3.5×8) of the HECTOR$^+$ array [32]. With these new data, we can search for difference in the excitation pattern for proton and alpha and we also expect to be able to determine the small branching to excited states and thus to provide more stringent tests to theory.

3. – Isospin mixing at finite temperature in the proton-rich ^{80}Zr

The question of isospin impurity in nuclei has been a long-standing open problem in nuclear physics. In particular the knowledge of the isospin impurity is interesting in connection with the properties of the Isobaric Analog States (IAS) and for the Fermi decay of the $N \approx Z$ nuclei near the proton drip line.

Moreover the isospin impurity on the beta decay has implications in the Fermi transition rates and thus on the Cabibbo-Kobayashi-Maskawa matrix. In the case of the IAS states it is known that they have a narrow width originating from Coulomb interaction coupling these states to the continuum. In general the breaking of isospin symmetry can be observed by decays, which would be forbidden by the selection rules if isospin mixing were not to occur. This is the case of the $E1$ decay from self-conjugate nuclei. To fully exploit this property of the $E1$ decay one can explore the region of the Giant Dipole Resonance (GDR) where the maximum strength of the $E1$ transitions is concentrated. Indeed this approach was employed for the $E1$ decay of the GDR in nuclei at finite temperature T, formed in fusion-evaporation reactions.

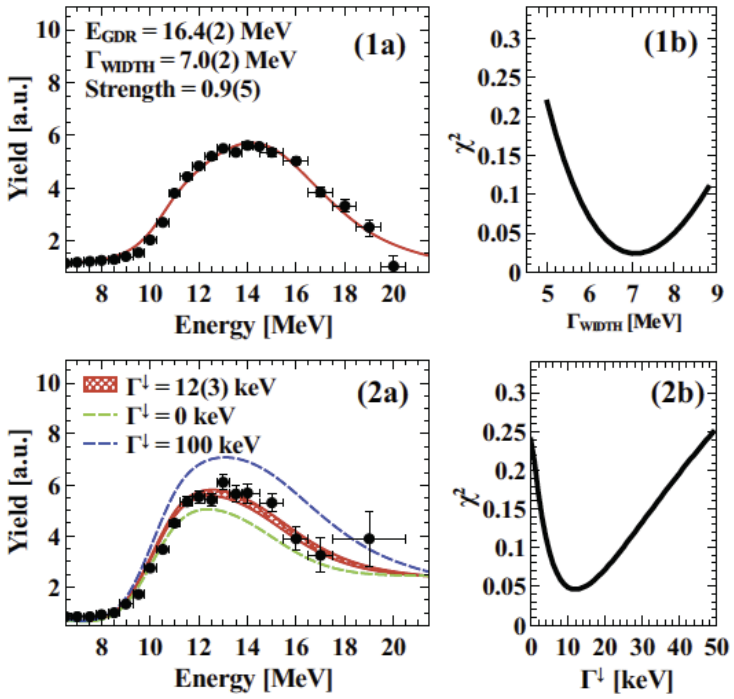

Fig. 5. – Linearized measured and calculated γ-ray spectra for $^{37}\mathrm{Cl} + {}^{44}\mathrm{Ca}$ (1a) and for $^{40}\mathrm{Ca} + {}^{40}\mathrm{Ca}$ (2a) in the GDR region. In (2a) the statistical-model calculations are shown corresponding to different values of the Coulomb spreading width: $\Gamma^{\downarrow}_{>} = 12\,\mathrm{keV}$ (red line), for no mixing $\Gamma^{\downarrow}_{>} = 0\,\mathrm{keV}$ (green dashed line), and for full mixing $\Gamma^{\downarrow}_{>} = 100\,\mathrm{keV}$ (blue dashed line) Right panels: χ^2 values obtained by varying the GDR width for $^{37}\mathrm{Cl} + {}^{44}\mathrm{Ca}$ (1b) and by varying the Coulomb spreading width for $^{40}\mathrm{Ca} + {}^{40}\mathrm{Ca}$ (2b).

Self-conjugated Compound Nuclei (CN) at high excitation energy can be formed using fusion-evaporation reactions. The use of self-conjugate projectile and target ensures population of CN with isospin $I = 0$ and thus with $E1$ decay from the GDR which is hindered. In contrast, if the initial state is not pure in isospin but contains an admixture of $I = 0, 1$ states, it can decay to the more numerous final states with isospin $I = 0$. At finite temperature there is an additional effect, that of a partial restoration of the isospin symmetry. This is because the degree of mixing in a compound nucleus is limited by its finite lifetime for particle decay [42]. It is particularly interesting to investigate isospin mixing in nuclei with $N = Z$ in the mass region $A = 80$–100 because there the different model predictions give the largest discrepancies among them.

The most recent works on the isospin mixing at finite temperature were made for the hot compound nucleus $^{80}\mathrm{Zr}$ populated using the fusion reactions $^{40}\mathrm{Ca} + {}^{40}\mathrm{Ca}$ at $E_{beam} = 136, 200\,\mathrm{MeV}$. The reaction $^{37}\mathrm{Cl} + {}^{44}\mathrm{Ca}$ at $E_{beam} = 95, 153\,\mathrm{MeV}$ was also measured in the same set-up to have a reference for the gamma-ray emission from the

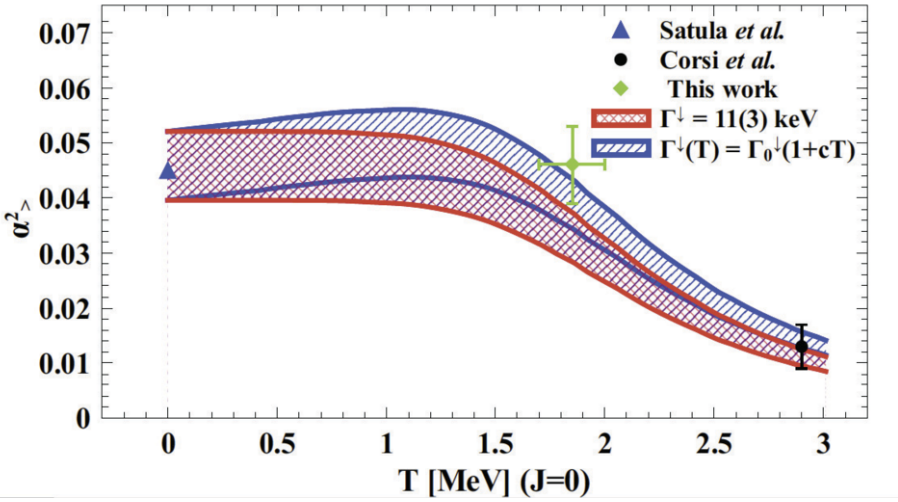

Fig. 6. – The isospin mixing $\alpha^2_>$ as a function of T obtained with the procedure of [42] corresponding to $\Gamma^\downarrow = 11 \pm 2.1$ keV (red region), constant with T. For the blue band $\Gamma^\downarrow$ was assumed to vary mildly and linearly with T (see text). The blue triangle is the theoretical value at $T = 0$ from [49], the green circle is the datum from [40], the black diamond is the datum from [41].

GDR for a nucleus with the same excitation condition but without isospin hinderance. The statistical-model analysis of the measured spectra provided the value of the isospin mixing. More details can be found in refs. [40] and [41].

To show the importance of measuring a reference reaction in the same experimental conditions used for the measurement of the reaction in which the isospin mixing effects are expected to show up, one should examine fig. 5 that refers to the data obtained with the reactions ^{40}Ca + ^{80}Ca at $E_{beam} = 200$ MeV and ^{37}Cl + ^{44}Ca at $E_{beam} = 153$ MeV. In this figure one can see the details of the comparison between data and calculations. These quantities are shown in a linear scale following the linearization procedure which is usually applied in the study of the GDR in hot nuclei. Statistical-model calculations made without isospin mixing ($\Gamma^\downarrow_> = 0$ keV), with the value of $\Gamma^\downarrow_> = 10$ keV yielding the best fit and with a large mixing ($\Gamma^\downarrow_> = 100$ keV) are compared.

With the result obtained for the isospin mixing at finite temperature, the value at zero temperature was derived using the model of [42], which describes the variation of the mixing probability with T. The isospin mixing probability for a nucleus at finite temperature is defined as

$$\alpha^2_>(T) = \frac{1}{I_0 + 1} \frac{\Gamma^\downarrow_{IAS}}{\Gamma_{CN}(T) + \Gamma_{IVM}(IAS)}, \tag{1}$$

where $\Gamma^\downarrow_{IAS}$ is the Coulomb spreading width of the IAS, to be considered equal to $\Gamma^\downarrow_>$, $\Gamma_{IVM}(IAS)$ is the width of the Isovector Monopole Resonance (IVM) at the excitation

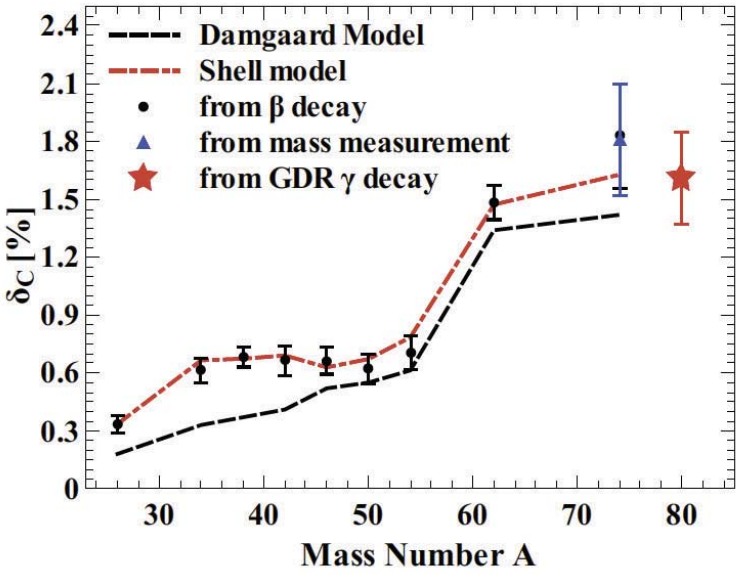

Fig. 7. – The isospin mixing correction δ_C as a function of the nuclear mass number A. The dashed black line is the prediction from the Damgaard model [46], while the red line is a shell model with Saxon-Woods radial wave function prediction [47]. Black circles are the experimental points extracted from β decay as reported in [44], the blue triangle is obtained using a new Q *value* of ^{74}Ru β decay deduced from mass measurements [45]. The red star is the value of δ_C reported in [41]. Adapted from [41].

energy of the IAS, which is expected to be constant with T. According to the systematics for the present case one has $\Gamma_{IVM}(IAS) = 240\,\text{keV}$ [40,42,48]. $\Gamma_{CN}(T)$ is the CN decay width increasing with temperature.

In fig. 6 the values of $\alpha^2_>$ calculated using eq. (1) are shown as a function of T. The red line is obtained with a value of $\Gamma^\downarrow_> = 11 \pm 2.1\,\text{keV}$, corresponding to the average of the two experimental values (the lower and upper curves corresponding to 8.9 and 13.1 keV, respectively). This calculation gives at $T = 0$ $\alpha^2_> = 4.6\% \pm 0.9\%$, in rather good agreement with the prediction shown with the blue triangle from [49]. Following the discussion in [42], we also considered a weak linear dependence on T of the Coulomb spreading width given by $\Gamma^\downarrow_>(T) = \Gamma^\downarrow_>(1 + cT)$. In this expression the chosen slope parameter $c = 0.1\,\text{MeV}^{-1}$ is such that the value of $\Gamma^\downarrow_>$ stays within the experimental error bar. The blue band in fig. 6 displays the dependence of $\alpha^2_>$ with T when such weak dependence of $\Gamma^\downarrow_>$ is considered (the limiting curves correspond to 8.9 and 13.1 keV). We performed also two calculations using $\Gamma^\downarrow_> = 11\,\text{keV}$ and $\Gamma_{IVM}(IAS) = 220$ and 260 keV and found that these two curves are well within the two colored bands of fig. 6.

It is very interesting to connect the isospin mixing parameter $\alpha^2_>$ with the isospin-correction term δ_C. As reported in ref. [43] the quantity δ_C is defined as

$$\delta_C = 4(I+1)\frac{V_1}{41\xi A^{2/3}}\alpha^2, \tag{2}$$

where $V_1 = 100\,\mathrm{MeV}$ and $\xi = 3$, while α^2 is the isospin impurity in the ground state and I is the isospin of the nucleus.

Using eq. (2) the value $\delta_C = 0.81(16)\%$ was obtained for ^{80}Zr. This value is shown in fig. 7 with the red star. In this figure the dashed black line is the prediction from the Damgaard model [46], while the red line is a shell model with Saxon-Woods radial wave function prediction [47]. Black circles are the experimental points extracted form the β decay as reported in [44], the blue triangle is the value reported using a new Q value of ^{74}Rb β decay deduced from mass measurements [45]. It is important to note that the quantity $\delta_C/I + 1$ is plotted in fig. 7 since β-decay measurements are for $I = 1$ nuclei, while that for ^{80}Zr is $I = 0$. The present result is consistent (within the error bars) with data for ^{74}Rb and the trend of predictions is also in agreement with the present new point. No calculations of the type of [44] are available for $A = 80$ and the δ_C data for ^{74}Rb are the only existing ones close to $N = Z = 40$.

The temperature dependence of the isospin mixing was obtained for the heaviest $N = Z$ nucleus that could be formed so far with fusion reactions with stable nuclei. The zero temperature value was deduced and provides a stringent test to theory. The isospin correction term used in the β-decay analysis was also extracted for the first time for $A = 80$ and found to be consistent with systematics from β-decay and mass measurements. This result supports the validity of the method based on the GDR at finite temperature to obtain the value of the isospin mixing in regions of Z not directly accessible at zero temperature.

4. – Concluding remarks

Progress has been made in the study of the nature of 1^- states and at around the neutron binding energy. This information is attracting interest to test models based on the Energy Density Functional used also for astrophysical applications such as those for neutron stars. High-resolution experiments using both hadron and electromagnetic probes are found to be key tools to understand the isospin character of the pygmy states. Interesting conclusions were obtained by comparing different results. Isoscalar strengths in general lower than 10% of the corresponding value of the ISGDR at 20–30 MeV were deduced from the analysis of the hadron data with the distorted-wave Born approximation approach.

More data are necessary to probe in detail the shape of the transition density and to deduce the mixing among the isoscalar and isovector components. In particular the study of isoscalar pygmy states in deformed nuclei, not yet performed, appears very interesting. The overall picture obtained from the available results supports the interpretation of the low-lying pygmy states as due to the excitation of the neutron skin.

In the future, it will be important to address open problems for stable nuclei and to search for 1^- states, with their isoscalar and isovector components, in nuclei far from

stability. For stable nuclei the transition between the PDR and GDR regime should be understood and information on the nuclear transition density should be obtained in order to provide stringent tests to theory.

Concerning the isospin mixing future work concerns studies in other mass regions. In the case of the light ^{28}Si nucleus results from ref. [50] show that the isospin mixing deduced from the GDR work is not in very good agreement with results deduced from beta decay studies. This aspect also needs further investigations.

REFERENCES

[1] SAVRAN D. *et al.*, *Prog. Part. Nucl. Phys.*, **70** (2013) 210.
[2] GORIELY S., *Phys. Lett. B*, **436** (1998) 10.
[3] REINHARD P.-G. and NAZAREWICZ W., *Phys. Rev. C*, **81** (2010) 051303.
[4] PIEKAREWICZ J., *Phys. Rev. C*, **83** (2011) 034319.
[5] KLIMKIEWICZ A. *et al.*, *Phys. Rev. C*, **76** (2007) 051603.
[6] CARBONE A. *et al.*, *Phys. Rev. C*, **81** (2010) 041301.
[7] VRETENAR D. *et al.*, *Phys. Rev. C*, **85** (2012) 044317.
[8] LATTIMER J. M. *et al.*, *Ann. Rev. Nucl. Part. Sci.*, **62** (2012) 485.
[9] TSANG M. B. *et al.*, *Phys. Rev. C*, **86** (2012) 015803.
[10] POELHEKKEN T. D. *et al.*, *Phys. Lett. B*, **278** (1992) 423.
[11] DERYA V. *et al.*, *Phys. Lett. B*, **730** (2014) 288.
[12] DERYA V. *et al.*, *J. Phys. Conf. Ser.*, **366** (2012) 012012.
[13] ENDRES J. *et al.*, *Phys. Rev. Lett.*, **105** (2010) 212503.
[14] ENDRES J. *et al.*, *Phys. Rev. C*, **80** (2009) 034302.
[15] SAVRAN D. *et al.*, *Phys. Rev. Lett.*, **97** (2006) 172502.
[16] ENDRES J. *et al.*, *Phys. Rev. C*, **85** (2012) 064331.
[17] BRACCO A. A., CRESPI F. C. L. and LANZA E. G., *Eur. Phys. J. A*, **51** (2015) 899.
[18] CRESPI F. C. L. *et al.*, *Phys. Rev. Lett.*, **113** (2014) 012501.
[19] PELLEGRI L. *et al.*, *Phys. Lett. B*, **738** (2014) 519.
[20] KRZYSIEK M. *et al.*, *Phys. Rev. C*, **93** (2016) 044330.
[21] CRESPI F. C. L. *et al.*, *Phys. Rev. C*, **91** (2015) 024323.
[22] VOLZ S. *et al.*, *Nucl. Phys. A*, **779** (2006) 1.
[23] GOVAERT K. *et al.*, *Phys. Rev. C*, **57** (1998) 2229.
[24] MENGONI D. *et al.*, *Nucl. Instum. Methods Phys. Res. A*, **764** (2014) 241.
[25] AKKOYUN S. *et al.*, *Nucl. Instum. Methods A*, **668** (2012) 26.
[26] GADEA A. *et al.*, *Nucl. Instum. Methods A*, **654** (2011) 88.
[27] FARNEA E. *et al.*, *Nucl. Instum. Methods A*, **621** (2010) 331.
[28] LANZA E. *et al.*, *Phys. Rev. C*, **84** (2011) 064602.
[29] LANZA E. *et al.*, *Phys. Rev. C*, **89** (2014) 041601(R).
[30] LITVINOVA E. *et al.*, *Phys. Rev. C*, **78** (2008) 014312.
[31] KUBO T., *Nucl. Instrum. Methods B*, **204** (2003) 97.
[32] GIAZ A. *et al.*, *Nucl. Instrum. Methods A*, **729** (2013) 910.
[33] NAKATSUKA N. *et al.*, *Phys. Lett. B*, **768** (2017) 387.
[34] TRYGGESTAD E. *et al.*, *Phys. Lett. B*, **541** (2002) 52.
[35] TRYGGESTAD E. *et al.*, *Phys. Rev. C*, **67** (2003) 064309.
[36] CO G. *et al.*, *Phys. Rev. C*, **87** (2013) 034305.
[37] BIANCO D. *et al.*, *J. Phys. G*, **41** (2014) 025109.
[38] HARAKEH M. N. and DIEPERINK A. E. L., *Phys. Rev. C*, **23** (1981) 2329.

[39] SWANN C. P. *et al.*, *Nucl. Phys. A*, **150** (1970) 300.
[40] CORSI A. *et al.*, *Phys. Rev. C*, **84** (2011) 041304(R).
[41] CERUTI S. *et al.*, *Phys. Rev. Lett.*, **115** (2015) 222502.
[42] SAGAWA H., BORTIGNON P. F. and COL G., *Phys. Lett. B*, **444** (1998) 1 and private communication.
[43] AUERBACH N., *Phys. Rev. C*, **79** (2009) 035502.
[44] TOWNER I. S. and HARDY J. C., *Phys. Rev. C*, **82** (2010) 065501.
[45] KELLERBAUER I. *et al.*, *Phys. Rev. Lett.*, **93** (2004) 072502.
[46] DAMGAARD J., *Nucl. Phys. A*, **130** (1969) 233.
[47] TOWNER I. S., HARDY J. C. and HARVEY M., *Nucl. Phys. A*, **284** (1977) 269.
[48] SUZUKI T., SAGAWA H. and COL G., *Phys. Rev. C*, **54** (1996) 2954.
[49] SATUŁA W., DOBACZEWSKI J., NAZAREWICZ W. and RAFALSKI M., *Phys. Rev. Lett.*, **103** (2009) 012502.
[50] MONDAL D. *et al.*, *Phys. Lett. B*, **763** (2016) 422.

Proceedings of the International School of Physics "Enrico Fermi"
Course 201 "Nuclear Physics with Stable and Radioactive Ion Beams", edited by F. Gramegna,
P. Van Duppen, A. Vitturi and S. Pirrone
(IOS, Amsterdam; SIF, Bologna) 2019
DOI 10.3254/978-1-61499-957-7-341

The $f_{7/2}$ shell: An optimum test bench for nuclear-structure studies

Silvia M. Lenzi

Dipartimento di Fisica e Astronomia, Università di Padova - Padova, Italy

INFN, Sezione di Padova - Padova, Italy

Summary. — The $f_{7/2}$ shell constitutes an ideal benchmark to investigate different nuclear-structure properties that can be studied in detail by means of the large-scale shell model. In particular, the systematic study of differences in excitation energy in isobaric nuclei has allowed to develop a theoretical method to deduce from the data, changes in the shape of the nuclei along a rotational band, the mechanism of the backbending, and the need to include an isospin-symmetry-breaking term in the nuclear interaction. Recently, these studies have been extended to other mass regions. In particular, I show here some results obtained in the *sd* shell where the method deduced for the $f_{7/2}$ nuclei seems to work well. A new approach based on a charge-dependent realistic nucleon-nucleon interaction is introduced. It allows to deduce the neutron skin at every excited state from the mirror energy differences. Moreover, a strong correlation between the skin and the difference of occupation numbers of neutrons and protons in the $s_{1/2}$ orbit is found.

1. – Introduction

Medium-light nuclei are suitable to investigate several nuclear properties and symmetries. In particular, nuclei in the region where valence neutrons and protons occupy the $f_{7/2}$ orbital present a richness of phenomena. Near the middle of the shell,

around ^{48}Cr, nuclei display rotational-like bands that can be described very accurately by large-scale shell model calculations. This offers the possibility to compare in the same physical system macroscopic and microscopic nuclear-structure models. As one moves away from ^{48}Cr, the doubly magic nuclei ^{40}Ca and ^{56}Ni are rapidly approached and the collective behavior gives way to more pronounced shell-model effects. Moreover, at high spin it becomes energetically favorable to the nuclei to align the particle spins along the rotational axis and backbending and band-termination phenomena show up. Nuclei in the $f_{7/2}$ shell thus provide an excellent opportunity to study the interplay between collective and single-particle degrees of freedom as functions of both angular momentum and valence particle number.

Another interesting feature that can be studied in these nuclei as a function of spin and mass number is the pairing interaction. While like-nucleon pairing is of $T = 1$ character, proton-neutron (pn) pairs can be coupled to isospin $T = 0$ and $T = 1$. Although the superfluid phenomenon in nuclei is a well-established feature, still a current issue in nuclear structure is the question of the role of $T = 0$ pn pairing and the existence of a $T = 0$ pairing condensate. The contribution of $T = 0$ pn pairing correlations, however, decreases rapidly with increasing proton or neutron excess and therefore, these studies concentrate on those nuclei that lie on the $N = Z$ line.

Around this line, another important property of the nuclear force can be studied: the isospin symmetry. This is based on the charge symmetry and independence of the nuclear interaction which allows to treat the proton and the neutron as the same particle, the nucleon, characterized by the isospin quantum number t with projection $t_z = +1/2$ in the case of the neutron and $t_z = -1/2$ for the proton. In a nucleus, the total isospin projection T_z will be the sum of those of the single nucleons, being the total isospin $T \geq T_z = (N-Z)/2$. One of the main consequences of isospin symmetry is that the structure of mirror nuclei (obtained interchanging neutrons and protons) should be identical. It is well known that the Coulomb interaction, experienced only by protons, breaks the isospin symmetry, but this is not enough to explain the differences observed experimentally. In mirror nuclei, for example, signatures of the isospin symmetry breaking are the differences between the excitation energy of analogue state (Mirror Energy Difference, (MED)) and the different strengths of the $E1$ transitions.

In recent years, the increase in sensitivity and resolving power of γ-ray spectrometers has allowed the study of $N \sim Z$ nuclei up to high spin and to extend the investigation to medium-heavy masses. In parallel, a remarkable improvement has also been obtained in the development of large-scale shell model calculations, leading to interesting results, in particular, in nuclei of the $f_{7/2}$ shell where it has been shown that the MED are sensitive to changes of nuclear-structure properties along rotational bands. They can give information on the alignment of nucleons, variation of the nuclear radius and, in some cases, on the configuration of the wave functions. It has also been shown that the Coulomb field is not the only responsible for the isospin symmetry breaking [1]. Until very recently these studies have been performed by using stable beams and targets [2]. Radioactive-ion beams allows now to populate mirror nuclei where the proton-rich partner is quite far from stability. In particular, knockout reactions induced by radioactive high-energy

beams have been performed at NSCL in the upper $f_{7/2}$ shell where $T = 3/2$ and $T = 2$ mirror nuclei have been studied [3].

Isospin-symmetry-breaking interactions produce states with isospin impurity. The degree of isospin mixing increases with mass and a fingerprint of the impurity can be studied in $T = 1$ isobaric triplets by measuring the reduced transition probabilities $B(E2 : 2^+ \rightarrow 0^+)$. If the involved states have good isospin, the $B(E2)$ of the three nuclei as a function of T_z should lie on a line. A deviation from this behavior is a signature of isospin mixing. Recently the $A = 46$, $T = 1$ triplet has been studied in GSI using the gamma-ray tracking array AGATA using radioactive beams at relativistic energies in Coulomb excitation reactions and plunger measurements. Preliminary results are compatible with a linear behavior [4].

In the following section a summary of the results obtained in the $f_{7/2}$ shell together with a brief description of the theoretical method is given. Section **3** is devoted to the extension of these studies to nuclei in the *sd* shell. In sect. **4** a new approach to the study of mirror nuclei is introduced and discussed. Section **5** summarizes the main results.

2. – Isospin-symmetry studies in the $f_{7/2}$ shell

The validity of the isospin symmetry for the strong interaction is a fundamental assumption in nuclear physics. One of the experimental manifestation of the isospin symmetry is the nearly identical spectra of pairs of mirror nuclei (obtained by interchanging protons and neutrons) and, more generally, in levels of isospin multiplets. A slight breakdown of isospin symmetry arises from the Coulomb potential, but it is well known that also the nuclear force has an isospin dependence as shown for example in difference of mass of protons and neutrons and in the phase shifts in *pp*, *nn* or *pn* scattering. Modern effective interactions derived from realistic, charge-dependent nucleon-nucleon potentials do not reproduce, however, the differences in excitation energy of analogue states, as shown in ref. [5, 6].

The Coulomb interaction has a large contribution to the binding energy of nuclei (hundreds of MeV). When comparing those of mirror nuclei, the difference in binding energy results of the order of tens of MeV and if we just consider the excitation energy of analogue states in mirror nuclei, the so-called Mirror Energy Differences (MED), we find values of the order of tens of keV. Very small values indeed. It is precisely because of this smallness that the MED are such efficient observatories: as the large contributions have been canceled, what remains gives direct insight into nuclear structure.

MED are obtained by subtracting the excitation energies of analogue states in mirror nuclei (same J and same T):

$$MED(J) = E^*_J(T, -T_z) - E^*_J(T, T_z). \tag{1}$$

In this respect, it is interesting to investigate the behavior of rotating mirror nuclei where MED acts as a magnifying glass, being sensitive to changes of shape and nucleon rearrangements. In particular, the $1f_{7/2}$ shell offers unique opportunities: it is the first

region where backbending rotors have been observed [7] that can be studied with the rigor of the shell model [8]. Detailed investigations of the high spin structure of these rather light nuclei have become experimentally feasible in the nineties due to the advent of high-efficiency gamma-ray spectrometers and ancillary particle detectors. It is interesting to note, in this respect, that high-performance shell model codes became available simultaneously.

From the systematic analysis of the MED in the $1f_{7/2}$ shell it was shown that they constitute a very useful tool to get insight into the nuclear structure of the involved states and the evolution as a function of the angular momentum and excitation energy. The results of these studies have been recently extended to other mass regions such as the *sd* and upper *pf* shells. However, in most of the cases the MED can be just followed up to very limited spin because the proton-rich partners of the mirror pairs become soon unbound.

Let us now enter into the details of the theoretical description of the MED. The main ingredient is, of course, the Coulomb potential which acts only between protons and breaks isospin symmetry. In the shell-model framework we calculate the Coulomb matrix elements in the harmonic-oscillator basis within the model space. Its contribution to the MED is sizable but not enough to reproduce the experimental data. In ref. [9] another Coulomb contribution of monopole origin was included that takes into account the changes in the nuclear radii when increasing angular momentum. Indeed the angular momentum is constructed by aligning the nucleon spins. The structure of nuclei in the $1f_{7/2}$ shell are not well described within a model space containing just this orbit for protons and neutrons. The full *pf* shell is needed to cope with the collective behavior and, in particular, the role of the $p_{3/2}$ orbital is crucial. Indeed, it is the quadrupole partner of the $f_{7/2}$ orbit in the quasi-$SU(3)$ dynamical symmetry framework [10].

The radius of the nucleus depends on the orbits that are being filled. In the main shell, the orbits with low angular momentum have larger radii than the others. In the *pf* shell, *p* orbits have much larger radii than *f* orbits. At low excitation energy, the occupation of the $p_{3/2}$ orbit in deformed nuclei is sizable but to increase the nuclear spin, nucleons prefer to fill the $f_{7/2}$ shell and the occupation of the *p* orbits decreases, reducing the nuclear radii. This affects the excitation energy of the states as the Coulomb repulsion increases. Of course this happens in both mirror pairs, but the Z value is different and therefore there is a net Coulomb effect on the MED. In the shell-model framework this radial effect is obtained as the difference of the average of the occupation numbers of protons *plus* neutrons in the *p* orbits with respect to the ground state, weighted with an empirical parameter, which is kept constant for all the mirror pairs in the $f_{7/2}$ shell. An example of the Coulomb contributions for the case of the mirror pair $A = 49$, $T = 1/2$ is given in fig. 1.

In fig. 1, the two Coulomb contributions are labeled V_{CM}, that takes into account the Coulomb contributions within the model space, and V_{Cr}, the radial-dependent contribution. By adding the two, the trend of the data as a function of the nuclear spin is qualitatively reproduced, but not enough satisfactory from the quantitative point of view. In ref. [1] an additional isospin-symmetry braking (ISB) term V_B was introduced

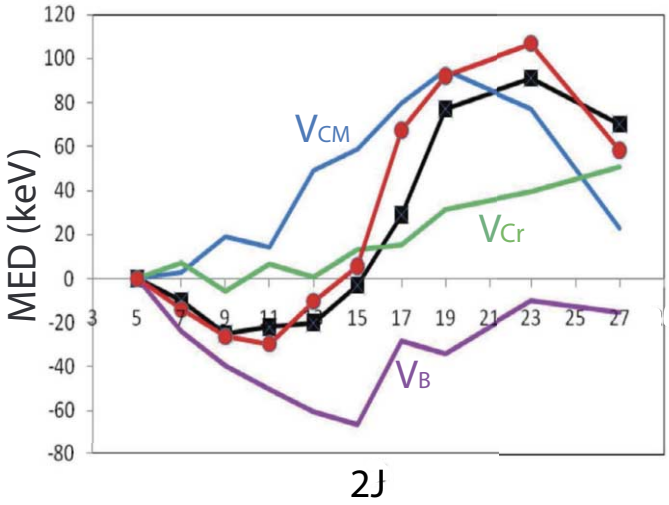

Fig. 1. – MED for the mirror nuclei ^{49}Mn-^{49}Cr: The experimental values (black line) are compared to the theoretical predictions (red curve) that consists on the sum of the three components V_{CM}, V_{Cr} and V_B (see text for details).

that allowed reproducing the data with high accuracy. It is a schematic isovector term, deduced from the data of the mirror pair ^{42}Ti-^{42}Ca and consists in the difference of the expectation values of a single diagonal matrix element for two nucleons in the $f_{7/2}$ shell coupled to $I = 2$ and with a strength of 100 keV,

$$\Delta_M \langle V_B \rangle_J = \langle V_B^{\pi\pi} \rangle_J - \langle V_B^{\nu\nu} \rangle_J, \tag{2}$$

where the difference of expectation values are obtained for each state with angular momentum J. Taking into account this contribution to the MED, they can be obtained in first-order perturbation theory as

$$MED(J) = \Delta_M \langle V_{CM} \rangle_J + \Delta_M \langle V_{Cm} \rangle_J + \Delta_M \langle V_B \rangle_J, \tag{3}$$

where Δ_M indicates that the difference of the expectation values is taken by subtracting to that of the proton-rich partner the corresponding value for the neutron-rich one. As can be seen in fig. 1 the V_B contribution is of the same order of magnitude of the Coulomb terms. The interesting result is that this simple prescription, together with the Coulomb terms, allow to reproduce with very good accuracy all the MED data that have been reported during the last two decades for mirror nuclei in the $f_{7/2}$ shell, even for nuclei quite far from stability [1, 2]. It is important to note that it is not compatible with the ISB contribution deduced from charge-dependent nucleon-nucleon realistic interactions.

As stated above, the ISB V_B term has been deduced from the MED in mass $A = 42$, where the value for two particles coupled to $I = 2$ is much larger than that of the other

$I = 0, 4, 6$ value. (We adopt the notation I to stress that this is the spin to which two nucleons are coupled, while we use J for the spin of a nuclear state, that involves many nucleons.) In a recent work by Bentley and collaborators [11], it has been shown that the MED are not sensitive to the absolute value of these matrix elements but to the relative values. Indeed they show, from a fit of all the so far experimentally known MED in the $f_{7/2}$ shell that taking a strength of $+100\,\mathrm{keV}$ in the $I = 2$ coupling is equivalent to consider a $I = 0$ coupling with a strength of $-100\,\mathrm{keV}$.

So far we have concentrated in mirror nuclei with $T_z = \pm T$. The isospin symmetry also implies that all nuclei with the same mass (isobaric multiplets) should show states with the same spin and configuration, the so-called analogue states, provided these states are characterized by the same value of T. The easiest cases are the isobaric triplets with $T = 1, T_z = 0, \pm 1$. If the $N = Z$ ($T_z = 0$) member of the triplet is an odd-odd nucleus, then $T = 0$ and $T = 1$ states coexist at low excitation energy. Triplet energy differences (TED) are obtained experimentally as

$$TED(J) = E^*_J(T, -T_z) + E^*_J(T, T_z) - 2E^*_J(T, T_z = 0). \tag{4}$$

Due to the way they are defined, TED are not sensitive to changes in the nuclear structure as a function of the spin and monopole contributions cancel out. In ref. [1] it has been shown that a good description of the TED can be achieved by adding to the multipole Coulomb term an ISB schematic interaction, as in the case of the MED,

$$\Delta_T \langle V_B \rangle_J = \langle V_B^{\pi\pi} \rangle_J + \langle V_B^{\nu\nu} \rangle_J - 2\langle V_B^{\pi\nu} \rangle_J, \tag{5}$$

with the triplet difference of the expectation values of a single diagonal matrix element for two nucleons in the $f_{7/2}$ shell coupled to $I = 0$ and with a strength of $100\,\mathrm{keV}$ [1,2].

The theoretical expression for the TED thus becomes

$$TED(J) = \Delta_T \langle V_{CM} \rangle_J + \Delta_T \langle V_B \rangle_J. \tag{6}$$

In fig. 2 some examples are shown evidencing the very good description of the TED for isobaric triplets in the $f_{7/2}$ shell. Note that the contribution arising from the ISB term is also in this case of the same order than the Coulomb one. The effect of this term is not compatible with that produced by effective interactions deduced from realistic nucleon-nucleon interactions, as discussed in ref. [5] and, more recently in ref. [6].

3. – Extension to the *sd*-shell nuclei

The very satisfactory description of MED and TED for nuclei the $f_{7/2}$ shell with the phenomenological method described above triggers some questions. First of all, one may wonder if the same or similar prescription applies to other mass regions where several orbitals are active and there is not the dominance of one isolated orbital. This is particularly important for the schematic ISB term that was deduced in the hypothesis

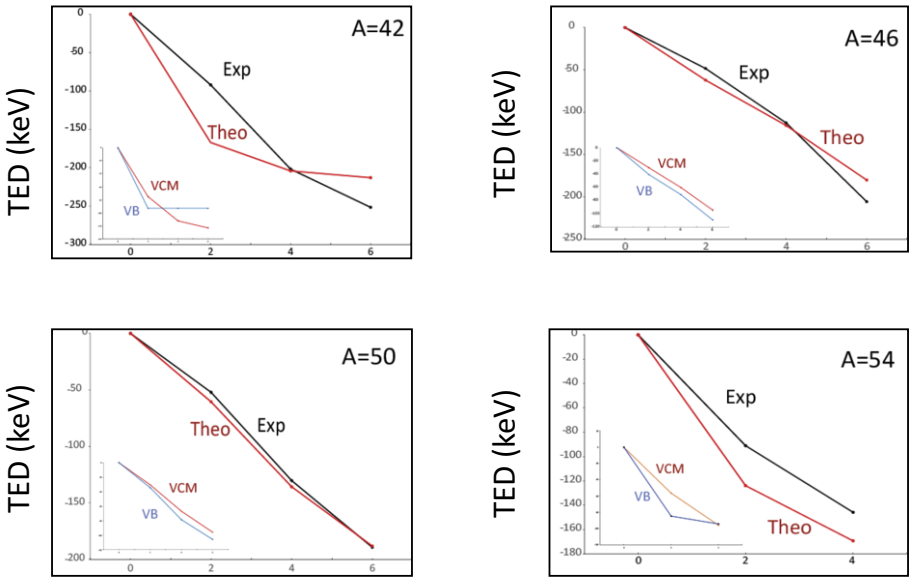

Fig. 2. – TED for the isobaric triplets $T = 1$ in nuclei della shell $f_{7/2}$. The experimental values are compared with the theoretical predictions. In the inset the separate contributions of the Coulomb and ISB term V_B are shown.

of a pure $f^2_{7/2}$ configuration in mass $A = 42$. The form of the ISB V_B term in both the MED and TED in complex configurations is not straightforward. Regarding the radial term, the single parameterization found in terms of the occupation of the $p_{3/2}$ orbital may change when other orbitals are at play.

In ref. [12] we have applied the same method to nuclei in the *sd* shell. Here data on MED and TED are limited to rather low spin. Two fundamental generalizations have been done in the theoretical approach. In the case of the MED, for the radial term, we assumed that it is the $s_{1/2}$ orbit the one of larger radius in this main shell. A quantitative estimate of this radial difference has been confirmed by a recent theoretical study [13]. The second generalization is related to the ISB term. The wave functions of nuclei in this shell are not dominated by a single orbital, as for the $f^2_{7/2}$-shell nuclei. Therefore we have to consider for the MED a schematic isovector ISB term for each orbit with the same strength of +100 keV for two nucleons coupled to $I = 2$, while a strength of +100 keV was used for the isotensor ISB term in the case of the TED. While in the $f_{7/2}$ shell single-particle corrections due to electromagnetic spin-orbit interaction (ls) [14] and the ll term introduced in ref. [15] have almost no influence on the MED, they have to be included in the description of *sd* MED. As an example, we show in fig. 3 the different contributions to the MED of the pairs ^{21}Na-^{21}Ne and ^{29}P-^{29}Si. These nuclei present a rotational-like structure and therefore the role of the radial term is evident, however, still more important is the contribution from the ISB terms that allows to reproduce the experimental data with very good accuracy.

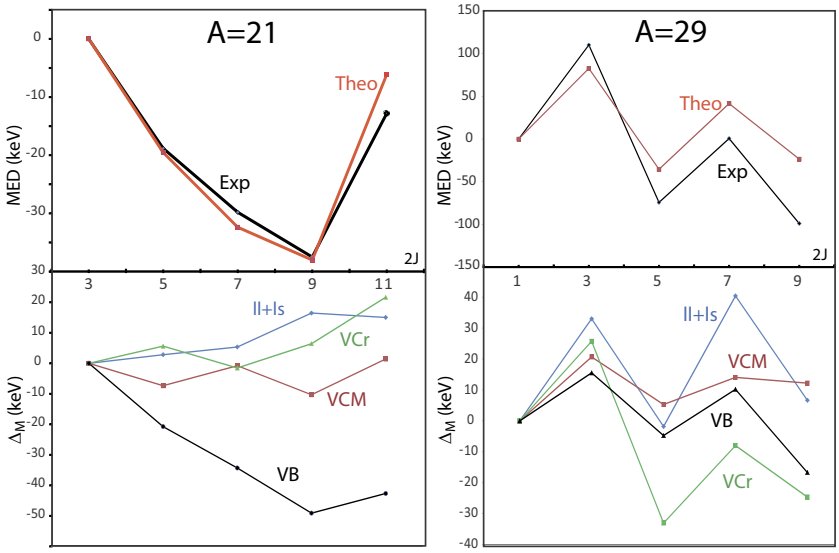

Fig. 3. – Upper panel: Mirror energy differences for the pairs ^{21}Na-^{21}Ne and ^{29}P-^{29}Si in comparison with shell model calculations, bottom panel: different components that contribute to the theoretical MED: V_{CM} and V_{Cr} are the Coulomb contributions together with those arising from the electromagnetic spin-orbit (ls) and orbital (ll) single-particle corrections. The ISB contribution V_B is calculated in all sd orbits.

A systematic study of the mirror nuclei in this shell shows that the prescription successfully used in the $f_{7/2}$ seems to apply also in the sd shell for both the MED and the TED. It is important to underline here that no best fit has been done at all and that the same parameters used in the mass $A = 40$–55 region have been taken identical for the sd nuclei. This means that the agreement with data could be improved for sure by adapting the parameters to these nuclei, although maintaining them constant for the full shell. But this was not the goal of the present investigation that aimed at exploring the generalization of the method developed in the $f_{7/2}$ shell.

4. – A new approach: MED and neutron skin

The satisfactory description of the MED and TED is based on the addition to the multipole Coulomb term of the radial term (V_{Cm}) and the ISB contribution. These two latter terms, crucial to account for the experimental findings, are schematic and phenomenological. Inspired on a recent work by Bonnard *et al.* [13] we have followed a new approach to obtain the MED. This consists in adopting in the shell model framework an effective interaction deduced in a no-core approach from a realistic charge-dependent nucleon-nucleon interaction recently developed by A.P. Zuker [13]. This includes naturally the ISB part of the nuclear field and produces the single-particle energies, which therefore are not taken from the experimental data. It also includes the electromagnetic spin-orbit correction.

The radial term is taken into account in this new approach by considering the effect of the isovector monopole polarizability introduced in ref. [13]: when a nucleon is added to a nucleus it polarizes both fluids, the protons and the neutrons. This causes a change in the respective radii that tend to equalize them, reducing the neutron skin independently of the neutron excess. This implies to consider a different potential well for each fluid, at difference with what is done in normal shell model calculations where the size parameter of the harmonic oscillator potential is obtained with a standard formula.

The size parameter is inversely proportional to the radius. Charge radii are measured for most of the stable nuclei at the ground state. They can be fitted using the Duflo-Zuker formula:

$$\rho_\pi = A^{1/3}\left(\rho_0 - \frac{\zeta}{2}\frac{t_z}{A^{4/3}} - \frac{v}{2}\left(\frac{t_z}{2}\right)^2\right)e^{g/A} + \lambda\mathcal{D}_{\nu\pi}, \tag{7}$$

where ρ_π is the charge radius and $t_z = N - Z$. The coefficients ρ_0, ζ, and v are associated with the scalar, vector and tensor components of ρ_π, while the $e^{g/A}$ factor corrects for the larger radii observed in light nuclei. The expression of the correction term $\mathcal{D}_{\nu\pi}$ may be found in refs. [15, 13] where its efficiency in providing very good radii and its physical interpretation in terms of correlations are also discussed. The 5 parameters are determined by fitting all measured charge radii up to mass $A = 60$. Once these are fixed, the neutron radii are calculated, using isospin symmetry arguments, by changing the sign of t_z in eq. (7). Still, relying on the isospin symmetry, we can assume that the proton radius of one of the mirrors is the same as the neutron radius of its mirror partner and viceversa. We can therefore deduce now the size parameters of the harmonic-oscillator potential to calculate the matrix elements of our effective interaction.

With all these elements taken into account we would be able to calculate the MED and, in particular, the mass difference between the two mirrors, which is also an experimental datum. This has been done in ref. [13] for closed-shell nuclei plus/minus one nucleon. There, Bonnard and collaborators have shown that a good fit of the data can be obtained by allowing the parameter ζ in eq. (7) to vary in the range 0.4–1.2. This parameter is related to the difference of neutron and proton radii, *i.e.* the neutron skin:

$$\Delta r_{\nu\pi} = \rho_\nu - \rho_\pi = \frac{\zeta t_z}{A}e^{g/A}. \tag{8}$$

Therefore, the MED are computed as a function of the parameter ζ until they match the experimental value. Interestingly, they have a linear dependence with ζ and the first important result of this research is that the MED provide an indirect measurement of the neutron skin for each excited state. A remarkable result indeed.

The new procedure is quite different from the previous one in the sense that most of the terms that have to be added to the nuclear plus Coulomb interaction in a schematic approach are now incorporated by adopting a charge-dependent chiral realistic interaction deduced in a no-core approach [12]. The only term that is not included here is the radial one due to the monopole Coulomb contribution and computed by considering the *sum*

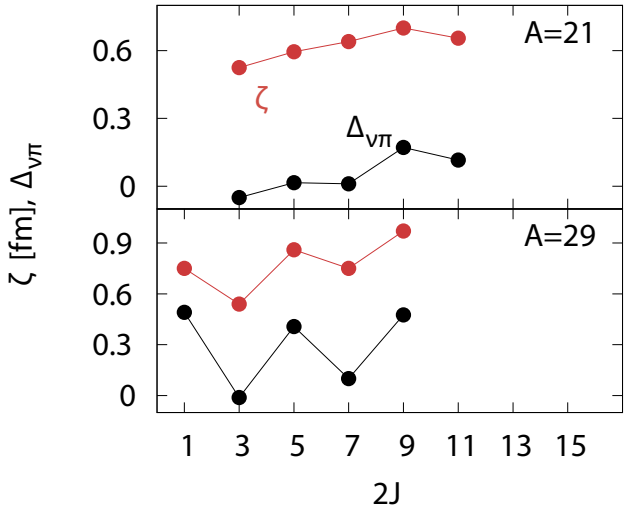

Fig. 4. – Correlation between the neutron skin parameter ζ and the difference of occupation numbers of neutrons and protons in the $s_{1/2}$ orbital ($\Delta_{\nu\pi}$) for the mirror pairs $A = 21$ and $A = 29$.

of proton *and* neutron occupation numbers in the $s_{1/2}$ orbital. On the other hand, the variation of the radii is accounted for in the new approach by adjusting the potential size parameters of both fluids in the two nuclei. Interestingly, the neutron skin deduced from the MED data is correlated with the *difference* in occupation number of neutrons and protons in the $s_{1/2}$ orbit. This correlation can be seen in fig. 4 for the two mirror pairs of fig. 3.

5. – Summary

Nuclei where the valence nucleons are filling the $f_{7/2}$ shell are an ideal ground to study nuclear-structures properties. Indeed, the wave function configurations are dominated by this orbital, which simplifies the interpretation of the evolution of the structure as a function of the angular momentum. Still, the contribution of other orbitals in the fp shell, in particular the $p_{3/2}$, are essential for the development of quadrupole deformation. Due to the relatively reduced number of valence particles, the properties of both rotational bands and single-particle structures can be described by means of large-scale shell-model calculations.

Along the $N = Z$ line, the study of MED in the $f_{7/2}$ has demonstrated very useful to put in evidence certain properties of the nuclear structure such as the mechanism at the backbending in rotational bands, changes in the nuclear radius, and the isospin symmetry breaking of the nuclear potential. This has been possible due to both a systematic experimental work in the region and a good shell model description. The application

of the same method to nuclei in the *sd* shell seems to apply as well using the same parameters deduced for the $f_{7/2}$ shell.

The new approach inspired in ref. [13] and applied in ref. [12] has shown that the MED can give information on the nuclear skin at every excited state. Moreover, is has been found that the skin is correlated with the difference between the occupation of the $s_{1/2}$ orbital by neutrons and protons. This new finding may open the possibility to predict the MED values by starting from the charge radii, provided a quantitative relation between nuclear skin and the difference of occupation numbers of neutrons and protons in the $s_{1/2}$ orbit is found.

* * *

The author acknowledges A. Boso, M.A. Bentley, J. Bonnard, F. Recchia and A.P. Zuker for the fruitful collaboration that led to the results reported in this contribution.

REFERENCES

[1] ZUKER A. P., LENZI S. M., MARTINEZ-PINEDO G. and POVES A., *Phys. Rev. Lett.*, **89** (2002) 142502.
[2] BENTLEY M. A. and LENZI S. M., *Prog. Part. Nucl. Phys.*, **59** (2007) 497.
[3] DAVIES P. J. *et al.*, *Phys. Rev. Lett.*, **111** (2013) 072501.
[4] BOSO A., PhD Thesis, University of Padova (2017).
[5] GADEA A. *et al.*, *Phys. Rev. Lett.*, **97** (2006) 152501.
[6] ORMAND W. E., BROWN B. A. and HJORTH-JENSEN M., *Phys. Rev. C*, **96** (2017) 024323.
[7] LENZI S. M. *et al.*, *Z. Phys. A*, **354** (1996) 117.
[8] CAURIER E., MARTÍNEZ-PINEDO G., NOWACKI F., POVES A. and ZUKER A. P., *Rev. Mod. Phys.*, **77** (2005) 427.
[9] LENZI S. M. *et al.*, *Phys. Rev. Lett.*, **87** (2001) 122501.
[10] ZUKER A. P., POVES A., NOWACKI F. and LENZI S. M., *Phys. Rev. C*, **92** (2015) 024320.
[11] BENTLEY M. A. *et al.*, *Phys. Rev. C*, **92** (2015) 024310.
[12] BOSO A. *et al.*, *Phys. Rev. Lett.*, (2018) in press.
[13] BONNARD J., LENZI S. M. and ZUKER A. P., *Phys. Rev. Lett.*, **116** (2016) 212501.
[14] NOLEN J. A. and SCHIFFER J. P., *Annu. Rev. Nucl. Sci.*, **19** (1969) 471.
[15] DUFLO J. and ZUKER A. P., *Phys. Rev. C*, **66** (2002) 051304(R).

This page intentionally left blank

Proceedings of the International School of Physics "Enrico Fermi"
Course 201 "Nuclear Physics with Stable and Radioactive Ion Beams", edited by F. Gramegna,
P. Van Duppen, A. Vitturi and S. Pirrone
(IOS, Amsterdam; SIF, Bologna) 2019
DOI 10.3254/978-1-61499-957-7-353

Structure function and collective effects in particle evaporation

L. G. Moretto

University of California Berkeley and Nuclear Science Division
Lawrence Berkeley National Laboratory, University of California
Berkeley, CA 94720, USA

Summary. — We explore the role of intrinsic and collective modes in the evaporation spectra of particles emitted by a compound nucleus. Collective effects are found to determine the gross features of the spectra, dramatically distorting the exit channel phase space of the free particle. We are also trying to determine whether the spectra retain information on the preformation of the particle inside the compound nucleus. Alpha particle evaporation spectra are analyzed and interesting modulations at the level of 1% are observed.

1. – Introduction

Fusion reactions have demonstrated the role of a variety of degrees of freedom, both intrinsic and collective, in determining the cross section, especially in the peribarrier region [1]. Intrinsic degrees of freedom are usually accounted for in terms of an optical model. The survival of a particle and its motion (neutron, proton alpha particle, etc.) inside the nucleus before relaxation affects and modulates the entrance channel cross section.

Similarly, collective degrees of freedom, like shape multipole deformation can be excited, giving rise to an apparent distribution of fusion barriers and to other significant effects [2].

In this paper we present an attempt to unveil similar effects in the exit channel, more specifically in the evaporation spectra of particles emitted by a compound nucleus. The amalgamation of a particle with a nucleus in fusion reactions, and the segregation of the same particle in evaporation, pose the question of the existence of complex particles in the nuclear medium [3]. Even for nucleons, the interaction with the nuclear medium makes their existence as independent particles rather fleeting. In general, one wonders to what extent the total nuclear wave function is factorizable into the product of the wave function of the particle in question and that of the residual nucleus. This problem is analogous to the problem of the interaction of a solute molecule with the molecules of the solvent in solutions. The properties of a solute molecule, or even of an individual solvent molecule, are dramatically renormalized by the interaction with the other molecules. Geometric conformation, bond lengths, and, in general, all other spectroscopic features are at the very least changed with respect to the corresponding quantities *in vacuo*. In the most extreme cases, the existence of the molecule itself may be compromised due to dissociation, or to other chemical reactions. In the nuclear case, one can consider the nuclear medium as the solvent, and the various kinds of (complex) particles as the solute. Individual neutrons and protons, at least in ground-state nuclei, behave more or less as non-interacting particles in the shell model potential. However, single-particle excited states couple rather quickly into the many-body degrees of freedom. The width of the corresponding strength function gives a direct estimate of the "lifetime" of the nucleon in the medium. Qualitatively one can expect that tightly-bound particles such as alphas may have more than a fleeting existence in the nuclear medium, certainly much longer than that of a weakly-bound particle such as the deuteron. Cluster models have described complex particles within the nuclear medium. This problem has also been addressed, in the case of nuclear reactions, by the optical model theory. The interaction of the projectile with the nucleus is described in terms of a complex one-body potential, where the imaginary part describes the removal of flux from the elastic channel, or the "absorption" of the particle into the collective unconscious of the nuclear many-body system. While the optical potential may adequately describe elastic scattering, it tells us little about the actual behavior of the particle inside the nucleus. Although the problem has been studied theoretically for ground-state nuclei, very little experimental information does in fact exist. No information is at hand concerning hot nuclei. This is true even for nucleons. We know nothing on how the shell/optical model potential evolves with temperature. We know just as little about the existence and properties of clusters in hot nuclei. One may wonder whether this information is at all accessible experimentally. Should it be so, it would provide us with an important and totally novel chapter of nuclear physics. We believe that the questions outlined above, and possibly others, can be addressed by looking at compound nucleus evaporation of nucleons and complex particles in a fresh way.

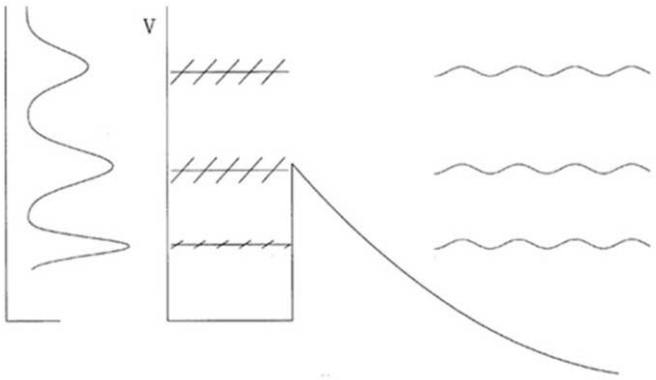

Fig. 1. – Schematic drawing of the states of a particle in a potential well. The wavelengths change with energy, as it may not be clear from the drawing.

2. – Particle evaporation from compound nuclei

As a particle is "segregated" from a compound nucleus state and prepares to exit, it senses its environment. This environment could be a mean field, like a shell/optical potential, or a local polarization field of some sort. This should result in states that acquire a width through the coupling with the continuum and the remaining many-body degrees of freedom. A strength function should arise that modulates the spectrum of the emitted particle. This is illustrated qualitatively in fig. 1. The states inside and above the well are the states of the particle in the nucleus, which, in the case of protons, tend to the shell model states well below the barrier, and to the optical model resonances in the continuum above the barrier. This modulation should be observable in very high statistics evaporation spectra. Since the particle to be emitted is in a hot nucleus, whose excitation energy is under experimental control, the strength function obtained from the modulation of the spectrum refers to that specific excitation energy or temperature. Thus the possibility exists of studying these fields not only for a variety of particles, but also for different temperatures. Another way of looking at this problem is to consider the standard expression for the evaporation spectrum.

The decay width differential in the particle kinetic energy is

$$\Gamma(\varepsilon) \propto \sigma_{\mathrm{inv}}(\varepsilon)\varepsilon\rho(E - B - \varepsilon), \tag{1}$$

where B is the particle binding energy and $\sigma_{\mathrm{inv}}(\varepsilon)$ is the inverse cross-section. A first-order expansion of the log of the level density in the kinetic energy of the particle gives the transparent form:

$$\Gamma(\varepsilon) \propto \sigma_{\mathrm{inv}}(\varepsilon)\varepsilon e^{-\varepsilon/T}, \tag{2}$$

where T is the nuclear temperature.

Thus the spectrum is the product of a structure factor, namely the "inverse" cross section, and of a phase-space factor. Removal of the latter should leave the former with its potentially interesting modulations. Usually evaporation codes calculate the inverse cross section, or the corresponding transmission coefficients, from an optical model. There are two difficulties with this. The first is related to the fact that the residual nucleus to which the inverse cross section refers is an excited nucleus, while the optical potential is known for ground-state nuclei. This is not a problem here, since we intend to extract the "inverse" cross section directly from the data, and infer the temperature dependence of the optical potential. The second is associated with shape polarization effects in the exit channel. These are due, for instance, to the Coulomb interaction, and are very different from those in the entrance channel. Let us consider this interesting problem in more detail.

3. – Shape polarization and evaporation spectra

In order to exit from a nucleus, a charged particle must overcome the Coulomb barrier. If the nucleus deforms in the direction of emission, the Coulomb barrier decreases. Therefore, it pays for the nucleus to invest some energy in deformation in order to lower the barrier. More quantitatively, let us consider a configuration formed by the emitted particle just in contact with the residual nucleus. Now we deform the residual nucleus always keeping the light particle in contact, and we plot the total energy as a function of deformation. The total energy has a minimum at some finite prolate deformation. This is the location of the saddle point, as shown in fig. 2. The unbound mode, or reaction coordinate, is the distance between centroids. A particle crossing over the saddle point with zero kinetic energy acquires a kinetic energy at infinity smaller than the Coulomb barrier associated with a spherical configuration. This is not sub-barrier emission, of course, in the sense that it is not associated with quantum barrier penetration [4].

Thermal fluctuations along this deformation coordinate Z lead to large fluctuations in the Coulomb interaction energy, as shown in fig. 2.

While the total potential energy V_T has a minimum at some prolate deformation, the fragment-fragment Coulomb interaction $V_{\rm Coul}$ is a monotonically decreasing function of the deformation coordinate.

Therefore, we can expand the total potential energy and the Coulomb interaction energy about the saddle point along the deformation coordinate Z ($Z = 0$ at the saddle):

$$V_T = V_T^0 + KZ^2, \qquad V_{\rm Coul} = V_{\rm Coul}^0 - cZ. \tag{3}$$

Now, if we allow the shape to fluctuate involving an energy of the order of the temperature T, we obtain a corresponding fluctuation of the Coulomb energy:

$$\Delta V_{\rm Coul} = 2\sqrt{\frac{Tc^2}{K}} = 2\sqrt{pT}. \tag{4}$$

This fluctuation will, of course, be reflected in the final kinetic energy of the particle.

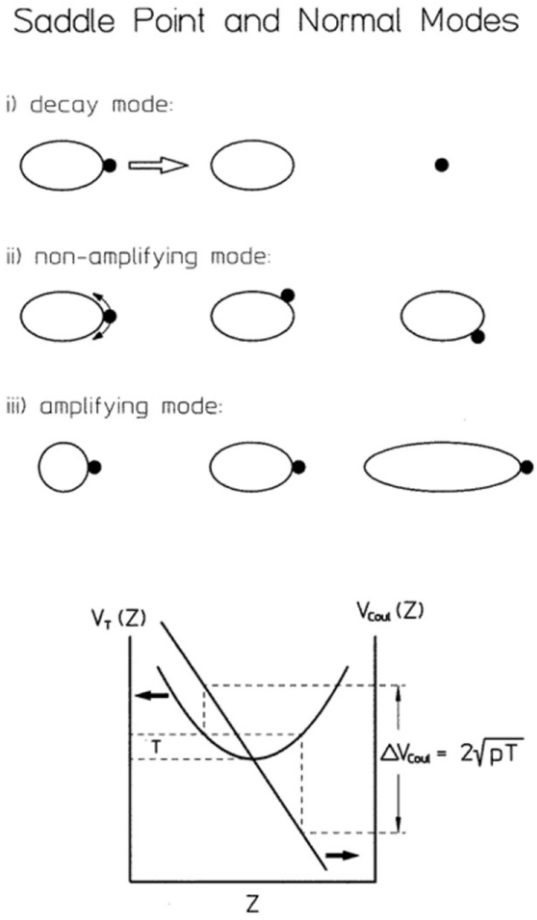

Fig. 2. – Top: Normal modes at the saddle point. Bottom: Total potential energy V_T and Coulomb energy $V_{\rm Coul}$ as a function of the deformation coordinate Z.

Because of this, we call the parameter p the amplification parameter. More quantitative considerations lead to an expression for the kinetic energy of the particle [5]

$$P(x) \propto e^{-x/T} \operatorname{erfc}\left(\frac{p-2x}{2\sqrt{pT}}\right), \tag{5}$$

where $x = \varepsilon - V^0_{\rm Coul}$.

This formula is easily generalized to include: 1) a larger number of amplifying and non-amplifying degrees of freedom at the saddle; 2) their quantization; 3) true quantal barrier penetration along the reaction coordinate [6]. We see immediately that, by using a formula like eq. (5) to fit experimental spectra, we can obtain information on the shape polarization associated with particle emission and on its excitation energy dependence.

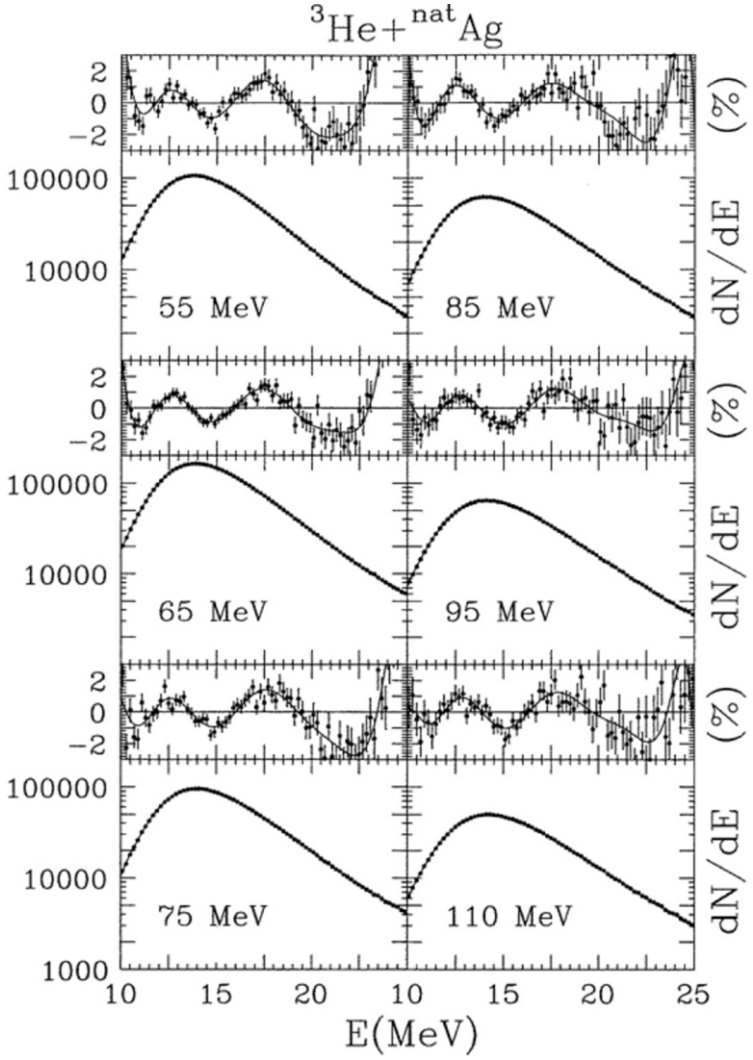

Fig. 3. – Lower panels: the experimentally measured α spectra and the linear combination of the orthogonal functions (eq. (6) (full curves)). Upper panels: the dots represent the percentage difference between the experimental data and the fits with eq. (5). The error bars represent the statistical errors of the experimental data. The full curves represent the percentage difference of the combination of the orthogonal functions and the fits.

4. – Experimental particle structure functions

We are now going to explore high statistics evaporation spectra from the reaction ^{3}He + ^{nat}Ag from 55 to 110 MeV bombarding energy [2, 5, 6] in order to see whether physical modulations similar to those expected from optical potentials are present.

The plan is to fit the spectra shown in the lower panel of each sextant in fig. 3 with a smooth function, and to search the residuals for modulations. Standard expressions for the evaporation spectra do not provide adequate fits since they do not incorporate shape polarization, etc. On the other hand, expressions like eq. (5) and similar ones, have demonstrated the necessary flexibility.

The resulting fits to the experimental spectra shown in fig. 3 are of extremely high quality. The percentage residuals of the fits are also shown in fig. 3, in the upper panel of each sextant. They are of the order of 1% throughout the energy range, which shows the goodness of the fitting functions. These residuals show a statistically significant modulation with amplitude of about 1.5% which is approximately repeated in both amplitude and phase at all bombarding energies.

In order to extract information on the modulations observed at the various excitation energies, we have devised an analytical procedure based upon orthogonal polynomials. We write down the experimental spectrum as a linear combination of orthogonal polynomials

$$F(\varepsilon) = \sum a_n S(\varepsilon) P_n(\varepsilon), \tag{6}$$

where $S(\varepsilon)$ is a suitably chosen weight function that generates the polynomials $P_n(\varepsilon)$.

The orthogonality condition is

$$\int_a^b S^2(\varepsilon) P_n(\varepsilon) P_m(\varepsilon) \mathrm{d}\varepsilon = \delta_{nm}. \tag{7}$$

The choice of $S(\varepsilon)$ is dictated by the desire of concentrating the bulk of the spectral shape into the single coefficient a_0. The modulations then appear in the higher-order coefficients, hopefully in only one or two. This goal can be achieved by choosing for $S(\varepsilon)$ the form given by eq. (5) with parameters obtained from the least-squares fit. This guarantees that a_0 will take up the bulk of the spectrum. The amplitudes a_n can be obtained from the dot product of the experimental spectrum with the n-th polynomial

$$a_n = b \int_a^b F(\varepsilon) S(\varepsilon) P_n(\varepsilon) \mathrm{d}\varepsilon \tag{8}$$

and the corresponding strength s_n can be defined as

$$s_n = \frac{a_n^2}{\int_a^b F^2(\varepsilon) \mathrm{d}\varepsilon}. \tag{9}$$

The strength coefficients, as defined above are shown in fig. 4 for the usual sequence of energies. As expected, all the physical information is contained in a few low modes.

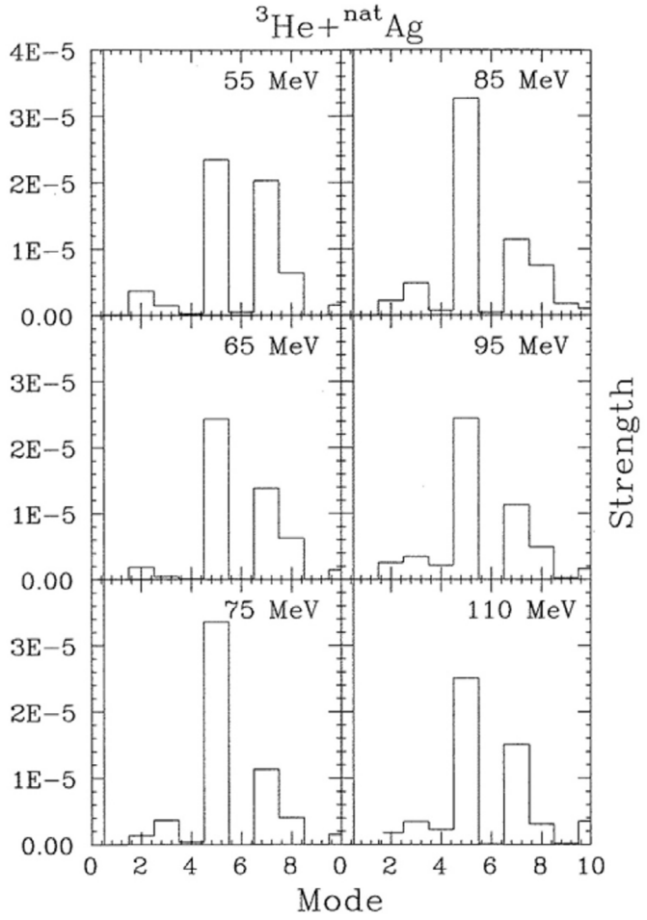

Fig. 4. – The strength s_n of the n-th order as defined in eq. (9) plotted against the order n.

5. – Significance of the shape polarization parameters

The exceedingly good quality of the fit to the spectra by means of eqs. (5) and (6) suggests that it may be possible to extract information regarding shape polarization both as a function of particle energy and of excitation energy. It is tempting to make a connection between this physics and that of sub-barrier fusion. This connection is best seen by considering eqs. (5) and (6). By eliminating the phase-space part of the spectrum one is left with the inverse cross section as a function of particle energy. As we said before, this cross section refers to a hot target. By studying this cross section at low particle energy we are effectively exploring the "sub-barrier" region. Thus the apparent oxymoron: "sub-barrier fusion in hot nuclei". This aspect of the problem is quite tantalizing. In principle one could attempt the same analysis as done in sub-barrier fusion. The product $\varepsilon\sigma_{\rm inv}(\varepsilon)$ can be extracted from the spectrum as shown by eq. (4)

and the barrier distribution can be obtained:

$$B(\varepsilon) = \frac{\partial^2 \varepsilon \sigma_{\mathrm{inv}}}{\partial \varepsilon^2} \,.$$

However, no effort has been made in this direction as yet.

6. – Possible interpretations of the observed modulations

The "wavelength" of the modulations and their small amplitude suggest that they could be modulations associated with the optical potential felt by the α-particle inside the nucleus. Although a fit with an optical model calculation may be premature, the features are consistent with a ground-state–like optical potential with a moderate to large imaginary part. Interesting is the persistence and stability of the modulation with increasing energy. This can be seen from the weak evolution of the extracted coefficient a_n with energy. These results are also consistent with the above interpretation. The temperature involved in the experiment is small and changes little over the excitation energy range investigated. In the temperature range covered by the experiment we expect that the geometries associated with the decay are not greatly altered yet (nuclei do not expand so easily). Similarly, there are good reasons to expect that the strength of the potential has a weak temperature dependence. While we hope that a finer inspection might reveal temperature effects, the gross stability of the modulation with temperature is comforting.

7. – Moment expansion of the evaporation spectra

In the same spirit as in the introduction of barrier distributions functions in fusion reactions, we can try to introduce Gaussian distribution functions associated with the fitting parameters. We have found a very powerful method of doing so through the moment expansion of the spectra.

The moment expansion method can be introduced in the following way: it is always possible to expand the spectral function in Taylor series about the zeroth moments of its parameters, like B, T, p, etc.

Up to second order the expansion gives

$$\bar{P}(\varepsilon, B, T) = P(\varepsilon, \bar{B}, \bar{T}) + \frac{1}{2}\frac{\partial^2 P}{\partial B^2}\bigg|_{\bar{B},\bar{T}} \sigma_B^2 + \frac{1}{2}\frac{\partial^2 P}{\partial T^2}\bigg|_{\bar{B},\bar{T}} \sigma_T^2 + \frac{\partial^2 P}{\partial B \partial T}\bigg|_{\bar{B},\bar{T}} \mathrm{Cov}(B,T) + \ldots, \tag{10}$$

where

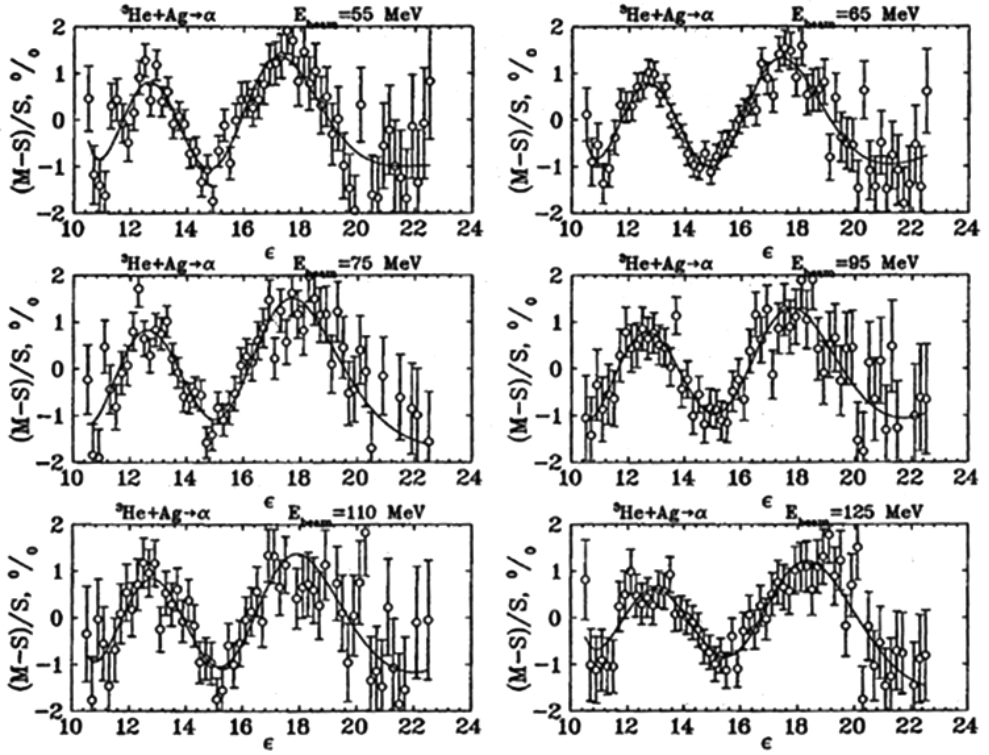

Fig. 5. – Examples of fitting the data with the moment expansion method at different excitation energies. The oscillations are completely described. The circles represent the relative residual of the zeroth-order fit to the data, while the solid lines represent the relative difference between the zeroth-order fit and the actual fit.

$$\sigma_B^2 = \iint_{B,T} w(B,T)(B-\bar{B})^2 \mathrm{d}B\,\mathrm{d}T, \tag{11}$$

$$\sigma_T^2 = \iint_{B,T} w(B,T)(T-\bar{T})^2 \mathrm{d}B\,\mathrm{d}T,$$

$$\mathrm{Cov}(B,T) = \iint_{B,T} w(B,T)(B-\bar{B})(T-\bar{T}) \mathrm{d}B\,\mathrm{d}T$$

The first moments are of course zero since the expansion is about a minimum.

For the function itself we can take eq. (5) or a similar one, since it can reproduce the data to better than 1%. The same equation can be used to evaluate the second derivatives analytically.

An attempt to fit the data has been made with eq. (12) in terms of its seven unknown

parameters.

$$
\begin{aligned}
(12)\quad \bar{P}(\varepsilon,B,T) = {} & A\exp\left(-\frac{\varepsilon-\bar{B}}{T}\right)\operatorname{erfc}\left(\frac{p-2(\varepsilon-\bar{B})}{2\sqrt{p\bar{T}}}\right)\left[1+\frac{\sigma_B^2}{2\bar{T}^2}\right.\\
& \left.+\frac{\sigma_B^2(\varepsilon-\bar{B})}{2\bar{T}^3}\left(\frac{\varepsilon-\bar{B}}{T}-2\right)+\frac{\operatorname{Cov}(B,T)}{\bar{T}^2}\left(\frac{\varepsilon-\bar{B}}{\bar{T}}-1\right)\right]\\
& +\frac{A}{(pT)^{3/2}\sqrt{\pi}}\exp\left(-\frac{\varepsilon-\bar{B}}{T}\right)\exp\left(-\left(\frac{p-2(\varepsilon-\bar{B})}{2\sqrt{p\bar{T}}}\right)^2\right)\\
& \times\left[-\sigma_B^2(p-2(\varepsilon-\bar{B}))+\frac{\sigma_T^2}{16\bar{T}^2}((p-2(\varepsilon-\bar{B}))^2-6p\bar{T})(p-2(\varepsilon-\bar{B}))\right.\\
& \left.+\frac{p\bar{T}-(\varepsilon-\bar{B})p-2(\varepsilon-\bar{B})^2}{T}\operatorname{Cov}(B,T)\right].
\end{aligned}
$$

The results of the fitting procedure can be seen in fig. 5.

We can see that the fits are as good as those obtained with the orthogonal polynomial approach, giving a χ^2 per degree of freedom of order unity.

The conclusion is that the gross and fine features of the experimental evaporation spectra can be expressed in terms of distributions of the model parameters, very much like in the case of sub-barrier fusion, where the cross sections can be reproduced in terms of barrier distribution.

Although it is premature to attempt an interpretation of these results, it is already clear that they contain potentially interesting information on the intrinsic and collective degrees of freedom involved in the evaporation exit channel as a function of the compound nucleus temperature.

8. – Conclusion

Two distinct, though connected, aspects can be discussed in the physics of evaporation spectra.

1) A gross aspect relating to the polarization of the nucleus in the process of emitting the particle. This should become more and more relevant as the atomic number of the particle out of the compound nucleus increases.

2) A fine aspect dealing with the lifetime of the particle inside the nucleus. This should be most important for evaporated nucleons and light particles. In particular, one may learn about the dependence of the imaginary part of the optical potential upon particle binding energy.

In both cases the possibility of performing the studies as a function of excitation energy or temperature is of paramount interest.

* * *

This work was supported by the Director, Office of Energy Research, Office of High Energy and Nuclear Physics, Nuclear Physics Division of the US Department of Energy, under contract DE-AC03-76SF00098.

REFERENCES

[1] See for instance Beckerman M., *Rep. Prog. Phys.*, **51** (1988) 8 and references therein.
[2] Moretto L. G. *et al.*, *J. Phys. G: Nucl. Part. Phys.*, **23** (1997) 1323.
[3] Moretto L. G., *Nucl. Phys. A*, **247** (1975) 211.
[4] Moretto L. G. and Bowman D. R., LBNL report, LBL-23228 (1987).
[5] Jing K. X., PhD Thesis, UCB, Berkeley, (1999) `https://www.osti.gov/scitech/servlets/purl/760325`.
[6] Breus D. E., PhD Thesis, UCB, Berkeley, (2005) `https://digital.library.unt.edu/ark:/67531/metadc787150/`.

Proceedings of the International School of Physics "Enrico Fermi"
Course 201 "Nuclear Physics with Stable and Radioactive Ion Beams", edited by F. Gramegna,
P. Van Duppen, A. Vitturi and S. Pirrone
(IOS, Amsterdam; SIF, Bologna) 2019
DOI 10.3254/978-1-61499-957-7-365

Fission dynamics in systems of intermediate fissility

G. La Rana and E. Vardaci

Dipartimento di Fisica "Ettore Pancini", Università di Napoli Federico II and INFN, Sezione di Napoli - Via Cinthia, 80126 Napoli, Italy

A. Di Nitto

Johannes Gutenberg-Universität Mainz - 55099 Mainz, Germany

P. N. Nadtochy

Omsk State Technical University - Mira prospekt 11, 644050 Omsk, Russia

Summary. — This lecture is aimed at reviewing recent results on the study of fission dynamics. It is well established that fission is a slow process dominated by nuclear viscosity. This is demonstrated by many experimental observations, mainly based on measurements of fission fragment Total Kinetic Energy (TKE), pre-scission light particle, GDR γ-ray multiplicities and energy spectra. Fission time-scale as well as the nature of energy dissipation during the process and its dependence on the nuclear shape and the temperature are the main aspects which have been addressed. In spite of the extensive work, there are still many open questions on the dynamics of the process, mainly due to the lack of constraints on the models and to the different probes used. Intermediate fissily systems are particularly suited for this study as they present comparable cross sections in the fusion-fission and fusion-evaporation channels, allowing to measure observables in both channels, and therefore to further constrain the models. Furthermore, for these systems the path from equilibrium to saddle configuration is expected to dominate with respect to saddle-to-scission one, reducing the complexity of the physical process to be studied. As a case study, we present the study performed on the nucleus ^{132}Ce, which shows the limits of the Statistical Model in accounting for the whole set of observables. We further present the analysis of the data with a 3D Langevin dynamical approach which proves to be capable of reproducing the values of a large set of observables. Our analysis reinforces the fact that extended data sets are essential to achieve reliable simulations to address the open questions on fission dynamics and strongly suggests the use of setups of high efficiency.

1. – Introduction

Several studies on the fission decay of composite systems with $A \approx 180$–250 have shown that the pre-scission multiplicities of neutrons and charged particles increase monotonically with the bombarding energy in contrast with the calculations of the standard statistical model (SM) of evaporation based on the detailed balance principle [1-17]. This finding is considered as the evidence that fission is a slow process with respect to the lifetime for the emission of light particles. With increasing excitation energy, the particle decay lifetime decreases and becomes smaller than the time necessary for building up the collective motion of the nuclear matter towards the saddle point. Consequently, fission does not compete as effectively as predicted by the SM in the early stages of the decay, and particles and γ-ray emissions can occur more favorably. The overall cause of the establishment of these transient effects is believed to be associated with the nuclear matter viscosity which slows down the collective flow of mass from equilibrium to scission and does not allow the fission decay lifetime to be reduced with increasing excitation energy as in the case of light particles. This is equivalent to the assumption that fission is delayed, namely, that the fission probability is not to its full Bohr-Wheeler value in the initial phase of the decay as assumed by the SM. An energy domain has been further identified above which the SM predictions begin to deviate from the data.

A strong dissipation due to nuclear viscosity can indeed trigger a variety of effects of dynamical origin, among which the possibility that a compound nucleus (CN) committed to fission (already at the saddle-point configuration) can still become an evaporation residue (ER) if enough particles are evaporated and the fissility reduced. This correlation between the enhanced yield of pre-scission particles and the survival of evaporation residues might be an important channel for the feeding of evaporation residues having large deformations in the mass region of $A \approx 150$–160.

Most of the estimates of fission time-scale have been obtained from the neutron prescission multiplicities on the basis of the SM. However, several variants of the SM have been proposed in the literature to explicitly consider transient effects, time-scales as well as viscosity. Following the initial idea of the "neutron clock" [4], the common trend is to split the path from the equilibrium point to the scission point configuration into two regions, the pre- and the post-saddle [5]. The total fission time is defined as $\tau_f = \tau_d + \tau_{ssc}$, where τ_d is the pre-saddle delay, namely, the characteristic time that the composite system spends inside the barrier, and τ_{ssc} is the time necessary to travel the path from saddle-to-scission. The relevant observables are computed using τ_d and τ_{ssc} as free parameters, along with the other input parameters relative to the specific ingredients of the model, and fit to the experimental data. However, τ_d and τ_{ssc} are also considered dependent on the viscosity parameter γ. Following Kramer's work [18], the inclusion of dissipative effects results in an effective time-dependent fission decay width $\Gamma_f(t)$ which is smaller than the standard Bohr-Wheeler decay width by a hindrance factor,

$$\Gamma_f(t) = \Gamma_{BW} \left[\sqrt{1+\gamma_{pre}^2} - \gamma_{pre}\right] [1 - \exp(-t/\tau_d)]. \tag{1}$$

Here τ_d is a delay parameter, Γ_{BW} is the Bohr-Wheeler fission decay width, and γ_{pre} is the nuclear viscosity parameter in the pre-saddle that can be written as $\gamma_{pre} = \beta/2\omega_o$. β is the so-called reduced dissipation parameter and ω_o is the potential curvature at the saddle point.

The saddle-to-scission time τ_{ssc} (post-saddle), in this very simplified way of splitting the time scale of a complex phenomenon, might also be dependent on the nuclear viscosity. One widely used ansatz is the following:

$$\tau_{ssc} = \tau_{ssc}(\gamma_{post} = 0)\left[\sqrt{1+\gamma_{post}^2} + \gamma_{post}\right]. \tag{2}$$

In general, the nuclear viscosity parameter might be different inside and outside the saddle point. Furthermore, τ_d, τ_{ssc}, γ_{pre} and γ_{post} are dependent on the excitation energy available, the temperature of the nucleus, the fission barrier, the angular momentum, but are kept constant along the decay chain.

In spite of the extensive work, estimates of the fission time-scales are however quite controversial, ranging from ≈ 5 to $\approx 500 \times 10^{-21}$ s, depending on the system and experimental probe. Furthermore, such estimates are weakened by the fact that different sets of input parameters can result in equally good fits within the same model [7, 12-14].

Dynamical models [19, 20, 22-27], based on the Euler-Lagrange, Fokker-Planck or Langevin equations, have been proposed to estimate the reduced viscosity parameter β and to gain insight on the nature of dissipation. In this approach, the time evolution of properly chosen collective variables on a potential energy surface, when a dissipation term is included, describes the fission process. The dissipation term specifies the mechanism through which excitation energy is exchanged between collective and single-particles degrees of freedom. Once collective variables are chosen, single-particle degrees of freedom are treated as a heat bath. Therefore, one of the main issues is whether the nuclear dissipation mechanism proceeds by means of individual two-body collisions (two-body friction), as in the case of ordinary fluids, or by means of nucleons colliding with a moving potential wall (one-body friction). The analysis of the fission fragment TKE [19], using the one-body or two-body prescriptions in the dissipation function, indicates that this observable alone is not sufficient to clarify this point.

One of the very first application of the Langevin approach was proposed by Wada *et al.* to disentagle between the one-body or two-body dissipation mechanisms [20]. Two-dimensional Langevin equations were used to analyze simultaneously the TKE and the pre-scission neutron multiplicity for the ^{200}Pb nucleus. In this case, it turned out that one-body dissipation allows reproducing both quantities, while an unusually strong two-body viscosity allows reproducing only neutron multiplicity. In a similar study, the values of the reduced viscosity parameter $\beta = 15 \times 10^{21}$ and $24 \times 10^{21}\,\mathrm{s}^{-1}$, extracted from the prescission neutron multiplicities for the composite nucleus ^{188}Pt at $E_x = 99.7$ and 101.4 MeV, were found consistent with one-body dissipation [21]. The observed value of $\beta = 6 \times 10^{21}\,\mathrm{s}^{-1}$ for the same CN but at $E_x = 66.3$ MeV allowed to even infer a possible increase with temperature of nuclear viscosity. A different result was

found however for the ^{220}Th system by Rubchenya *et al.* [10], on the basis of pre-scission neutron multiplicities. They found that the effective average value of β decreases with increasing excitation energy, similarly to the temperature dependence expected for the two-body viscosity. A systematic study was also carried out by Bhattacharya *et al.* [22]. They found that the values of viscosity coefficient used to reproduce the observed neutron multiplicities alone increase with the mass and the excitation energy per nucleon of the composite system and follows a kind of a global relation. In conclusion, on the basis of a review of the current studies on the subject, the β values are found to range from ≈ 2 up to $30 \times 10^{21}\,\mathrm{s}^{-1}$. However, the estimates of β, from the fits to the particle and GDR γ-rays multiplicities with the statistical models, provide a contradictory picture of the values of β, which range over an order of magnitude, and rather controversial conclusions on the nature of nuclear dissipation and its dependence on the shape and temperature.

2. – Dynamical *vs.* statistical approach

Besides the specialistic details, there are a few characteristic features of the description of the fission process that appear out of these two entirely different approaches that are quite surprising. In the SM approach, the viscosity parameters are treated as constant free parameters to be adjusted on the experimental data. From the fits to the data it turns out that the viscosity is higher in the post-saddle path than in the pre-saddle one, and increases with the temperature or the square of the temperature [12,13]. Light particles and/or GDR γ-rays are emitted mostly in the post-saddle region where viscosity is higher [12]. Added to this is the fact that the same data can be reproduced equally well if the viscosity is considered to be temperature- or deformation-dependent [11, 12, 14]. In the dynamical approach, the CN can pass the saddle point several times before eventually undergoing fission and there is no free parameter in the dissipation model (one- or two-body) except for a strength parameter [26, 27]. In the one-body model, the dissipation is shape-dependent but not temperature-dependent. Contrary to what occurs in the statistical approach, it turns out that viscosity is higher in the pre-saddle shape configuration and, hence, light particles and/or GDR γ-rays are emitted mostly in the pre-saddle region. This behaviour does not change if the one-dimensional (1D) version of the dynamical approach [26, 27] is used. Furthermore, in both one- or two-body dissipation models there is no explicit dependence on the temperature. The question is how it could be possible to disentangle this apparent contradiction between the statistical and dynamical description of the fission process. Somehow the answer could be straightforward because the statistical approach, for instance, can only mimic a dissipation model by introducing *ad hoc* parameters and average shapes in the deformation space. To draw a more consistent description of nuclear dissipation, and its connection with the shape and temperature, it seems reasonable and crucial to start by taking into account a larger number of observables which can be expected to be sensitive to nuclear dissipation and try to reproduce their measured values with a unique set of input parameters.

3. – Dissipation in systems of intermediate fissility

Composite systems of intermediate fissility ($\chi = 0.5$–0.6) are very little studied, although they offer quite a unique environment where nuclear viscosity can be effectively studied. They are characterized by an ER cross-section comparable to or larger than the fission cross-section, and by a shorter path in the deformation space from the saddle-to-scission point [30]. Consequently, 1) models, as well as their input parameters, can be further constrained by the energy spectra and multiplicities of light particles in the ER channel; 2) the effect of the fission delay over fission and ER cross-section is much more pronounced with respect to heavier systems because the emission of a charged particle in the pre-saddle region strongly enhances the probability of producing an ER as a consequence of both reduction of the fissility and the larger value of the angular momentum necessary to ignite fission. The fact that the potential energy surface is characterized by a shorter path from the saddle-to-scission point implies that the role of the pre-saddle dynamics relative to the saddle-to-scission dynamics is enhanced and, therefore, some of the ambiguities on the not-well identified separation and interplay between pre-and post-saddle might be reduced in the interpretation of the data. We expect that the measurements of neutron and charged particle multiplicities and energy spectra in the two channels as well as the measurements of the cross-sections of the channels themselves will allow more severe constraints onto the models. This should provide more reliable values of fission delay and viscosity parameter, and contribute to a better comprehension of nuclear viscosity. To put this criterion into practice, the 8πLP Collaboration has started a research program at the Laboratori Nazionali di Legnaro (LNL), Italy, aimed at studying the fission dynamics in systems of intermediate fissility. In the following sections we will discuss a specific case study of such systems.

4. – The 8πLP apparatus

The 8πLP apparatus [31] (fig. 1) is a 4π light charged particle detector assembly consisting of two detector subsystems, each made of two-stage telescopes: the WALL and the BALL. The WALL contains 116 telescopes and is placed at 60 cm from the target. Each of the WALL telescopes consists of a 300 μm Si detector backed by a 15 mm Csi(Tl) crystal and has an active area of 25 cm^2 corresponding to an angular opening of about 4°. The WALL covers the angular range from 2° to 24°. The BALL has a diameter of 30 cm and consists of seven rings placed coaxially around the beam axis. Each ring contains 18 telescopes and covers an angular opening of about 17°. The telescopes of the BALL are made of a 300 μm Si detector mounted in the flipped configuration (particle entering from the Ohmic side) backed by a 5 mm CsI(Tl) crystal. The BALL has a total of 126 telescopes and covers the angular range from 34° to 177°. The rings are labelled from A to G from backward to forward angles.

Particle identification is carried out by the ΔE-E method for the ions that do not stop in the E stage. The particles stopping in the E stage are identified by the TOF method in the case of WALL telescopes, and by the pulse shape discrimination (PSD)

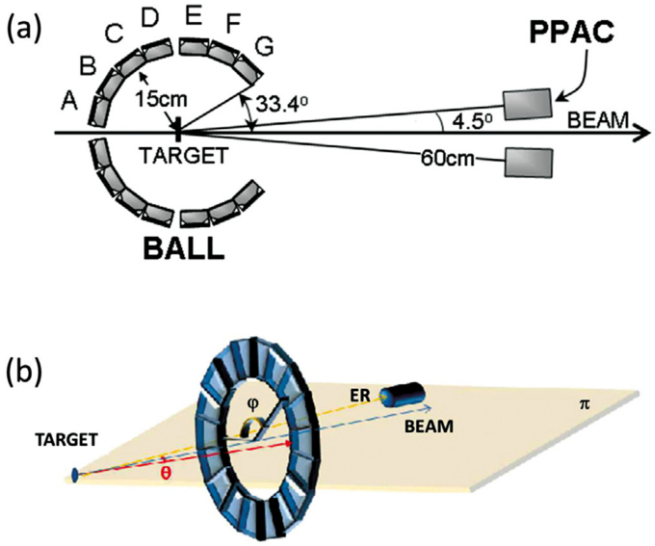

Fig. 1. – (a) Schematic layout of the experimental apparatus. The letters from A to G label the seven rings of the BALL section. (b) The geometry used for the angular distribution of LCP detected in a ring around the beam in coincidence with ER detected in a parallel-plate avalanche counter (PPAC) horizontal plane. π indicates the reaction plane, which is defined as the plane containing the beam and the PPAC.

technique in the case of BALL telescopes. In this configuration it is possible to measure energies up to 64 AMeV in the WALL and 34 AMeV in the BALL with energy thresholds of 0.5 and 2 MeV for protons and α-particles, respectively.

Heavy fragments can be detected in the telescopes of the BALL. The PSD technique allows the separation between heavy fragments and light particles stopping in the same detector. The selection between symmetric and asymmetric mass splittings can nevertheless be achieved on a kinematics ground [34]. In the 8πLP set-up it is also possible to detect ER. The WALL detectors between 2.5° and 7.5° around the beam axis are in fact replaced by four parallel-plate avalanche counter (PPAC) modules, each one subtending a solid angle of about 0.3 msr. Each module consists of two coaxial PPACs mounted and operating in the same gas volume at a distance of 15 cm from each other. By adjusting the gas pressure, it is possible to stop the ER between the two PPACs, and let the fission fragments and elastic scattered ions to impinge on the second PPAC. Consequently, ERs are sorted out from the first PPAC signals using the signals from the second PPAC as a VETO signal.

With this device it is possible to detect, in the same experiment, light charged particles in coincidence with fission fragments and evaporation residues. Furthermore, given the large angular coverage and the symmetrical location of the detectors around the beam axis, angular distributions, along with the differential multiplicity distributions, can be constructed, in- and out-of the reaction plane, by summing events recorded within the many equal angular correlations.

5. – A case study: the system $^{32}S + ^{100}Mo$ at 200 MeV

In order to highlight the benefits of studying fission dynamics with an approach based on systems of intermediate fissility and a dynamical model we start by specifying how such systems can guarantee a large set of observables that should all together be reproduced within the same dynamical model. We consider here the reaction $^{32}S + ^{100}Mo$ at 200 MeV that leads to the composite system ^{132}Ce at $E_x = 122$ MeV and fusion angular momentum $L_{fus} = 72\hbar$, derived from the measured fusion cross-section in the sharp cut-off approximation. We shall show the inability of the SM to provide an estimate of the fission time-scale when the ER channel is included as a further constraint in the procedure used to estimate the fission delay time. Afterwards, our study with an advanced realistic dynamical approach based on a 3D-Langevin approach will be discussed.

5˙1. *Experimental procedure and data analysis*. – The experiment was performed at the XTU Tandem-ALPI Superconducting LINAC accelerator complex of the LNL. A 200 MeV pulsed beam of ^{32}S of about 1 pnA intensity was used to bombard a self-supporting ^{100}Mo target of 300 μg/cm^2 thickness. A beam burst with a frequency of about 1.25 MHz and duration of about 2 ns was used. We used the BALL and the WALL sections of the 8πLP apparatus to detect light charged particles (LCP). The experimental method consists of measuring light charged particles (LCPs) in coincidence with both fission fragments (FFs) and evaporation residues (ERs). The fission fragments were detected in the telescopes of the rings F and G of the BALL. The PSD technique allows the separation between heavy fragments and LCP stopping in the same detector. ERs were detected through the four parallel-plate avalanche counter modules. In a separate experiment at LNL, ERs and FFs cross-sections were measured, respectively, using an electrostatic deflector and the double-arm time-of-flight spectrometer CORSET [32].

Figure 2 shows, for alpha-particles, the experimental differential multiplicity energy spectra (histograms) for 12 in-plane angular correlations. The multiplicity spectra are obtained by normalizing the area of each spectrum to the number of fission events measured by the trigger detectors. This conversion is easily done because single FFs (or ERs) events are measured simultaneously to the coincidences in the same run. In order to extract the pre-and post-scission angle integrated multiplicities, particle spectra were analysed assuming three evaporative sources [33, 34]: the composite nucleus prior to scission (CE) and the two fully accelerated fission fragments (F1 and F2). We have used a well-established procedure that employs the code GANES [37] and that takes advantage of the different kinematics of the three emission sources. In this procedure, proton and alpha particle evaporation spectra are computed separately for each emitting source in the experimental detection conditions within the window of angular momentum associated to FF. In our case the window is 67–72 $\hbar$ as extracted from the channel cross-sections σ_{ER} and σ_{FF}.

The full set of data is shown in table I along with the results of the SM calculations performed with the code PACE2 N97 [35] and a 3D Langevin dynamical code [24, 26] which implements one- and two-body dissipation models. The dynamical model was

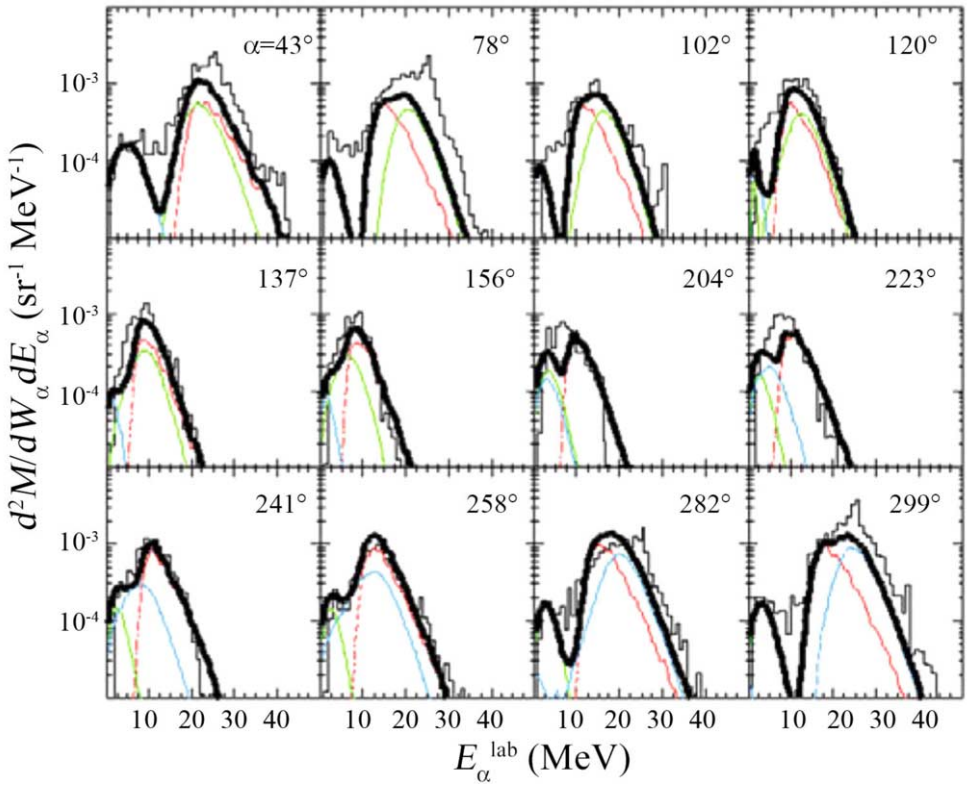

Fig. 2. – Experimental (histogram) in-plane multiplicity spectra of alpha-particles in coincidence with fission fragments detected in the rings F and G of the 8πLP apparatus. In red the evaporative component from the composite system prior to scission; in blue and green the evaporative components from the two fission fragments; in thick solid line the sum of the three components (for details see text).

Table I. – *Proton and α-particle multiplicities in the ER and pre-scission channels together with the FF and ER cross-sections for the* 200 MeV $^{32}S + ^{100}Mo$ *reaction. The SM calculation refers to the case where the parameters are chosen to best reproduce the FF channel data without time delay (see text for details).*

	ER channel			FF Channel				
	M_n	M_p	M_α	M_n	M_p	M_α	σ_{ER} (mb)	σ_{FF} (mb)
Exp.	–	0.90 ± 0.14	0.56 ± 0.09	–	0.055 ± 0.007	0.038 ± 0.05	828 ± 50	130 ± 13
SM	4.26	1.44	1.64	0.42	0.058	0.034	813	143
One body	5.30	1.198	0.556	0.63	0.064	0.0399	786	150

coupled with the statistical model Lilita N97 [36] to simulate the emission of protons, neutrons and α-particles from ERs and the composite system before scission (pre-scission emission).

The symbols are as follows: the multiplicities of the protons and α-particles are, respectively, M_p and M_α; σ_{ER} and σ_{FF} are, respectively, the ERs and FFs cross-sections.

5˙2. *Statistical model analysis.* – The measured quantities in table I were analysed with the SM implemented in the code PACE2. The original code has indeed been extended by including new options for the level density and the transmission coefficients as well as fission delay according to the prescription given in [1]. If we limit our analysis to the FF channel only, namely, if we try to reproduce only the multiplicities in the FF channel as usually done [1], the data shown in table I can be reasonably well reproduced by assuming $a_\nu = A/9$, $a_f/a_\nu = 1.04$, liquid-drop model (LDM) yrast line and optical model (OM) transmission coefficients, without any delay. The parameter $a_\nu = A/9$ is the Fermi gas level density parameter for particle evaporation and a_f is the level density parameter for fission. From this result one could conclude that no transient effect takes place in this decay, although it has been verified that a different combination of input parameters does not exclude the presence of a relatively small fission delay. On the other hand, with the same input parameters, the statistical model strongly overestimates the ERs particle multiplicities even though it reproduces the ERs cross-section. This is an evident contradiction: if the model is not able to reproduce the LCPs multiplicities in the ER channel, once the ER cross-section is well accounted for, the same model cannot be assumed to be a reliable tool to estimate the fission time-scale through the pre-scission light particle multiplicities.

To explore the possibility to reproduce the data in both channels with a unique set of input parameters we performed an extensive analysis with different prescriptions of the level density parameter and transmission coefficients (TC). Calculations were carried out by adopting three different and well-known directives for the yrast line: 1) Gilbert-Cameron, 2) LDM and 3) sharp rigid sphere with radius parameter $r_o = 1.2\,\mathrm{fm}$. Different prescriptions have also been used for the level density parameter a_ν: 1) a constant value ranging from $A/6$ to $A/12$, 2) inclusion of shell effects with a damping term as a function of the excitation energy and 3) a temperature-dependent prescription. Transmission coefficients derived from OM and Fusion Systematics (FS) were used. Different values of fission delay and a_f/a_ν were adopted to modulate the particle-fission competition. Calculations were constrained by the sum of the measured ER and fission cross-section $\sigma_{fus} = \sigma_{ER} + \sigma_{FF} = 958\,\mathrm{mb}$. In fig. 3 we show the experimental multiplicities for protons and α-particles, in the ER and FF channels, as well as the measured channel cross-sections, compared to the calculated values, as a function of the ratio a_f/a_ν. We report in fig. 3 also the SM results corresponding to the prescriptions labelled as (a), (b), (c) and (d), whose peculiarities are reported in table II. The prescriptions (a), (b), (c) and (d) presented here were chosen among the many combinations for which calculations were performed as they allow to explore the full range of variability of the calculated values of the observables under examination. No fission delay was included in the calcu-

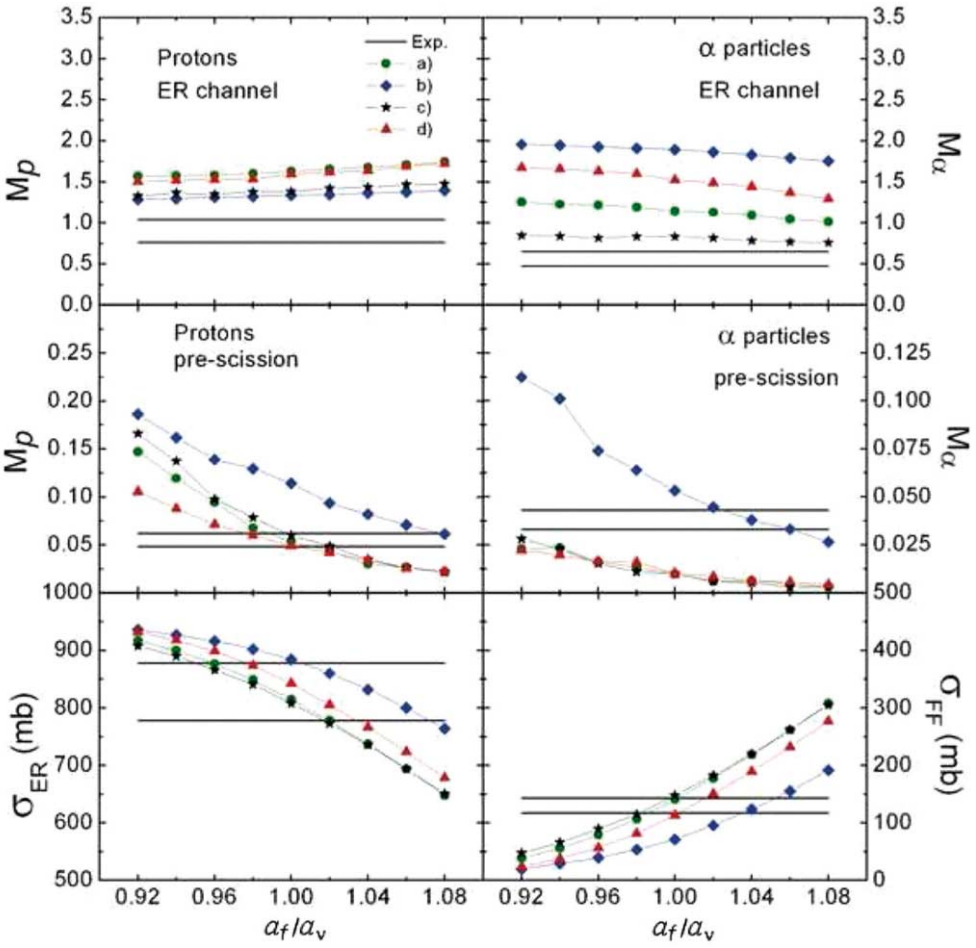

Fig. 3. – Measured ER and pre-scission LCP multiplicities along with the FF and ER cross-sections (horizontal solid lines indicate measured lower and upper limits due to the experimental errors), compared to the calculations of the SM changing i) the level density parameter a, ii) the yrast line and iii) the transmission coefficients (for details see text).

lations. From fig. 3 we infer that the SM strongly overestimates proton and α-particle multiplicities in the ER channel for this system, irrespective of the input parameters and prescriptions used for the level density and TCs. The same result is confirmed by the calculations performed with the well-known code Lilita N97 [36]. Furthermore, the inclusion of a time delay to further suppress the fission does not change the overall pattern of the calculated data with respect to the experimental data. At the same time, the influence of nuclear deformation would further enhance the predictions of SM particle multiplicities, resulting in a larger overestimation. On the other hand, the comparison of the measured proton and α-particle energy spectra with the SM does not show any evidence of nuclear deformation.

TABLE II. – *Summary of the SM parameters used in the calculations for the level density parameter a, yrast line (YR) and TC.*

Prescriptions	a_ν	YR	TC
(a)	$A/6$	RS	OM
(b)	$A/12$	LDM	OM
(c)	$A/6$	RS	FM
(d)	$A/6$	LDM	OM

It should be pointed out that the overestimate in the ER channel found for the present compound system was also found in other systems of similar mass. We have, in fact compared the experimental data taken from the literature with the predictions of our code PACE2 N97. Indeed, in the literature there are only few systems for which the ER channel LCP multiplicities were measured. From the calculations performed by us, once again we find that the SM overestimates protons and α-particle multiplicities in the ER channel which makes us to suspect that the SM is behaving surprisingly at variance with what is expected.

5˙3. *Dynamical model analysis*. – The contradictory results shown above outline the necessity of considering dynamical models. Recently, we have coupled the Lilita N97 code with a dynamical model [24, 26] which describes the fission process by using a 3D Langevin stochastic approach. This coupling was necessary to allow the evaporation of light particles from the composite system during the evolution along trajectories in the phase space. In this study, we have performed several sets of calculations for the $^{32}\mathrm{S} + {}^{100}\mathrm{Mo}$ system at $E_{Lab} = 200\,\mathrm{MeV}$ by assuming different prescriptions of TCs and level densities for particle evaporation, and by modulating the values of the strength of the one- and two-body dissipation schemes. From table I we see that the one-body model can reproduce most of the measured quantities, including the ones in the ER channel, by assuming full one-body dissipation. The value $a_\nu = A/6$ is used in the SM decay branch. To obtain a similar agreement with two-body dissipation, an unrealistic value of viscosity parameter has to be used, as already found in [20].

Experimental proton and α-particle energy spectra for both ER and FF channels have also been compared with the predictions of the dynamical model. Only emission from spherical nuclei has been assumed in the calculation for both channels. We know that this is an important limitation of the actual implementation of the model, and we are working on possible solutions which must take into account the fact that the shape of the fissioning nucleus is known step by step. However, from the comparison with the experimental data we can already infer how important the shape of the nucleus can be in the evaporation process, especially considering that the shape itself is connected with the dissipation strength. The comparison of the energy spectra for the ER channel is shown in fig. 4. The good agreement indicates that nearly spherical nuclei are involved in the

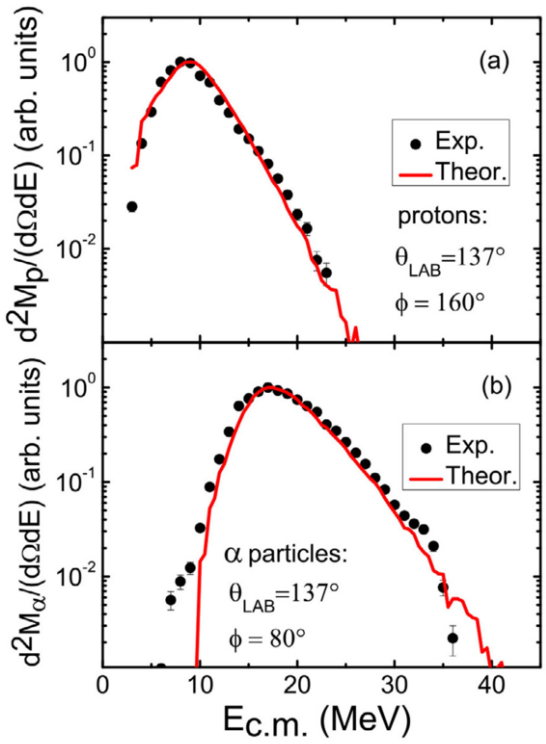

Fig. 4. – Measured proton (a) and α-particle (b) energy spectra in the center-of-mass system ($\theta_{LAB} = 137°$) for the ER channel compared with the prediction of the dynamical model obtained with the basic set of input model.

ER channel. A good agreement is also obtained for α-particles in the FF channel (cf. fig. 5), indicating, also in this case, that these particles are emitted from nearly spherical nuclei. This result also implies that pre-scission α-particle emission occurs in the early stage of fission, where small deformations are involved. This is in agreement with the findings of ref. [30], where a phenomenological analysis with the statistical model has been carried out. As far as pre-scission protons are concerned, the model is not able to reproduce the experimental spectra as well as in the case of the α-particles. The excess of measured low-energy protons with respect to the simulation is indicative of strong deformations of the emitter. This deformation should also produce a lowering of the high-energy part of the spectrum, with respect to the spherical case, because of the increase of the moment of inertia. This effect, however, is not observed. On the contrary, we observe an excess of high-energy protons with respect to the predictions of the model. The rigorous account of deformation dependence of the statistical model parameters like reduction of emission barriers for charged particles, change of level-density parameter for the deformed shapes of fissioning nucleus, could also change the shape of the spectra.

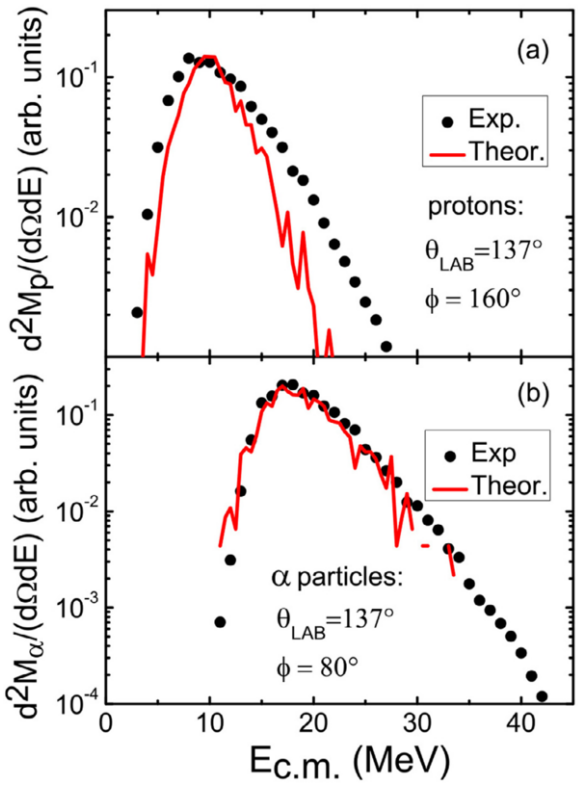

Fig. 5. – Same as fig. 4 but for the FF channel.

In this respect, the comparison of the data with calculations for deformed nuclei could be particularly elucidating. Such a study will be possible with a further extension of the model, which should include a consistent treatment of particle evaporation taking into account the instantaneous deformation of the compound nucleus determined from the solution of dynamical equations. Nevertheless, the possibility to compute the prescission particle energy spectra, even in a simplified way, clearly shows that this additional observable carries valuable information concerning the fission dynamics. A more detailed picture can be achieved when also energy spectra can be reproduced along with the other traditional observables.

5˙4. *Angular correlation ER-LCP*. – The angular correlation between LCPs and ERs is an observable that can be obtained using 8πLP. In fact, owing to the high granularity and the large number of used detectors it is possible to measure the coincidences with a large variety of geometrical configurations.

As shown in fig. 6, the angular distribution has an oscillating behavior as a consequence of a combined effect of kinematics and angular momentum, as shown in ref. [34]. With reference to the geometry in fig. 1, the maxima correspond to the events where ER

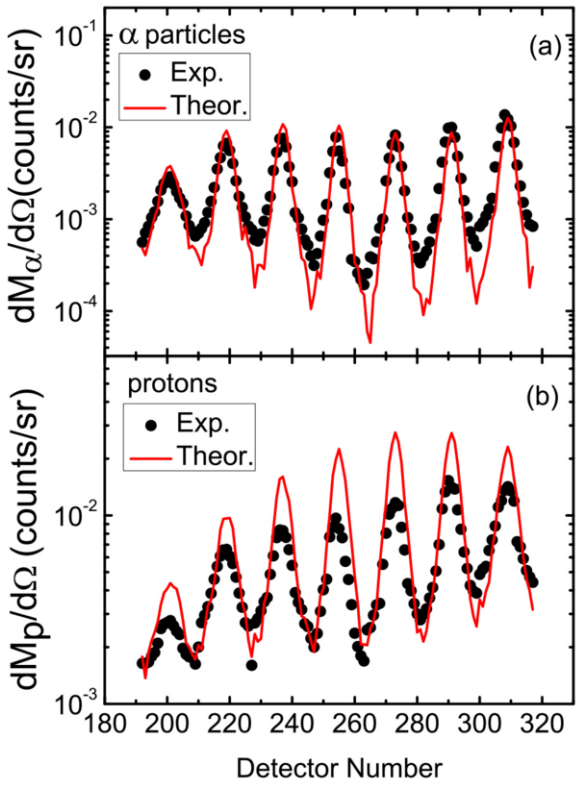

Fig. 6. – Measured ER-α (a) and ER-p (b) angular correlations, compared with the predictions of the dynamical model. LCP have been detected by 8πLP-BALL detectors, whose number is reported in the abscissa. Evaporation residues have been detected at $\theta_{LAB} = 4.5°$.

and LCP are in plane and on the opposite side of the beam; the minima occur when ER and LCP are in plane and on the same side with respect to the beam direction. The comparison between calculated and experimental data is shown in fig. 6. The ER-LCP angular distribution turned out to be more sensitive to the relevant parameters of the statistical model than the spectral shapes. The angular correlation for α-particles could be reproduced reasonably well, including the amplitude of the oscillations. The oscillating behavior is reasonably well reproduced also for protons, but mostly the maxima are overestimated by the model. This overestimation reflects the overevaluation of proton multiplicity in the ER channel p_{ER} reported in table I. As the values of the model parameters are constrained by the full set of experimental observables, we did not vary them to improve the agreement only for ER-proton angular correlation. A better agreement could indeed be obtained for this observable by changing the parameters of the statistical model which could decrease the p_{ER} value [34], but this would make worse the overall agreement for the full set of data, in contradiction with the approach of this work.

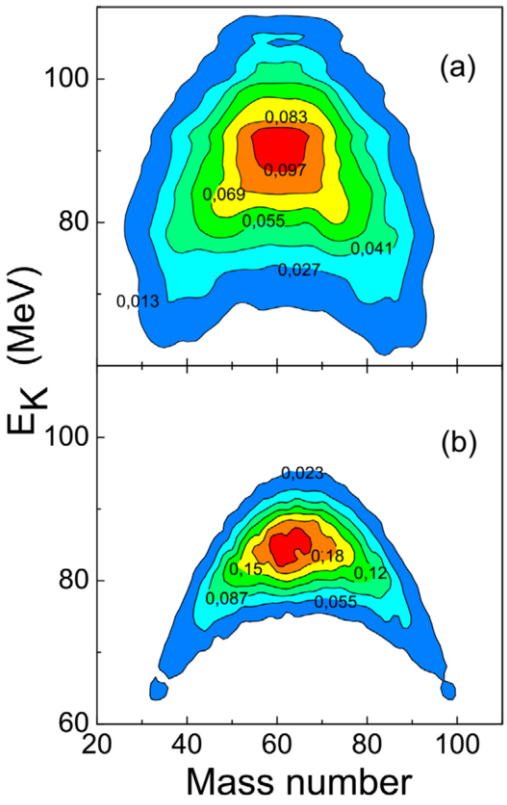

Fig. 7. – Experimental (a) and theoretical (b) MED of fission fragments for the ^{132}Ce composite system. See text for details.

5˙5. *Mass-energy distribution of fission fragments*. – Figure 7(a) shows the Mass Energy Distribution (MED) as measured and fig. 7(b) shows the MED computed with the dynamical model and the basic set of parameters. Mass-energy distributions have been measured at angles where the contribution from Deep Inelastic Collision (DIC) fragments is expected to be negligible with respect to that from fission fragments, on the basis of kinematics. One can see a qualitative agreement in the general behavior of the contours between the experimental and theoretical two-dimensional plots. However, the calculated distribution deviates from the experimental one particularly around the symmetric fission. In the calculations there are no events with $E_K > 95\,\text{MeV}$ and $E_K < 75\,\text{MeV}$ at nearly symmetric fission. This indicates that in the dynamical calculations, at the scission point, the parametric geometrical representation chosen for the shapes is not suitable to sample a sufficiently large variety of shapes of the fissioning nuclei. In particular, there is not enough variability in the elongation of the scission configurations for a given mass asymmetry. Introducing a more flexible shape parametrization at the scission region could generate a larger variety of E_K values, with the result of expanding the calculated MED with respect to the E_K axis.

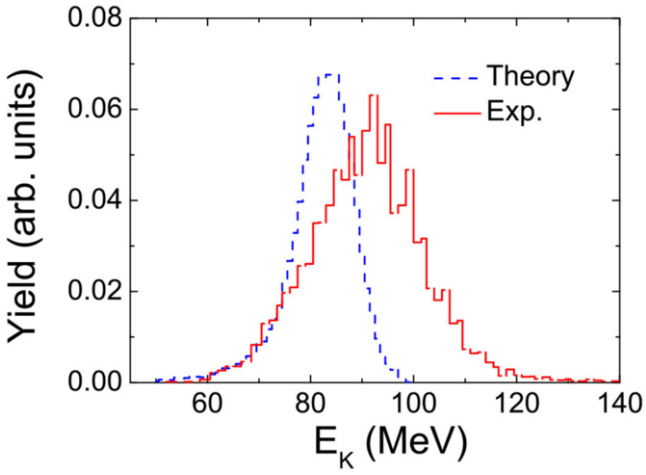

Fig. 8. – Experimental and theoretical kinetic-energy distribution of fission fragments.

5˙6. *Total kinetic-energy distribution of fission fragments.* – The kinetic-energy distribution of fission fragments is obtained by integration of two-dimensional MED over fission fragment mass. The comparison between calculated and experimental kinetic-energy distribution of fission fragments is presented in fig. 8, where the difference between them is clearly seen. The yield of calculated energy distribution is substantially lower than the experimental one in the range of high E_K values: $95\,\mathrm{MeV} < E_K < 120\,\mathrm{MeV}$, the latter being substantially wider than the calculated one. A similar result has been obtained in three-dimensional Langevin calculations in refs. [24, 28]. The maxima of kinetic-energy distributions show a difference of about 10 MeV.

To get a better reproduction of the experimental kinetic energy distribution, one needs to use lower values of the viscosity strength K_s, which does not make it possible to reproduce the pre-scission particle multiplicities [29]. Furthermore, the sensitivity of the standard deviation of the energy distribution σ_{EK} to the strength of the viscosity is found to be very small.

5˙7. *Mass distribution of fission fragments.* – The mass distribution of fission fragments is presented in fig. 9. One can see that the theoretical calculations with one-body dissipation is able to reproduce reasonably well the experimental data, although the model slightly underestimates the width of the distribution. Even in this case a lower value of K_s would improve the experimental mass distribution, but, as previously said, this would not reproduce the pre-scission particle multiplicities. The variance of the mass distributions for ^{132}Ce is not very sensitive to nuclear dissipation, it changes only about 25% when the viscosity coefficient K_s changes from 0.1 to 1. This feature of the mass distribution is attributable to a short descent from the saddle to the scission point for light nuclei. The fissioning system ^{132}Ce passes the region between saddle and scission point in approximately 3×10^{-21} s. Moreover, the stiffness of the potential energy with

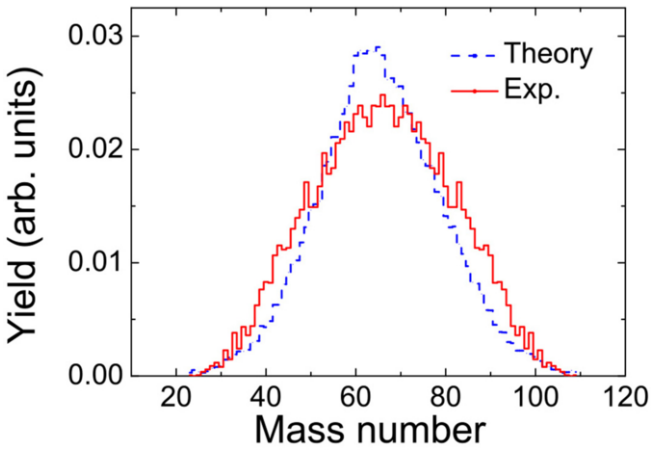

Fig. 9. – Experimental and theoretical mass distribution of fission fragments.

respect to the mass-asymmetry coordinate at saddle and scission points is approximately the same. Therefore, during the descent from the saddle to the scission point the fluctuations of mass-asymmetry collective coordinates, which determine the width of mass distribution, have not the opportunity to become large.

5˙8. *Fission time scale*. – In fig. 10(a) we show how the reduced friction coefficient varies with the deformation of the nucleus en route towards fission in the one-body dissipation model. The case that can give the best agreement with the full set of data is represented by the red line ($K_s = 1$), namely, full one-body dissipation. The two-body dissipation case is represented by the black line. It is clear that the one-body dissipation shows a stronger dependence on deformation. Furthermore, the viscosity grows at the beginning of the deformation until a maximum is reached; later, it decreases monotonically for increasing deformation. This implies that the viscosity shows the maximum strength only at the beginning of the collective motion and when the shape is still fairly compact. No dependence on temperature is assumed so far. From the model and the computational method it is also possible to build the time distribution of all fission events. This is shown in fig. 10(b).

This figure reveals indeed that fission can take place in quite a broad interval of time. In the time interval $0 < t < \tau_d$ there are no fission events at all. The time $\tau_d = 5 \times 10^{-21}$ s could be considered the analog of the delay parameter often used in fission studies [23, 38]. Furthermore, we observe a steep rise from $\tau_d = 5 \times 10^{-21}$ s up to the maximum at $t = t_f^{\max} = 30 \times 10^{-21}$ s. At $t_f > t_{\max}$ the fission time distribution has a nearly exponential decrease with a long tail lasting up to 10^{-18} s. The arrow at $t = 1250 \times 10^{-21}$ s indicates the mean fission time t_f. This value is strongly influenced by the tail of the fission time distribution. The parameters that characterize this fission time distribution are reported in table III. They are obtained from the calculation that provides the best description of the experimental data in ER and FF channels.

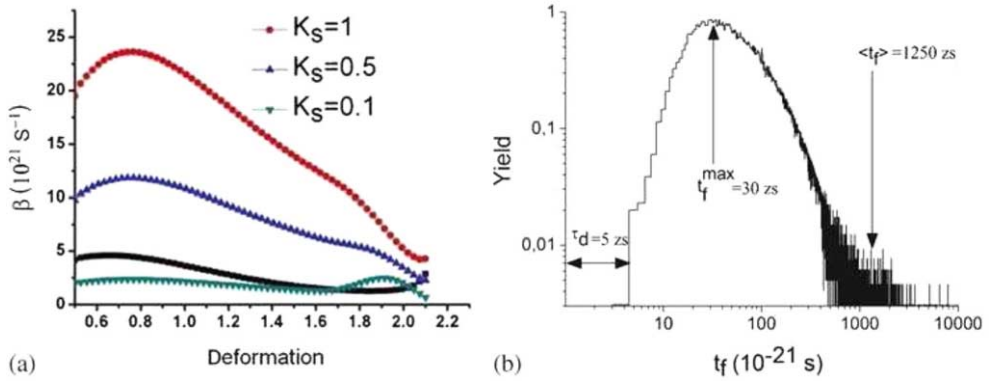

Fig. 10. – Reduced dissipation parameter *vs.* deformation of the compound nucleus. K_s is the strength of the one-body dissipation. $K_s = 1$ represents full strength. The black solid line is the functional dependency expected in the case of two-body dissipation. (b) Time distribution of all fission events for the ^{132}Ce nucleus in one-body dissipation.

To illustrate how particle evaporation is distributed in time before fission occurs, we show in fig. 11(a) the percentage yields of the first- $Y_{n1}(t)$, the second- $Y_{n2}(t)$, and the third-chance $Y_{n3}(t)$ pre-scission neutron as a function of time. The yields for the first-chance pre-scission proton and α-particle are presented in fig. 11(b). From these figures one can see that particle evaporation starts from $t = 0$. The yields for the first-chance neutron, proton, and α-particle have approximately the same behavior as a function of time. It is an exponential decrease from the maximum at $t = 0$, to zero at $t = 250 \times 10^{-21}$ s. Considering the multiple emission of neutrons, one can see that the emission of every further neutron requires a correspondingly larger time. The maxima for $Y_{2n}(t)$ and $Y_{3n}(t)$ are at nearly 100×10^{-21} s and 900×10^{-21} s, respectively. The main reason for such a behavior is the reduction of the excitation energy E_x after each evaporation step. From the investigation of the characteristic times of particle emissions one can estimate the time scales of the different steps accompanying the decay of the compound nucleus.

These results are quite informative because they show that fission can take place in

Table III. – *The parameters of fission time distribution extracted from the simulation with the dynamical model.*

Compound system	τ_d 10^{-21} s	$\tau_f^{\max}$ 10^{-21} s	$\langle\tau_f\rangle$ 10^{-21} s
^{132}Ce	5	30	1250

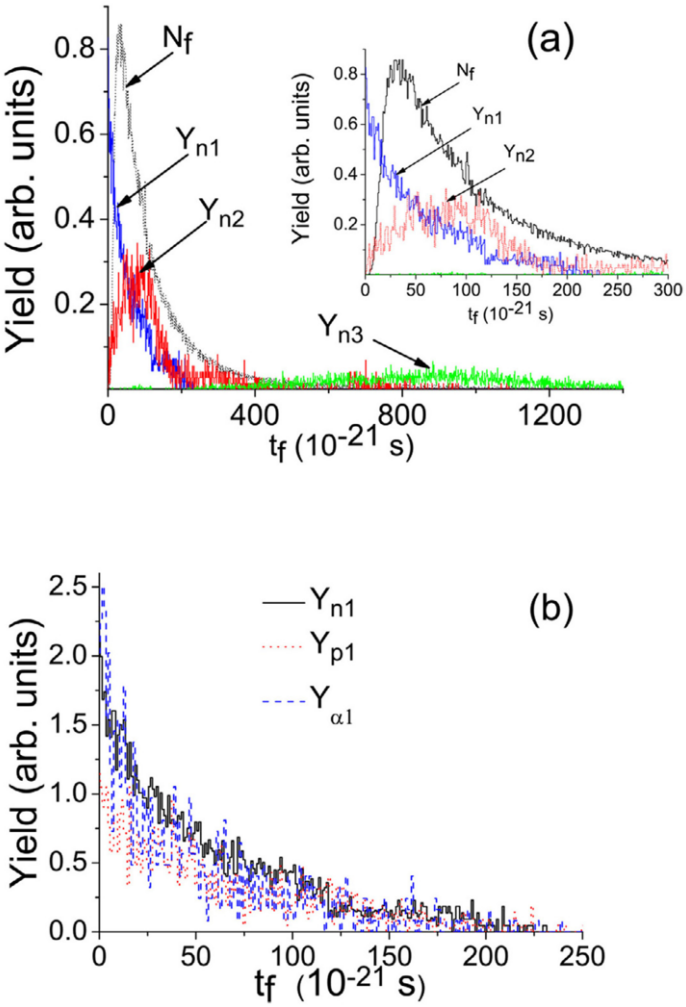

Fig. 11. – Distribution of the yields of pre-scission particle multiplicities *vs.* time of emission from equilibrium: (a) first-(Y_{n1}), second-(Y_{n2}), and third-(Y_{n3}) chance pre-scission neutrons together with time distribution of fission events (N_f); (b) first-chance neutron (Y_{n1}), proton (Y_{p1}) and α-particle ($Y_{\alpha 1}$). See text for details.

quite a large interval of time. The time delay parameter widely used in the statistical approach does not correspond to any of the above characteristic times of the distribution and this confirms the inadequacy of the SM approach to nuclear dissipation. The extension of time distribution may also explain why different time-scales are extracted with the SM approach when different probes are used.

6. – Conclusions and perspectives

The study on the system $^{32}S + ^{100}Mo$ at 200 MeV highlights the inadequacy of the SM in describing the LCP particle multiplicities in the ER channel. The same analysis performed on the data from literature in the region of mass number $A \approx 150$ and excitation energy $E_x \approx 100$–150 MeV, for the ER channel, provides similar conclusions. These findings repropose the problem of reliability of the SM in describing the CN decay and have a relevant impact on the extraction of the fission delay time through the use of SM. The dynamical approach to fission decay is indeed very promising in describing both fission and ER channel within the same model. Furthermore, the dynamical model may reveal more intimate details of the fission process. For instance, the time distribution of the fission events provides hints to interpret the large variety of fission time-scales found in the literature.

The model can be more and more refined. We have indeed enlarged the computational capabilities of our code to include the calculation of energy spectra and angular distribution of the pre-scission particles. This is a novel feature that constrains the model parameters even more. One observable which we also consider important is the isospin degree of freedom. In [27, 30] the importance of selecting the proper probe for testing a dissipation model according to the isospin of the CN is discussed. A component still missing in our computational model is the evaporation from the fission fragments. This is an important feature because post-scission light particle multiplicities are also measured. The comparison of these observables with the predictions of a model that follows the full decay chain, from equilibrium to fragment decays, would probe the models in more detail for the sharing of excitation energy and angular momentum between the fission fragments, and would provide a more direct link to the features of a nucleus at the scission point. An example for this is the temperature of the nucleus at the scission point. Such an extension of the model should also consider the possible dependence of nuclear viscosity on the temperature. Consequently, experiments should be designed to explore this particular aspect. Both of these developments are currently in progress.

REFERENCES

[1] Hilscher D. and Rossner H., *Ann. Phys. (France)*, **17** (1992) 471 and references therein.
[2] Gavron A. *et al.*, *Phys. Rev. C*, **35** (1987) 579.
[3] Hinde D. J. *et al.*, *Phys. Rev. C*, **39** (1989) 2268.
[4] Hinde D. J. *et al.*, *Phys. Rev. C*, **45** (1992) 1229.
[5] Lestone J. P. *et al.*, *Nucl. Phys. A*, **559** (1993) 277.
[6] Thoennessen M. and Bertsch G. F., *Phys. Rev. Lett.*, **71** (1993) 71.
[7] A Chatterijee A. *et al.*, *Phys. Rev. C*, **52** (1995) 3167.
[8] Saxena A. *et al.*, *Phys. Rev. C*, **49** (1994) 932.
[9] Fiore L. *et al.*, *Nucl. Phys. A*, **620** (1997) 71.
[10] Rubchenya V. A. *et al.*, *Phys. Rev. C*, **58** (1998) 1587.
[11] Back B. B. *et al.*, *Phys. Rev. C*, **60** (1999) 044602.
[12] Dioszegi I. *et al.*, *Phys. Rev. C*, **61** (2000) 024613.

[13] DIOSZEGI I. *et al.*, *Phys. Rev. C*, **63** (2000) 014611.
[14] SHAW N. P. *et al.*, *Phys. Rev. C*, **61** (2000) 044612.
[15] SAXENA A. *et al.*, *Phys. Rev. C*, **65** (2002) 64601.
[16] LA RANA G. *et al.*, *Eur. Phys. J. A*, **16** (2003) 199.
[17] CABRERA J. *et al.*, *Phys. Rev. C*, **68** (2003) 34613.
[18] KRAMER A., *Physica (Amsterdam)*, **7** (1940) 284.
[19] SIERK A. J. *et al.*, *Phys. Rev. C*, **21** (1980) 982.
[20] WADA T. *et al.*, *Phys. Rev. Lett.*, **70** (1993) 3538.
[21] BADIMON C., Ph.D. Thesis - CENBG, Bordeaux, (2001).
[22] BHATTACHARYA C. *et al.*, *Phys. Rev. C*, **53** (1996) 1012.
[23] FROBRICH P. and GONTCHAR I. I., *Phys. Rep.*, **292** (1998) 131.
[24] KARPOV A. V. *et al.*, *Phys. Rev. C*, **63** (2001) 54610.
[25] CHAUDHURI G. and PAL S., *Phys. Rev. C*, **65** (2002) 54612.
[26] NADTOCHY P. N. *et al.*, *Phys. Rev. C*, **65** (2002) 64615.
[27] NADTOCHY P. N. *et al.*, *Phys. Lett. B*, **685** (2010) 258.
[28] NADTOCHY P. N. *et al.*, *Phys. At. Nucl.*, **65** (2002) 799.
[29] NADTOCHY P. N. *et al.*, *Phys. At. Nucl.*, **66** (2003) 1203.
[30] ITKIS M. G. and RUSANOV A. YA, *Phys. Part. Nucl.*, **29** (1998) 160.
[31] FIORETTO E. *et al.*, *IEEE Trans. Nucl. Sci.*, **44** (1997) 1017.
[32] KOZULIN E. M. *et al.*, *Instrum. Exp. Tech.*, **51** (2008) 44.
[33] VARDACI E. *et al.*, *Eur. Phys. J. A*, **43** (2010) 127.
[34] DI NITTO A. *et al.*, *Eur. Phys. J. A*, **47** (2011) 83.
[35] PACE2 N97, is a modified version of PACE2 by A Gavron, *Phys. Rev. C*, **21** (1980) 230.
[36] LILITA N97, is an extensively modified version of the original Lilita program made by GOMEZ DEL CAMPO J. and STOCKSTAD R. G., ORNL Report No. TM7295, 1981 (unpublished).
[37] AJITANAND N. N. *et al.*, *Nucl. Instrum. Methods Phys. Res. A*, **243** (1986) 111.
[38] GRANGÉ P. *et al.*, *Phys. Rev. C*, **27** (1983) 2063.

This page intentionally left blank

Proceedings of the International School of Physics "Enrico Fermi"
Course 201 "Nuclear Physics with Stable and Radioactive Ion Beams", edited by F. Gramegna,
P. Van Duppen, A. Vitturi and S. Pirrone
(IOS, Amsterdam; SIF, Bologna) 2019
DOI 10.3254/978-1-61499-957-7-387

The time scale of nuclear reactions from Coulomb to Fermi energies

A. Pagano

INFN, Sezione di Catania and Dipartimento di Fisica e Astronomia, Università di Catania - Catania, Italy

Summary. — Important progresses in Heavy Ion (HI) physics at medium energies have been achieved in the field of nuclear structure and reaction mechanism over the last three decades. The ultimate goal of such studies was to pin down basic properties of the effective in-medium interaction. In particular, large efforts have been devoted to understand dynamical and thermal instabilities *versus* isospin asymmetries of nuclei. In this scenario, a prominent role has been played by the design of innovative devices covering a large part of the available phase space. In this lecture, the contribution of the 4π detector CHIMERA is emphasized with respect to the relevant case of the time scale in neck fragmentation around 40 MeV/nucleon of beam energy.

1. – Introduction

The main object of the present lecture was the "reaction mechanism" in nucleus-nucleus collisions in the range of 20–100 MeV/nucleon, the so-called Fermi domain. The typical energy value of 35 MeV/nucleon corresponds to the Fermi Energy, that is a key reference value in nuclear physics in the frame of the Fermi-gas model. In a heuristic picture, we can say that this value is related to the average kinetic energy of the nucleon

(n or p) in the nucleus, in its ground state; classically, it corresponds to a velocity of about 0.25 c (c = the speed of the light). When a projectile nucleus is accelerated at a beam velocity close to the Fermi one to bombard a target nucleus, a transition in the reaction mechanism of the nucleus-nucleus collision is expected from the gentle low-energy dissipation mechanism dominated by the mean-field dynamics to the nucleon-nucleon (NN) dissipation process with the formation of exotic matter out of equilibrium [1]. At Coulomb energy ($E/A \leq$ 5–10 MeV/nucleon) the reaction mechanism is dominated by the nucleus-nucleus interaction (one-body dissipation mechanism): the energy and angular momentum are dissipated into intrinsic degrees of freedom by excitations of single particle states and/or collective modes, such as resonances and high spin states excitations. Dominant reactions are: scattering processes (including inelastic excitation and both direct and sequential break-up), transfer reactions, compound-nucleus formation (characterized by different de-excitation modes including that one deriving by the high-energy gamma decay from giant dipole resonances (GDR)) and fission [2]. A this low bombarding energy the time scale of the reactions are quite well understood, although still different aspects have to be better detailed (see for example the fission case). Direct reactions occur very rapidly, in a time of the order of 10–20 fm/c, that is in the range of the time scale involved by the projectile for passing through the target field [3]. In direct reactions the incident projectile interacts primarily at the surface of the target nucleus and the number of nucleons involved is small with respect to the atomic mass number of the interacting nuclei, typically one or two nucleons from both projectile and target; such reactions are also called peripheral processes and the cross sections are strongly dependent on the de Broglie wavelength of the incident particle. In contrast, compound nucleus formation and fission decays require a longer time scale, typically of the order of 4–5 orders of magnitude more than the direct ones. This longer time is necessary for distribution, rearrangement and sharing of the incident energy among all nucleons of the composite system formed by the fusion of the projectile and target, in order to achieve the full thermodynamic equilibrium.

With the increase of the beam energy around 10–20 MeV/nucleon and for interacting heavy nuclei, the relative kinetic energy dissipation is dominated by the concept of deep inelastic reactions. The essential unifying role of the semi-classic deflection function modeled by both conservative mean fields (Nuclear + Coulomb)and dissipative nuclear surface viscosity forces were successful introduced for the first time by Wilczyński [4]. The reactions is dominated by the decay of a short-living di-nuclear system into two main excited fragments: a Projectile-like Nucleus (PLF) and a Target-like nucleus (TLF) of relative kinetic energy of the final two-body channel close to the value of the Coulomb barrier between the two nuclei. The available kinetic energy of the entrance channel is dissipated in internal degrees of freedom and it is shared between the two main partners. We have to add, for a more complete description of the physics connected to deep inelastic collisions, the major role played by the concept of nucleon mass transfer in determining the large dissipation of kinetic energy that occurs in the reaction [5].

The time scale of the deep inelastic reactions was proved to be in the range between the one for direct reactions and the one for compound nucleus and sequential decay. In

contrast, at relativistic energy ($E/A \geq 200\,\mathrm{MeV/nucleon}$) the reaction is characterized by the NN elementary interactions (two-body dissipation mechanism). The picture of the participant-spectator model is useful to describe the reaction in this domain: a fast abrasion (removal) of nucleons from projectile and target nuclei [6] produces a high compressed piece of nuclear matter (fireball) located in the overlap region between the projectile and the target nuclei, where transport calculations predict nuclear density well above the normal one, *i.e.*, 2–3 times larger than the value $\rho_0 \sim 0.17$ nucleon/fm^3 [1]. Consequently, sub-nuclear degrees of freedom, that are "frozen" at lower energies due to the dominant role of the Pauli blocking, become effective in dictating the reaction dynamics. Intra-nucleon cascade calculations are required to explain the phase space characteristics of the abundant production of particles and resonances [7]. The reaction mechanism is dominated by the formation of hot exotic matter and decay and, asymptotically, at much higher energies, *e.g.*, available at CERN, by Quark Gluon Phase (QGP) phase transition [8]. At the Fermi energy ($20\,\mathrm{MeV/nucleon} < E/A < 200\,\mathrm{MeV/nucleon}$) the coexistence of the mean field dynamics and NN two-body interactions is the main characteristic of the dominant phenomenon of this domain: the huge production of nuclear clusters, *i.e.*, the fast disassembling of the excited highly compressed "composite system" created in central collisions, *i.e.*, the so-called Multifragmentation phenomena [9]. The full explanation of the multifragmentation process is not still, after many years of investigation, well understood. The dynamical evolution in the early phase of the nucleus-nucleus collision ($\sim$ 10–50 fm/c) leads to the formation of a freeze out highly excited configuration of low nuclear density ($\rho \sim 0.3$–$0.6\ \rho_0$) in a time scale of the order of $\sim 100\,\mathrm{fm}/c$. In this exotic states, both surface and bulk instabilities induce the conditions for a clusterization process, having similarity with a first-order liquid-vapor phase transition [10]. Depending on the mass (charge) of the collision system, and in the range $\sim$ 20–50 MeV/nucleon of incident beam energy, the occurrence of the multifragmentation process can be predicted by transport models [11]. Under the condition of multifragmentation reaction the full disassembling of the composite system is expected in light charged particles (LCP) and neutrons, intermediate mass fragments (IMF) and, under the extreme case, in the vaporization of the whole system in nucleons [12]. The detection of a multifragmentation event in HI collisions at Fermi energy represents a real challenge for the experimental point of view. Large efforts have been devoted during the last twenty years to face and solve the experimental problem by the construction of a variety of powerful detectors in different laboratories all around the world [13]. Careful experiments with heavy ions represent a unique source of information to build a phenomenological model of the nucleus-nucleus interaction as a link between the observed properties of the nucleus and the effective in medium interaction, that should be in agreement with the theory of bare NN forces [14].

2. – The concept of detection in nuclear reactions

Since the pioneer work of Rutherford and co-workers at the beginning of the XX century, a steady progress in nuclear physics had been possible by the development and refinement of the detection systems, including magnetic analysis for charged particles [15]

and gamma spectroscopy [16]. With respect to the heavy-ion reaction studies at Fermi energy, it is important to notice that a full reconstruction of the collision event is determined by the experimental possibility to detect basic quantities, such as, masses, charges, kinetic energies, emission angles, velocities and linear momenta. The evolution of the detection methods during the last twenty years was impressive and allowed the concept of 4π detector measurements for both the inclusive (construction of global variables, such as: multiplicity, transverse energy, flow,..etc) and exclusive analysis (reaction product correlations) of almost all the particles produced in the collision event. It is important to notice that the simultaneous detection of neutral (n, γ) and charged particles (in the same detection cell), it remains an open experimental problem. So, mostly of the existing devices were highly specialized, and separately, for charged particles or neutrons or gamma rays. However, the coincidence method was in some cases applied among various detection systems in order to match with the necessity of a complete detection of the produced particles [13]. In the frame of this lecture it is not possible to describe the evolutionary character of the detection systems during the last twenty years, and only the concept of the CHIMERA detector will be briefly described in connection with the innovative role played in studying nuclear reactions at Fermi energy. A synthesis of the work done with CHIMERA during the last ten years is found in refs. [17,18]. Typical performances of the identification methods adopted in the CHIMERA detector are given in fig. 1 and fig. 2. In this lecture an application of the detection capability of CHIMERA to the physics case of the time scale determination in semi-peripheral collisions (neck fragmentation) is presented in some details.

In fig. 1 a summary of the basic detection structure of CHIMERA (on the left) together with the adopted identification methods (on the right) are presented. The apparatus assembles a number of 1192 Si-CsI(Tl) elementary telescopes and it covers the laboratory angular range between 1° and 176°, in an azimuthal symmetry around the beam axis. The forward part of the detector ($\leq 30^\circ$) is made by nine rings allocating globally 688 Si-CsI(Tl) telescopes. It is relatively easy to dismount and, consequently, adapted for reaction studies in coupling modality with other devices that are working in different laboratories, all around Europe. Relevant examples of this flexibility were exploited in the third INDRA campaign [19], where the first ring of CHIMERA was coupled with INDRA at GANIL(FR), and in the ASY-EOS measurement of symmetry energy [20], where the four forward rings of CHIMERA were coupled with an ensemble of detectors at GSI(D), including neutrons detection. The detector is able to efficiently include the time-of-flight technique (TOF) for mass measurements. The typical intrinsic resolution of the first-stage silicon detector of each telescope is $\approx 500\,\mathrm{ps}$, allowing for mass by mass identification of fragments with kinetic energy less than $10\,\mathrm{MeV/nucleon}$, that are stopped in the active $300\,\mu\mathrm{m}$ silicon stickiness. In fig. 2 an illustration of typical performances of the identification methods adopted in the CHIMERA detector is shown. In figs. 2a) and b) two typical 2D-Plots energy loss matrices, *i.e.*, ΔE (Y axis)-E (X axis), are shown for the reaction $^{124}\mathrm{Sn} + ^{64}\mathrm{Ni}$ investigated at the beam (^{124}Sn) energy of $35\,\mathrm{MeV/nucleon}$. The ΔE signal was obtained by the silicon detector and the E signal by the CsI(Tl) scintillator. The two matrices have been obtained with two different gains

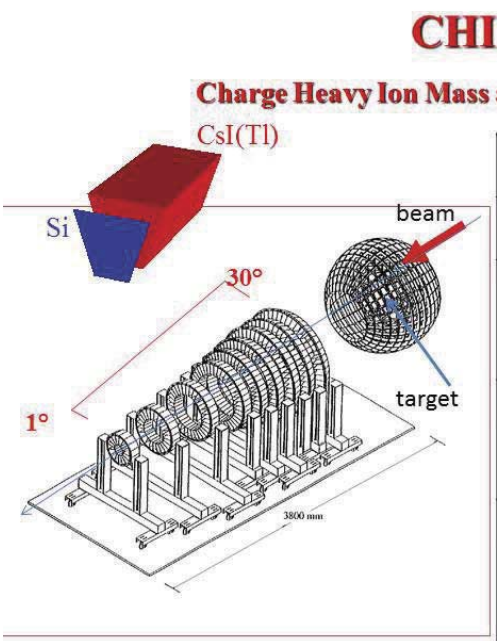

Granularity	1192 telescopes Si (300μm) +CsI(Tl)
Geometry	RINGS: 688 telescopes 100-350 cm SPHERE: 504 telescopes 40 cm
Angular range	RINGS: $1° < \theta < 30°$ SPHERE: $30° < \theta < 176°$ Geometrical efficiency : 94% of 4π
Identification method:	ΔE-E Si-CsI(Tl) E-TOF Si PSD Si- CsI(Tl) PSD Si
Experimental observables and performances	TOF $\delta t \leq 1$ ns (time resolution) Energy resolution: $\delta E/E$ for Light Charged Particles) ≈ 2% $\delta E/E$ for Heavy Ions ≤ 1% Energy, Velocity, A, Z, angular distributions primary quantities
Detection threshold	≈ 1 MeV/nucleon for Heavy nuclei ≈ 2 MeV/A for charged particles

Fig. 1. – Summary of basic CHIMERA detection structure and the adopted identification methods. A recent list of experimental activity and data analysis performed by the CHIMERA collaboration in the field of heavy-ion collisions, has been reported in ref. [17].

of the main DAC (digital-to-analogic converter), *i.e.*, the low gain (fig. 2a) and the high gain (fig. 2b). The procedure allows for the separation of isotopes of light fragments of intermediate mass. The charge spectrum of the produced particles at 2.5° from $Z = 1$ to $Z = 50$ atomic numbers is observed in fig. 2a. Figure 2c) shows a typical 2D-Plot pulse shape discrimination (PSD) performed on the Silicon signals, *i.e.*, kinetic energy (Y-axis)-rise time (X-axis). In the matrix only signals corresponding to the particles that are stopped in the silicon detector are reported. Rise time was evaluated by measuring, by proper constant fraction discrimination techniques, the rise time of the signal starting from 10% up to 80% of the maximum. Atomic number identifications of fragments are seen in fig. 2c) starting from an energy threshold of about 4.5 MeV/nucleon. The unique characteristic of CHIMERA among the existing 4π detector is reported in the 2D-plot, energy (Y-axis)-time-of-flight (X-axis), of fig. 2d, where the time-of-flight identification for mass measurements is shown. In doing this mass identification, evidently, the time resolutions of both the silicon detectors (stop- see above) and pulsed beam produced by the LNS superconductive cyclotron (start ~ 0.7 ns) are crucial ingredients. However,

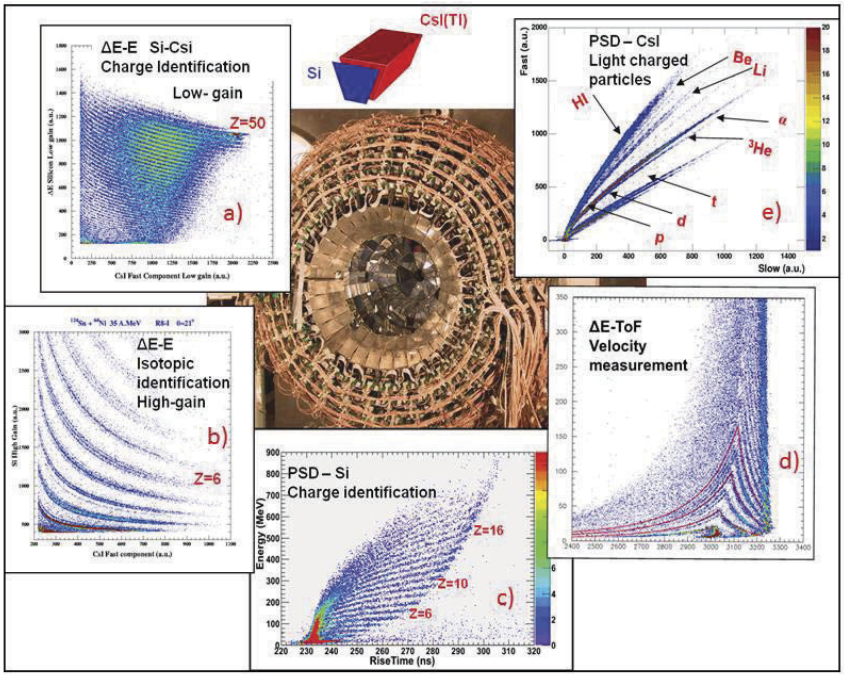

Fig. 2. – Illustration of typical performances of the identification methods adopted in the CHIMERA detector, including the recent upgrade of pulse shape discrimination (PSD) technique, based on the hardware determination of the rise time of signals induced by charged particles that are stopped ($E/A \leq 10\,\mathrm{MeV/nucleon}$) in the silicon detector. For the descriptions of fig. 1a) up to fig. 1e) see text.

the path of the particle from the target to the detectors, of the order of few meters (see the left drawing in fig. 1) allows to identify light fragments (atomic number $A \leq 10$) produced by multifragmentation of interacting nuclei in central collisions and to have a good estimation of the velocity of all the fragments. PSD method is also employed in CHIMERA to measure the Light Charged Particles (LPC) stopped in the CsI(Tl), *i.e.*, the second stage of the single telescope. This latter method is basically different from the PSD method applied to Si detectors (fig. 2c). It is based on the charge evaluation of the current signal, produced in the crystal by the absorption of the particle, by two different portions of the time pulse. Typically, a fast and slow charge components are easily evaluated and reported in 2D-Plot identification array of fig. 2e. Isotopic identification of atomic numbers: $Z = 1$, $Z = 2$, $Z = 3$ and $Z = 4$ are there easily seen.

3. – The time scale of nuclear reactions in neck fragmentation

At the Fermi energy (20–100 MeV/nucleon) and for semi-peripheral collisions, signatures of binary deep inelastic collisions (low energy regime) and participant-spectator

scenario (high energy regime) coexist in the same pattern [21]. The participant region (*i.e.*, the overlapping matter between the projectile and the target nuclei) in peripheral collisions assumes the characteristic of a transient expanding neck-like structure connecting (on a short time scale $\sim 100\,\mathrm{fm}/c$) the Projectile-like (PLF) and the Target-like (TLF) nuclei [11]. The dynamic evolution of this neck fragmentation process has been clearly elucidated in the context of CHIMERA data [22,23]. This device [18] is the unique 4π in the world for its ability to detect fragments in the full dynamic range from very slow TLF to very fast PLF, allowing to study in details different correlations among various observable of the emitted fragments. Indeed, the Wilczyński-2 plot (WILC2, see fig. 4) is one of these powerful correlations, as it is briefly discussed below, for the particular application in ternary (*i.e.* three bodies in the final state, in contrast to the deep inelastic reactions where essentially two bodies are observed) reactions where the three biggest fragments in the final state correspond to a fast PLF, having velocity very close to the projectile one, a slow TLF, practically at rest in the laboratory system of reference, and a fragment of intermediate mass IMF, with velocity that is reminiscent of the CM velocity of the collision, respectively (see fig. 3). In ternary reactions, the three fragments are observed together with few light particles, as is seen by inspecting the total charged particles multiplicity (M_c in fig. 3) that shows a value lower than seven (including the three biggest fragments). Notice that neutrons have not been observed since no detectors for neutron signals are included in CHIMERA. However, especially for a future use of such a device with exotic beams, some experimental efforts are undergoing in this interesting direction to study new methods for neutron detection together with charged particles [24]. Important results on the production mechanism of these three fragments were obtained from the analysis of the relative fragment-fragment velocities for selected binary sub-systems of the three-body reaction, as it follows. The relative velocity of the IMF with respect to PLF one and the relative velocity of the same IMF with respect to the TLF one, *i.e.*, $V_{rel(IMF,PLF)}$ and $V_{rel(IMF,TLF)}$, have been measured in an event-by-event analysis. The two relative velocities were normalized to the relative velocity corresponding to the Viola systematics [25,26], as given by the expression: $E_{Viola} = (0.775\frac{Z_1 Z_2}{{A_1}^{1/3}+{A_2}^{1/3}} + 7.3)\,\mathrm{MeV}$ that gives the relative kinetic energy of the pure Coulomb repulsion between the two sub-systems (PLF-IMF and TLF-IMF, respectively) in a sequential binary decay. In fig. 4 the experimental correlation plot between the two previously defined normalized relative velocities $V_{rel(IMF,PLF)}/V_{Viola(IMF,PLF)}$ and $V_{rel(IMF,TLF)}/V_{Viola(IMF,TLF)}$ is shown for light IMFs selected in the $4 \leq Z \leq 10$ atomic number range, for the reaction $^{124}\mathrm{Sn} + {}^{64}\mathrm{Ni}$ at the bombarding energy of 35 MeV/nucleon. It can be readily checked that the correlation between the two ratios gives information (together with simple kinematics analysis) on the scenario of IMF emission, and particularly on the time scale when the neck region separates from the PLF* or TLF* (or from both in the case of instantaneous ternary splitting). In fig. 4, as a solid line, an evaluation of the time scale of the process is shown. It is obtained by assuming that the IMF separates in a collinear configuration with respect to the relative PLF-TLF velocity vector, and it is performed by assuming two step processes(see the right side of fig. 4). In the first step the projectile and the target undergoes a binary fast neck-like inelastic process in the center-of-mass

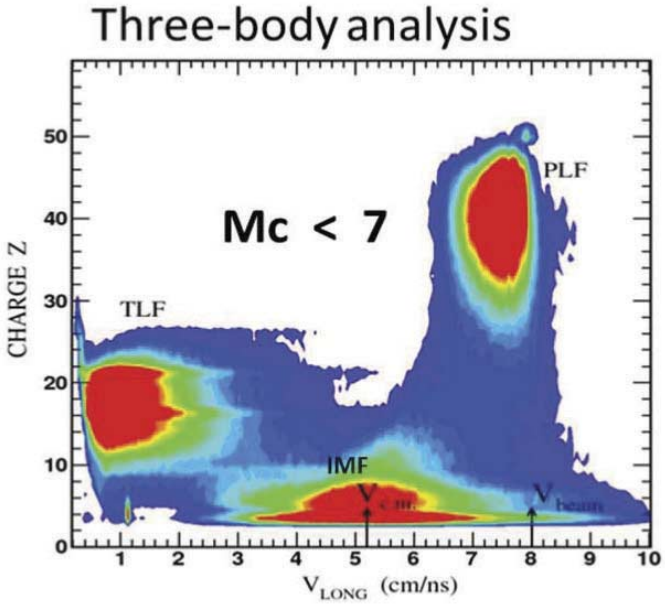

Fig. 3. – The three fragments: PLF, TLF and IMF as a function of the observed laboratory respective velocities.

system, producing an excited binary system PLF* + TLF*. After some delay (second step) from the first primary re-separation, either the projectile or the target emit one IMF (only three-body final decay channels are considered). As an example, the case of PLF decay is described as it follows: projectile+target (interation) $\rightarrow$ PLF* + TLF* (first step separation) $\rightarrow$ TLF+PLF+IMF (second step separation). A similar process is assumed for the TLF decay. The light IMF experiences the Coulomb repulsion from both the TLF and PLF residues. Any distortion with respect to a binary relative velocity in the PLF+IMF (or IMF+TLF) sub-system induced by the repulsive action of the third body (the TLF, in the case of PLF decay) may indicate a deviation from the pure binary Coulomb interaction given by the Viola systematics valid for sequential decay. As examples of computations, the second steps separation times of 40, 80 and 120 fm/c, respectively, have been considered after the (binary) first step TLF*-PLF* separation (see more details and kinematical calculations in the appendix of ref. [23]). In fig. 4, these evaluations based on Coulomb numerical one-dimension trajectory calculations (three squares for PLF emission and three circles for TLF one) are associated with the numeric symbols, 1, 2 and 3, respectively, and connected by a solid line.

In particular, events close to the diagonal of the WILC2-Plot of fig. 4 (this diagonal is also drawn in fig. 4) correspond to prompt (ideal) ternary divisions of the PLF, IMF and TLF in closing approach and in a co-linear configuration at the moment of the separation, whereas the events approaching the values of $V_{rel(IMF,PLF)}/V_{Viola(IMF,PLF)} = 1$ or

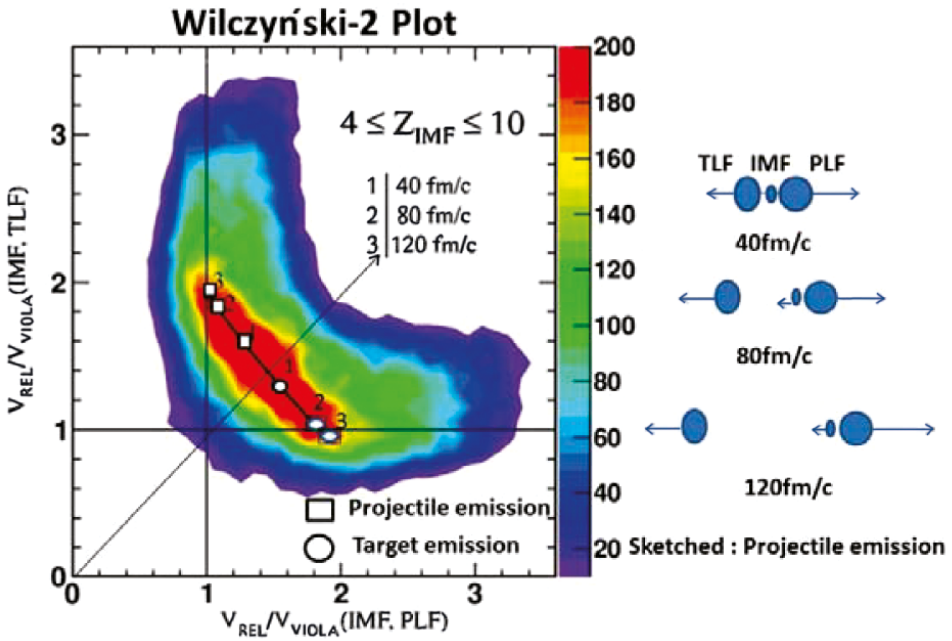

Fig. 4. – Summary of the data analysis (see text) of the unique time scale determination in neck fragmentation reactions at Fermi energy obtained by CHIMERA data. The diagram represents a new correlation plot (WILC2) obtained by relative velocity measurements between PLF-IMF and TLF-IMF sub-systems. The diagonal arrow separates the region of the PLF emission (top) from the one of the TLF emission (bottom). On the right side of the figure, a schematic representation of the idealized dynamics adopted in the time computations of the IMF emission is sketched.

$V_{rel(IMF,TLF)}/V_{Viola(IMF,TLF)} = 1$ correspond to the sequential splitting of the primary projectile-like nucleus or the target-like nucleus, respectively, (also sketched in fig. 4 by two lines: one is representing the projectile-like sequential decay (vertical-up) and the other (horizontal-bottom) is representing the target-like sequential decay). The time scales illustrated in fig. 4 span a time interval in the range lower than $\approx 120\,\mathrm{fm}/c$. Beyond that value, the evaluations of the ratio of the relative velocity correlations move no further and are undistinguishable from much slower true sequential decay processes ($> 300\,\mathrm{fm}/c$). On the other hand, sensitivity of the WILC2-Plot within a time scale of less than $40\,\mathrm{fm}/c$, is limited by the relative linear momentum resolving power of the used correlator CHIMERA, largely due to the size of the detectors angular opening in the investigated region. Notice that, according to the yield-scale reported on the right side of fig. 4, the most probable value of the fragment yield is well accounted by the computation (full line connecting the squares and circles in fig. 4), so clearly demonstrates that at least in the case of light IMFs, the majority are emitted in almost prompt (dynamical) or fast two-step processes, within times in the range ≈ 40–$120\,\mathrm{fm}/c$.

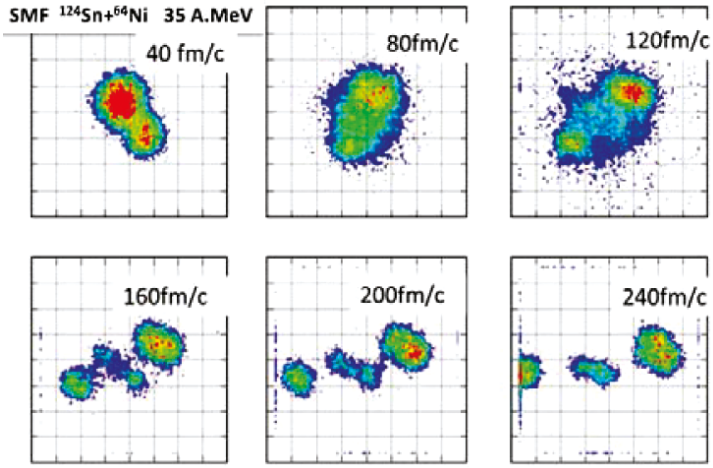

Fig. 5. – Time evolution of the density profile in the reaction plane in a ternary event produced at the impact parameter of value, $b = 6$ fm. Density profile is shown by time step of 40 fm/c. Calculations : Stochastic Mean Field (SMF) transport code. Figure adapted from ref. [29].

The time scale calibration discussed above was an important step in the understanding of the dynamical component of the reaction mechanism in peripheral collisions: the neck-fragmentation process. This new kind of Wilczyński plot (see fig. 4) is the most persuasive correlation to calibrate the time scale of IMF emission in semi-peripheral collisions, under the condition that both the slow (TLF) and the fast (PLF) are measured in coincidence in the same event. It demonstrates at the same time that the IMF emission is collinear with the relative PLF-TLF velocity vector, established at the instant of their binary separation. The analysis of the reaction ^{124}Sn + ^{64}Ni showed for the first time a well defined chronology: light IMFs ($Z \leq 10$), (as the example plotted in fig. 3 and fig. 4) are emitted either on a short time scale (within 50 fm/c) with a prompt neck rupture mechanism or sequentially (> 120 fm/c) after the re-separation of the primary binary PLF*-TLF* system. These results were supported by different approaches of transport model simulations like the stochastic mean field (SMF) [11,27] and constrained molecular dynamical model (CoMD-II) [28]. As a relevant example of theoretical predictions of a neck-fragmentation process in ternary reaction (and for the same system and energy of fig. 4), the time evolution of the density profile of the projectile-target interation as simulated by transport SMF code of ref. [29] is shown in fig. 5. The density profile is studied for an impact parameter of value $b = 6$ fm. The production of a light IMF ($Z_{IMF} < 10$) is observed. Notice that the simulation indicates a time slabs of about 120 fm/c, starting from the first instant of the collision, for the full rearrangement of the density profile in order to create an intermediate region of matter (the neck) located between the PLF and TLF interacting system. The ternary re-separation of PLF-IMF-TLF is observed between the values of 120 fm/c and 160 fm/c (*i.e.*, in a slab of 40 fm/c).

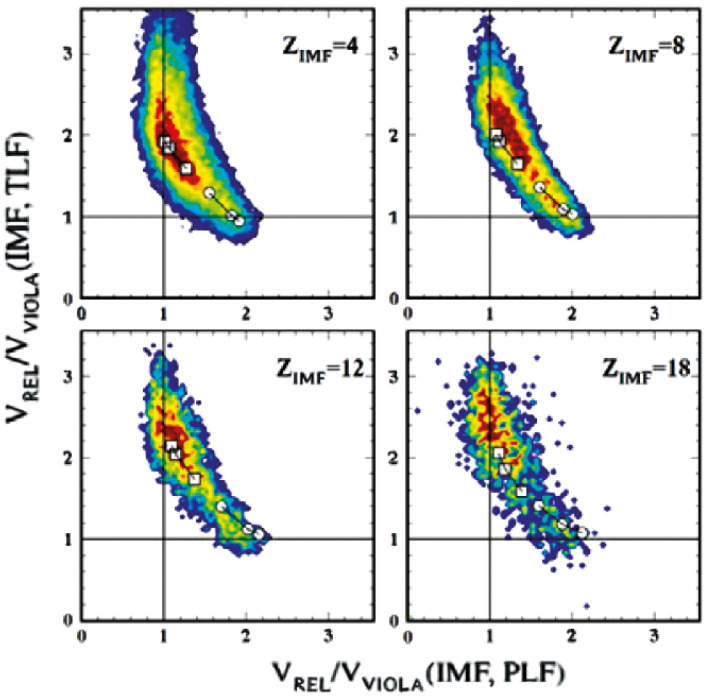

Fig. 6. – WILC2 plot correlations for different IMFs of charge: Z_{IMF} = 4, 8, 12 and 18, separately shown (colors indicate yield-scale, as in fig. 4).

After this time the evolution of the density profile is essentially determined by an aligned Coulomb trajectory (mutual repulsion) that is simulated up to the value of 240 fm/c. So, the event simulation shown in fig. 5 is consistent with the physics case of the IMF emission that is observed at the position labeled by the symbol 1 (40 fm/c) in fig. 4. In fact, the experimental WILC2-Plot (as described above) is sensitive only to the time at which the ternary nuclear complex is created, so starting to experience the three-body final-state Coulomb interaction. The WILC2 Plot tells us nothing about the "production time" of the IMF, that, at present, is estimated by the transport simulation to be about 120 fm/c. Experimental methods useful to pin down the time scale of the first phase of the IMF production could be obtained by femtoscopy studies (intensity interferometry methods) of the particle-particle (including the uncharged particles) correlation function [30]. The SMF simulation indicates a substantial difference in the mechanism between a "direct" reaction, typical of the low-energy regime, and the neck-fragmentation process typical of the Fermi regime. Direct reactions are relatively fast processes with respect to the neck fragmentation one. The experimental information obtained in studying this latter process are unique sources to pin down a more complete understanding of the cluster production mechanism in heavy ion collision at Fermi energy that still is a topic of major challenge.

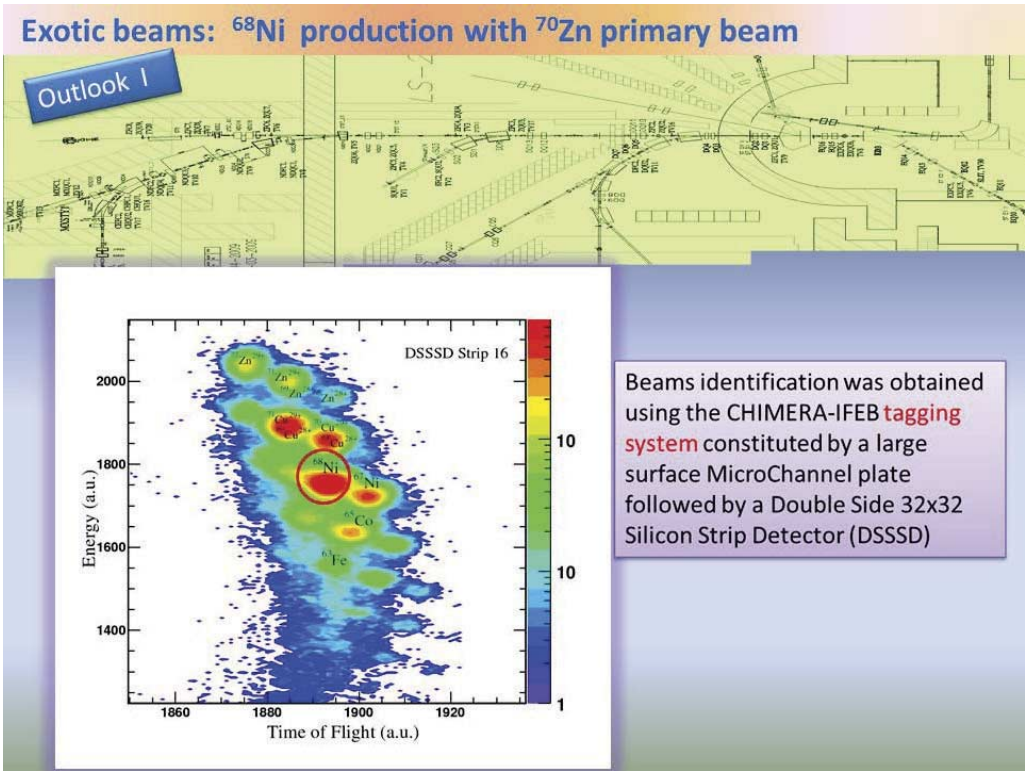

Fig. 7. – Identification of exotic beams ^{68}Ni by in-flight fragmentation reactions of a primary beam produced by the cyclotron at LNS and impinging on a thick beryllium target. The ΔE-Time-of-flight matrix was obtained using the CHIMERA tagging system constituted by a large surface MicroChannel plate followed by a Double Side 32×32 Silicon Strip Detector (DSSSD).

To complete the picture, and in contrast with light fragment emission, heavy fragments ($Z \geq 10$) have been proven to be emitted in a longer time scale ($> 300\,\mathrm{fm}/c$) ranging from a non-equilibrated fission-like splitting to a fully equilibrated fission process of much longer time scale [31]. In fig. 6 the observed PLFs in the same reaction are separately shown in the WILC2-Plot for increasing values of the atomic number. The figure illustrates the clear tendency of the IMFs to approach the value of the sequential PLF decay as their atomic number progressively increases from the light fragment with $Z_{IMF} = 4$ up to the heavier one with $Z_{IMF} = 18$, supporting the picture of the time scale for the emission longer than $120\,\mathrm{fm}/c$. These observations are important constrains for transport simulations. Unfortunately, in contrast with the light IMF production, transport simulations are not still available to be compared with data concerning heavy IMF emission, as the ones shown in fig. 6. As matter of fact, the cluster production phenomenon at Fermi energy is still a challenging topic in the frame of transport theories.

More recently, CHIMERA has been oriented toward a new challenge: the study of nuclear reactions with exotic beams produced at the National Laboratories of Sud (LNS) in

Catania by the in-flight method [32]. Time scale and other studies will be highly improved at the Fermi energy by the new facility. The influence of the isospin degree of freedom on the EOS will be explored in more details in regions of the nuclear chart far from the stability valley, thus opening fascinating perspectives. Notice that, in exotic nuclei the detection of neutrons together with charged particles will be a necessary requirement for new investigations. In fig. 7, the production of a 30 MeV/nucleon ^{68}Ni beam at LNS was investigated by the fragmentation of $^{70}Zn^{19+}$ primary beam at 40 MeV/nucleon impinging on a 250 μm ^{9}Be target. The maximum intensity obtained for the primary beam was ≈ 300 enA with 30 watt dissipation and the production rate was ≈ 7 kHz. With the implementation of the high intensity of the primary beam of a factor ≥ 30, expected to be in operation in the next couple of years at LNS [32], the exotic beam production by fragmentation will be a common facility for reaction studies with CHIMERA or different sophisticated detection systems.

4. – Conclusion

The time scale of nuclear reaction is an important concept in heavy-ion physics in order to describe the time evolutionary character of the reaction from the early phase of the collision ($10\,\mathrm{fm}/c$) up the later stage of the sequential decay and equilibrium emission ($\geq 1000\,\mathrm{fm}/c$). Measurements of the reaction time involved in different reaction channels are unique tools to probe the in medium effective interaction and to constrain advanced reaction simulations in order to predict heavy-ion collision dynamics. In future investigations, we stress the importance of reaction studies induced by Exotic beams. They represent fundamental and necessary steps towards the study of the dependence of the equation of state of nuclear matter with respect to the baryon density and the isospin degrees of freedom.

* * *

The author is grateful to the Varenna School organization staff for the kind hospitality and to Prof. Sara Pirrone for the careful reading of the manuscript prior to publication.

REFERENCES

[1] PEILERT G., STOCKER H. and GREINER W., *Rep. Prog. Phys.*, **57** (1994) 533.
[2] PRESTON M. A. and BHADURI R. H., in *Structure of the Nucleus*, second printing (Westview press) 1982.
[3] KRANE KENNETH S., in *introductory Nuclear Physics* (John Wiley & Sons, Inc.) 1988.
[4] WILCZYŃSKI J., *Phys. Lett. B*, **47** (1973) 484.
[5] RANDRUP J., *Nucl. Phys. A*, **383** (1982) 468.
[6] DAYRAS R. and PAGANO A. *et al.*, *Nucl. Phys. A*, **460** (1986) 299.
[7] CUGNON J., KNOLL J., RIEDEL C. and YARIV Y., *Phys. Lett. B*, **109** (1982) 167.
[8] `http://aliceinfo.cern.ch/ArtSubmission/publications`.
[9] LYNCH W. G., *Nucl. Phys. A*, **583** (1995) 471.
[10] PHOCHODZALLA J. *et al.*, *Phys. Rew. Lett. A*, **75** (1995) 140.

[11] Baran V., Colonna M. and Di Toro M., *Nucl. Phys. A*, **730** (2004) 329.
[12] Bacri O. Ch., Borderie B. and Charvet J. L. *et al.*, *Phys. Lett. B*, **353** (1995) 27.
[13] De Souza R. T., Le Neindre N., Pagano A. and Schmidt A. H., *Eur. Phys. J. A*, **30** (2001) 275.
[14] Amaldi U., in *Conoscere Fermi nel centenario della nascita 29 Settembre 1901-2001*, 1st edition (SIF, Bologna) 2001.
[15] Duckworth H. E., in *Mass Spectroscopy* (Cambridge University Press) 1958.
[16] Ricci R. A., *65 years with Nuclear Physics*, this volume, p. 401.
[17] De Filippo E. and Pagano A., *Eur. Phy. J. A*, **50** (2014) 1.
[18] Pagano A., *Nucl. Phys. News*, **22** (2012) 25 and references therein.
[19] Manduci L. *et al.*, *Nucl. Phys. A*, **811** (2008) 93.
[20] Russotto P. *et al.*, *Phys. Rev. C*, **94** (2016) 034608.
[21] Guerreau D., *Nucl. Phys. A*, **447** (1985) 37c.
[22] Wilczyński J., De Filippo E. and Pagano A. *et al.*, *Int. J. Mod. Phys. E*, **14** (2004) 353.
[23] De Filippo E., Pagano A. and Wilczyński J. *et al.*, *Phys. Rev. C*, **71** (2005) 044602.
[24] Pagano E. V. *et al.*, *Nuclear Instrum. Methods Phys. Res. A*, **889** (2018) 83.
[25] Viola V. E., Kwiatkowski K. and Walker M., *Phys. Rev. C*, **31** (1985) 1550.
[26] Hinde D. J., Leigh J. R., Bokhorst J. M., Newton J. O., Walsh R. L. and Boldeman J. E., *Nucl. Phys. A*, **472** (1987) 044602.
[27] Rizzo J. *et al.*, *Nucl. Phys. A*, **79** (2008) 806.
[28] Papa M. *et al.*, *Phys. Rev. C*, **75** (2007) 054616.
[29] Colonna M. *et al.*, *J. Phys. Conf. Ser.*, **413** (2013) 012018.
[30] Ghetti R. *et al.*, *Nucl. Phys. A*, **765** (2006) 307.
[31] Russotto P. *et al.*, *Phys. Rev. C*, **81** (2010) 064605.
[32] HIB2015-workshop; `http://agenda.infn.it/conferenceDisplay.py?confId=10053`.

Proceedings of the International School of Physics "Enrico Fermi"
Course 201 "Nuclear Physics with Stable and Radioactive Ion Beams", edited by F. Gramegna,
P. Van Duppen, A. Vitturi and S. Pirrone
(IOS, Amsterdam; SIF, Bologna) 2019
DOI 10.3254/978-1-61499-957-7-401

65 years with Nuclear Physics

R. A. Ricci

Laboratori Nazionali di Legnaro - Padova, Italy

"It's a long way to Tipperary"

Summary. — An excursus along the 65 years of a scientific activity mostly dedicated to Nuclear Physics is presented. The overwiew goes back to the first experiments on radioactivity and nuclear decays employing extensively the scintillation spectometry (Turin, Amsterdam, 1952–1957) and to the foundation of the experimental Nuclear Spectrscopy in Italy starting from the systematic researches in Naples in the '60s of the last century. The extension to Florence and Padua and to the just founded Legnaro Laboratory which could become in the '70s a national center for nuclear physics research with the institution by the INFN of the LNL (Laboratori Nazionali di Legnaro) is outlined. The domain of the research with particular emphasis on the spectroscopy of $1f_{7/2}$ nuclei as well as the international collaborations with Amsterdam, Orsay, Munich groups is underlined. The evolution following the advent of heavy-ion accelerators and of the new more performant gamma-ray detectors, together with the invented in-beam spectroscopy is accounted for in describing the important achievements in this field of that collaboration. A report is presented about the further developments in Italy with the installation at the LNL of the XTU Tandem, the first national *heavy-ion accelerator*, opening also in Italy a large area of investigation including the advent of other facilities (LNS with a second Tandem accelerator; the coupling of the two Tandems with the superconducting Cyclotron at LNS and LINAC at LNL, respectively The extension to new areas of research and to new collaborations are mentioned. Finally the promotion of and the participation to the enterprises concerning nuclear physics programs at CERN in the frame of large national and international collaborations concerning experiments with anti-nucleons at LEAR (OBELIX) and relativistic heavy ions at the SPS and at the LHC (ALICE) are pointed out shedding some light on the most interesting results. Conclusions about the different steps of a long journey with physics are drawn.

Introduction([1])

Exactly ten years ago (July 17–27, 2007), here in Varenna, a Course (the 169th of this wonderful School entitled to Enrico Fermi) was organized on *Nuclear Structure far from stability: New Physics and New Technology* and directed by A. Covello, F. Iachello and myself. In fact there was a particular dedication to my 80th anniversary and for that occasion I could personally contribute with a lecture on "*Phenomenological Nuclear Spectroscopy (a personal recollection)*" [1]. I wish also to mention that, even before, in 2002 (August 16–26) another nuclear physics course on *From nuclei and their constituents to stars* was held under the direction of A. Molinari and L. Riccati and dedicated to the 50 years of my career as a physicist. My contribution to that course was a lecture on: "*From* $1f_{7/2}$ *nuclei to the quark-gluon plasma*" [2]. Moreover I have not to forget that in 2003, still here in Varenna an *International Conference* on *Nuclear Reaction Mechanisms* directed by E. Gadioli was held also with a dedication to my scientific career [3]. Therefore, since in such successive events, I had the opportunity to report on a large part of my long journey with nuclear physics, I wish to refer to such contributions also in my lecture here.

I can summarize my impressions and acknowledgments by quoting few words of my previous reports in 2002 and 2007. In both cases I mentioned the fact that 50 years (2002) with nuclear physics (65 now) and 80 years (2007) of life (90 now) "*are quite a lot*" and that: "*... this quite a long journey has been gratified not only by interesting activities and results in a pleasant, even if intriguing, field of research, but also by the communion with a lot of nice people, excellent physicists and wonderful friends*". Moreover: "*It is perhaps exaggereted to emphasize my commitment and contributions to nuclear physics but I assume it correct to speak about my "passion" for such a field during my scientific and academic career*". Now, that emphasis was present in the words of the dedication of the 2003 Conference (I quote) "*He was a most successful teacher and several of the leading Italian nuclear physicists have been his alumni.... He introduced in Italy the experimental study of nuclear spectroscopy and gave numerous and important contributions to this field... he was one of the leaders of the experiments made at CERN with the antiproton beams and started here the relativistic heavy-ion physics*". Taking also into account the kind presentation of Franco Iachello in his specific seminar for the "Ricci 90th" day, as well as the friendly words of the directors of this course, I fill more than gratified and allowed to avoid any further reference to my personal merits.

([1]) To complete this introduction I wish to mention that 18 courses in Nuclear Physics have been organized in Varenna starting in 1955 with the one devoted to: *Questioni di struttura nucleare e dei processi nucleari a basse energie* and directed by C. Salvetti with the participation as lecturers of A. Bohr, D.M. Brink, S. Yoshida, A. De Shalit, I. Rabi and J. Horowitz. The subjects of the various nuclear physics courses cover a large spectrum of specific problems whose relevance and evolution will be outlined in my lecture. Among them I wish to mention here the one held in 1979 on *Nuclear Structure and Heavy-Ion Collisions* (Course LXXVII), under the direction of R. Broglia, C. H. Dasso and myself with lecturers as A. Gobbi, L. Moretto, H. J. Specht, J. Randrup, A. Winther, H. A. Weidenmuller, G. Bertrand, G. Bertsch, J. De Boer, J. Vervier, A. Vitturi.

I actually started my research activities in 1952, after taking the university degree in Theoretical Physics in Pisa (1950) by discussing a thesis on "*The pressure broadening of spectroscopic lines*" with T. Derenzini and a diploma of the Scuola Normale Superiore (1951) with a a thesis on "*The energetic component of Cosmic Rays*" (with M. Conversi as supervisor). In that period, I moved to Paris with a grant and I spent my stay there (1951–52) at the Ecole Politechnique under the supervision of L. de Broglie (*Mècanique ondulatoire des systemes de corpuscules*) and at the Collège de France under the direction of F. Joliot-Curie (*Radioactivité et Fission Nucléaire*). I wish to note in passing, that this period marked my final decision to move from theoretical approaches to experimental phenomenology.

Back to Italy, after a short period in Pisa with a temporary position at the Istituto di Fisica under the direction of M. Conversi, I went to Turin (Department of Physics of the Politecnico) having obtained a permanent position as Assistant at the Physics chair held by E. Perucca. These were the years (1950–1956) of the explosion of the nuclear spectroscopy phenomenology. On the experimental side, the massive use of dedicated accelerators and the advent of scintillation detectors allowed the production of new radioactive nuclear species whose decay schemes could be extensively investigated while, on the theoretical side, more appropriate approaches were provided by the description of peculiar properties (*i.e.* magic numbers, quantum orbitals, collective states) with the shell-model (M. Goppert-Mayer, J.H. Jensen) [4] and/or with collective models (A. Bohr and B. Mottelson) [5].

The discovery of scintillation counters (H. Kalmann 1947, R. Hofstadter 1948) [6] and their coupling with the already invented photomultipliers [7] did allow a rapid evolution of such a simple instrument to an extraordinary measuring device, especially for γ-ray spectroscopy. The main reason was the simplicity and the handiness of the experimental set-up consisting of a scintillator and a photo-cell with electron multiplier connected to a pulse-height analyzer providing quite a good efficiency in spite of a non-excellent resolution. As I will show in the following the advent of technical refinements and the availability of multichannel analyzers made it possible to treat even quite complicated spectra and extract important features of the nuclei under investigation. Of course, other detection techniques as magnetic and crystal spectrometry were still in use (excellent resolution but very poor efficiency); in fact in such cases one needed quite a strong intensity of the sources under investigations (of the order of hundreds of millicuries *i.e.* some 10^7 Becquerel)([2]).

I mentioned also the theoretical approaches to describe the nuclear-structure features.

([2]) Later on, and particularly in the years 2000, the impressive improvements of the gamma-ray spectrometry with new detection techniques (gamma-arrays) displaying very high efficiency, excellent resolution and geometry (close to 4π), and the possibility of exploring new features in more details of the nuclear structure, has been largely amplified. The final touch has been and is the advent of the radioactive beam acceleration and the study of exotic nuclear species. That possibility has been open to the LNL with the SPES (Selective Production of Exotic Species) Facility consisting of a high-performance cyclotron and an ISOL-type target.

Those years were indeed marked by the advent of the two prominent points of view concerning the description of the nuclear quantum states: the *shell-model* and the *collective model*. Highlights of the evolution of the nuclear models together with the continuous progresses of the experimental techniques are largely represented in the various Varenna courses. I wish to report here a good example concerning the earlier confrontations between the two (simplified at the time) extreme interpretations *i.e.* the *independent-particle shell-model* (Rehovoth School) and the *collective model* (Copenhagen school). I am referring to the second Nuclear Physics course held in 1960 and directed by G. Racah [8] with the significant title *Nuclear Spectroscopy*, where the presence of both I. Talmi (lecturing on "*Shell-model spectra in nuclei*") and B. Mottelson (lecturing on "*Selected topics in the theory of collective phenomena in nuclei*") was of particular significance. I need only to quote Racah himself in his presentation of the course introducing the *nuclear structure problem*: "*... They* (Talmi and Mottelson) *are typical representatives of two different approaches: the independent particle model and the collective model. I hope that the clash* (!) *between these two opposite points of view will be one of the most interesting features of the course*". No doubt about the interest of this "confrontation" along a history of many years. We know today that, due to more than 50 years of experimental and theoretical progresses, the "opposite" views are both consistent (one can use the apt expression of T. Otsuka [9]: "*Single particle and collective modes are not enemies but friends*!"). In fact the coexistence, together with the competition (I would better say the "interplay") of different modes of excitations in nuclear spectra are today an experimental fact. As I will report later, the investigations performed in the era of the advent of the *heavy-ion accelerators* and of the *in-beam gamma spectrometry* (years '70s–'80s) together with the better performances of the γ-detection techniques with germanium counters, have been very successful in selecting nuclear states at high excitation energies and with high angular momenta characterizing the compound system evaporation into still rapidly rotating and highly excited states of the residual nuclei which will cool down via γ-ray cascades forming *yrast* bands.

This period coincides with that of the first part of my career (1955–1985) as a nuclear physicist, during the most fruitful years of my research activity (1952–1990).

This has not affected, of course, my interest and engagement, in the second part (starting from 1990) of my scientific career, to other nuclear aspects and phenomena such as the reaction dynamics, the mechanisms of nucleus-nucleus interactions at the Tandem energies, the proton-antiproton reactions and relativistic heavy-ion collisions at CERN as well as some relevant applied nuclear physics experiments (see refs. [2] and [3]). Let me now come back to the beginning of the story.

1. – The beginning and the years of nuclear spectroscopy: The Amsterdam group

As already mentioned the first part of my real research activity started in Turin, after my return to Italy. Since the Physics Laboratory of the Politecnico directed by E. Perucca, was engaged in an experimental program, initiated by F. De Michelis and

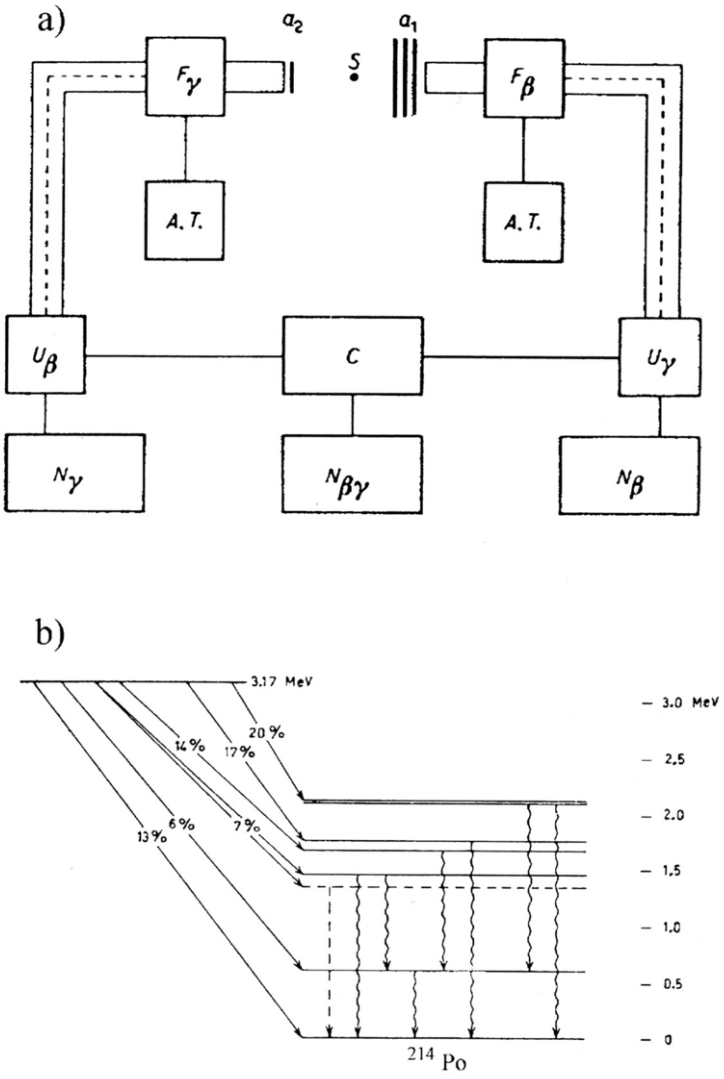

Fig. 1. – a) Experimental set up for detecting β- and γ-rays and β-γ coincidences with scintillation counters from the decay of ^{214}Bi (RaC); S is a source of ^{226}Ra (16 μCi) in equilibrium with its decay products up to RaD ($T_{1/2} = 22$ years), F_β and F_γ are naphthalene and NaI(Tl) crystals connected with RCA and Dumont photomultipliers, respectively, and to standard electronics for pulse amplification and shaping and recording single N_β, N_γ and coincidences $N_{\beta\gamma}$ events (Torino Politecnico 1953, ref. [10]) and b) the corresponding γ-spectrum for ^{214}Po.

R. Malvano, dealing with the production and performances of scintillation detectors and their use in radioactive decays, I started there some experiments concerning the radioactivity of some heavy natural radioisotopes (namely of the radium family). In fact

my first published paper [10] concerns the β-decay of ^{214}Bi (RaC) and the corresponding γ-spectrum of ^{214}Po (see fig. 1) as measured completely with scintillation counters (for the first time in Italy) *i.e.* with a homemade naphthalene crystal for β-rays and a commercial NaI(Tl) one for γ-rays, coupled with RCA and Du Mont photomultipliers and a standard electronics for measuring single events (N_β and N_γ) and β-γ coincidences. We were in the middle of the first revolution of gamma-ray spectroscopy (the scintillation era).

Other experiments were performed on this line [11] and this allowed me to enter in contact with the Amsterdam group (namely R. Van Lieshout and A.H. Wapstra) of the IKO (*Institut voor Kernphysics Onderzoek, i.e. the Institute for Nuclear Research*), where one of the most important and active research center for nuclear spectroscopy investigations at that time was set up. The established collaboration was further extended in the years 1955–1958 when I could stay in Amsterdam first with a grant (1956) and then as a visiting researcher (1957–58). The fact that I had acquired some experience with the performance of scintillation counters was of a quite important help for my complete introduction in the IKO research program on nuclear spectroscopy. Just

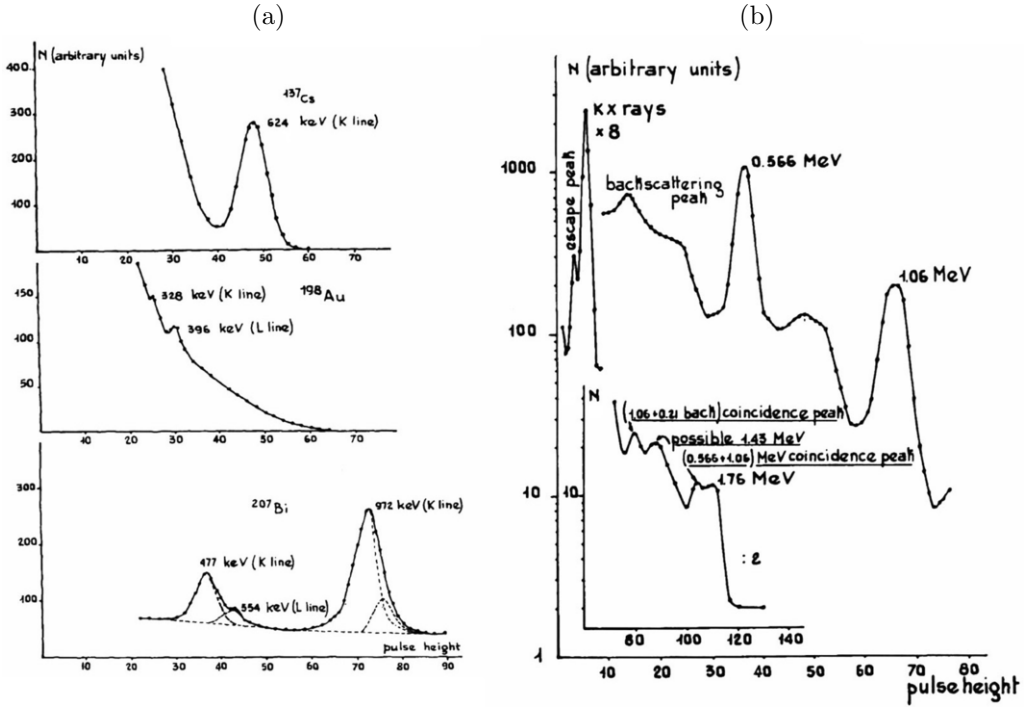

Fig. 2. – a) Electron and conversion spectra of ^{137}Cs, ^{196}Au and ^{297}Bi as obtained with a scintillation spectrometer (anthracene crystal ($2.5 \times 1.3\,\mathrm{cm}$) mounted on a Du Mont 6292 photomultiplier; b) gamma scintillation spectrum from the ^{207}Bi decay measured with a NaI(Tl) crystal ($2.5 \times 2.5\,\mathrm{cm}^2$); the two detectors were connected with single-cannel analyzers (ref. [12]).

to give an idea of the results one could obtain even with simple devices (*primitive* as compared with the sophisticated and complex *gamma arrays* of today) I wish to mention two examples of my personal experience in the field during the stay in Turin and in Amsterdam. The first [12] refers to the performance of a beta scintillation spectrometer especially used for measuring electrons and conversion spectra (cases in point ^{137}Cs, ^{196}Au and ^{207}Bi). It is interesting to note that, in the latter case, the reported values of the *K conversion lines* (477 and 972 keV) of the two stronger γ-transitions (570 and 1064 keV, respectively), (see fig. 2) were adopted to calibrate the liquid scintillation detector used in the famous experiment of Reines and Cowan [13] leading to the first neutrino detection.

The second example is a "poor-man method" (ref. [14] and the appendix of ref. [2]) useful to calibrate and measure the efficiency of a NaI(Tl) gamma scintillation spectrometer for laboratories where only few standard sources with known γ-decay are at disposal, as in the case of the Turin Politecnico at that time). This "home-made technique" making use of only one well-known radioactive source (^{137}Cs in my case) emitting monochromatic γ-rays (662 keV) consisted in measuring, as a function of the angle and of the primary energy, the photopeak areas of the different Compton scattered radiations produced in an Al scatterer placed at the center of a circumference described by the standard source (note that the number of photons scattered at a certain direction into the unit solid angle is obtained by applying the well-known Klein-Nishina formula (cfr [14]). This method has been used for the experiments reported in ref. [11].

With Wapstra, Van Lieshout and R.H. Girgis (a graduate student coming from Egypt) we formed a group very active in studying the decay schemes of many radioisotopes produced by the IKO syncrocyclotron. Quite a number (17) of new nuclear species were produced and investigated in details [15]. A powerful technique for the analysis of the gamma-ray spectra was developed [16] and became a "*trade mark*" of the gamma scintillation spectrometry in those years (see fig. 3 and ref. [16]).

The case of ^{48}Sc is reported also because it is a typical *1particle-1hole configuration* in the $1f_{7/2}$ shell region (see later); the corresponding γ-ray spectrum is taken using also the *summing technique* (well crystal) in order to single out γ-γ and even γ-γ-γ coincidences (see the cascade $6^+ \to 4^+ \to 2^+ \to 0^+$).

The Amsterdam period was therefore very successful in the field of nuclear spectroscopy along the *gamma scintillation era* (namely the *first revolution* in the gamma spectroscopy). The numerous investigations we could perform gave rise to a specific program of research concerning a systematic of the collective and shell-model states in some even-even nuclei and of the particle core-excitations in odd nuclei. This research program was extended later to a strong collaboration with the nuclear physics group I could form in Naples starting from the year 1960 when I moved there from Turin. I will show few of the most interesting results as obtained in the frame of such a program dealing with: *a) shell-model single-particle states in medium-mass nuclei, b) vibrational and rotational states in even-even nuclei*, and *c) particle-core excitations coupling in odd nuclei with even-even core.*

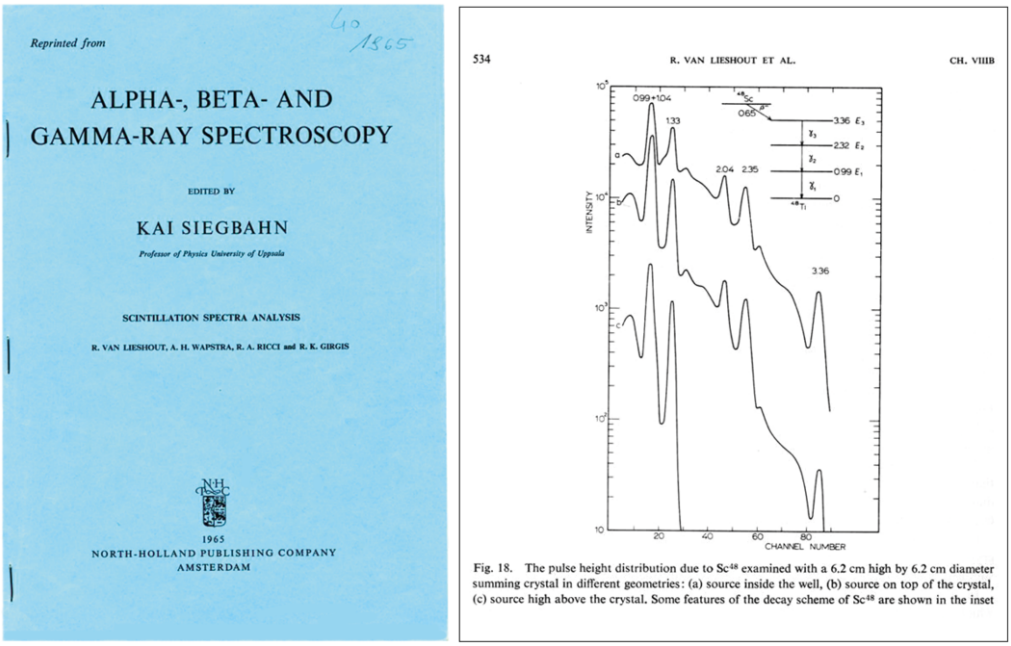

Fig. 3. – Cover of the Amsterdam "Summa" on the scintillation spectra analysis. On the right a typical example of a gamma scintillation spectrum taken with a 6.2 cm high by a 6.2 cm diameter NaI(Tl) summing crystal in different geometries showing the direct spectrum and the double and triple coincidences due to the γ_1-γ_2-γ_3 cascade in the summing spectrum (source insight the crystal). The corresponding feature of the ^{48}Sc is shown in the insert (ref. [16]).

Among the first experiments performed at IKO (Amsterdam) the one concerning the ^{66}Ge $\beta+$ decay (γ-spectrum of ^{66}Ga) is a special case [17], quoted by Bohr and Mottelson [18] as a test of the "*isobaric invariance*". It is in fact a good example of *isospin-forbidden Fermi beta transition* with $\Delta T \neq 0$ ($0^+ \rightarrow 0^+$, $\Delta T = 1$ in our case with a hindrance factor of the order of 10^{-4}–10^{-5} taken from the ft value). Figure 4 shows, as a typical example, the Fermi-Kurie plot of the positon spectrum and the γ scintillation spectra measured with stilbene and NaI(Tl) crystal, respectively. The analysis of the β^+ spectrum was performed taking into account the resolution corrections (see ref. [11]), while the γ spectra were analyzed with the "*peeling method*" as described in ref. [16].

Another interesting case concerning γ-transitions between pure shell-model states particularly with respect to *magnetic dipole effects* in single-particle configurations, is that of the γ-spectrum of ^{207}Pb. The crucial experiment [19] was the ^{207}Bi $\rightarrow$ ^{207}Pb decay and the determination of the ratio of the single-particle $f_{7/2}$-$p_{3/2}$ transition ($E2$) to the $f_{7/2}$-$f_{5/2}$ one ($M1$). This experiment was performed in 1963 at the Nuclear Physics Institute in Naples in the frame of the collaboration with Amsterdam.

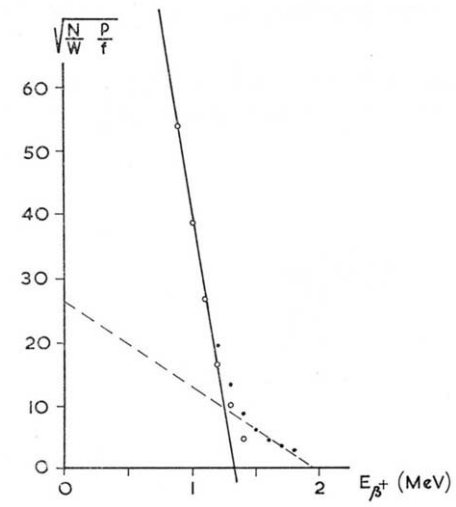

(a)

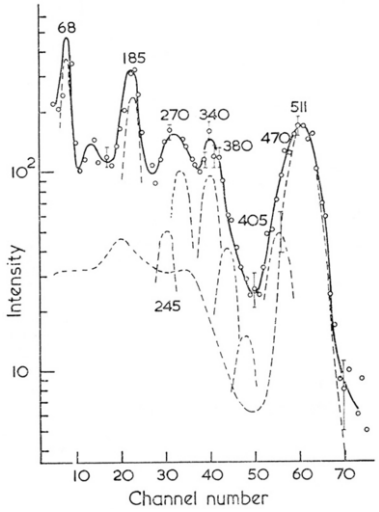

(b)

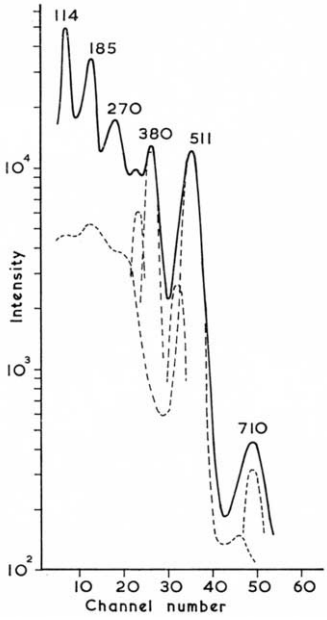

(c)

Fig. 4. – a) Fermi-Kurie diagram of the positon spectrum of ^{66}Ge; contributions due to ^{68}Ga and ^{69}Ge were subtracted; b) part of the direct gamma-ray spectrum from the decay of ^{66}Ge analyzed with the peeling method; the tail of 511 keV peak due to the annihilation in flight of the positons and the backscattering coincidences is also shown (ref. [16]); c) example of γ-γ coincidences: the γ-spectrum in coincidence with a 46 keV photopeak, showing the analyzed lines as dashed curves (ref. [17]).

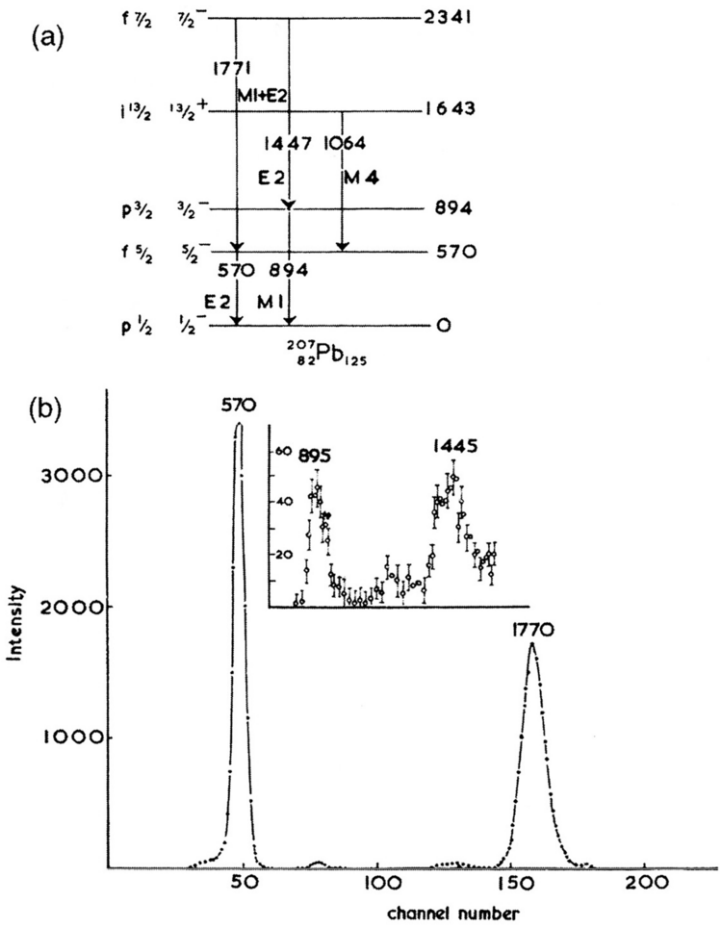

Fig. 5. – a) Level scheme of ^{207}Pb from the decay of ^{207}Bi; b) sum coincidence with 2340 keV sum energy; the insert shows the central part enlarged (ref. [19]).

Figure 5 shows in a) the level scheme of ^{207}Pb clearly displaying the single-hole sequence in the 126 neutron unfilled shell and in b) the coincidence γ-spectrum taken via a summing scintillation technique revealing the decay of the $f_{7/2}$ level at 2341 keV to the $p_{3/2}$ one at 894 keV ($E2$ transition of 1445 keV) and to the $f_{5/2}$ one at 570 keV (pure spin-flip $M1$ transition of 1445 keV). The measured $M1/E2$ ratio (0.023 ± 0.002) showed an hindrance factor ≈ 4 for the $M1$ transition and is one of the best example of this feature as reported by Bohr and Mottelson [20].

Of some interest at the time was also the question of the structure of the excited states in even-even nuclei due to the possibility of simple description in terms of the seniority scheme ($4^+ \to 2^+ \to 0^+$ sequence) as a consequence of a short-range two-body force (pairing force for instance) and the problem of a mixing with collective modes as induced for instance by residual interactions like quadrupole forces. Such a question was

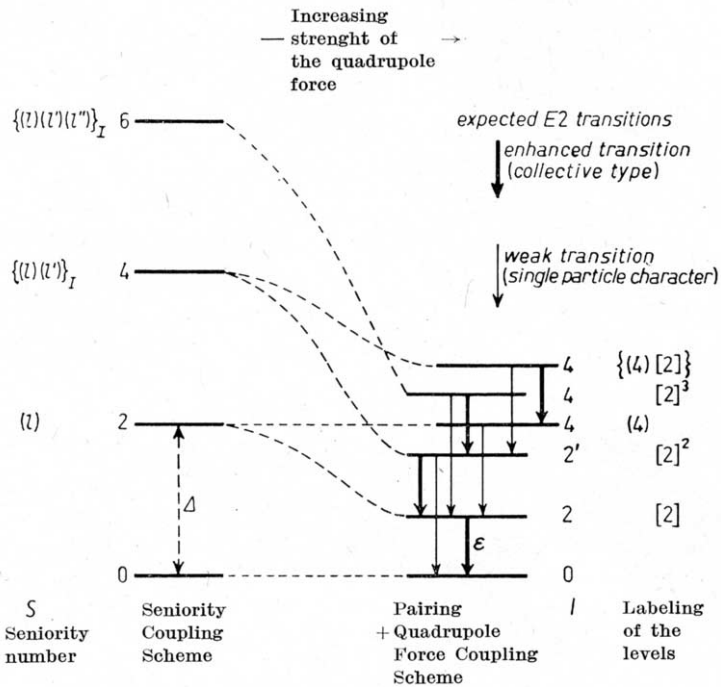

Fig. 6. – Energy levels in the pairing plus quadrupole force coupling scheme in spherical even-even nuclei. The level sequence is only qualitative and refers to the lowest part of the situation expected for vibrational nuclei. Among the possible higher excited states only the $I = 4^+$ one has been drawn. A simplified picture is assumed, in which an even number of nucleons of the same kind are confined to a single j shell.

considered in the frame of a more extended collaboration including the theoretical group of Orsay (namely M. Jean and J. Touchard)([3]).

In fig. 6 I show a qualitative level scheme following the effect of a pairing plus quadrupole force coupling in even-even vibrational nuclei as reported in ref. [21]. That possible interpretation was a consequence of a systematic investigation about some regularities in the branching ratios of excited sates of vibrational character in even-even nuclei [22] pointing out a specific behaviour in the deexcitation of the levels above the low well established vibrational states. The suggestion made by M. Jean, R. Van Lieshout and myself was that the *"pairing" plus long range forces* coupling scheme could be the basis of a more general interpretation of the electromagnetic properties of even-even spherical nuclei.

([3]) The Naples-Amsterdam collaboration was in fact extended to the Institut de Physique Nucléaire of Orsay where I could stay for some time in the years 1964–65 establishing a pleasant collaboration with M. Jean and with the experimental group directed by M. Riou, with whom I could perform a series of experiments on inelastic and quasi-free scattering with protons at 155 MeV provided by the Orsay synchro-cyclotron (see later).

2. – The foundation of Nuclear Spectroscopy in Italy. Naples 1959–1966; the collaboration with Amsterdam and Orsay

As mentioned before, I moved from Turin to Naples in 1959 where I was invited by G. Cortini and by E. Caianiello (directors of the *Istituto di Fisica Superiore* and of the *Istituto di Fisica Teorica* of the Universiy of Naples, respectively) in order to promote there a research activity on Nuclear Physics, namely on nuclear structure studies. Starting with the basic Amsterdam experience I could organize a Laboratory equipped with the necessary instrumentation for advanced gamma spectrometry and form a group of researchers active in the field. In the beginning we did perform some measurements with radioactive sources provided by the IKO cyclotron (*i.e.* with a not too short half-life); later on we could dispose of a 400 keV Van de Graaf accelerator used as 14 MeV neutron generator via the (d, t) reaction, which has been for a certain time, an excellent home-facility for producing a number of radioisotopes we could study in the frame of a specific nuclear spectroscopy program.

Of course we started with measurements of the γ-decays of nuclei already under investigation during my stay at IKO (Amsterdam). The physical case was the particle-core excitations in odd nuclei and the validity of the *center-of-gravity theorem in nuclear spectroscopy* as postulated by R.D. Lawson and J.L. Uretsky [23].

The first example is the γ-spectrum of ^{63}Cu following the positon and electron capture decay of ^{63}Zn produced by Cu (d, n) reactions with the IKO synchrocyclotron and measured with a standard scintillation techniques [24]. In this case ($Z = 27$) a quartet of levels with spins $1/2^-$, $3/2^-$, $5/2^-$, $7/2^-$, is expected by the addition of the 29th proton in a $p_{3/2}$ state, outside the ^{62}Ni core, to the first 2^+ excited state of this latter. This was indeed found for the levels at 668 keV, 1412 keV, 961 keV, 1327 keV, respectively, confirming the results of inelastic scattering experiments (as reported in ref. [24], see fig. 7).

Our γ-ray measurements allowed to establish for some states, the quite correct multipolarities and branching ratios of the different transitions. However this kind of coupling which should be weak with respect to the excitation energy of the core-state and to the separation energy of the various single-particle states, was not very satisfactory. For this reason we decided to perform also in Naples a detailed investigation on the γ-spectrum of ^{57}Co ($Z = 27$; a proton-hole in the 28 proton shell of the ^{58}Ni core) by the β^+-decay of ^{57}Ni (produced at the Betatron of the Turin Institute of Physics by (γ, n) reactions.) [25]. The results are shown in fig. 8, where the level scheme of ^{57}Co is compared with that of ^{59}Co (having ^{60}Ni as a core), as known at that time.

In both nuclei a quintet of levels with spin $3/2^-$, $5/2^-$, $7/2^-$, $9/2^-$ and $11/2^-$ is expected from the coupling of the $1f_{7/2}$ proton hole with the 2^+ core state at 1452 keV in ^{58}Ni and at 1329 keV in ^{60}Ni, respectively. The results, taking into account the incompleteness of the data, showed a promising agreement as found in Cu isotopes for the energies. However, concerning the deexcitation properties (*i.e.* the transition probabilities which should be the same as compared with the deexcitation of the core state) the agreement is less satisfactory.

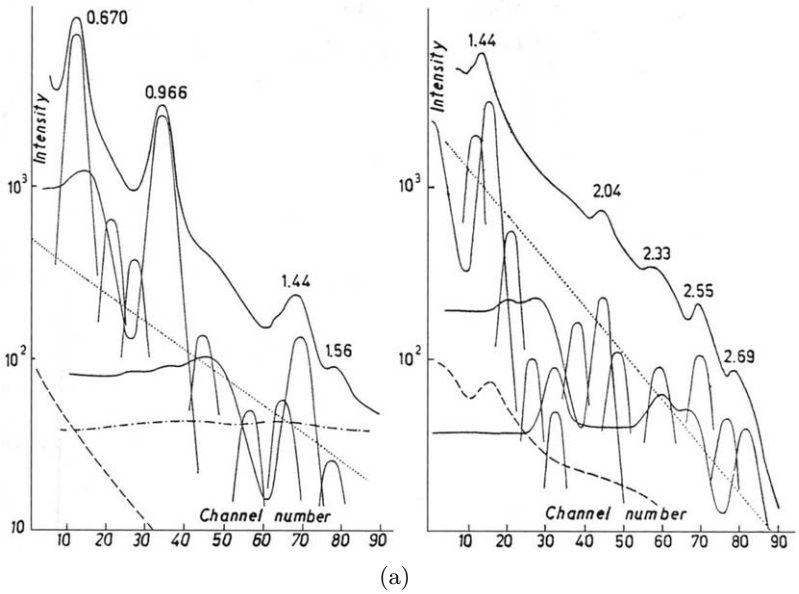

(a)

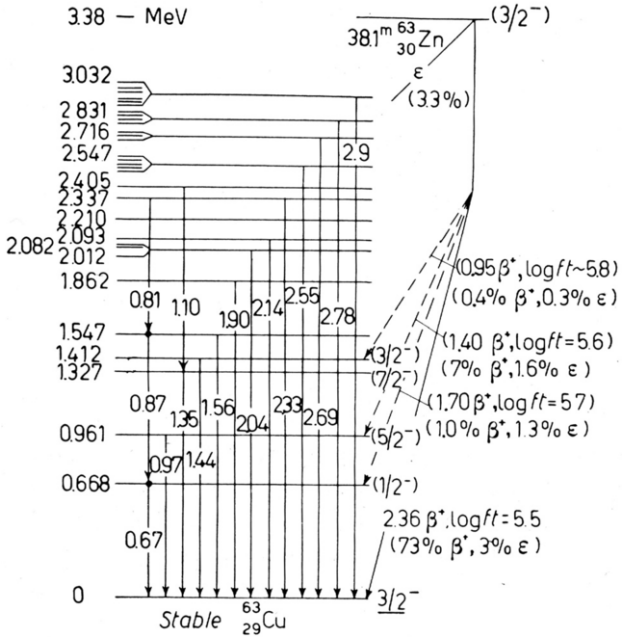

(b)

Fig. 7. – a) Gamma-ray scintillation spectrum following the decay of ^{63}Zn in two different energy region, showing the analysis made by means of the "peeling" method (cfr. ref. [16]). The dotted and dashed lines represent the continuous pulse contributions of annihilation In flight and bremsstrahlung, respectively (see appendix of ref. [24]). b) Level scheme of ^{63}Cu with spin assignement to levels considered as belonging to the center-of-gravity multiplet.

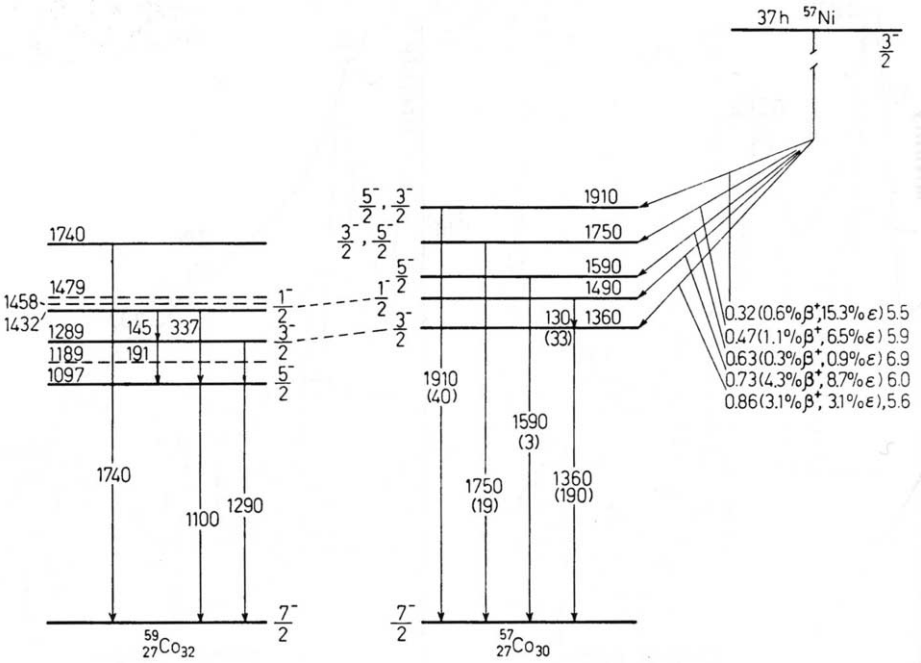

Fig. 8. – Level scheme of ^{57}Co as obtained from the decay of ^{57}Ni; the spin assignement to the higher levels is only tentative. The level structure of ^{59}Co is also reported for comparison: levels consistent with the center of gravity theorem in both nuclei are connected with dashed lines.

In fact, apart from the simplest case of the coupling of a $j = 1/2$ single-particle state and for doubly magic core nuclei, such a weak coupling scheme holds in very peculiar situations where the different single-particle states of the odd nuclei are quite apart and the core excitations and well separated from each other so that the center-of-gravity level multiplet can be treated as a small perturbation [26]. Specific cases for instance are the coupling of the octupole (collective vibrations) 3^- states, in ^{40}Ca and in ^{208}Pb coupled with the $1d_{3/2}$ proton hole in the 20 magic proton shells and the $h_{9/2}$ proton out of the 82 magic proton shells, respectively. Anyhow the evidence of *core-excitation coupling states* in odd nuclei was quite well established by inelastic scattering of charged particles, for instance with 155 MeV protons at Orsay, during my stay there, in the $1d$-$2s$ and $1f$-$2p$ shell-model nuclear region. A typical case was indeed that of the core coupling states in ^{39}K for which we could establish the validity of the center-of-gravity theorem (see ref. [27]).

The very successful activity of the Naples team did find an important achievement with the full exploitement of the facilities at our disposal. This was the case of the investigation of a key nucleus like ^{50}Ti ($Z = 22$, $N = 28$) for the characterization of the *two-particle spectrum* in a quite interesting nuclear region, that of the $1f_{7/2}$ shell. This experiment turned out to be very convenient because the ^{50}Ti gamma-spectrum

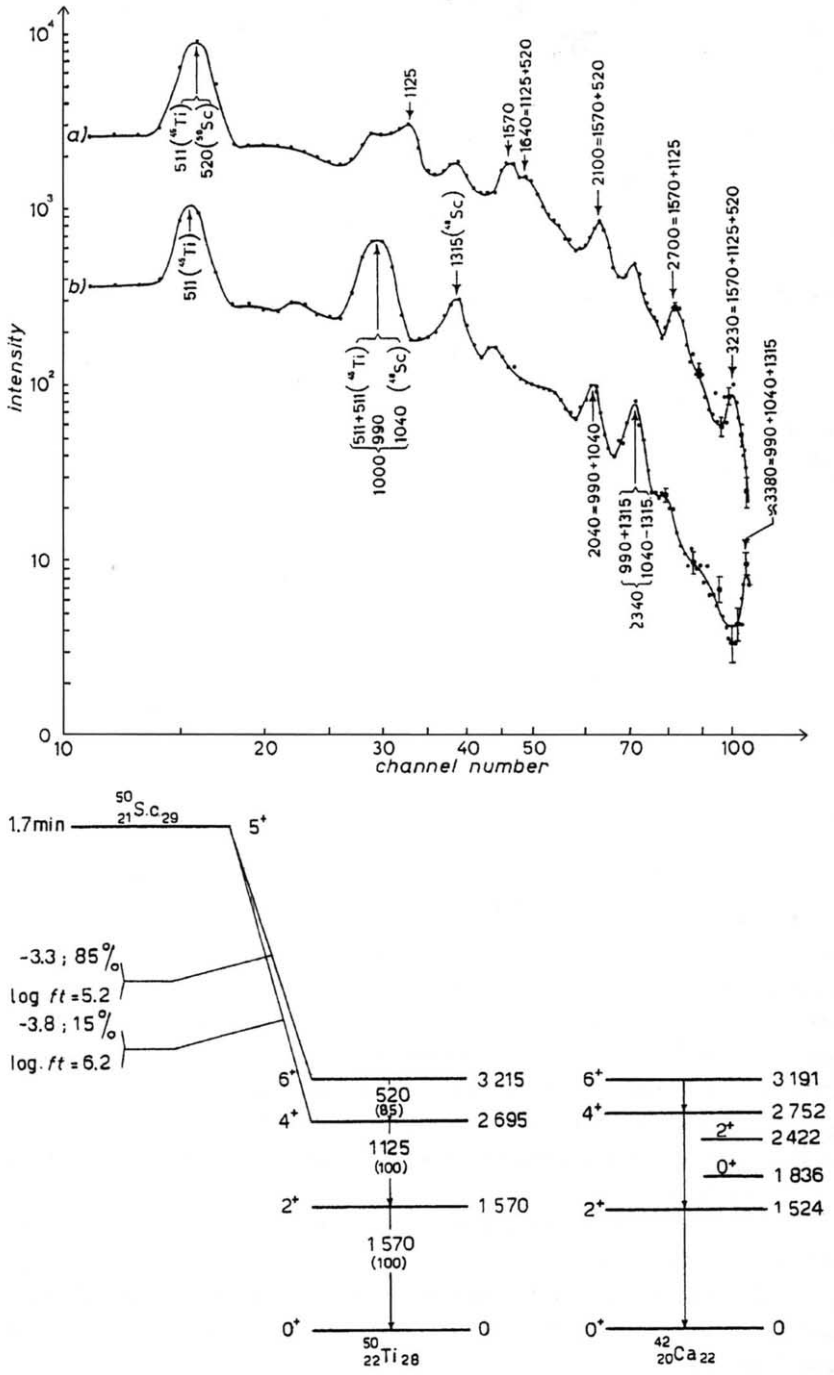

Fig. 9. – The γ-ray and γ summing coincidences spectrum and level scheme of ^{50}Ti compared with the ^{42}Ca one; the extra 0^+ and 2^+ states in this latter are assumed as core excitations (deformed) states (1963, ref. [28]).

follows the β-decay of ^{50}Sc with a half-life of 1.7 min., which could be easily produced via the (n, p) reaction by bombarding titanium metallic foils (99.9% purity) with the 14 MeV neutrons generated by the (d, t) reaction at the 400 keV electrostatic accelerator and measuring the β and γ-ray spectra with standard scintillation detectors (antracene and NaI(Tl) crystals, respectively) coupled to Du Mont photomultipliers and connected with a 200 channel (LABEN) analyzer [28]. This is also a case where the complete scintillation analysis including the observation of γ-γ and γ-γ-γ coincidences by means of the *summing* technique (*hollow crystal*) was performed (see fig. 9).

The importance of the results we obtained is due to the fact that, on the one hand the $(j)^2$ and more generally $(j)^n$ could be a quite good approximation in the $1f_{7/2}$ shell, on the other, that, taking into account the comparison with the ^{42}Ca spectrum, it was shown, for the first time, that the *effective two-body interaction* both for protons ($(\pi 1f_{7/2})^2$ configuration) and neutrons ($(\nu 1f_{7/2})^2$ configuration) in the $T = 1$ isospin states (0^+, 2^+, 4^+, 6^+), is the same (*charge independence of the effective nuclear force*). The problem of the presence of the other states (0^+ and 2^+) in ^{42}Ca was and is still explained with different configurations in the ^{42}Ca core (like collective states due to core excitations or, more generally, deformed states). *So started the* $1f_{7/2}$ *story.*

3. – The $1f_{7/2}$ story

Following the investigations on shell-model and collective states in "spherical" even-even nuclei and on excited states of odd nuclei with a spherical core, the program I started in Naples was then mainly devoted to a particular region, that of the so-called "$1f_{7/2}$ *nuclei*" *i.e.* nuclei with nucleons filling the major $1f_{7/2}$ shell. It was realized that this is a real rich domain of research in many aspects and it became in fact a kind of *trade mark* of our collaboration with Amsterdam and Orsay and, later on and more extensively, with Florence, Padua and Munich. I will not report this story (that I called "The $1f_{7/2}$ saga") in details also because one can find quite a number of specific articles and general reviews (see refs. [1] and [2] and more specifically ref. [29]). As mentioned by H. Morinaga in his conclusion of the topical conference we did organize at the Laboratori Nationali di Legnaro in 1971, entirely devoted to the "*Structure of* $1f_{7/2}$ *nuclei*" (see ref. [29], 4)), we started by the so-called **MBZ** work [30] whose preprint was send to a number of people interested in the field with an accompanying letter addressed "*Dear friends of* $f_{7/2}$ *shell*". This is a kind of an historical introduction together with the fact that in 1947 when the shell-model was proposed "*It was only qualitative and probably* —I am quoting Morinaga— *one of the earliest effort to make quantitative calculations... was done by Levinson and Ford in 1955 for the* $1f_{7/2}$ *shell. It is no wonder that this is a single shell*". At that time the experimental knowledge of the key nuclei from which one could extract the single-particle energies (^{41}Ca) and the two-body residual interaction (^{42}Ca) as referred to the doubly magic ^{40}Ca was quite poor so as for other possible reference nuclei in the region and the presence of states of doubtful origin in ^{42}Ca was a further complication. For this reason our results on ^{50}Ti together with those concerning the extra 0^+ and 2^+ (core excited) states in ^{42}Ca out of the normal (0^+,

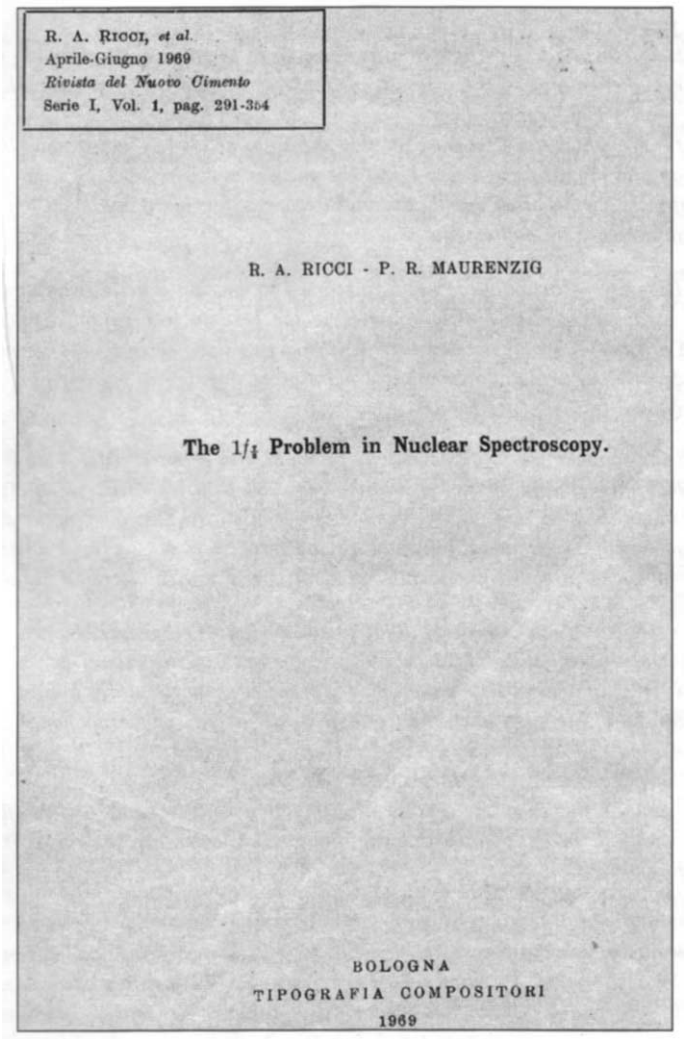

Fig. 10. – Cover of the "Bible" of $1f_{7/2}$ nuclei (1969, ref. [29], 2)). The definition is due to Gerry Brown in the '60s.

2^+, 4^+) seniority sequence, designating this nuclear region as "*the* $1f_{7/2}$ *nuclei*" could preserve some meaning.

Thereafter the series of measurements and results so as the various theoretical approaches concerning this nuclear region in the years 1960–1976 were reviewed successively in a number of "classical" papers presented and discussed in specific or "topical" conferences and meetings. A list of them is reported in ref. [29]. The main fundamental aspects were summarized and analyzed in the so called "*Bible*" of the $1f_{7/2}$ nuclei (see fig. 10 and ref. [29], 2)) and in the lecture I gave here in Varenna in 1969 on "*Experimental Nuclear Spectroscopy in the* $1f_{7/2}$ *nuclei*" (cfr. ref. [29], 3)).

Particularly in refs. [29] and [31] a summary can be found of the significant progress made in investigating the properties of nuclei with Z and N ranging from 20 to 28 including the more recent data especially with reference to the more advanced facilities with the possibility of going from the stability walley towards exotic regions with radioactive ion beams. A real "*Revival of* $1f_{f7/2}$ *nuclei*". This is mostly due to the various revolutions occurred in the years 1970–2000 concerning the gamma-ray spectroscopy with the advent, first *of germanium detectors* (great improvement of the resolution), then of the more complex and sophisticated *gamma-arrays* (optimazition of resolution and efficiency and even of the position sensitivity). The advent of *heavy-ion accelerators*, allowing the production of high-energy and high-spin nuclear states and of the *in-beam spectroscopy* were essential. The final touch is the radioactive beam acceleration with the possibility of producing exotic nuclear species. One should not forget that the extensive use of nuclear reactions has also been of great help and I wish here to underline some peculiar *findings* not particularly related to gamma spectroscopy. In our case the collaboration with Orsay, as already mentioned, was very fruitful, particularly with the experimental group held by M. Riou, well equipped and expert in the domain of nuclear reactions induced by medium–high energy protons (155 MeV from the Orsay synchrocyclotron). It was very interesting for me to join them and suggest to extend their measurements performed in the $2s$-$1d$ region also to the $1f_{7/2}$ nuclei. Important results were found concerning the observation by *inelastic proton scattering* of collective *vibrational states* (*i.e.* 2^+ quadrupole and 3^- octupole) in even-even nuclei and of excited states in odd nuclei

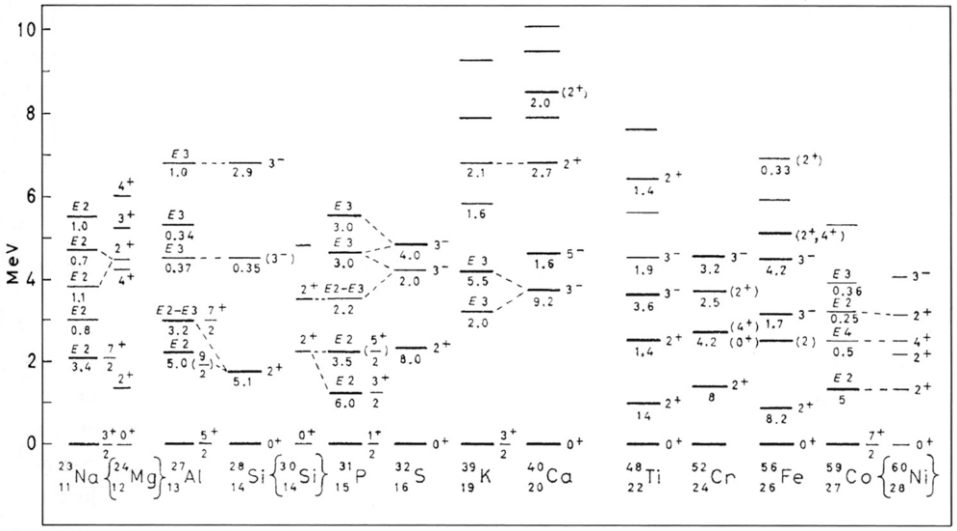

Fig. 11. – Nuclear states excited by inelastic 155 MeV proton scattering in nuclei from $A = 23$ to $A = 59$ at Orsay (1963, ref. [27]); the strongly excited (collective) levels of even-even nuclei are indicated in bold type while in odd nuclei the levels corresponding to core excitations are connected to the parent states in the even-even cores by dashed lines.

arising from a *core-single particle coupling* in the $1d_{3/2}$-$1f_{7/2}$ region (namely from ^{23}Na to ^{59}Co). They are summarized in fig. 11 as obtained by measuring energies, differential cross-sections and angular distributions, which clearly indicate the $E2$ and $E3$ multipolarities. The connection of levels in odd nuclei arising by the core-particle-excitation were also clearly identified (namely by the angular distributions and by the statistical distribution of the excitation intensities).

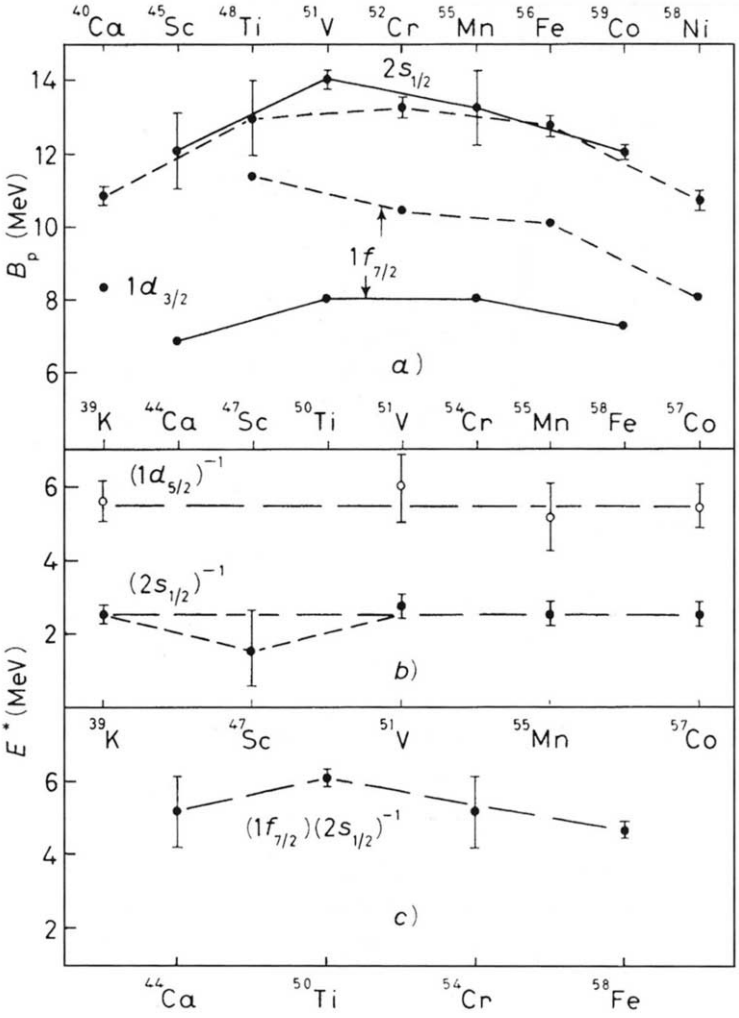

Fig. 12. – a) Binding energies of $2s_{1/2}$ states in $1f_{7/2}$ nuclei from (p, 2p) reactions at 155 MeV. Target nuclei are indicated on the top; the full line connects even-even residual nuclei; the separation between $1d_{3/2}$ and $1f_{7/2}$ states as from the proton binding energies in target nuclei is indicated. b) Excitation energies $2s_{1/2}$ and $1d_{3/2}$ proton-hole states in the odd nuclei reported in a). The main difference between b) and c) is due to pairing effects (ref. [32]).

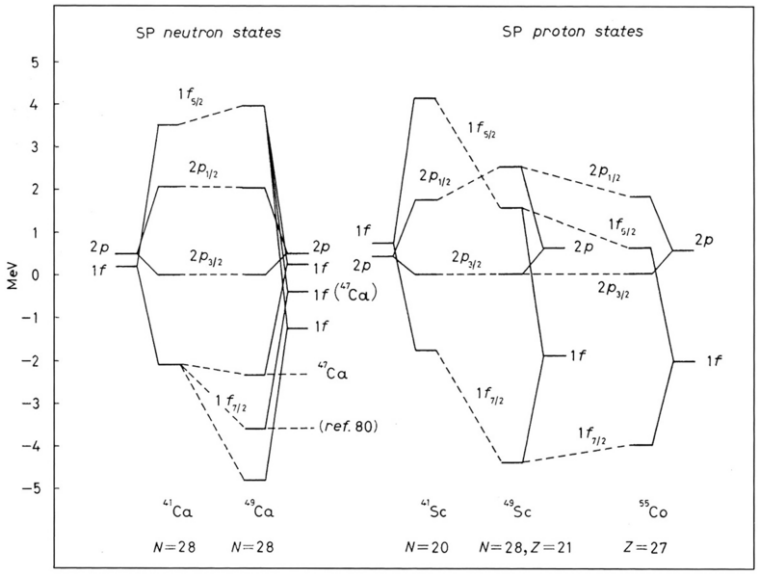

(a)

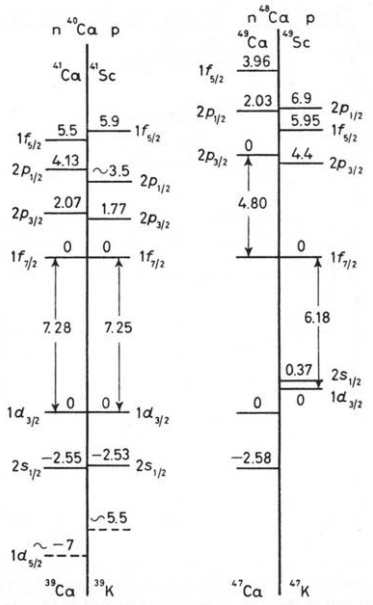

(b)

Fig. 13. – a) Single-particle energies (centroids derived from stripping, pick-up and knock-out reactions taking into account the spectroscopic strengths and the isospin splitting in the proton case) relative to the $2p_{3/2}$ state of ^{41}Ca, ^{47}Ca, ^{49}Ca (neutron states) and of ^{41}Sc, ^{49}Sc and ^{55}Co (proton states). The centroid of $1f$ and $2p$ states are indicated with the corresponding spin-orbit splitting. b) Summary of the spacing between the unperturbed single-particle states referred to the ^{40}Ca and ^{48}Ca cores (see ref. [29], 3)).

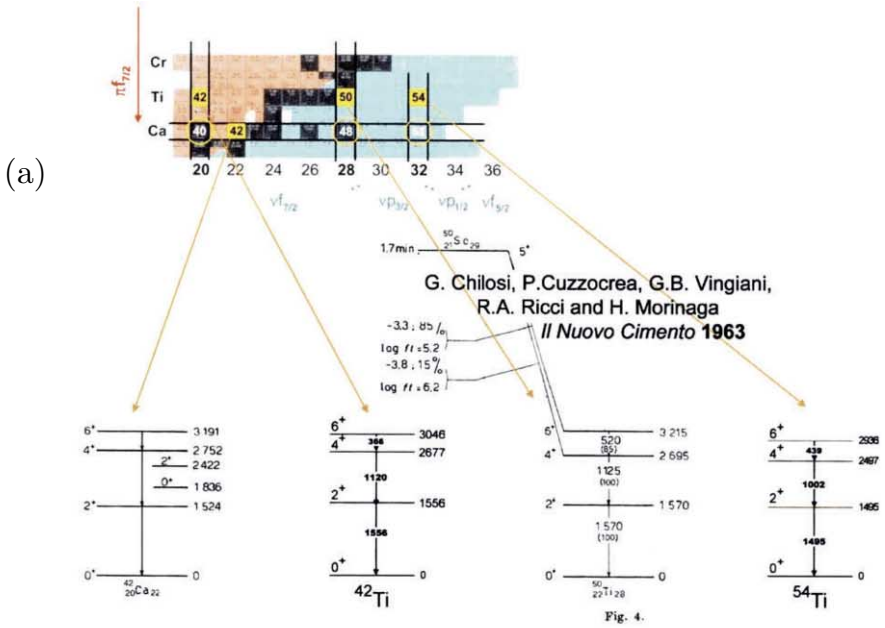

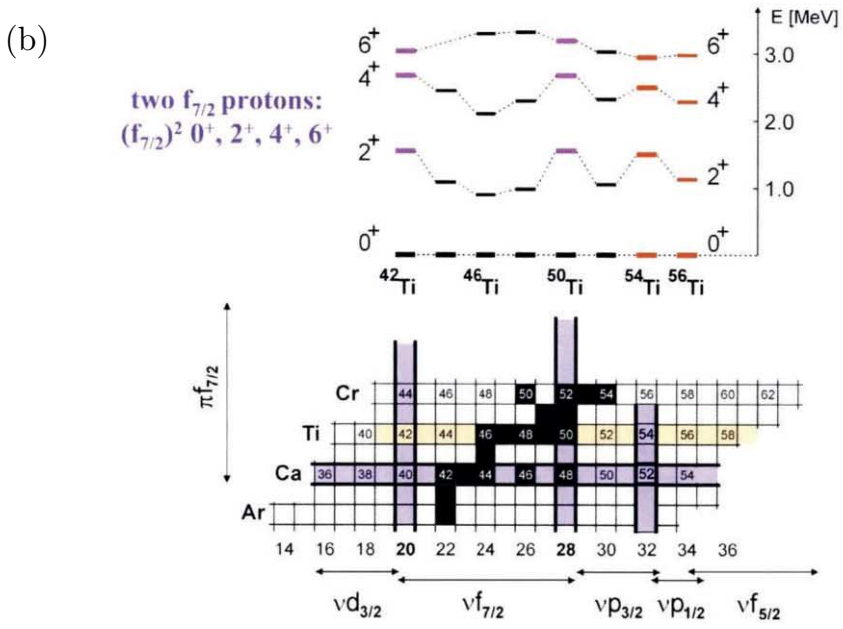

Fig. 14. – a) Two-particle (proton) spectra in the $1f_{7/2}$ nuclei; the ^{42}Ca two-neutron spectrum is reported for comparison. b) Evolution of the $1f_{7/2}$ proton spectra of the even Ti isotopes and of the filling of the neutron single-particle states in the f-p shells (see ref. [31]).

A second important investigation concerns the measurement of the proton binding energies in the ($1f$-$2p$) region by (p, 2p) knock-out reactions (quasi-free proton scattering) performed at the 155 MeV synchrocyclotron in Orsay in 1967 (cfr refs. [27] and [32]). Figure 12 displays the results concerning in particular the $1f_{7/2}$-$1d_{3/2}$ *energy separations* together with the excitation energies of s and d holes states in some $1f_{7/2}$ nuclei.

Our results could add new data to those found in the (e, e′p) important experiments performed by the Group of the Istituto Superiore di Sanità (Rome) (see ref. [33]) and gave also a direct demonstration of *the existence of nuclear shells*.

Another important piece of information was obtained by those data for evaluating the behaviour of the single-particle (or single-hole) states in the $1f$-$2p$ region. From a systematic analysis of the various reaction data already known at that time (stripping, pick-up and knock-out reactions) one could construct a sort of diagram as that reported in fig. 13a. Moreover fig. 13b shows, as a summary, the spacing between single-particle states referred to the ^{40}Ca and ^{48}Ca cores; the presence of a quite consistent $1f_{7/2}$-$2p_{3/2}$ energy gap is quite evident near the ^{48}Ca core. One should already argue about the possibility of an evolution of the nuclear states in this region pointing to an increase of the energy separation (namely in the neutron filling of the $1f_{7/2}$ and $2p_{3/2}$ shells).

What is significant in this context is that, as pointed out recently by B. Fornal [31], the evolution of the shell-model single-particle states $f_{7/2}$, $p_{3/2}$, $f_{5/2}$ and $p_{1/2}$ did already show that with the filling of the $p_{3/2}$ orbital, it appears a *subshell closure at* $N = 32$ *(energy gap)* and possibly at $N = 34$. That $N = 32$ could be associated with a new quasi-magic number has been demonstrated by the data recently obtained for the 2^+ lowest states of even-even Ti isotopes until ^{54}Ti ($N = 32$) as produced and investigated thanks to radioactive-beam γ-ray spectroscopy (see fig. 14 and ref. [31]). The evolution of the $(1f_{7/2})^2$ two-body spectra shows the strong similarity of ^{54}Ti ($N = 32$) with ^{42}Ti ($N = 20$) and ^{50}Ti ($N = 28$), whereas ^{56}Ti ($N = 34$) does not present the same behaviour.

4. – The second and third revolution of nuclear spectroscopy: the germanium detectors for γ-spectrometry; the heavy-ion accelerators and the in beam spectroscopy

The coincidence of all these events in the years 1960–65 was certainly essential in the impressive development of the systematic experimental investigation of peculiar properties concerning nuclear structure and dynamics. Just at the end of 1965 I moved from Naples to Florence. In fact a quite efficient collaboration was already started with the Florence group giving rise to the first investigation in Italy of a nuclear gamma spectrum with Ge(Li) detectors.

The case in point was the measurement of the γ-spectrum of ^{174}Yb following the decay of ^{174}Lu searching for two-particle states in deformed nuclei: fig. 15 shows the relevant part of the spectrum where a specific 1265 keV summing peak arising from a γ-γ cascade from the 1518 keV state, was resolved (this was difficult in a previous

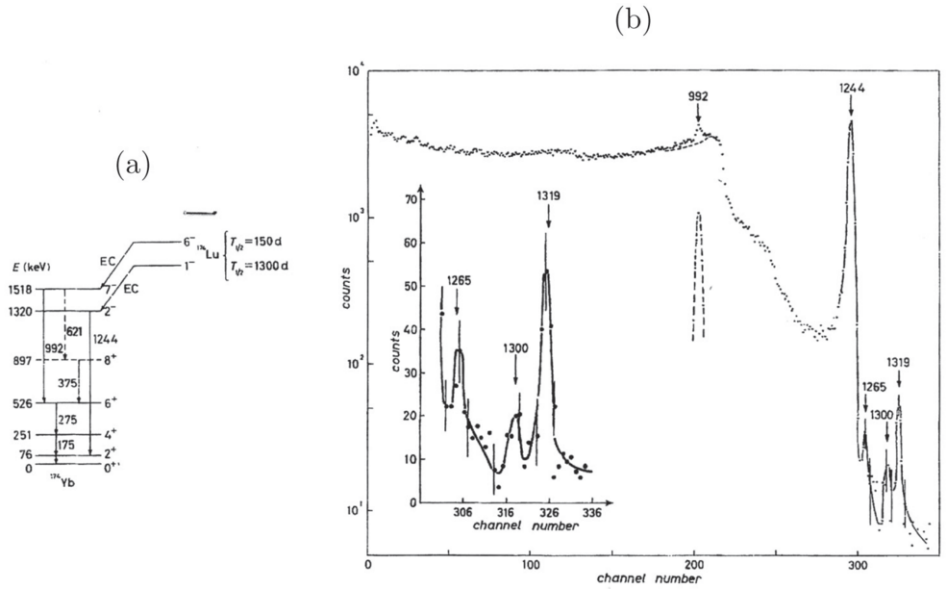

Fig. 15. – a) Level scheme of ^{174}Yb From the decay of the isomeric pair of ^{174}Lu; the 1518 keV level with spin 7^- is definitely established as a two-particle shell-model state. b) Gamma-spectrum (high energy part) measured with a Ge(Li) detector ($4\,\mathrm{cm}^2 \times 0.6\,\mathrm{cm}$); the summing peak at 1265 keV clearly shown in the insert exhausts completely the $992 + 275$ keV γ-γ cascade confirming the 7^- assignement to the 1518 keV state (ref. [34]).

experiment performed in Naples with a scintillation counter) and establishing the spin assignement 7^- as expected for a two-neutron shell-model state. This is a typical case of the coexistence of shell-model states with deformed ones in heavy nuclei [34].

Now, the *coexistence and competition of pure shell-model configurations with collective behaviour* was of course an important feature to be confirmed also in our priviledged region of $1f_{7/2}$ nuclei. Therefore the research program initiated in Naples was extended to the collaboration with Florence and then with Padua and at the Laboratori of Legnaro where, starting from 1965, I could organize a well founded research activity based on the efficient collaboration of groups of Naples, Florence. Padua, and Trieste making use of the more advanced facility at disposal in Italy for nuclear structure at that time *i.e.* the 5 MV Van de Graaf accelerator. A series of interesting experiments was performed and it could be very fruitful making use of the *in-beam gamma-ray spectroscopy* which was just invented in 1963 in Amsterdam by H. Morinaga and P. Gugelot [35].

The results we could obtain already at the Legnaro Van de Graff are summarized in ([29], 4)) and [36], where specific important examples are also quoted, as investigated by (p, n), (p, p′), (α, n), (^{3}He, n), (^{3}He, α) reactions, via high-resolution gamma-spectrometry, measuring also excitation functions, transition probabilities, angular distributions and correlations, half-lives, linear polarization. particle-gamma and

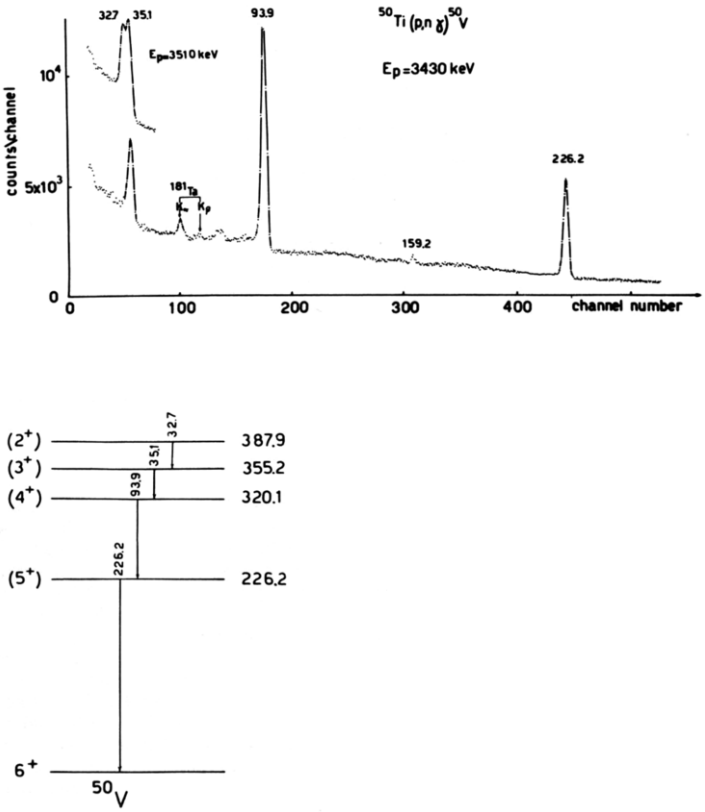

Fig. 16. – The low-lying levels of the od-odd ^{50}V ($Z = 23$, $N = 27$) as an example of shell-model states belonging to the $(\pi f_{7/2})^3(\nu f_{7/2})^{-1}$ configuration (ref. [36]).

gamma-gamma coincidences. Results of particular interest were: i) the characterization of particle-hole states by (^{3}He, α) reactions (neutron pick-up) in even Ca isotopes ($2s$-$1d$ core excitations) with decreasing strength from ^{40}Ca to ^{48}Ca (which is one of the experimental indication of ^{48}Ca being a better inert core than ^{40}Ca); ii) the preliminary identification of rotational bands with positive and negative parity in odd $1f_{7/2}$ nuclei (typical example ^{45}Sc) that I will discuss later considering also high-spin states; iii) pure shell-model configurations in some odd-odd nuclei (cfr ^{50}V, see fig. 16); iv) measurements of electromagnetic transitions and mean lives in $(1f_{7/2})^3$ nuclei as ^{43}Ca and ^{53}Mn and critical tests of nuclear models with a further proof that nuclei lying between ^{48}Ca and ^{56}Ni are better described by the spherical shell-model than by those near ^{40}Ca.

I will come back to these systematic investigations later in resuming the more general achievements obtained by the Legnaro-Padua-Florence-Munich (LPMF)collaboration in the years '70s–'80s. I wish to mention here another important topic covered by our research program at the Legnaro Van de Graaff accelerator: the search and character-

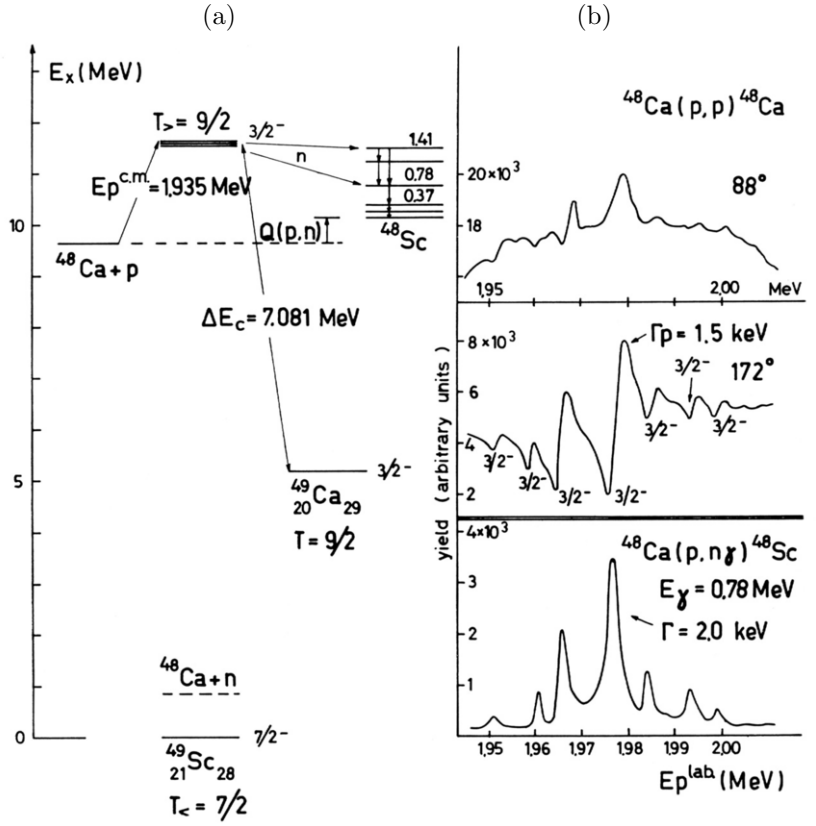

Fig. 17. – a) Reaction diagram for the excitation and decay of the ^{49}Ca ground-state IAR in the ^{48}Ca+p system and b) the corresponding fine structure found in (p, p) and (p, nγ) experiments (ref. [37] and text).

ization of *Isobaric Analogue States* (IAS) *or Resonances* (IAR) in medium-light nuclei (namely in the $1f_{7/2}$ region). In fact, this exciting research field was open to low-energy accelerators in connection with properly used high-resolution facilities. Among the various interesting cases studied, I will quote at least that of the fine structure distribution of the ^{49}Ca (angular momentum $J^\pi = 3/2^-$, isospin $T = 9/2$) ground-state analogue in ^{49}Sc, which could give information on the properties of single-particle shell-model states beyond the $1f_{7/2}$ shell. The reaction ^{48}Ca+p (for ^{48}Ca $J^\pi = 0^+$ and isospin $T_0 = 4$) is the proper one with proton energy corresponding at least to three open decay-channels (p, p), (p, γ) and (p, nγ) for the ^{49}Sc compound nucleus states (see fig. 17a). Since the last one will feed levels in the ^{48}Sc residual nucleus ($T = T_0 - 1/2 = 7/2$)) followed by γ-decay, the measurement of the corresponding γ-yield as a function of the proton energy would show the corresponding analogue state as a resonance (IAR). In fact the IAR in question was resolved into components singled out in the isospin forbidden (p,

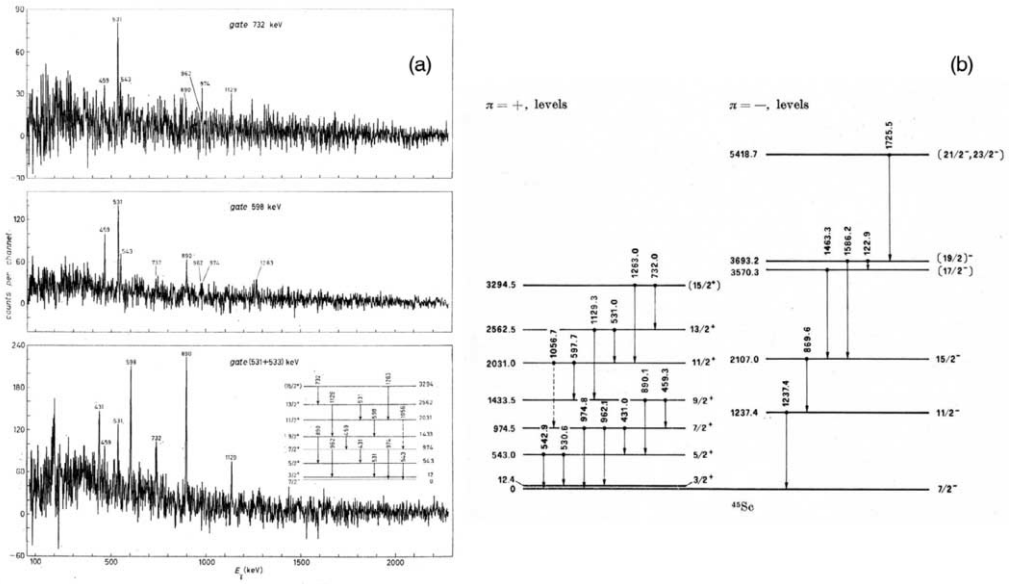

Fig. 18. – a) A typical example of in-beam γ-γ coincidence spectrum in ^{45}Sc produced by the (30 MeV) ^{30}Si + ^{18}O reaction at the Munich Tandem accelerator; the insert shows the corresponding deduced level scheme. b) Partial level scheme of ^{45}Sc showing the two positive- and negative-parity bands with high-spin states up to $15/2^-$ and $23/2^+$, respectively (ref. [38]).

nγ) reaction, indicating for the first time a quite detailed structure due to the mixing of the IAS ($T_> = T_0 + 1/2 = 9/2$) and the surrounding compound nucleus (^{49}Sc) states (corresponding to particle-hole excitations) with the same angular momentum and parity ($J^\pi = 3/2^-$) and lower isospin ($T_< = T_0 - 1/2 = 7/2$) which will allow the neutron decay of the ^{49}Sc-IAS into the normal $T_<$ states of ^{48}Sc (see fig. 17). Therefore the shell-model description of IAS is related to the isospin splitting of single-particle states [37].

Let me now come back to the extended research program concerning the structure of the "$1f_{7/2}$ *nuclei*" as allowed by the advent of heavy-ion (HI) facilities in connection with the beam γ-ray spectroscopy and the higher-resolution detection techniques. The LPFM collaboration could profit of the 11 *MV Tandem* accelerator of the Munich University and undertake a series *of* important experiments based on the *selective population of high-energy and high-spin states* of quite a number of $1f_{7/2}$ nuclei. I will confine myself only to few specific cases showing significant findings concerning the identification and the interplay of single-particle shell-model and collective states in this peculiar region. Figure 18 shows the two bands of positive and negative parities in ^{45}Sc with identification of high-spin levels (up to $15/2^*$ and $23/2^-$, respectively) as an extension of the results found in the lower energy investigation performed at the Legnaro Van de Graaff. The positive-parity band has clearly a rotational-like character based on the $3/2^+$ hole state

and it is seen to continue up to the fairly high spins whereas for the negative-parity one it was found that particularly for what concerns the high-spin states both collective and shell-model can be applied with a preference to the last one since it predicts an upper limit for the highest spin (23/2) as experimentally observed.

The great quantity of collected data in those years with systematic measurements of γ-ray excitation functions, γ-γ coincidences and angular distributions, linear polarization and life-time of nuclear states, was quite impressive and we could obtain quite a number of significant informations [39]. Among them I wish to outllne the quite general feature in this region, besides the coexistence of collective and spherical shell-model states, *i.e.* the confirmation that collective effects are more confined at lower energies and that, in some cases, at high excitation, the collectivity seems to be totally washed out. To summarize taking also into account the results at the Legnaro VdG: i) for several odd nuclei, besides ^{45}Sc (^{43}Sc, ^{45}Ti, ^{47}V, ^{49}V), the existence of $K = 3/2^+$ and $K = 1/2^+$ bands based on *s*-*d* holes, was confirmed up to high-spin states, while in ^{51}V and ^{53}Mn (single-closed shell nuclei) the $(1f_{7/2})^3$ configuration was clearly observed and other states with $J^\pi = 15/2^-$

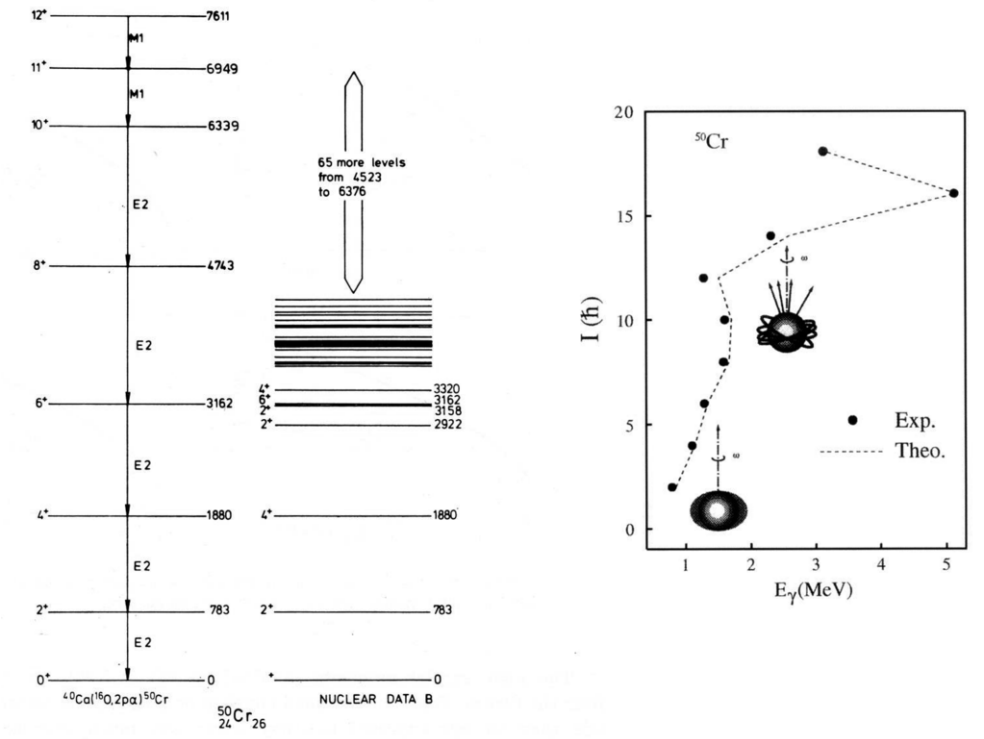

Fig. 19. – a) Levels observed in ^{50}Cr from heavy-ion–induced reactions compared with what is known from other type of reactions). b) Back-bending plot (J *vs.* E_γ) of the corresponding yrast band (ref. [39]).

were found and described in terms of excitation of a single neutron from the $N = 28$ core to higher shells; ii) in odd-odd nuclei like ^{48}V and ^{44}Sc, non natural (negative) parity states with rotational character were definitely established, which are lacking in ^{52}Mn as expected from the systematic of deformed hole-states. As a general fact, the results concerning the selective population of yrast states is very spectacular as shown in fig. 19 where the levels seen from heavy ion reactions are reported in comparison with all the levels actually known in ^{50}Cr. Also the behaviour of the angular momentum J as a function of the excitation energy E_γ is reported showing a clear double back-bending effect as predicted, which is in very good agreement with shell-model calculation [39]. This interesting feature *i.e.* the fact that the collective behaviour is well accounted for in the frame of the shell-model is also present in the case of ^{48}Cr ($N = Z = 24$) [39].

On the other hand, a particular feature of ^{50}Cr is that, along the yrast sequence ($12^+ \to 11^+ \to 10^+ \to 8^+ \to 6^+ \to 4^+ \to 2^+ \to 0^+$), "unstretched" $M1$ transitions connecting the 12-11-10 states were observed on the top of the subsequent "stretched" (*i.e.* with $J_i > J_f$) $E2$ cascade, as a clear example of a sort of "purification" of the low-energy collective band, at high excitation, in shell-model configurations, as already mentioned.

Of particular interest, in this context, was therefore the case of the even Ti ($Z = 22$) isotopes, namely ^{46}Ti ($N = 24$) and ^{48}Ti ($N = 26$) for which a similar behaviour was

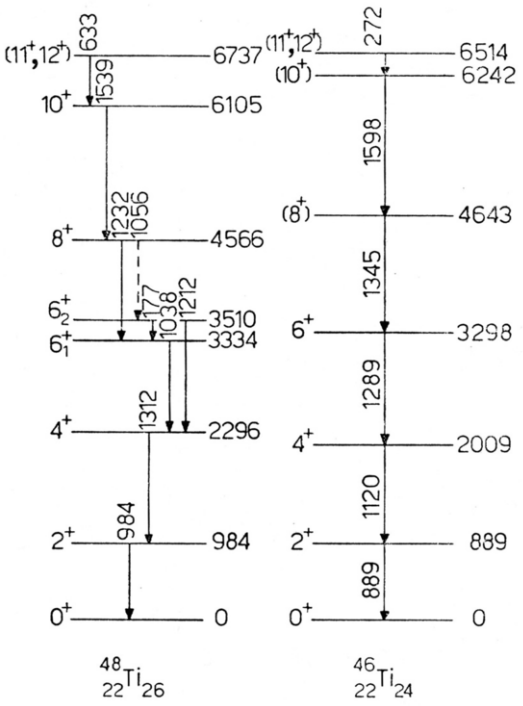

Fig. 20. – Decay schemes of ^{48}Ti and ^{46}Ti as observed in (HI) selective reactions (ref. [40]).

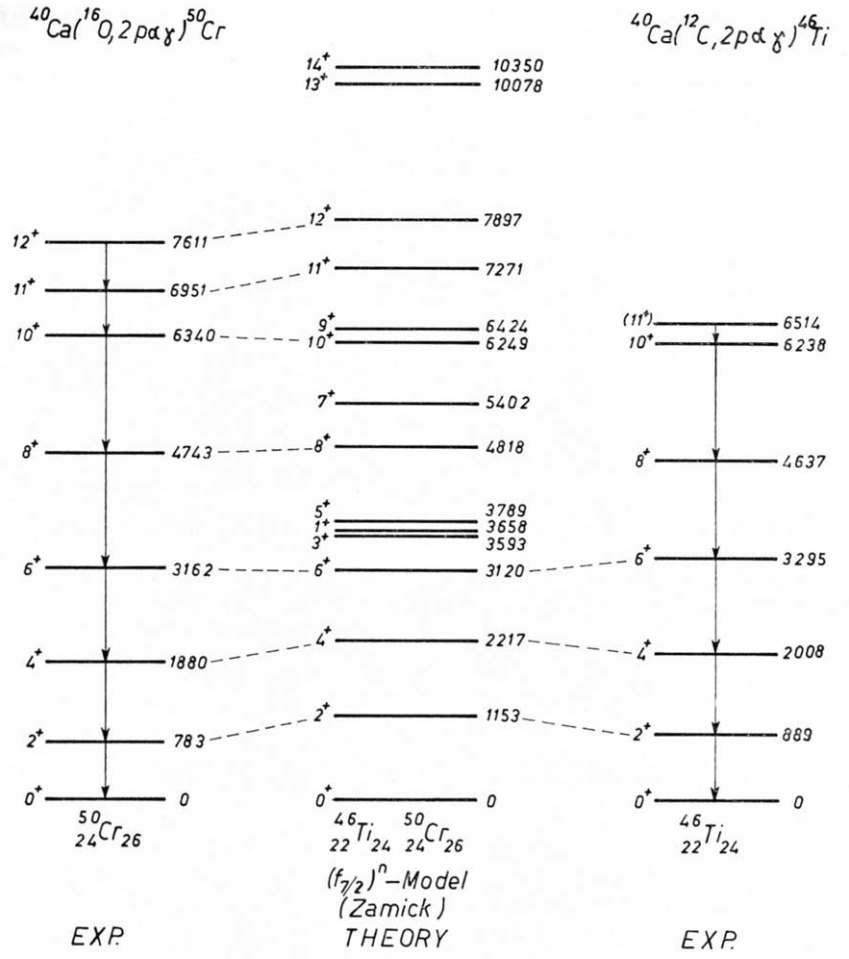

Fig. 21. – High-spin (shell-model) states observed in ^{50}Cr and in ^{46}Ti compared with the predictions of M.B.Z. calculations (refs. [39, 40]).

found [40]. In fig. 20 the decay schemes of both nuclei are shown as observed with HI reactions at the Munich Tandem, whereas in fig. 21, just as an example, a comparison of the ^{50}Cr and ^{46}Ti observed yrast states with the pure $(f_{7/2})^n$ shell-model configuration is reported.

The fact that yrast states with collective character can be described with quite a good approximation in the frame of the shell-model, is a peculiar aspect of the $1f_{7/2}$ region. Similar results were found in other even-even nuclei with non-closed core like ^{44}Ti, ^{48}Cr and ^{52}Fe, with calculations always performed in the pure $(1f_{7/2})^n$ space using different sets of the empirical $(f_{7/2})^n$ matrix elements (deduced from the ^{42}Sc, ^{54}Co and ^{48}Sc) (see refs. [39] and [40]). One has to mention that ^{48}Cr show the most collective features

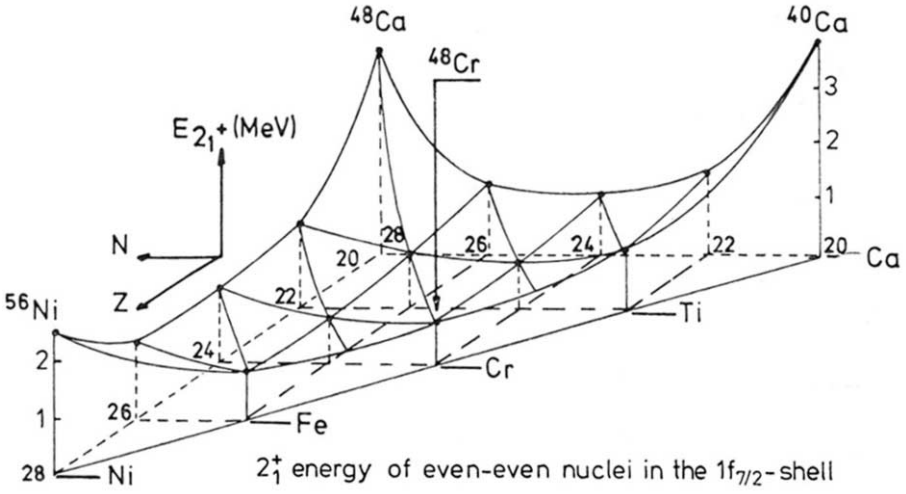

(a)

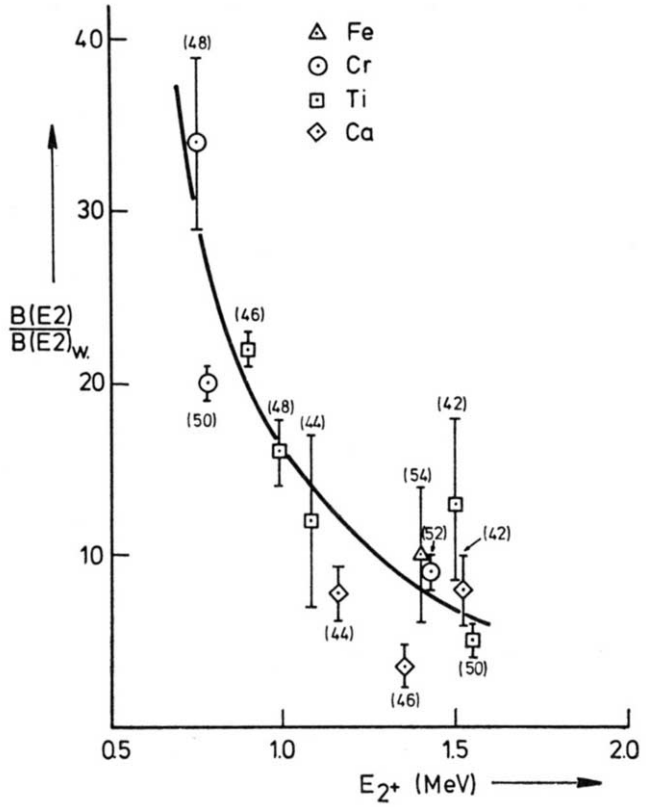

(b)

Fig. 22. – a) Height of the first 2^+ state in the even-even nuclei in $1f_{7/2}$ shell; b) $E2$ strength in W.u.) of the first 2^+ state in the even-even nuclei of the $1f_{7/2}$ shell (ref. [39]).

in the region.

One can understand our satisfaction for all these findings: the interplay of collective and single-particle shell-model features in the $1f_{7/2}$ nuclei has been in fact a sound program of research which was further developed in the subsequent years at the Tandem accelerator in Legnaro. As a summary (see ref. [39]) of the results mentioned above I wish to present the evolution of the height of the first 2^+ state, which is usually taken as an indication of the collectivity, for the nuclei lying inside the triangle ^{40}Ca-^{48}Ca-^{56}Ni (the double magic vertices)([4]). Figure 22a displays the situation and shows how this height is sinking towards the middle of the $1f_{7/2}$ shell (^{48}Cr as already mentioned). The strengths of the corresponding $B(E2)\,2^+ \to 0^+$ are reported in fig. 22b and rise very rapidly again around ^{48}Cr The corresponding value is 40 W.u. (Weisskopf units).

In this context it is worth to remind that the possibility open by he new facilities to go beyond the drip line towards neutron-rich isotopes was of great help in establishing the evolution of the various structure properties of $1f_{7/2}$ nuclei. As I have already mentioned the systematics of 2^+ states in the even Titanium isotopes (and in the even calcium ones) effectively shows the presence of a quasi-magic $N = 32$ neutron number in agreement with the $1f_{7/2}$-$2p_{3/2}$ gap already foreseen (see refs. [29], 3), [31] and fig. 14) about fifty years ago.

In summary one can repeat, once again that the $1f_{7/2}$ nuclei are still a real mine for investigating and understanding a lot of peculiar properties of the nuclear structure such as: the evolution of shell-model states and deformations, the exploration of the neutron-rich territory and related isospin effects, the possible quenching of spin-orbit coupling, the shape coexistence and the high excitation-energy effects.

As a matter of fact the recent revolutions in nuclear spectroscopy (*i.e. radioactive ion beams and high resolution, high efficiency gamma arrays*), together with the new important perspectives they will open in the nuclear domain, will also provide a powerful tool for leaving the "$1f_{7/2}$ *problem*" still alive.

5. – Nuclear physics with heavy ions. The advent of the 16 MV Tandem at LNL. The evolution of nuclear physics in Italy (years 1980–90)

Here I have to mention briefly the story of the installation at the LNL of the 16 MV (HVEC-XTU) Tandem Accelerator, the first Italian facility for heavy ions. It was a real

([4]) The collaboration with the Munich group held by H. Morinaga has been the most intense in the systematic research program concerning the nuclear structure of $1f_{7/2}$ nuclei in which the LNL-Padua-Florence groups took part working on this interesting problem for at least ten years (1970–1980). The Morinaga-Ricci personal relationship and collaboration began in the '60s (Amsterdam) and continued via Naples-Florence-Padua-Legnaro-Munich until the '90s. The names of the people belonging to the various groups are reported in the references. **Note added in proofs: One can understand how deeply I have been touched by the recent sad news that Haruhiko Morinaga passed away (May 2018). I wish to dedicate to him this part of my lecture.**

Fig. 23. – Left: Celebration of the extraction of the first ion beams (acceptance test in November 1981 with ^{32}S and ^{127}I) and right: a photogroup of the inauguration of the XTU tandem ("Moby Dick") at the LNL (January 1982).

milestone for the development of nuclear physics in Italy and for its role in the context of the INFN (Istituto Nazionale di Fisica Nucleare); a turning point in its strategy and evolution. In fact this was an exceptional step not only for providing a very powerful tool in nuclear structure investigations (production of high energy, high-spin states, new nuclear species...) but also for opening to Italian laboratories the possibility of performing a larger program of investigation in the field of *heavy-ion physics* and in understanding the physics of the *nucleus-nucleus interaction* in different aspects and at different energies. Concerning the story of such an installation I wish only to remind that this goal was achieved in 1982 after 10 years of hard work and confident waiting. Some of the various steps of this event are reported in ref. [41] so as the summary of the first experiments dealing with the research program organized around the new facility. Figure 23 shows two pictures of the celebration of the first ion-beam extraction (november 1981) and of an aspect of the inauguration (January 1982) of *MOBY DICK* (this is the name given to the Tandem recalling the 10 years of hunting the "*White Whale*").

The advent of the LNL Tandem not only gave rise to a larger area of research but opened the way for the installation and construction of other important facilities for the evolution of nuclear physic in Italy. It was followed by a second Tandem accelerator (HVEC-MP, 14 MV) installed at the Laboratori Nazionali del Sud (LNS) in Catania (1984) in order to increase with a better geographical distribution, the national capability of the INFN in the field of heavy-ion physics. The nuclear physics strategy marked other

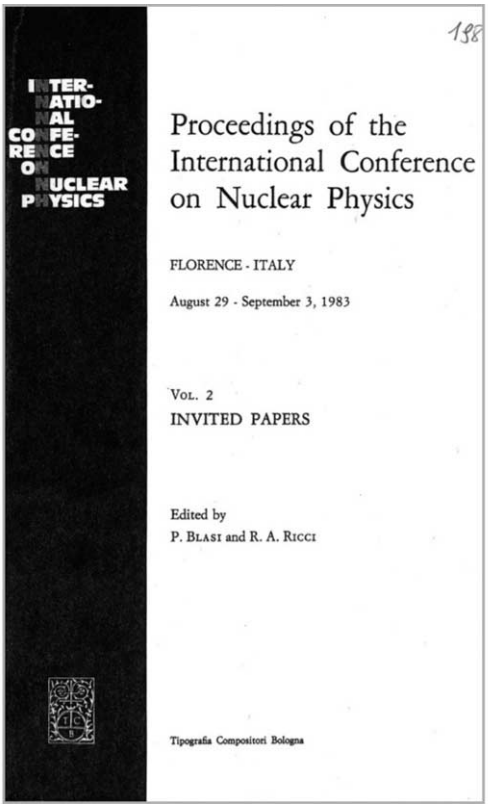

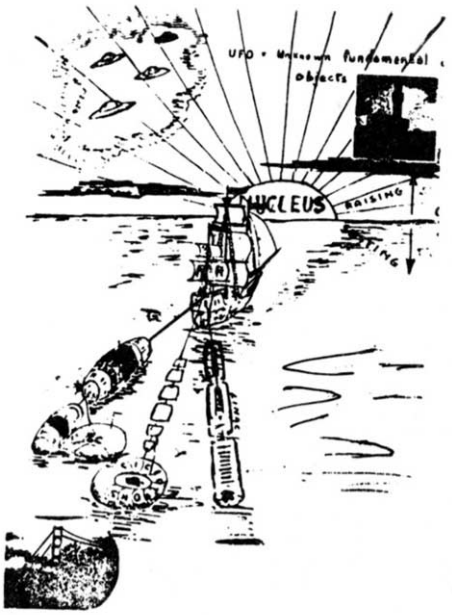

Fig. 24. – The nuclear physics ship sailing from Berkeley (INPC 1980) to Florence (INPC 1983) carrying the various facilities provided for the development of the Italian nuclear physics program (see text and ref. [42]).

important points with the building in Milano, under the direction of F. Resmini, of a superconducting cyclotron conceived as a booster (post-accelerator) for a national Tandem and, following a decision of the council of INFN, installed at the LNS and coupled with the MP Tandem. Meanwhile a superconducting Linear Accelerator ALPI (Acceleratore Lineare Per Ioni) was built and installed at the LNL (1993) coupled to the XTU Tandem increasing the capability of the Legnaro facilities in producing ions with mass and energy spanning from hydrogen to uranium and from several tens to a few MeV/amu. Figure 24 shows a picture that I did present in my introductory talk at the *International Nuclear Physics Conference* held in Florence in 1983, showing the nuclear physics ship coming from Berkeley, where the previous Conference was held in 1980, and in the way to reach Florence, considered as a starting point for the launching of the new Italian facilities (ref. [42]). It is worth noting here that the future development of the LNL concerning the acceleration of radioactive ion beams has been ensured by the installation in the recent years of the new SPES (Selective Population of Exotic Species) facility (see ref. [45]).

Concerning the advent of heavy ions one has to stress the two peculiar aspects of this extraordinary probe of investigation: one is the nucleus-nucleus collision as a physics case in itself related to the dynamics of such a peculiar type of nuclear reaction (the *physics of heavy ions*), the other is the use of this kind of reaction as a tool for better investigating in a selective way the nuclear structure which, together with the in-beam gamma spectroscopy and the impressive evolution of the modern gamma-arrays, gave rise to a very powerful technique for nuclear spectroscopy (*the 4th revolution*). These two aspects of course are connected and it is the interplay between them that constitutes the "salt" of the physics we are dealing with.

Note that all these aspects are covered in many of the nuclear physics courses held here in Varenna. Among them I wish to mention at least the one on *Nuclear Structure and Nuclear reactions* (1967) directed by M. Jean and myself [43] with lectures on nuclear structure, given by R. Van Lieshout, G. Alaga, S.G. Nilsson, M.H. Macfarlane, M. Baranger, M. Jean and myself, and nuclear dynamics given by H.F. Bayman, N.K. Glendenning, R.H. Lemmer and D.A. Bromley; that on *Nuclear Spectroscopy and Nuclear Reactions with heavy ions* (1974) directed by H. Faraggi and myself [44], with lectures devoted to the physics of heavy-ion reactions given by R. Giraud; D. Kurath, M. Lefort, J.P. Bondorf, F. Colombani, M. Mermaz, N. Cindro, P. Armbruster and to the structure properties revealed by the heavy-ion reactions (B. Buck, M. Harvey, S.G. Nilsson, H. Morinaga; C. Signorini), and the one on *Elemenary Modes of Excitations in Nuclei*, directed by A. Bohr and R. Broglia (1976), which could be considered as an amplified continuation of the Racah's course in 1960 as I have already quoted in connection with the interplay between shell and collective models taking also into account the participation of lecturers as A. Bohr, B. R. Mottelson, I. Talmi, K. Kerman, G. R. Satchler G. B. Wildenthal, F. S. Stephens and L. Hamamoto.

The scientific program at the LNL-Tandem and, later on, with the Tandem-ALPI facility, was of course extended to more advanced investigations in the field of nuclear structure due to the larger variety of *ion beams* and to the *new γ-ray spectroscopy* made possible by the new detection techniques, as already mentioned. At the LNL, advanced *γ-arrays* have been installed (GASP, EUROBALL, AGATA) in the frame of a large European collaboration and extensively used with excellent results concerning, for instance, superdeformed yrast bands, characterization of shell-model states and even a shell closure at $N = 40$ (^{68}Ni), together with the new results in the $1f_{7/2}$ nuclear region that I have already discussed. They can be found in ref. [45] where up to date reviews concerning also heavy-ion facilities are reported.

Just after the installation of the Tandem at the LNl, having established a sound research program in the field of nuclear structure, I turned my attention and efforts to the parallel field of dynamic problems. Therefore, let me now touch such aspects which, by the way, are related to the second part of my personal activity and interest. I do not wish to enter into details; I will rather mention a few of the most interesting experiments and results as found in the frame of different research programs.

Coming to the *nuclear dynamics with heavy ions*, strictly speaking the nucleus-nucleus interacting process can be considered as part of the more general problem of the statis-

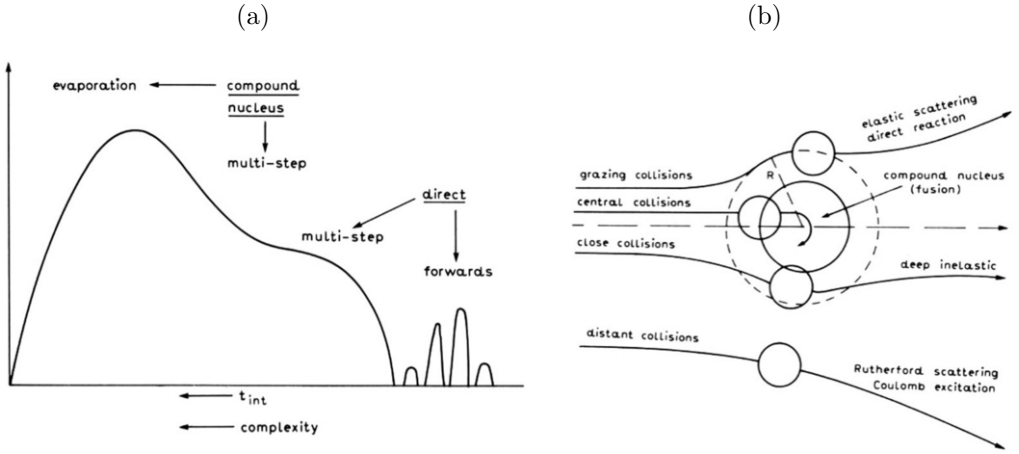

Fig. 25. – a) The Fesbach diagram: evolution, with increasing interaction time (right to left), from direct to compound (evaporation) process through multistep intermediate stages (ref. [46] and text). b) Classical picture of different types of nucleus-nucleus collisions as a function of the impact distance (see text).

tical distribution of systems formed by a relatively small number of strongly interacting particles. In this context, the complex nature of the interacting partners make the nucleus-nucleus collisions, at relatively low and moderate energies, *strongly absorbing processes* related to the existence of different stages of the evolution of the composite system (*multistep processes*) between two extremes such as the simplest direct and the compound-nucleus modes. This is shown in fig. 25a, where the famous *Fesbach-diagram* is reported [46], indicating such an evolution as a function of the interaction time. Since the absorbing interaction will depend on the overlap of the two systems, in fig. 25b also the classical picture of classifying the heavy-ion reactions, as a function of the impact distance of the two colliding nuclei, is shown.

Following our research program, we started with experiments dealing with *dissipative phenomena*. In fact at bombarding energies not higher than 10 MeV/amu, the two main dissipative mechanisms *i.e. fusion-evaporation-fission* (FF) *and deep inelastic collisions* (DIC) were considered in the early description on the basis of a schematic picture of the collision processes. Depending on the topology of the entrance channel potential either attractive forces, leading to a *mononucleus* as a composite system, or repulsive forces, leading to a *dinucleus* were considered to describe the reaction path. Since some experimental evidence was reported of intermediate dissipative regimes, phenomenological descriptions were reported as "*fast-fission-*" or "*extra-push*" statistical models, [47]. Therefore, systematic investigations were performed at the Legnaro and at the Strasbourg Tandem facilities [48] with the results that *transitional dissipative mechanisms* are indeed present and that the *fission-like* fragmentation of composite systems formed at incident energies around (4–7) MeV/amu, exhibits certain peculiar characteristics which cannot be understood in terms of pure fusion or DIC processes nor in the framework of

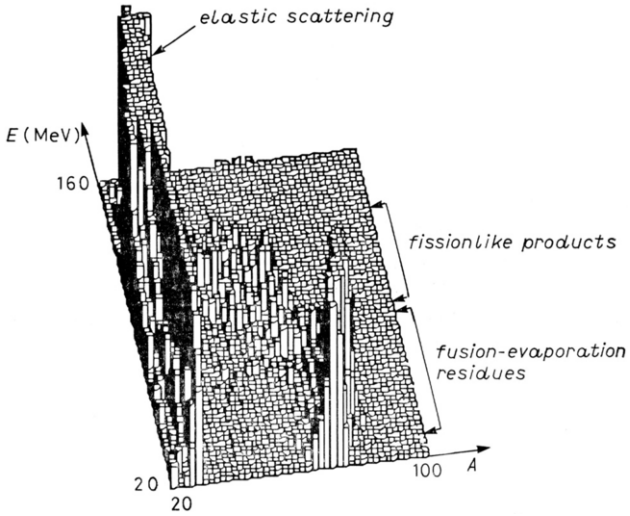

Fig. 26. – Mass-energy spectrum for the ^{28}Si+^{63}Cu reaction at bombarding energy $E_i = 158$ MeV and at a laboratory angle $\vartheta_L = 20°$.

the above-mentioned models. Rather, the interesting results found by the joint Legnaro-Padua-Bologna-Milano-Strasbourg Collaboration [49] were, *first*, that, in general, the reaction mechanism of dissipative collisions for different medium-mass systems could be described in terms of a *continuous relaxation process* leading the composite system from the entrance channel to more or less equilibrated configurations, depending on the system lifetime, at the extremes of which DIC or fusion-fission processes are found; *second*, that *ternary processes* can occur as prompt ternary break-up, *i.e. three-body fragmentation*, as observed in ^{32}S + ^{59}Co and ^{32}S + ^{63}Cu, besides the sequential binary process [49]. Figure 26 shows, as an example, the presentation of the fission-like events of the ^{28}Si + ^{63}Cu, lying on a locus in the mass-energy plot, corresponding to the Coulomb repulsion of two charged spheres.

Such results were part of a systematic investigation with a series of target nuclei of mass ranging from 45 to 80 including of course the finding of clear examples of deep inelastic and fusion-evaporation (fission) processes as well as the sequential binary decay (see ref. [50] where also the collaboration with the Bari and Messina groups is included).

Another interesting field was the search for *quasi-molecular resonances* as a more general feature in some exit channels of heavy-ion reactions. This resonant-like behaviour, observed for the first time in 1960 by Bromley *et al.* at the Yale Tandem [51] as correlated structures in ^{12}C + ^{12}C scattering, was confirmed and widely reported in the '80s in collisions, particularly of identical nuclei, leading to composite systems in the range of $A_{CS} \approx 50$ (*i.e.* ^{24}Mg + ^{24v}Mg or ^{28}Si + ^{28}Si). Our investigations promoted by the collaboration with Nikola Cindro (Zagreb) and with the Trieste, Bologna and Giessen groups, (see ref. [52]) were therefore concentrated to heavier systems (elastic ad inelastic scattering of ^{58}Ni + ^{46}Ti, ^{58}Ni + ^{58}Ni, ^{58}Ni + ^{62}Ni) finding for the first time *non-statistical structures* in the excitations functions and angular distributions. Figure 27 shows the

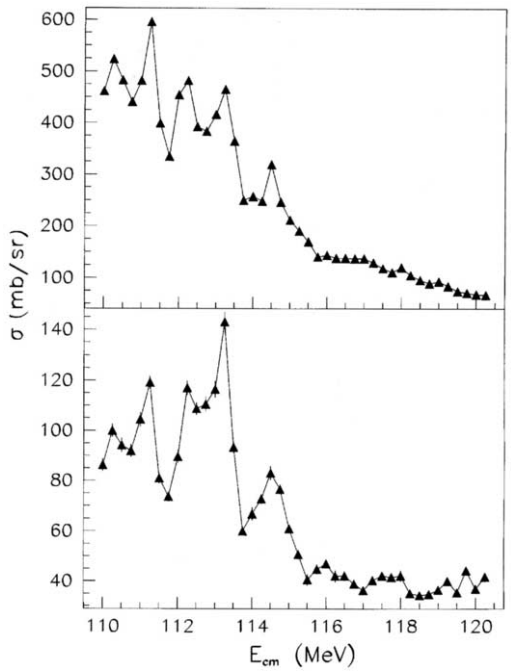

Fig. 27. – Excitation functions of the angle-summed ($76^\circ \leq \vartheta_{cm} \leq 104^\circ$) elastic scattering (top) and inelastic ($Q = 1.45\,\mathrm{MeV}$, first excited state of ^{58}Ni) scattering (bottom) differential cross-sections of $^{58}\mathrm{Ni} + {}^{58}\mathrm{Ni}$. The correlation between the two distributions is evident.

excitation functions for elastic and inelastic scattering of the differential cross-sections for the case of $^{58}\mathrm{Ni} + {}^{58}\mathrm{Ni}$. Such structures were generally interpreted including the presence of intermediate *dinuclear states* (virtual diatomic molecules).

6. – Nuclear physics at CERN. Antinucleon probes (LEAR), the OBELIX experiment, the relativistic heavy ions at SPS and at LHC, the Quark-Gluon Plasma, ALICE in wonderland

Already in the '80s INFN opened up to more extensive collaborations and activities at CERN in the field of nuclear physics. Personally, as a Chairman, in that period, of the INFN Nuclear Physics Committee, I sponsored this operation and I formed a group in Legnaro to work with the OBELIX Collaboration [53]. It was a very interesting experience for me, a physicist coming from small research groups in which everything was almost hand-created, being part of big CERN collaborations (this was even more evident later on in the case of ALICE). I would say that it was also educational because I realized that one has to better consider not only the proper sharing of the job but also the way to contribute with some cultural humility and collaborative spirit, to the common goals. Of course what you lose in a certain amount is the familiarity with your colleagues and young collaborators whom, in smaller groups, you know personally one by one.

Speaking about OBELIX I wish to mention first the contribution of the Legnaro group (with Padua and Pavia) in building the *vertex detector*, *i.e.* the Spiral Projection Chamber (SPC) and, as far as the physics program was concerned, in the sectors of atomic and nuclear physics and meson spectroscopy, including search for exotic matter like glueballs, hybrids, quark-antiquark states in antiproton-proton and antiproton-deuterium interactions at rest [53]. Interesting results with specific contributions of our group can be found in ref. [54]. They concern namely: i) the annihilation of antiprotons and antineutrons (produced with special techniques) on nucleon and light nuclei; ii) the first measurement of the antineutron-proton total cross-section (50 to $400\,\mathrm{MeV}/c$) finding the dominance of the isospin $T = 0$ channel over the $T = 1$ one (at low energy); iii) the strangeness production in antiproton-deuterium *Pontecorvo reactions* at rest with two-body final states consisting of baryon-meson and baryon-baryon pairs.

The other relevant jump was the promotion of a significant contribution of Padua and LNL to the Italian participation in the important enterprise concerning the CERN relativistic heavy-ion project, first at SPS (Na57 and WA97 experiments) then at LHC (ALICE). I would mention the strong collaboration between CERN and LNL in the installation of the heavy-ion beam line; LNL did provide the *Radio Frequency Quadrupole (RFQ)* to accelerate Pb ions to 250 keV and the medium-energy beam transport following the RFQ ($\sim 70\,\mu$A of $^{208}Pb^{27+}$ ions). The higher energy part was provided by the Turin group. As a consequence the Padua-LNL group could contribute in a significant way to the experiments with sulfur and lead ions leading to the enhanced production of strange particles, a preliminary indicator of the presence of the Quark-Gluon Plasma (QGP) [55].

Moving to ALICE (*A Large Ion Collider Experiment*), let me say, about my personal participation, that, after having contributed to its promotion and its design phase, I played my part as consultant in the definition and analysis of some aspects of its physics program [56]. Among the numerous findings of such an impressive enterprise, I wish to mention at least two results, in my opinion particulalry interesting. One is the production of light *antinuclei* (and *antihypernuclei*) providing also a test of unprecedented precision of the CPT invariance. The latest measurement in this field concerns the production of *antialpha*, the heaviest antimatter nucleus found so far [57]. The second concerns the abundance of strange-particle production in the high-multiplicity proton-proton collisions [58]; a quite intriguing result for the insight it provides into collective effects in the interaction between protons and not only between complex nuclei. It could indicate that the behaviour of QGP has to do, in a quite decisive way, microscopically speaking, with the multiplicity of the particles produced. In fig. 28 I report the titles and references concerning the first report of our group in Legnaro dealing with our participation to the ALICE collaboration and the two related to the items just mentioned.

7. – Final considerations. Facing Nuclear Physics

What about the following question: what is really nuclear physics? What is really its domain? Well. The traditional domain, looking at it with the eyes of 65 years ago, was the investigation of the structure and dynamic properties of atomic nuclei in an energy interval not too far from the binding energy of their constituents ("cold" nuclei near the

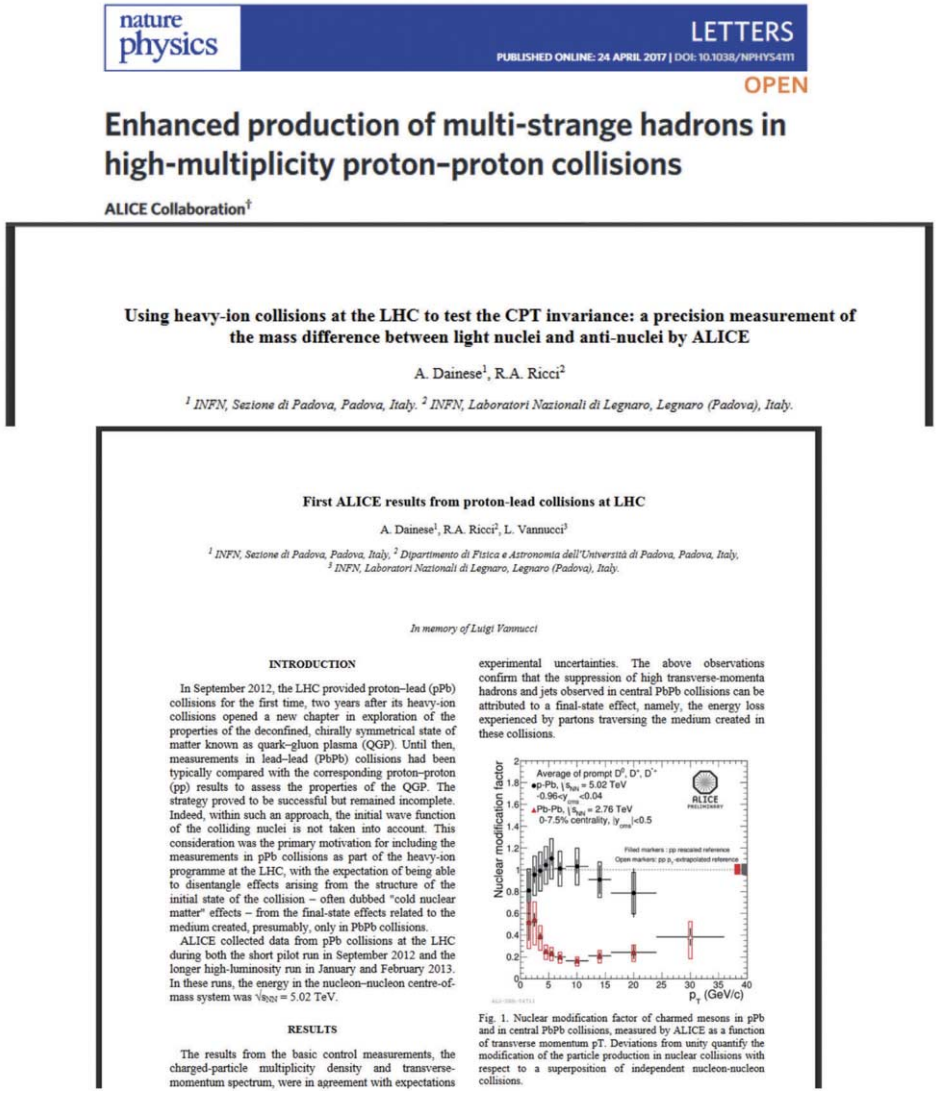

nature physics

LETTERS

PUBLISHED ONLINE: 24 APRIL 2017 | DOI: 10.1038/NPHYS4111

OPEN

Enhanced production of multi-strange hadrons in high-multiplicity proton–proton collisions

ALICE Collaboration†

Using heavy-ion collisions at the LHC to test the CPT invariance: a precision measurement of the mass difference between light nuclei and anti-nuclei by ALICE

A. Dainese[1], R.A. Ricci[2]

[1] INFN, Sezione di Padova, Padova, Italy. [2] INFN, Laboratori Nazionali di Legnaro, Legnaro (Padova), Italy.

First ALICE results from proton-lead collisions at LHC

A. Dainese[1], R.A. Ricci[2], L. Vannucci[3]

[1] INFN, Sezione di Padova, Padova, Italy, [2] Dipartimento di Fisica e Astronomia dell'Università di Padova, Padova, Italy, [3] INFN, Laboratori Nazionali di Legnaro, Legnaro (Padova), Italy.

In memory of Luigi Vannucci

INTRODUCTION

In September 2012, the LHC provided proton–lead (pPb) collisions for the first time, two years after its heavy-ion collisions opened a new chapter in exploration of the properties of the deconfined, chirally symmetrical state of matter known as quark–gluon plasma (QGP). Until then, measurements in lead–lead (PbPb) collisions had been typically compared with the corresponding proton–proton (pp) results to assess the properties of the QGP. The strategy proved to be successful but remained incomplete. Indeed, within such an approach, the initial wave function of the colliding nuclei is not taken into account. This consideration was the primary motivation for including the measurements in pPb collisions as part of the heavy-ion programme at the LHC, with the expectation of being able to disentangle effects arising from the structure of the initial state of the collision – often dubbed "cold nuclear matter" effects – from the final-state effects related to the medium created, presumably, only in PbPb collisions.

ALICE collected data from pPb collisions at the LHC during both the short pilot run in September 2012 and the longer high-luminosity run in January and February 2013. In these runs, the energy in the nucleon–nucleon centre-of-mass system was $\sqrt{s_{NN}} = 5.02$ TeV.

RESULTS

The results from the basic control measurements, the charged-particle multiplicity density and transverse-momentum spectrum, were in agreement with expectations experimental uncertainties. The above observations confirm that the suppression of high transverse-momenta hadrons and jets observed in central PbPb collisions can be attributed to a final-state effect, namely, the energy loss experienced by partons traversing the medium created in these collisions.

Fig. 1. Nuclear modification factor of charmed mesons in pPb and in central PbPb collisions, measured by ALICE as a function of transverse momentum pT. Deviations from unity quantify the modification of the particle production in nuclear collisions with respect to a superposition of independent nucleon-nucleon collisions.

Fig. 28. – ALICE's Adventures in Wonderland.

ground state, low spin and low excitation energy) and the main concept of the nucleus as a nucleon complex only was dominating. Now, already in the '80s of the last century, a significant change did occur, as we have seen in what I have presented here. Even more important changes did occur at the beginning of this century, if one looks in the various directions, *i.e.* angular momentum, isospin and, with particular emphasis, temperature ("hot" nuclei and hìgh interaction energies).

In fact the nucleus is a two-faceted object with a variety of, sometime contradictory, properties and phenomena: it is too small to be considered as a microscopic piece of a real

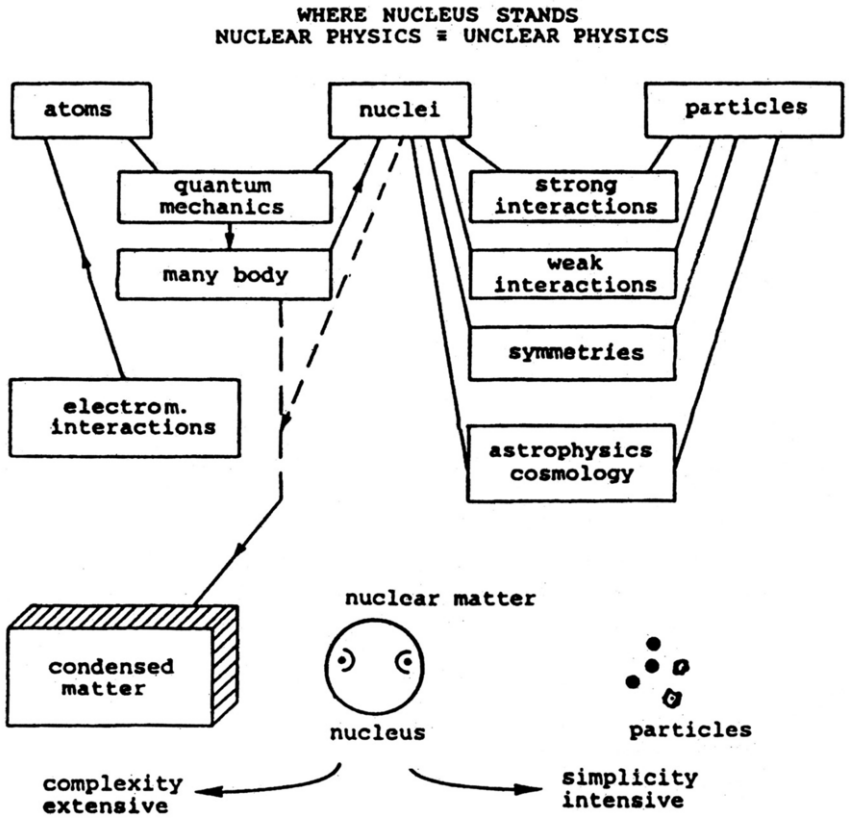

Fig. 29. – Standing position of the atomic nucleus and of nuclear physics and their relationships with fundamental problems.

nuclear matter (a *dwarf*) and too big to derive all its properties from the simple motion of its fundamental constituents (a *giant*); we could speak of a kind of *mesoscopic* system and both the *holistic* and *reductionistic* views are allowed for its (partial) description. This is one of the main reasons why nuclear physics (the anagram *"unclear physics"* was properly found) is a complex matter which one is dealing with. On the other hand, its connections with fundamental aspects and interactions are so relevant that one cannot avoid its properties and phenomenology in order to understand the universal laws (see fig. 29).

The new developments in understanding the links between collective and elementary properties both present in the nuclear system as well as in exploring fundamental problems inside the nucleus bring into light common features of nuclear and subnuclear physics as far as the intimate structure of the matter of the Universe is concerned. In fact we did learn how the nucleus could be considered as a wonderful laboratory for studying the behaviour of its primary constituents, for instance in nucleus-nucleus collisions in extreme conditions. Figure 30 shows the nuclear and subnuclear roots to approach the primordial matter of the "early" Universe. The *subnuclear root* provides the addition

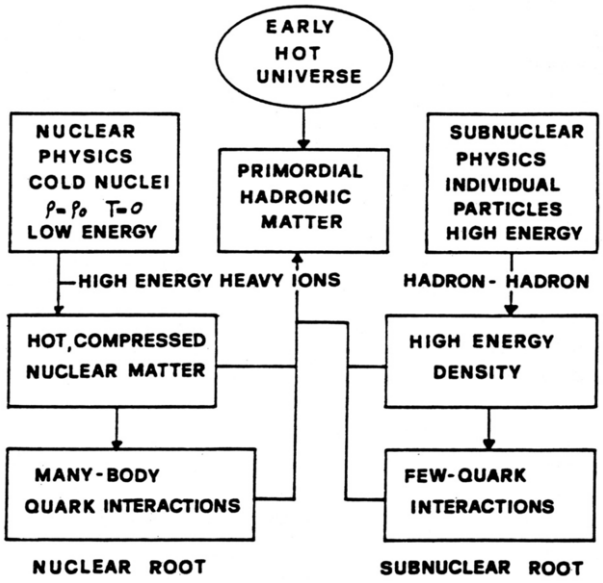

Fig. 30. – Fundamental problems and corresponding roots to approach them for nuclear and subnuclear physics, respectively.

of ever more energy to regions of ever decreasing sizes: this is done via the interaction between individual hadrons with *a restricted number of quarks*. The major problem here is the "*confinement*" of the elementary constituents. On the other hand the *nuclear root* to the primordial hadronic matter (nucleus-nucleus collisions) is related to the possible observation of *many-body quark interactions*. Ever higher energy is added to volumes containing many nucleons; this is the reason why one expects that bringing together a large number of quarks and gluons at ever higher density (compression) they can be released as a QGP (see ref. [59]).

Of course one should not forget that the *common interface* between nuclear and elementary-particle physics is also related to the possibility of identifying *sub-nuclear effects* in the nuclear behaviour due to the more elementary degrees of freedom (*mesons, quarks, gluons*). We know that these effects exist and that the problem of relating the nuclear properties with the primary strong interaction is still open. However let me quote, for the sake of saving our oversimplified description still employed today, the "old" statement of V. Weisskopf (1969!) (see ref. [59]): "*... The complete understanding of nuclear phenomena would imply a description of the nucleus as a system of nucleons in interaction with a common meson field: nucleons that are not identified as protons or neutrons swimming in a sea of virtual mesons. Fortunately, and somewhat surprisingly, the nucleus can be rather accurately described as a system of well-defined neutrons and protons with certain forces between them. The meson origin of these forces does not seem to play an essential role in the nuclear behaviour at lower energies. Hence the theory of the nuclear structure is not interested in the theory of the nuclear force itself; it is taken*

for granted that such a force exists and its properties are accepted as an experimental fact". Of course other problems arise today from the extension of the energy and of the map of the nuclear systems, as we know. A more detailed discussion on all these considerations can be found in refs. [59] and [60].

Closing

I have to conclude. The excursus I have made could be related to the way one could have understood nuclear physics and managed with it either as an actor or as an interested spectator. Since at the age of 90, even if I am still active both consciously and intellectually and interested in what is going on, I cannot say that I could be considered as an actor. 65 years with nuclear physics is a lot and is a substantial part of my life. But, fortunately, they do not exhaust all the aspects of my life. *Let me mention, last but not least, my family (65 years also with my wife Claudine Abraham) the children (Marco and Françoise) the grandchildren (Giorgio and Carlo), the many friends, the students (also many) to whom I wish to dedicate this last paper, and the other activities and problems outside of Science.*

About this Course and Varenna I have obviously something to say: My introduction has been added in the written version of my lecture because of two reasons.

First I wanted to better clarify the context in which the course proposed to and accepted by the Council of the Italian Physical Society has been in some sense related to the celebration of my 90th anniversary and therefore I have to express my special gratitude to the SIF President Luisa Cifarelli, to the friends and colleagues of the SIF Council, to the Directors of the course Fabiana Gramegna, Peter Van Duppen and Andrea Vitturi together with the Scientific Secretary Sara Pirrone for their kindness in organizing a special session, so as the SIF Secretary Staff here at Villa Monastero and in Bologna. And of course, for their unvaluable technical support in working on the written version of my lecture, to Angela Oleandri (SIF) and Valentino Rigato (LNL).

Second, to be here in Varenna is not so occasional. This School and this place are also of particular significance for my scientific (and not only) life, as a SIF President for many years and as a participant and/or director of a number of physics courses, some of which I have mentioned in my lecture. It is gratifying to aknowledge once again the presence of friends and of colleagues and I like to express my appreciation for the presence of Franco Iachello and Luciano Moretto, with whom I shared the responsibility of a number of courses of the School. Moreover It is not only a duty but also a pleasure for me to express my appreciacion to all the directors([5]) of the LNL who, in succeeding after me, in this office, gave me always the opportunity to remain an active participant of the LNL research programs and to describe in different ways this story along many years.

([5]) I wish to report their names as a token of my affection and esteem: Paolo Blasi, Cosimo Signorini, Piero Dalpiaz, Massimo Nigro, Graziano Fortuna, Gabriele Puglierin, Gianni Fiorentini, Diego Bettoni. All together we have written an interesting part of the story of Nuclear Physics in Italy. A further appreciation is due to the Presidency and Council of INFN for the Italian strategy concerning Nuclear Physics along the years.

In writing this lecture, I had in mind my teachers, my mentors, my students, my pupils, my collaborators. As you could have seen, in my references I quoted all the names of the authors, except of course in the case of very large collaborations (OBELIX and ALICE for instance) In fact I don't like the extensive use of the term "*et al.*" with no identification of all the people who did the job. All those I quoted are not just names but real persons to whom I am indebted for the friendly collaboration and the precious help during this long trip.

At the end of which I, leave you with the last two remarks. The first is just a "poetic" representation of a "long" career with a quite complete parabolic pathway. The second points out two simple statements: 1) that the *long way to Tipperery was really long* (no regrets however!); 2) that he best answer to the "unfailing" question you have to face in getting old "*What is your vision of*...?" which by the way is resumed in closing (or in opening) many meetings by the more "scientific" one "*What next?*"), is that given by the statement of Freeman Dyson.

REFERENCES

[1] RICCI R. A. in *Proceedings of the International School of Physics "Enrico Fermi", Course CLXIX*, edited by COVELLO A., IACHELLO F., RICCI R. A. and MAINO G. (IOS Press Amsterdam and SIF Bologna) 2008, pp. 29–56.

[2] RICCI R. A. in *Proceedings of the International School of Physics "Enrico Fermi", Course CIII*, edited by MOLINARI A., RICCATI L., ALBRICO W. and MORANDO M. (IOS Press, Amsterdam and SIF Bologna) 2003, pp. 627–667.

[3] RICCI R. A. in *Proceedings of the 10th International Conference on Nuclear Reactions and Mechanisms*, Varenna, 2003 edited by GADIOLI E. (Università di Milano, Ricerca Scientifica ed Educazione Permanente) 2003, pp. IX–XXI.

[4] GOPPERT-MAYER M., *Phys. Rev.*, **75** (1949) 1969; HAXEL O., JENSEN J. H. and SUESS H. E., *Phys. Rev.*, **75** (1949) 1766; GOPPERT-MAYER M. and JENSEN J. H., *Elementary Theory of Nuclear Shell Structure* (J. Wiley and Sons) 1955; see also: TALMI I. and DE SHALIT A., *Nuclear Shell Theory* (Academic Press) 1963. It is interesting to note that the idea of a possible *spin-orbit coupling* in the nuclear potential was discussed by Maria MAYER with Enrico FERMI during a conversation in Chicago (as reported by WALI K. C., *Robert Green Sachs, 1916–1999, Biographical Memoirs*, Vol. **84** (National Academy of Sciences, Washington) 2004.

[5] BOHR A. and MOTTELSON B. R., *Mat. Fys. Medd. Dan. Vid. Selsk.* **27**, no.16 (1953); BOHR A. and MOTTELSON B. R., *Nuclear Structure*, Vol. **I** *Single-particle motion* and Vol. **II**, *Nuclear Deformations* (W. A. Benjamin, New York, Amsterdam) 1969, 1975.

[6] KALMANN H., *Nature and Technique*, July 1947; HOFSTADTER R., *Phys. Rev.*, **74** (1948) 100.

[7] See CURRAN S. C. *Luminescence and the scintillation counter* (Academic Press, New York) 1953. *Note:* the coupling of a scintillator with a photomultiplier did realize the transformation of a simple counter into a spectrometer.

[8] RACAH G. (Editor), *Proceedings of the International School of Physics "Enrico Fermi", Course XV* (Academic Press, New York and London) 1960.

[9] OTSUKA T., "Recent developments in shell model studies of atomic nuclei", this volume, p. 1. One can realize this evolution by referring to the previous lectures given by Otsuka ("Shell structure of exotic nuclei") ten years ago here in Varenna at the course on *Nuclear structure far from stability* (see ref. [1] p. 261).

[10] RICCI R. A. and TRIVERO G., *Nuovo Cimento*, **1** (1955) 717; **2** (1955) 745.

[11] DE MICHELIS F. and RICCI R. A., "β-γ angular correlations of ^{208}Tl (ThC$''$)", *Nuovo Cimento*, **4** (1956) 96; for other applications of the scintillation technique see also: RICCI R. A., "On the internal bremstrahlung of the ^{204}Tl beta decay", *Physica*, **XXIV** (1958) 297.

[12] RICCI R. A., *Physica*, **XXIII** (1957) 693.

[13] REINES F. and COWAN C. L., *Phys. Rev.*, **113** (1959) 273; the specific description is in the report concerning the improved experimental method as reported by NEZRICH F. A. and REINES F., *Phys. Rev.*, **142** (1966) 142.

[14] RICCI R. A., *Physica*, **XXIV** (1958) 289. Note: this method has also been applied extensively for the calibration of γ-ray sources used for medical purposes in some British hospitals.

[15] See, for instance, RICCI R. A. in ref. [1] and references quoted herein; see also: RICCI R. A., "L'evoluzione della spettroscopia nucleare in Italia-La spettroscopia gamma", *Q. Storia Fis.*, **19** (2017) 94.

[16] VAN LIESHOUT R., WAPSTRA A. H., RICCI R. A. and GIRGIS R. K., "Scintillation Spectra Analysis", in *α, β, γ-ray Spectroscopy*, edited by SIEGBAHN K. (North Holland, Amsterdam) 1965, pp. 501–538.

[17] RICCI R. A., GIRGIS R. K. and VAN LIESHOUT R., *Nucl. Phys.*, **21** (1966) 177; see also: DE BOER F. W. N., LINGEMAN E. W. A., VAN LIESHOUT R. and RICCI R. A., *Nucl. Phys. A*, **158** (1970) 168.
[18] BOHR A. and MOTTELSON B. R., in ref. [5], *Nuclear Structure*, Vol. **I**, p. 53, table 1–3.
[19] CHILOSI G., RICCI R. A., TOUCHARD J. and WAPSTRA A. H., *Nucl. Phys.*, **53** (1964) 235.
[20] BOHR A. and MOTTELSON B. R., in ref. [5], Vol. **I**, p. 344 and table 3–4.
[21] RICCI R. A., JEAN M. and VAN LIESHOUT R., *Nuovo Cimento*, **25** (1962) 1389 and references quoted herein; see also SARTORIS G. and TOUCHARD J., **25** (1962) 1375; and RICCI R. A., *Suppl. Nuovo Cimento*, **1** (1960) 141. A more detailed review can be found in RICCI R. A. "Proprietés des états excites des noyaux pairesr-paires spheriques", *Colloques sur la Physique Nucléaire de basse energie* (Institut Interuniversitaire de Sciences Nucléaire, Bruxelles) 1962.
[22] VAN LIESHOUT R., RICCI R. A. and GIRGIS R. K., *Nuovo Cimento*, **21** (1961) 379; GIRGIS R. K. *Thesis* (Amsterdam 1959); cases in point, among others, arising from the data of the Amsterdam and Napoli groups are: ^{74}Ge, ^{76}Se, ^{94}Mo, ^{104}Pd, ^{126}Ba, ^{150}Sm.
[23] LAWSON R. D. and URETSKY J. L., *Phys. Rev.*, **108** (1957) 1300.
[24] RICCI R. A., GIRGIS R. H. and VAN LIESHOUT R., *Nuovo Cimento*, **11** (1959) 156 and references quoted herein. In particular the quoted proton inelastic scattering data are due to MAZARI M., BUECHNER W. W. and FIGUEIREDO R. P., *Phys. Rev.*, **108** (1957) 373.
[25] CHILOSI G., MONARO S. and RICCI R. A., *Nuovo Cimento*, **26** (1962) 440.
[26] For a more detailed discussion see RICCI R. A. and VAN LIESHOUT R., *Excited states in odd mass nuclei with spherical core. Remarks on the validity of the Center of Gravity Theorem in Nuclear Spectroscopy*, Seminar Workshop IKO, Amsterdam 1962.
[27] See RICCI R. A., "Inelastic and quasi-free proton scattering on medium-weight nuclei at 155 MeV", in *Proceedings of the International School of Physics "Enrico Fermi", Course XXXVI*, edited by BLOCH C. (Academic Press, New York and London) 1966, pp. 566–589; see also: JACMART J. C., LIU M., RICCI R. A., RIOU M. and RUHLA C., *Phys. Lett.*, **84** (1964) 273; LIU M., JACMART J. C., RICCI R. A., RIOU M. and RUHLA C., *Nucl. Phys.*, **75** (1966) 481 and: RICCI R. A., JACMART J. C., LIU M., RIOU M. and RUHLA C., *Nucl. Phys. A*, **91** (1967) 609, and references quoted herein.
[28] CHILOSI G., CUZZOCREA P., VINGIANI G. B., RICCI R. A. and MORINAGA H., *Nuovo Cimento*, **27** (1963) 407.
[29] As a general "historical" review see: 1) RICCI R. A., "The $1f_{7/2}$ saga", in *The Nuclear Physics from $f_{7/2}$ to the Quark-Gluon Plasma, Workshop in honour of the 80th birthday of R. A. Ricci*, edited by GRAMEGNA F., CINAUSERO M. and FABRIS D., *Conf. Proc. SIF*, Vol. **96** (SIF, Bologna) 2007, pp. 151–162; for the main general reviews see: 2) RICCI R. A. and MAURENZIG P., 'The $f_{7/2}$ Problem in Nuclear Spectroscopy", *Riv. Nuovo Cimento*, **1** (1969) 291; 3) RICCI R. A., "Experimental Nuclear Spectroscopy in the $1f_{7/2}$ shell", in *Proceedings of the International School of Physics "Enrico Fermi", Course XL*, edited by JEAN M. and RICCI R. A. (Academic Press New York, London) 1969, pp. 80–140; for specific Conferences see: 4) RICCI R. A. (Editor), *Proceedings of the Topical Conference on the Structure of $1f_{7/2}$ nuclei, Legnaro 1971* (Editrice Compositori, Bologna) 1971 and the contributions there of RICCI R. A., p. 1, ZAMICK L., p. 9, SCHIFFER J. P., p. 37, TALMI I., p. 511, LAWSON R. D., p. 519 and MORINAGA H., p. 529; and 5) BLASI P. and RICCI R. A. (Editors), *Proceedings of the International EPS Conference on Physics of Medium-Light nuclei, Florence 1977* (Editrice Compositori, Bologna) 1978 and the contributions there of RICCI R. A., p. 1, ARIMA A., p. 19. SCHULZ N., p. 79, KUTSCHERA W., p. 120, SIGNORINI C., p. 198, MORINAGA H., p. 421 and TALMI I., p. 424.; for more recent and advanced findings see ref. [31].

[30] Mc Cullen J. D., Bayman B. F. and Zamick L., *Phys. Rev.*, **134** (1955) B515; see also Ginocchio J. N. and French J. B., *Phys. Lett.*, **7** (1963) 137. See also: Ford K. and Levinson C., *Phys. Rev.*, **99** (1955) 792; **100** (1955) 1,13; and Lawson R. D. and Uretski J. L., *Phys. Rev.*, **106** (1957) 1369.

[31] Fornal B., in *The Nuclear Physics from $f_{7/2}$ to Quark-Gluon Plasma*, edited by Gramegna F., Cinausero M. and Fabris D., *Conf. Proc. SIF*, Vol. **96** (SIF, Bologna) 2008, pp. 163–173, and references quoted herein; the more recent data are from Fornal B., unpublished and private communication, see also Lenzi S., this volume p. 341 and references quoted herein; concerning the possible full fp shell-model calculations see for instance: Honma M., Otsuka T., Brown B. A., Mizusaki T., *Phys. Rev. C*, **65** (2002) 061301, and *Eur. Phys. J. A*, **25** (2005) 499.

[32] Ruhla C., Riou M., Ricci R. A., Arditi M., Doubre H., Jacmart J. L., Liu M. and Valentin L., *Phys. Lett.*, **10** (1964) 326; Ruhla C., Arditi M., Jacmart J. C., Liu M., Ricci R. A., Riou M. and Roynette J. C., *Nucl. Phys. A*, **95** (1967) 526; see also Ricci R. A., ref. [27].

[33] See Amaldi U. jr., Campos Venuti G., Cortellessa G., De Sanctis E., Frullani S., Lombard R. and Salvadori P., *Phys. Lett.*, **22** (1966) 593 and references herein.

[34] Barone A., Greco G., Ricci R. A., Blasi P., Maurenzig P. and Sona P., *Nuovo Cimento B*, **46** (1965) 134; for the low energy results see: Ricci R. A., Pautrat M., Drosi M., Chilosi G. and Cuzzocrea P., *Nuovo Cimento*, **36** (1965) 1398.

[35] Morinaga H. and Gugelot P. C., *Nucl. Phys.*, **46** (1963) 210; see also Morinaga H. and Yamazaki T., in *In-Beam Gamma-Ray Spectroscopy* (North Holland, Amsterdam) 1976.

[36] See Ricci R. A., *Nuclear Structure Studies with a Van de Graaff accelerator*, lecture given at the Advanced Institute of Electron Scattering and Nuclear Structure, Cagliari Sept. 1970, and references quoted herein; for the ^{50}V case see: Blasi P., Maurenzig P. R., Taccetti N. and Ricci R. A., *Phys. Lett. B*, **28** (1969) 555.

[37] For the specific case see: Chilosi G., Ricci R. A. and Vingiani G. B., *Phys. Lett.*, **20** (1968) 159: Vingiani G. B., Ricci R. A., Giacomich R. and Poiani G., *Nuovo Cimento B*, **57** (1968) 453; Vingiani G. B., Chilosi G. and Bruynenstein W., *Phys. Lett. B*, **26** (1968) 285; for more general reviews see: Ricci R. A. "Isobaric Analogue Resonances in the $f_{7/2}$ region by (p, n γ) reactions", in *Fundamentals in Nuclear theory* (IAEA, Vienna) 1967, pp. 257–265; and: Ricci R. A. "The Isobaric Analogue Resonances in Phenomenological Nuclear Spectroscopy", in *Evolution of Particle Physics* (a volume dedicated to Edoardo Amaldi in his sixtieth birthday), edited by Conversi M. (Academic Press, New York, London) 1970, p. 218; see also: Vingiani G. B. and Ricci R. A., *Proceedings of the Topical Conference on The Structure of $1f_{7/2}$ nuclei* (Editrice Compositori, Bologna) 1971, pp. 303–325.

[38] Bizzeti P. G., Bizzeti-Sona A. M., Bucciolini M., Huber R. B., Kutschera W., Morinaga H., Ricci R. A. and Signorini C., *Nuovo Cimento A*, **26** (1975) 25; for the low-energy results see: Blasi P., Fazzini T., Maurenzig P., Taccetti N. and Ricci R. A., *Nuovo Cimento A*, **68** (1970) 49.

[39] See Signorini C. "Selective Population of the High-Spin States in the $1f_{7/2}$ shell", in *Proceedings of the International School of Physics "Enrico Fermi", Course LXII*, edited by Faraggi E. and Ricci R. A. (Editrice Compositori, Bologna) 1976, p. 499; and Ricci R. A. "Collective and Single-Particle States in $1f_{7/2}$ nuclei", in *Proceedings of the International Symposium on Nuclear Structure*, Vol. **II**, n. 45, Budapest, 1976; and references quoted herein. The data concerning ^{50}Cr can be found here; for ^{48}Cr see: Lenzi S. M., *et al. Z. Phys. A*, **354** (1996); *Phys. Rev. C*, **60** (1999) 1303.

[40] See FORTUNA G., HUBER R. B., KUTSCHERA W., MORANDO M., MORINAGA H., RICCI R. A. and SIGNORINI C., *Nuovo Cimento A*, **34** (1976) 321 and references quoted herein.

[41] See RICCI R. A and SIGNORINI C., *Nucl. Instrum Methods*, **146** (1977) 93; and **184** (1981) 35; SIGNORINI C., BEZZON G., CERVELLERA F., SPOLAORE P. and RICCI R. A., *Nucl. Instrum. Methods*, **220** (1984) 30; for the scientific program see: RICCI R. A., *Nuovo Cimento A*, **81** (1984) 1; see also: RICCI R. A., "Electrostatic Accelerators in the development of nuclear physics in Italy" *Nucl. Intstrum Methods Phys. Res. A*, **328** (1993) 355.

[42] RICCI R. A. in *Proceedings of the International Conference on Nuclear Physics*, Florence 1983, edited by BLASI P. and RICCI R. A., Vol. **2** (Editrice Compositori, Bologna) 1983, pp. 45–60, for a more general presentation of the nuclear physics problems at the time, see BROMLEY D. A., the same volume, pp. 3–44.

[43] JEAN M. and RICCI R. A. (Editors), *Proceedings of the International School of Physics "Enrico Fermi", Course XL* (Academic Press, New York, London) 1969.

[44] FARAGGI H. and RICCI R. A. (Editors), *Proceedings of the International School of Physics "Enrico Fermi", Course LXII* (North Holland, Amsterdam) 1976.

[45] Concerning the evolution of the gamma-spectrometry at LNL, see RICCI R. A. in ref. [15]; for the specific installations (the GASP. EUROBALL, AGATA, GALILEO gamma arrays) and experiments, see ROSSI-ALVAREZ C., *Nucl. Physics News Europa*, **3** (1993) 10; LUNARDI S. *et al.*, *Phys. Rev. Lett.*, **72** (1994) 1427: VIESTI G. *et al.*, *Phys. Lett. B*, **382** (2012) 24 and references quoted herein; FARNEA P. and BAZZACCO D., *Nucl. Phys.*, **22** (2012) 27; see also FORNAL B. in ref. [31]; and LENZI S. M., this issue; for the recent results on $1f_{7/2}$ nuclei see also: LENZI S. M. *et al.*, *Nuovo Cimento A*, **6-7** (1998) 739; MODAMIO V. *et al.*, *Phys. Rev. C*, **88** (2013) 044326; GADE A. *et al.*, *Phys. Rev. Lett.*, **112** (2014) 112503; BRAUNROTH T. *et al.*, *Phys. Rev. C*, **92** (2015) 034306. For the new advanced facilities at the LNL (SPES and gamma arrays) see, *e.g.*, DEANGELIS G. and FIORENTINI G., *Phys. Scripta*, **91** (2016) 113001.

[46] FESBACH H., in *Heavy Ion Physics and Nuclear Physics* edited by SALVADORI L. and VILLI C. (North-Holland, Amsterdam) 1983, p. 423c; see also RICCI R. A. in *Hadronic Physics at Intermediate Energy* edited by BRESSANI T. and RICCI R. A. (Elsevier Science Publ.) 1986, p. 235.

[47] See for instance: GREGOIRE C., NGO C. and TOMASI E., *Nucl. Phys. A*, **387** (1982) 37e; SWIATECKI W. J., *Phys. Rev.*, **24** (1981) 113. For a more general explanation see RICCI R. A. "Dissipative Phenomena and Fragmentation in Low-Energy Heavy-Ion Reactions of Medium-Mass Region", in *Proceedings of the International School of Physics "Enrico Fermi", Course CIII*, edited by KIENLE P., RICCI R. A. and RUBBINO A. (North-Holland, Amsterdam) 1989, pp. 585–600.

[48] For LNL see: IORI I., GENTILI M., MASSA I., VANNINI G., BOCCACCIO P., REFFO F. and RICCI R. A., *Phys. Lett. B*, **132** (1983) 304; AGNOLI S., MASSA I., VANNINI G., BOCCACCIO P., REFFO F., VANNUCCI L., IORI I. and RICCI R. A., *Nucl. Phys. A*, **464** (1987) 103; for Strasbourg Tandem Facility see: COFFIN J. P., GUILLAUME G., FAHLI A., RAMI F., HEUTSCH B., WAGNER P., ENGELSTEIN P., FINTZ P. and CINDRO N., *Phys. Rev. C*, **30** (1984) 539 and references quoted herein.

[49] For deep inelastic (^{32}S + ^{58}Ni): FORNAL B., GRAMEGNA F., MICZINSKI W., PRETE G., RICCI R. A., VIESTI G., D'ERASMO G., FIORE L., GUARINO G., PANTALEO A., IORI I., MORONI A., BLASI P., LUCARELLI F., *Z. Phys. A*, **328** (1987) 227; and (^{32}S + ^{100}Mo): GRAMEGNA F., PAVANATI M., PRETE G., RICCI R. A., VIESTI G., IORI I., LI ZU YU, MORONI A., D'ERASMO G., FIORE L. and PANTALEO A., *Nuovo Cimento A*, **79** (1984) 373.

[50] For fusion-fission and fusion-evaporation (^{28}Si+^{28}Si): FUSCHINI E., MALAGUTI F., OSTUNI S., VERONDINI E., VANNINI G., BRACCO A., IORI I., MORONI A., FIORETTO E., RICCI

R. A., Boccaccio P., Vannucci L., D'Arrigo A., Giardina G. and Taccone A., *Phys. Rev. C*, **46** (1992) R27. See also for the measurement of time scale in heavy-ion reactions with the crystal-blocking technique: Fuschini E., Malaguti F., Fioretto E., Ricci R. A., Vannucci L., D'Arrigo A., Giardina G., Taccone A., Moroni A., Eremin N., Yuminov O. and Vannini G., *Phys. Rev. C*, **50** (1994) 1965.

[51] Bromley D. A., Kuchner J. A. and Almquist E., *Phys. Rev. Lett.*, **4** (1960) 365.

[52] First evidence found at the LNL-Tandem ($^{32}S + {}^{24}Mg$): Abbondanno U., Demanins F., Boccaccio P., Vannucci L., Ricci R. A., Vannini G. and Cindro N., *Nuovo Cimento A*, **97** (1987) 205 and references quoted herein; more details for elastic and inelastic scattering of $^{58}Ni + {}^{58}Ni$ and $^{58}Ni + {}^{62}Ni$ can be found in Vannucci L., Abbondanno U., Bettiolo M., Bruno M., Cindro N., D'Agostino M., Milazzo P. M., Ricci R. A., Ritz T., Scheid W. and Vannini G., *Z. Phys. A*, **335** (1996) 41, and references quoted herein. About the possible interpretations of the quasi-molecular resonances see: Abbondanno U., Cindro N. and Milazzo P. M., *Nuovo Cimento A*, **110** (1997) 955; for Statistical Analysis see: Vannucci L. Abbondanno U., Bologna A., Bruno M., Cindro N., D'Agostino M., Milazzo P. M., Ricci R. A., Scheid W. and Vannini G., *Heavy Ion Phys.*, **11** (2000) 319.

[53] See: Bendiscioli G., Boccaccio P. *et al.*, *LNL/INFN Annual Report* 1990; see also Cagliari-Padova-Torino Collaboration (Agnello M. *et al.*), *Europhys. Lett.*, **7** (1988) 13.

[54] Obelix Collaboration, *Nucl. Phys. A*, **558** (1993) 369c; *Phys. Lett. B*, **337** (1994) 226: *Nucl. Phys. A*, **594** (1995) 375, *Phys. Atom. Nucl.*, **59** (1996) 1455; *Phys. Lett. B*, **475** (2000) 378 and references quoted herein.

[55] See, WA97 Collaboration, *Phys. Lett. B*, **449** (1999) 401; *J. Phys. G*, **25** (1999) 171; Na57 Collaboration, *J. Phys. G*, **25** (1999) 473.

[56] See, ALICE Collaboration, ALICE technical Design Report, *CERN–LHCC-99-32* (1999); see also: Ricci R. A. and Vannucci L., for the ALICE Collaboration, *LNL/INFN Annual Rport* 2011.

[57] Alice Collaboration, *Nat. Phys.*, **11** (2015) 811; see also: Dainese A. and Ricci R. A., for the ALICE Collaboration *LNL/INFN Annual Report* 2016.

[58] See, Alice Collaboration, *Nat. Phys.*, **13** (2017) 535; and *CERN ArXiv*, **1709**, 08522 v1 (nucl.exp).

[59] See, for instance, Ricci R. A., in *Hadronic Physics at intermediate energy*, edited by Bressani T. and Ricci R. A. (Elsevier Science Publishing) 1986, and in *Common Problems and Ideas of Modern Physics*, edited by Bressani T., Minetti B. and Zenoni A. (World Scientific Publishing Co.) 1992, p. 191. See also Ricci R. A. *Nuclear Physics at the Fermi's time and Today* in *Proceedings of the Symposium dedicated to Enrico Fermi on the occasion of he 50th anniversary of the first Reactor* (Accademia dei Lincei, Roma) 1992, pp. 55–69.

[60] See: Ricci R. A., "Fisica Nucleare", in *Enciclopedia delle Scienze Fische*, Vol. **II** (Istituto dell'Enciclopedia Italiana) 1993, pp. 612-621; and "Radioattività", pp. 693-701. It is also worth mentioning here: Focardi S. and Ricci R. A., "The beta-decay and the Fundamental Properties of Weak Interactions", *Riv. Nuovo Cimento*, **6**, N. 11 (1983) (as quoted by Iachello F., this volume, p. 31); Ricci R. A., "Nuclear Physics at the Fermi's time and today", Accademia dei Lincei, Atti Convegni 104, Roma, 1993, pp. 55–69; Ricci R. A., "The Italian study Project for ICF (Inertial Confinement Fusion) driven by Heavy ion beams", in *Particle Accelerators*, **17** (1992) 31; Ricci R. A., "Energia Nucleare. Prospettive della Fusione termonuclneare controllata", in *Raccontare la Fisica* (CLUEB University, Bologna) 1992, pp. 27–59; Ricci R. A., "The nuclear energy problem and its scientific information", *Proc. Accad. Lincei*, **163** (2000) 105.

International School of Physics "Enrico Fermi"

Villa Monastero, Varenna

Course 201

14 – 19 July 2017

Nuclear Physics with Stable and Radioactive Ion Beams

Directors

Fabiana Gramegna
INFN Laboratori Nazionali di Legnaro
Viale dell'Università 2
35020 Legnaro (PD)
Italy
tel: 0039 0498068442
gramegna@lnl.infn.it

Andrea Vitturi
Dipartimento di Fisica "Galileo Galilei"
Università di Padova
Via Marzolo 8
35131 Padova
Italy
tel: 0039 0498277194
andrea.vitturi@unipd.it

Piet Van Duppen
Instituut voor Kern- en Stralingsfysica
Departement Natuurkunde
en Sterrenkunde
University of Leuven
Celestijnenlaan 200 D
3001 Leuven
Belgium
tel: 0032 16327272
Piet.VanDuppen@kuleuven.be

Scientific Secretary

Sara Pirrone
INFN Sezione di Catania
Via S. Sofia 64
95123 Catania
Italy
tel: 0039 0955425394
sara.pirrone@ct.infn.it

Lecturers

Giovanna Benzoni
Dipartimento di Fisica
Università di Milano e INFN
Via Celoria 16
20133 Milano
Italy
tel: 0039 0250317217
giovanna.benzoni@mi.infn.it

Gianluca Colò
Dipartimento di Fisica
Università di Milano e INFN
Via Celoria 16
20133 Milano
Italy
tel: 0039 0250317241
colo@mi.infn.it

Francesco Iachello
Department of Physics
Yale University
217 Prospect Street
P.O. Box 208120
New Haven, CT 06520-8120
USA
tel: 001 2034326944
francesco.iachello@yale.edu

Yoshiko Kanada-En'yo
Department of Physics
Kyoto University
Yoshida-honmachi
Sakyo-ku, Kyoto 606-8501
Japan
tel: 0081 757537531
yenyo@ruby.scphys.kyoto-u.ac.jp

Wolfram Korten
CEA Saclay
DRF/IRFU/SPhN
Gif-sur-Yvette
91191 Cedex
France
tel: 0033 169087584
wolfram.korten@cea.fr

Antonio Moro
Departamento de Física Atómica,
Molecular y Nuclear
Universidad de Sevilla
Apdo. 1065
41080 Sevilla
Spain
tel: 0034 954552890
moro@us.es

Wilfried Nörtershäuser
Technische Universität Darmstadt
Institut für Kernphysik
Gebäude: S2—14
Raum: 410
Schlossgartenstrasse 9
64289 Darmstadt
Germany
tel: 0049 61511623575
wnoertershaeuser@ikp.tu-darmstadt.de

Takaharu Otsuka
University of Tokyo
7-3-1 Hongo, Bunkyo-ku
Tokyo 113-0033
Japan
tel: 0081 484644195
otsuka@phys.s.u-tokyo.ac.jp

Riccardo Raabe
Institute for Nuclear and Radiation
Physics
University of Leuven
Celestijnenlaan 200d
Box 2418
3001 Leuven
Belgium
tel: 0032 16327273
riccardo.raabe@kuleuven.be

Seminar Speakers

Angela Bracco
Dipartimento di Fisica
Università di Milano e INFN
Via Celoria 16
20133 Milano
Italy
tel: 0039 0250317252
Angela.Bracco@mi.infn.it

Giovanni La Rana
Dipartimento di Fisica "Ettore Pancini"
Università di Napoli "Federico II" e INFN
Via Cintia
Complesso Monte S. Angelo
80126 Napoli
Italy
tel: 0039 0817682426
larana@na.infn.it
giovanni.larana@unina.it

Silvia Lenzi
Dipartimento di Fisica "Galileo Galilei"
Università di Padova
Via Marzolo 8
35131 Padova
Italy
silvia.lenzi@pd.infn.it

Luciano Moretto
Lawrence Berkeley National Laboratory
Department of Chemistry
University of California
419 Latimer Hall
Berkley, CA 94720-1460
USA
tel: 001 5106425882
lgmoretto@lbl.gov

Angelo Pagano
INFN Sezione di Catania
Via Santa Sofia 64
95123 Catania
Italy
tel: 0039 0953785348
angelo.pagano@ct.infn.it

Renato Angelo Ricci
Università Padova e INFN
Laboratori Nazionali di Legnaro
Viale dell'Università 2
35020 Legnaro (PD)
Italy
tel: 0039 3479831150
Renato.A.Ricci@lnl.infn.it

Students

Vira Bondar	University of Leuven, Belguim
Alberto Camaiani	Università di Firenze, Italy
Salvatore Calabrese	Università di Catania, Italy
Magda Cicerchia	Università di Padova, Italy
Petra Colovic	Ruder Boskovic Institute, Croatia
Brunilde Gnoffo	Università di Catania, Italy
Diego Gruyer	Università di Firenze, Italy
Kushal Kapoor	Panjab University, India
Asli Kusoglu	ELI Nuclear Physics, Romania
Giorgia Mantovani	Università di Ferrara, Italy
Nunzia Martorana	INFN Laboratori Nazionali del Sud, Italy
Pietro Ottanelli	INFN Sezione di Firenze, Italy
Giuseppe Pastore	Università di Firenze, Italy
Simone Perrotta	INFN Laboratori Nazionali del Sud, Italy
Denise Piatti	Università di Padova, Italy
Federico Pinna	Politecnico di Torino, Italy
Oleksii Poleshchuk	Instituut voor Kern- en Stralingsfysica, Belgium
Marek Stryjczyk	University of Leuven, Belguim
Silvia Vignals i Onses	Istituto de Estructura de la Materia, Spain
Jiecheng Yang	University of Leuven, Belguim

Observers

Elena Santopinto	INFN Sezione di Genova, Italy
Korneliya Yordanova Spasova	Institute for Nuclear Research and Nuclear Energy, Bulgaria

Finito di stampare
nel mese di Aprile 2019

This page intentionally left blank